# A STUDY ON THE MECHANISM OF STRESS CORROSION CRACKING OF DUPLEX STAINLESS STEELS IN HOT ALKALINE-SULFIDE SOLUTION

A Dissertation
Presented to
The Academic Faculty

By

Kevin Robert Chasse

In Partial Fulfillment
Of the Requirements for the Degree
Doctor of Philosophy in Materials Science and Engineering

Georgia Institute of Technology
December 2011

# A STUDY ON THE MECHANISM OF STRESS CORROSION CRACKING OF DUPLEX STAINLESS STEELS IN HOT ALKALINE-SULFIDE SOLUTION

Approved by:


Dr. Preet M. Singh, Advisor
School of Materials Science and Engineering
*Georgia Institute of Technology*

Dr. Arun M. Gokhale
School of Materials Science and Engineering
*Georgia Institute of Technology*

Dr. W. Brent Carter
School of Materials Science and Engineering
*Georgia Institute of Technology*

Dr. Naresh N. Thadhani
School of Materials Science and Engineering
*Georgia Institute of Technology*

Dr. Thomas F. Fuller
School of Chemical and Biomolecular Engineering
*Georgia Institute of Technology*


Date Approved: September 8 , 2011

# ACKNOWLEDGEMENTS

Life is a continuous adventure that brings new understanding and meaning with every experience. The past few years of life have been incredibly rewarding both personally and professionally, and the assistance I received along the way was nothing less than remarkable. I would especially like to thank my advisor Dr. Preet M. Singh who taught me that being an effective researcher requires open-mindedness, patience, and perspective. His guidance and encouragement gave me momentum throughout this learning process. My fellow researchers in the Corrosion and Materials Research Laboratory, in particular Jamshad Mahmood, were very helpful and made every day pleasurable. I would also like to thank my committee members, Dr. Naresh Thadhani, Dr. W. Brent Carter, Dr. Tom Fuller, and Dr. Arun Gokhale for challenging me to consider the fundamental as well practical implications of this research. Funding for this project was provided by the PSE Foundation Fellowship Program at the Institute of Paper Science and Technology and the State of Georgia – TIP3 Program. I would like to thank my colleagues in Helsinki, Finland for their insight on different aspects of this project, in particular: Heikki Leinonen, Dr. Hannu Hänninen, Dr. Petri Kinnunen, Dr. Timo Saario, Jyrki Romu, Timo Kiesi, and Tapio Saukkonen. Financial support while I was a visiting researcher at VTT Technical Research Centre of Finland and Aalto University was provided by the International Center for Materials Research fellowship through the National Science Foundation. I never would have challenged myself to such an extent or received as much fulfillment doing it if it were not for the love and support of my wife Kate and our family members. Finally, I would like to thank our animals, Isabel and Molybdenum, who made me smile and laugh on some of the more demanding days.

# TABLE OF CONTENTS

ACKNOWLEDEMENTS iii

LIST OF TABLES xii

LIST OF FIGURES xiv

**CHAPTER 1: INTRODUCTION 1**

1.1 Motivation 1

1.2 Research Objectives and Technical Approach 8

1.3 Organization of Dissertation 10

1.4 REFERENCES 11

**CHAPTER 2: BACKGROUND 17**

2.1 Introduction 17

2.2 Duplex Stainless Steels 17

2.2.1 Effect of Composition 17

2.2.2 Influence of Microstructure 21

2.2.3 Mechanical Behavior of Individual Phases 23

2.3 Stress Corrosion Cracking 26

2.3.1 General Definition 26

2.3.2 Existing Models for SCC 30

2.3.2.1 Anodic Dissolution Models 31

2.3.2.2 Mechanical Fracture Models 33

2.3.2.2.1 Film-induced Cleavage 34

2.3.2.2.2 Hydrogen Embrittlement 35

2.3.2.2.3 Other Mechanical Models 38

2.4 Effect of Environment on SCC of DSS 39

2.4.1 Effect of Potential and Solution pH 39

2.4.2 Effect of Ionic Species on Corrosion and SCC 41

2.5 Summary 46

2.6 REFERENCES 47

**CHAPTER 3: EXPERIMENTAL PROCEDURE 57**

3.1 Introduction 57

3.2 Microstructural Characterization of the As-Received DSS Materials 57

3.2.1 Metallography 57

3.2.2. Phase Distribution and Ratio 58

3.2.3 Composition of the Austenite and Ferrite Phases 61

3.2.4 Hardness of Austenite and Ferrite Phases 62

3.3 Tests to Evaluate the Effect of Alloy Composition and Environment on the General Corrosion Behavior of Stainless Steels 62

3.3.1 Materials 62

3.3.2 Test Environments 63

3.3.3 Coupon Exposure Tests for Corrosion Susceptibility 65

3.4 Electrochemical Tests and Film Characterization to Evaluate Selective Dissolution of DSS 67

3.4.1. Potentiodynamic Polarization Scans 68

3.4.2. Film Properties at the Open Circuit Potential 70

3.4.2.1 Physicoelectrical Behavior of Surface Films 70

3.4.2.2 Surface Film Composition 72

3.4.2.2.1 Cross-Sectioned Film Characterization with Scanning Electron Microscope 72

3.4.2.2. Surface Film Characterization with X-ray Photoelectron Spectroscopy 72

3.5 Slow Strain Rate Tests for SCC Susceptibility 73

3.6 Mechanical Properties of Anisotropic Microstructure 77

3.6.1 Residual Stress Measurements 77

3.6.2 Hardness of Austenite and Ferrite Phases 79

3.7 Cathodic Polarization Study to Evaluate Hydrogen Embrittlement 79

3.7.1 Electrochemical Study of Hydrogen Behavior 80

3.7.1.1 Potentiodynamic Behavior 80

3.7.1.2 Diffusion Studies 80

3.7.1.3 Hydrogen Microprinting 82

3.7.2 Mechanical Behavior during Cathodic Polarization 83

3.7.2.1 Effect on Hydrogen Absorption on Hardness 83

3.7.2.2 Slow Strain Rate Test to Evaluate Hydrogen Embrittlement 84

3.8 Summary 84

3.9 REFERENCES 85

**CHAPTER 4: CORROSION AND ELECTROCHEMICAL BEHAVIOR OF DUPLEX STAINLESS STEELS IN HOT ALKALINE ENVIRONMENTS 87**

4.1. Introduction 87

4.2 Corrosion Behavior in Alkaline Environments 88

4.2.1 Corrosion Rates 88

4.2.2 Forms of Corrosion 90

4.3 Electrochemical Behavior 94

4.3.1 Effect of Alloy Composition and Temperature 94

4.3.1.1 Behavior of Pure Elements at 90 $^{o}$C and 170 $^{o}$C 94

4.3.1.1 Behavior of Alloys at 90 $^{o}$C and 170 $^{o}$C 104

4.3.2 Effect of Alkalinity 109

4.4 Passive Film Behavior 111

4.4.1 Role of Temperature on Physicoelectrical Behavior 112

4.4.1.1 Behavior of Alloying Elements 112

4.4.1.1 Behavior of Alloys 125

4.4.2 Film Morphology and Composition 142

4.5 Conclusions 156

4.6 REFERENCES 159

**CHAPTER 5: INFLUENCE OF SULFIDE AND CHLORIDE ON CORROSION OF DUPLEX STAINLESS STEELS IN HOT ALKALINE ENVIRONMENTS 162**

5.1. Introduction 162

5.2. Effect of Sulfide 163

5.2.1 Influence of Environment on Corrosion Rates and Morphology 163

5.2.2 Effect of Sulfide on Electrochemical Behavior 174

5.5.5.1 Anodic Polarization of Individual Alloying Elements 174

5.5.5.1 Anodic Polarization of Stainless Steel Alloys 180

5.2.3 Role of Sulfide on Surface Film Formation 185

5.2.3.1 Electrochemical Impedance Spectroscopic Measurements 185

5.2.3.2 Film Composition 197

5.3 Effect of Chloride 214

5.3.1 Role of Chloride in NaOH Environments 215

5.3.1.1 Influence on Electrochemical Behavior 215

5.3.1.3 Film Morphology and Composition in Chloride-Containing NaOH Solution 217

5.3.2 Role of Chloride in NaOH + $Na_2S$ Environment 223

5.3.2.1 Influence on Corrosion Rates and Morphology 224

5.3.2.2 Surface Film Properties 230

5.3.2.2.1 Electrochemical Impedance Spectroscopic Measurements 230

5.3.2.2.2 Surface Film Composition 235

5.4 Conclusions 242

5.5 REFERENCES 246

**CHAPTER 6: EFFECT OF SULFIDE AND CHLORIDE ON STRESS CORROSION CRACKING OF DUPLEX STAINLESS STEELS IN HOT ALKALINE ENVIRONMENTS 252**

6.1. Introduction 251

6.2 Effect of Alkalinity 252

6.2.1 Stress Corrosion Cracking Susceptibility of DSS in Caustic Solutions 252

6.2.2 Crack and Fracture Surface Morphology 257

6.3 Effect of Sulfide 274

6.3.1 Stress Corrosion Cracking Susceptibility of DSS in Sulfide-Containing Caustic Solutions 274

6.3.2 Crack and Fracture Surface Morphology 277

6.4 Effect of Chloride 290

6.4.1. NaOH + NaCl Environments 290

6.4.1.1 Stress Corrosion Cracking Susceptibility of DSS in Chloride-Containing Caustic Solutions 290

6.4.1.2 Crack and Fracture Surface Morphology 292

6.4.2. NaOH + $Na_2S$ + NaCl Environments 299

6.4.2.1 Stress Corrosion Cracking Susceptibility of DSS in Chloride- and Sulfide-Containing Caustic Solutions 299

6.4.1.2 Crack and Fracture Surface Morphology 306

6.5 Conclusions 322

6.6 REFERENCES 324

**CHAPTER 7: ROLE OF ANISOTROPIC MICROSTRUCTURE ON SCC BEHAVIOR OF DUPLEX STAINLESS STEELS IN HOT ALKALINE ENVIRONMENTS 330**

7.1 Introduction 328

7.2 Anisotropy in Mechanical Properties 330

7.2.1 Effect of Large Plastic Deformation 330

7.3.2 Effect of Annealing and Quenching 339

7.3 Stress Corrosion Cracking Behavior 343

7.3.1 Slow Strain Rate Testing in Chloride- and Sulfide-Containing Caustic Solution to Determine Anisotropic Effects in Microstructure on Fracture Features 343

7.3.2 Crack Statistics 345

7.4 Conclusions 351

7.5 REFERENCES 352

**CHAPTER 8: HYDROGEN EMBRITTLEMENT OF UNS S32205 DUPLEX STAINLESS STEEL IN ALKALINE-SULFIDE SOLUTION 358**

8.1 Introduction 356

8.2 Electrochemical Conditions Required for Hydrogen Embrittlement 357

8.2.1 Effect of Sulfide on Cathodic Polarization 357

8.2.2 Effect of Cathodic Polarization on Hydrogen Diffusion 358

8.3 Effect on Mechanical Behavior 363

8.3.1 Influence of Hydrogen Absorption on Microhardness 363

8.3.2 Effect of Cathodic Polarization on Slow Strain Rate Testing 364

8.4 Conclusions 379

8.5 REFERENCES 380

**CHAPTER 9: PROPOSED MECHANISM FOR STRESS CORROSION CRACKING OF DUPLEX STAINLESS STEELS IN HOT ALKALINE SULFIDE SOLUTION 385**

9.1 Introduction 383

9.2 Summary of Results 390

9.3 Proposed Mechanism 392

9.3.1 Crack Initiation 390

9.3.2 Crack Propagation 396

9.4 Conclusions 403

9.5 REFERENCES 403

**CHAPTER 10: CONCLUSIONS 406**

10.1 Practical Implications 406

10.1.1 Process Optimization Considerations 406

10.1.2 Material Considerations 407

10.2 Suggestions for Future Work 408

10.2.1 Crack Tip Chemistry and Morphology 408

10.2.2 Electrochemical Behavior 409

10.2.3 Fracture Mechanics Approach 409

**APPENDIX A: MATERIAL CERTIFICATION SHEETS 411**

**APPENDIX B: PROCEDURE FOR REFEENCE ELECTRODE 417**

**APPENDIX C: MECHANICAL TEST RESULTS AND SAMPLE DIMENSIONS FROM VTT TECHNICAL RESEARCH CENTRE OF FINLAND 421**

**VITA 426**

# LIST OF TABLES

Table 2.1 Nominal chemical composition (wt %) and pitting resistance equivalent numbers (PREN) of select grades of DSS ..... 19

Table 3.1: Quantitative stereology parameters for the austenite phase (light etching phase) of as-received materials evaluated in this study ..... 60

Table 3.2: Quantitative stereology parameters for the austenite phase (light etching phase) of as-received materials evaluated in this study ..... 61

Table 3.3: Vickers microhardness ($HV_{25}$) of as-received DSS S32205 and S32101..... 62

Table 3.4: Nominal chemical compositions of materials in this study (wt. %) ..... 63

Table 3.5: Compositions and of test solutions used in static exposure tests (per liter).. 65

Table 3.6: Compositions and of test solutions used in SCC (strained) specimen tests (per liter). ..... 75

Table 4.1: Summary of electrochemical parameters for elements tested in 2.5 M NaOH at 90 $^{o}$C and 170 $^{o}$C based on Tafel extraction.....98

Table 4.2: Summary of electrochemical parameters for alloys tested in 2.5 M NaOH at 90 $^{o}$C and 170 $^{o}$C based on Tafel extraction.....108

Table 5.1: Anodic polarization parameters of Fe, Cr, Ni, Mo, and Mn tested in alkaline (A) and alkaline-sulfide (AS) solution at 90 $^{O}$C determined from Tafel extraction..... 176

Table 5.2: Anodic polarization parameters of S31603, S44660, S32101, and S32205 tested in alkaline-sulfide solution at 90 $^{O}$C and 170 $^{O}$C determined from Tafel extraction. Pt is shown for comparison. ..... 185

Table 5.3: Binding Energies (BE) of the Different Chemical States for Fe(2p3/2), Cr(2p3/2), Ni(2p3/2), and O(1s) Photoelectron Spectra of Control Samples (this study).....200

Table 5.4: Binding Energies (BE) of the Different Chemical States for Fe(2p3/2), Cr(2p3/2), Ni(2p3/2), and O(1s) Photoelectron Spectra for References on Various Model Compounds.....201

Table 5.5: Solubility Products for the Dominant Species the Fe-Cr-Ni ternary System at 170 $^{O}$C. ..... 213

Table 5.6: Anodic polarization parameters of alloys (S31603, S44660, S32101, S32205, S32304) and their alloying elements (Fe, Cr, Ni, Mo, Mn) tested in alkaline (A) and alkaline chloride (AC) solution at 90 $^{O}$C determined from Tafel extraction..... 217

Table 6.1: SCC data for S32205 and S32101 tested in alkaline environments at 170 $^{o}$C.. ..... 255

Table 6.2: SCC data for S32205 and S32101 tested in alkaline-sulfide environments at 170 $^{O}$C. S44660 and S44627 were tested for comparison using U-bend specimens. ..... 276

Table 6.3: SCC data for S32205 and S32101 tested in alkaline chloride environments at 170 $^{O}$C. ..... 292

Table 6.4: SCC data for S32205 and S32101 tested in alkaline-sulfide environments with and without 0.17 M NaCl at 170 $^{O}$C. ..... 301

Table 6.5: SCC data for S32205 and S32101 tested in alkaline-sulfide solution (3.75 M NaOH + 0.64 M $Na_2S$) with various amounts of NaCl at 170 $^{O}$C. ..... 304

Table 7.1: Macroscopic mechanical properties for rolling direction (RD) and transverse direction (TD) of standard DSS S32205 tested by VTT Technical Research Centre of Finland. ..... 333

Table 7.2: Microhardness values ($HV_{25}$) of austenite and ferrite phase in rolling direction (RD) of as-received annealed and 20 % cold worked standard DSS S32205 ..... 334

Table 7.3: Residual microstresses of austenite and ferrite for different orientations (scattering vector is parallel to RD for $\psi$ = 0 degrees) of annealed and 20 % cold rolled standard DSS S32205. ..... 338

Table 7.4: Quantitative stereology parameters for the austenite phase (light etching phase) of as-received and annealed standard DSS S32205 materials evaluated in this study..... 342

Table 7.5: Vickers microhardness ($HV_{25}$) of as-received and annealed DSS S32205. 342

# LIST OF FIGURES

Figure 1.1: Micrograph showing SCC in a corroded section from a 2205 DSS hot black liquor tank that failed in service due to chloride contamination [3]. ..... 1

Figure 1.2: Continuous digester (left) and batch digesters (right) used in the kraft pulping process to extract lignin from cellulose. ..... 3

Figure 1.3: Banded microstructure of standard grade DSS S32205 in (a) rolling longitudinal and (b) short transverse orientation. Austenite (light etching) phase is distributed in a ferrite (dark etching phase) matrix. ..... 6

Figure 2.1: Schaffler diagram used to determine the composition of DSS that will result in a balanced microstructure [1]. ..... 18

Figure 2.2: Schematic of different sections of a (a) continuous digester and (b) batch digester used in the kraft pulping process. ..... 20

Figure 2.3: Isothermal cooling curve for the ternary Fe-Cr-Ni system showing possible precipitates that can form upon cooling [2]. ..... 22

Figure 2.4: Schematic showing the interdependence of environmental, metallurgical, and stress conditions required for stress corrosion cracking [3]..... 27

Figure 2.5: Schematic of (a) intergranular stress corrosion cracking and (b) transgranular stress corrosion cracking. ..... 27

Figure 2.6: Schematic anodic polarization curve showing zones of susceptibility to stress corrosion cracking [46]. ..... 28

Figure 2.7: Schematic showing variation of crack growth rate (a) with stress intensity factor during a stress corrosion cracking test and (b) per stress cycle during a corrosion fatigue test [3]. ..... 30

Figure 2.8: Schematic showing the film rupture model for stress corrosion cracking. (a) Slip is initiated at film-metal interface, (b) dissolution facilitates crack initiation, and (c) crack grows through discontinuous film growth and rupture [78]. ..... 32

Figure 2.9: Schematic showing the slip dissolution model for stress corrosion cracking [73]. ..... 32

Figure 2.10: Schematic showing the film-induced cleavage model for stress corrosion cracking. ..... 34

Figure 2.11: Schematic showing the hydrogen embrittlement model for stress corrosion cracking. ..... 36

Figure 2.12: E-pH diagram for the dominant Fe species in the Fe-Cr-Ni system at 25 $^{o}$C [106]. ..... 41

Figure 2.13: Stress corrosion cracks in lean grade DSS S32101 sample tested in simulated white liquor at 170 $^{o}$C. Crack propagation occurs in austenitic phase (γ) [31]. ..... 42

Figure 2.14: Fractography showing crack initiation sites in the austenite phase (γ) in S32205 welded specimen tested in simulated white liquor at 200 $^{o}$C [31]. ..... 43

Figure 2.15: Micrograph showing cracks in the ferrite phase (α) of DSS S32205 tested in 26 wt% NaCl solution [100]. ..... 44

Figure 3.1: Microstructure for different orientations of as-received (a) standard DSS S32205 and (b) lean DSS S32101 evaluated in this study. ..... 59

Figure 3.2: Micrograph showing a 14 x 14 grid overlaid on the RL orientation microstructure of as-received lean DSS S32101 evaluated in this study. Each block represents 20 μm. ..... 60

Figure 3.3: Experimental setup used for corrosion rate tests (weight loss) showing (left) samples isolated by PTFE washers on holder, and autoclave used for exposure. ..... 66

Figure 3.4: Experimental setup used for potentiodynamic scans at 90 $^{o}$C showing the working electrode holder, reference electrode, and counter electrode. ..... 69

Figure 3.5: Experimental setup used for potentiodynamic scans at 170 $^{o}$C showing the working electrode, reference electrode, and counter electrode. ..... 70

Figure 3.6: Typical DSS S32205 and S32101 specimen dimensions used in slow strain rate testing to assess SCC. ..... 74

Figure 3.7: Slow strain rate test setup with autoclave for high temperature SCC experiments. ..... 75

Figure 3.8: Modified slow strain rate test autoclave setup to accommodate corrosion potential monitoring during high temperature experiments. ..... 76

Figure 3.9: Modified ψ goniometer [4] used in residual stress measurements. The diffraction plane is marked with a squared pattern. The tilt axis T lies in the specimen surface and in the diffraction plane. The rotation vector ϕ was

varied between measurements. A value of $\phi = 0^o$ corresponded to the rolling direction. ..... 79

Figure 3.10: Summary of experimental approach used to understand corrosion and SCC mechanisms of DSS in alkaline-sulfide environments with respect to environment, alloy composition, and microstructure. ..... 85

Figure 4.1: Corrosion rates of austenitic (N08904, S31703, S31603, S30403), duplex (S32705, S32205, S32101, S32003), and superferritic grades (S44660, S44627) of stainless steel tested in 2.5 M, 3.13 M, and 3.75 M NaOH at 170 $^o$C. Austenitic, duplex, and superferritic types are arranged left to right by descending molybdenum content. ..... 89

Figure 4.2: SEM micrograph showing general corrosion on austenitic (S31603) and superferritic grades (S44660) of stainless steel tested in 3.75 M NaOH at 170 $^o$C. ..... 91

Figure 4.3: SEM micrograph showing general corrosion on lean DSS (S32101) and standard DSS grade (S32205) of stainless steel tested in 2.5 M NaOH at 170 $^o$C. ..... 92

Figure 4.4: Optical micrograph showing corrosion morphology on (a) super grade DSS (S32705), (b) lean grade DSS (S32101), and standard grade DSS (S32205) tested in 3.75 M NaOH at 170 $^o$C. ..... 93

Figure 4.5: Anodic polarization scans for pure elements (Fe, Cr, Ni, Mo, and Mn) tested in 2.5 M NaOH at 90 $^o$C. ..... 95

Figure 4.6: The E-pH diagram for the Mn-$H_2O$ system at 90 $^o$C [14]. ..... 96

Figure 4.7: Anodic polarization scans for pure elements (Fe, Cr, Ni, and Mo) tested in 2.5 M NaOH at 170 $^o$C. ..... 97

Figure 4.8: The E-pH diagram for the Fe-$H_2O$ system at 170 $^o$C [14]. ..... 100

Figure 4.9: The E-pH diagram for the Cr-$H_2O$ system at 170 $^o$C [14]. ..... 101

Figure 4.10: The E-pH diagram for the Ni-$H_2O$ system at 170 $^o$C [14]. ..... 102

Figure 4.11: The E-pH diagram for the Mo-$H_2O$ system at 170 $^o$C [14]. ..... 103

Figure 4.12: Anodic polarization scans for austenitic (S31603), superferritic (S44660),lean DSS (S32101 and S3204), and standard DSS (S32205) grades tested in 2.5 M NaOH at 90 $^o$C. ..... 105

Figure 4.13: Anodic polarization scans for lean DSS grade (S32101) and primary alloying elements (Fe, Cr, Ni, Mo, and Mn) tested in 2.5 M NaOH at 90 $^{o}$C. ..... 106

Figure 4.14: Anodic polarization scans for austenitic (S31603), superferritic (S44660), lean DSS (S32101 and S3204), and standard DSS (S32205) grades tested in 2.5 M NaOH at 170 $^{o}$C..... 107

Figure 4.15: Anodic polarization scans for lean DSS grade (S32101) and primary alloying elements (Fe, Cr, Ni, Mo, and Mn) tested in 2.5 M NaOH at 170 $^{o}$C. ..... 108

Figure 4.16: E-pH diagram for the Fe-Cr-Ni-$H_20$ system at 170 $^{o}$C [14]. ..... 109

Figure 4.17: Anodic polarization curves for lean grade DSS S32101 and standard grade DSS S32205 tested in 2.5 M NaOH and 12.5 M NaOH at 170 $^{o}$C..... 110

Figure 4.18: Corrosion rates based on Tafel extraction for lean grade DSS S32101 and standard grade DSS S32205 tested in 2.5 M NaOH and 12.5 M NaOH at 170 $^{o}$C. ..... 111

Figure 4.19: Comparison of polarization resistance values measured using linear polarization resistance and electrochemical impedance spectroscopy for alloying elements tested in 2.5 M NaOH at 170 $^{o}$C..... 113

Figure 4.20: Comparison of electrochemical impedance spectra for Fe tested in 2.5 M NaOH at 90 and 170 $^{o}$C. ..... 115

Figure 4.21: Electrochemical impedance spectra for Fe tested in 2.5 M NaOH at 90 $^{o}$C. Points – experimental points, lines – best fit results obtained from simulation.116best fitting parameters are: $R_s$ = 2.39 Ω cm$^2$, $R_1$ = 3240 Ω cm$^2$, $CPE_1$ = 156 μF cm$^{-2}$, $\alpha_1$ = 0.939, $R_2$ = 13.7 kΩ cm$^2$, $CPE_2$ = 1.11 mF cm$^{-2}$, and $\alpha_1$ =0.577. ($\chi^2$ = 6.27 e-4) ..... 116

Figure 4.22: Electrochemical impedance spectra for Fe tested in 2.5 M NaOH at 170 $^{o}$C. Points – experimental points, lines – best fit results obtained from 117simulation. The best fitting parameters are: $R_s$ = 2.11 Ω cm$^2$, $R_1$ = 763.8 Ω117$^2$, and $\alpha_1$ = 0.826. ($\chi^2$ = 4.14 e-4) ..... ..... 117

Figure 4.23: Equivalent circuit used to simulate the electrochemical behavior of Fe in 2.5 M NaOH at 90 and 170 $^{o}$C..... 118

Figure 4.24: Comparison of electrochemical impedance spectra for Cr tested in 2.5 M NaOH at 90 and 170 $^{o}$C. ..... 122

Figure 4.25: Comparison of electrochemical impedance spectra for Cr tested in 2.5 M NaOH at 90 and 170 $^{o}$C. ..... 123

Figure 4.26: Comparison of electrochemical impedance spectra for Mo tested in 2.5 M NaOH at 90 and 170 $^{o}$C. ..... 124

Figure 4.27: Electrochemical impedance spectra for S32205 tested in 2.5 M NaOH at 90 $^{o}$C. Points – experimental points, lines – best fit results obtained from simulation. The best fitting parameters are: $R_s$ = 1.94 Ω cm$^2$, $R_1$ = 1617 Ω cm$^2$, $CPE_1$ = 135.3 μF cm$^{-2}$, $\alpha_1$ = 0.927, $R_2$ = 9.29 kΩ cm$^2$, $CPE_2$ = 0.870 mF cm$^{-2}$, and $\alpha_1$ = 0.556. ($\chi^2$ = 5.38e-4) ..... 126

Figure 4.28: Electrochemical impedance spectra for S32201 tested in 2.5 M NaOH at 90 $^{o}$C. Points – experimental points, lines – best fit results obtained from 127simulation. The best fitting parameters are: $R_s$ = 2.32 Ω cm$^2$, $R_1$ = 44.0 Ω cm$^2$,127$CPE_1$ = 66.8 μF cm$^{-2}$, $\alpha_1$ = 0.909, $W_1$-R = 7989 Ω cm$^2$, $W_1$-T = 142 s, $W_1$-P = 0.530. ($\chi^2$ = 1.85e-3) ..... 127

Figure 4.29: Equivalent circuit used to simulate the electrochemical behavior of S32101 in 2.5 M NaOH at 90 $^{o}$C. ..... 128

Figure 4.30: Comparison of electrochemical impedance spectra for S32205 tested in 2.5 M NaOH at 90 and 170 $^{o}$C. Points – experimental points, lines – best fit results obtained from simulation. The best fitting parameters are: $R_s$ = 71.18 Ω cm$^2$, $R_1$ = 656 Ω cm$^2$, $CPE_1$ =95.6 μF cm$^{-2}$, $\alpha_1$ = 0.706, $R_2$ = 2.17 kΩ cm$^2$, $CPE_2$ = 1.31 mF cm$^{-2}$, and $\alpha_1$ = 0.932. ($\chi^2$ = 1.97e-3) ..... 130

Figure 4.31: Comparison of electrochemical impedance spectra for S32101 tested in 2.5 M NaOH at 90 and 170 $^{o}$C. Points – experimental points, lines – best fit results131 obtained from simulation. The best fitting parameters are: $R_s$ = 0.658 Ω cm$^2$,131$R_1$= 4270 Ω cm$^2$, $CPE_1$ = 10.6 mF cm$^{-2}$, $\alpha_1$ = 0.829, $W_1$-R = 2179 Ω cm$^2$, $W_1$-T131= 142 s, $W_1$-P = 0.736. ($\chi^2$ = 1.63e-3) ..... 131

Figure 4.32: Comparison of electrochemical impedance spectra after 24 h for austenitic (S31603), superferritic (S44660), and lean DSS (S32101), and standard DSS (S32205) grades tested in 2.5 M NaOH at 170 $^{o}$C. The Nyquist plots are shown on the left, and the Bode plots are shown on right. ..... 133

Figure 4.33: Linear polarization resistance values during 168 h exposure of austenitic (S31603 and S30403), superferritic (S44660 and S44627), and lean DSS (S32101), and standard DSS (S32205) grades tested in 2.5 M NaOH at 170 $^{o}$C. ..... 134

Figure 4.34: Comparison of electrochemical impedance spectra after 168 h for austenitic (S31603), superferritic (S44660), and lean DSS (S32101), and

standard DSS (S32205) grades tested in 2.5 M NaOH at 170 $^{o}$C. Points – experimental points, lines – best fit results obtained from simulation of S32205 results. The best fitting parameters for S32205 are: $R_s$ = 33.38 Ω cm$^2$, $R_1$ = 80.86 Ω cm$^2$, $CPE_1$ = 3.05 mF cm$^{-2}$, $\alpha_1$ = 0.764, $R_2$ = 180.9 kΩ cm$^2$, $CPE_2$ = 6.09 mF cm$^{-2}$, and $\alpha_1$ = 0.902. ($\chi^2$ = 3.05e-3)..... 136

Figure 4.35: Comparison of electrochemical impedance spectra for S32205 tested in 2.5 M or 12.5 M NaOH at 170 $^{o}$C. Points – experimental points, lines – best fit results obtained from simulation. The best fitting parameters are: $R_s$ = 2.46 Ω cm$^2$, $R_1$ = 7.14 Ω cm$^2$, $CPE_1$ = 266.1 mF cm$^{-2}$, $\alpha_1$ = 0.924, $R_1$ = 5.92 Ω cm$^2$ $W_1$-R = 214.5 Ω cm$^2$, $W_1$-T = 5697 s, $W_1$-P = 1. ($\chi^2$ = 8.95e-3) ..... 138

Figure 4.36: Equivalent circuit used to simulate the electrochemical behavior of S32205 in 12.5 M NaOH at 170 $^{o}$C. ..... 139

Figure 4.37: Comparison of electrochemical impedance spectra for S32101 tested in 2.5 M or 12.5 M NaOH at 170 $^{o}$C. Points – experimental points, lines – best fit results obtained from simulation. The best fitting parameters are: $R_s$ = 1.088 Ω cm$^2$, $R_1$ = 239.1 Ω cm$^2$, $CPE_1$ = 122.5 mF cm$^{-2}$, $\alpha_1$ = 0.818, $W_1$-R = 10.07 Ω cm$^2$, $W_1$-T = 77.2 s, $W_1$-P = 1. ($\chi^2$ = 1.31e-3) ..... 140

Figure 4.38: Linear polarization resistance values for 24 h exposure of lean DSS (S32101) and standard DSS (S32205) grades tested in 2.5 M and 12.5 M NaOH at 170 $^{o}$C. ..... 141

Figure 4.39: Cross-sectional SEM micrograph showing surface film on standard DSS S3220) tested in 2.5 M NaOH at 170 $^{o}$C. EDS from outer later and inner layer captured using an accelerating voltage of 15kV indicated by arrows. ..... 144

Figure 4.40: Cross-sectional SEM micrograph showing surface film on lean DSS S32101 tested in 2.5 M NaOH at 170 $^{o}$C. EDS from outer later an inner layer captured using an accelerating voltage of 15 kV indicated by arrows. ..... 145

Figure 4.41: X-ray photoelectron spectroscopy depth profile of surface film on standard DSS S32205 formed at corrosion potential in 2.5 M NaOH at 170 $^{o}$C. . 147

Figure 4.42: X-ray photoelectron spectroscopy depth profile of surface film on standard DSS S32101 formed at corrosion potential in 2.5 M NaOH at 170 $^{o}$C. . 148

Figure 4.43: High resolution X-ray photoelectron spectra from surface film formed on standard DSS S32205 formed at corrosion potential in 2.5 M NaOH at 170 $^{o}$C for (a) Fe 2p and (b) Cr 2p. Filled symbols represent the scan corresponding to the half maximum O 1s peak intensity (ca. 1920 nm). 149

Figure 4.43 (cont'd):High resolution X-ray photoelectron spectra from surface film formed on standard DSS S32205 formed at corrosion potential in 2.5 M NaOH at 170 $^{o}$C for (c) Ni 2p and (d) O 1s. Filled symbols represent the scan corresponding to the half maximum O 1s peak intensity (ca. 1920 nm). ..... 150

Figure 4.44: Peak fitting results for high resolution X-ray photoelectron spectra from surface film formed on standard DSS S32205 formed at corrosion potential in 2.5 M NaOH at 170 $^{o}$C for (a) Fe 2p and (b) Cr 2p. Curve fitting was performed at the half maximum O 1s peak intensity (ca. 1920 nm). ..... 152

Figure 4.44 (cont'd): Peak fitting results for high resolution X-ray photoelectron spectra from surface film formed on standard DSS S32205 formed at corrosion potential in 2.5 M NaOH at 170 $^{o}$C for (c) Ni 2p and (d) O 1s. Curve fitting was performed at the half maximum O 1s peak intensity (ca. 1920 nm). .... ..... 153

Figure 4.45: (a) High resolution X-ray photoelectron spectra from surface film formed on standard DSS S32205 formed at corrosion potential in 2.5 M NaOH at 170 $^{o}$C for Mo $3d_{5/2}$. (b) Peak fitting results for Mo $3d_{5/2}$. Curve fitting was performed at the half maximum O 1s peak intensity (ca. 1920 nm)..... 155

Figure 4.46: High resolution X-ray photoelectron spectra from surface film formed on standard DSS S32205 formed at corrosion potential in 2.5 M NaOH at 170 $^{o}$C for Mn 2p. ..... 156

Figure 5.1: Corrosion rates of austenitic (N08904, S31703, S31603, S30403) stainless steel tested in alkaline-sulfide and alkaline solutions at 170 $^{O}$C. Alloys have been arranged by left to right by decreasing Ni content within each type of stainless steel. ..... 164

Figure 5.1 (cont'd): Corrosion rates of (b) duplex (S32705, S32205, S32101, S32003, and (c) superferritic grades (S44660, S44627) of stainless steel tested in alkaline-sulfide and alkaline solutions at 170 $^{O}$C. Alloys have been arranged by left to right by decreasing Ni content within each type of stainless steel..... 165

Figure 5.2: SEM micrograph showing general corrosion on austenitic grades (a) S31603 and (b) S30403 tested in 3.75M NaOH + 0.64 M $Na_2S$ at 170 $^{O}$C. ..... 168

Figure 5.3: SEM micrographs showing (a) intergranular corrosion on superferritic grade S44660 and (b) negligible attack on superferritic grade S44627 tested in 3.75 M NaOH + 0.64 M $Na_2S$ at 170 $^{O}$C. ..... 169

Figure 5.4: SEM micrograph showing preferential corrosion on lean DSS (S32101) tested in solutions of (a) 35 % sulfidity (2.5M NaOH + 0.70 M $Na_2S$) and (b) 25 % sulfidity (150 g/l NaOH + 0.64 M $Na_2S$) at 170 $^{O}$C. ..... 170

Figure 5.5: SEM micrograph showing preferential corrosion on standard DSS (S32205) tested in solutions of (a) 35 % sulfidity (2.5M NaOH + 0.70 M $Na_2S$) and (b) 25 % sulfidity (150 g/l NaOH + 0.64 M $Na_2S$) at 170 $^{O}$C. ..... 171

Figure 5.6: Cross-sectional SEM micrographs showing relatively uniform corrosion on lean DSS (S32101) stainless steel tested in 35 % sulfidity solution (2.5M NaOH + 0.70 M $Na_2S$) at 170 $^{O}$C. ..... 172

Figure 5.7: Cross-sectional SEM micrograph of standard DSS S32205 exposed to 35 % sulfidity solution (2.5M NaOH + 0.70 M $Na_2S$) at 170 $^{O}$C. Arrows correspond to EDS spectra of Cr-rich region (ferrite) that was unoxidized and EDS spectra of S-rich, oxidized region. ..... 172

Figure 5.8: Anodic polarization curves for Fe, Cr, Ni, Mo, and Mn tested in 2.5M NaOH + 0.70 M $Na_2S$ at 90 $^{O}$C. ..... 175

Figure 5.9: Anodic polarization curves for Fe, Cr, Ni, Mo, and Mn tested in 2.5M NaOH + 0.70 M $Na_2S$ at 170 $^{O}$C. ..... 177

Figure 5.10: Anodic polarization curves for Pt tested in alkaline (2.5M NaOH) and alkaline-sulfide (2.5 M NaOH + 0.70 M $Na_2S$) solution at 170 $^{O}$C..... 178

Figure 5.11: E-pH diagram for the S- $H_20$ system at 170 $^{O}$C and 0.77 MPa. Molar concentration of sulfur is 0.70 M [49]. ..... 179

Figure 5.12: Anodic polarization curves for austenitic (S31603), superferritic (S44660), and DSS (S2205 and S32101) tested in alkaline-sulfide (2.5 M NaOH + 0.70 M $Na_2S$) solution at 90 $^{O}$C. ..... 182

Figure 5.13: Anodic polarization curves for austenitic (S31603), superferritic (S44660), and DSS (S32205 and S32101) tested in alkaline-sulfide (2.5 M NaOH + 0.70 M $Na_2S$) solution at 170 $^{O}$C. ..... 183

Figure 5.14: E-pH diagram for the Fe-Cr-Ni-S $H_20$ system (S dominant) at 170 $^{O}$C and 0.77 MPa [49]. Molar concentration of metal cations is 0.001 M and sulfur is 0.70 M. ..... 183

Figure 5.15: Comparison of electrochemical impedance spectra at the corrosion potential for Fe tested in 2.5 M NaOH and 2.5 M NaOH + 0.70 $Na_2S$ at 170 $^{O}$C..... 187

Figure 5.16: Comparison of electrochemical impedance spectra at the corrosion potential for Cr tested in 2.5 M NaOH and 2.5 M NaOH + 0.70 $Na_2S$ at 170 $^{O}$C..... 188

Figure 5.17: Comparison of electrochemical impedance spectra at the corrosion potential for Ni tested in 2.5 M NaOH and 2.5 M NaOH + 0.70 $Na_2S$ at 170 $^{O}$C..... 189

Figure 5.18: Comparison of electrochemical impedance spectra at the corrosion potential for Mo tested in 2.5 M NaOH and 2.5 M NaOH + 0.70 $Na_2S$ at 170 $^{O}$C. .. 190

Figure 5.19: Comparison of electrochemical impedance spectra at the corrosion potential for S31603, S44660, S32101, and S32205 tested in 2.5 M NaOH + 0.70 $Na_2S$ at 170 $^{O}$C. Points – experimental points, lines – best fit results obtained from simulation on S32101. The best fitting parameters are: $R_s$ = 21.58 Ω $cm^2$, $R_1$ = 368 Ω $cm^2$, $CPE_1$ =189.9 mF $cm^{-2}$, $\alpha_1$ = 0.855, $R_2$ = 375 Ω $cm^2$, $CPE_2$ = 957 mF $cm^{-2}$, and $\alpha_2$= 0.98. ($\chi^2$ = 8.94e-3) ..... 193

Figure 5.20: Electrochemical impedance spectra at the corrosion potential for S32205 tested in 2.5 M NaOH + 0.70 $Na_2S$ at 170 $^{O}$C. Points – experimental points, lines – best fit results obtained from simulation. The best fitting parameters are: $R_s$ = 8.73 Ω $cm^2$, $R_1$ = 61.8 Ω $cm^2$, $CPE_1$ =5.89 mF $cm^{-2}$, $\alpha_1$ = 0.455, $R_2$ = 206 Ω $cm^2$, $CPE_2$ = 369 mF $cm^{-2}$, $\alpha_2$= 0.947, R3=4.02 Ω $cm^2$, and C1 = 46.9 μF. ($\chi^2$ = 2.74e-3)..... 194

Figure 5.21: Equivalent circuits used to simulate the electrochemical behavior of (a) S31603, S44603, S32101, and (b) S32205 in 2.5 M NaOH + 0.70 M $Na_2S$ at the corrosion potential at 170 $^{O}$C. ..... 195

Figure 5.22: Linear polarization resistance values for austenitic S31603, superferritic S44660, lean DSS S32101 and standard DSS S32205 tested in 2.5 M and 2.5 M NaOH + 0.70 M $Na_2S$ at 170 $^{O}$C. Pt is shown for comparison. ..... 196

Figure 5.23: Cross-sectional SEM micrograph of superferritic S44660 exposed to 35 % sulfidity solution (2.5M NaOH + 0.70 M $Na_2S$) at 170 $^{O}$C. Arrows correspond to EDS spectra of S-rich outer layer and EDS spectra of Fe and Cr enriched inner layer..... 198

Figure 5.24: Cross-sectional SEM micrograph of austenitic S31603 exposed to 35 % sulfidity solution (2.5M NaOH + 0.70 M $Na_2S$) at 170 $^{O}$C. Arrows correspond to EDS spectra of S-rich outer layer and EDS spectra of Cr and Ni enriched inner layer..... 199

Figure 5.25: X-ray photoelectron spectroscopy depth profile of surface film on (a) austenitic S3160 formed at corrosion potential in 2.5 M NaOH + 0.70 M $Na_2S$ at 170 $^{O}$C. ..... 202

Figure 5.25(cont'd): X-ray photoelectron spectroscopy depth profile of surface film (b) superferritic S44660, (c) lean DSS S32101, and (d) standard DSS S32205 formed at corrosion potential in 2.5 M NaOH + 0.70 M $Na_2S$ at 170 $^{O}$C. . 203

Figure 5.26: High resolution X-ray photoelectron spectra from surface film formed on standard DSS S32205 formed at corrosion potential in 2.5 M NaOH + 0.70 M Na2S at 170 $^{O}$C for (a) Fe 2p and (b) Cr 2p. Filled symbols represent the scan corresponding to the half maximum O 1s peak intensity (ca. 1920 nm).. ..... 205

Figure 5.26 (cont'd):High resolution X-ray photoelectron spectra from surface film formed on standard DSS S32205 formed at corrosion potential in 2.5 M NaOH + 0.70 M Na2S at 170 $^{O}$C for (c) Ni 2p and (d) O 1s. Filled symbols represent the scan corresponding to the half maximum O 1s peak intensity (ca. 1920 nm). ..... 206

Figure 5.27: High resolution X-ray photoelectron spectra of S $2p_{3/2}$ from surface film formed at corrosion potential in 2.5 M NaOH + 0.70 M $Na_2S$ at 170 $^{O}$C for (a) austenitic S31603 and (b) superferritic S44660. ..... 208

Figure 5.28: High resolution X-ray photoelectron spectra of S $2p_{3/2}$ from surface film formed at corrosion potential in 2.5 M NaOH + 0.70 M $Na_2S$ at 170 $^{O}$C for DSS S32205. ..... 208

Figure 5.29: Peak fitting results for high resolution X-ray photoelectron spectra from surface film formed on standard DSS S32205 formed at corrosion potential in 2.5 M NaOH + 0.70 M $Na_2S$ at 170 $^{O}$C for S $2p_{3/2}$ . Curve fitting was performed at the half maximum O 1s peak intensity (ca. 1920 nm)..... 210

Figure 5.30: E-pH diagram for the Fe-Cr-Ni-S $H_20$ system (Fe dominant) at 170 $^{O}$C and 0.77 MPa. Molar concentration of metal cation is 0.001 M and sulfur is 0.70 M [49]. ..... 211

Figure 5.31: E-pH diagram for the Fe-Cr-Ni-S $H_20$ system (Cr dominant) at 170 $^{O}$C and 0.77 MPa. Molar concentration of metal cation is 0.001 M and sulfur is 0.70 M [49]. ..... 212

Figure 5.32: E-pH diagram for the Fe-Cr-Ni-S $H_20$ system (Ni dominant) at 170 $^{O}$C and 0.77 MPa. Molar concentration of metal cation is 0.001 M and sulfur is 0.70 M [49]. ..... 212

Figure 5.33: Anodic polarization curves for alloying elements (Fe, Cr, Ni, Mo, and Mn) tested in alkaline chloride (2.5 M NaOH + 0.17 M NaCl) solution at 90 $^{O}$C.. ..... 216

Figure 5.34: Anodic polarization curves for alloys (S31603, S44660, S32101, S32205, S32304) tested in alkaline chloride (2.5 M NaOH + 0.17 M NaCl) solution at 90 $^{O}$C. ..... 216

Figure 5.35: Optical micrographs showing (a) relatively uniform corrosion of S32205 and (b) preferential corrosion of austenitic phase in S32101 tested in 2.5 M NaOH + 0.17 M NaCl at 170 $^{O}$C. ..... 218

Figure 5.36: Cross-sectional SEM micrograph of S32205 exposed to 2.5M NaOH + 0.17 M NaCl at 170 $^{O}$C. Arrows correspond to EDS spectra of Fe-rich outer layer and EDS spectra of Cr and Ni enriched inner layer. ..... 219

Figure 5.37: (a) & (b) Cross-sectional SEM micrograph of S32101 exposed to 2.5M NaOH + 0.17 M NaCl at 170 $^{O}$C. Arrows correspond to (c) EDS spectra of Fe-rich outer layer and (d) EDS spectra of Cr enriched inner layer. ..... 220

Figure 5.38: X-ray photoelectron spectroscopy depth profile of surface film on (a) standard DSS S32205 and (b) lean DSS S32101 formed at corrosion potential in 2.5 M NaOH + 0.17 M NaCl at 170 $^{O}$C. ..... 222

Figure 5.39: Corrosion rates of (a) austenitic (N08904, S31703, S31603) and (b) superferritic grades (S44660, S44627) of stainless steel tested in alkaline-sulfide solutions at 170 $^{O}$C. Alloys have been arranged by left to right by decreasing Ni content within each type of stainless steel. ..... 225

Figure 5.39 (cont'd): Corrosion rates of (c) DSS (S32705, S32205, S32101, S32003)tested in alkaline-sulfide solutions at 170 $^{O}$C. Alloys have been arranged by left to right by decreasing Ni content within each type of stainless steel. ..... 226

Figure 5.40: Cross-sectional SEM micrograph of S32205 exposed to 2.5M NaOH + 0.70 M $Na_2S$ + 0.17 M NaCl at 170 $^{O}$C. Arrows correspond to EDS spectra of Ni and S-rich outer layer and EDS spectra of Cr and Ni enriched inner layer. 228

Figure 5.41: (a) & (b) Cross-sectional SEM micrograph of S32101 exposed to 2.5M NaOH + 0.70 M $Na_2S$ + 0.17 M NaCl at 170 $^{O}$C. Arrows correspond to (c) EDS spectra of Fe and S -rich outer layer and (d) EDS spectra of Cr and Ni enriched inner layer. ..... 229

Figure 5.42: Comparison of electrochemical impedance spectra at the corrosion potential for S31603, S44660, S32101, and S32205 tested in 2.5 M NaOH + 0.70 $Na_2S$ + 0.17 M NaCl at 170 $^{O}$C. ..... 231

Figure 5.43: Electrochemical impedance spectra at the corrosion potential for S32205 tested in 2.5 M NaOH + 0.70 $Na_2S$ + 0.17 M NaCl at 170 $^{O}$C. Points – experimental points, lines – best fit results obtained from simulation. The best fitting parameters are $R_s$ = 10.5 Ω cm$^2$, $R_1$ = 8.24 Ω cm$^2$, $CPE_1$ =8.99 mF cm$^{-2}$, $\alpha_1$ = 0.850, $R_2$ = 594 Ω cm$^2$, $CPE_2$ =40.3 mF cm$^{-2}$, $\alpha_2$ = 0.816. ($\chi^2$ = 6.98e-4) ..... 232

Figure 5.44: Electrochemical impedance spectra at the corrosion potential for S32101 tested in 2.5 M NaOH + 0.70 $Na_2S$ + 0.17 M NaCl at 170 $^{O}$C. Points – experimental points, lines – best fit results obtained from simulation. The best fitting parameters are: $R_s$ = 11.2 Ω cm$^2$, $R_1$ = 5.45 Ω cm$^2$, $CPE_1$ =15.4 mF cm$^{-2}$, $\alpha_1$ = 0.802, $R_2$ = 660 Ω cm$^2$, $CPE_2$ =18.3 mF cm$^{-2}$, $\alpha_2$ = 0.778. ($\chi^2$ = 3.57e-4) ..... 233

Figure 5.45: Linear polarization resistance values for austenitic S31603, superferritic S44660, lean DSS S32101 and standard DSS S32205 tested in 2.5 M NaOH + 0.70 M $Na_2S$ with and without 0.17 M NaCl at 170 $^{O}$C. ..... 235

Figure 5.46: X-ray photoelectron spectroscopy depth profile of surface film on (a) standard DSS S32205 and (b) lean DSS S32101 formed at corrosion potential in 2.5 M NaOH + 0.70 M $Na_2S$ + 0.17 M NaCl at 170 $^{O}$C..... 236

Figure 5.47: High resolution X-ray photoelectron spectra from surface film formed on standard DSS S32205 formed at corrosion potential in 2.5 M NaOH + 0.70 M Na2S at 170 $^{O}$C for (a) Fe 2p and (b) Cr 2p. Filled symbols represent the scan corresponding to the half maximum O 1s peak intensity (ca. 1920 nm).. ..... 238

Figure 5.47(cont'd):High resolution X-ray photoelectron spectra from surface film formed on standard DSS S32205 formed at corrosion potential in 2.5 M NaOH + 0.70 M Na2S at 170 $^{O}$C for (c) Ni 2p and (d) O 1s. Filled symbols represent the scan corresponding to the half maximum O 1s peak intensity (ca. 1920 nm). ..... 239

Figure 5.48: High resolution X-ray photoelectron spectra of S $2p_{3/2}$ from surface film formed at corrosion potential in 2.5 M NaOH + 0.70 M $Na_2S$ + 0.17 M NaCl at 170 $^{O}$C for (a) S32205 and (b) S32101. ..... 241

Figure 6.1: Engineering stress - % elongation curves for S32205 tested at an initial strain rate of 2 x 10$^{-6}$ s$^{-1}$ in different alkaline environments at 170 $^{o}$C. ..... 253

Figure 6.2: Engineering stress - % elongation curves for S32101 tested at an initial strain rate of 2 x 10$^{-6}$ s$^{-1}$ in different alkaline environments at 170 $^{o}$C. ..... 254

Figure 6.3: Engineering stress - % elongation curves for S32205 tested at an initial strain rate of 2 x 10$^{-6}$ s$^{-1}$ in 12.5 M NaOH at 170 $^{o}$C while monitoring the corrosion potential..... 256

Figure 6.4: Engineering stress - % elongation curves for S32101 tested at an initial strain rate of 2 x 10$^{-6}$ s$^{-1}$ in different alkaline environments at 170 $^{o}$C. ..... 257

Figure 6.5: Optical micrograph showing stress corrosion cracks for lean DSS S32101 in (a) 2.5 M NaOH in austenite (light etching phase) and (b) 3.75 M NaOH in ferrite phase (dark etching phase) tested at 170 $^{o}$C. ..... 258

Figure 6.6: (a) Low magnification and (b) high magnification SEM micrographs showing fracture surface of lean DSS S32101 tested in 3.75 M NaOH at 170 $^{o}$C. Arrow corresponds to region shown in (b). ..... 260

Figure 6.7: Micrographs of DSS S32205 tensile specimens tested in (left) sand and (right) 12.5 M NaOH at 170 $^{o}$C show influence of environment..... 261

Figure 6.8: Micrographs of DSS S32101 tensile specimens tested in (left) sand and (right) 12.5 M NaOH at 170 $^{o}$C show influence of environment..... 262

Figure 6.9: Optical micrograph showing stress corrosion cracks for (a) standard DSS S32205 tested in 12.5 M NaOH at 170 $^{o}$C. ..... 262

Figure 6.9 (cont'd): Optical micrograph showing stress corrosion cracks for (b) lean DSS 32101 tested in 12.5 M NaOH at 170 $^{o}$C. ..... 263

Figure 6.10: High resolution backscattered image and energy dispersive X-ray spectra maps of the surface of a standard DSS S32205 slow strain rate specimen tested in 12.5 M NaOH at 170 $^{o}$C. ..... 264

Figure 6.11: (a) Backscatter scanning electron micrograph of surface of a standard DSS S32205 slow strain rate specimen and corresponding electron back scattered diffraction maps of the tested in 12.5 M NaOH at 170 $^{o}$C. (b)Phase map showing austenite (dark) and ferrite phases (light). ..... 266

Figure 6.11 (cont'd): Electron back scattered diffraction maps of the tested in 12.5 M NaOH at 170 $^{o}$C (c) misorientation maps (step size 0.3µm), and (d) pole Figure crystal orientation map. ..... 267

Figure 6.12: Energy dispersive X-ray spectra maps of the surface of a lean DSS S32101 slow strain rate specimen tested in 12.5 M NaOH at 170 $^{o}$C. ..... 269

Figure 6.13: (a) Backscatter scanning electron micrograph of surface of a lean DSS S32101 slow strain rate specimen and corresponding electron back scattered diffraction maps of the tested in 12.5 M NaOH at 170 $^{o}$C: (b) phase map showing austenite (dark and ferrite (light. ..... 271

Figure 6.13 (cont'd): Electron back scattered diffraction maps of the tested in 12.5 M NaOH at 170 $^{o}$C: (c)Misorientation maps (step size 0.3µm), and (d) pole Figure crystal orientation map. ..... 272

Figure 6.14: Engineering stress - % elongation curves for S32205 tested at an initial strain rate of 2 x $10^{-6}$ $s^{-1}$ in different alkaline environments with and without $Na_2S$ at 170 $^{O}C$. ..... 275

Figure 6.15: Engineering stress - % elongation curves for S32101 tested at an initial strain rate of 2 x $10^{-6}$ $s^{-1}$ in different alkaline environments with and without $Na_2S$ at 170 $^{O}C$. ..... 275

Figure 6.16: Micrographs of DSS S32205 tensile specimens tested in (left) sand, (center) 2.5 M NaOH + 0.70 M $Na_2S$, and (right) 3.75 M NaOH + 0.64 M $Na_2S$ at 170 $^{o}C$ show the influence of environment on SCC. ..... 277

Figure 6.17: Micrographs of DSS S32101 tensile specimens tested in (left) sand, (center) 2.5 M NaOH + 0.70 M $Na_2S$, and (right) 3.75 M NaOH + 0.64 M $Na_2S$ at 170 $^{o}C$ show the influence of environment on SCC. ..... 278

Figure 6.18: (a) Micrographs of S44660 and U-bend specimens tested in 2.5 M NaOH + 0.70 M $Na_2S$ at 190 $^{o}C$ show the influence of environment. No SCC was observed on these superferritic steel samples in tested environments. ..... 278

Figure 6.18 (cont'd):(b) Micrographs of S44627 U-bend specimens tested in 2.5 M NaOH + 0.70 M $Na_2S$ at 190 $^{o}C$ show the influence of environment. No SCC was observed on these superferritic steel samples in tested environments. 279

Figure 6.19: Optical micrograph showing stress corrosion crack growth (a) along austenite/ferrite phase boundaries and (b) through austenite phase in standard DSS S32205 tested in 3.75 M + 0.64 M $Na_2S$ at 170 $^{o}C$. ..... 280

Figure 6.20: Optical micrograph showing stress corrosion cracks for lean DSS S32101 in (a) 2.5 M + 0.70 M $Na_2S$ and (b) 3.75 M + 0.64 M $Na_2S$ tested at 170 $^{o}C$. 281

Figure 6.21: (a) Low magnification and (b) high magnification SEM micrographs showing fracture surface of lean DSS S32205 tested in 3.75 M NaOH + 0.64 M $Na_2S$ at 170 $^{o}C$. Arrow corresponds to region shown in (b)..... 282

Figure 6.22: SEM micrographs showing cross-sectional views of SCC cracks oriented (a) along the loading direction and (b) normal to load direction on standard DSS S32205 slow strain rate specimen tested in 3.75 M NaOH + 0.64 M $Na_2S$ at 170 $^{o}C$. The "O" and "I" indicate the outer and inner regions of the surface layers examined with EDS, respectively. ..... 284

Figure 6.23: (a) Low magnification and (b) high magnification SEM micrographs showing fracture surface of lean DSS S32101 tested in 3.75 M NaOH + 0.64 M $Na_2S$ at 170 $^{o}C$. Arrow corresponds to region shown in (b)..... 286

Figure 6.24: SEM micrographs showing cross-sectional views of SCC cracks oriented (a) along the load direction and (b) normal to the loading direction on standard DSS S32101 slow strain rate specimen tested in 3.75 M NaOH + 0.64 M $Na_2S$ at 170 $^{o}$C. The "O" and "I" indicate the outer and inner regions of the surface layers examined with EDS, respectively. ..... 288

Figure 6.25: Engineering stress - % elongation curves for S32205 tested at an initial strain rate of 2 x $10^{-6}$ $s^{-1}$ in different alkaline environments with and without NaCl at 170 $^{O}$C. ..... 291

Figure 6.26: Engineering stress - % elongation curves for S32101 tested at an initial strain rate of 2 x $10^{-6}$ $s^{-1}$ in different alkaline environments with and without NaCl at 170 $^{O}$C. ..... 291

Figure 6.27: Micrographs of DSS S32205 tensile specimens tested in (left) 2.5 M NaOH and (right) 2.5 M NaOH + 0.17 M NaCl at 170 $^{o}$C show influence of environment. ..... 293

Figure 6.28: Micrographs of DSS S32101 tensile specimens tested in (a) 2.5 M NaOH and (b) 2.5 M NaOH + 0.17 M NaCl at 170 $^{o}$C show influence of environment. ..... 294

Figure 6.29: Optical micrograph showing stress corrosion cracks for lean DSS S32101 in (a) 2.5 M NaOH + 0.17 M NaCl showing in austenite (light etching phase) and (b) 3.75 M NaOH in ferrite phase (dark etching phase) tested at 170 $^{o}$C. . ..... 295

Figure 6.30: Optical micrograph showing stress corrosion cracks for lean DSS S32101 in (a) 2.5 M NaOH + 0.17 M in ferrite (dark etching phase) and (b) 3.75 M NaOH + 0.17 M in ferrite phase (dark etching phase) tested at 170 $^{o}$C. .... 296

Figure 6.31: (a) Low magnification and (b) high magnification SEM micrographs showing fracture surface of lean DSS S32101 tested in 3.75 M NaOH + 0.17 M NaCl at 170 $^{o}$C. Arrows corresponds to regions shown in (b) and (c). .. 298

Figure 6.32: Engineering stress - % elongation curves for S32205 tested at an initial strain rate of 2 x $10^{-6}$ $s^{-1}$ in different alkaline-sulfide environments with and without NaCl at 170 $^{O}$C..... 299

Figure 6.33: Engineering stress - % elongation curves for S32101 tested at an initial strain rate of 2 x $10^{-6}$ $s^{-1}$ in different alkaline-sulfide environments with and without NaCl at 170 $^{O}$C..... 300

Figure 6.34: Engineering stress - % elongation curves for S32205 tested at an initial strain rate of 2 x $10^{-6}$ $s^{-1}$ in different alkaline-sulfide environment (0.375 M NaOH + 0.64 M $Na_2S$) with various amounts of NaCl at 170 $^{O}$C. ..... 302

Figure 6.35: Engineering stress - % elongation curves for S32101 tested at an initial strain rate of 2 x $10^{-6}$ $s^{-1}$ in alkaline-sulfide solution (0.375 M NaOH + 0.64 M $Na_2S$) with various amounts of NaCl at 170 $^{O}$C. ..... 303

Figure 6.36: Percent reduction in area for standard DSS S32205 and lean DSS S32101 tested at an initial strain rate of 2 x $10^{-6}$ $s^{-1}$ in alkaline-sulfide environment (0.375 M NaOH + 0.64 M $Na_2S$) with various amounts of NaCl at 170 $^{O}$C. ... ..... 305

Figure 6.37: Micrographs showing crack coalescences in the necked region of S32205 specimens tested at an initial strain rate of 2 x $10^{-6}$ $s^{-1}$ in alkaline-sulfide solution (0.375 M NaOH + 0.64 M $Na_2S$) with (a) 0 M, (b) 0.034 M, (c) 0.17 M, and (d) 1.7 M NaCl at 170 $^{O}$C. ..... 306

Figure 6.38: Micrographs showing the typical crack morphologies on SSRT S32205 specimens tested in alkaline-sulfide solution (150 g/l NaOH + 50 g/l $Na_2S$) containing (a) 0.034 M and (b) 0.085. Arrow indicates slip-step emergence... ..... 307

Figure 6.38 (cont'd):Micrographs showing the typical crack morphologies on SSRT S32205 specimens tested in alkaline-sulfide solution (150 g/l NaOH + 50 g/l $Na_2S$) containing (c) 0.17 M, and (d) 1.7 M NaCl at 170 $^{o}$C. Arrow indicates slip-step emergence..... 308

Figure 6.39: Micrographs showing preferential corrosion of the austenite phase (γ) of S32205 specimens tested in alkaline-sulfide solution (150 g/l NaOH + 50 g/l $Na_2S$) containing (a) 0.034 M, and (b) 0.085 M NaCl at 170 $^{o}$C..... 309

Figure 6.40: Micrographs showing the typical crack morphologies on SSRT S32101 specimens tested in alkaline-sulfide solution (150 g/l NaOH + 50 g/l $Na_2S$) containing (a) 0.034 M and (b) 0.085 M, (c) 0.17 M at 170 $^{o}$C..... 311

Figure 6.40 (cont'd):Micrographs showing the typical crack morphologies on SSRT S32101 specimens tested in alkaline-sulfide solution (150 g/l NaOH + 50 g/l $Na_2$ with (c) 0.17 M, and (d) 1.7 M NaCl at 170 $^{o}$C. ..... 312

Figure 6.41: Micrographs showing preferential corrosion of the austenite phase (γ) of S32101 specimens tested in alkaline-sulfide solution (150 g/l NaOH + 50 g/l $Na_2S$) containing (a) 0.034 M, and (b) 0.085 M NaCl at 170 $^{o}$C..... 313

Figure 6.42: Micrographs showing the fractured surface of SSRT S32205 specimens tested in alkaline-sulfide solution (3.75 M NaOH + 0.64 M $Na_2S$) containing (a) 0 M, (b) 0.034 M, (c) 0.085 M, and (d) 0.17 M NaCl at 170 $^{o}$C..... 314

Figure 6.43: (a) Low magnification and (b) high magnification SEM micrographs showing fracture surface of lean DSS S32205 tested in 3.75 M NaOH + 0.64 M $Na_2S$ + 0.17 M NaCl at 170 $^oC$. Arrow corresponds to region shown in (b). ..... 315

Figure 6.44: (a) Low magnification and (b) high magnification SEM micrographs showing fracture surface of lean DSS S32101 tested in 3.75 M NaOH + 0.64 M $Na_2S$ + 0.17 M NaCl at 170 $^oC$. Arrow corresponds to region shown in (b). ..... 316

Figure 6.45: Cross-sectional view of oxide film of (a) S32205 and (b) S32101 DSS samples tested in alkaline-sulfide solution (3.75 M NaOH + 0.64 M $Na_2S$) with 0.17 M NaCl at 170 $^oC$. Arrows indicate the sites where inner, barrier film composition was measured with EDS. ..... 318

Figure 6.46: Top-down SEM micrographs showing film morphology of S32205 samples tested in alkaline-sulfide solution (3.75 M NaOH + 0.64 M $Na_2S$) with (a) 0 M, and (b) 0.034 M at 170 $^oC$. ..... 320

Figure 6.46 (cont'd): Top-down SEM micrographs showing film morphology of S32205 samples tested in alkaline-sulfide solution (3.75 M NaOH + 0.64 M $Na_2S$) with (c) 0.085 g/l, and (d) 1.7 M NaCl at 170 $^oC$. ..... 321

Figure 7.1: Micrographs showing the (a) RL orientation, (b) TS orientation, and (c) TL orientation microstructure of annealed standard DSS S32205 evaluated in this study. ..... 331

Figure 7.2: Micrographs showing the (a) RL orientation, (b) TS orientation, and (c) TL orientation microstructure of 20 % cold worked standard DSS S32205 evaluated in this study. ..... 332

Figure 7.3: Micrographs showing the microstructure (RL orientation) of (a) annealed and (b) 20 % cold worked standard as-received DSS S32205 evaluated in this study. Microhardness indents show similarity in hardness of the two phases and increased hardness of the cold worked specimen. ..... 334

Figure 7.4: Experimental and fitted $\sin^2\psi$ curves determined using X-ray diffraction for the annealed and 20 % cold worked standard DSS S32205 (scattering vector is parallel to RD for $\psi = 0$). Lattice spacing of austenite {311} is shown. 336

Figure 7.5: Experimental and fitted $\sin^2\psi$ curves determined using X-ray diffraction for the annealed and 20 % cold worked standard DSS S32205 (scattering vector is parallel to RD for $\psi = 0$ degrees). Lattice spacing of ferrite {211} is shown. ..... 337

Figure 7.6: Micrographs showing the (a) RL orientation, (b) TS orientation, and (c) TL orientation microstructure of annealed standard DSS S32205 evaluated in this study. ..... 341

Figure 7.7: (a) Micrograph showing the relatively round fracture surface of DSS S32205 tested in 3.75 M NaOH + 0.64 M Na2S + 0 M NaCl at 170 $^{o}$C. (b) A more elliptical fracture surface was observed for the fracture surface of a DSS S32205 sample tested in 3.75 M NaOH + 0.64 M Na2S + 1.7 M NaCl due to increased ductility associated with the failure. ..... 344

Figure 7.8: Histogram showing the frequency of cracks of a given length in DSS S32205 tested by SSRT in 3.75 M NaOH + 0.64 M $Na_2S$ with various amounts of chloride at 170 $^{o}$C..... 345

Figure 7.9: Histogram showing the frequency of cracks of a given length in DSS S32101 tested by SSRT in 3.75 M NaOH + 0.64 M $Na_2S$ with various amounts of chloride at 170 $^{o}$C..... 346

Figure 7.10: (a) Average crack density and (b) maximum crack velocity measured on the surface of DSS S32205 SSRT specimens tested in 3.75 M NaOH + 0.64 M $Na_2S$ with various amounts of chloride at 170 $^{o}$C..... 347

Figure 7.11: (a) Average crack density and (b) maximum crack velocity measured on the surface of DSS S32101 SSRT specimens tested in 3.75 M NaOH + 0.64 M $Na_2S$ with various amounts of chloride at 170 $^{o}$C..... 348

Figure 8.1: Cathodic polarization behavior of DSS S32205 tested in deaerated 3.75 M NaOH with and without 0.64 M $Na_2S$ at room temperature. The potential was increased at a rate of 2 mV $s^{-1}$. ..... 358

Figure 8.2: Hydrogen permeation curves for DSS S32205 coupons tested in alkaline-sulfide solution (3.75 M NaOH + 0.64 M $Na_2S$) under applied cathodic potential of -1500 and -1200 mV vs. SCE as well as at the stabilized corrosion potential (~ -700 mV vs. SCE after 1 h) at room temperature.... 359

Figure 8.3: Scanning electron micrograph of 2205 DSS polarized to -1200 mV vs. SCE in a sulfide-free (3.75 M NaOH) solution at for 24 h. Silver grains are present on ferrite phase. ..... 361

Figure 8.4: Vickers microhardness data for S32205 DSS polarized to -1200 mV vs. SCE and 1500 mV vs. SCE in alkaline-sulfide solution (3.75 M NaOH + 0.64 M $Na_2S$). The sample tested at the OCP (approximately -700 mV cs. SCE after stabilization) is shown for comparison (control). ..... 364

Figure 8.5: Stress-strain curves measured on S32205 DSS tested in alkaline-sulfide solution (3.75 M NaOH + 0.64 M $Na_2S$) at the OCP and with applied

potentials of -1500, -1200, -1100, and -1000 mV vs. SCE. A sample was tested in air for comparison..... 365

Figure 8.6: The % RA values measured on the fracture surfaces of S32205 DSS tested in alkaline-sulfide solution (3.75 M NaOH + 0.64 M $Na_2S$) at the OCP and applied cathodic potentials..... 367

Figure 8.7: Optical micrographs (a) low magnification and (b) high magnification of S32205 DSS polarized to -1500 mV vs. SCE in alkaline-sulfide solution (3.75 M NaOH + 0.64 M $Na_2S$) at room temperature. Cracks initiated in the ferrite phase (darker etching phase) in (b). ..... 368

Figure 8.8: (a) SEM fractographs of S32205 DSS that was strained to failure at 2 X $10^{-6}$ $s^{-1}$ in sulfide-containing (3.75 M NaOH + 0.64 M $Na_2S$) solution polarized to -1500 mV vs. SCE at room temperature. ..... 369

Figure 8.8 (cont'd):SEM fractographs of S32205 DSS that was strained to failure at 2 X $10^{-6}$ $s^{-1}$ in sulfide-containing (3.75 M NaOH + 0.64 M $Na_2S$) solution polarized to (a) -1500 mV vs. SCE (b) -1200 mV vs. SCE, (c) -1100 mV vs. SCE, and (d) OCP at room temperature..... 370

Figure 8.9: Fracture surface of the S32205 DSS that was strained to failure at 2 X $10^{-6}$ $s^{-1}$ in alkaline-sulfide solution (3.75 M NaOH + 0.64 M $Na_2S$) polarized to -1500 mV vs. SCE at room temperature: (a) low magnification of surface and (b) high magnification of edge near failure initiation indicated by arrow.. 372

Figure 8.10: Micrographs showing high magnification fracture features of the S32205 DSS strained to failure at 2 X $10^{-6}$ $s^{-1}$ in alkaline-sulfide solution (3.75 M + 0.64 M $Na_2S$) polarized to (a) -1200 mV vs. SCE and (b) -1100 mV vs. SCE. ..... 374

Figure 8.11: SEM micrographs showing the fracture features of S32205 DSS that was strained to failure at 2 X 10-6 $s^{-1}$ at room temperature: (a) OCP (ca. -700 mV vs. SCE) in alkaline-sulfide solution (3.75 M NaOH + 0.64 M $Na_2S$) and (b) air. ..... 376

Figure 8.12: E-pH diagram for the Fe-Cr-Ni system at 25 $^{o}$C [27] showing the thermodynamic stability of water as indicated by the solid red lines. ..... 378

Figure 9.1: Schematic showing steps involved in crack initiation caused by selective dissolution of DSS tested in hot alkaline environments in the absence of other anions: (a) material forms film in absence of stress (b) initiation in austenite phase ($\gamma$) due to film rupture (slip dissolution) model, and (c) intergranular corrosion at ferrite ($\alpha$) grain boundaries. ..... 392

Figure 9.2: Schematic showing steps involved in crack initiation caused by sulfidation of the inner, barrier film formed on DSS tested in hot alkaline environments in the presence of sulfide and chloride: (a) film on alloy in absence of stress, (b) initiation in austenite phase due to film rupture (slip dissolution) model ,and (c) sulfides are adsorbed on the surface and enhance metal oxidation by $OH^-$, $S^{2-}$, or $Cl^-$ , and (c) sulfidation of the austenite phase ($\gamma$) is enhanced by the presence of $Cl^-$..... 395

Figure 9.3: Schematic showing steps involved in stress corrosion crack initiation and growth on DSS tested in hot alkaline environments in the absence of sulfide and chloride: (a) initiation in austenite phase due to film rupture (slip dissolution model) or in ferrite phase at grain boundaries, (b) selective dissolution of Fe, Mo, and Mn creates vacancies near crack tip, and (c) vacancies are consumed by dislocations and enable crack advance through creep. ..... 399

Figure 9.4: Schematic showing steps involved in stress corrosion crack initiation and growth on DSS tested in hot alkaline environments in the presence of sulfide and chloride: (a) initiation inaustenite phase due to sulfidation of the inner, barrier layer causes unstable passivity at the crack tip, (b) dislocations are dissolved at slip-steps (slip-step model), and (c) crack advance proceeds in discontinuous steps due to unstable passivity. ..... 400

Figure A.1: Material certification sheet for standard grade DSS UNS S32205 used in slow strain rate tests for stress corrosion cracking susceptibility.

Figure A.2 Material certification sheet for standard grade DSS UNS S32205 used in hydrogen embrittlement studies

Figure A.3 Material certification sheet for standard grade DSS UNS S32205 used to understand film formation and role of composition.

Figure A.4 Material certification sheet for austenitic grade UNS S31603 (type 316L) used for exposure coupons to understand film formation and role of composition.

Figure A.5 Material certification sheet for superferritic grade UNS S44660 used for exposure coupons to understand film formation and role of composition.

Figure B.1: Image showing silver/silver sulfide external pressure-balanced reference electrode connected to lid of high temperature autoclave assembly using high pressure PTFE tubing.

Figure B.2: Potential measurement during a 48 h exposure for the $Mo/MoS_2$ pseudo reference electrode vs. a silver/silver sulfide (SSS) external pressure-balanced reference.

Figure C.1: Mechanical test results and nominal chemical composition of standard grade DSS UNS S32205 (2205) received from VTT Technical Research Centre of Finland.

Figure C.2: Mechanical test results and nominal chemical composition of lean grade DSS UNS S32101 (2101) received from VTT Technical Research Centre of Finland.

Figure C.3: Sample dimensions for tensile specimens used to determine mechanical properties of standard grade DSS UNS S32205 (2205) and lean grade DSS UNS S32201 (2101) received from VTT Technical Research Centre of Finland.

Figure C.4: Sample dimensions for U-bend specimens used to determine stress corrosion cracking susceptibility of superferritic grades UNS S44660 and UNS S44427.

# SUMMARY

Duplex stainless steels (DSS) generally have superior strength and corrosion resistance as compared to most standard austenitic and ferritic stainless grades owing to a balanced microstructure of austenite and ferrite. As a result of having favorable properties, DSS have been selected for the construction of equipment in pulp and paper, chemical processing, nuclear, oil and gas as well as other industries. The use of DSS has been restricted in some cases because of stress corrosion cracking (SCC), which can initiate and grow in either the ferrite or austenite phase depending on the environment.

Thorough understanding of SCC mechanisms of DSS in chloride- and hydrogen sulfide-containing solutions has been useful for material selection in many environments. However, understanding of SCC mechanisms of DSS in sulfide-containing caustic solutions is limited, which has restricted the capacity to optimize process and equipment design in pulp and paper environments. Process environments may contain different concentrations of hydroxide, sulfide, and chloride, altering corrosion and SCC susceptibility of each phase. Crack initiation and growth behavior will also change depending on the relative phase distribution and properties of austenite and ferrite.

The role of microstructure and environment on the SCC of standard grade UNS S32205 and lean grade UNS S32101 in hot alkaline-sulfide solution were evaluated in this work using electrochemical, film characterization, mechanical testing, X-ray diffraction, and microscopy techniques. Microstructural aspects, which included residual stress state, phase distribution, phase ratio, and microhardness, were related to the propensity for SCC crack initiation in different simulated alkaline pulping liquors at 170 $^{o}$C. Other grades of DSS and reference austenitic and superferritic grades of stainless

steel were studied using exposure coupons for comparison to understand compositional effects and individual phase susceptibility. Environments having different ionic concentrations of inorganic salts, i.e. sodium hydroxide, sodium sulfide, and sodium chloride, were used to understand the effect of liquor alkalinity, percent sulfidity, and chloride content on the corrosion and SCC behavior. Hydrogen embrittlement of S32205 was studied to understand the electrochemical conditions and fracture features associated with this failure mode.

The results showed that there is an appreciable increase in the susceptibility of DSS to SCC in the presence of sulfide and chloride in hot alkaline environments. Sulfide and chloride adsorption at active sites on the metal surface caused unstable passivity and defective film formation. Chloride and sulfide available at the electrolyte/film surface reduced the charge transfer resistance and shifted the response of the films to lower frequencies indicating the films became more defective. The surface films had an outer, discontinuous layer, and an inner, barrier layer. Fe, Mo, and Mn were selectively dissolved in hot alkaline environments. The onset of SCC was related to the extent of selective dissolution and was consistent with a slip-step dissolution mechanism.

Selective corrosion of the austenite phase depended on percent sulfidity and liquor alkalinity. Chlorides enhanced crack initiation and coalescence along the austenite/ferrite boundaries. Crack initiation and transgranular growth strongly depended on the phase distribution in the banded microstructure of DSS. These findings will augment understanding of SCC in this alloy-environment combination and facilitate materials selection in hot alkaline-sulfide environments, particularly in the petrochemical, nuclear, chemical processing, and pulp and paper industries.

# CHAPTER 1

# INTRODUCTION

## 1.1 Motivation

Stress corrosion cracking (SCC) is a particularly detrimental form of environmentally assisted cracking (EAC) because failure is often sudden and unpredictable and can occur below the design stress. Many industrial accidents, including the rupture of high-pressure gas transmission pipes, the explosion of boilers, the collapse of infrastructure, and the destruction of power stations, and oil refineries [1] have been attributed to SCC. Equipment failure from SCC (Figure 1.1) is therefore a serious concern, costing industries in the United States ~$300 billion dollars annually [2].

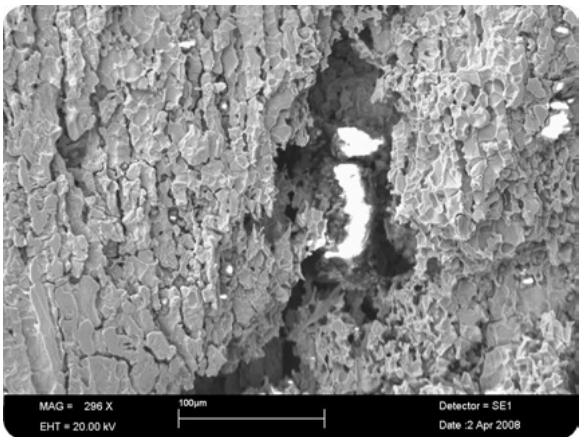


***Figure 1.1:*** ***Micrograph showing SCC in a corroded section from a 2205 DSS hot black liquor tank that failed in service due to chloride contamination [3].***

Extensive research efforts have been conducted to mitigate the risk of SCC by determining the underlying mechanisms and limitations of selected alloys in a variety of corrosive environments. Austenitic and ferritic stainless steels have widely been studied

because of their extensive use in industrial applications [4], but their use in some chemical process and manufacturing industries can be limited due to SCC [5]. Different grades of duplex stainless steels (DSS) have been developed for these industries to combine toughness, formability, corrosion, and SCC resistance. DSS grades are generally divided into three sub-classes based on their composition: lean duplex (UNS S32003, S32101, S32304), standard duplex (UNS S32205), and superduplex (UNS S32705) [6]. Superior corrosion performance results from alloying elements such as Cr, Mo, and N, which increase the resistance to environmental effects in a number of chemical environments [7-9]. SCC has been widely studied in solutions containing chlorides [10-14] and hydrogen sulfide ($H_2S$) [15-17]; however, far fewer studies have reviewed the SCC behavior of DSS alloys in strong alkaline or caustic environments. Caustic environments are common in a number of chemical process industries including the modified Bayer processes used in alumina ore processing, the Girdler-sulfide (GS) process used in heavy water production, hydrocarbon processing for the treatment of acidic impurities such as hydrogen sulfide and mercaptans, and various process streams in pulp mills utilizing the kraft pulping process [18-24].

The pulp and paper industry has been inundated by the high cost attributed to maintenance and downtime from corrosion susceptibilities of plant equipment, estimated at $6 billion dollars annually in the United States [2]. Plant equipment such as batch and continuous digesters shown in Figure 1.2, as well as accumulators, clarifiers, and storage tanks have historically been constructed from carbon steel, mild steel, and cladded carbon steel [5, 22]. Recent modifications to the kraft pulping process have resulted in higher operating temperatures, processing pressures, alkalinity, and percent sulfidity, requiring

more corrosion resistant materials. More stringent environmental legislation has also increased the need to reuse water throughout the chemical circulation loop, resulting in the accumulation of corrosive non-process elements such as chloride.

***Figure 1.2:*** ***Continuous digester (left) and batch digesters (right) used in the kraft pulping process to extract lignin from cellulose.***

The pulp and paper industry has been using several grades of DSS for more critical components to thwart the expensive cost associated with equipment maintenance and to increase the safety of paper mill employees. Mild steel has traditionally been used in most North American digesters, but the use of DSS corrosion-resistant coatings or claddings has been adopted to extend equipment life in many cases. Scandinavian mills have instead replaced many aging mild steel digesters entirely with DSS. While DSS have been a reliable alternative in many pulp mills, several equipment failures from general corrosion and SCC have been reported [3, 25-27]. Recent field and laboratory

studies have also shown that these materials are susceptible to general corrosion and SCC, particularly with elevated temperature, alkali content [24, 26, 28-30], and chloride content [3]. Additional research needs to address the fundamental mechanism of corrosion and SCC of DSS in hot alkaline environments with different concentrations of sulfide and chloride to optimize alloying compositions, enhance the safety and durability of equipment, and provide data for the accurate prediction of component performance.

Understanding the underlying mechanisms for SCC of DSS in caustic environments is of both scientific and industrial importance, particularly to the pulp and paper industry, which uses pressurized digesters containing concentrated solutions of sodium hydroxide (NaOH) and sodium sulfide ($Na_2S$) at temperatures of 160 – 180 $^oC$. Researchers have demonstrated that under laboratory conditions, DSS are susceptible to general corrosion and SCC in simulated pulping liquors at temperatures above ~140 $^oC$ [20-21, 26, 28-32]. Welded regions are particularly susceptible to SCC due to residual stresses from fabrication [29-30]. Selective corrosion of the individual phases can also influence crack initiation behavior. Indeed, the austenitic phase has been reported to be the preferred phase for crack initiation in alkaline-sulfide solutions; however, the ferrite phase and austenite/ferrite phase boundaries were found to be favorable sites for SCC initiation in solutions containing chloride or hydrogen sulfide [10-17].

Previous studies [12, 33-34] have shown that hydrogen may also influence the SCC behavior of DSS. Hydrogen absorption causes a drastic loss of ductility and change in the fracture morphology in seawater (chlorides) and sour gas (hydrogen sulfide) environments. Several researchers have suggested [24, 35-36] that hydrogen may also contribute to SCC of stainless steels in alkaline solutions. The evolution of hydrogen has

been evaluated on stainless steel electrodes in NaOH [37-38] and it was shown that hydrogen can be generated under alkaline conditions with an applied cathodic potential.

The process of SCC is broadly divided in two stages: crack initiation and crack propagation. Crack initiation is generally due to microstructural features such as phase distribution, residual stress, and secondary phases. The microstructures of DSS typically have an equal volume fraction of austenite and ferrite. Fabrication of DSS plates often results in a banded microstructure as shown in Figure 1.3. Secondary phases formed during hot working can act as crack initiation sites. Residual microstresses are generated upon cooling because of a difference in the CTE between the two phases [39-42]. These stresses affect the anisotropic deformation behavior of these alloys.

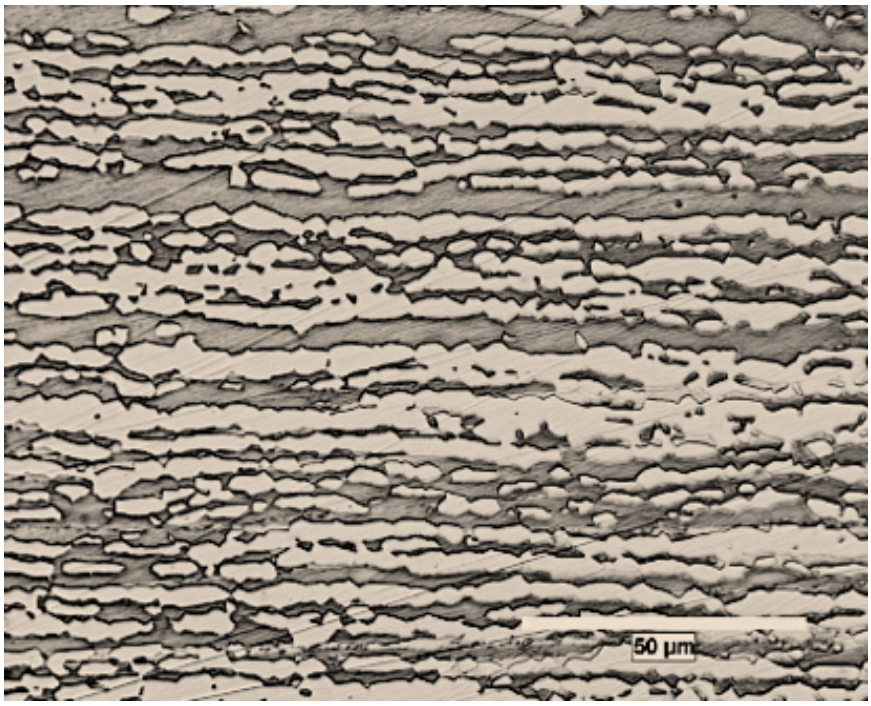


(a)

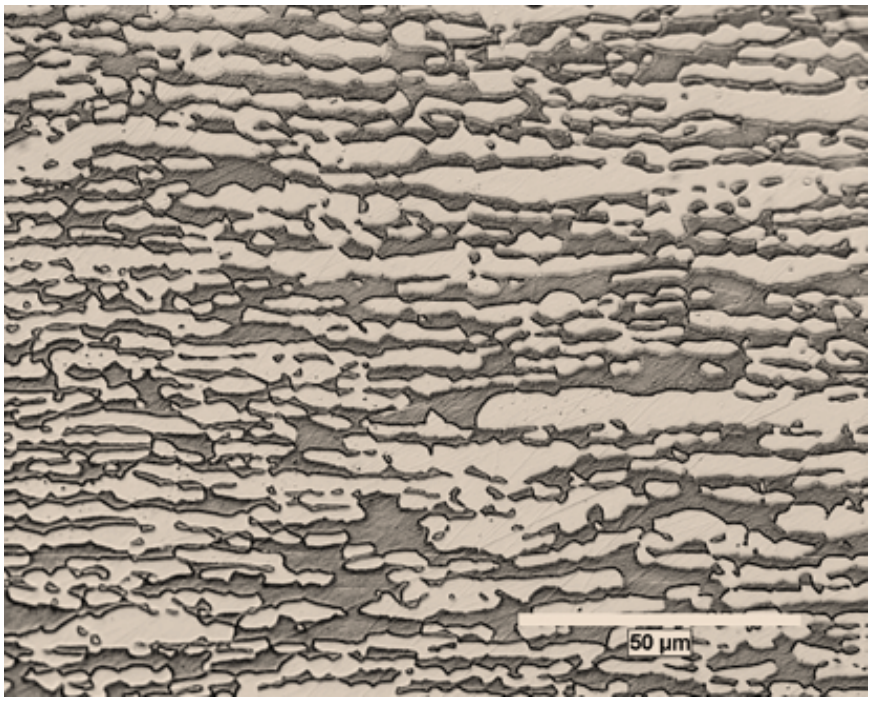


(b)

***Figure 1.3:*** ***Banded microstructure of standard grade DSS S32205 in (a) rolling longitudinal and (b) short transverse orientation. Austenite (light etching) phase is distributed in a ferrite (dark etching phase) matrix.***

The electrochemical and passivation behavior of DSS varies from single-phase austenitic or ferritic grades of stainless steel. An electrochemical potential difference between the two phases has been shown to vary for DSS S32705 in chloride solutions at room temperature, resulting in selective corrosion of the ferritic phase [43-44]. Precipitates and intermediate phases can also alter the electrochemical behavior of DSS. Alloying elements such as Cr, Mo, and Si partition to the ferritic phase, while Ni, N, C, and Cu partition to the austenitic phase [45-49]. The ability of the individual phases to form a stable passive film is influenced by the local composition and environment. Crack initiation and growth will depend on electrochemical conditions at the electrolyte/film interface and film composition, thus it is important to understand film formation mechanisms on DSS in alkaline solutions.

Crack growth occurs at a rate that is a function of the local solution, microstructure distribution, and stress at the crack tip. The stress condition at the crack tip, such as constant strain or load, can affect the susceptibility to SCC by either favoring dynamic straining or facilitating stress relaxation. The creep rate at the crack tip has been shown to be an important factor in determining SCC susceptibility [50]. A number of studies have shown that the conditions at the crack tip can greatly differ from that at the surface [51-53]. The loading condition will influence crack initiation and propagation.

There are many dissolution and mechanical fracture models to explain the SCC initiation and growth in different alloy-environment combinations [4, 54-55]. No single mechanism of SCC has been able to explain the complex interaction of the environment, material, and loading condition in every circumstance. Dissolution models (e.g., film rupture, slip-step dissolution, and localized surface plasticity) are generally applied to

intergranular SCC (IGSCC), whereby crack growth proceeds along ferrite grain boundaries [4]. Mechanical fracture models (e.g., hydrogen embrittlement, adsorption-induced cleavage, film-induced cleavage) are typically based on the adsorption of aggressive anions that weakens metal bonds near the crack tip, hydrogen absorption, or cleavage due to a brittle surface film. Fracture features are essential for determining if a dissolution or mechanical fracture model is operative under particular environmental conditions.

Researchers have applied an active path, slip-step dissolution model to TGSCC of stainless steels in several environments [56-59], particularly at potentials near the transpassive region. This process is facilitated by a mechanochemical effect, whereby dissolution is accelerated in the presence of an applied stress. A more recent study [60] of austenitic stainless steels in strong caustic environment established a connection between a de-alloyed surface film and SCC, supporting a film-induced cleavage model. Of the existing mechanical fracture modes, only film-induced cleavage, hydrogen embrittlement, and slip-step dissolution have been supported by experimental data in stainless steels [12, 24, 36, 60-63]. The conditions under which these mechanisms are prevalent will depend on the concentration of ions in the solution and the composition of the particular grade of DSS.

### 1.2 Research Objectives and Technical Approach

The main goal of the current investigation is to evaluate the role of microstructure and environment on the mechanism of SCC of DSS in hot sulfide-containing caustic environments. The specific technical objectives are the following:

(1) To understand selective dissolution (de-alloying) in DSS by studying the corrosion and electrochemical behavior of austenitic and ferritic grade stainless steels and their alloying elements (Fe, Cr, Ni, Mo, and Mn) in caustic solutions containing chloride and sulfide.

(2) To evaluate passive film formation and breakdown on DSS in caustic solutions containing chloride and sulfide.

(3) To address the role of microstructural anisotropy on the initiation and growth of stress corrosion cracks under constant strain in as-received standard grade DSS S32205 and lean grade DSS S32101 in alkaline-sulfide solution with different amounts of chloride.

(4) To assess the electrochemical conditions necessary to cause hydrogen embrittlement of DSS S32205 in alkaline-sulfide solution.

(5) To investigate the mechanism for SCC initiation and growth in standard grade DSS S32205 and lean DSS grade S32101 DSS in caustic solutions containing chloride and sulfide.

Mechanical, electrochemical, and characterization studies were conducted in this work to accomplish these objectives. Slow strain rate testing (SSRT) and exposure coupon tests were used to evaluate the SCC and general corrosion susceptibility in different alkaline environments. Stereology techniques were used to quantify the crack distribution for different material-environment combinations. The use of *ac* and *dc* electrochemical tests, such as electrochemical impedance spectroscopy (EIS), potentiodynamic polarization, linear polarization resistance (LPR), open circuit potential, and (OCP) monitoring were used to understand the corrosion behavior and film formation

on the surface of DSS with changes in the solution composition, temperature, and potential range. The composition and structure of the surface films formed in caustic environments on pure elements and different grades of stainless steels were studied with X-ray photoelectron spectroscopy (XPS), scanning electron microscopy (SEM), and energy dispersive X-ray spectroscopy (EDS). The residual stress state of cold worked DSS plates was evaluated with X-ray diffraction (XRD) to understand the behavior of the different phases after large plastic deformation. The influence of an applied cathodic potential on the electrochemical and mechanical behavior of DSS S32205 was studied to understand hydrogen embrittlement in caustic solution.

### 1.3 Organization of Dissertation

The following chapters are organized to present the work in a clear manner. Chapter 2 provides a general review of the experimental and industrial experience with DSS in different applications, existing proposed mechanisms for SCC, and previous work to study the corrosion and SCC of DSS in caustic environments. Chapter 3 summarizes the experimental techniques, materials, and testing conditions used in this study. Chapter 4 addresses the corrosion susceptibilities, electrochemical behavior, and film properties associated with selective dissolution of different grades of stainless steel in alkaline environments. Chapter 5 focuses on the corrosion susceptibilities, electrochemical behavior, and film properties of different grades of stainless steel in caustic environments containing sulfide and chloride. Chapter 6 assesses the SCC behavior of DSS in caustic environments containing sulfide and chloride. Chapter 7 evaluates the role of microstructure of DSS on the SCC crack initiation and growth behavior in alkaline-sulfide environments containing chloride. Chapter 8 investigates hydrogen uptake and its

affect on hydrogen embrittlement of DSS in caustic environments. Chapter 9 reviews existing models for SCC of stainless steels and proposes a mechanism of SCC of DSS in hot alkaline and alkaline-sulfide environments based on the experimental results. Chapter 10 provides a summary of the results, practical implications, and several recommendations for future studies on this topic.

## 1.4 REFERENCES


[1] D.J. Wulpi, "Understanding how Components Fail", American Society for Metals, Cleveland, OH, 1985.

[2] H.K. Gerhardus, M.P. Brongers, N.G. Thompson, Y.P. Virmani, J.H. Payer, "Corrosion Costs and Preventive Strategies in the United States," NACE Report FHWA-RD-01-156, 2001.

[3] Bergquist, A., and Wegrelius, W. "Experiences in Pulp and Paper Industry of a 30 Years Old Steel Grade," 2009 TAPPI Conference Proceedings, 10 – 14 October, 2009, Memphis, TN.

[4] D.A. Jones, Principles and Prevention of Corrosion, Prentice Hall, 1996.

[5] D.C. Bennett, "Continuous Digester Cracking: Task Group Report," TAPPI J, vol. 64, 1981, p. 75-77.

[6] Outokumpu, "Duplex Stainless Steel," uhttp://www.outokumpu.com/36719.epibrw (accessed on 09/2011).

[7] J.E. Truman and K.R. Pirt, "Properties of a Duplex (Austenitic-Ferritic) Stainless Steel and Effects of Thermal History," Duplex Stainless Steels, 1982, pp. 113-142.

[8] H.J. Grabke, "The Role of Nitrogen in the Corrosion of Iron and Steels," ISIJ International, vol. 36, 1996, pp. 777-786.

[9] J. Foct et al., "Nitrogen Alloying of Duplex Stainless Steels," 1991.

[10] S. Kim, D.B. Mitton, and R.M. Latanision, "Corrosion Resistance of Stainless Steels in Chloride Containing Supercritical Water Oxidation System," Korean J. Chem. Eng, vol. 17, 2000, p. 58.

[11] Oltra, A. Desestret, E. Mirabal, J.P. Bizouard, "A Critical Study of Stress Corrosion Cracking of Duplex Stainless Steels in Environments Containing

Chlorides and H2S. Study of the Ferrite Phase Behavior," Corrosion Science, Vol. 27, I. 10-11, 1987, pp. 1251-1269.

[12] Tsai and S.L. Chou, "Environmentally Assisted Cracking Behavior of Duplex Stainless Steel in Concentrated Sodium Chloride Solution," Corrosion Science, vol. 42, 2000, pp. 1741-1762.

[13] H.S. Kwon and H.S. Kim, "Investigation of stress corrosion susceptibility of duplex( alpha+ gamma) stainless steel in hot chloride solution," Materials Science and Engineering A(Switzerland), 1993, pp. 159-166.

[14] M. Puiggali, D. Desjardins, L. Ajana, "A Critical Study of Stress Corrosion Cracking Testing Method for Stainless Steels in Hot Chloride Media," Corrosion Science, Vol. 27, I. 6, 1987, pp. 585-594.

[15] K. Van Gelder et al., "The Stress Corrosion Cracking of Duplex Stainless Steel in $H_2S/CO_2/Cl$ environments," Corrosion science, vol. 27, 1987, pp. 1271-1279.

[16] K. Klyk-Spyra and M. Sozanska, "Quantitative Fractography of 2205 Duplex Stainless Steel after a Sulfide Stress Cracking Test," Materials Characterization, vol. 56, 2006, pp. 384-388.

[17] M. Barteri et al., "Microstructural Study and Corrosion Performance of Duplex and Superaustenitic Steels in Sour Well Environment," Corrosion, vol. 43, 1987, pp. 518-525.

[18] A. Boateng, J.A. Begley, and R.W. Staehle, "Corrosion Fatigue and Stress Corrosion Cracking of Type 304 Stainless Steel in Boiling NaOH Solution," Metallurgical and Materials Transactions A, vol. 10, 1979, pp. 1157-1164.

[19] A.K. Agrawal et al., "The Polarization Behavior of Fe-Ni-Cr Alloys in Concentrated Sodium Hydroxide Solutions in the Temperature Range 25° to 150° C," Journal of The Electrochemical Society, vol. 119, 1972, p. 1637.

[20] M. Honda et al., "Stress Corrosion Cracking of Stainless Alloys in Alkaline-Sulfide Solutions.," 1991.

[21] M. Honda, Y. Kobayashi, and A. Tamada, "Stress Corrosion Cracking of Stainless Alloys in Alkaline-sulfide Solutions," Corrosion (USA), vol. 48, 1992, pp. 822-829.

[22] D. Singbeil and A. Garner, "Caustic Stress Corrosion Cracking of Pressure Vessel Steels in Dilute Alkaline-Sulfide Solutions," Materials Performance, vol. 24, 1985, pp. 9-15.

[23] A.J. Sedriks, “Corrosion of Stainless Steel,” John-Wiley & Sons, New York, 1979.

[24] G. Rondelli, B. Vicentini, and E. Sivieri, “Stress Corrosion Cracking of Stainless Steels in High Temperature Caustic Solutions,” Corrosion Science, vol. 39, 1997, pp. 1037-1049.

[25] M. Gorog, “Digester Outlet Device Scraper Arm Cracking,”2006 Engineering, Pulping and Environmental Conference, Atlanta, GA, USA, 5-8 November 2006.

[26] H.T. Leinonen, P. Pohjanne, “Stress Corrosion Cracking Susceptibility of Duplex Stainless Steels and their Welds in Simulated Cooking Environments. NACE Corrosion 2006, paper no. 06244, San Diego, CA, USA, 12-16 March 2006.

[27] C. Reid, “Stress Corrosion Cracking of Austenitic and Duplex Stainless Steels in the Pulp and Paper Industry,” TAPPI Engineering Conference Proceedings, 1999, pp. 1315-1357.

[28] P.M. Singh, J. Mahmood, P. Conde, “Stress Corrosion Cracking and Corrosion Susceptibility of Duplex Stainless Steels in Caustic Solutions,” NACE Corrosion 2005, paper no. 05196, Houston, TX, USA, 3-7 April 2005.

[29] A. Bhattacharya, P. M. Singh, H. Leinonen, J. Mahmood, “Effect of Welding Related Microstructure on Stress Corrosion Cracking Susceptibility in Caustic Solutions,” NACE Corrosion 2006, paper no. 06497, San Diego, CA, USA, 12-16 March 2006.

[30] A. Bhattacharya and P.M. Singh, “Stress Corrosion Cracking of Welded 2205 Duplex Stainless Steel in Sulfide-containing Caustic Solution,” Journal of Failure Analysis and Prevention, vol. 7, 2007, pp. 371-377.

[31] A. Harrison, “Corrosion Control Offers Paper Mills a Method of Cost Control, “Pulp & Paper, vol. 68, I. 10, October 2005, pp. 135-137.

[32] K.C. Bendall, “Duplex Stainless Steel in the Pulp and Paper Industry,” Anti-Corrosion Methods and Materials, vol. 44, 1997, pp. 170-174.

[33] S.L. Chou and W.T. Tsai, “Effect of Grain Size on the Hydrogen-Assisted Cracking in Duplex Stainless Steels,” Materials Science and Engineering: A, vol. 270, 1999, pp. 219-224.

[34] A.A. El-yazgi and D. Hardie, “The Embrittlement of a Duplex Stainless Steel by Hydrogen in a Variety of Environments,” Corrosion Science, vol. 38, 1996, pp. 735-744.

[35] L. Dahl, T. Dahlgren and N. Lagmyr, High Temperature High Pressure Electrochemistry in Aqueous Solutions, NACE-4 (ed. R.W. Staehle, D. De G. Jones and J.E. Slater), NACE, Houston, TX, 1986, p. 533.

[36] G.J. Theus and R.W. Staehle, 1977. Review of Stress Corrosion Cracking and Hydrogen Embrittlement in the Austenitic Iron-Chromium-Nickel Alloys. In: Staehle, R.W., Hockman, J., McCright, R.D. and Slater, J.E., Editors, 1977. Stress Corrosion Cracking and Hydrogen Embrittlement of Iron Based Alloys, NACE-5, Houston, pp. 845–892.

[37] R.N. O'Brien and P. Seto, "The Mechanism of Hydrogen Evolution at a Stainless Steel Electrode in Basic Solution," Journal of the Electrochemical Society, vol. 117, 1970, p. 32.

[38] J.M. Olivares-Ramirez, M.L. Campos-Cornelio, J. Uribe Godinez, E. Borja-Arco, R.H. Castellanos, "Studies on the Hydrogen Evolution Reaction on Different Stainless Steels," Int. J. of Hyd. Ener., vol. 32, 2007, pp.3170-3173.

[39] E. Werner, T. Siegmund, and F. Fischer, "A Computer Study of the Thermomechanical Deformation Behavior of a Duplex Steel," Computational Materials Science, vol. 3, 1994, pp. 279-285.

[40] T. Siegmund, E. Werner, and F.D. Fischer, "On the Thermomechanical Deformation Behavior of Duplex-type Materials," Journal of the Mechanics and Physics of Solids, vol. 43, 1995, pp. 495-532.

[41] V.V. Silberschmidt and E. Werner, "Analysis of Thermal Residual Stresses in Duplex-type Materials," Computational Materials Science, vol. 16, 1999, pp. 39-52.

[42] J. Johansson, M. Odén, and X.H. Zeng, "Evolution of the Residual Stress State in a Duplex Stainless Steel during Loading," Acta Materialia, vol. 47, 1999, pp. 2669-2684.

[43] R.A. Perren et al., "Corrosion Resistance of Super Duplex Stainless Steels in Chloride Ion Containing Environments: Investigations by Means of a New Microelectrochemical Method I. Precipitation-free States," Corrosion Science, vol. 43, 2001, pp. 707-726.

[44] R. Perren et al., "Corrosion Resistance of Super Duplex Stainless Steels in Chloride Ion Containing Environments," Corrosion Science, vol. 34, 2001, p. 727-745.

[45] J. Nilsson, "Super Duplex Stainless Steels," Materials Science and Technology, vol. 8, 1992, pp. 685-700.

[46] H.D. Solomon and T.M. Devine Jr, “Keynote Address: A Tale of Two Phases,” Duplex Stainless Steels (Conference Proceedings of the American Society for Metals), RA Lula (ed.), Metals Park, Ohio, vol. 44073, 1983, pp. 693-756.

[47] P. Combrade and J.P. Audouard, “Duplex Stainless Steels' 91, 28.±30.10. 1991, Beaune, Bourgonge, France, J,” S, pp. 257-270.

[48] L.F. Garfias-Mesias, J.M. Sykes, and C.D.S. Tuck, “The Effect of Phase Compositions on the Pitting Corrosion of 25 Cr Duplex Stainless Steel in Chloride Solutions,” Corrosion Science, vol. 38, 1996, pp. 1319-1330.

[49] M. Femenia, J. Pan, and C. Leygraf, “Characterization of Ferrite-Austenite Boundary Region of Duplex Stainless Steels by SAES,” Journal of the Electrochemical Society, vol. 151, 2004, p. B581.

[50] R. Parkins, “Environmental Effects in Crack Growth,” The Journal of Strain Analysis for Engineering Design, vol. 10, 1975, pp. 251-257.

[51] R.H. Jones, “Analysis of Brittle Intergranular Crack Propagation During Stress Corrosion,” Russell H. Jones Pacific Northwest Laboratory Richland, UA 99352,” Structure/Property Relationships for Metal/Metal Interfaces: Symposium Held April 29-May 1, 1991, Anaheim, California, USA, 1990.

[52] A. Turnbull, Progress in the Understanding of the Electrochemistry in Cracks, Embrittlement by the Local Crack Environment, R.P. Gangloff, Ed., The Metallurgical Society, 1984, pp. 3.

[53] U.K. Chatterjee, “Stress Corrosion Cracking and Component Failure: Causes and Prevention,” Sadhana, vol. 20, 1995, pp. 165-184.

[54] R.C. Newman, “Stress-Corrosion Cracking Mechanisms,” Corrosion Mechanisms in Theory and Practice, 1995.

[55] J. Scully and T. Hoar, “Mechanochemical Anodic Dissolution of Iron-Nickel Alloys in Hot Chloride Solution at Controlled Electrode Potential,” International Congress on Metallic Corrosion: Proceedings, 1966.

[56] Z. Fang et al., “Stress Corrosion Cracking of Austenitic Type 304 Stainless Steel in Solutions of Hydrochloric Acid and Sodium Chloride at Ambient Temperature,” Corrosion (Houston), vol. 50, 1994, pp. 873-878.

[57] J.H. Zheng, W.F. Bogaerts, and M.J. Brabers, “Stress Corrosion Cracking and Anodic Dissolution of 316L Stainless Steel in Hot Lithium Hydroxide,” 1992.

[58] E.M. Gutman, G. Solovioff, and D. Eliezer, “The Mechanochemical Behavior of Type 316L Stainless Steel,” Corrosion Science, vol. 38, 1996, pp. 1141-1145.

[59] R. Nishimura, Y. Maeda, "SCC Evaluation of Type 304 and 316 Austenitic Stainless Steels in Acidic Chloride Solutions using the Slow Strain Rate Technique," Corrosion Science, Vol. 46, 2004, pp. 769-785.

[60] J. Deakin et al., "De-alloying of Type 316 Stainless Steel in Hot, Concentrated Sodium Hydroxide Solution," Corrosion Science, vol. 46, 2004, pp. 2117-2133.

[61] J.F. Newman, "The Stress Corrosion of Steel in Sodium Hydroxide Solution: A Film-Rupture Model," Corrosion Science, vol. 21, 1981, pp. 487-503.

[62] W.J. Nisbet, G.W. Lorimer and R.C. Newman, "A Transmission Electron Microscopy Study of Stress Corrosion Cracking in Stainless Steels," Corrosion Science, vol. 35, 1993, pp. 457-469.

[63] K. Sieradzki and R.C. Newman, "Brittle Behavior of Ductile Metals During Stress-Corrosion Cracking," Philosophical Magazine A, vol. 51, 1985, pp. 95-132.

# CHAPTER 2

# BACKGROUND

## 2.1 Introduction

Accurate prediction of stress corrosion cracking (SCC) of duplex stainless steel (DSS) components in hot alkaline-sulfide environments requires understanding of the metallurgical, environmental, and mechanical factors that influence the initiation and growth behavior. There has been an extensive amount of research conducted on different aspects of the three critical conditions needed for SCC in DSS, particularly in chloride environments, but there is limited understanding of the combination of all three aspects in caustic conditions. The following chapter will explore some of the research and industrial experiences described in the literature necessary to understand the motivation for this research and the problem it has addressed. Many subjects not presented in the background are described in more detail in subsequent chapters.

## 2.2 Duplex Stainless Steels

### 2.2.1 Effect of Composition

Duplex stainless steels (DSS) having 20 – 29 wt % Cr, 1 – 7 wt % Ni, 1 – 4 wt %, and 0.15 – 0.25 wt % N acquire their duplex name because they have a balanced microstructure of ferrite and austenite. The phase balance can be maintained by controlling the composition. The austenite phase is primarily stabilized by Ni, C, Cu, Mn and N and ferrite is stabilized by Cr, Mo, and Si. The Schaffler diagram [1], shown in Figure 2.1, is commonly used to predict the phase balance in stainless steels. Elements

are expressed in terms of Ni equivalence (austenite stabilizers) or Cr equivalence (ferrite stabilizers). Cr and Mo improve intergranular and pitting resistance while N improves structural strength [2-4]. The superior mechanical and corrosion properties of DSS as compared to other types of stainless steel depend on a balanced microstructure.

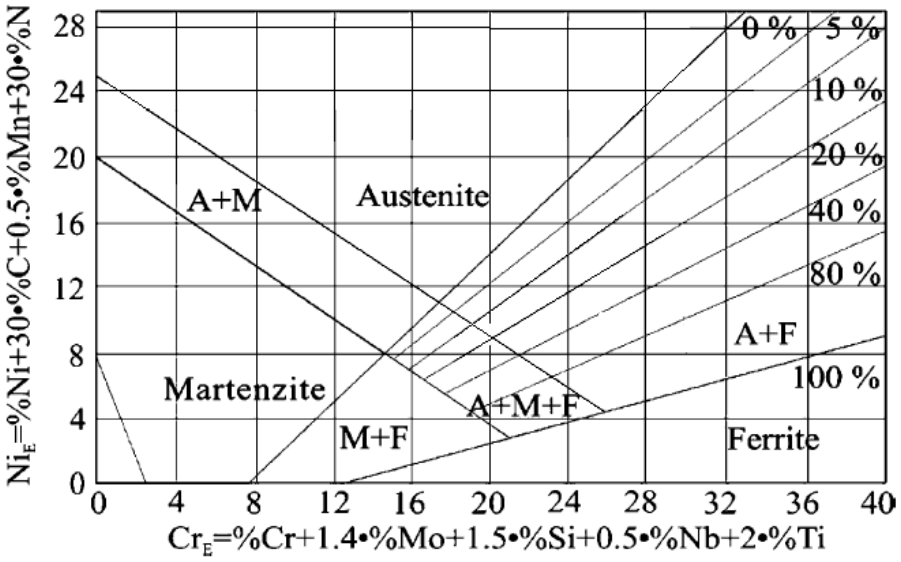


***Figure 2.1:*** ***Schaffler diagram used to determine the composition of DSS that will result in a balanced microstructure [1].***

Different forms of DSS are commercially available as standard, lean, and super grades depending on their composition. Due to volatility associated with the price of alloying elements such as Ni, newer lean grades (e.g., S32101, S32003, and S32304) that have Mn or Cu substitutions for Ni have been developed. Each grade can be advantageous in a particular environment depending on the relative concentration of alloying elements. A majority of plant equipment in service is constructed of standard grade DSS S32205, but lean grades are steadily gaining popularity as understanding of

their behavior is established in different environments. Super DSS are typically chosen when pitting is a concern due to a high pitting resistance equivalent number (PREN) [2].

$$PREN = Cr + 3.3Mo + 16N \quad [2.1]$$

The nominal compositions of some common DSS grades and their associated PREN are provided in Table 2.1.

***Table 2.1 Nominal chemical composition (wt %) and pitting resistance equivalent numbers (PREN) of select grades of DSS***

| | | *Chemical Composition %, Typical Values* | | | | | | |
|---|---|---|---|---|---|---|---|---|
| *Alloy* | *UNS Number* | *PREN* | *C max* | *N* | *Cr* | *Ni* | *Mo* | *Other* |
| 2003 | S32003 | 27 | 0.03 | 0.14 | 19.5 | 3.0 | 1.5 | 2 Mn |
| 2101 | S32101 | 26 | 0.03 | 0.22 | 21 | 1.5 | 0.3 | 5 Mn |
| 2205 | S32205/S31803 | 35 | 0.02 | 0.17 | 22 | 5.7 | 3.1 | - |
| 2304 | S32304 | 25 | 0.02 | 0.10 | 23 | 4.8 | 0.3 | 0.2 Cu |
| 2507 | S32750 | 43 | 0.02 | 0.27 | 25 | 7.0 | 4.0 | - |

DSS offer advantages to austenitic and ferritic stainless steels in many industrial applications because of their mechanical strength, ductility, toughness, corrosion and SCC resistance, formability, and cost savings due to lower Ni and Mo content. As a result of their beneficial attributes, section thicknesses and thus the weight of the structure can often be reduced. DSS is available from suppliers in wrought or cast forms including: tubing, pipes, extrusions, plates, bars, forgings, and sheets. The wide array of forms

offers versatility in the design process of industrial structures. Wrought plates are most commonly welded together to form the different sections of the pulping digester shown in Figure 2.2.

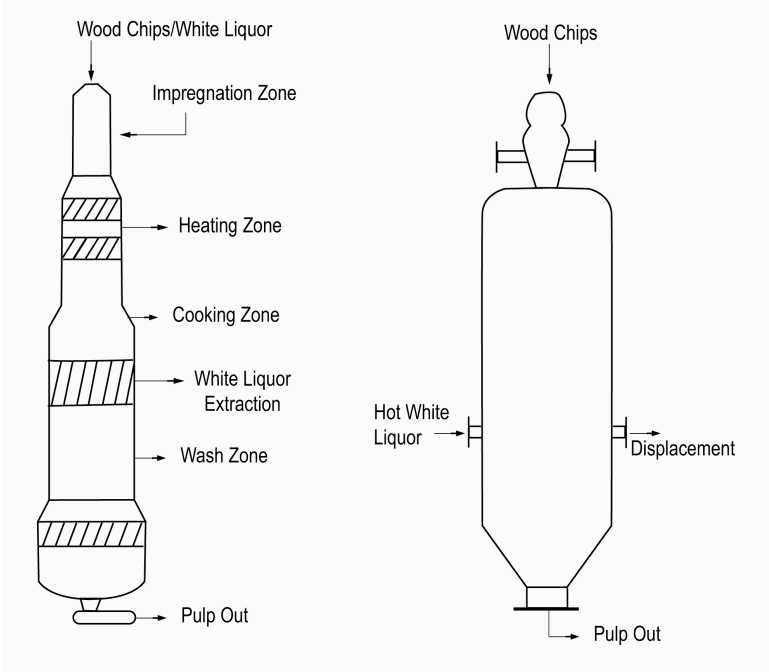


***Figure 2.2:*** ***Schematic of different sections of a (a) continuous digester and (b) batch digester used in the kraft pulping process.***

The influence of alloying elements on the behavior of DSS has been reviewed extensively, with Cr, Mo, Ni, and N constituting the four most essential elements with respect to corrosion resistance [5-9]. Partitioning of the alloying elements to the austenite and ferrite phases has been shown to influence corrosion and SCC susceptibility of the individual phases. The diffusivity of alloying elements is generally faster in the ferrite phase. Femenia et al [9] used scanning Auger electron spectroscopy to study the austenite/ferrite interface of grades S32705, S32304, and S32205 and showed that Cr and

Mo partitioned to the ferrite phase and Ni and N partitioned to the austenite phase. This partitioning effect was shown to cause a galvanic interaction [10-11] between the two phases in chloride environments, which lead to a higher dissolution of the ferrite phase. In highly alloyed DSS such as S32705, the elements are partitioned a manner that is favorable to homogeneous dissolution. Wensley et al [12-14] have attributed the increased susceptibility of the austenite phase in alkaline pulping liquors to lower Cr content as compared to the ferrite phase.

The individual alloying elements have a strong role in improving the corrosion resistance of DSS by promoting the formation of a stable passive film. Cr and Ni have been found to increase the corrosion potential in alkaline environments, thus increasing the SCC resistance of DSS [15-17]. N and Mo have been shown to have a strong role on passive film stability. Sridar and Kolts [15] investigated the effect of N in DSS and found that corrosion preferentially occurred in the austenite phase for low-nitrogen DSS, whereas the ferrite and austenite phases were equally susceptible for high-nitrogen DSS. Tseng et al [16] considered the SCC susceptibility of grade S32205 in chloride media and found that N improved the strength and ductility, increased the stacking fault energy, and enhanced the passivation ability. The role of Mo has also been investigated in different environments. Mo was shown to increase SCC and pitting resistance in chloride-containing environments [18-20], but its influence on SCC resistance in caustic solutions was shown to be detrimental [21-23].

### 2.2.2 Influence of Microstructure

The degree of heterogeneity arising from the complex microstructure obfuscates the study of SCC mechanisms. Particular care must be exercised when welding or heat

treating DSS due to disruption of phase balance as well as the formation of intermetallic particles and secondary phases. The isothermal cooling curve for the ternary Fe-Cr-Ni system in Figure 2.3 [2] indicates that many precipitates and intermetallic phases may form. Precipitates and intermetallic phases are preferred initiation sites for SCC. The role of heat treatments on precipitation in DSS has been studied in different environments to understand general corrosion and SCC susceptibility [24-27, 15-17].

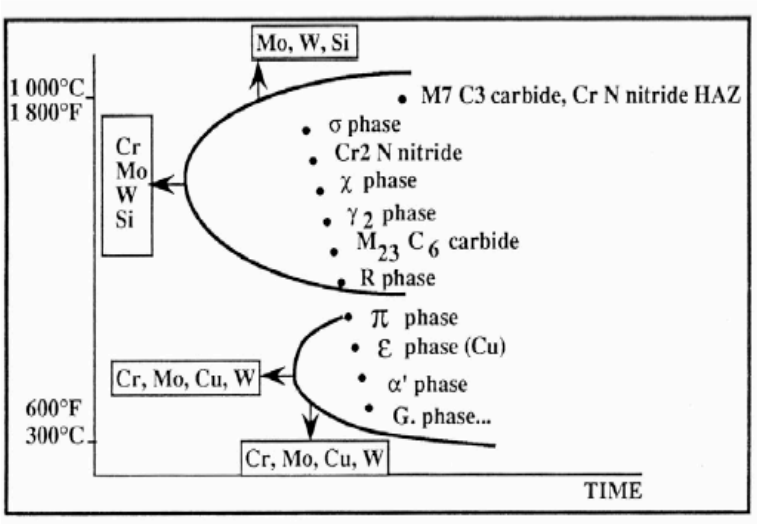


***Figure 2.3:*** ***Isothermal cooling curve for the ternary Fe-Cr-Ni system showing possible precipitates that can form upon cooling [2].***

Precipitates and secondary phases can reduce the fracture toughness and thereby increase the susceptibility of DSS to general corrosion and SCC in certain environments. In the temperature range of 300 – 600 $^{o}$C, DSS can also undergo spinodal decomposition of the ferrite phase into a Cr-rich α' and Fe-rich α phase, which is known as "475 $^{o}$C embrittlement" [28]. The formation of this phase has been associated with enhanced corrosion susceptibility in chloride solution [29]. Bhattacharya [30-31] also showed that the α' phase rendered the ferrite phase of grade S32205 susceptible to transgranular SCC

in caustic solutions when the ferrite content was approximately 50 % volume fraction. Intergranular SCC caused by the α' phase was observed in S32205 samples when ferrite content was increased to 60 % volume fraction.

Phase transformations can result in the formation of chromium nitrides and chromium carbides as well as a number of intermetallic phases when exposed to temperatures between 600 - 1000 $^{o}$C. The sigma phase has been the subject of most studies. A number of researchers have shown that the sigma phase consumes Cr and Mo from the matrix, providing favorable conditions for SCC. Perren and co-workers [10-11] studied the electrochemical behavior of individual micron-sized features using a microcell technique. These researchers were able to determine the corrosion behavior of the single austenite and ferrite phases as well as the detrimental influence of the sigma phase, chromium nitrides, and secondary austenite on the corrosion resistance of a super DSS in a dilute chloride solution. Dominquez-Aguilar et al [32] have also shown the role of deleterious phases (chromium nitride, chi, and sigma) in chloride solutions using an anodic galvanostatic polarization technique. Conversely, sigma and chi phase were shown to have a negligible effect on SCC initiation in simulated pulping liquor [30-31] showing the strong influence of environment.

### 2.2.3 Mechanical Behavior of Individual Phases

Many mechanical and physical properties describing the macroscopic behavior of DSS, such as yield and ultimate tensile strength, fatigue resistance, fracture toughness, and corrosion resistance, varies widely for different material forms. Processing of DSS can influence the properties of the individual phases resulting in inhomogeneous or anisotropic behavior. The load sharing capacity of the austenitic and ferritic phases,

residual microstresses, crystallographic orientation, and substructural features can also affect the localized stress distribution [33-45].

The two phases of DSS have different coefficients of thermal expansion (CTE) hence thermal microstresses are introduced during cooling from an elevated temperature [33-36]. Silberschmidt and Werner [35] demonstrated that an irreversible, plastic deformation occurs during cooling and heating cycles conducted in the 20 – 900 $^{o}$C temperature range. Siegmund et al [34] determined that the CTE for the austenite and ferrite phases were approximately 15.8 X $10^{-6}$ and 11.6 X $10^{-6}$ $^{o}C^{-1}$, respectively. The CTE mismatch results in compressive stresses in the ferrite phase and tensile stresses in the austenite phase, thereby providing a favorable condition for crack initiation. The difference in CTE contributes to a highly anisotropic microstructure.

Owing to the complexity of the stress state between the two phases, micromechanical modeling in conjunction with experimentation was used to determine the role of CTE mismatch on the deformation behavior of DSS. Johansson et al [36] used X-ray diffraction to study the load sharing capacity of the two phases and the evolution of micro- and macrostresses during cyclic loading of lean grade S32304. The cyclic loading response of the material was controlled by the plastic properties of the austenite phase, which had a larger extent of permanent deformation, and a higher hardness and yield strength than the ferritic phase. Larger load transference to ferrite phase resulted from the compressive residual stresses, which increased fatigue life resistance.

Alignment of the individual phases, e.g. texture, during rolling operations may further lead to preferential orientations in both phases, which causes anisotropy in the mechanical behavior of these materials [37-39]. Hutchinson et al [37] showed that DSS

sheet processed by hot and cold rolling underwent texture strengthening due to reinforcement of the ferrite matrix by a continuous and harder austenite phase. Ul-Haq et al [38-39] have shown that tensile deformation caused texturing in the austenite and ferrite phases. The degree of deformation of the respective phases was also shown to be dependent on the deformation direction [38]. Texturing effects were more pronounced for the ferrite phase than the austenite phase. These texture effects did not significantly alter the elastic properties, but acted to reduce the stress concentrations in the ferrite phase by adopting lower energy configurations.

Substructural features such as dislocation interactions, substructure development, and stacking fault energy (SFE) have also been studied [40-45]. The substructural changes that DSS experience during deformation have been evaluated using transmission electron microscopy [40]. The SFE of the austenitic and ferritic phases has been shown to be a critical feature for SCC. The body-centered cubic (bcc) ferrite phase has a high SFE and many slip systems, which are only activated by thermal effects. The face-centered cubic (fcc) austenite phase is more ductile than the bcc ferrite phase because the slip systems of the fcc phase consist of close-packed planes and are activated at lower temperatures. Reick et al [42] showed that the austenite phase underwent more strain hardening, had a more homogeneous dislocation distribution, and contained a higher incidence of stacking faults after cold deformation. Polak et al [40] also studied the dislocation substructure of fatigued DSS and found a complex dislocation structure for the austenitic phase. The austenite phase has an unusual strain-hardening response because of its stacking fault energy, ability to form deformation twins, and tendency to

form planar dislocation structures. Collectively, these features of the fcc austenite phase can strongly influence the SCC behavior of DSS.

## 2.3 Stress Corrosion Cracking

A number of models have been developed to explain SCC initiation and growth in stainless steels in select environments. The following section will provide an overview of the fundamental topics required to understand SCC. The factors that influence SCC and the associated dissolution and mechanical fracture models will be described.

### 2.3.1 General Definition

SCC results from the conjoint interaction of a corrosive environment, a susceptible material, and an applied or residual stress. The susceptibility is further influenced by the rate of solution renewal, oxide rupture, and passivation at the crack tip as shown in Figure 2.4 [3]. There are thus many interdependent variables that influence whether or not a particular material will become susceptible in a corrosive environment. Furthermore, the cracking process can proceed along grain boundaries (intergranular SCC) or through grains (transgranular SCC) as shown in Figure 2.5, but the crack always follows a general macroscopic path that is normal to the tensile component of the stress. Crack growth may also occur through both mechanisms depending on the metallurgical condition and thermal history of the alloy [3].

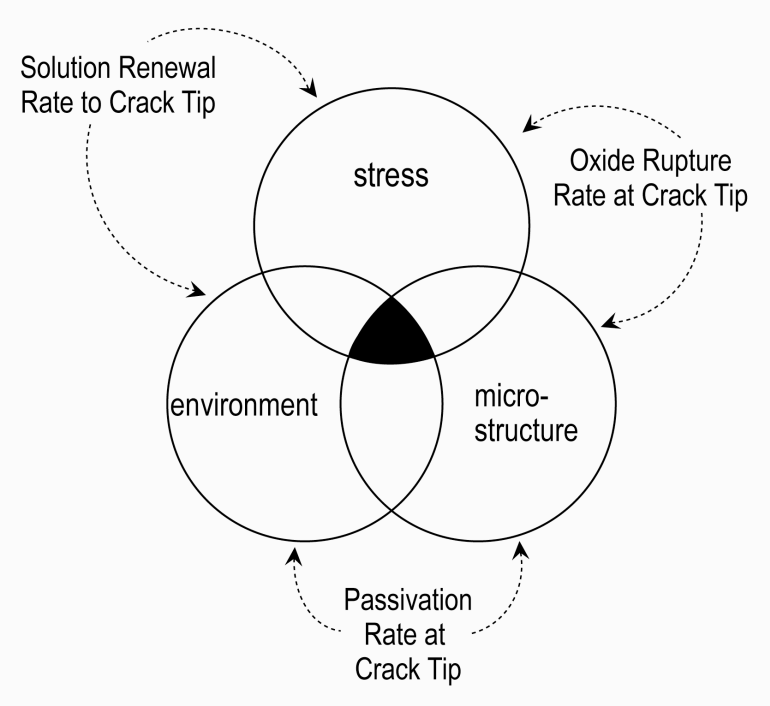


***Figure 2.4:*** ***Schematic showing the interdependence of environmental, metallurgical, and stress conditions required for stress corrosion cracking [3].***

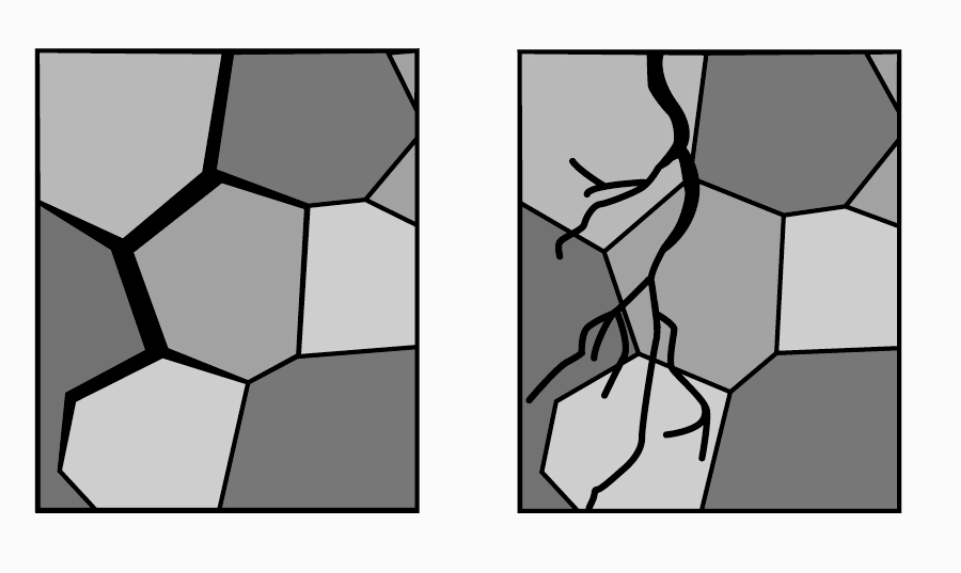

(a) (b)

***Figure 2.5:*** ***Schematic of (a) intergranular stress corrosion cracking and (b) transgranular stress corrosion cracking.***

The onset of SCC requires the formation of a protective passive film on the metal surface that forms at critical electrochemical potentials [3]. Figure 2.6 shows the schematic potentiodynamic anodic polarization curve for a typical active-passive alloy with the different zones that correspond to SCC [46]. The two zones of susceptibility appear at the potential boundaries where the passive film is less stable. In Zone 2, SCC and pitting are present as has been observed for austenitic stainless steel in $MgCl_2$ solutions [46]. SCC can also occur in Zone 1 under active conditions when the passive film is defective and passivation is difficult. SCC in Zone 1 has been observed for carbon steel in strong caustic solutions [47]. Anodic current densities decrease with time, thus film formation and growth is likely present even in the active potential range. Other factors (pH, dissolved oxidizers, aggressive ions, inhibitors) can also influence the anodic polarization behavior.

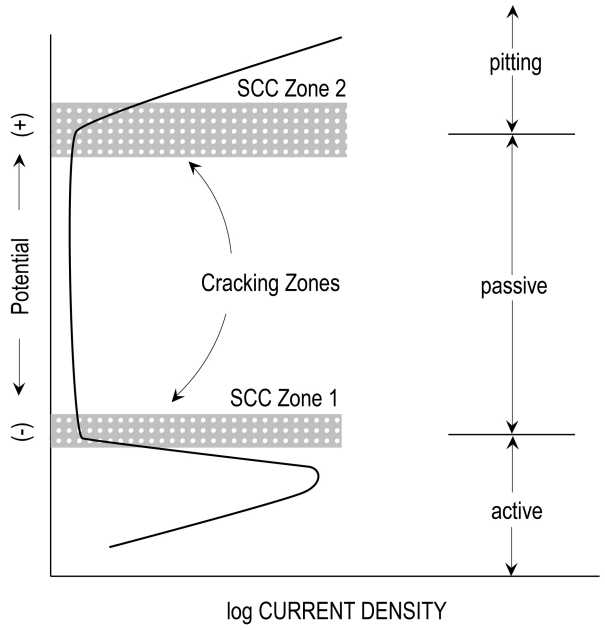


***Figure 2.6:*** ***Schematic anodic polarization curve showing zones of susceptibility to stress corrosion cracking [46].***

A fracture mechanics approach has commonly been used to study the critical mechanical features of the crack propagation processes in SCC as well as a complementary process, corrosion fatigue, whereby the crack growth behavior is controlled by a cyclic load in lieu of a sustained load. Threshold stress intensities and stresses, the presence of a stress-independent crack growth regime, and a dependence of crack growth rate on strain rate are common features of both processes. Crack growth behavior is typically divided into several stages. The relationship between subcritical crack propagation rate and stress-intensity for mode I loading (tensile) is demonstrated for each stage in Figure 2.7 [3]. The conditions that are required for crack initiation incubation and crack propagation of a stress corrosion crack are complex because of the conjoint effect of chemical and mechanical processes, and the stress at which crack growth will occur depends on the particular environmental conditions. An important aspect of SCC behavior is the critical stress intensity factor for SCC, $K_{1SCC}$, which is a function of the crack geometry and applied stress. For stress intensities less than $K_{1SCC}$, SCC will not occur. When the stress intensity exceeds this critical value, crack growth will proceed, eventually leading to sudden fracture at $K_{1C}$.

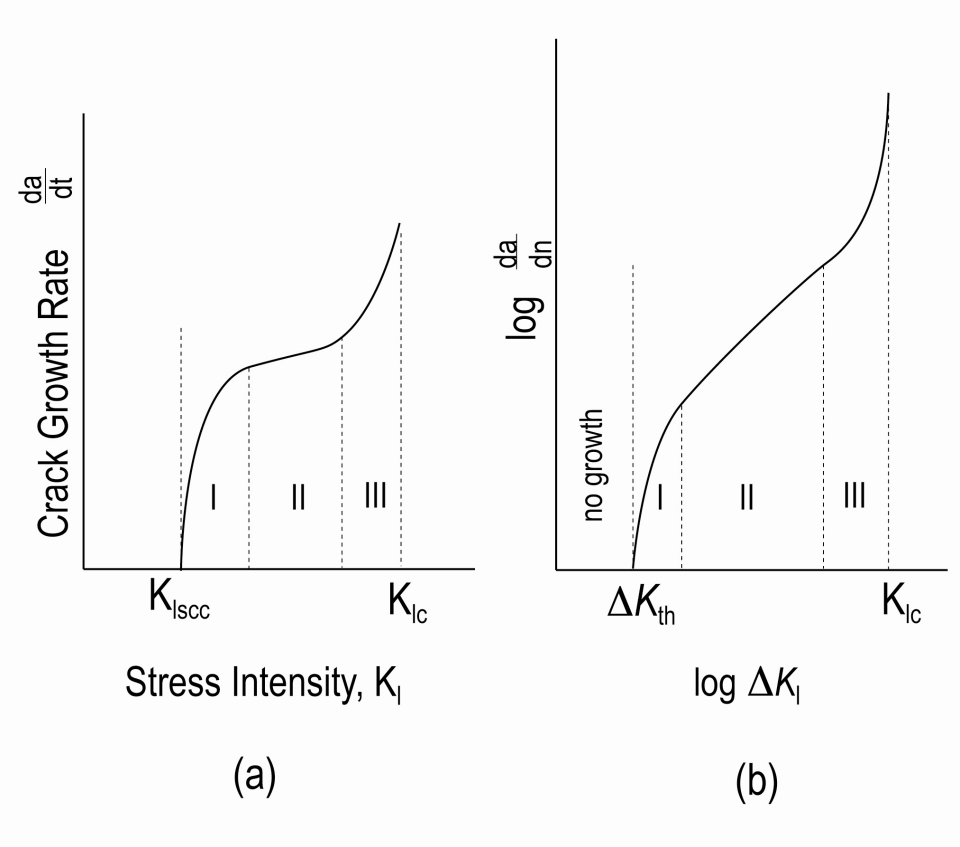


***Figure 2.7:*** ***Schematic showing variation of crack growth rate (a) with stress intensity factor during a stress corrosion cracking test and (b) per stress cycle during a corrosion fatigue test [3].***

### 2.3.2 Existing Models for SCC

Many studies have evaluated the corrosion and SCC behavior of stainless steels in caustic environments [12-14, 30-31, 48-72]. Austenitic stainless steels are more susceptible than ferritic stainless steels with equivalent chromium content in caustic media [46]. Researchers have proposed numerous dissolution and mechanical fracture models [73 – 83] to explain the SCC phenomenon in a number of alloy-environmental systems: slip-step dissolution model or active-path model, corrosion tunnel model, tarnish-rupture model, film-induced cleavage model, adsorption-induced brittle fracture, and hydrogen embrittlement. No single mechanism of SCC can explain the interaction of

the environment, material, and applied or residual stress in every alloy-environment combination; indeed, several operative mechanisms may be acting simultaneously. The various models for SCC mechanisms will be explored further in the following section.

#### 2.3.2.1 Anodic Dissolution Models

Dissolution models [73, 78] such as film rupture [78] (Figure 2.8) assumes that crack advancement is facilitated by preferential dissolution at the crack tip. Preferential dissolution at the crack tip has been attributed to the formation or existence of active paths in the material, stresses at the crack tip, and mechanochemical interactions. The slip-step dissolution model [73] shown in Figure 2.9 has received serious consideration for various systems and is based on the film rupture model. This model assumes that stresses act to open the crack and rupture the protective surface film. Considerable evidence supports an active dissolution mechanism for intergranular SCC; however, the observation of discontinuous cracking and crack arrest markings is an indication that the crack propagation process is not continuous. Furthermore, TGSCC fracture surfaces are flat, crystallographically orientated, and match on opposite sides of the fracture surface, which indicates that there is limited dissolution during crack advance.

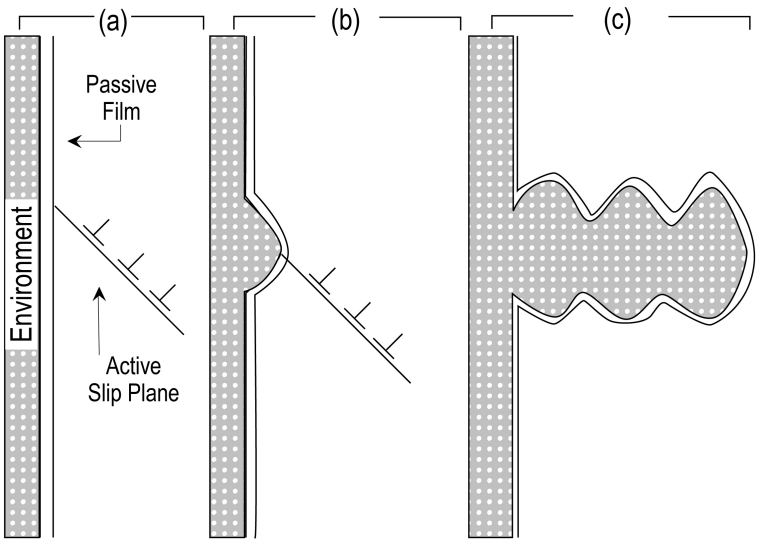


*Figure 2.8:* ***Schematic showing the film rupture model for stress corrosion cracking. (a) Slip is initiated at film-metal interface, (b) dissolution facilitates crack initiation, and (c) crack grows through discontinuous film growth and rupture [78].***

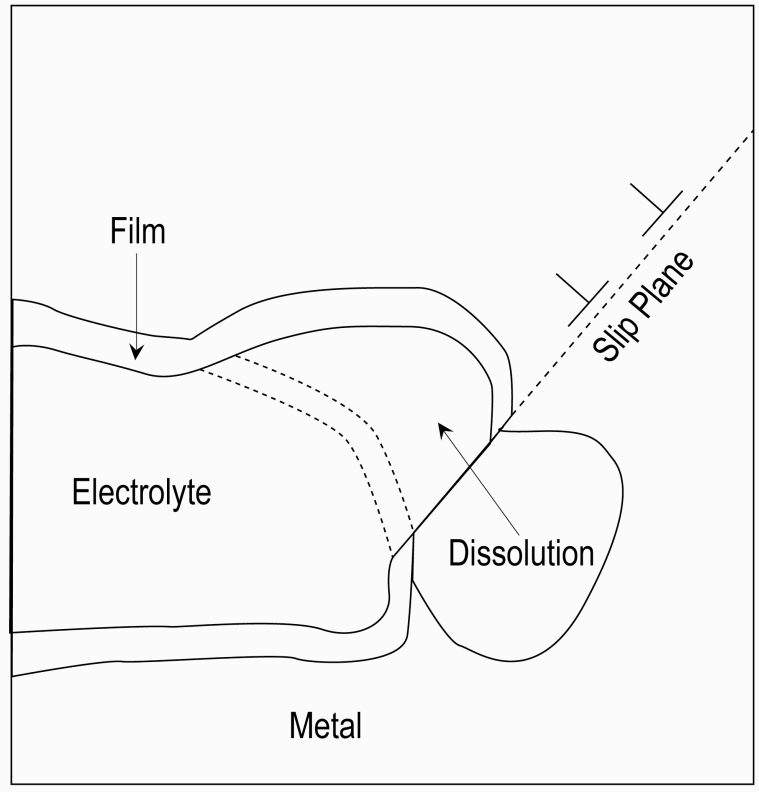


*Figure 2.9:* ***Schematic showing the slip dissolution model for stress corrosion cracking [73].***

TGSCC is widely thought to propagate by discontinuous brittle fracture (cleavage), but there is some evidence to support a mechanochemical dissolution mechanism in austenitic stainless steels. Early work on mechanochemical anodic dissolution [83] showed that 18 Cr-8 Ni stainless steel tested in 42 wt% MgCl solution underwent a large increase in the anodic current density in the presence of plastic deformation. The authors attributed this effect to the arrival of dislocation pile-ups produced by restricted slip at the crack tip, thereby producing more active sites at the dissolving surface. Zheng et al [76] showed that 316L stainless steel experienced a mixed, intergranular and transgranular failure at intermediate potentials in a hot lithium hydroxide solution and concluded that anodic dissolution occurred at either slip-steps or grain boundaries due to transpassive anodic dissolution of chromium. Gutman [74] studied 316L stainless steel in acidified sodium sulfate and demonstrated an increase the anodic current density as a function of plastic deformation, attaining a maximum during the strain hardening stages of deformation. Newman [78] evaluated 3% CrMo steel in a hot concentrated sodium hydroxide and attributed slower crack propagation rates at cathodic potentials to a slip-step dissolution mechanism. The slip-step dissolution model has been presented in more detail elsewhere [3-4].

#### 2.3.2.2 Mechanical Fracture Models

A number of mechanical fracture models have been proposed to explain intergranular and transgranular mechanisms of SCC. The models that have been most commonly associated with discontinuous, TGSCC of stainless steels are film-induced cleavage, hydrogen embrittlement, and corrosion-enhanced plasticity.

*2.3.2.2.1 Film-Induced Cleavage*

Sieradzki and Newman [81-82] have proposed that TGSCC in ductile, fcc materials is attributed to a film-induced cleavage mechanism. There has been empirical and analytical evidence to support this model, whereby TGSCC occurs via a series of discontinuous, microcleavage events. Each event is triggered by a thin, brittle surface film or de-alloyed layer of several hundred nm in thickness, which has formed at the crack tip due to an anodic process. A crack initiates in this brittle surface layer and propagates across the film-matrix interface with little loss in velocity, and continues to grow into the ductile material until it eventually blunts and arrests. A schematic of this model is shown in Figure 2.10.

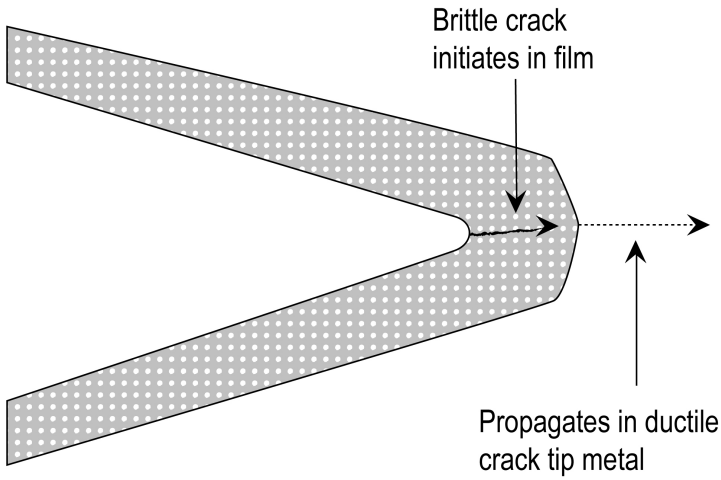


***Figure 2.10:*** ***Schematic showing the film-induced cleavage model for stress corrosion cracking.***

The film-induced cleavage model has widely been used to explain SCC behavior in a number of Cu alloy systems (Cu-Zn, Cu-Au, Ag-Cu, Cu-Al, and Ag-Cd) [79-82] and stainless steel [69]. De-alloying (selective dissolution) occurs in solid solutions or intermetallic compounds where there is a large difference in the reactivity between the alloying elements. The compositional dependence of SCC in Cu-Al and Cu-Zn alloys has been shown to correlate exactly with the compositional dependence of de-alloying the less noble metal element from these alloy systems [79]. For example, transgranular SCC in Cu-Al and Cu-Zn occurs when the solute (Zn or Al) is less than about 20 at. %. A critical Fe/Ni ratio of approximately 1.3 has been found for type 316 stainless steel alloys exposed to concentrated sodium hydroxide solution. Chromium was mostly dissolved or reprecipitated during the process, resulting in a solid solution of intermediate composition. The removal of only half the Fe explains the existence of a connected nanoporous network. Evidence of a de-alloyed layer was also found on type 304 stainless steel exposed to sodium hydroxide [69]. The compositional dependence increases the planar dislocation distribution, reducing the SFE. The compositional dependence was explained via percolation theory, whereby a continuously-connected pathway of solute atoms is selectively dissolved out the noble matrix.

*2.3.2.2.2 Hydrogen Embrittlement*

Cathodic hydrogen has been known to cause TGSCC in many material-environment combinations [83-104]. Experimental data shows that hydrogen-induced crack growth is involved in the SCC mechanism for ferritic steels, nickel-base alloys, aluminum alloys, and intermetallic compounds. Specific mechanisms of hydrogen-induced subcritical crack growth have not been developed. The macroscopic observations

have shown a reduction in elongation and fracture toughness, inducing a change in the fracture morphology from ductile to brittle failure. The hydrogen influence on flow stress in pure iron has yielded mixed results; a decrease in the flow stress has been found in several studies, while an increase has been observed in others [83]. It is generally agreed that hydrogen enhances dislocation mobility.

The prevailing mechanisms used to explain the effect of hydrogen on the macroscopic material behavior are the hydrogen-induced de-cohesion (HID) [84] and hydrogen-enhanced localized plasticity (HELP) [85] models. In the hydrogen embrittlement process, hydrogen ions present on the crack tip surface combine with an electron to form cathodic hydrogen. The hydrogen then diffuses into the material at the crack tip and acts to dilate the lattice, thus reducing the ductility of the exposed material as shown in Figure 2.11.

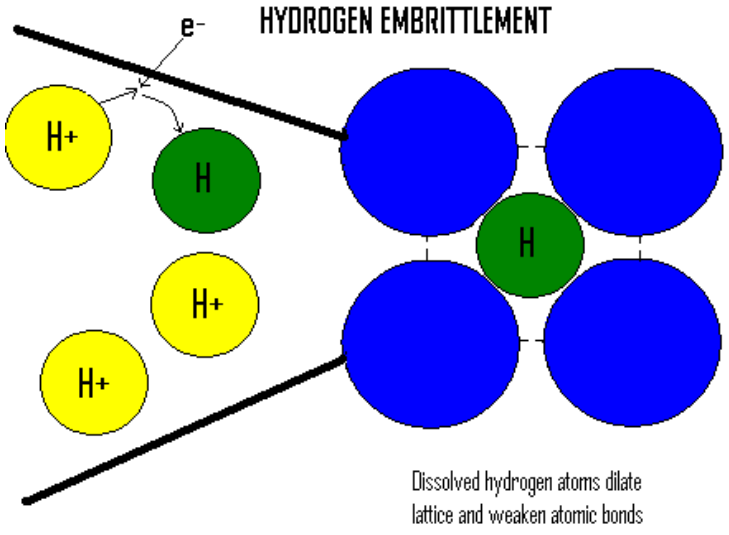


***Figure 2.11:*** ***Schematic showing the hydrogen embrittlement model for stress corrosion cracking.***

The corrosion enhanced plasticity model [86] describes localized plasticity at the crack tip arising from anodic dissolution and localized hydrogen entry in ductile, fcc alloys. The coupled effect of an anodic dissolution process and a hydrogen absorption process has been able to explain the discontinuous cleavage-like fracture observed during SCC of austenitic stainless steels, copper alloys, aluminum alloys, and pure copper. This model supposes that a slip-step initiates at the crack tip because of localized anodic dissolution. Localized plasticity is then enhanced at {111} slip planes because of is favored dissolution and absorption of hydrogen. Plasticity is localized near the surface, which emits dislocations that interact with obstacles (grain boundaries, precipitates, dislocation networks) in front of the crack tip, forming pile-ups that act increase the local stress. A crack embryo then forms if the localized stress exceeds $K_{1C}$. The energy of de-cohesion of the {111} microfacets decreases, opening the crack on the {111} plane and causing further emission of dislocations. Depending on the crystallographic orientation, cracks may also grow on the {100} or {110} facets leading to a regular zigzag microcracking.

A few authors have proposed that hydrogen could enhance SCC susceptibility of stainless steels in caustic solutions [53, 83]. Hydrogen absorption in alkaline solutions may be enhanced by the presence of S-containing compounds, which are a known catalyst poison [93-95], preventing nascent hydrogen from recombining on the sample surface, thereby promoting hydrogen absorption. Only 1 ppm of sulfide ions was required to enhance the severity of HE of DSS in artificial seawater [98]. Rondelli et al [53] asserted that hydrogen could play an important role in the crack propagation process of grade S32205. At the open circuit potentials (OCP) in the 300 g $l^{-1}$ sodium hydroxide and

20 g $l^{-1}$ of $Na_2S$-9*$H_2O$ solutions that were studied, hydrogen was the only possible cathodic reaction. The SCC susceptibility increased with decreasing strain rate, which is indicative of a hydrogen mechanism. SCC susceptibility was also enhanced in the presence of sulfide ions. Zakroczymski et al [87] studied UNS S31803 (DSS 2205) in 100 g $l^{-1}$ sodium hydroxide solutions under cathodic polarization and found a significant loss of ductility. Conversely, there is considerable data that is contrary to a hydrogen embrittlement mechanism in caustic solutions [83].

Hydrogen transport of different grades of DSS has been studied in various solutions using the Devanathan and Stachurski method [88]. Hydrogen effects have been shown to be more detrimental to the ferrite phase and austenite/ferrite interfaces than the austenite phase [87]. The permeability and diffusivity of the ferrite phase is much greater [3]. Moreover, the hydrogen microprint technique developed by Perez and Garcia [90] has been used by Chen et al [91] to show a greater distribution of hydrogen in the ferrite phase. Researchers have also shown that the extent of cold working (i.e. higher dislocation density) decreases the effective hydrogen diffusivity and increases the effective permeability through the generation of trapping sites, which increases the susceptibility to hydrogen degradation [92].

*2.3.2.2.3 Other Mechanical Models*

There are other mechanical fracture models for SCC, which include the corrosion tunnel, tarnish rupture, and adsorption-induced brittle fracture models; however, experimental evidence for these models remains limited [3]. The corrosion tunnel model supposes that a fine array of small corrosion tunnels form at emerging slip-steps, which grow until the remaining ligaments cause fracture. Cracks propagating via this

mechanism should result in grooved fracture surfaces with evidence of microvoid coalescence on the peaks. The absorption-enhanced plasticity model concludes that the continuous fracture process results from chemisorption, which would result in the formation of small voids as well as slip bands ahead of the crack tip. In the tarnish-rupture model, the crack propagates by alternating brittle film growth and fracture. Crack arrest-markings on intergranular fracture surfaces and discontinuous acoustic emission during crack propagation would confirm this model. The adsorption-induced brittle fracture is similar to hydrogen embrittlement, whereby the absorption of environmental species lowers the interatomic bond strength and the stress required for cleavage fracture. This model supposes that crack grow in a continuous manner at a rate that is proportional to rate of embrittling species arriving at the crack tip. Collectively, the mechanical fracture models share many similarities [3].

## 2.4 Effect of Environment on SCC of DSS

### 2.4.1 Effect of Potential and Solution pH

The effect of environment on the corrosion and SCC susceptibility of DSS in alkaline environments will be a strong function of the film that forms under high pH, reducing conditions. The E-pH diagrams [105] (Pourbaix) provide thermodynamic predictions for the stability of species that can form at a given temperature, pH, and potential. These diagrams are useful for predicting the compounds in the passive film. These diagrams assume that insoluble compounds stable in any system will form a protective film at the surface and describe the conditions at which film formation and metal oxidation will occur. Environmental parameters such as pH, oxygen concentration, and temperature, can be related to the thermodynamic conditions with these diagrams.

For example, the stability of water can readily be determined by the hydrogen (2.1) and oxygen evolutions (2.2) reactions:

$$2H_2O + 2e^- = H_2 + 2OH^- \quad (2.1)$$

$$E_{H_2/H_2O} = -0.059\,pH$$

$$O_2 + H_2O + 4e^- = 4OH^- \quad (2.2)$$

$$E_{O_2/H_2O} = +1.229 - 0.059\,pH$$

The E-pH diagram for iron species in the Fe-Cr-Ni-$H_2O$ system at 25 $^oC$ is shown in Figure 2.12 [106]. This diagram illustrates the effect of changing the pH (x-axis) and oxidation potential versus standard hydrogen electrode (SHE) (y-axis) on the stability of spinel oxides trevorite ($NiFe_2O_4$) and chromite ($CrFe_2O_4$), which have the lowest solubility under the evaluated conditions. A decrease in the pH at fixed potential results in a shift of iron from a region of stability to one of active corrosion. Susceptibility to corrosion generally decreases at higher pH because of the increased stability of the passive film. Oxygen concentration generally alters the electrode potential, with increasing oxygen concentration resulting in more oxidizing conditions. The effect of temperature on the diagram needs to be evaluated at each value of interest.

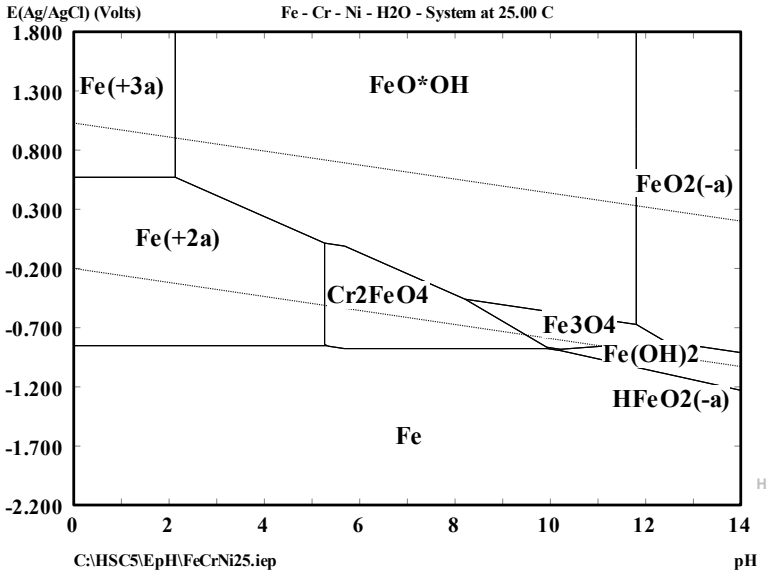


*Figure 2.12:* ***E-pH diagram for the dominant Fe species in the Fe-Cr-Ni system at 25 $^{o}$C [106].***

### 2.4.2 Effect of Ionic Species on Corrosion and SCC

The kraft process makes use of a number of corrosive solutions, particularly white liquor. Pulping liquor composition was evaluated previously [107-108]. White liquor contains sodium sulfide, sulfate, sodium thiosulfate, sodium carbonate, and sodium hydroxide. Additionally, sodium chloride may be present as an impurity that can originate from the local water supply or from the wood chips. There are many chemical species available for SCC in a typical pulping mill. To simplify this environment for research, simulated white liquors are typically composed of the most aggressive species, sodium hydroxide and sodium sulfide.

Bhattacharya et al [31] evaluated the general corrosion and SCC susceptibility of DSS S32205, S32101, S32304, and S32003 in different simulated pulping liquors. The corrosion rates and SCC susceptibility increased with increasing temperature, and the threshold temperature for SCC was lower in the lean grades. All of the grades of DSS

that were evaluated were found to be susceptible to SCC in liquors having 3.75 M NaOH + 0.64 M $Na_2S$ at temperatures above 170 $^oC$. Figure 2.13 shows cracking of a grade S32101 sample that experienced crack initiation in the austenitic phase at 170 $^oC$.

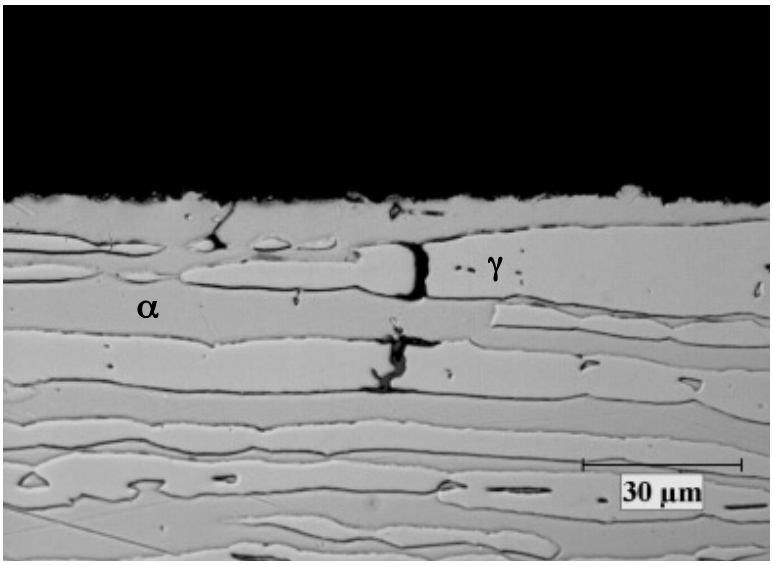


***Figure 2.13:*** ***Stress corrosion cracks in lean grade DSS S32101 sample tested in simulated white liquor at 170 $^oC$. Crack propagation occurs in austenitic phase (γ) [31].***

Other studies have investigated the general corrosion and SCC resistance in alkaline-sulfide solutions. Singh et al [57] compared the corrosion behavior of DSS grades S32205 and S32304 to carbon steel and austenitic stainless steel in different solution compositions. Austenitic and DSS were more resistant to general corrosion than carbon steel 516-Gr70. All of the steels in the study were found to be susceptible to SCC above 170 $^oC$. The maximum crack velocities in the DSS were two orders of magnitude lower than the carbon steel. Cracks have also been found in and near the welding zone in several DSS batch digesters exposed to pulping liquors [31]. Leinonen et al [55] reviewed the SCC behavior of welded grade S32205 material in simulated batch cooking liquor as well as an industrial digester at 170 $^oC$. The susceptibility to SCC was increased in the

welded region. Crack initiation and propagation occurred in the austenitic phase or the interface between the weld metal and heat affected zone. The severity was found to increase with increasing austenite content. Bhattacharya et al [31] found similar results as shown in Figure 2.14. The severity of SCC and degradation of mechanical properties were found to increase as a function of temperature.

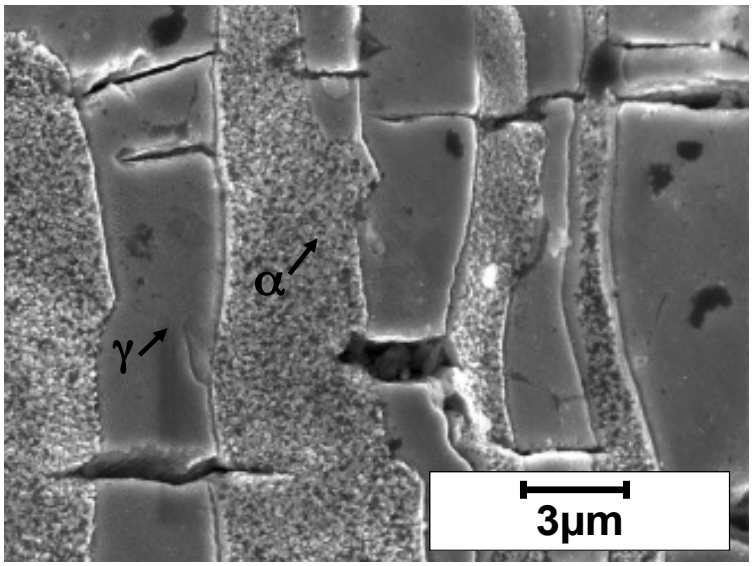


***Figure 2.14:*** ***Fractography showing crack initiation sites in the austenite phase (γ) in S32205 welded specimen tested in simulated white liquor at 200 $^{o}$C [31].***

The mechanism of SCC of DSS has widely been studied in chloride-containing environments [100, 108-112]. Singh et al [108] studied heat-treated cast duplex stainless steel (similar to UNS J93372) used in white waters, which is a waste solution emanating at the end of the paper machine that contains chloride and thiosulfate ions. Crack initiation in these environments occurred by pitting within ferrite grains or near ferrite grain boundaries. Pitting has not been observed in caustic solutions. Tsai and Chou [100] studied grade 2205 in a 26 wt % NaCl solution and found that the ferrite phase was less resistant to SCC as shown in Figure 2.15. In the absence of a sensitized microstructure,

SCC in austenitic stainless steels in hot 42 % MgCl solution was found to nucleate at slip-steps and propagated in a transgranular mode [109] showing that chlorides may also cause SCC of the ferrite phase of DSS under certain conditions.

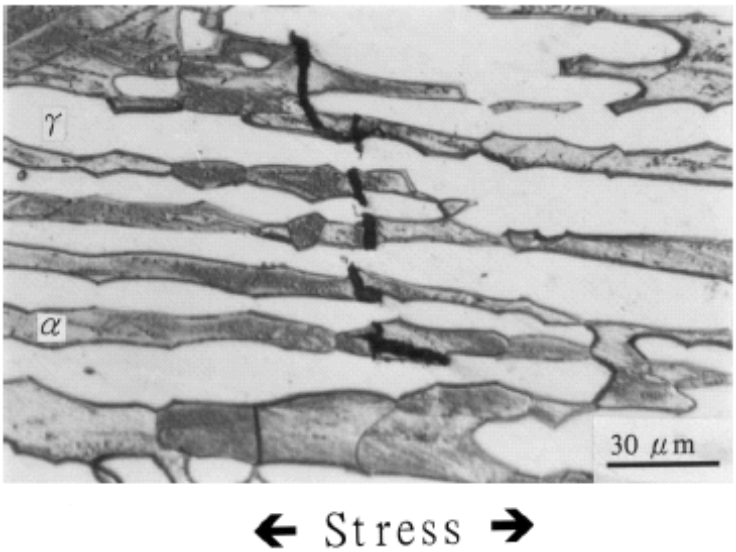


***Figure 2.15:*** ***Micrograph showing cracks in the ferrite phase (α) of DSS S32205 tested in 26 wt% NaCl solution [100].***

DSS components are also susceptible to SCC in sour environments containing hydrogen sulfide ($H_2S$), which are common to the oil and gas industries [113-115]. In sour environments, the SCC failure occurred at ferrite/austenite interfaces or the interior of ferrite grains. The failure in this environment proceeded by a combination of repetitive slip-step emergence accompanied by anodic dissolution and a cathodic hydrogen embrittlement process. Temperature has a dramatic effect on the occurrence of SCC in sour environments.

Laboratory and field experience [49-51, 68] have shown that DSS are susceptible to general corrosion and SCC at elevated temperatures in solutions containing $Cl^-$ and $S^{2-}$ ions. SCC occurs in a wide range of environments containing more than one corrodent,

namely chlorides, sulfides, or hydroxides. The combined effect of multiple corrodents can have an extraordinary effect on the SCC behavior. SCC behavior of carbon steel and austenitic stainless steel in complex, multiple corrodent solutions has been well known for decades [4]. In many chemical process streams, chlorides are always present in limited amounts as non-process elements and are a concern for the reliability of alloys. More stringent environmental regulations have caused many chemical processing plants to conserve or re-use water resources, resulting in increased chloride contamination [108]. Chloride contamination in alkaline solutions may become a concern under certain conditions where pH or temperature fluctuations can influence the stability of the protective films formed on the surface of equipment, facilitating either localized corrosion or SCC. The effects of chloride concentration on the corrosion susceptibility of DSS have widely been studied in acidic or near neutral environments [108-112]. Few studies have sought to determine the role of chlorides in alkaline environments.

Recent field experience [68] showed that elevated chloride content (~1.0%) in a heavy black liquor tank constructed of DSS S32205 resulted in accelerated corrosion and SCC. Several techniques have been used to study the corrosion behavior of DSS in alkaline-sulfide solutions containing chloride. Wensley et al [12] evaluated the corrosion rate and corrosion potential of several austenitic and DSS used in industrial white and black liquors. The results showed that increasing the Cr content above 25 wt. % was necessary for enhanced corrosion resistance, and the austenitic phase was attacked preferentially in the standard DSS S32205 and super DSS S32705 at potentials more noble than the corrosion potential. Wensley and Champagne [13] have also shown that sulfidity did not play a strong role on the corrosion susceptibility of stainless steel (UNS

S30403, S32304, S31803) in the white, green, and black liquors containing limited amounts of chlorides that were tested. Rämo et al [64] studied the corrosion behavior of grades UNS S30400, S31603, S32205, and S32304 in simulated and industrial liquors containing hydroxide, sulfur anions, carbonates, and chlorides. Their work showed that hydroxide content was found to correlate linearly with the adhesion of sulfur onto the steel, whereby hydroxide enhanced the sulfur-rich film formation on stainless steel surfaces. Adhesion of sulfur onto surfaces increased in the order S32304, S32205, S30400, and S31603. Bhattacharya [31] evaluated pitting corrosion of standard grade DSS S32205 and lean grade DSS S32101 in low pH (pH~0.5) acidic solution containing ferric-chloride ($FeCl_3$) and high pH (pH~12.5) caustic solution containing $Na_2S$. Selective corrosion of the ferrite phase was apparent at low pH in the presence of chloride ions, but at high pH the materials were immune to localized corrosion. The concentration of ionic species and their relative ratios will therefore influence the corrosion and SCC susceptibility in alkaline-sulfide solution.

## 2.5 Summary

The capacity to accurately predict the failure of DSS components in kraft pulping environments requires understanding of the following interdependent controlling variables:

- Metallurgical features (composition, microstructure, and fabrication history)
- Mechanical loading condition (stress intensity at the crack tip, extent of deformation, and rate of deformation)

- Environmental parameters (ionic concentrations of anions, temperature, presence of oxidizing agents, concentration of organic constituents, and potential)

The absolute and relative concentrations of anions (i.e., $OH^-$, $S^{2-}$, and $Cl^-$) in hot alkaline pulping liquors will influence the corrosion and SCC susceptibilities of DSS. The susceptibility of the individual phases of DSS will depend on the formation of a stable passive film in the presence of sulfide and chloride. Thermo-mechanical processes during fabrication of DSS will result in anisotropy in the banded structure of austenite islands in a ferrite matrix. The relative phase ratio and distribution of the austenite islands in the ferrite matrix will vary depending on the fabrication history. The propensity for crack initiation in a particular plate orientation and growth along favorable paths will depend on the environment. Composition, residual stress state, and mechanical properties of the individual phases will also have an important role on SCC crack initiation and growth behavior. Hydrogen embrittlement may influence SCC of DSS if the conditions are thermodynamically favorable at the crack tip.

## 2.6 REFERENCES


[1] Schaeffler, A.L. 1949. Constitution diagram for stainless steel weld metal. Metal Progress 56(11):680 - 680B.

[2] J. Charles, "The Duplex Stainless Steels: Materials to Meet Your Needs", Duplex Stainless Steels, Vol. 1, 1991, pp. 3-48.

[3] R.H. Jones, "Stress-Corrosion Cracking," ASM International, 1992.

[4] D.A. Jones, Principles and Prevention of Corrosion, Prentice Hall, 1996.

[5] J. Nilsson, "Super Duplex Stainless Steels," Materials Science and Technology, vol. 8, 1992, pp. 685-700.

[6] H.D. Solomon and T.M. Devine Jr, “Keynote Address: A Tale of Two Phases,” Duplex Stainless Steels (Conference Proceedings of the American Society for Metals), RA Lula (ed.), Metals Park, Ohio, vol. 44073, 1983, pp. 693-756.

[7] P. Combrade and J.P. Audouard, “Duplex Stainless Steels' 91, 28.±30.10. 1991, Beaune, Bourgonge, France, J,” S, pp. 257-270.

[8] L.F. Garfias-Mesias, J.M. Sykes, and C.D.S. Tuck, “The Effect of Phase Compositions on the Pitting Corrosion of 25 Cr Duplex Stainless Steel in Chloride Solutions,” Corrosion Science, vol. 38, 1996, pp. 1319-1330.

[9] M. Femenia, J. Pan, and C. Leygraf, “Characterization of Ferrite-Austenite Boundary Region of Duplex Stainless Steels by SAES,” Journal of the Electrochemical Society, vol. 151, 2004, p. B581.

[10] R.A. Perren et al., “Corrosion Resistance of Super Duplex Stainless Steels in Chloride Ion Containing Environments: Investigations by Means of a New Microelectrochemical Method I. Precipitation-free States,” Corrosion Science, vol. 43, 2001, pp. 707-726.

[11] R. Perren et al., “Corrosion Resistance of Super Duplex Stainless Steels in Chloride Ion Containing Environments,” Corrosion Science, vol. 34, 2001, p. 727-745.

[12] Wensley, A., Moskal, M., and Wilton, W., "Materials Selection for Kraft Batch Digesters," Corrosion/97, NACE Paper No. 378, 1997, Houston, TX.

[13] Wensley, A., and Champagne, P. NACE Corrosion, Paper No. 281, 1999, Houston, TX.

[14] Wensley, A., NACE Corrosion, Paper No. 589, 2000, Houston, TX.

[15] N. Sridhar and J. Kolts, “Corrosion 43 (1987),” p. 646.

[16] C.M. Tseng, H.Y. Liou, and W.T. Tsai, “The Influence of Nitrogen Content on Corrosion Fatigue Crack Growth Behavior of Duplex Stainless Steel,” Materials Science & Engineering A, vol. 344, 2003, pp. 190-200.

[17] K. Hashimoto, K. Asami, K. Teramoto,, An X-Ray Photo-Electron Spectroscopic Study on the Role of Molybdenum in Increasing the Corrosion Resistance of Ferritic Stainless Steels in HCl,”Corros. Sci. vol. 19, 1979, p. 251.

[18] H. Okamoto, The Effect of Tungsten and Molybdenum on the Performance of Super Duplex Stainless Steels, Proceedings of Application of Stainless Steel ’92, Stockholm, Sweden, Jernkontoret, 1992, p. 360.

[19] M. Femenia, J. Pan, and C. Leygraf, “Characterization of Ferrite-Austenite Boundary Region of Duplex Stainless Steels by SAES,” Journal of The Electrochemical Society, vol. 151, 2004, p. B581.

[20] F. El-Taib Heakal, A.A. Ghoneim, and A.M. Fekry, “Stability of Spontaneous Passive Films on High Strength Mo-containing Stainless Steels in Aqueous Solutions,” Journal of Applied Electrochemistry, vol. 37, 2007, pp. 405-413.

[21] G. Rondelli et al., “Effect of Alloy Element Contents on Caustic Stress Corrosion Cracking of Several Stainless Steels,” Werkstoffe und Korrosion, vol. 44, 1993, pp. 57-61.

[22] C.M. Abreu et al.,”Comparative Study of Passive Films of Different Stainless Steels Developed on Alkaline Medium,” Electrochimica Acta, Vol. 49, 2004, pp. 3049-3056.

[23] P. Crook, N. S. Meck and P. Houlle, “The Caustic Dealloying of Molybdenum-Bearing Nickel Alloys,” Eurocorr 2005, Paper O-645-F, 4-8 September 2006, Lisbon, Portugal.

[24] T.Amadou, A.Ben Rhouma, H.Sidhom, C.Braham, J.Ledion, "Influence of Thermal Aging on the Reactivity of Duplex Stainless Steel Surfaces," Metallurgical and Materials Transactions A, Volume 31A, pp. 2000-2015.

[25] T.H.Chen, K.L.Weng, J.R.Yang, "The Effect of High-temperature Exposure on the Microstructural Stability and Toughness Property in a 2205 Duplex Stainless Steel," Materials Science and Engineering A, Volume 338, 2002, pp. 259-270.

[26] K.L. Weng, T.H. Chen, J.R. Yang, "The High-Temperature and Low-Temperature Aging Embrittlement in a 2205 Duplex Stainless Steel," Bulletin of the College of Engineering, Issue 89, Oct. 2003.

[27] B. Josefsson, J.O. Nilsson, A. Wilson, “ Phase Transformations in Duplex Stainless Steels and the relation Between Continuous Cooling and Isothermal Heat Treatment ”,Duplex Stainless Steels, Vol. 1,1991, pp. 67-78.

[28] P.J. Grober, R.F. Steigerwald, JOM 29 (1977) 17.

[29] C.J. Park and H.S. Kwon, Mat. Chem. and Phys. 91 (2005) 355-360.

[30] A. Bhattacharya and P. Singh, “Effect of Heat Treatment on Corrosion and Stress Corrosion Cracking of S32205 Duplex Stainless Steel in Caustic Solution,” Met. and Mat. Trans. A 40A (2009), 1388-1399.

[31] A. Bhattacharya, ”Stress Corrosion Cracking of Duplex Stainless Steels in Caustic Solutions, Ph.D. Thesis, Georgia Institute of Technology, Atlanta, GA (2008).

[32] M.A. Domínguez-Aguilar and R.C. Newman, "Detection of Deleterious Phases in Duplex Stainless Steel by Weak Galvanostatic Polarization in Alkaline Solution," Corrosion Science, vol. 48, 2006, pp. 2560-2576.

[33] E. Werner, T. Siegmund, and F. Fischer, "A Computer Study of the Thermomechanical Deformation Behavior of a Duplex Steel," Computational Materials Science, vol. 3, 1994, pp. 279-285.

[34] T. Siegmund, E. Werner, and F.D. Fischer, "On the Thermomechanical Deformation Behavior of Duplex-type Materials," Journal of the Mechanics and Physics of Solids, vol. 43, 1995, pp. 495-532.

[35] V.V. Silberschmidt and E. Werner, "Analysis of Thermal Residual Stresses in Duplex-type Materials," Computational Materials Science, vol. 16, 1999, pp. 39-52.

[36] J. Johansson, M. Odén, and X.H. Zeng, "Evolution of the Residual Stress State in a Duplex Stainless Steel during Loading," Acta Materialia, vol. 47, 1999, pp. 2669-2684.

[37] Hutchinson, W.B., Ushioda, K., and Runnsjő, G., "Anisotropy of tensile behavior in a duplex stainless steel sheet," Mat. Sci. and Tech, Vol. 1 (1985), p.728.

[38] A. ul-Haq, H. Weiland, and H.J. Bunge, Mat. Sci. and Tech. 10 (1994) 289-298.

[39] A. ul-Haq, H. Weiland, and H.J. Bunge, J. of Mat. Sci. 29 (1994) 2168-2176.

[40] J. Polak, T. Kruml, and S. Degallaix, "Dislocation Structures in Fatigued Duplex Steel," Scripta Metall, vol. 29, 1993, p. 1553.

[41] L. Llanes et al., "Aging Effects on the Cyclic Deformation Mechanisms of a Duplex Stainless Steel," Acta Materialia, vol. 44, 1996, pp. 3967-3978.

[42] W. Reick, M. Pohl, and A.F. Padilha, "Recrystallization–Transformation Combined Reactions during Annealing of a Cold rolled Ferritic–Austenitic Duplex Stainless Steel," ISIJ International, vol. 38, 1998, pp. 567-571.

[43] W. Reick, M. Pohl, and A. Padilha, "Determination of Stacking Fault Energy of Austenite in a Duplex Stainless Steel," Steel Research, vol. 67, 1996, pp. 253-256.

[44] S. Fréchard et al., "AFM and EBSD Combined Studies of Plastic Deformation in a Duplex Stainless Steel," Materials Science & Engineering A, vol. 418, 2006, pp. 312-319.

[45] I.A. Yakubtsov, A. Ariapour, and D.D. Perovic, “Effect of Nitrogen on Stacking Fault Energy of fcc Iron-based Alloys,” Acta Materialia, vol. 47, 1999, pp. 1271-1279.

[46] R.W. Staehle et el, Stress Corrosion Cracking and Hydrogen Embrittlement of Iron Base Alloys, R.W. Staehle et al, eds. NACE-5, NACE, Houston, (1977) p. 193.

[47] R.N. Parkins, Proc. 5th Symposium on Line Pipe Research, Am. Gas Assoc. Arlington, VA (1974), P. U-1.

[48] A.K. Agrawal et al., “The Polarization Behavior of Fe-Ni-Cr Alloys in Concentrated Sodium Hydroxide Solutions in the Temperature Range 25° to 150° C,” Journal of The Electrochemical Society, vol. 119, 1972, p. 1637.

[49] M. Honda et al., “Stress Corrosion Cracking of Stainless Alloys in Alkaline-Sulfide Solutions.,” 1991.

[50] M. Honda, Y. Kobayashi, and A. Tamada, “Stress Corrosion Cracking of Stainless Alloys in Alkaline-sulfide Solutions,” Corrosion (USA), vol. 48, 1992, pp. 822-829.

[51] D. Singbeil and A. Garner, “Caustic Stress Corrosion Cracking of Pressure Vessel Steels in Dilute Alkaline-Sulfide Solutions,” Materials Performance, vol. 24, 1985, pp. 9-15.

[52] A.J. Sedriks, “Corrosion of Stainless Steel,” John-Wiley & Sons, New York, 1979.

[53] G. Rondelli, B. Vicentini, and E. Sivieri, “Stress Corrosion Cracking of Stainless Steels in High Temperature Caustic Solutions,” Corrosion Science, vol. 39, 1997, pp. 1037-1049.

[54] M. Gorog, “Digester Outlet Device Scraper Arm Cracking,”2006 Engineering, Pulping and Environmental Conference, Atlanta, GA, USA, 5-8 November 2006.

[55] H.T. Leinonen, P. Pohjanne, “Stress Corrosion Cracking Susceptibility of Duplex Stainless Steels and their Welds in Simulated Cooking Environments. NACE Corrosion 2006, paper no. 06244, San Diego, CA, USA, 12-16 March 2006.

[56] C. Reid, “Stress Corrosion Cracking of Austenitic and Duplex Stainless Steels in the Pulp and Paper Industry,” TAPPI Engineering Conference Proceedings, 1999, pp. 1315-1357.

[57] P.M. Singh, J. Mahmood, P. Conde, "Stress Corrosion Cracking and Corrosion Susceptibility of Duplex Stainless Steels in Caustic Solutions," NACE Corrosion 2005, paper no. 05196, Houston, TX, USA, 3-7 April 2005.

[58] D.C. Bennett, "Continuous Digester Cracking: Task Group Report," TAPPI J, vol. 64, 1981, p. 75-77.

[59] G. Rondelli and B. Vicentini, "Susceptibility of Highly Alloyed Stainless Steels to Caustic Stress Corrosion Cracking," Materials and Corrosion, Vol. 53, 2002, pp. 813-819.

[60] P.M. Singh and A. Anaya, "Effect of Wood Species on Corrosion Behavior of Carbon Steel and Stainless Steels in Black Liquors," Corrosion Science, vol. 49, 2007, pp. 497-509.

[61] Truman, J.E. and Pirt, K.R., Duplex Stainless Steel, ed. Lula, R.A. ASM, p. 113-142, 1983, Materials Park, OH.

[62] Singbeil, D.L., and Garner, A., NACE Corrosion 84, April 2-6, 1984, New Orleans, LA.

[63] Svensson, C., Pulliainen, M., Huttunen, M., and Niemelainen, P., 2005 TAPPI Engineering, Pulping, Environmental Conference, August 28-31, 2005, Philadelphia, PA.

[64] Ramo, J., Sillanpaa, Kujalao, A., Hyokyvirta, O., and Peltonen, S., Mat. and Corr. Vol. 52 (2001), p741.

[65] ERC Project Report, Institute of Paper Science and Technology at Georgia Tech, August 2006.

[66] Bhattacharya, A. and Singh, P.M."Corrosion and Stress Corrosion Cracking of Duplex Stainless Steels in Pulping Liquors," CORROSION/2007, Paper No. 07206. (Houston, TX: NACE, 2007).

[67] Bhattacharya, A., and Singh, P.M. "Effect of Heat Treatment on Corrosion and Stress Corrosion Cracking of S32205 Duplex Stainless Steel in Caustic Solution." Metallurgical and Materials Transactions A: Physical Metallurgy and Materials Science, Vol. 40A (6) (2009), p.1388.

[68] Bergquist, A., and Wegrelius, W. "Experiences in Pulp and Paper Industry of a 30 Years Old Steel Grade," 2009 TAPPI Conference, Paper No. Memphis, TN.

[69] J. Deakin et al., "De-alloying of Type 316 Stainless Steel in Hot, Concentrated Sodium Hydroxide Solution," Corrosion Science, vol. 46, 2004, pp. 2117-2133.

[70] W.J. Nisbet, G.W. Lorimer and R.C. Newman, “A Transmission Electron Microscopy Study of Stress Corrosion Cracking in Stainless Steels,” Corrosion Science, vol. 35, 1993, pp. 457-469.

[71] P.P.Snowden, "Comparative Stress-Corrosion Behaviour of Some High-Alloy Steels," Journal of the Iron and Steel Institute, London, Volume 197, 1961, pp. 136-141.

[72] E.M.Horn et al, "Performance of Duplex Stainless Steels in Caustic Solutions," Duplex Stainless Steels, Volume 2, 1991, pp. 1111-1119.

[73] F.P. Ford, “Slip Dissolution Model,” Corrosion Sous Contrainte-Phénoménologie et MécanismesLes Editions de Physique, Les Ulis, France, vol. 307, 1992.

[74] E.M. Gutman, “An Inconsistency in Film Rupture Model of Stress Corrosion Cracking,” Corrosion Science, vol. 49, 2007, pp. 2289-2302.

[75] K. Sieradzki et al., “The Relationship Between Dealloying and Transgranular Stress-Corrosion Cracking of Cu-Zn and Cu-Al Alloys,” Journal of the Electrochemical Society, vol. 134, 1987, p. 1635.

[76] J.H. Zheng, W.F. Bogaerts, and M.J. Brabers, “Stress Corrosion Cracking and Anodic Dissolution of 316L Stainless Steel in Hot Lithium Hydroxide,” 1992.

[77] F. Zucchi et al., “Influence of P, As and Sb on the Susceptibility to SCC of Alpha Brasses,” Materials and Corrosion, vol. 49, 1998, pp. 864-869.

[78] J.F. Newman, “The Stress Corrosion of Steel in Sodium Hydroxide Solution: A Film-Rupture Model,” Corrosion Science, vol. 21, 1981, pp. 487-503.

[79] R.C. Newman, J. Shahrabi, and K. Sieradzki, “Film-induced Cleavage of Alpha-brass,” Scripta Metall, vol. 23, 1989, p. 71.

[80] R. Li and K. Sieradzki, “Ductile-brittle Transition in Random Porous Au,” Physical Review Letters, vol. 68, 1992, pp. 1168-1171.

[81] K. Sieradzki and R.C. Newman, “Brittle Behavior of Ductile Metals During Stress-Corrosion Cracking,” Philosophical Magazine A, vol. 51, 1985, pp. 95-132.

[82] K. Sieradzki and R.C. Newman, “Stress-Corrosion Cracking,” J. Phys. Chem. Solids, vol. 48, 1987, pp. 1101-1113.

[83] G.J. Theus and R.W. Staehle, 1977. Review of Stress Corrosion Cracking and Hydrogen Embrittlement in the Austenitic Iron-Chromium-Nickel Alloys. In: Staehle, R.W., Hockman, J., McCright, R.D. and Slater, J.E., Editors, 1977. Stress

Corrosion Cracking and Hydrogen Embrittlement of Iron Based Alloys, NACE-5, Houston, pp. 845–892.

[84] J.G. Morlet, H.H. Johnson, A.R. Troiano, "A New Concept of Hydrogen Embrittlement in Steel," J. of the Iron and Stl. Inst., Vol. 189, 1958, pp. 37-41.

[85] H.K. Birnhaum, P. Sofronis, "Hydrogen-enhanced Localized Plasticity – a Mechanism for Hydrogen-related Fracture," Mat. Sci. and Eng., Vol. A176, 1994, pp. 191-202.

[86] T. Magnin, A. Chambreuil, B. Bayle, "The Corrosion-Enhanced Plasticity Model for Stress Corrosion Cracking in Ductile fcc Alloys," Acta. Met., Vol. 44, 1996, pp. 1457-1470.

[87] T. Zakroczymski, A. Glowacka, and W. Swiatnicki, "Effect of Hydrogen Concentration on the Embrittlement of a Duplex Stainless Steel," Corrosion Science, vol. 47, 2005, pp. 1403-1414.

[88] M.A.V. Devanathan and Z. Stachurski, "The Adsorption and Diffusion of Electrolytic Hydrogen in Palladium," Proceedings of the Royal Society of London. Series A, Mathematical and Physical Sciences (1934-1990), vol. 270, 1962, pp. 90-102.

[89] E. Owczarek and T. Zakroczymski, "Hydrogen Transport in a Duplex Stainless Steel," Acta Materialia, vol. 48, 2000, pp. 3059-3070.

[90] T.E. Pérez and J. Ovejero García, "Direct Observation of Hydrogen Evolution in the Electron Microscope Scale," Scripta Metallurgica, vol. 16, 1982, pp. 161-164.

[91] S.S. Chen, T.I. Wu, and J.K. Wu, "Effects of Deformation on Hydrogen Degradation in a Duplex Stainless Steel," Journal of Materials Science, vol. 39, 2004, pp. 67-71.

[92] A.A. El-yazgi and D. Hardie, "The Embrittlement of a Duplex Stainless Steel by Hydrogen in a Variety of Environments," Corrosion Science, vol. 38, 1996, pp. 735-744.

[93] J.H. Barber and B.E. Conway, J. Chem. Soc. Faraday Trans. Vol. 92 (20) (1996) p. 3709.

[94] P. Kedzierzawski, Z. Szklarska-Smialowska, and M. Smialowski, J. Electrochem. Soc. Vol. 127 (1980), p. 2550.

[95] J.F. Newman, and L.L. Shreir, Corrosion Science, Vol. 9: (1969) p. 631.

[96] T. Zakroczymski, A. Glowacka, and W. Swiatnicki, "Effect of Hydrogen Concentration on the Embrittlement of a Duplex Stainless Steel," Corrosion Science, vol. 47, 2005, pp. 1403-1414.

[97] R.N. O'Brien and P. Seto, "The Mechanism of Hydrogen Evolution at a Stainless Steel Electrode in Basic Solution," Journal of the Electrochemical Society, vol. 117, 1970, p. 32.

[98] S.T. Tsai, k.P. Yen, and H.C. Shih, "The embrittlement of duplex stainless steel in sulfide-containing 3.5 wt% NaCl solution," Corr. Sci. 40 (1998), 281-295.

[99] M.A.V. Devanathan and Z. Stachurski, "The Adsorption and Diffusion of Electrolytic Hydrogen in Palladium," Proceedings of the Royal Society of London. Series A, Mathematical and Physical Sciences (1934-1990), vol. 270, 1962, pp. 90-102.

[100] S.T. Tsai and S.L. Chou, "Environmentally Assisted Cracking Behavior of Duplex Stainless Steel in Concentrated Sodium Chloride Solution," Corrosion Science, vol. 42, 2000, pp. 1741-1762.

[101] S.L. Chou and W.T. Tsai, "Effect of Grain Size on the Hydrogen-Assisted Cracking in Duplex Stainless Steels," Materials Science and Engineering: A, vol. 270, 1999, pp. 219-224.

[102] E. Owczarek and T. Zakroczymski, "Hydrogen Transport in a Duplex Stainless Steel," Acta Materialia, vol. 48, 2000, pp. 3059-3070.

[103] T.E. Pérez and J. Ovejero García, "Direct Observation of Hydrogen Evolution in the Electron Microscope Scale," Scripta Metallurgica, vol. 16, 1982, pp. 161-164.

[104] S.S. Chen, T.I. Wu, and J.K. Wu, "Effects of Deformation on Hydrogen Degradation in a Duplex Stainless Steel," Journal of Materials Science, vol. 39, 2004, pp. 67-71.

[105] M. Pourbaix, "Applications of Electrochemistry in Corrosion Science and in Practice," Corr. Sci., Vol. 14, 1974, pp. 25-82.

[106] HSC Chemistry 5.11, Outokumpu Technology Engineering Research.

[107] C.B. Christiansen and J.B. Lathrop, "Field Investigation of Corrosion in Alkaline Pulping Equipment," Pulp and Paper Magazine of Canada, Nov, 1954, p. 119.

[108] P.M Singh et al., "Stress Corrosion Cracking and Corrosion Fatigue Cracking of a Duplex Stainless Steel in White Water Environments," Corrosion (Houston, Tex.), vol. 60, 2004, pp. 852-861.

[109] T.P. Hoar, J.M. West, "Mechano-chemical Anodic Dissolution of Austenitic Stainless Steel in Hot Chloride Solution," Proc. Of the Roy. Soc. Of London, Vol. 268, 1962, pp. 304-315.

[110] R. Oltra, A. Desestret, E. Mirabal, J.P. Bizouard, "A Critical Study of Stress Corrosion Cracking of Duplex Stainless Steels in Environments Containing Chlorides and $H_2S$. Study of the Ferrite Phase Behavior," Corrosion Science, Vol. 27, I. 10-11, 1987, pp. 1251-1269.

[111] H.S. Kwon and H.S. Kim, "Investigation of stress corrosion susceptibility of duplex (alpha+ gamma) stainless steel in hot chloride solution," Materials Science and Engineering A(Switzerland), 1993, pp. 159-166.

[112] M. Puiggali, D. Desjardins, L. Ajana, "A Critical Study of Stress Corrosion Cracking Testing Method for Stainless Steels in Hot Chloride Media," Corrosion Science, Vol. 27, I. 6, 1987, pp. 585-594.

[113] K. Van Gelder et al., "The Stress Corrosion Cracking of Duplex Stainless Steel in $H_2S/CO_2/Cl$ environments," Corrosion science, vol. 27, 1987, pp. 1271-1279.

[114] K. Klyk-Spyra and M. Sozanska, "Quantitative Fractography of 2205 Duplex Stainless Steel after a Sulfide Stress Cracking Test," Materials Characterization, vol. 56, 2006, pp. 384-388.

[115] M. Barteri et al., "Microstructural Study and Corrosion Performance of Duplex and Superaustenitic Steels in Sour Well Environment," Corrosion, vol. 43, 1987, pp. 518-525.

# CHAPTER 3

# EXPERIMENTAL PROCEDURE

## 3.1 Introduction

The effect of microstructure and environment on the stress corrosion cracking (SCC) susceptibility of duplex stainless steel (DSS) was evaluated in this work. The phase distribution and phase ratio in the DSS microstructures of the as-received materials were characterized with a stereological approach. Mechanical behavior was evaluated by microhardness, stress-strain experiments, and X-ray techniques. Corrosion behavior and SCC were evaluated on exposure coupon and strained specimens, respectively. Both *ac* and *dc* electrochemical techniques in conjunction with film characterization were used to understand corrosion behavior in caustic environments containing chloride and sulfide. Slow strain rate testing (SSRT) was used to understand SCC susceptibilities in caustic environments. Samples were studied with optical and scanning electron microscopy (SEM) following testing to observe the failure characteristics. Test environments, materials, equipment, and experimental procedures are discussed in this chapter.

## 3.2 Microstructural Characterization of the As-Received DSS Materials

### 3.2.1 Metallography

Representative samples were sectioned from the as-received DSS S32205 and S32101 plates and prepared for optical microstructural characterization. These specimens were mounted in resin, wet ground to 1500 grit SiC paper finish, polished with diamond paste to 0.25 μm finish, and vibratory polished in a 0.05 μm alumina suspension.

Samples were rinsed in distilled water, and degreased in an ultrasonic bath following each step. Electrolytic etching was conducted with 40 % NaOH at 2.5 V for approximately 5 s using a stainless steel counter electrode to reveal the phases. Austenite ($\gamma$) is the light etching phase and ferrite ($\alpha$) is the dark etching phase in subsequent optical micrographs. Secondary phases were not observed in the optical images or in backscattered electron (BSE) SEM images in the as-received condition of either S32205 or S32101.

### 3.2.2. Phase Distribution and Ratio

The materials under study were standard DSS grade, S32205 (Fe – 22.5 Cr – 5.5 Ni – 3 Mo – 0.25 N) and lean grade S32101 (DSS 2101) (Fe – 21.5 Cr –1.5 Ni – 0.5 Mo – 0.20 N). Round tensile samples were machined from the as-received material, which was provided as 9.5 mm thick, hot rolled and coil-processed DSS plate with a No. 1 finish in accordance with ASTM A480. The microstructure was anisotropic for these alloys as shown in Figure 3.1. Orientations are described as the following: transverse direction (TD), rolling direction (RD), normal direction (ND), rolling longitudinal (RL), transverse longitudinal (TL) and transverse short (TS).

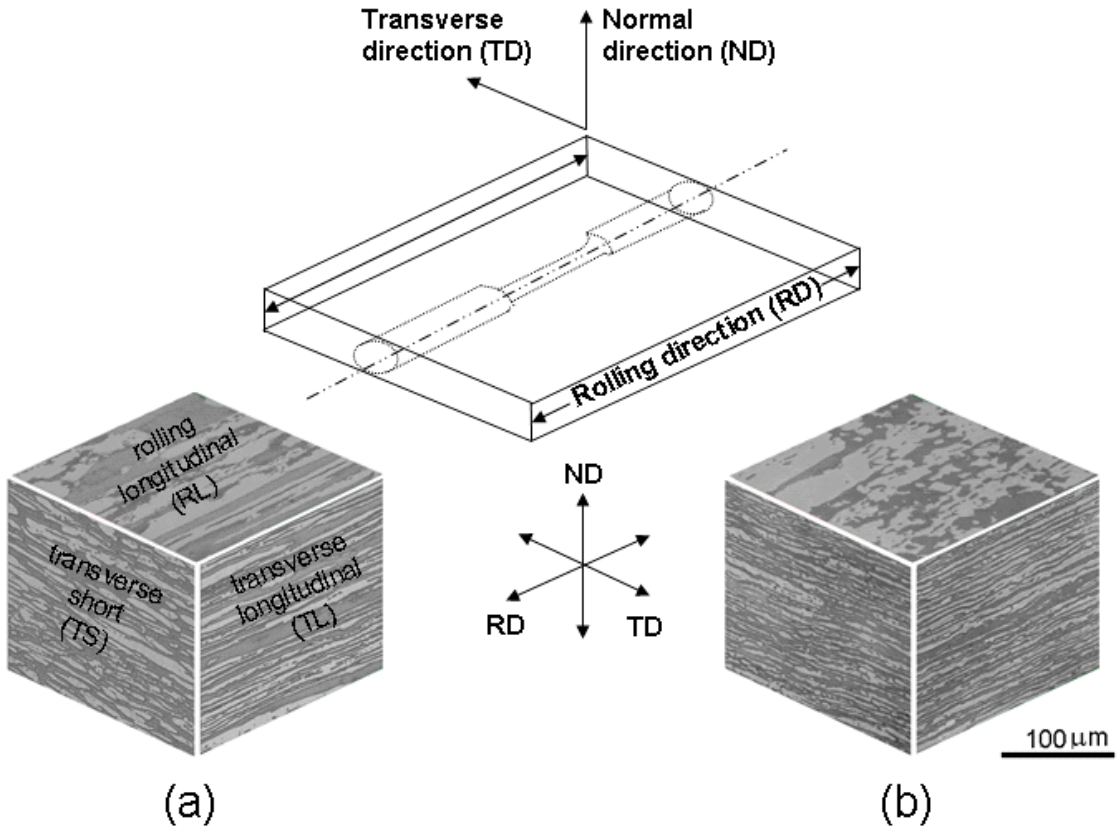


***Figure 3.1:*** ***Microstructure for different orientations of as-received (a) standard DSS S32205 and (b) lean DSS S32101 evaluated in this study.***

Table 3.1 provides a summary of quantitative stereology conducted to characterize the microstructure. Two fields of view (quadrants) from each orthogonal orientation were photographed with optical microscopy at 200x magnification. A grid was intentionally placed parallel to the elongated bands of austenite. An example of an overlaid grid on a micrograph of the RL orientation of the S32101 microstructure is shown in Figure 3.2. Quantification of the austenite phase (light etching regions in Figure 3.2) in the ferrite matrix was undertaken using the method of point counting [1] to determine the average area fraction of austenite ($A_\gamma$), number of point interceptions per test length ($N_L$), and lineal fraction ($L_L$) for the RL and TL orientations. Crack growth

was primarily along the TD or ND as the load was applied normal to these directions. The mean intercept length was calculated based on $L_L$/ $N_L$. A higher mean intercept length is indicative of a longer continuous austenite phase in a given orientation, providing higher probability of preferential stress corrosion crack growth in that direction. The results indicate that the highest mean intercept length corresponded to the RL orientation in both materials under study.

***Table 3.1:*** ***Quantitative stereology parameters for the austenite phase (light etching phase) of as-received materials evaluated in this study***

| | *RL Orientation* | | | | *TL Orientation* | | | |
|---|---|---|---|---|---|---|---|---|
| *Alloy (UNS No.)* | *$A_\gamma$ (%)* | *$N_L$ ($\mu m^{-1}$)* | *$L_L$* | *$L_L$/ $N_L$ ($\mu m$)* | *$A_\gamma$ (%)* | *$N_L$ ($\mu m^{-1}$)* | *$L_L$* | *$L_L$/ $N_L$ ($\mu m$)* |
| S32205 | 43±2 | 0.046±0.006 | 0.68±0.09 | 15 | 48±3 | 0.121± 0.008 | 0.69±0.04 | 6 |
| | | | | | | | | |
| S32101 | 43±4 | 0.021±0.008 | 0.46±0.13 | 22 | 51±2 | 0.055± 0.006 | 0.59±0.05 | 11 |

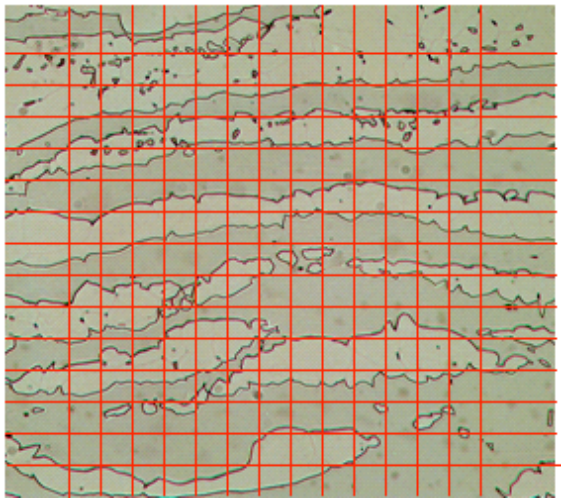

***Figure 3.2:*** ***Micrograph showing a 14 x 14 grid overlaid on the RL orientation microstructure of as-received lean DSS S32101 evaluated in this study. Each block represents 20 µm.***

### 3.2.3 Composition of the Austenite and Ferrite Phases

The chemical compositions (Table 3.2) of austenite and ferrite in the as-received DSS S32205 and S32101 were evaluated with a SEM equipped with energy dispersive X-ray spectroscopy (EDS) to understand partitioning of alloying elements. The average of 15 measurements (wt. %) is presented for each element. The accelerating voltage was set to 15 kV and the working distance was approximately 8 mm. The ratio of elements in the austenite to ferrite phase is presented as $P_\gamma$. A $P_\gamma$ value of 1 indicates there was negligible partitioning. Cr and Mo are bcc stabilizers and were enriched in the ferrite phase. Ni, N, and Mn are fcc stabilizers and were partitioned to the austenite phase. Alloying effects have been studied extensively in DSS with respect to their general and localized corrosion resistance (Chapter 2). A greater extent of partitioning for Ni and Mo was observed in S32205 than in S32101.

***Table 3.2:*** ***Quantitative stereology parameters for the austenite phase (light etching phase) of as-received materials evaluated in this study***

| | | *Fe (at. %)* | *Cr (at. %)* | *Ni (at. %)* | *Mn (at. %)* | *Mo (at. %)* | *Si (at. %)* |
|---|---|---|---|---|---|---|---|
| S32205 | Austenite | 63.2 | 21.9 | 6.4 | 1.2 | 1.4 | 0.9 |
| | Ferrite | 61.4 | 25.1 | 3.8 | 1.1 | 2.3 | 1.1 |
| | Pγ | 1.0 | 0.9 | 1.7 | 1.1 | 0.6 | 0.8 |
| | | | | | | | |
| S32101 | Austenite | 70.4 | 21.1 | 1.8 | 5.3 | < 0.5 | 0.7 |
| | Ferrite | 69.6 | 22.8 | 1.4 | 4.7 | < 0.5 | 0.9 |
| | Pγ | 1.0 | 0.9 | 1.3 | 1.1 | 1.0 | 0.8 |

### 3.2.4 Hardness of Austenite and Ferrite Phases

Vickers microhardness ($HV_{25}$) was measured for the austenite and ferrite phases of as-received DSS S32205 and S32101 as shown in Table 3.3. Ten measurements were made in the two phases for each orientation of the materials using a micro-hardness tester with a dwell time of 15 s. The results show that the austenite and ferrite phases had similar hardness in the DSS S32205 material. Moreover, there was a relatively small difference in hardness for the different orientations. However, there was an appreciable difference in the hardness of the austenite and ferrite phases of DSS S32101. Austenite was harder than ferrite in this alloy with the largest differences in the TS orientation.

***Table 3.3: Vickers microhardness ($HV_{25}$) of as-received DSS S32205 and S32101***

| | *Austenite Phase* | | | *Ferrite Phase* | | |
|---|---|---|---|---|---|---|
| *UNS No.* | *RL* | *TS* | *TL* | *RL* | *TS* | *TL* |
| S32205 | 306±14 | 306±9 | 306±9 | 317±20 | 297±14 | 287±13 |
| | | | | | | |
| S32101 | 274±12 | 292±9 | 251±9 | 224±11 | 230±10 | 220±6 |

## 3.3 Tests to Evaluate the Effect of Alloy Composition and Environment on the General Corrosion Behavior of Stainless Steels

### 3.3.1 Materials

Select grades of DSS (UNS S32003, S32101, S32205, S32705), austenitic (S30403, S31603, S31703, S08904) and superferritic stainless steels (S44660, S44627) were exposed to select environments to understand alloying effects on film formation and corrosion behavior. The nominal chemical compositions of the materials used in this

study are listed in Table 3.4. Material certification sheets for select alloys with actual chemical compositions are provided in Appendix A.

***Table 3.4: Nominal chemical compositions of materials in this study (wt. %)***

| *Alloy* | *UNS No* | *C max* | *Cr* | *Mn* | *Mo* | *Ni* | *N* | *Other* |
|---|---|---|---|---|---|---|---|---|
| 304L | S30403 | 0.03 | 18-20 | 2.0 max | - | 8 - 12 | 0.1 max | P. S, Si |
| 316L | S31603 | 0.03 | 16 - 18 | 2.0 max | 2.0 - 3.0 | 10.0 - 14.0 | 0.1 max | P, S, Si |
| 317L | S31703 | 0.03 | 18 - 20 | 2.0 max | 3.0 - 4.0 | 11.0 - 15.0 | 0.1 max | P, S, Si |
| 904L | N08904 | 0.02 | 19 - 23 | 2.0 max | 4.0 - 5.0 | 23.0 - 28.0 | - | P, S, Si, Cu |
| | | | | | | | | |
| 2101 | S32101 | 0.04 | 21-22 | 4.0 - 6.0 | 0.1 - 0.8 | 1.35 - 1.70 | 0.2 - 0.25 | P, S, Si, Cu |
| 2205 | S32205 | 0.03 | 22-23 | 2.0 max | 3.0 - 3.5 | 4.5 - 6.5 | 0.14 - 0.20 | P, S, Si |
| 2003 | S32003 | 0.03 | 19 - 22.5 | 2.0 max | 1.5 – 2 | 3 - 4 | 0.12 - 0.20 | P, S, Si |
| 2507 | S32705 | 0.03 | 24 - 26 | 1.2 max | 3 – 5 | 6 - 8 | 0.24 - 0.32 | P, S, Si, Cu |
| | | | | | | | | |
| E-Brite® | S44627 | 0.01 | 25 - 27.5 | 0.4 max | 0.75 - 1.50 | 0.5 max | 0.015 max | P, S, Si, Cu |
| SeaCure® | S44660 | 0.03 | 25- 28 | 1.0 max | 3.0 - 3.5 | 1.0 - 3.5 | 0.04 max | P, S, Si, Ti, Nb |

### 3.3.2 Test Environments

The test solutions were prepared from reagent-grade sodium hydroxide (NaOH), sodium sulfide ($Na_2S$), and sodium chloride (NaCl). Solutions used in this study were compared on the basis of percent sulfidity, active alkali (g/l), and effective alkali (g/l), expressed in their equivalents as $Na_2O$.

$$Percent\ \ Sulfidity = 100 * \frac{[Na_2S]}{[Na_2S] + [NaOH]} \quad [3.1]$$

$$Effective\ \ Alkali = 0.5 * [Na_2S] + [NaOH] \quad [3.2]$$

$$Active\ \ Alkali = [Na_2S] + [NaOH] \quad [3.3]$$

The environments shown in Table 3.5 were chosen to represent typical concentrations of pulping liquors used in North American (3.75 M NaOH + 0.64 M $Na_2S$), Swedish (3.13 M NaOH + 0.96 M $Na_2S$), and Finnish (2.5 M NaOH + 0.70 M $Na_2S$) digesters. Test solutions of sodium hydroxide without sulfide were used to evaluate the effect of alkalinity. The effect of chloride was studied in the three simulated pulping liquors with an addition of 0.17 M NaCl. The effect of chloride was also studied in 3.75 M NaOH without sulfide addition. The pH of each solution was measured at room temperature prior to each exposure test and was approximately 13.3 - 13.4 in all cases. All tests were conducted at 170 $^{O}$C.

***Table 3.5: Compositions and of test solutions used in coupon exposure tests (per liter).***

| | *Constituent* | | | *Alkalinity* | |
|---|---|---|---|---|---|
| *Hydroxide, as NaOH (M)* | *Sulfide, as $Na_2S$ (M)* | *Chloride, as NaCl (M)* | *EA (g $L^{-1}$)* | *AA (g $L^{-1}$)* | *% Sulfidity* |
| 2.5 | 0 | 0 | 100 | 100 | 0 |
| 2.5 | 0.7 | 0 | 127.5 | 155 | 35.5 |
| 2.5 | 0.7 | 0.17 | 127.5 | 155 | 35.5 |
| | | | | | |
| 3.13 | 0 | 0 | 125 | 125 | 0 |
| 3.13 | 0.96 | 0 | 162.5 | 200 | 37.5 |
| 3.13 | 0.96 | 0.17 | 162.5 | 200 | 37.5 |
| | | | | | |
| 3.75 | 0 | 0 | 127.5 | 150 | 0 |
| 3.75 | 0 | 0.17 | 127.5 | 150 | 0 |
| 3.75 | 0.64 | 0 | 175 | 200 | 25 |
| 3.75 | 0.64 | 0.17 | 175 | 200 | 25 |

### 3.3.3 Coupon Exposure Tests for Corrosion Susceptibility

All experiments were carried out in a 2 liter laboratory autoclave constructed from DSS S32205 with an external temperature control through a K-type thermocouple to 170 $^{o}$ C ±1 $^{o}$ C for 7 days (168 h) held in a thermowell in the autoclave lid. It took approximately 2 h to reach the test temperature. Samples were placed on a polytetrafluoroethylene (PTFE) - insulated rod and electrically isolated with PTFE washers. The setup used for exposure testing is shown in Figure 3.3.

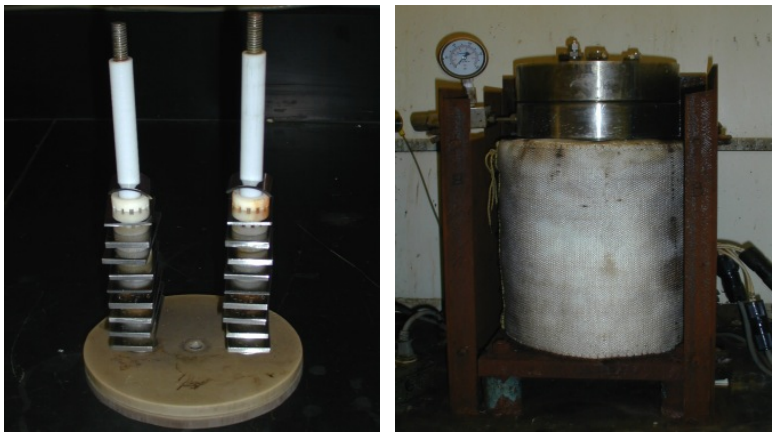

***Figure 3.3:*** ***Experimental setup used for corrosion rate tests (weight loss) showing (left) samples isolated by PTFE washers on holder, and autoclave used for exposure.***

Duplicate samples were used in several tests (all 2.5 M NaOH environments) and (3.75 M + 0.64 M $Na_2S$) to ensure there was minimal sample-to-sample variation, which was found to be ± 10% for all materials. All other tests were run with single specimens.

Prior to each experiment, samples were weighed with a precise scale with an accuracy of ±0.0001 g. The dimensions were measured with a dial caliper having an accuracy of ± 0.01 mm. The average corrosion rate calculations in mils per year (MPY) were based on

$$MPY = \frac{534 \times W}{D \times A \times T} \qquad [3.4]$$

where W is mass loss in g, D is density in g/cm$^3$, A is surface area in cm$^2$, and T is time in h.

Upon completion of each weight loss test, samples were rinsed in distilled water. The samples were then placed in an airlock bag and placed in an evacuated chamber that

contained desiccant to preserve the sample surface condition. Films were removed on select samples with an inhibited acid solution (Clark's solution) having a concentration of HCl, 50 g $SnCl_2$ + 20 g/l $SbCl_3$ prior to weight loss measurements. Blank samples were also exposed to the acid solution and weighed to ensure metal loss from the cleaning process was minimal. Weight loss measurements were taken on a high precision scale accurate within ±0.0001 g.

The sample surfaces were examined with standard microscopy techniques following the weight loss tests to detect the form of corrosion and surface morphology. Optical microscopy was used to characterize the surface at low magnifications (< 500x), and SEM was used to study the surface morphology at higher magnifications. The surfaces were analyzed with accelerating energy of 15 kV using the secondary electron detector (SE) or BSE detector.

### 3.4 Electrochemical Tests and Film Characterization to Evaluate Selective Dissolution of DSS

SCC behavior is dependent on certain electrochemical reactions that can occur in a narrow potential range. Temperature will also influence the potentials at which these reactions occur. Selective dissolution of less noble elements can occur in stainless steels if the corrosion potential lies in a particular range, thus potentiodynamic polarization scans were conducted on different grades austenitic (S31603), superferritic (S44660), and DSS (SS2205, S32101, S32304) and their alloying elements (Fe, Cr, Ni, Mo, Mn) to study selective dissolution as a function of alloy composition. Physicoelectrical properties of the surface films were studied with *ac* and *dc* techniques at the open circuit

potential (OCP). Film composition of the samples exposed at the OCP was studied with X-ray photoelectron spectroscopy (XPS) and under SEM using EDS.

### 3.4.1. Potentiodynamic Polarization Scans

Experiments were conducted at 90 $^{o}$C in 2.5 M NaOH, 2.5 M NaOH + 0.17 M NaCl, and 2.5 M NaOH + 0.17 M $Na_2S$. The solutions were prepared by dissolving 150 g of NaOH, 150 g of NaOH + 10 g of NaCl, or 150 g of NaOH + 169.7 g of Na2S* $9H_2O$ into 1000 ml of deionized water, respectively. Solutions were not deaerated prior to testing.

Austenitic (S31603), superferritic (S44660), and DSS (SS2205, S32101, S32304) and their alloying elements (Fe, Cr, Ni, Mo, Mn) were studied. The nominal material compositions of the alloys were provided in Table 3.4. The alloying elements were commercially pure. The surfaces of the specimens were mechanically wet polished with 600 grit SiC paper, rinsed with deionized water, and degreased with acetone before each test. The exposed surface area of the specimens was approximately 2 $cm^2$, which was maintained by an o-ring in a PTFE sample holder.

The experiments were conducted using a conventional three-electrode setup as shown in Figure 3.4. The cell was constructed of PTFE that was secured with 4 tie rods. The reference potentials were vs. external Ag/AgCl (0.199 mV vs. a standard hydrogen electrode) connected to the cell through a salt bridge. No attempt was made to correct for ohmic losses due to the liquid junction potential, which was approximately 20 mV. The counter electrode was a carbon rod.

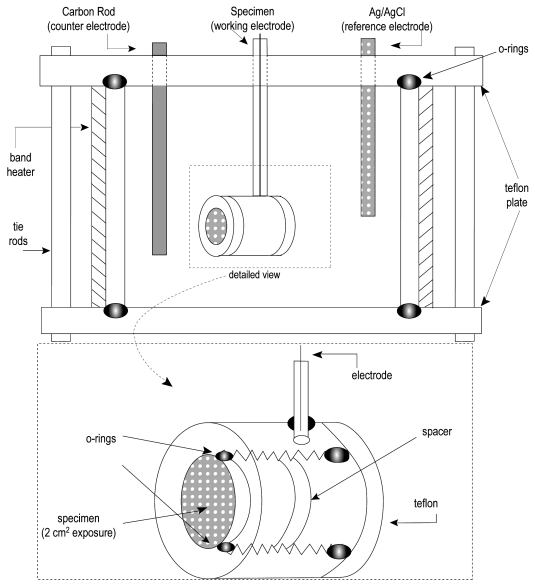


***Figure 3.4:*** ***Experimental setup used for potentiodynamic scans at 90 $^{o}$C showing the working electrode holder, reference electrode, and counter electrode.***

The OCP was allowed to stabilize prior to running each scan. During the potentiodynamic scans, the potential was increased in the anodic direction at a sweep rate of 2 mV $s^{-1}$ beginning -0.3 V vs. the OCP while the current was measured. The scans were stopped when the current was 0.5 A, which was the upper limit of the potentiostat-galvanostat. Experiments were repeated in several cases to ensure reliability of the results.

Similar experiments were conducted at 170 $^{o}$C in an autoclave using a Mo pseudo-reference electrode and a Pt counter electrode (Figure 3.5). Samples were machined from plate into cylindrical rods that were connected by PTFE-coated leads through the autoclave lid. The exposed area was approximately 5 $cm^2$. Quasi-steady-state current vs. potential curves were measured using the same parameters as used at 90 $^{o}$C. All potential values are referenced vs. Mo/$MoS_2$ (the potential at the experimental

temperature was approximately -1050 mV vs. Ag/AgCl). The potential was determined with the procedure in Appendix B.

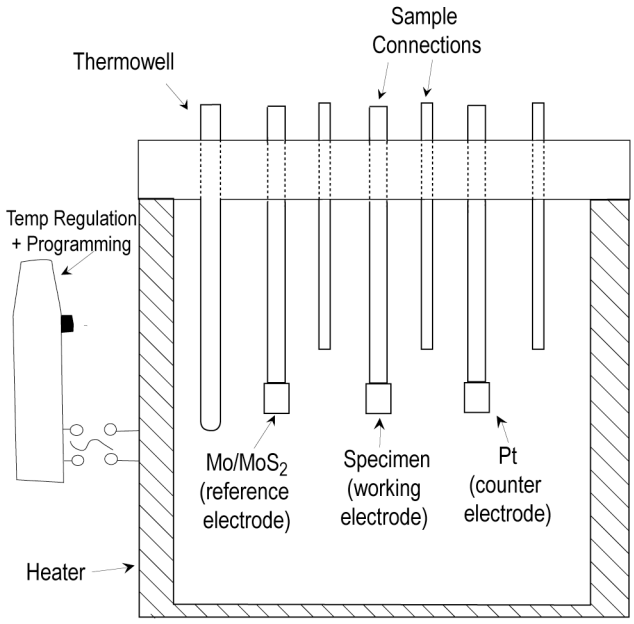


***Figure 3.5:*** ***Experimental setup used for potentiodynamic scans at 170 $^{o}$C showing the working electrode, reference electrode, and counter electrode.***

### 3.4.2. Film Properties at the Open Circuit Potential

Corrosion processes and SCC of stainless steels depends on the formation of a stable passive film on the surface. The composition of this film can vary among different grades of stainless steel depending on their composition. Ionic species, i.e., $Cl^-$ and $S^{2-}$, will influence the passivation ability of the alloys.

#### 3.4.2.1 Physicoelectrical Behavior of Surface Films

Experiments were conducted in 2.5 M NaOH, 2.5 M NaOH + 0.70 M $Na_2S$, and 2.5 M NaOH + 0.70 M $Na_2S$ + 0.17 M NaCl at 170 $^{o}$C in the autoclave setup shown in

Figure 3.5. The solutions were prepared by dissolving 150 g of NaOH, 150 g of NaOH + 169.7 g of Na2S* $9H_2O$, or 150 g of NaOH + 169.7 g of Na2S* $9H_2O$ + 10 g of NaCl into 1000 ml of deionized water, respectively. The material and surface preparation procedure was the same as used in the potentiodynamic scans. The samples were exposed to the environments for 168 h (7 days) at the OCP.

Linear polarization resistance (LPR) was measured every 24 h at a sweep rate of 0.01 mV $s^{-1}$ beginning -10 mV vs. the OCP and ending +10 mV vs. the OCP. Measurements of the OCP were made prior to each scan. The corrosion rate, r, and polarization resistance, $R_p$, values were determined with by curve fitting with electrochemical analysis (Gamry Echem Analyst) software based on

$$r = \frac{ia}{nF} \qquad [3.5]$$

$$i = \frac{\beta_a \beta_c}{2.303 R_p (\beta_a + \beta_c)} \qquad [3.6]$$

where i, the current density, equals I/A, the current divided by the surface area. The atomic weight, a, and number of electrons n depend on the particular element and are expressed as the equivalent weight. F is Faraday's constant. The Tafel constants, $\beta_a$ and $\beta_c$ were extrapolated from the potentiodynamic scans using a logarithmic fit. $R_p$ is taken as the linear slope of the line over the 20 mV range.

Electrochemical impedance spectroscopy (EIS) was measured on the samples after 24, 72, and 168 h to understand film formation and reactions at the surface film interfaces using *ac* amplitude of 10 mV rms in the frequency range of 50 kHz – 1 mHz at

6 points per decade. The capacitance of the electrical connections was checked independently with a digital voltmeter. Inductance effects from the connections were minimized by using the shortest possible connections. Commercial software (Scribner Associates ZView) was used for the fitting of the experimental data.

3.4.2.2 Surface Film Composition

*3.4.2.2.1 Cross-Sectioned Film Characterization with Scanning Electron Microscope*

Duplicate samples tested during the 168 h exposure at the corrosion potential. These samples were rinsed with deionized water and placed in a desiccator until analysis was performed. Samples were cross-sectioned and mounted in conductive resin. The samples were polished in lapping oil with SiC paper to 1000 grit, followed by polishing with diamond paste to 0.25 μm. The surface was then rinsed with acetone. The morphology and composition of the surface films were examined under SEM equipped with EDS microanalysis. The accelerating voltage was 15 kV. A minimum of 15 points were sampled in different regions of the sample film. The magnification depended on the film thickness.

*3.4.2.2.2 Surface Film Characterization with X-ray Photoelectron Spectroscopy*

A section of each 168 h exposure sample was stored in a desiccator until analysis could be performed. Surface analysis of the films was made under ultra high vacuum with a K-Alpha (Thermo Scientific) X-ray spectrometer equipped an Ar ion gun for sputtering capability. Monochromatised Al $K_{\alpha}$ radiation was used for excitation. An Al anode (1486.7 eV) was used to generate photoelectrons. A flood gun was used to maintain charge neutrality on the surface. Photoelectrons were collected over an analysis

region of 1.25 $mm^2$ with the surface orientated normal to the analyzer entrance. A survey scan in the energy range 0 – 1100 eV with pass energy of 50 eV was first acquired to detect elements on the surface layer. The C 1s peak (284.6 eV) was used to check the energy scale. High resolution scans were performed using pass energy of 20 eV on the primary alloying elements and solution constituents. Total energy resolution of the X-ray radiation and the energy analyzer was 0.4 eV. Sputtering was performed with energy of 3 kV over a 2 mm raster size. Sputter depths were estimated based on the rate (0.73 nm $s^{-1}$) for a $Ta_2O_5$ reference material. Semi-quantitative analysis of each scan was achieved using data processing software capable of peak fitting, elemental, and chemical state determination. Data analysis was performed with commercial fitting software (Thermo Scientific Avantage) using Shirley background subtraction and Lorentzian-Gaussian peak fitting to determine the composition and chemical states at the oxide/metal interface taken as approximately one half the maximum O 1s peak intensity.

### 3.5 Slow Strain Rate Tests for SCC Susceptibility

SSRT specimens were machined from the as-received plate (S32205 and S32101) with the longitudinal axis along the rolling direction. The gage length of each cylindrical sample was 25.4 mm and the gage diameter was 3.175 mm. Specimen geometry is shown in Figure 3.6. The gage length was ground and polished down to a 1000 grit surface finish. The final finish was applied along the rolling direction. The samples were then rinsed with distilled water, ultrasonically degreased in acetone, and allowed to dry prior to each test.

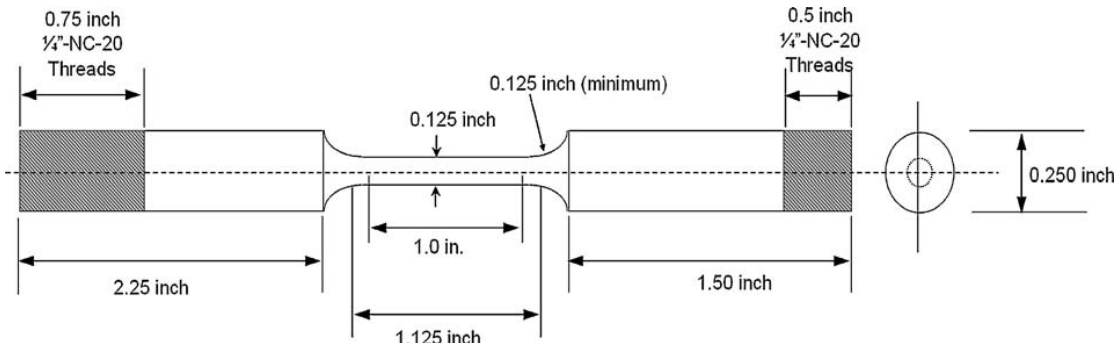


***Figure 3.6:*** ***Typical DSS S32205 and S32101 specimen dimensions used in slow strain rate testing to assess SCC.***

The tests were all conducted at an initial strain rate of 2 X $10^{-6}$ $s^{-1}$ in the solutions in Table 3.6. The test solutions were prepared from reagent-grade chemicals. All tests were carried out in an autoclave equipped with a rigid slow strain rate rig as shown in Figure 3.7. The potential was monitored with a high impedance voltmeter in certain experiments. The setup was modified to accommodate a Mo pseudo-reference electrode and Pt counter electrode for electrochemical measurements as shown in Figure 3.8. A separate lead was used to maintain a connection to the sample. The specimens were mounted in a fixture using ceramic washers to prevent galvanic effects with the autoclave. All of the tests were carried out at the corrosion potential. Each sample was preloaded to 15 kg to minimize system compliance (reduction gear, grips, etc.). The load was measured with a load cell and the % elongation was calculated based on the displacement rate of the crosshead times the duration of each test.

***Table 3.6:*** ***Compositions and of test solutions used in SCC (strained) specimen tests (per liter).***

| *Constituent* | | | *Alkalinity* | | |
|---|---|---|---|---|---|
| *Hydroxide, as NaOH (M)* | *Sulfide, as $Na_2S$ (M)* | *Chloride, as NaCl (M)* | *EA (g $L^{-1}$)* | *AA (g $L^{-1}$)* | *% Sulfidity* |
| 2.5 | 0 | 0 | 100 | 100 | 0 |
| 2.5 | 0 | 0.17 | 100 | 100 | 0 |
| 2.5 | 0.7 | 0 | 127.5 | 155 | 35.5 |
| 2.5 | 0.7 | 0.17 | 127.5 | 155 | 35.5 |
| | | | | | |
| 3.75 | 0 | 0 | 127.5 | 150 | 0 |
| 3.75 | 0 | 0.17 | 127.5 | 150 | 0 |
| 3.75 | 0.64 | 0 | 175 | 200 | 25 |
| 3.75 | 0.64 | 0.0085 | 175 | 200 | 25 |
| 3.75 | 0.64 | 0.034 | 175 | 200 | 25 |
| 3.75 | 0.64 | 0.085 | 175 | 200 | 25 |
| 3.75 | 0.64 | 0.17 | 175 | 200 | 25 |
| 3.75 | 0.64 | 0.34 | 175 | 200 | 25 |
| 3.75 | 0.64 | 1.7 | 175 | 200 | 25 |
| | | | | | |
| 12.5 | 0 | 0 | 500 | 500 | 0 |

***Figure 3.7:*** ***Slow strain rate test setup with autoclave for high temperature SCC experiments.***

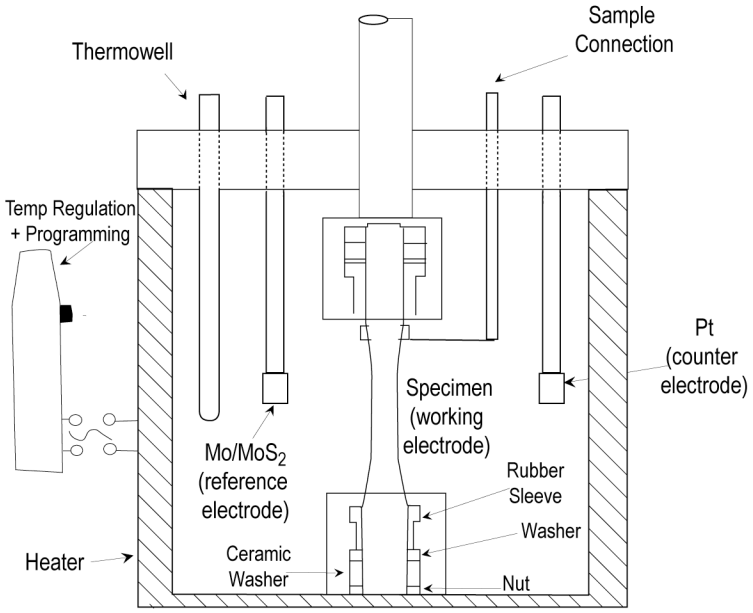


***Figure 3.8:*** ***Modified slow strain rate test autoclave setup to accommodate corrosion potential monitoring during high temperature experiments.***

Upon completion of each test, one half of the fractured tensile samples were mounted, polished, and electrolytically etched. The maximum crack velocity was calculated based on the length of the deepest crack in mm $s^{-1}$. The average crack density was determined based on the number of cracks that were in the gage section divided by the length of the fractured section. The fracture morphology was also observed to determine the preferred phase for crack initiation. The fracture morphology of the other half of the fractured specimen was observed in the SEM. The % reduction in area (% RA) was also determined after each test.

## 3.6 Mechanical Properties of Anisotropic Microstructure

### 3.6.1 Residual Stress Measurements

Samples were machined from DSS S32205 cold rolled, as-received sheet. The samples were provided by VTT Technical Research Centre of Finland (VTT) in the annealed as well as the 20 % cold work condition. Mechanical test data and chemical compositions were also provided by VTT (Appendix C). The surface was mechanically polished to 1000 grit, rinsed with deionized water, and degreased with acetone. The surfaces were electropolished for 15 s with A2 solution (78 ml perchloric acid ($HClO_4$), 120 ml deionized water, 700 ml ethanol, and 100 ml ethylene glycol ($C_6H_{14}O_2$)) using 70 mA, 25 V, and low flow at 25 $^oC$. The exposed region was approximately 1 $cm^2$.

All experiments were conducted at Aalto University by an experienced user with a commercial X-ray Stress Analyzer system (XSTRESS 3000 American Stress Technologies, Inc.). Stresses were obtained by measuring lattice spacing in different directions on the face of the longitudinal rolling orientation of the plates with the face orientated normal to the beam. The macrostress was assumed to be the same in both phases and the microstresses were assumed to be balanced by the phases [2]. The elastic moduli and Poisson ratio of the phases were assumed to be 205 GPa and 0.28, respectively.

Residual stress measurements of the DSS S32205 specimens were conducted using the $\sin^2\psi$ X-ray method [3]. The initial residual stresses were determined from measured $\langle a \rangle_{\{hkl\}}$ lattice parameters (where $\langle a \rangle_{\{hkl\}}$ are calculated from corresponding $\langle d \rangle_{\{hkl\}}$ spacing), using elastic constants. The phase stresses $\sigma_{ij}^{ph}$ were calculated based on the lattice spacing. Obtained stresses are statistically representative as they are

averaged over a 7 $mm^2$ area containing a large number of grains having different lattice orientations. The high absorption of X-ray radiation in the studied material enables the study of stress state in the surface volume of the sample. It was assumed the principal macrostress normal to the surface ${}^{M}\sigma_{33}$ (where 3 represented the axis normal to the main axis) equaled zero due to relaxation of the forces normal to the surface. A non-zero value phase stress may have been present due to phase interactions.

The average total stress at any point in phase $\alpha$ (ferrite) is the sum of the macrostress and microstress components.

$$\left\langle {}^{t}\sigma_{ij}^{\alpha} \right\rangle = {}^{M}\sigma_{ij} + \left\langle {}^{\mu}\sigma_{ij}^{\gamma} \right\rangle \qquad [3.7]$$

The microstresses in the ferrite (${}^{\mu}\sigma^{\alpha}$) and austenite (${}^{\mu}\sigma^{\gamma}$) phases can be determined by the equilibrium equation for a two-phase material

$$(1-V_f)\left\langle {}^{\mu}\sigma_{ij}^{\alpha} \right\rangle + V_f \left\langle {}^{\mu}\sigma_{ij}^{\gamma} \right\rangle = 0 \qquad [3.8]$$

where $V_f$ denotes the volume fraction of phase $\alpha$ (ferrite) and where the carats refer to the average over a given volume. The phase ratio of ferrite to austenite was assumed to be 60:40 based on the microstructural characterization.

The X-ray tube in the ferrite measurement used Cr $K_\alpha$ radiation measured on the {211} planes. Mn $K_\alpha$ radiation was used to measure the {311} plane of austenite. Lattice displacements were determined in three $\phi$-directions ($0^o$, $45^o$, and $90^o$) for 12 $\psi$-angles between $\pm 43^o$ for the ferrite and $\pm 47^o$ for the austenite. The sample orientation is shown in Figure 3.9 [4]. The locations of the peaks were determined by a least squares fit in the X3000 software. At least 5 measurements were made for each phase.

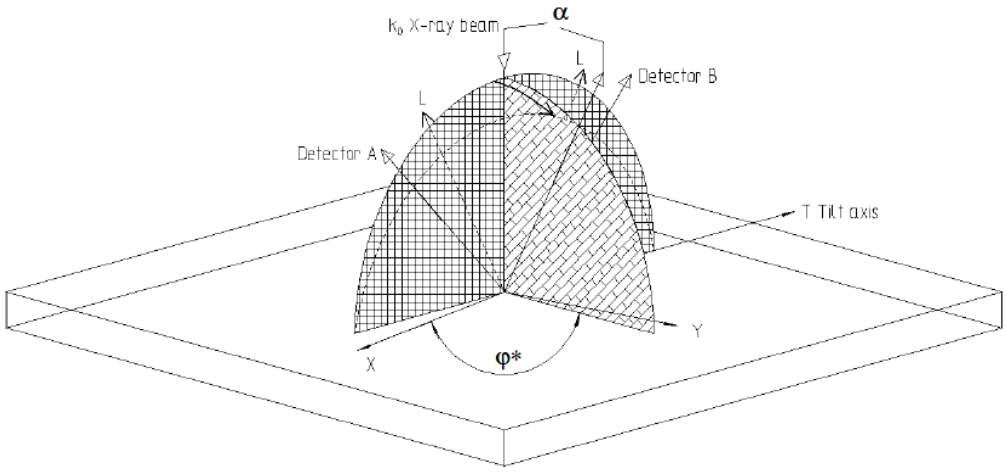


*Figure 3.9:* ***Modified ψ goniometer [4] used in residual stress measurements. The diffraction plane is marked with a squared pattern. The tilt axis T lies in the specimen surface and in the diffraction plane. The rotation vector ϕ was varied between measurements. A value of ϕ = 0° corresponded to the rolling direction.***

### 3.6.2 Hardness of Austenite and Ferrite Phases

Vickers microhardness measurements were performed on the as-received material from VTT using a 25 g load and a dwell time of 15 s on the rolling longitudinal orientation of the samples. The phase regions were smaller than the indents in the other sample orientations. The distance between the indentations was at least five times the diagonal to prevent stress-field effects from nearby indentations. Twenty measurements were made on each sample.

## 3.7 Cathodic Polarization Study to Evaluate Hydrogen Embrittlement

The test solutions were prepared from reagent-grade NaOH and $Na_2S \bullet 9H_2O$. With the exception of the hydrogen diffusion experiments, which utilized 3.75 M NaOH, tests were conducted in an alkaline-sulfide solution composed 3.75 M NaOH and 0.64 M

$Na_2S$ in order to simulate white liquor used in kraft pulping. All experiments were carried out at ambient room temperature. DSS S32205 material was evaluated in this study.

### 3.7.1 Electrochemical Study of Hydrogen Behavior

#### 3.7.1.1 Potentiodynamic Behavior

Electrochemical polarization tests were conducted on plate specimens of approximately 10 mm (h) x 10 mm (w) x 3 mm (t) exposing 3.2 $cm^2$ to sulfide-free and sulfide-containing alkaline solutions. Prior to each test, the samples were wet ground with silicon carbide paper to a 600-grit finish, rinsed with distilled water, and degreased by ultrasonic cleaning in acetone. The samples were placed in a conventional three-electrode cell using a saturated calomel reference electrode (SCE) and Pt counter electrode in a polytetrafluoroethylene (PTFE) electrochemical cell analogous to the cell in Figure 3.4. Nitrogen was continuously bubbled into the cell to purge dissolved oxygen. The scans were performed in the anodic direction at a sweep rate of 2 mV $s^{-1}$ beginning -0.3 V vs. the OCP and ending when the current was 0.5 A.

#### 3.7.1.2 Diffusion Studies

Plate specimens were machined to 25.4 mm X 25.4 mm X 3.1 mm and were sectioned into 200 μm thick wafers using a low speed diamond blade saw such that the rolling direction was orientated normal to the specimen thickness. The wafers were wet ground with SiC paper to 600-grit finish to have a final thickness of 170 – 200 μm. The samples were rinsed with deionized water, and degreased with acetone. The membranes were mounted between two electrochemical glass cells having flanges and fluoroelastomer o-rings. The circular area exposed to the solution was 3.1 $cm^2$. The entry

side of the membrane was subjected to cathodic charging in a sulfide-containing (3.75 M NaOH and 0.64 M $Na_2S$) solution at potentials of -1500 and -1200 mV vs. SCE as well as at the OCP. The exit side of the membrane was polarized in 0.1 M NaOH at a constant potential of 0.300 V vs. SCE. The anodic current measured on the exit side was a measure of the permeation rate of hydrogen. Once the permeation rate achieved a steady-state level, the experiment was terminated. These experiments were conducted at ambient room temperature. Both sides of the cell were continuously bubbled with nitrogen to purge dissolved oxygen. The hydrogen flux was directed normal to the rolling direction. The instrumentation and procedures for the hydrogen permeation tests have been described elsewhere [5].

The hydrogen flux through the specimen [5] was calculated in terms of the steady-state current density $i_p^{\infty}$ ($mA \cdot cm^{-2}$) and was converted into the steady-state hydrogen permeation flux, $J_{\infty}$ ($mol \cdot cm^{-2} \cdot s^{-1}$), according to

$$J_{\infty} = \frac{i_p^{\infty}}{nF} \qquad [3.9]$$

where n is the number of electrons transferred and F is Faraday's constant. The hydrogen permeation rate ($mol \cdot cm^{-1} \cdot s^{-1}$) is given by

$$J_{\infty} L = \frac{i_p^{\infty}}{nF} L \qquad [3.10]$$

where L is the specimen thickness in cm. For diffusion as the rate-limiting step, the effective diffusivity, $D_{eff}$ ($cm^2 \cdot s^{-1}$) is related to the time lag, $t_L$ (s) by

$$D_{eff} = \frac{L^2}{6t_L} \qquad [3.11]$$

3.7.1.3 Hydrogen Microprinting

The hydrogen microprint technique (HMT) [6] was used to detect and observe the hydrogen distribution on the microstructure in a sulfide-free (3.75 M NaOH) solution. HMT was also attempted on samples that were exposed to the sulfide-containing solution, but the thermodynamic stability of silver sulfide ($Ag_2S$) presented practical limitations to the use of the technique with this solution. Samples of approximately 10 mm (h) x 10 mm (w) x 3 mm (t) were polished to 0.05 μm finish, rinsed in distilled water, and degreased in acetone. The samples were then etched with the method described previously to reveal the phases. They were held potentiostatically at -1200 mV vs. SCE in the test environment for 24 h using the potentiostatic setup discussed previously to ensure that hydrogen absorption had occurred. After exposure, the samples were rinsed in distilled water and placed in an ultrasonic acetone bath to removal debris from the surface.

Under dark room conditions, a silver bromide (AgBr) nuclear emulsion (Ilford L4), with a grain size of 140 nm, was diluted into 2 ml of 5 wt % solution of $NaNO_2$. $NaNO_2$ reduces corrosion and prevents false accumulation of silver grains. The diluted solution was heated to 45 $^{o}$C and held for 20 min. A 3 cm diameter wire loop of AWG 20 gauge stainless steel wire was used to apply a uniform, monolayer of the nuclear emulsion to the etched sample surface. The coating was allowed to sit for 1 h. Dissolved hydrogen in the ferrite and austenite phases diffused to the surface and reacted with the AgBr in the emulsion to from silver by

$$AgBr + \frac{1}{2}H_2 \rightarrow Ag^0 + H^+ + Br^- \quad (3.1)$$

The samples were then soaked in a fixing solution composed of 152 g/l of $Na_2S_2O_3$, 10 g/l of $Na_2SO_3$, 25 g/l of $NaHSO_3$, and 30 g/l of $NaNO_2$ for 4 min. The samples were then rinsed with double-distilled water, dried with hot air, and rapidly transported to an SEM for observation.

SEM equipped with EDS was used to observe the silver grains on the surface. A non-polarized specimen was also subjected to HMT to ensure that no silver grains were present on the surface due to etching. EDS was used for phase identification as well as verifying that silver was present on the surfaces of the charged samples.

### 3.7.2 Mechanical Behavior during Cathodic Polarization

#### 3.7.2.1 Effect on Hydrogen Absorption on Hardness

Samples of approximately 10 mm (h) x 10 mm (w) x 3 mm (t) were cut from DSS S32205 plate material. Prior to each test, the samples were wet ground with silicon carbide paper to a 600-grit finish, rinsed with distilled water, and degreased by ultrasonic cleaning in acetone. DSS were held potentiostatically in the sulfide-containing solution for varying lengths of time, exposing 3.2 $cm^2$ to the solution. The potentiostatic setup was similar to the one shown in Figure 3.4. The tests were conducted at ambient room temperature. Nitrogen was continuously bubbled into the cell to purge dissolved oxygen. After exposure, the samples were rinsed in distilled water and ultrasonically rinsed in acetone.

3.7.2.2 Slow Strain Rate Test to Evaluate Hydrogen Embrittlement

The tests were all conducted at an initial strain rate of 2 X $10^{-6}$ $s^{-1}$ in solutions. All tests were carried out on a rigid slow strain rate rig. Each sample was preloaded to 15 kg to minimize system compliance (reduction gear, grips, etc.) effects. The potential was controlled with an external potentiostat. The solution was exposed to the atmosphere and maintained at ambient room temperature. The tests were carried out at the corrosion potential and under applied potentials ranging from -1500 mV vs. SCE to the corrosion potential. The load was measured with a load cell and the % elongation was calculated based on the displacement rate of the crosshead times the duration of each test.

## 3.8 Summary

The experimental approach used in this research project is summarized in Figure 3.10. The primary goal of this study is to understand the role of microstructure and environment on the SCC mechanism of DSS in hot alkaline-sulfide environments. Microstructural features such as mechanical behavior, phase distribution, and phase ratio will be related to SCC initiation and growth. The effect of environment will be studied with respect to ionic concentration and alloy composition as well as to understand selective dissolution. The corrosion rates, surface morphologies, and film properties will collectively be evaluated to understand the corrosion behavior of DSS in alkaline-sulfide environments. The SCC behavior of DSS will studied using SSRT in different environments and examined to understand fracture features. The effect of hydrogen absorption on the failure characteristics will also be examined.

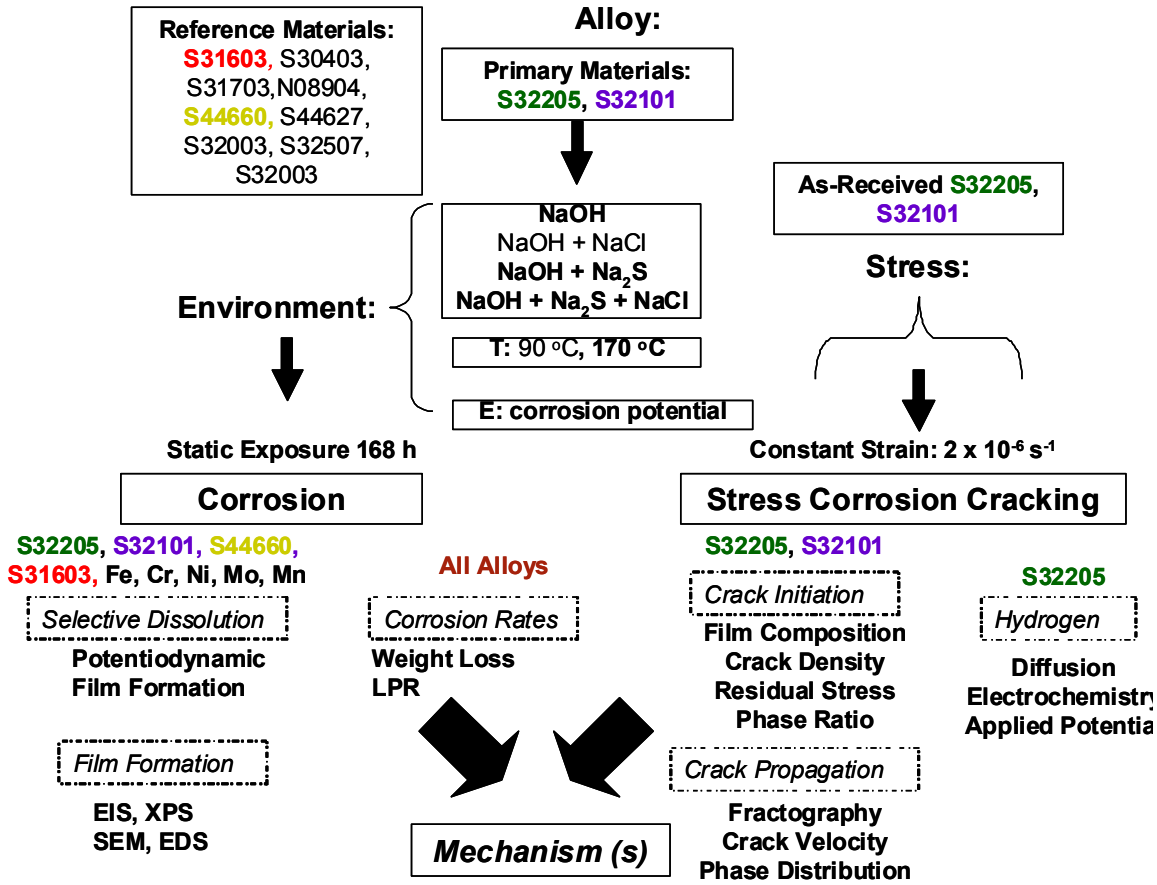


*Figure 3.10:* ***Summary of experimental approach used to understand corrosion and SCC mechanisms of DSS in alkaline-sulfide environments with respect to environment, alloy composition, and microstructure.***

## 3.9 REFERENCES


[1] L.M. Karlsson and A.M. Gokhale, Journal of Microscopy, 186 (1997) 143-152.

[2] H. Leinonen and P. Pohjanne, "Stress Corrosion Cracking Susceptibility of Duplex Stainless Steels and their Welds in Simulated Cooking Environments," CORROSION 2006, NACE , March 12- 16 (2006) San Diego, CA.

[3] I.C. Noyan and J.B. Cohen, "Residual Stress Measurements by Diffraction and Interpretation," Springer-Verlag, New York, NY (1987).

[4] Stresstech Group, "Software User's Guide X3000 V. 1.22d," American Stress Technologies, Cheswick, PA (2007), p91.

[5] ASTM G148, “Standard Practice for Evaluation of Hydrogen Uptake, Permeation, and Transport in Metals by an Electrochemical Technique,” ASTM International, West Conshohocken, PA (2003), p. 1-10.

[6] T.E. Pérez, J. Ovejero García, Scripta Metallurgica, Vol. 16 (1982), p. 161.

# CHAPTER 4

# CORROSION AND ELECTROCHEMICAL BEHAVIOR OF DUPLEX STAINLESS STEELS IN HOT ALKALINE ENVIRONMENTS

## 4.1. Introduction

Iron-chromium-nickel alloy vessels, digesters, and piping are used in high-temperature, high-pressure applications in chemical manufacturing, oil refining, alumina processing, nuclear power plant operation, and pulp and paper production. Reliable service of various stainless steel alloys in strong alkaline or caustic solutions is therefore of practical importance, particularly to the constructors and operators of equipment who attempt to mitigate major maintenance and safety concerns. Hydroxide ($OH^-$) is highly corrosive and will have a complex role in the corrosion mechanisms occurring in composite alkaline environments. Industrial environments composed of sodium hydroxide (NaOH) in the absence of other constituents (e.g., chlorides, sulfates, sulfides, carbonates, etc.) are rarely encountered in industry; nonetheless, NaOH is the most aggressive constituent that can cause corrosion and stress corrosion cracking (SCC), and it is useful to isolate its effect to further the mechanistic understanding. A phenomological study of the corrosion susceptibility, electrochemical behavior, and passive film characteristics has been undertaken to contribute to the fundamental understanding of corrosion behavior in pure NaOH environments as well as provide a control environment for solutions that contain reactive constituents such as chloride and sulfide.

Studying environmental effects on the general corrosion and electrochemical behavior of different types of stainless steel grades (austenitic, ferritic, and duplex) as

well as their primary alloying elements (Fe, Cr, Ni, Mo, and Mn) in simple caustic environments will also elucidate the role of alloy composition. The following chapter will describe the effect of temperature, solution composition, and alloy composition on the corrosion susceptibilities and electrochemical behavior of select grades of DSS in caustic environments. The results can be used to understand the corrosion behavior of stainless steel in caustic environments without the involvement of other aggressive constituents, which will be the subject of subsequent chapters.

## 4.2 Corrosion Behavior in Caustic Environments

### 4.2.1 Corrosion Rates

Figure 4.1 shows the effect of alkalinity (concentration of NaOH) on the corrosion rates of alloys tested in caustic solutions at 170 $^{o}$C for 168 h. An appreciable increase in the corrosion rates was found for alloys tested in 150 g/l NaOH (3.75 M NaOH) as compared to 100 g/l NaOH (2.5 M NaOH) and 125 g/l NaOH (3.13 M NaOH). DSS and austenitic stainless steels had low corrosion rates in simple caustic solution solution, which was demonstrated previously [1-6]. Super grade DSS S32705 was more susceptible in these solutions than the lean (S32101 and S32003) or standard (S32205) grades of DSS. Furthermore, superferritic grade S44660 was more susceptible in these solutions than superferritic grade S44627. Corrosion rates for the latter alloy were negligible in these strong alkaline environments.

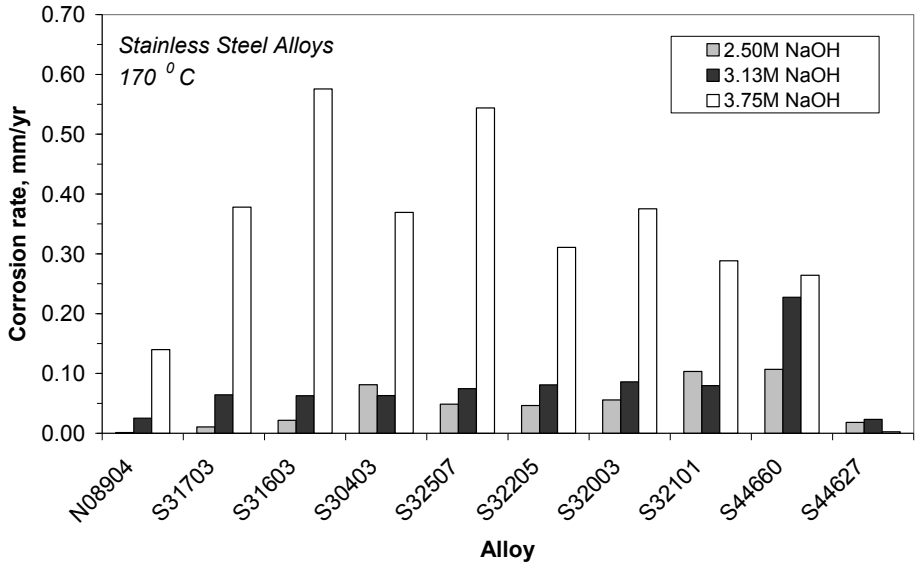


***Figure 4.1:*** ***Corrosion rates of austenitic (N08904, S31703, S31603, S30403), duplex (S32705, S32205, S32101, S32003), and superferritic grades (S44660, S44627) of stainless steel tested in 2.5 M, 3.13 M, and 3.75 M NaOH at 170 °C. Austenitic, duplex, and superferritic types are arranged left to right by descending molybdenum content.***

Comparison of the corrosion rates for the different types of stainless steel indicates that higher Cr and nickel Ni content were beneficial for corrosion resistance in alkaline environments. Previous studies have also shown that the improved corrosion resistance of DSS is due to higher amount of Cr and moderate additions of Ni [1-6]. Mo was detrimental to the corrosion resistance of stainless steels in alkaline environments, which is readily apparent by the higher corrosion rates of S31603 and S44660 as compared to similarly composed S30403 and S44627, everything else being equivalent. This finding has been demonstrated previously for austenitic and DSS tested in caustic environments [5-7]; however, the current study shows that superferritic grades may also benefit from lower Mo additions in alkaline environments. It is not possible to deduce the role of other alloying elements such as Mn or N based on the data in Figure 4.1.

Increased alkalinity had less of an effect on increasing the corrosion rates of the superferritic grades.

### 4.2.2 Forms of Corrosion

The form of corrosion affecting each grade of stainless steel was examined following exposure using optical and scanning electron microscopy (SEM). No appreciable change in the form of corrosion was found for the 2.50 – 3.75 M NaOH range of alkalinities tested. General corrosion for the austenitic (S31603) and superferritic (S44660) grades of stainless steel in alkaline environments can be seen in the micrographs in Figure 4.2. Figure 4.3 shows that the duplex grades were affected by localized preferential corrosion, which is apparent by the surface roughness. Both the ferrite and austenite phases have been dissolved in Figure 4.3. The localized selectivity is due to higher dissolution rates of the austenite phase in alkaline environments. This observation is consistent with the corrosion rate data in Figure 4.1.

Lean grade DSS S32101 and standard grade DSS S32205 showed distinct differences between the austenite (high contrast) and ferrite (low contrast) phases in the top-down images of Figure 4.3. Samples of DSS were also cross-sectioned and observed with optical microscopy to show the localized selectivity of the corrosion behavior. Figure 4.4 shows the depth of corrosion penetration is minimal for super grade DSS S32705. The preferential attack of the austenite phase (light etching phase) is more apparent in lean grade DSS S32101 and standard grade DSS S32205 as compared to the super grade S32705. The difference in selectivity is due to the composition differences among these grades of DSS. Earlier work [8] showed that selective corrosion of the

austenite or ferrite phase of DSS in $CaCl_2$ solution at 100 $^oC$ with pH 6.5 depended on alloy composition.

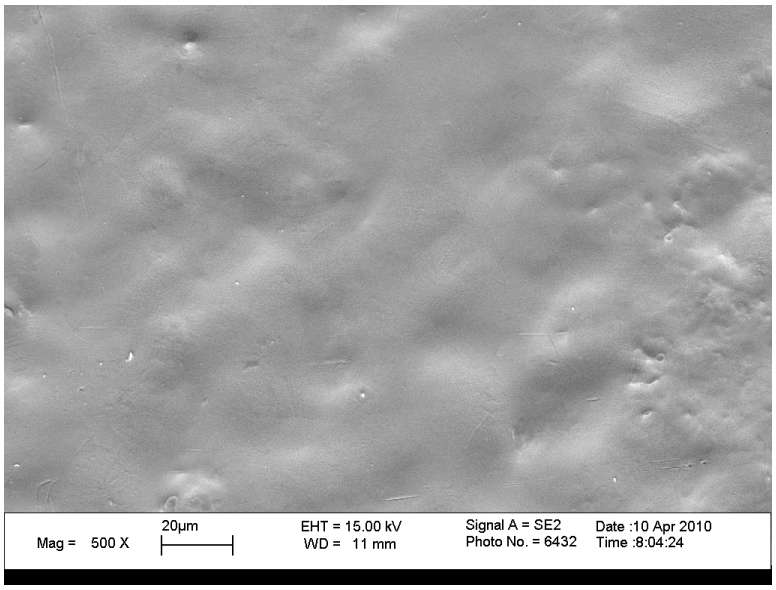


(a)

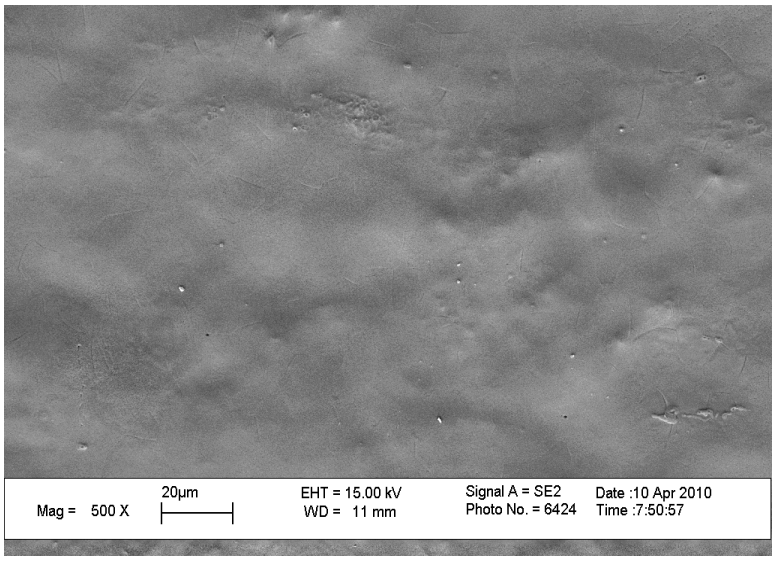


(b)

***Figure 4.2:*** ***SEM micrograph showing general corrosion on austenitic (S31603) and superferritic grades (S44660) of stainless steel tested in 3.75 M NaOH at 170 $^oC$.***

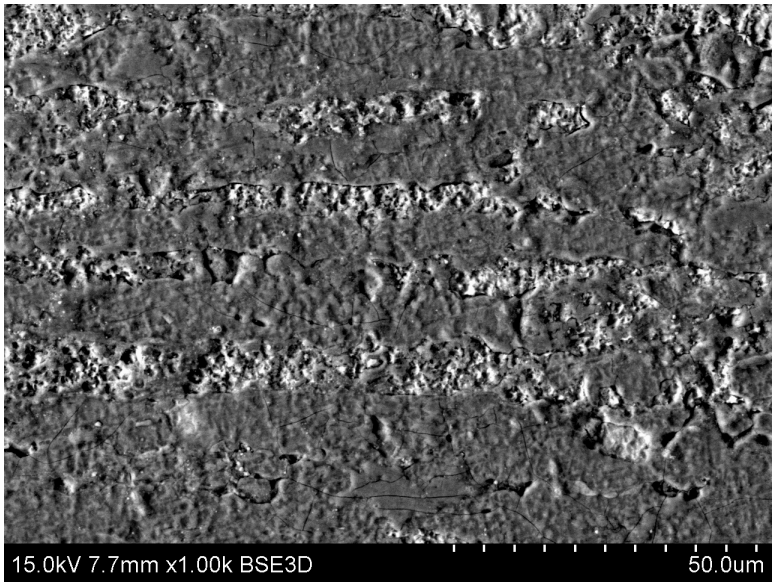


(a)

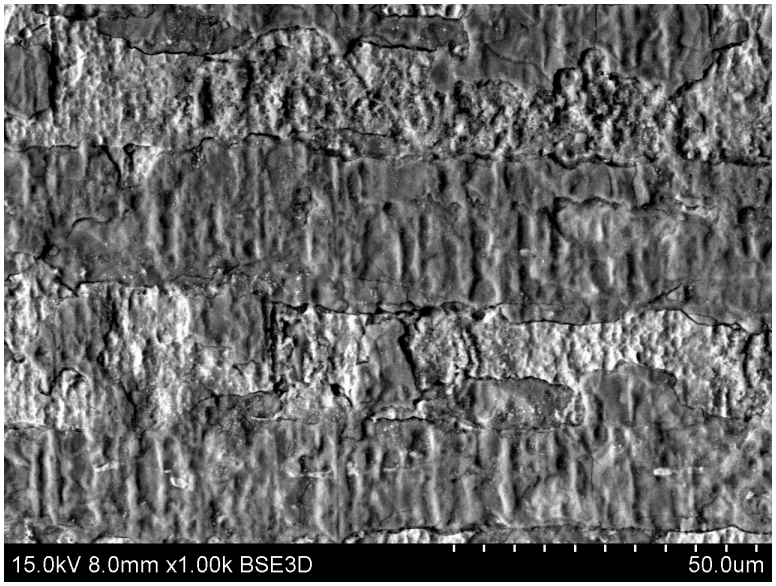


(b)

***Figure 4.3:*** ***SEM micrograph showing general corrosion on lean DSS (S32101) and standard DSS grade (S32205) of stainless steel tested in 2.5 M NaOH at 170 $^{o}$C.***

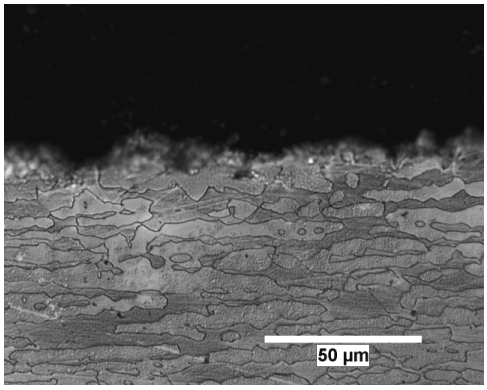


(a)

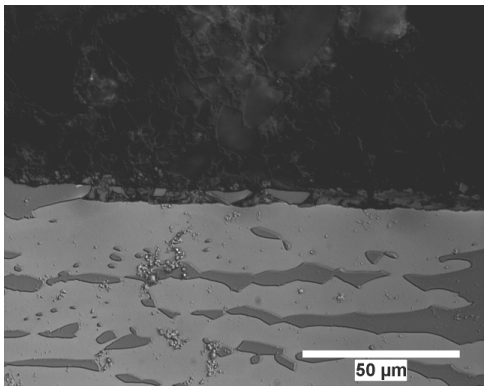


(b)

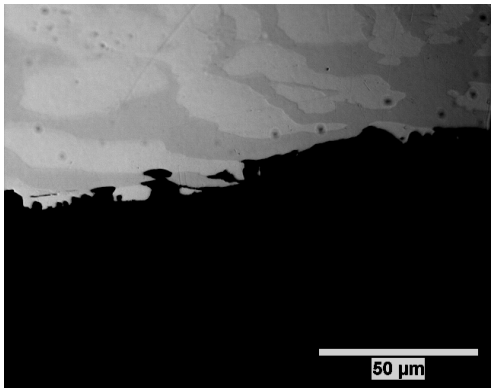


(c)

***Figure 4.4:*** ***Optical micrograph showing corrosion morphology on (a) super grade DSS (S32705), (b) lean grade DSS (S32101), and standard grade DSS (S32205) tested in 3.75 M NaOH at 170 $^{o}$C.***

## 4.3 Electrochemical Behavior

### 4.3.1 Effect of Alloy Composition and Temperature

Nominal compositions of the alloys and pure elements used in this work are shown in Chapter 3, Table 3.4. Prior studies [5-6] in alkaline environments showed that increased Cr content in austenitic stainless steel reduced the critical current density required for passivation and shifted the corrosion potential in the electropositive direction. A separate study [9-10] in hot lithium hydroxide also showed that Cr was beneficial due to the formation of chromium hydroxide or oxide compounds. A more recent study [6] showed that the electrochemical behavior of DSS was similar in a 3.75 M NaOH solution regardless of composition; however, it is currently unclear from the literature if alkalinity can influence the susceptibility of the different types of stainless steel and their alloying elements, which is useful for understanding selective dissolution or de-alloying. The anodic polarization behavior of various types of stainless steel and their primary alloying elements tested in 2.5 M NaOH have been evaluated at both 90 $^{o}$C and 170 $^{o}$C to determine composition and temperature effects on the electrochemical behavior.

#### 4.3.1.1 Behavior of Pure Elements at 90 $^{o}$C and 170 $^{o}$C

Results from pure elements (Fe, Cr, Ni, Mo, and Mn) tested at 90 $^{o}$C in 2.5 M NaOH are shown in Figure 4.5 versus a standard saturated silver-silver chloride (Ag/AgCl) reference electrode (E = 0.197 V versus a standard hydrogen electrode). Earlier studies [5-6, 9-11] evaluated the polarization behavior of Fe, Cr, Ni, and Mo in alkaline environments at 90 $^{o}$C and showed that Fe, Cr, and Ni were passive due to the formation of stable oxides and hydroxides, whereas Mo was active due to the formation

of molybdate ions. Similar results were found for the current concentration of NaOH. Because the electrochemical reactions for Fe, Cr, Ni, and Mo have been determined in previous studies at 90 $^{o}$C, they will not be discussed further.

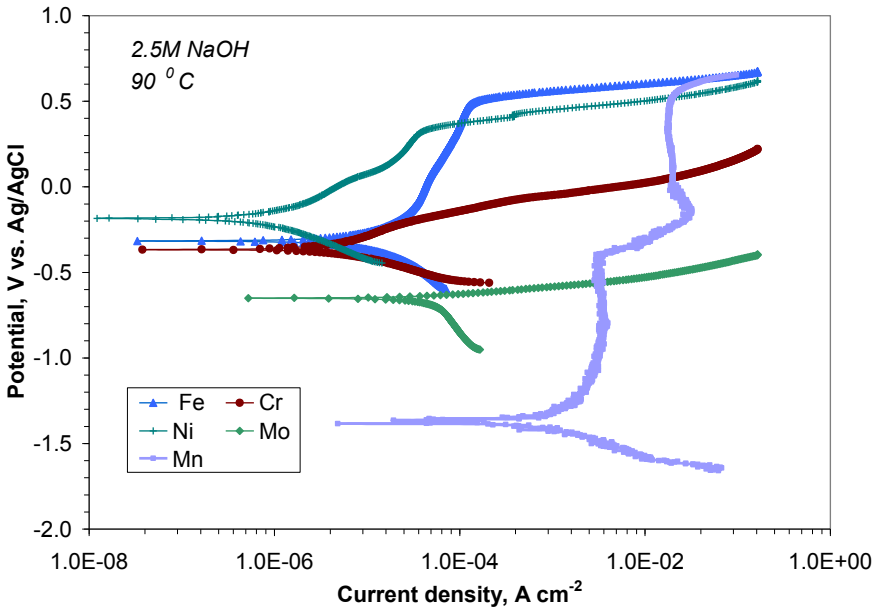


***Figure 4.5:*** ***Anodic polarization scans for pure elements (Fe, Cr, Ni, Mo, and Mn) tested in 2.5 M NaOH at 90 $^{o}$C.***

Few studies have evaluated the electrochemical behavior of Mn in alkaline environments [12-13]. The results for Mn in Figure 4.5 were compared to thermodynamic predictions for the stable species in alkaline environments. The Pourbaix (E-pH) diagram [14] for Mn-$H_2O$ system at 90 $^{o}$C is shown in Figure 4.6. Several assumptions were made when generating the E-pH diagram. Actual pH can change with temperature due to changes in hydrogen activity in solution. Temperature compensation based on an increased activity of hydrogen reduced the pH from 13.4 at 25 $^{o}$C to 12.2 at 90 $^{o}$C based on calculation. The ionic concentration was assumed to be $10^{-3}$ M. The potential is referenced versus the standard saturated Ag/AgCl reference potential. Comparing Figure

4.5 to Figure 4.6 reveals that the corrosion potential of Mn was near the MnO/Mn equilibrium. MnO formation through reaction (4.1) [12-13] was already present at the corrosion potential based on the absence of an active-passive transition in the polarization scan. MnO was stable over a broad potential range based on Figure 4.5 and the predictions of Figure 4.6. The transpassive behavior near -0.400 V vs. Ag/AgCl is attributed to the formation of $Mn_3O_4$. Secondary passivation is attributed to the formation of MnO(OH). The large increase in current at +0.550 V vs. Ag/AgCl is due to the evolution of oxygen.

$$Mn + 2H_2O = MnO + 2H^+ + 2e^- \qquad (4.1)$$

$$E_{MnO/Mn} = -0.295 - 0.0591pH$$

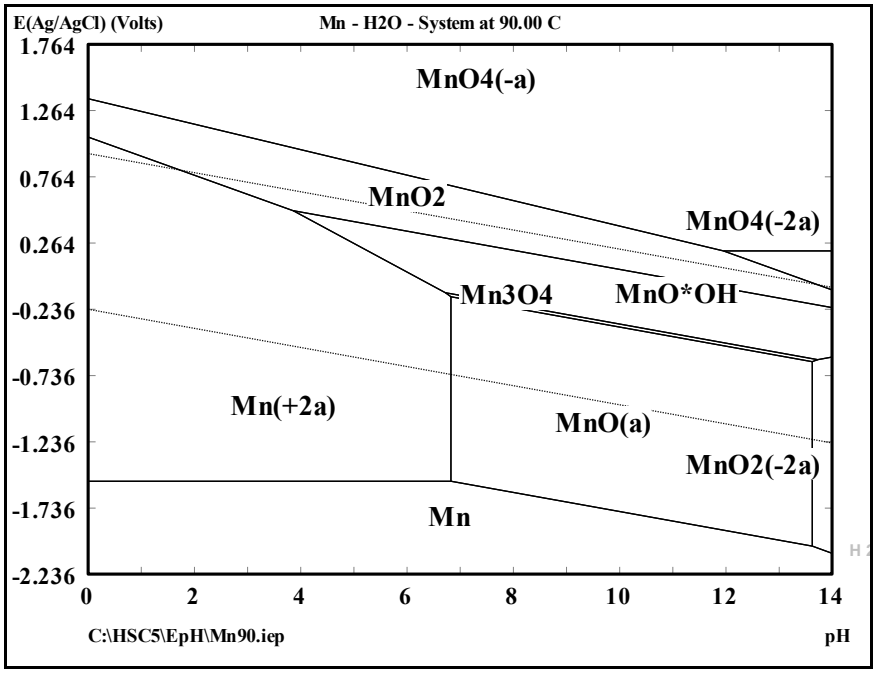


***Figure 4.6:*** ***The E-pH diagram for the Mn-$H_2O$ system at 90 $^oC$ [14].***

The influence of temperature on the electrochemical behavior of the alloying elements is found by comparing the results in Figure 4.5 and Figure 4.7, which shows the results at 170 $^{o}$C. The work conducted at 170 $^{o}$C was conducted with respect to a Mo pseudo reference electrode and potential values were converted to Ag/AgCl scale by assuming the potential of Mo/$MoS_2$ electrode in the alkaline solution as -1050 mV vs. Ag/AgCl as determined from the procedure in Appendix B and described elsewhere [15]. Comparison of Figure 4.5 and Figure 4.7 shows that there was an increase in the current densities of all of the alloying elements and a reduction in the corrosion potentials with temperature. The reduction in corrosion potential cannot be attributed solely to Nernst behavior based on calculation and was therefore due to increased corrosion activity.

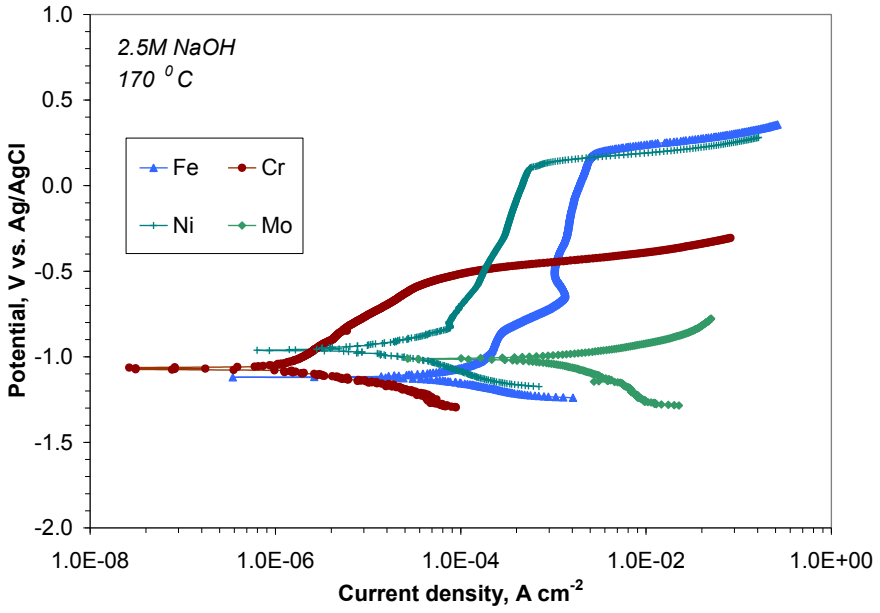


***Figure 4.7:*** ***Anodic polarization scans for pure elements (Fe, Cr, Ni, and Mo) tested in 2.5 M NaOH at 170 $^{o}$C.***

Table 4.1 compares the results from the two temperatures determined by the Tafel extraction technique for further comparison. Mn was not tested at 170 $^{o}$C because the electrode was not compatible with the setup. The results at 90 $^{o}$C clearly indicated high critical current densities and corrosion rates of this material in alkaline environments. The trends in Table 4.1 show that the corrosion rates were nearly an order of magnitude greater for Fe and Ni, whereas the corrosion rate of Cr was nearly unaffected by the increase in temperature. Mo was found to undergo active dissolution with a corrosion rate that was nearly two orders of magnitude greater at 170 $^{o}$C as compared to 90 $^{o}$C. These results are similar to earlier findings [5-6, 9-10] that showed that Ni and Cr lower the critical current density required for passivation and shift the corrosion potential in the electropositive direction in alkaline environments. These results show that Fe, Mo, and Mn will be dissolved in stainless steels when the passive film becomes unstable in alkaline environments.

***Table 4.1:*** ***Summary of electrochemical parameters for elements tested in 2.5 M NaOH at 90 $^{o}$C and 170 $^{o}$C based on Tafel extraction.***

| *Element* | *T, $^{o}$C* | *jcorr. μA cm$^{-2}$* | *Ecorr, mV vs. Ag/AgCl* | *Ba, mV dec$^{-1}$* | *Bc, mV dec$^{-1}$* | *Corrosion rate, mm yr$^{-1}$* |
|---|---|---|---|---|---|---|
| Fe | 90 | 92 | -319 | 1000000 | 1090 | 1.07 |
| Fe | 170 | 352 | -1116 | 1000000 | 339 | 10.21 |
| | | | | | | |
| Cr | 90 | 9 | -326 | 228 | 179 | 0.10 |
| Cr | 170 | 2 | -966 | 419 | 97 | 0.03 |
| | | | | | | |
| Ni | 90 | 2 | -189 | 371 | 310 | 0.02 |
| Ni | 170 | 11 | -962 | 155 | 108 | 0.52 |
| | | | | | | |
| Mo | 90 | 41 | -648 | 47 | 356 | 0.48 |
| Mo | 170 | 1026 | -1010 | 81 | 205 | 51.18 |
| | | | | | | |
| Mn | 90 | 2600 | -1370 | 1000000 | 422 | 30.28 |
| Mn | 170 | - | - | - | - | - |

Based on the corrosion potentials measured at 90 and 170 $^{o}$C it is possible to use thermodynamic predictions to determine the reactions that can occur at various applied potentials. Temperature compensation based on an increased activity of hydrogen would reduce the pH from 13.4 at 25 $^{o}$C to 11.5 at 170 $^{o}$C through calculation. All molar concentrations are assumed to be $10^{-3}$ M for the ionic species.

The E-pH diagram for Fe-$H_2O$ system at 170 $^{o}$C [14] is shown in Figure 4.8. The corrosion potential of Fe at 170 $^{o}$C in Table 4.1 and a pH of 11.5 are in the region of the Fe/$HFeO_2^-$ equilibrium. The stable oxide under these conditions was $Fe_3O_4$ based earlier studies [11]. The anodic Tafel slope for Fe and the absence of an active-passive transition further indicated the electrode was already passivated in 2.5 M NaOH at the test temperature. The transpassive behavior observed in Figure 4.8 is due to the formation of $Fe_2O_3$ through reaction (4.2). The large increase in current near 0.220 V vs. Ag/AgCl was associated with oxygen ($O_2$) evolution.

$$3HFeO_2^- + H^+ = Fe_3O_4 + 2H_2O + 2e^- \qquad (4.2)$$

$$E_{Fe_3O_4/HFeO_2^-} = -1.74 + 0.037\,pH - 0.037\log[HFeO_2^-]^3$$

$$2Fe_3O_4 + 2H_2O = 3Fe_2O_3 + 2H^+ + 2e^- \qquad (4.3)$$

$$E_{Fe_2O_3/Fe_3O_4} = +0.261 - 0.074\,pH$$

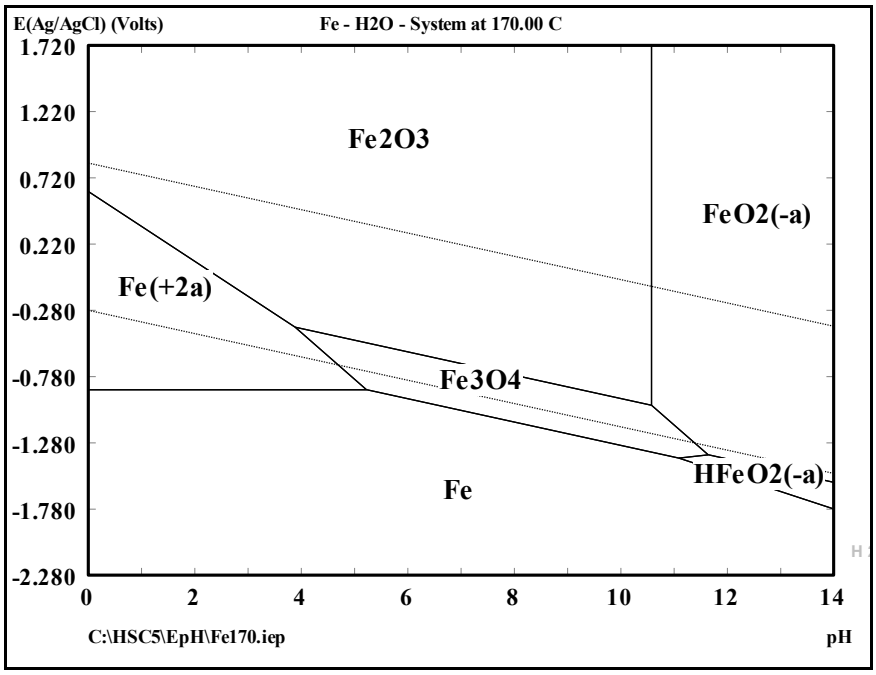


***Figure 4.8:*** ***The E-pH diagram for the Fe-$H_2O$ system at 170 $^oC$ [14].***

The E-pH diagram for Cr-$H_2O$ system at 170 $^oC$ [14] is shown in Figure 4.9. Early work [16] to study the E-pH diagram of the Cr-$H_2O$ system was performed at 150 $^oC$. The corrosion potential of Cr at 170 $^oC$ in Table 4.1 is in the region of the $Cr(OH)_3/CrO_4^{2-}$ equilibrium. The stable hydroxide under these conditions was $Cr(OH)_3$, which is also referred to as $Cr_2O_3$ – hydrate [17]. The anodic Tafel slope for Cr and the absence of an active-passive transition near the corrosion potential further indicated the electrode was passivated in 2.5M NaOH at the test temperature. Agarwal et al. [11] studied the electrochemical behavior of Cr in alkaline environments at 90 $^oC$ and attributed the transpassive behavior in Figure 4.7 to the formation of $CrO_4^{2-}$ through reaction 3. Others [5-6. 9-10] have drawn similar conclusions. The passive film on alloys containing Cr became unstable when $CrO_4^{2-}$ formed at more noble potentials.

$$Cr_2O_3 + 5H_2O = 2CrO_4^{2-} + 10H^+ + 6e^- \quad (4.4)$$

$$E_{Cr_2O_3/CrO_4^{2-}} = +1.386 - 0.0985\,pH + 0.0197\log[CrO_4^{2-}]$$

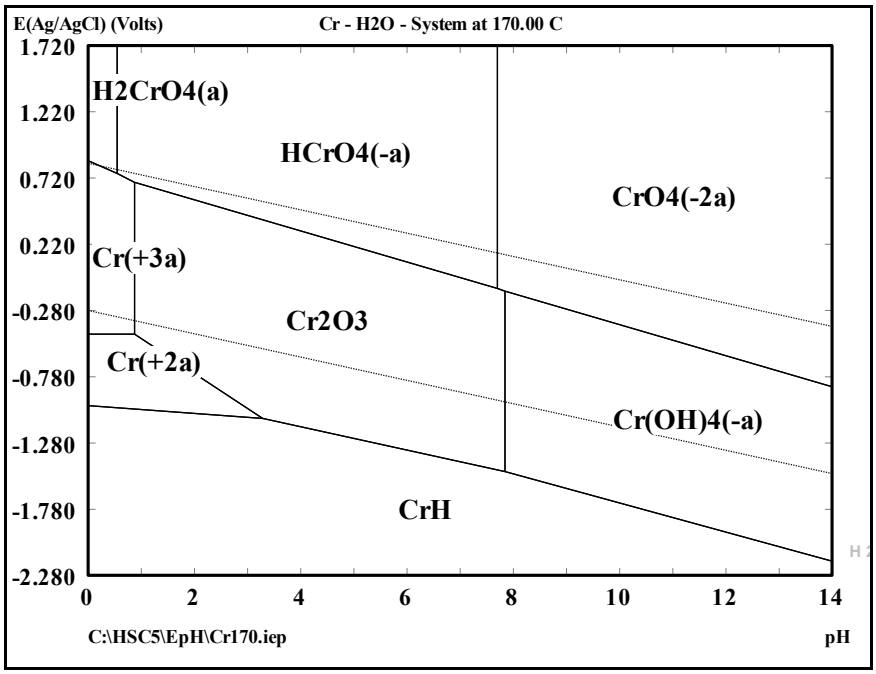


***Figure 4.9:*** ***The E-pH diagram for the Cr-$H_2O$ system at 170 $^oC$ [14].***

The E-pH diagram for Ni-$H_2O$ system at 170 $^oC$ [14] is shown in Figure 4.10. Many studies have described the thermodynamic behavior of Ni in alkaline environments [16-18]. The corrosion potential of Ni at 170 $^oC$ in Table 4.1 and a pH of 11.5 are in the region of the NiO/Ni equilibrium based on Figure 4.10. NiO can form through reaction 5. $Ni(OH)_2$ can also form through reaction 6 under strong alkaline conditions (pH > 14) depending on the molar concentration of Ni ions. The anodic Tafel slope for Ni and the absence of an active-passive transition near the corrosion potential further indicated that $NiO/Ni(OH)_2$ had formed in 2.5 M NaOH at the test temperature. Beverskog [18] used thermodynamic predictions to show that Ni shares a region with the stable area of water,

thus Ni cannot reduce water in this area of the E-pH diagram. Ni is therefore a relatively noble metal in neutral to alkaline solutions and is far less active than Fe [19] or Cr [20] under high pH conditions. Others [5-6, 9-10] have shown similar behavior. Alkaline solutions corrode Ni by the formation of $Ni(OH)_3^-$ and $Ni(OH)_4^{2-}$, which are not shown in Figure 4.10 due to the limited pH range. At very high potential ranges, NiO and $Ni(OH)_2$ are oxidized into beta and gamma phases. The stability of Ni could change drastically in the presence of complexing agents [18], which is the subject of the next Chapter. The large increase in current observed near +0.200 V vs. Ag/AgCl in Fig 4.7 is due to oxygen evolution.

$$NiO + 2H^+ = Ni^{2+} + H_2O \tag{4.5}$$

$$Ni^{2+} + 2H_2O = Ni(OH)_2 + 2H^+ \tag{4.6}$$

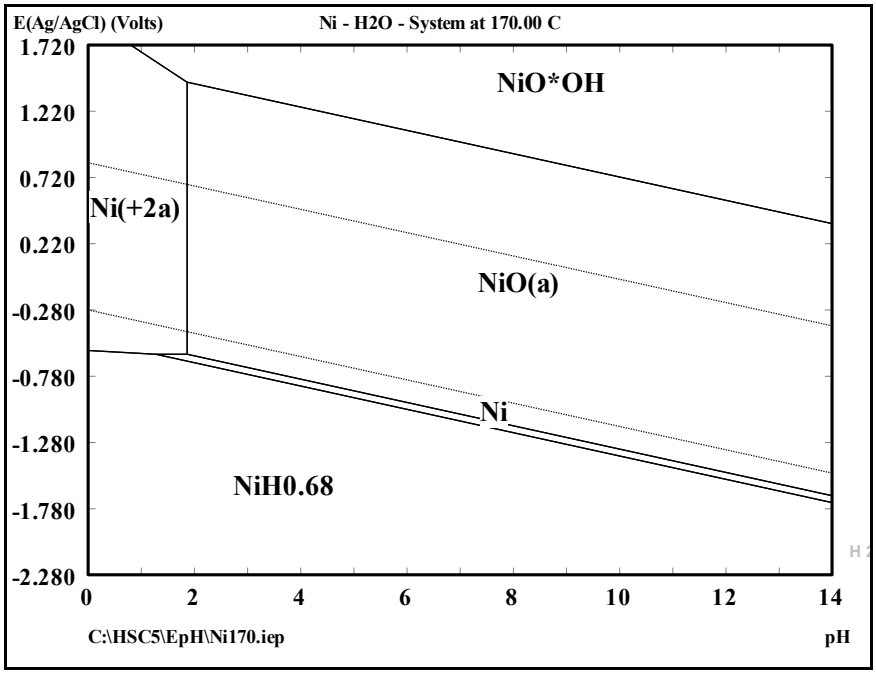


***Figure 4.10:*** ***The E-pH diagram for the Ni-$H_2O$ system at 170 $^oC$ [14].***

Mo had high corrosion rates in 2.5 M NaOH at 90 $^{o}$C and 170 $^{o}$C due to limited passivation in alkaline environments. The E-pH diagram for Mo-$H_2O$ system at 170 $^{o}$C [14] is shown in Figure 4.11. The corrosion potential (-1010 mV vs. SCE) of Mo was active to Cr and Ni in these environments. A rapid increase in the anodic current is apparent in Table 4.1, which shows the low anodic Tafel slope value. An increase in potential beyond the corrosion potential of Mo resulted in rapid dissolution due to the formation of $MoO_4^{2-}$ according to

$$MoO_2 + 2H_2O = MoO_4^{2-} + 4H^+ + 2e^- \qquad (4.7)$$

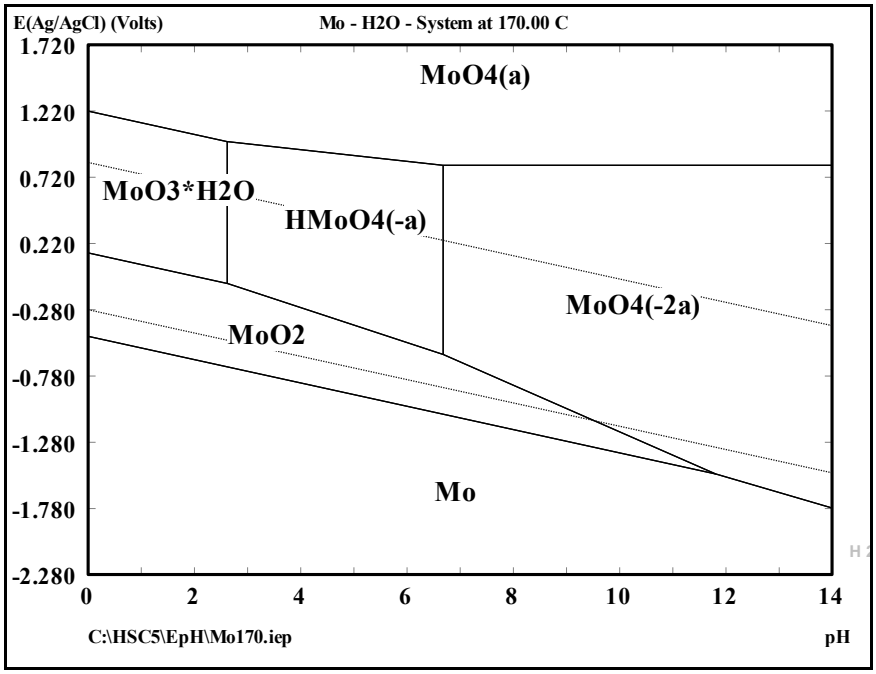


***Figure 4.11:*** ***The E-pH diagram for the Mo-$H_2O$ system at 170 $^{o}$C [14].***

4.3.1.1 Behavior of Alloys at 90 $^{o}$C and 170 $^{o}$C

The anodic polarization behavior of austenitic grade S31603 and superferritic grade S44660 were compared to lean DSS grades S32101 and S32304 and standard grade S32205 at 90 $^{o}$C and 170 $^{o}$C in 2.5 M NaOH to further understand composition and temperature effects. Results from 170 $^{o}$C have been compared to thermodynamic stability predictions to determine likely electrochemical reactions.

Results of alloys tested at 90 $^{o}$C are shown in Figure 4.12. There are no appreciable differences near the corrosion potential; however, the transpassive behavior near 0 V vs. Ag/AgCl and secondary passivation behavior do differ depending on the alloy composition. The transpassive behavior is attributed to the formation of $CrO_4^{2-}$ from $Cr(OH)_3$ as shown in other studies [11]. Previous work [21] showed the transpassive behavior of model Ni-Cr alloys at 200 $^{o}$C in buffered borate solutions (pH 8.7) was determined by Ni content. A similar conclusion was made in the current study, where higher corrosion potentials and an increase in anodic current were more apparent for the lowest Ni-containing stainless steels (S32101 and S44660). The current density of highest Ni-containing alloy (S31603) was lowest in the secondary passive region. This result indicated that austenitic or DSS grades having higher Ni content are favorable for corrosion -resistant applications in oxidizing environments.

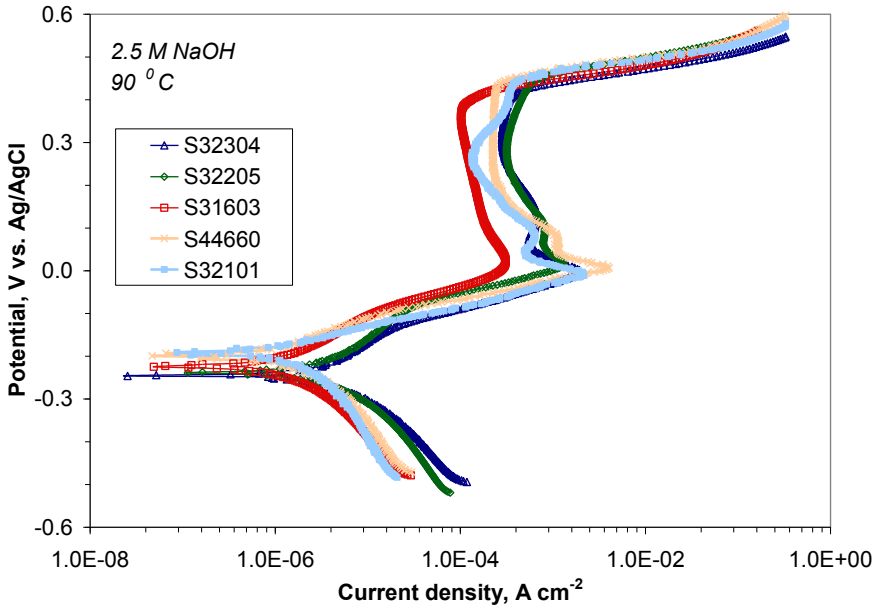


***Figure 4.12:*** ***Anodic polarization scans for austenitic (S31603), superferritic (S44660), lean DSS (S32101 and S3204), and standard DSS (S32205) grades tested in 2.5 M NaOH at 90 °C.***

The polarization curves of Fe, Ni, Mo, Cr, and Mn were compared to lean grade DSS S3201 (Figure 4.13) to understand the role of each alloying element, particularly Ni, on the electrochemical behavior. The corrosion potential of S32101 appears to be determined by the transpassive dissolution $CrO_4^{2-}$. Based on the transpassive behavior of S32101 and S44660, it can be concluded that the corrosion resistance of stainless steel is limited in oxidizing, alkaline environments due to localized instability in the passive film.

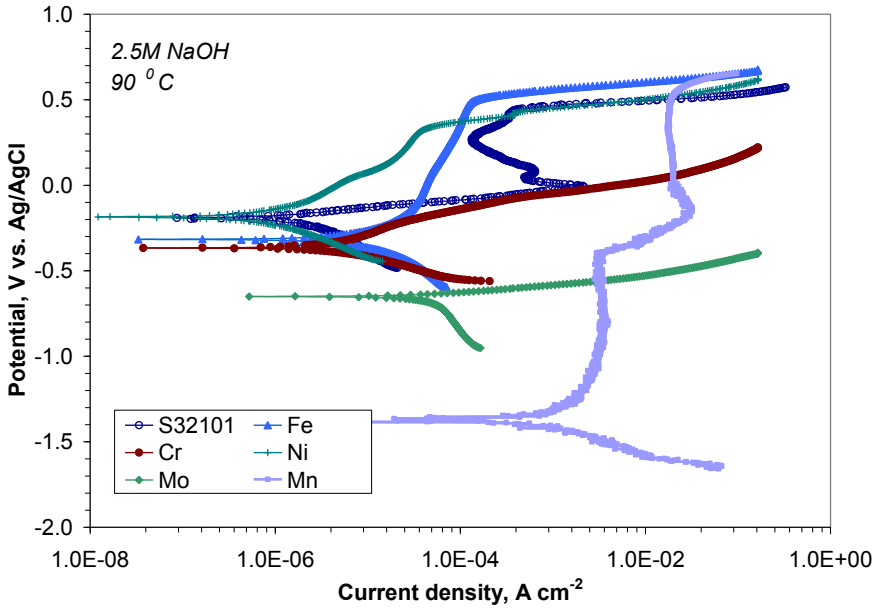


***Figure 4.13:*** ***Anodic polarization scans for lean DSS grade (S32101) and primary alloying elements (Fe, Cr, Ni, Mo, and Mn) tested in 2.5 M NaOH at 90 °C.***

The effect of temperature on the electrochemical behavior of the alloys can be found by comparing Figure 4.12 to Figure 4.14, which shows the results at 170 °C. Further comparisons are provided in Table 4.2, which indentifies the parameters determined by Tafel extraction. Results showed that there was an appreciable reduction in the corrosion potentials of the alloys at 170 °C accompanied by a substantial increase in the corrosion rates, particularly for the austenitic grade S31603. Indeed, corrosion rates were found to increase by nearly two orders of magnitude with the increase in temperature. The corrosion potentials for the DSS grades decreased with decreasing Cr content. Lean DSS grade S32101 was the only DSS grade to have an active-passive transition. The addition of Mn as an austenite stabilizer is the only significant alloying change in S32101 and other DSS grades, which likely accounts for the lower corrosion potential. It is worth noting that the superferritic grade S44660 was less active than

austenitic grade S31603 near the corrosion potentials of the DSS grades, which indicates that the austenite phase in the tested alloys were anodic to the ferrite phase. This finding was corroborated by Figure 4.4. Corrosion rates of DSS grades were similar to the superferritic grade S44660 in alkaline environments, which was consistent with the weight loss experimental results.

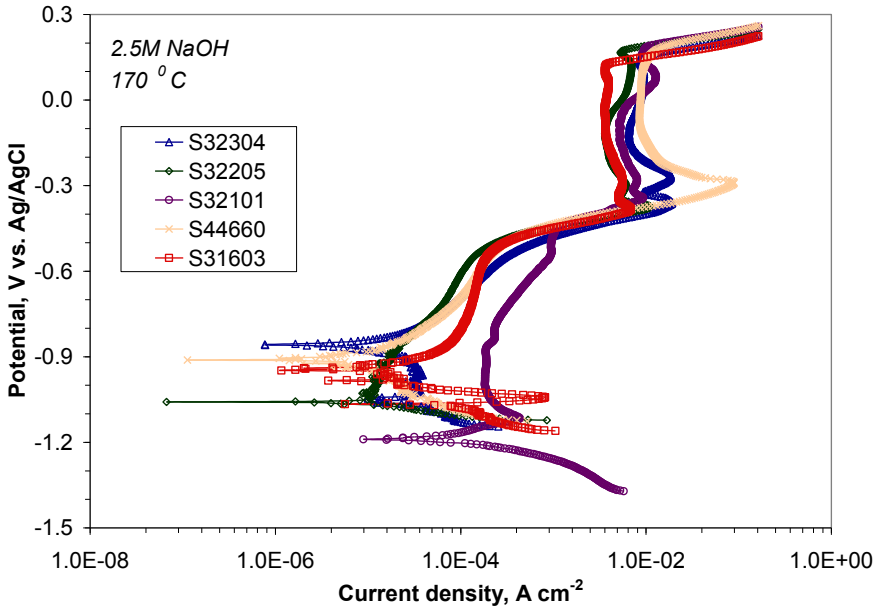


***Figure 4.14:*** ***Anodic polarization scans for austenitic (S31603), superferritic (S44660), lean DSS (S32101 and S3204), and standard DSS (S32205) grades tested in 2.5 M NaOH at 170 °C.***

The individual electrochemical reactions for the alloying elements were compared to the behavior of lean DSS grade S32101 as shown in Figure 4.15. Determining oxide composition from thermodynamic predictions alone is insufficient in the alloys. Nonetheless, the dominant reactions of the elements were readily apparent in the figure. Hydrogen evolution is also thermodynamically possible near the corrosion potential. Hydrogen effects will be discussed more in Chapter 8.

*Table 4.2: Summary of electrochemical parameters for alloys tested in 2.5 M NaOH at 90 °C and 170 °C based on Tafel extraction.*

| Alloy (UNS No.) | T, °C | jcorr. μA cm-2 | Ecorr, mV vs. Ag/AgCl | Ba, mV dec-1 | Bc, mV dec-1 | Corrosion rate,mm $yr^{-1}$ |
|---|---|---|---|---|---|---|
| S31603 | 90 | 7 | -250 | 278 | 181 | 0.08 |
| S31603 | 170 | 131 | -942 | 318 | 1000000 | 6.07 |
| | | | | | | |
| S44660 | 90 | 2 | -188 | 109 | 214 | 0.02 |
| S44660 | 170 | 80 | -910 | 613 | 1000000 | 3.69 |
| | | | | | | |
| S32304 | 90 | 6 | -241 | 213 | 185 | 0.07 |
| S32304 | 170 | 60 | -858 | 557 | 671 | 3.51 |
| | | | | | | |
| S32205 | 90 | 7 | -236 | 247 | 241 | 0.08 |
| S32205 | 170 | 151 | -1072 | 315 | 116 | 1.75 |
| | | | | | | |
| S32101 | 90 | 4 | -195 | 104 | 338 | 0.04 |
| S32101 | 170 | 158 | -1134 | 206 | 104 | 1.84 |

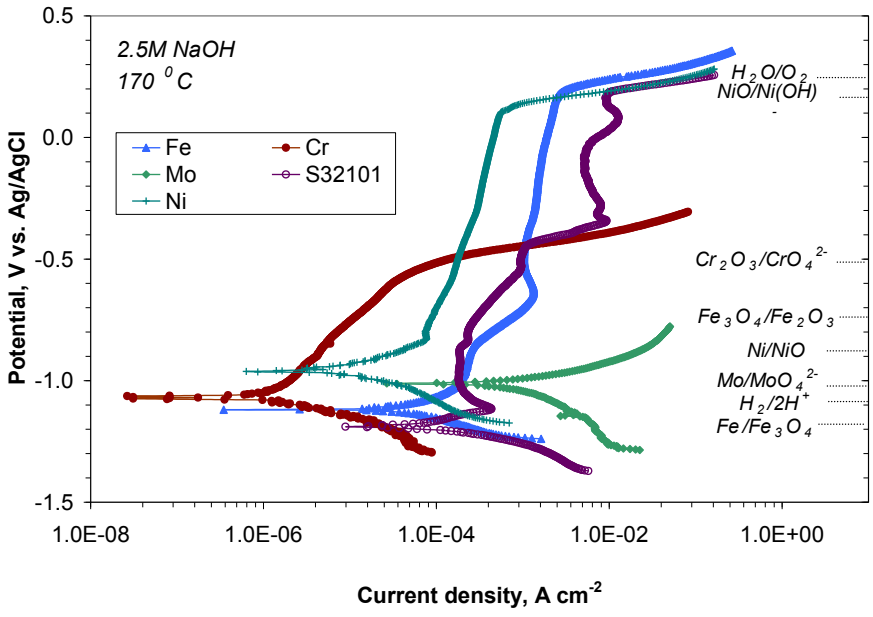


*Figure 4.15: Anodic polarization scans for lean DSS grade (S32101) and primary alloying elements (Fe, Cr, Ni, Mo, and Mn) tested in 2.5 M NaOH at 170 °C.*

The E-pH diagram for Fe-Cr-Ni-Mo-Mn-$H_2O$ system (Fe species dominant) at 170 $^oC$ [14]is shown in Figure 4.16. Film structure of DSS in alkaline environments has been studied previously with X-ray diffraction [5-6], and the results showed that the film on DSS grade S32205 was composed of primarily spinel oxides composed of Fe and Cr, which is consistent with the thermodynamic predictions of Figure 4.16. The film was likely composed primarily of chromite ($Cr_2FeO_4$) and magnetite ($Fe_3O_4$) based on thermodynamic predictions.

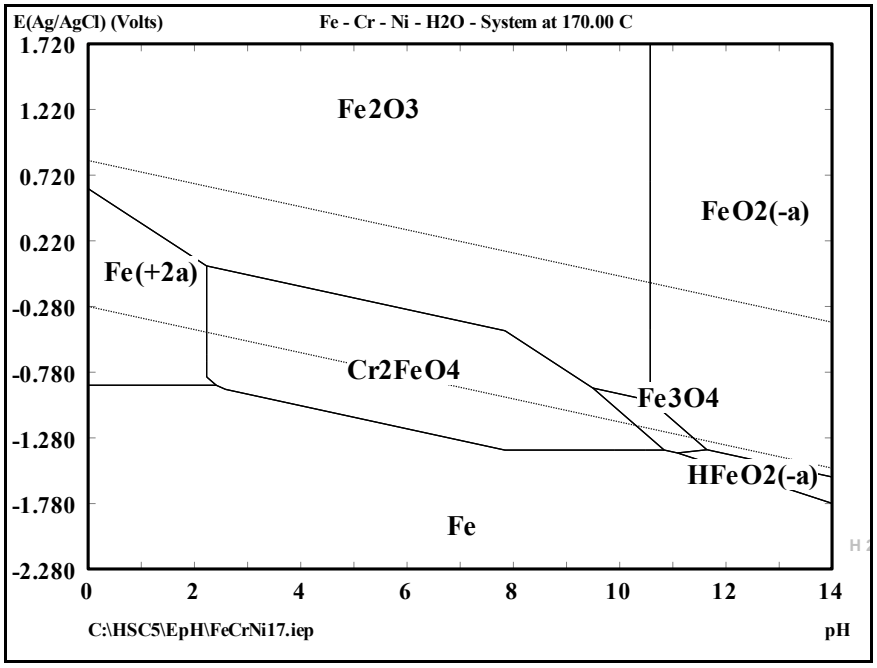


***Figure 4.16:*** ***E-pH diagram for the Fe-Cr-Ni-$H_20$ system at 170 $^oC$ [14].***

### 4.3.2 Effect of Alkalinity

Anodic polarization was used to assess the influence of alkalinity on the electrochemical behavior of lean grade DSS S32101 and standard grade DSS S32205 in 2.5 M NaOH and 500 g/l NaOH (12.5 M NaOH) at 170 $^oC$. An earlier study [6] evaluated

the electrochemical behavior of select grades of DSS in 3.75 M NaOH solution using anodic polarization at 170 $^{o}$C and found similar behavior regardless of DSS grade. Figure 4.17 shows there is an appreciable effect of alkalinity on the polarization behavior between S32205 and S32101 depending on the concentration. The transpassive behavior at -0.900 V vs. Ag/AgCl (near $Fe_3O_4/Fe_2O_3$ equilibrium in Figure 4.15) was drastically influenced in 12.5 M NaOH, whereas in 2.5 M NaOH this effect was not apparent.

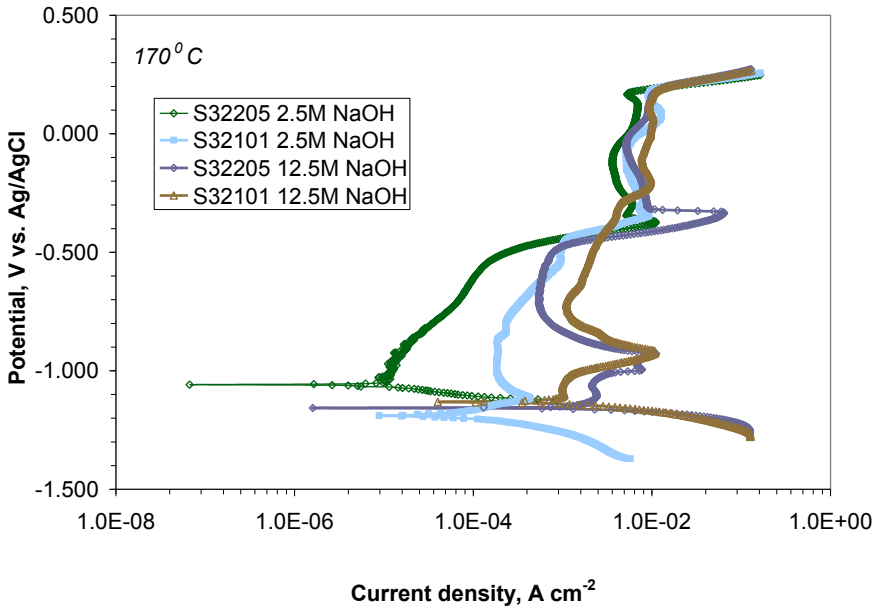


***Figure 4.17:*** ***Anodic polarization curves for lean grade DSS S32101 and standard grade DSS S32205 tested in 2.5 M NaOH and 12.5 M NaOH at 170 $^{o}$C.***

The Tafel extraction technique was used to calculate the corrosion rates from the data provided in Figure 4.17. The results are plotted in Figure 4.18 and show that the corrosion rates for the two alloys were similar in the two environments; however, the rates were greater by nearly an order of magnitude in 12.5 M NaOH. These data demonstrate qualitative comparisons for the different alloys because this technique is

subject to large errors depending on the anodic and cathodic slopes that are used. Furthermore, measurements were made after 24 h, which may not have been sufficient time to ensure steady state conditions. Nonetheless, the influence of alkalinity is apparent. The corrosion rate results in Figure 4.1 also showed that alkalinity has a strong influence on the corrosion rates of DSS.

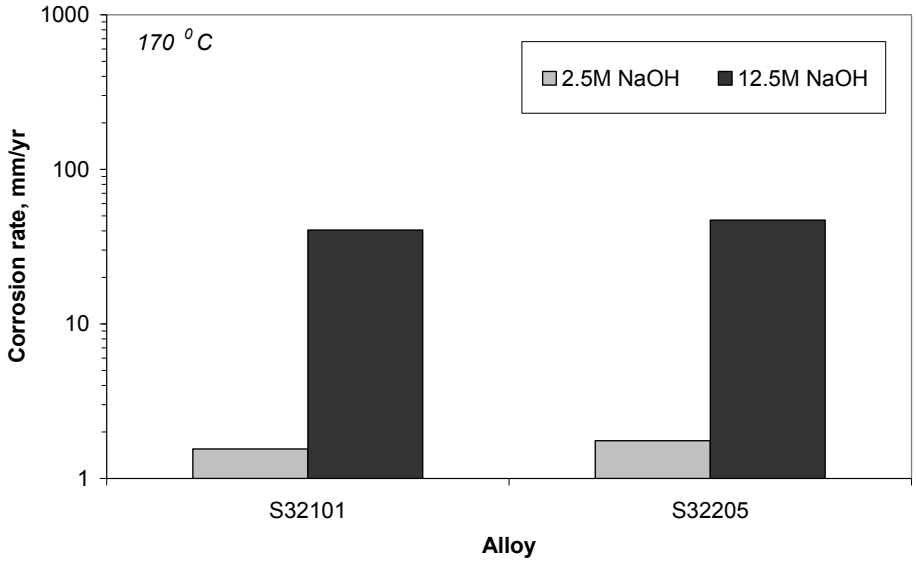


***Figure 4.18:*** ***Corrosion rates based on Tafel extraction for lean grade DSS S32101 and standard grade DSS S32205 tested in 2.5 M NaOH and 12.5 M NaOH at 170 $^o$C.***

## 4.4 Passive Film Behavior

The corrosion resistance of stainless steels is determined solely by their ability to rapidly form and repair a stable passive film on the surface. The resistive properties of this oxide layer are a determined by their composition and morphology. The corrosion susceptibility of each grade of stainless steel will thus be a function of alloy composition

and environment. The following section will focus on the physicoelectrical properties and composition of passive films formed in alkaline environments.

### 4.4.1 Role of Temperature on Physicoelectrical Behavior

The film characteristics of the primary alloying elements (Fe, Cr, Ni, and Mo) were studied during exposure to 2.5 M NaOH at 90 $^{o}$C as well as 170 $^{o}$C using *ac* electrochemical impedance spectroscopy (EIS). Linear polarization resistance (LPR) measurements were compared to the results from EIS. Both *ac* and *dc* techniques have benefits in electrochemistry. The *ac* technique is advantageous near the corrosion potential because limited current is passed and behavior can be observed over a broad frequency range. The *dc* technique can provide useful information about electrochemical behavior over a wider potential range. The performance of austenitic (S31603), superferritic (S44660), lean duplex DSS (S32101), and standard grade DSS (S32205) were evaluated during a 168 h exposure and compared with respect to composition. The corrosion potential was continuously monitored during the experiments.

#### 4.4.1.1 Behavior of Alloying Elements

Passive film formation at the corrosion potential in alkaline environment was evaluated throughout the first 24 h of exposure in 2.5 M NaOH using EIS at 90 $^{o}$C and 170 $^{o}$C. LPR values measured in a separate experimental setup and compared to the results of each EIS scan. Polarization resistance from the LPR measurements can be compared directly to the impedance modulus in the EIS scans at approximately 5 mHz based on the following calculation: a scan rate of 0.1 mV/s and a range of 10 mV to the corrosion potential results in a frequency of 1 cycle per 200 s or 0.005 Hz. Table 4.3 compares the measurements from LPR and EIS measurements after 24 h of exposure at

170 $^{o}$C. Reasonable repeatability, i.e. within an order of magnitude, was found for the two experimental setups. Results showed that passive film formed on Cr had a higher resistance than any of the other alloying elements. Polarization resistance of Mo was significantly lower than the other alloying elements, which supports the higher corrosion rates of this material. Betova et al [15] have shown similar behavior for the alloying elements in alkaline environments.

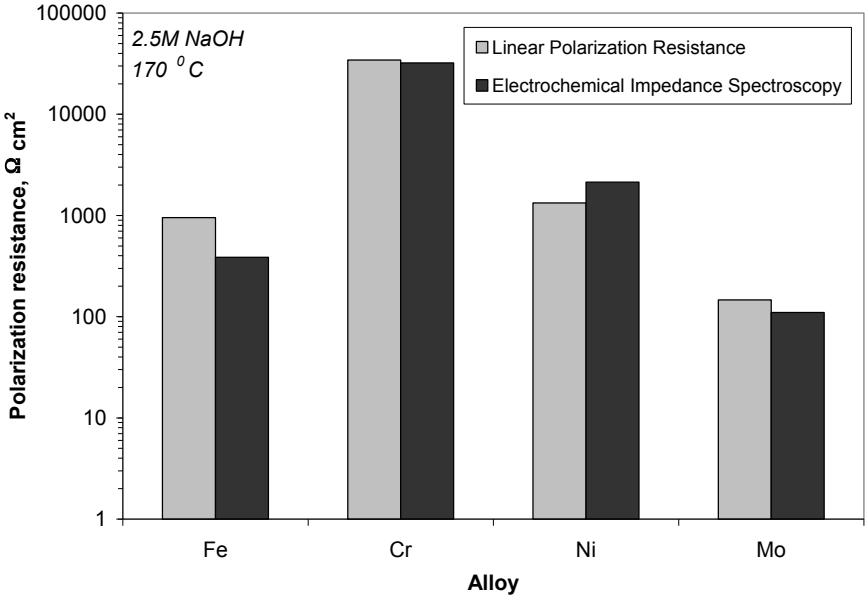


***Figure 4.19:*** ***Comparison of polarization resistance values measured using linear polarization resistance and electrochemical impedance spectroscopy for alloying elements tested in 2.5 M NaOH at 170 $^{o}$C.***

EIS results were fit to analogous electrical circuits using a complex non-linear least squares (CNLS) linear regression algorithm to burgeon mechanistic understanding of the corrosion processes occurring on the electrodes surface near the corrosion potential at 90 and 170 $^{o}$C. Resistivity of the passive film or charge transfer resistance is the single most important parameter that can be determined using EIS modeling. Other surface

phenomena, i.e., adsorption, diffusion, or dissolution, can also be studied with EIS. EIS spectra for Fe, Cr, Ni, and Mo were collected in the frequency range of 50 kHz to 1 mHz after a 24 h stabilization of the system, whereby the potential remained within a mV for a 10 minute period. Spectra for Fe are provided in Figure 4.20 – 4.22. Figure 4.20 is experimental results for Fe tested in the solution at 90 and 170 $^{o}$C. Experimental results from Figure 4.20 have been re-plotted in Figure 4.21 and Figure 4.22 and compared to the best-fit results from simulations.

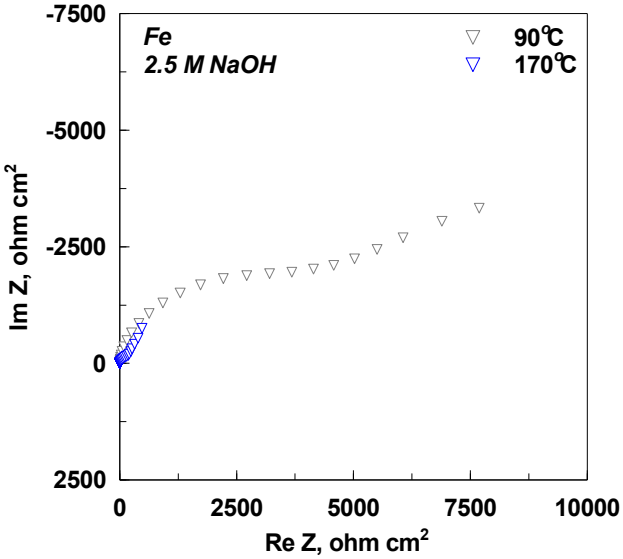


(a)

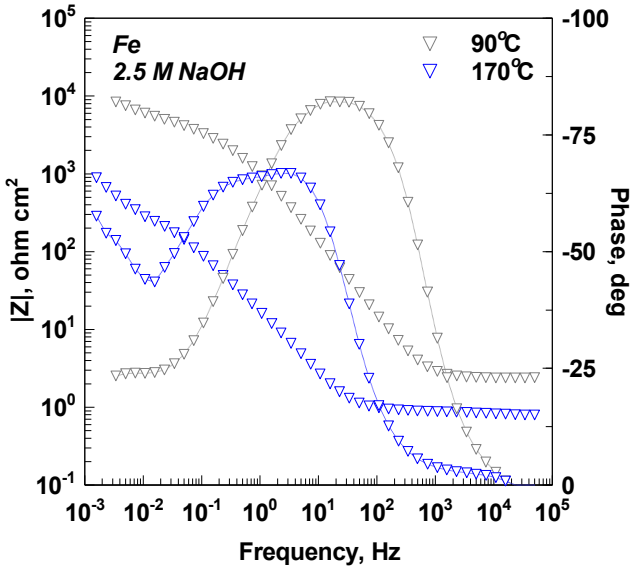


(b)

*Figure 4.20:* ***Comparison of electrochemical impedance spectra for Fe tested in 2.5 M NaOH at 90 and 170 °C.***

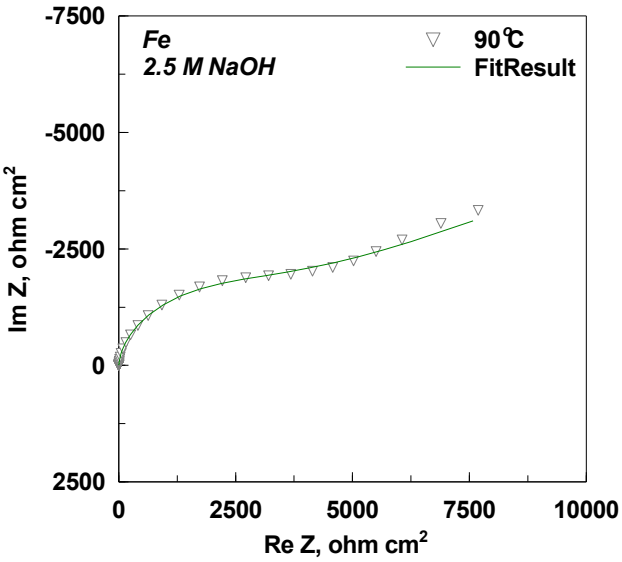


(a)

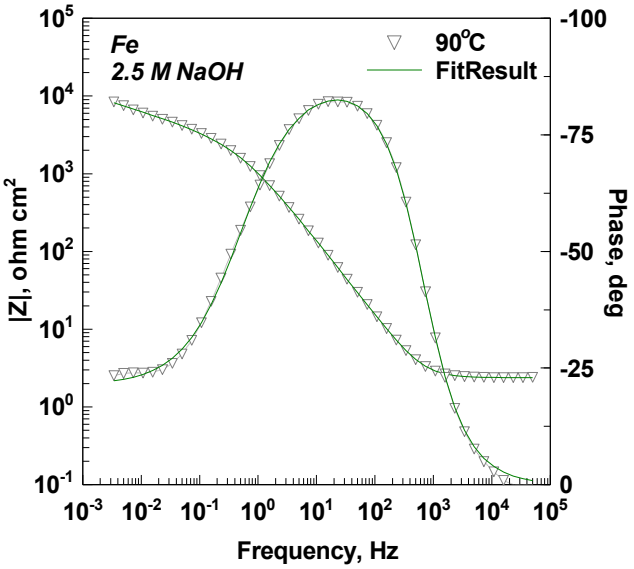


(b)

*Figure 4.21:* ***Electrochemical impedance spectra for Fe tested in 2.5 M NaOH at 90 °C. Points – experimental points, lines – best fit results obtained from simulation. The best fitting parameters are: $R_s$ = 2.39 Ω cm$^2$, $R_1$ = 3240 Ω cm$^2$, $CPE_1$ = 156 μF cm$^{-2}$, $\alpha_1$ = 0.939, $R_2$ = 13.7 kΩ cm$^2$, $CPE_2$ = 1.11 mF cm$^{-2}$, and $\alpha_1$ = 0.577. ($\chi^2$ = 6.27 e-4)***

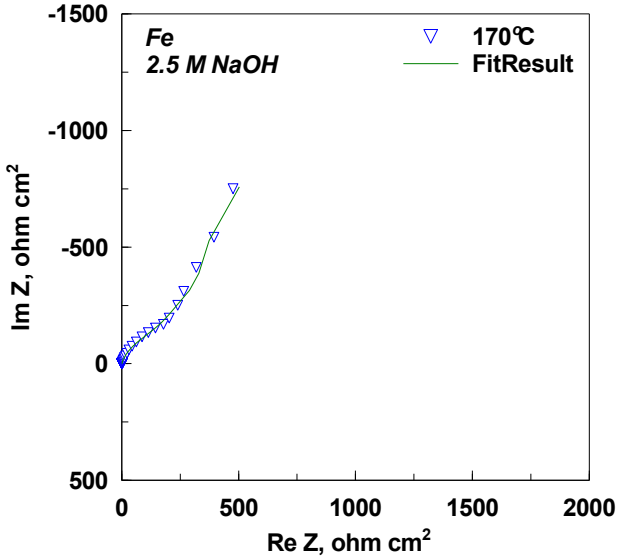


(a)

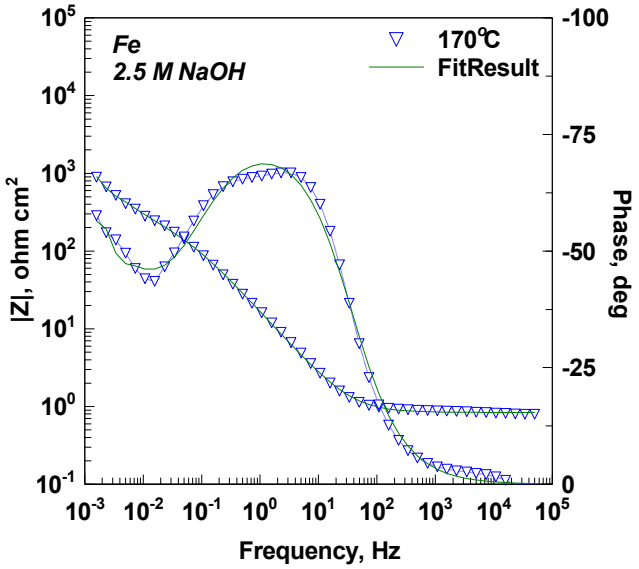


(b)

*Figure 4.22:* ***Electrochemical impedance spectra for Fe tested in 2.5 M NaOH at 170 °C. Points – experimental points, lines – best fit results obtained from simulation. The best fitting parameters are: $R_s$ = 2.11 Ω cm$^2$, $R_1$ = 763.8 Ω cm$^2$, $CPE_1$ = 5.32 mF cm$^{-2}$, $\alpha_1$ = 0.826, $R_2$ = 10.4 kΩ cm$^2$, $CPE_2$ = 17.4 mF cm$^{-2}$, and $\alpha_1$ = 0.826. ($\chi^2$ = 4.14 e-4)***

Reasonable agreement between the experimental data and the simulations was found at both temperatures. Validity of the models was verified by a goodness of fit (chi-squared statistics) having a significance level less than 0.005. Electrical circuits were chosen to represent the simplest analogous model that fit the data. Two resistance capacitance (RC) time constants were observed for the Fe spectra. The results from the EIS measurements have been fit to the hierarchically distributed equivalent circuit (Figure 4.23) using a simplex method. Other studies of Fe in alkaline environments have shown either two [21] or three [15] RC circuits for Fe depending on the solution concentration and temperature.

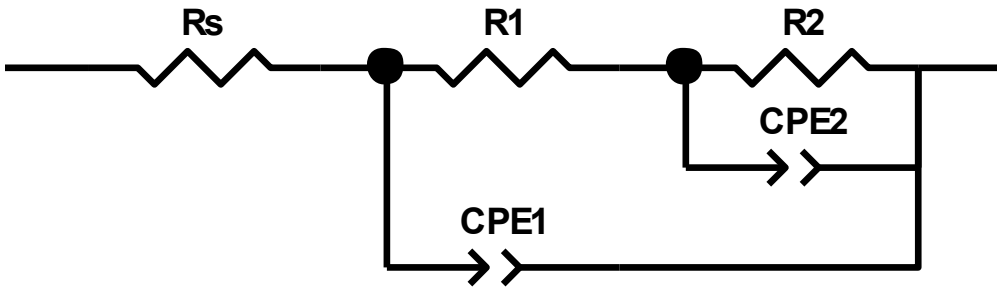


***Figure 4.23:*** ***Equivalent circuit used to simulate the electrochemical behavior of Fe in 2.5 M NaOH at 90 and 170 $^{o}$C.***

A constant phase element (CPE) was used to model the low frequency domain at 90 $^{o}$C. The impedance results at 90 $^{o}$C are compatible with two oxidation/reduction reactions corresponding to a blocking electrode process and a redox process taking place in the passive layer. The solution resistance ($R_S$) was found to decrease with an increase in temperature. The model element ($R_2$) represents the charge transfer resistance occurring at lowest frequencies at the electrode-passive film interface, which was also

found to decease from approximately 15 kΩ $cm^2$ to 10 kΩ $cm^2$ with the increase in temperature. The charge transfer resistance can be taken as a first-approximation measure for the polarization resistance. The double layer capacitance at low frequencies ($CPE_2$) increased in value and shifted to lower frequencies with increased temperature, which indicates that the oxide film was thicker at 170 $^oC$. Moreover, the high capacitance value at this temperature has been shown to correspond to an oxidation/reduction process occurring on a roughed surface texture in previous work [22-23]. Magnetite was the stable oxide expected near the corrosion potential at 90 $^oC$ based on thermodynamic calculations. This oxide is conductive and results in a roughened surface. According to previous work on Fe and carbon steel in borate buffer solution in temperatures of 150 – 300 $^oC$ [24-28] the RC time constant at high frequencies is likely associated with electronic properties of the passive film.

The impedance of the analogous electrical circuit at 90 $^oC$ and 170 $^oC$ are provided in equations [4.1] – [4.5] [29]. An analogous circuit whereby the RC circuit at low frequencies is replaced by a Warburg impedance element as shown below. The variable d is the Nernst diffusion layer thickness, and D is the ionic diffusion coefficient

$$Z(\omega) = R_S + \frac{R_1}{\frac{1}{1+\left(Z_2(\omega)/R_1\right)} + \left(j\omega R_1 CPE_1\right)^{\alpha_1}} \qquad [4.1]$$

$$\text{where } Z_2(\omega) = \frac{R_2}{1+\left(j\omega R_2 CPE_2\right)^{\alpha_2}} \qquad [4.2]$$

$$Z(\omega) = R_S + \frac{R_1}{\frac{1}{1 + \left( Z_{\omega_S}(\omega) \Big/ R_1 \right)} + \left( j\omega R_1 CPE_1 \right)^{\alpha_1}} \quad [4.3]$$

where $Z_{W_S}(\omega) = \frac{W_{1-R}}{\sqrt{\omega}}(1-j)\tanh\left[W_{1-T}\sqrt{j\omega}\right]$ [4.4]

and $W_{1-T} = \frac{d}{\sqrt{D}}$ [4.5]

A Warburg Short ($W_S$) diffusion element could also have been used to model finite-length diffusion with a transmissive boundary, which was apparent by the 45 $^{o}$ phase angle at lower frequencies in Figure 4.22. The Warburg element $W_{1-R}$ is the Warburg coefficient, σ, which is given by the equation:

$$\sigma = W_{1-R} = \frac{RT}{[M^{n+}]n^2F^2A\sqrt{2D}} \quad [4.6]$$

where R is the gas constant, T is temperature, $[M^+]$ is the molar ionic concentration, n is the number of electrons, F is Faraday's constant, A is surface area. Diffusion processes can be dominated by one of the following mechanisms: diffusion of anionic vacancies, diffusion of cationic vacancies, or diffusion of cationic interstitials. Based on previous

work [30] for Fe and carbon steel in alkaline environments, the low frequency behavior was likely limited by cation diffusion. It was outside of the scope of the current work to understand the kinetic behavior of passive film formation, but to provide a comparison of alloying elements. Other studies have been devoted to kinetic considerations [27-28, 31-34].

The other alloying elements were also fit using CNLS fitting algorithms to simulate analogous electrical circuits. Up to three RC time constants were apparent for Cr and Ni in the alkaline environments. Only one time constant was found for Mo. The experimental EIS spectra for Cr, Ni, and Mo are shown in Figure 4.24 – 4.26, respectively. Results show that temperature reduced the charge transfer resistances at 170 $^{o}$C, which accounts for the higher corrosion rates at this temperature. Indeed, the charge transfer resistance for Cr and Ni (ca. 20 kΩ cm$^2$) was reduced by nearly 50 % with the increase in temperature. A diffusion element could be fit to the low frequency behavior in Cr and Ni at 90 $^{o}$C, but due to the frequency range of the experiment it was not clear if the redox reaction at the film-metal interface was limited by diffusion. Other work [24] has attributed this behavior to the cation diffusion. Mo had a significantly lower charge transfer resistance (< 1 kΩ cm$^2$) at both temperatures and showed no ionic diffusion in the time scale of the experiment. The increase in temperature also accounted for an increase in the capacitance character of the electrodes, signifying that the oxide films were thicker and rougher at 170 $^{o}$C.

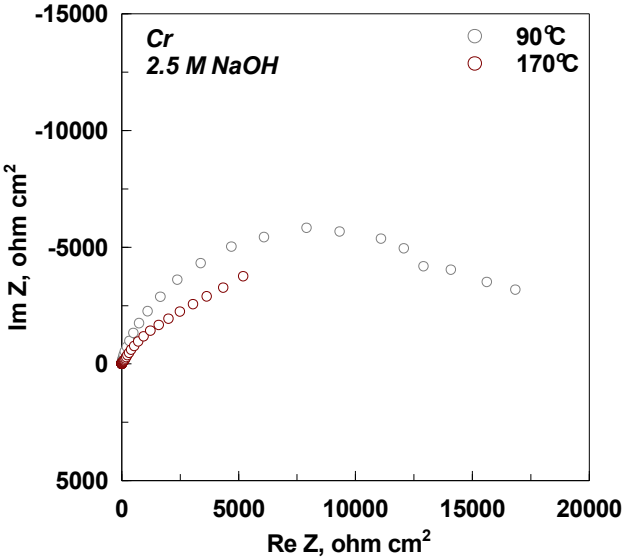


(a)

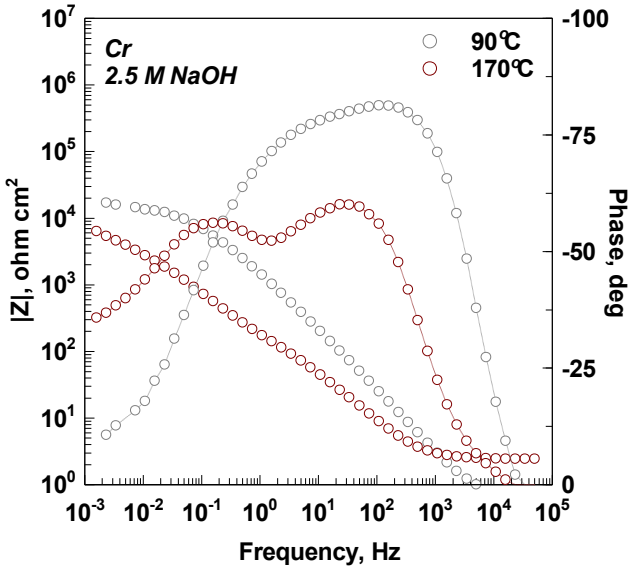


(b)

*Figure 4.24:* ***Comparison of electrochemical impedance spectra for Cr tested in 2.5 M NaOH at 90 and 170 °C.***

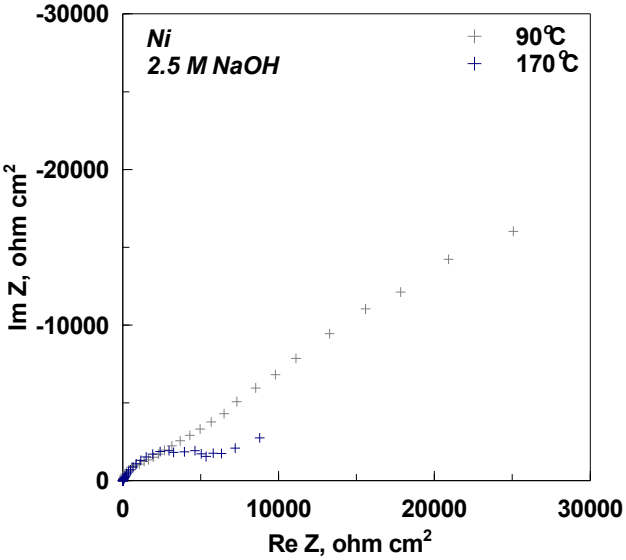


(a)

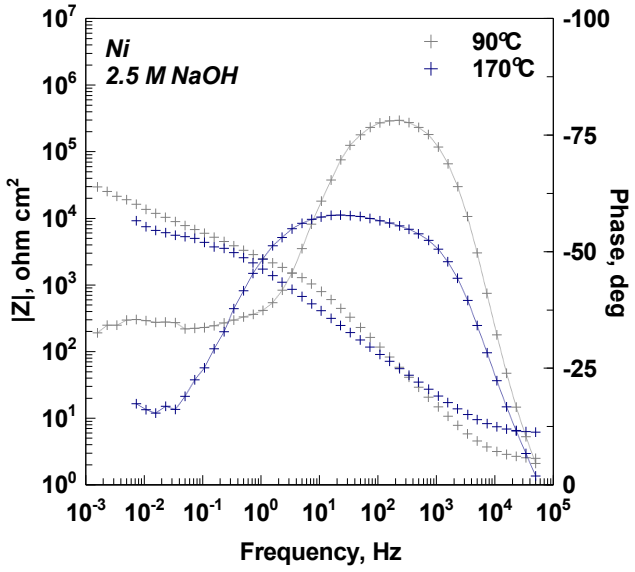


(b)

*Figure 4.25:* ***Comparison of electrochemical impedance spectra for Cr tested in 2.5 M NaOH at 90 and 170 °C.***

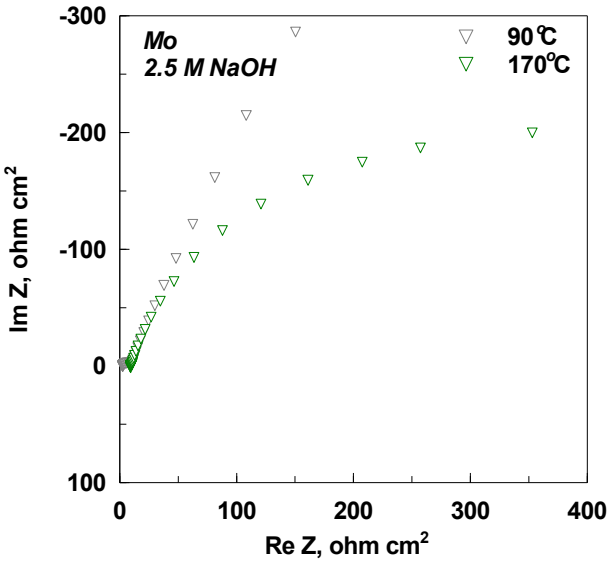


(a)

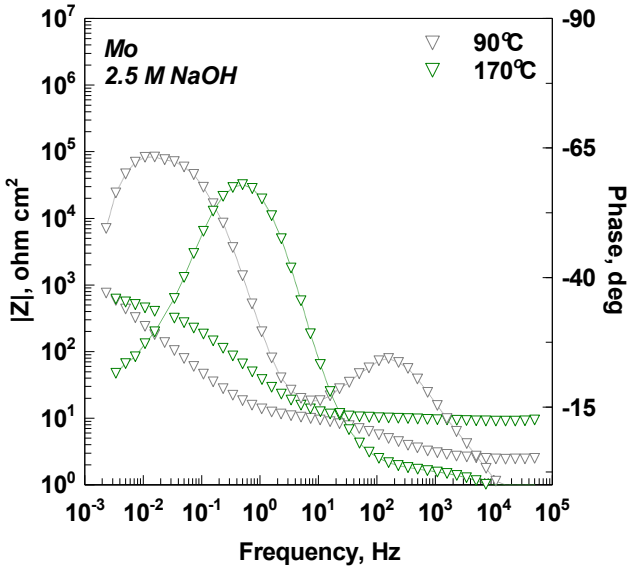


(b)

*Figure 4.26:* ***Comparison of electrochemical impedance spectra for Mo tested in 2.5 M NaOH at 90 and 170 °C.***

4.4.1.1 Behavior of Alloys

EIS and LPR measurements were used to gain an understanding of the role of alloy composition and temperature on the physicoelectrical properties of the passive films formed on austenitic (S31603), superferritic (S44660), lean DSS (S32101), and standard grade DSS (S32205) in alkaline environments. Of particular interest was how compositional differences between the different DSS grades, particularly Ni and Mn, would influence the resistivity of the passive films. For these particular alloys, a separate study to evaluate the effect of alkalinity was performed comparing 2.5 M and 12.5 M NaOH at 170 $^{o}$C.

A comparison of the EIS spectra for the lean (S32101) and standard (S32205) DSS grades at 90 $^{o}$C is shown in Figure 4.27 and Figure 4.28, respectively. Two distinct RC time constants were found in the Nyquist plots for both alloys. The first time constant observed at low frequencies is associated with the at the electrode-passive film interface. The second time constant is attributed to a Faradic process in the passive film, which is more rapid in S32101 as compared to S32205 based on the CPE values.

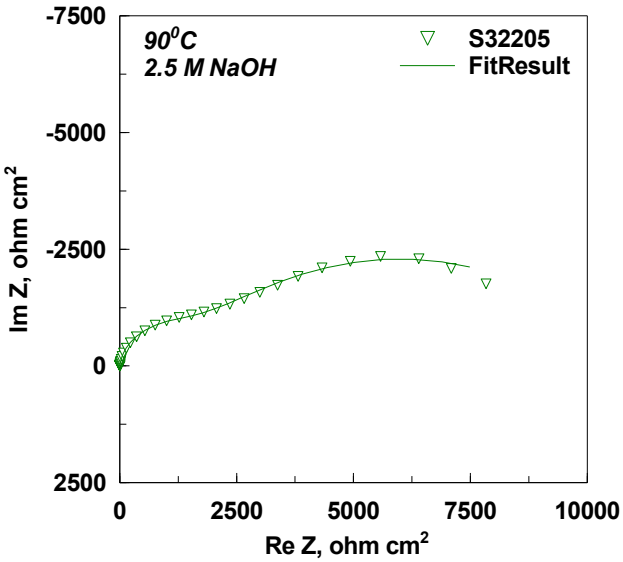


(a)

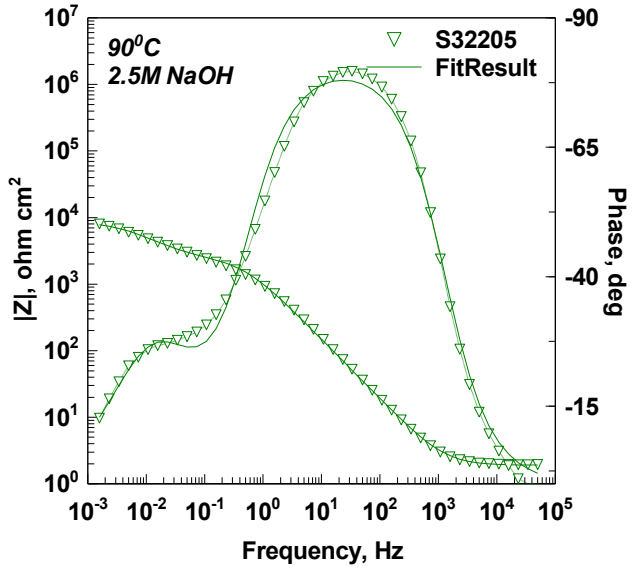


(b)

*Figure 4.27:* ***Electrochemical impedance spectra for S32205 tested in 2.5 M NaOH at 90 $^{o}$C. Points – experimental points, lines – best fit results obtained from simulation. The best fitting parameters are: $R_s$ = 1.94 Ω cm$^2$, $R_1$ = 1617 Ω cm$^2$, $CPE_1$ = 135.3 μF cm$^{-2}$, $\alpha_1$ = 0.927, $R_2$ = 9.29 kΩ cm$^2$, $CPE_2$ = 0.870 mF cm$^{-2}$, and $\alpha_1$ = 0.556. ($\chi^2$ = 5.38e-4)***

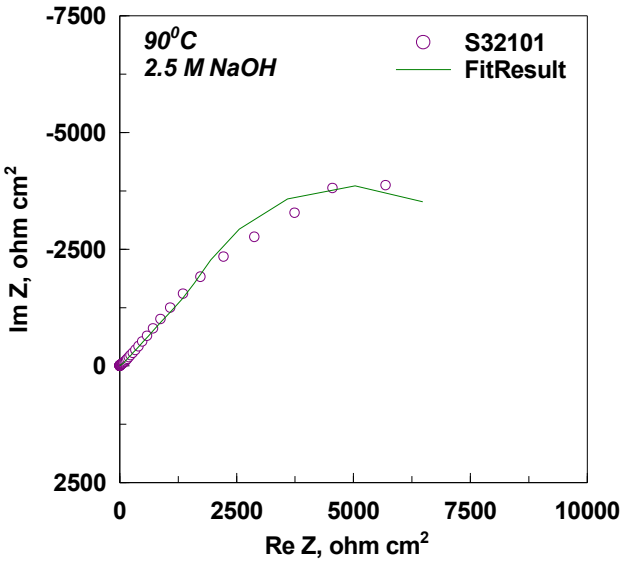


(a)

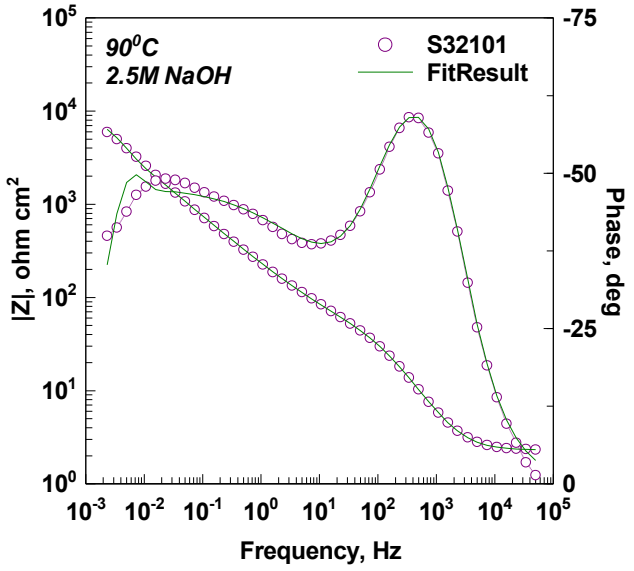


(b)

*Figure 4.28:* ***Electrochemical impedance spectra for S32201 tested in 2.5 M NaOH at 90 $^{o}$C. Points – experimental points, lines – best fit results obtained from simulation. The best fitting parameters are: $R_s$ = 2.32 Ω cm$^2$, $R_1$ = 44.0 Ω cm$^2$, $CPE_1$ = 66.8 μF cm$^{-2}$, $\alpha_1$ = 0.909, $W_1$-R = 7989 Ω cm$^2$, $W_1$-T = 142 s, $W_1$-P = 0.530. ($\chi^2$ = 1.85e-3)***

Lean grade DSS S32101 has been modeled with a Warburg diffusion component to facilitate the fit with an analogous Randles circuit shown in Figure 4.29. Based on the rapid electronic transport and distinct $45^{o}$ low frequency behavior (i.e., $\alpha = 0.5$), a diffusion process was rate-limiting in DSS S32101.

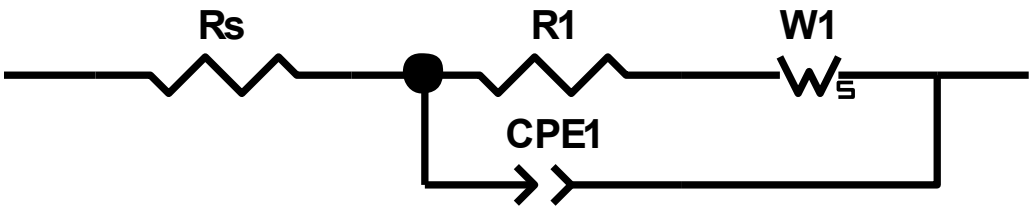


***Figure 4.29:*** ***Equivalent circuit used to simulate the electrochemical behavior of S32101 in 2.5 M NaOH at 90 $^{o}$C.***

The best fitting parameters for the two grades of DSS differ with respect to the double layer capacitance, which suggests that the passive film on S32205 was more resistant to current leakage. Differences in film composition, primarily Mo and Ni, will be discussed in the next section with respect to passive film formation.

The influence of temperature on the physicoelectrical properties of the passive films formed on standard (S32205) and lean (S32101) grade DSS at 90 and 170 $^{o}$C in 2.5 M NaOH are shown in Figure 4.30 and Figure 4.31, respectively. The increase in temperature reduced the resistivity of the films formed on the two DSS materials. The double layer capacitance was shifted to lower frequencies and became more capacitive. The passivation process was significantly altered by increased temperature for S32205. Two overlapped RC time constants were found at 90 $^{o}$C as well as 170 $^{o}$C in the Bode plots in Figure 4.30; however, there was a decrease in the impedance modulus at lower

frequencies at 170 $^{o}$C, which is indicative of inductance behavior. A pseudo-inductive time constant at low frequencies is typically observed for a passive electrode when an increase in the surface fraction causes an increase in the local current [35]. Active dissolution, adsorption, or surface roughening may cause increased surface fraction. Non-Faradaic processes (involving no transfer of charge), such as adsorption of species, reorientation of surface molecules, and diffusion may also occur at low frequencies [35].

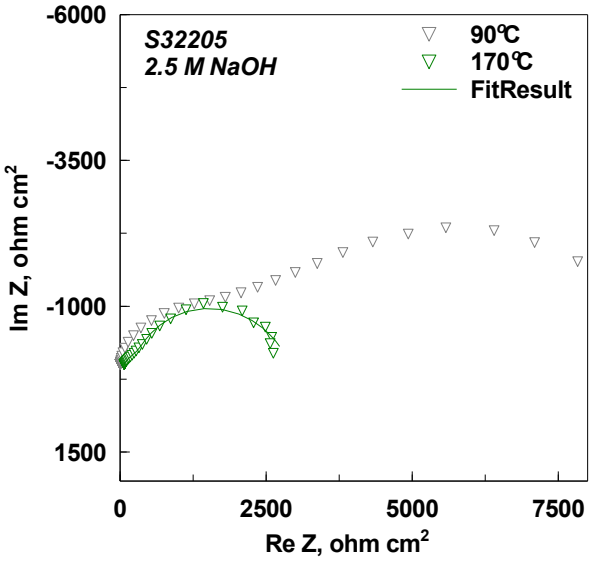


(a)

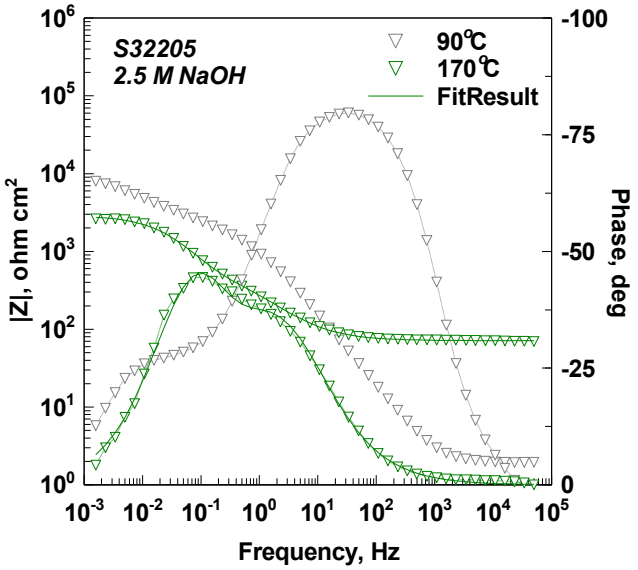


(b)

*Figure 4.30:* ***Comparison of electrochemical impedance spectra for S32205 tested in 2.5 M NaOH at 90 and 170 $^{o}$C. Points – experimental points, lines – best fit results obtained from simulation. The best fitting parameters are: $R_s$ = 71.18 Ω cm$^2$, $R_1$ = 656 Ω cm$^2$, $CPE_1$ =95.6 μF cm$^{-2}$, $\alpha_1$ = 0.706, $R_2$ = 2.17 kΩ cm$^2$, $CPE_2$ = 1.31 mF cm$^{-2}$, and $\alpha_1$ = 0.932. ($\chi^2$ = 1.97e-3)***

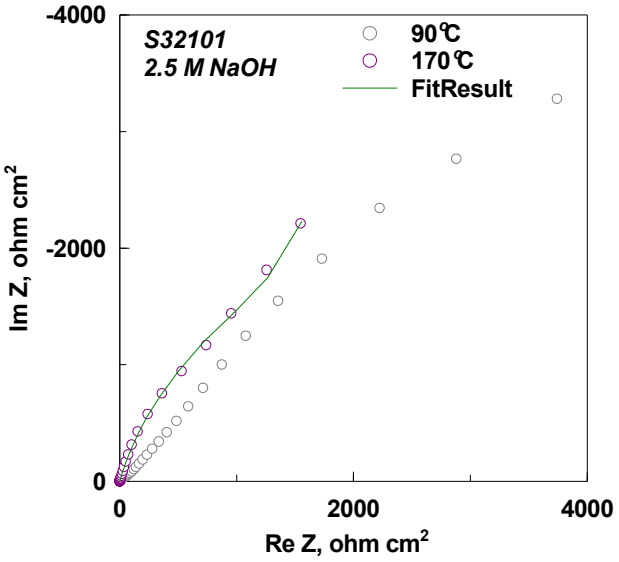


(a)

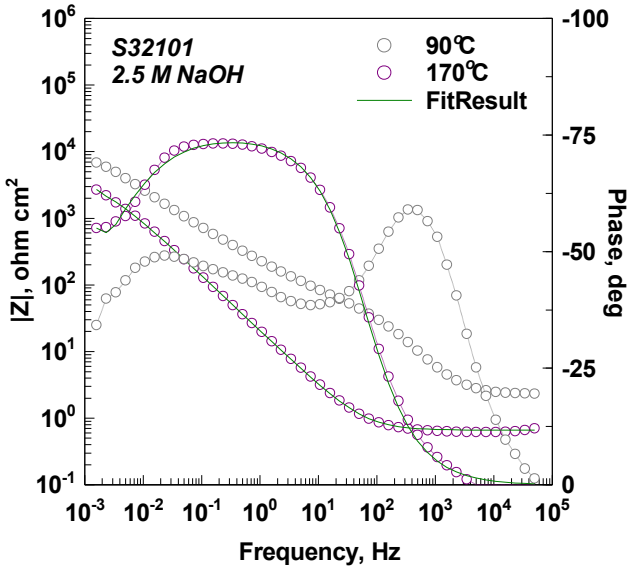


(b)

*Figure 4.31:* ***Comparison of electrochemical impedance spectra for S32101 tested in 2.5 M NaOH at 90 and 170 °C. Points – experimental points, lines – best fit results obtained from simulation. The best fitting parameters are: $R_s$ = 0.658 Ω cm², $R_1$ = 4270 Ω cm², $CPE_1$ = 10.6 mF cm$^{-2}$, $\alpha_1$ = 0.829, $W_1$-R = 2179 Ω cm², $W_1$-T = 142 s, $W_1$-P = 0.736. ($\chi^2$ = 1.63e-3)***

Differences in the low frequency domain of the standard and lean grade DSS were apparent by comparing the behavior at 170 $^{o}$C in Figure 4.30 and 4.31, respectively. To determine if the behavior at low frequencies was attributed to a redox reaction occurring at the metal-passive film interface or a diffusion process, a separate set of experiments were conducted for a duration of 168 h. Results for austenitic (S31603), superferritic (S44660), lean DSS (S32101), and standard DSS (S32205) grades after 24 h are shown in Figure 4.32. It is clear that the low frequency behavior for lean DSS (32101) differs from the other grades of stainless steel, which can be seen in the Nyquist plots. Constant 45 $^{o}$ Warburg behavior is observed for S32101, while the other grades show a reduction in the phase angle to nearly pure resistance

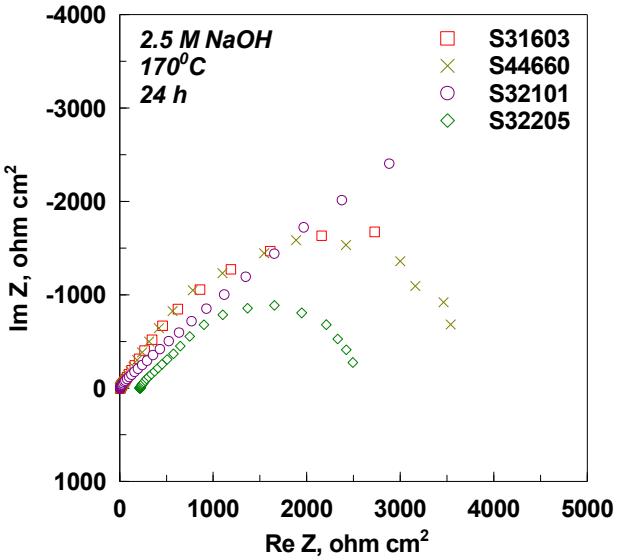


(a)

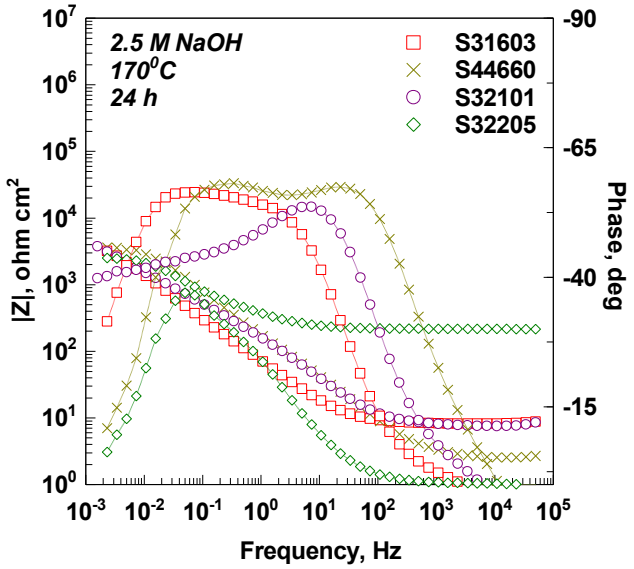


(b)

*Figure 4.32:* ***Comparison of electrochemical impedance spectra after 24 h for austenitic (S31603), superferritic (S44660), and lean DSS (S32101), and standard DSS (S32205) grades tested in 2.5 M NaOH at 170 °C. The Nyquist plots are shown on the left, and the Bode plots are shown on right.***

LPR measurements were made every 24 h over the duration of the experiment to determine differences in the behavior of the stainless steel grades with exposure to the 2.5 M NaOH solution. Austenitic (S30403) and superferritic (S44627) stainless steel, which have negligible Mo additions, were tested for comparison. Results from the LPR measurements shown in Figure 4.33 indicate that the polarization resistance values for S32101 were stable after 24 h, whereas the other alloys did not stabilize until 72 h. LPR values for S32101 were considerably lower than the other alloys. Austenitic grade S30403 had appreciably higher values than S31603.

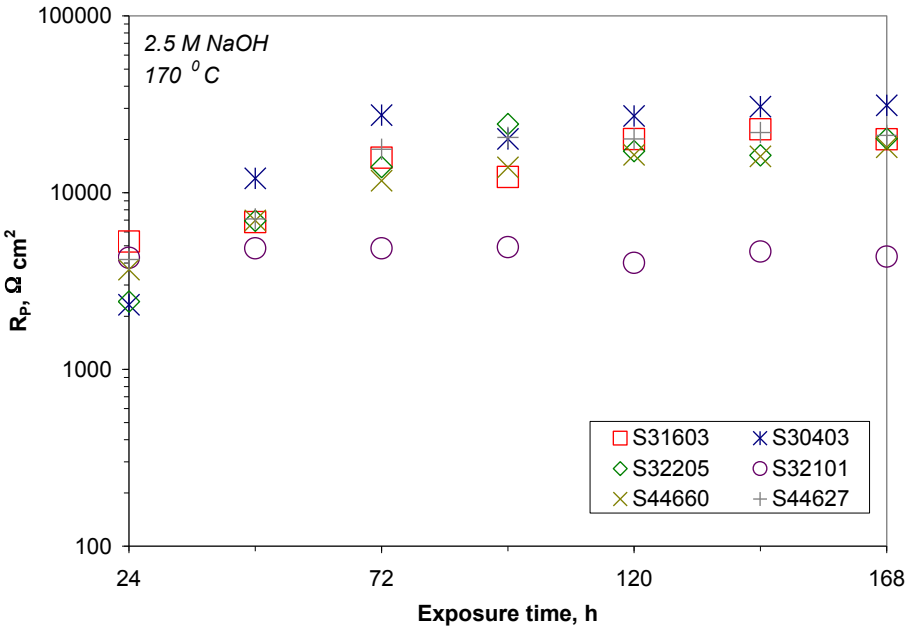


***Figure 4.33:*** ***Linear polarization resistance values during 168 h exposure of austenitic (S31603 and S30403), superferritic (S44660 and S44627), and lean DSS (S32101), and standard DSS (S32205) grades tested in 2.5 M NaOH at 170 °C.***

The EIS spectra captured after 72 h and 168 h did not show differences with exposure time. The difference in passive film behavior among the grades of stainless steel after 168 h is shown in Figure 4.34. Based on the results in Figure 4.34, it can be

concluded that S32101 was indeed under diffusion control. Therefore, the use of a modified Randles circuit for this alloy was also justified at 170 $^{o}$C. Two time constants can be observed in the frequency domain of all of the stainless grades that were tested, which is consistent with the findings after 24 h. The charge transfer resistance increased from 24 h to 168 h, which supports the LPR measurements. Finally, the Faradaic process occurring in the passive film and double layer capacitance of the metal-passive film interface was shifted to lower frequencies in all of the alloys indicating that the film had increased surface area.

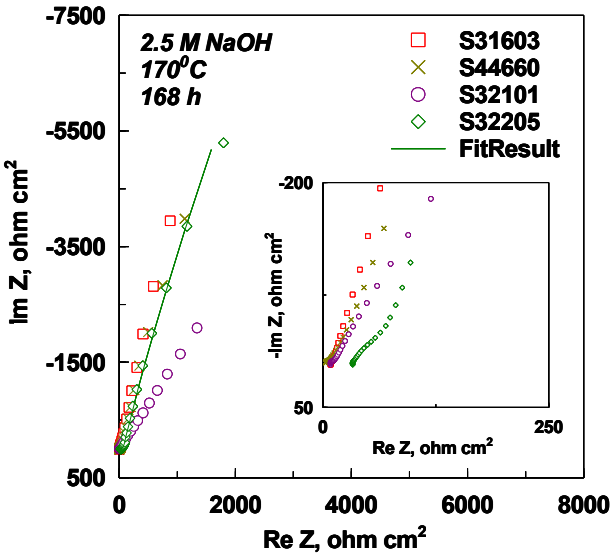


(a)

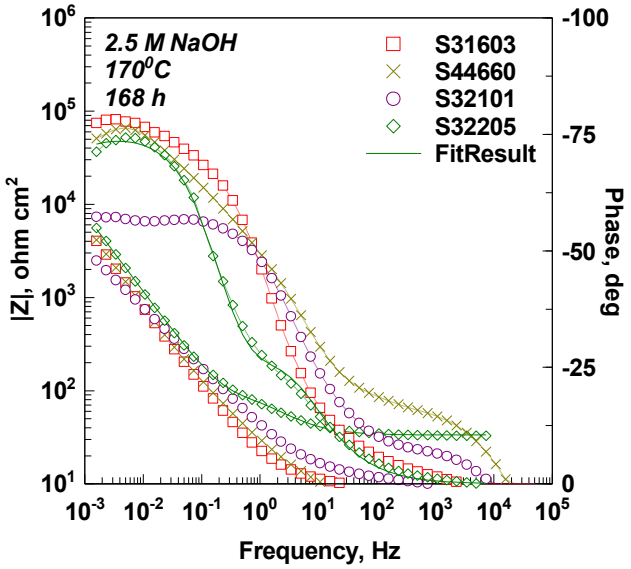


(b)

*Figure 4.34:* ***Comparison of electrochemical impedance spectra after 168 h for austenitic (S31603), superferritic (S44660), and lean DSS (S32101), and standard DSS (S32205) grades tested in 2.5 M NaOH at 170 °C. Points – experimental points, lines – best fit results obtained from simulation of S32205 results. The best fitting parameters for S32205 are: $R_s$ = 33.38 Ω cm², $R_1$ = 80.86 Ω cm², $CPE_1$ = 3.05 mF cm⁻², $\alpha_1$ = 0.764, $R_2$ = 180.9 kΩ cm², $CPE_2$ = 6.09 mF cm⁻², and $\alpha_1$ = 0.902. ($\chi^2$ = 3.05e-3)***

The effect of alkalinity on the passivation of DSS (S32205 and S32101) was evaluated during exposure to 2.5 M and 12.5 M NaOH at 170 $^{o}$C for comparison. Spectra for standard (S32205) DSS tested in the two environments are provided in Figure 4.35. Two time constants were observed in the Nyquist plot in both solutions; however, clear differences in film properties can be seen in the figure. The resistivity of the film was reduced by approximately two orders of magnitude. Furthermore, the response of the film became more capacitive with increased alkalinity, which could be attributed to increased surface area or decreased film thickness. An attempt was made to fit the behavior of the film using CNLS, but large errors in the calculation resulted in a poor agreement with the theoretical model of Figure 4.23, particularly the charge transfer resistance of the metal-passive film interface. An alternative model that used Warburg impedance (Figure 4.36) to describe the ionic transport mechanism due to diffusion resulted in a reasonable fit. Warburg impedance has been used to describe ionic transport in passive films has largely been used within the frames of the Mixed Conduction Model for Oxides [27-28], Point Defect Model [31-32], and other kinetic approaches [33-34]. Kinetic modeling was outside the scope of this evaluation, hence the fit parameters are provided for qualitative comparisons.

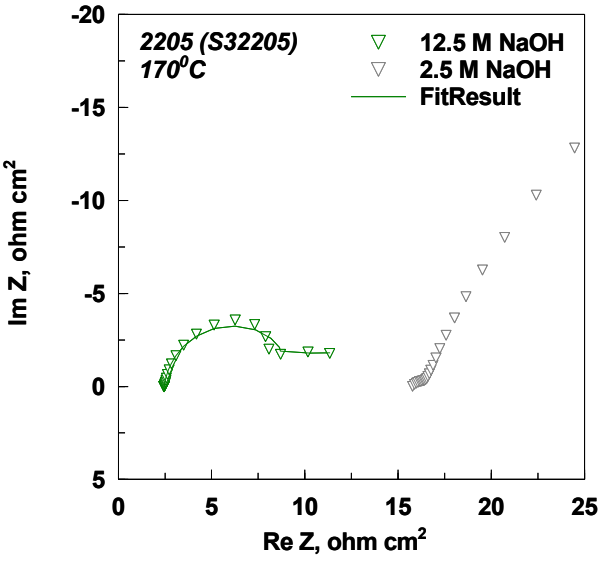


(a)

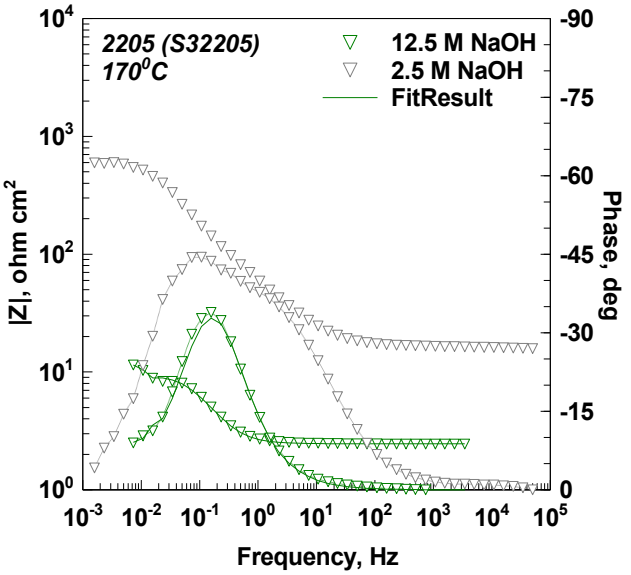


(b)

*Figure 4.35:* ***Comparison of electrochemical impedance spectra for S32205 tested in 2.5 M or 12.5 M NaOH at 170 °C. Points – experimental points, lines – best fit results obtained from simulation. The best fitting parameters are: $R_s$ = 2.46 Ω cm², $R_1$ = 7.14 Ω cm², $CPE_1$ = 266.1 mF cm$^{-2}$, $\alpha_1$ = 0.924, $R_1$ = 5.92 Ω cm² $W_1$-R = 214.5 Ω cm², $W_1$-T = 5697 s, $W_1$-P = 1. ($\chi^2$ = 8.95e-3)***

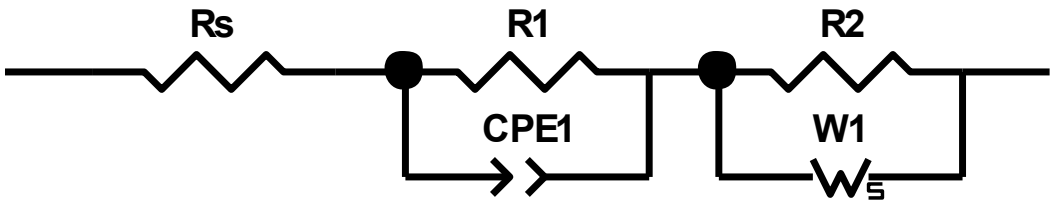


*Figure 4.36:* ***Equivalent circuit used to simulate the electrochemical behavior of S32205 in 12.5 M NaOH at 170 $^{o}$C.***

The effect of increased alkalinity on the electrochemical behavior of S32101 is shown in Figure 4.37. The general trends for S32205 and S32101 were similar in the more aggressive environment with respect to decreased film resistivity and increased film capacitance, although the mechanism did not seem to change in S32101 with increased alkalinity as it did for S32205. A modified Randles circuit was used to fit the results from S32101 tested in the 12.5 M NaOH solution with reasonable agreement. The best fit parameters in Figure 4.37 can be compared directly to those in Figure 4.31 to see the changes in film behavior.

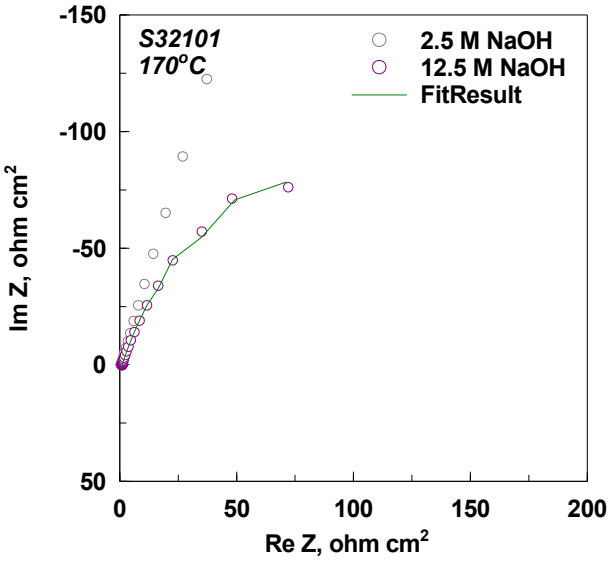


(a)

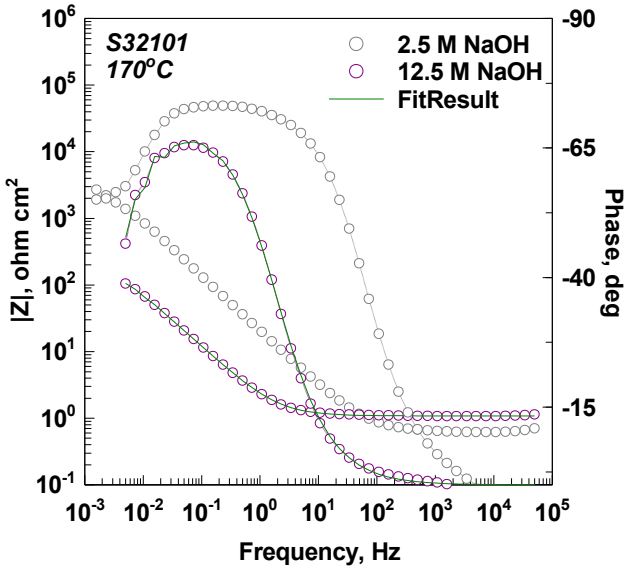


(b)

*Figure 4.37:* ***Comparison of electrochemical impedance spectra for S32101 tested in 2.5 M or 12.5 M NaOH at 170 °C. Points – experimental points, lines – best fit results obtained from simulation. The best fitting parameters are: $R_s$ = 1.088 Ω cm², $R_1$ = 239.1 Ω cm², $CPE_1$ = 122.5 mF cm$^{-2}$, $\alpha_1$ = 0.818, $W_1$-R = 10.07 Ω cm², $W_1$-T = 77.2 s, $W_1$-P = 1. ($\chi^2$ = 1.31e-3)***

The polarization resistance values for S32205 and S32101 tested in 2.5 M and 12.5 M NaOH solution at 170 $^{o}$C are shown in Figure 4.38. Increased alkalinity had a greater effect on reducing the resistivity of the passive film on S32205; however, the general trends for the two alloys are similar. The LPR and EIS data showed that the films had significantly lower resistivity with increased alkalinity. The corrosion mechanism in alkaline environments did not change with increased alkalinity in S32101, but differences in the mechanism were apparent for S32205 on the basis of the EIS and LPR results. Further work is needed to determine the kinetic parameters associated with ionic transport at the metal/film interface.

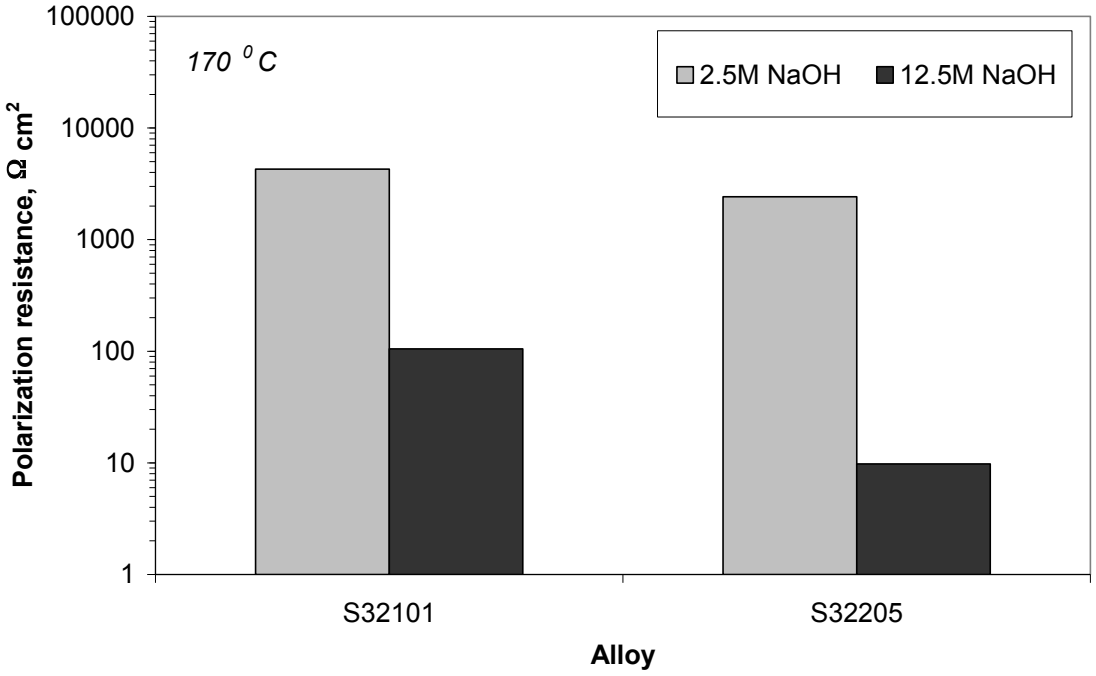


***Figure 4.38:*** ***Linear polarization resistance values for 24 h exposure of lean DSS (S32101) and standard DSS (S32205) grades tested in 2.5 M and 12.5 M NaOH at 170 $^{o}$C.***

The EIS and LPR results indicated that the physicoelectrical behavior of the surface films formed on DSS S32205 and S32101 were adversely affected by higher alkalinity. The response of the surface films became more capacitive with increased alkalinity, which could be attributed to increased surface area due to porosity or defects [35]. The increase in alkalinity also altered the resistivity of the films making them more conductive and susceptible to increased corrosion rates. The polarization values measured from LPR were found to be similar to the low frequency impedance response, which showed consistency in the behavior with two experimental setups. The resistivity of the films decreased by nearly two orders of magnitude in the 12.5 M NaOH solution as compared to the 2.5 M NaOH solution. These findings demonstrate the profound influence of alkalinity on the corrosion susceptibilities of DSS in caustic environments.

### 4.4.2 Film Morphology and Composition

Film morphology and composition were studied to further the understanding of corrosion mechanisms for lean grade DSS S32101 and standard grade DSS S32205 in alkaline environments. SEM in conjunction with energy dispersive X-ray spectroscopy (EDS) was used to study film cross-sections on DSS after exposure to 2.5 M NaOH at 170 $^{o}$C. X-ray photoelectron spectroscopy (XPS) equipped with an argon (Ar) ion sputtering gun was also used to evaluate the composition and oxidation state of the ionic species in the surface film as a function of depth. Reference materials of Fe, Cr, Ni, and Mo were also studied to determine the binding energies (BE) and full width half maximum (FWHM) values of reference materials. All BE values were corrected using the fortuitous carbon (C 1s) peak at 284.6 eV.

Cross-sectional SEM micrographs of the surface film that formed on S32205 are shown in Figure 4.39 at both low and high magnification. Evidence for preferential corrosion is apparent in Figure 4.39a. The depth of corrosion penetration was ca. 10 μm. Representative spectra from EDS of the high magnification image showed that the outer layer was enriched in Fe and the inner layer was both Cr and Ni rich. The EDS spectra were normalized and compared based on the ratio of each cation to total cation percentage for qualitative comparisons. Outer layer was (93 wt % Fe, 4 wt % Cr, 2 wt % Ni, and 1 wt % Mo) and inner layer was approximately (49 wt % Fe, 34 wt % Cr, 13 wt % Ni, and 4 wt % Mo) based on the average of 15 measurements. The Mo-$L_{\alpha}$ peak with emission energy of 2.3 keV overlaps with the S- $K_{\alpha}$ peak, accounting for the erroneous S in the spectra. Mn was detected in trace amounts in the outer layer of the surface film. Care was exercised in the interpretation of the EDS results because the outer layer may have formed after exposure.

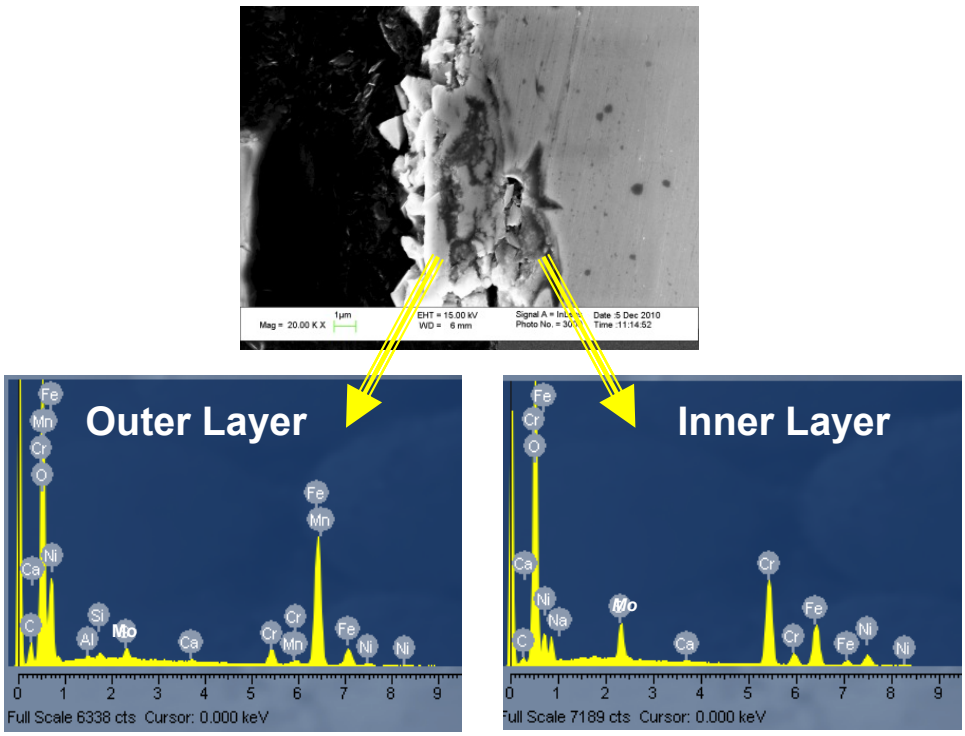


***Figure 4.39:*** ***Cross-sectional SEM micrograph showing surface film on standard DSS S3220) tested in 2.5 M NaOH at 170 $^{o}$C. EDS from outer later and inner layer captured using an accelerating voltage of 15kV indicated by arrows.***

DSS S32101 was also cross-sectioned and observed under SEM and analyzed using EDS following exposure to 2.5 M NaOH at 170 $^{o}$C. The micrograph in Fig 4.40a shows that corrosion on lean grade DSS was uniform. Furthermore, the surface film (ca. 2 μm thick) on S32101 was less protective and adherent based on the higher corrosion rate as compared to the standard grade of DSS. Further evidence for an increased corrosion rate of S32101 as compared to S32205 was provided in the electrochemical results. The EDS spectra in Fig 4.40 show that the outer layer was Fe rich and the inner layer was Cr and Ni rich. The outer layer composition was approximately (93 wt % Fe, 6 wt % Cr, and <2 wt % other (Ni + Mn) and the inner layer was approximately (64 wt % Fe, 29 wt % Cr, 3 wt % Ni, and 4 wt % Mn) based on the normalized EDS results. The outer layer surface compositions of S32205 and S32101 were similar, but the inner layer

compositions differed with respect to the concentrations of Ni and Mn. Ni was enriched in S32205 and Mn was enriched in S32101.

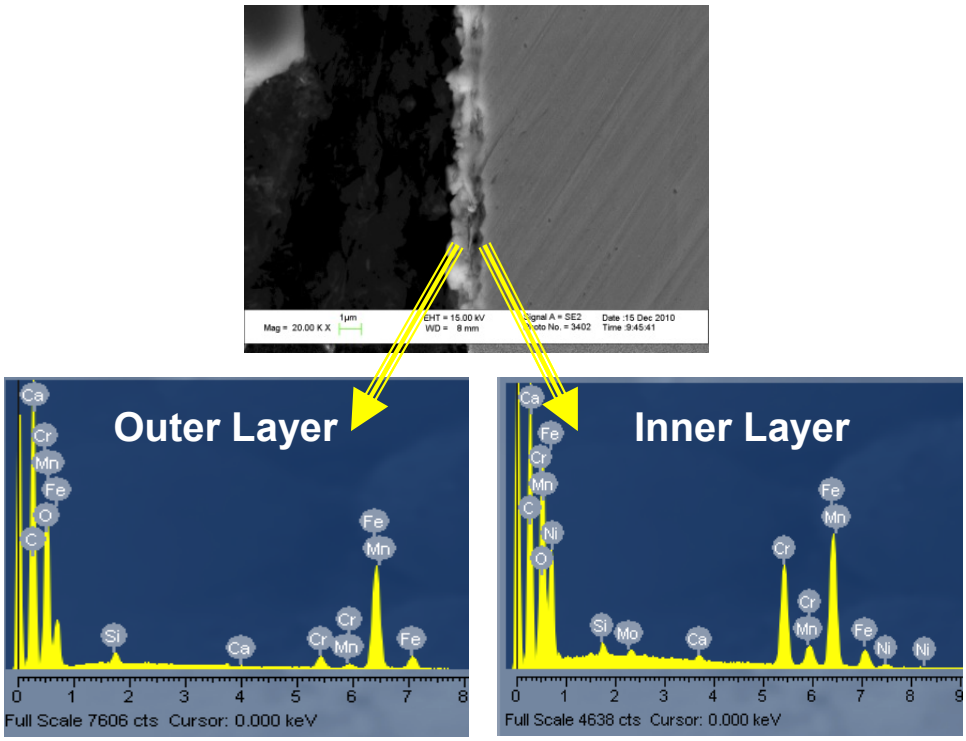


***Figure 4.40:*** ***Cross-sectional SEM micrograph showing surface film on lean DSS S32101 tested in 2.5 M NaOH at 170 $^{o}$C. EDS from outer later an inner layer captured using an accelerating voltage of 15 kV indicated by arrows.***

Surface films formed on S32205 and S32101 after 168 h exposure to 2.5 M NaOH at 170 $^{o}$C were analyzed using XPS with sputtering capability. Reference materials of Fe, Cr, and Ni were also studied to determine the binding energies (BE) of the Fe $2p_{3/2}$, Ni $2p_{3/2}$, and Cr $2p_{3/2}$ signals. Quantitative analysis of each scan was achieved using data processing software capable of peak fitting, elemental, and chemical state determination. Values for the BE of the various chemical states of alloys and reference materials are provided in Table 4.3. Results in Table 4.3 are consistent with published data [36-38].

***Table 4.3:*** ***Binding Energies (BE) of the Different Chemical States for $Fe(2p_{3/2})$, $Cr(2p_{3/2})$, $Ni(2p_{3/2})$, and O(1s) Photoelectron Spectra of Control Samples.***

| *Sample* | *Chemical State* | *BE (eV)* |
|---|---|---|
| Iron | $Fe^{o}$ $(2p_{3/2})$ | 707.1 |
| | | |
| Chromium | $Cr^{o}$ $(2p_{3/2})$ | 574.3 |
| | | |
| Nickel | $Ni^{o}$ $(2p_{3/2})$ | 852.6 |
| | | |
| S32205 | $Fe^{o}$ $(2p_{3/2})$ | 707.0 |
| | $Cr^{o}$ $(2p_{3/2})$ | 574.3 |
| | $Ni^{o}$ $(2p_{3/2})$ | 852.4 |
| | | |
| S32101 | $Fe^{o}$ $(2p_{3/2})$ | 707.1 |
| | $Cr^{o}$ $(2p_{3/2})$ | 574.3 |
| | $Ni^{o}$ $(2p_{3/2})$ | 852.5 |
| | | |
| Oxidized Iron | $Fe^{+2}$ $(2p_{3/2})$ | 708.9 |
| | $Fe^{+3}$ $(2p_{3/2})$ | 711.2 |
| | $O^{-2}$ (1s) | 530.3 |
| | | |
| Oxidized Chromium | $Cr^{+3}$ $(2p_{3/2})$ | 576.6 |
| | $O^{-2}$ (1s) | 530.3 |
| | | |
| Oxidized Nickel | $Ni^{+2}$ $(2p_{3/2})$ | 854.3 |
| | $O^{-2}$ (1s) | 530.2 |

Figure 4.41 shows a comparison of the major constituents of the surface film between XPS sputter depth profiles acquired from S32205. The primary y-axis shows the normalized cation concentration (at %), and the secondary y-axis shows the measured anion concentration (at. %). Cr enrichment was apparent on the outermost surface layer, but these data are not representative of the surface film due to redeposition and surface contamination. The surface film composition is usually taken at half the maximum value of the O concentration or approximately 2000 nm in the figure. The surface film on S32205 was Fe enriched and contained Cr and Ni. Ni was slightly enriched near the

oxide/metal interface. Mo was mostly dissolved in the alkaline environment, which supports the results from the electrochemical measurements. Spot size for these measurements was 400 µm, which is larger than the phase regions for this S32205 material (ca. 50 µm).

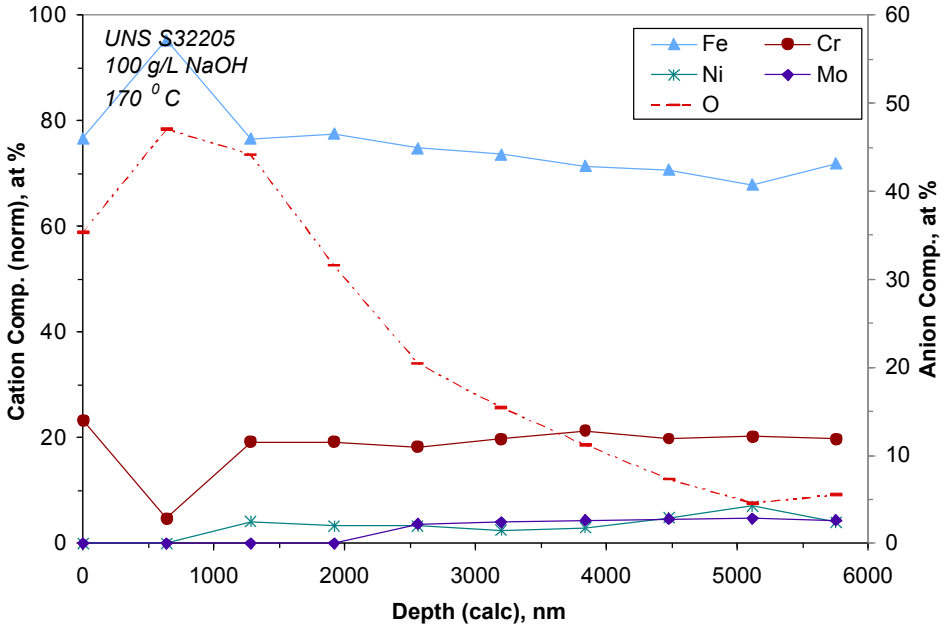


***Figure 4.41:*** ***X-ray photoelectron spectroscopy depth profile of surface film on standard DSS S32205 formed at corrosion potential in 2.5 M NaOH at 170 °C.***

Figure 4.42 shows a comparison of the major constituents of the surface film between XPS sputter depth profiles acquired from S32101. Similar trends in composition were found in S32101 and S32205 with respect to Fe enrichment near the surface; however, Cr and Mn enrichment was more noticeable in S32101. Mn was depleted from the outermost layers (ca. 1000 nm), but was detected throughout the surface film in compositions consistent with the base material of approximately 5 at. %. Results from XPS that show Fe enrichment on outer layer are consistent with the EDS spectra.

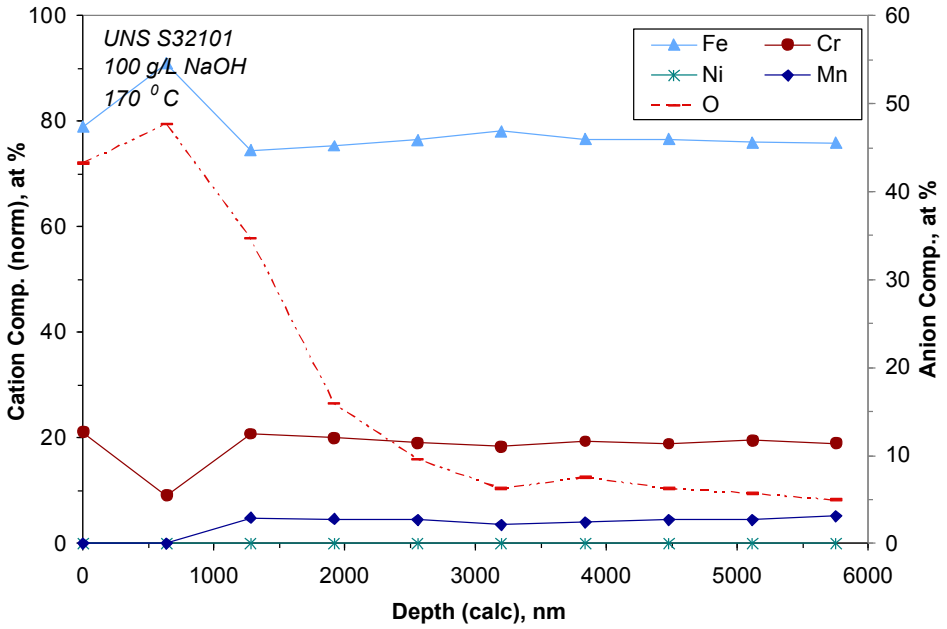


***Figure 4.42:*** ***X-ray photoelectron spectroscopy depth profile of surface film on standard DSS S32101 formed at corrosion potential in 2.5 M NaOH at 170 °C.***

XPS spectra of high resolution scans of Fe 2p, Ni 2p, and Cr 2p and O 1s from the top surface layers formed on S32205 are shown in Figure 4.43. The spectra corresponding to half the maximum of the O 1s signal (ca. 1920 nm depth) is plotted using filled symbols. Results of Figure 4.43 showed that the oxidation states shifted from higher BE values to lower BE values with sputtering depth, indicating that the species were oxidized in the surface film. The BE of the O 1s signal on the outer levels was consistent with a hydroxide layer. The surface films that form on Fe-Cr-Ni alloys in many environments [36-38] have been shown to have two primary layers: an outer hydroxide layer and inner oxide layer. The spectra from half the maximum O 1s signal depth (ca. 1920 nm) were analyzed to determine the oxidation states of each element.

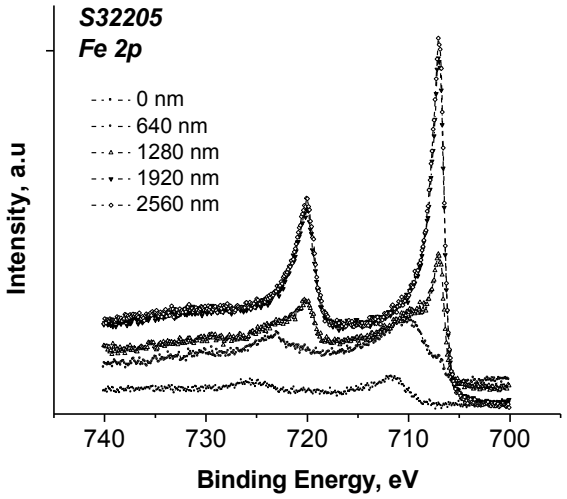


(a)

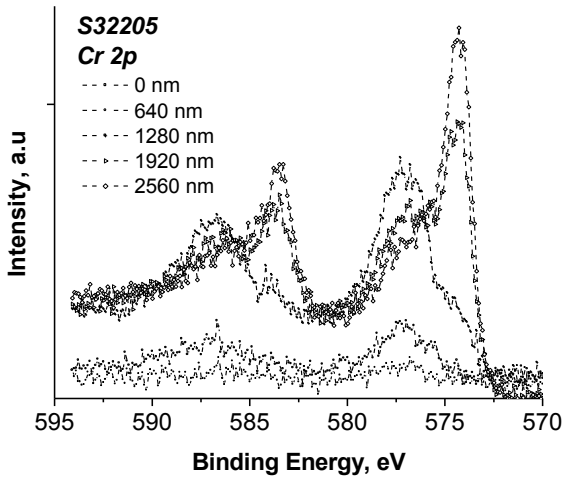


(b)

***Figure 4.43:*** ***High resolution X-ray photoelectron spectra from surface film formed on standard DSS S32205 formed at corrosion potential in 2.5 M NaOH at 170 $^{o}$C for (a) Fe 2p and (b) Cr 2p. Filled symbols represent the scan corresponding to the half maximum O 1s peak intensity (ca. 1920 nm).***

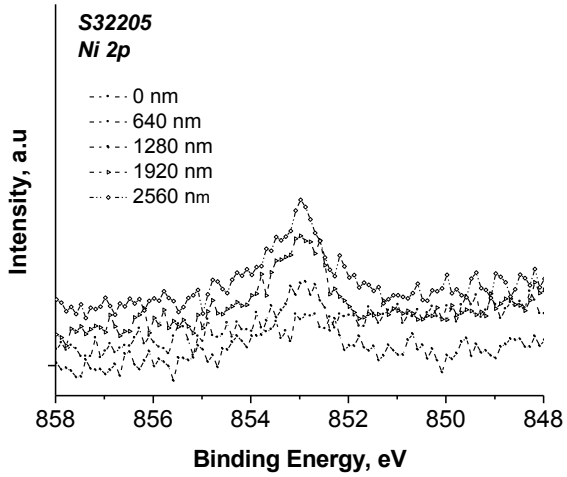


(c)

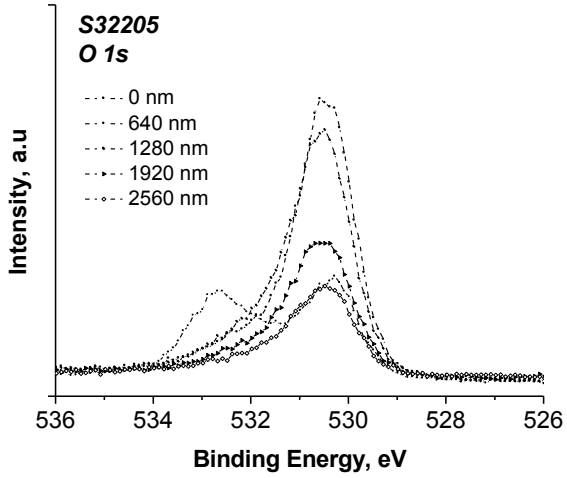


(d)

***Figure 4.43 (cont'd):*** ***High resolution X-ray photoelectron spectra from surface film formed on standard DSS S32205 formed at corrosion potential in 2.5 M NaOH at 170 °C for (c) Ni 2p and (d) O 1s. Filled symbols represent the scan corresponding to the half maximum O 1s peak intensity (ca. 1920 nm).***

Peak fitting of Fe 2p (Figure 4.44) performed using Gaussian-Lorentzian line shapes after Savitzky - Golay smoothing and Shirley background subtraction indicated that the oxide was primarily $Fe_3O_4$ or FeOOH based on the integrated area of the $Fe^{3+}$

peak. Ionization due to sputtering is possible with depth profiling, thus semi-quantitative interpretation of the data showed that Fe was present in two oxidation states. $Fe^{2+}$ was stable as ferrous oxide (FeO) under the electrochemical conditions used to form the passive films, but $Fe_2O_3$ may have formed during cooling when the corrosion potential became more positive as indicated by Table 4.1. Cr was predominantly in the form of $Cr^{3+}$ as chromium oxide ($Cr_2O_3$) with trace amounts of metallic form. Ni was in metallic form with limited amount of $Ni^{2+}$, which was likely nickel oxide (NiO) based on thermodynamic predictions.

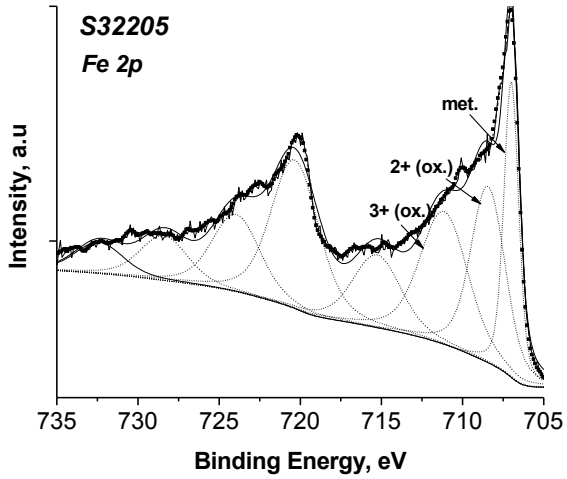


(a)

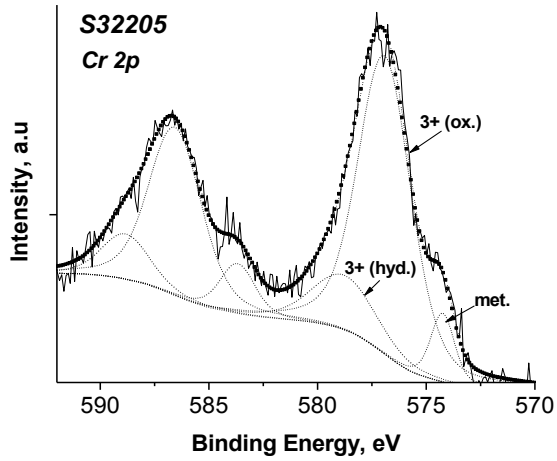


(b)

*Figure 4.44:* ***Peak fitting results for high resolution X-ray photoelectron spectra from surface film formed on standard DSS S32205 formed at corrosion potential in 2.5 M NaOH at 170 $^{o}$C for (a) Fe 2p and (b) Cr 2p. Curve fitting was performed at the half maximum O 1s peak intensity (ca. 1920 nm).***

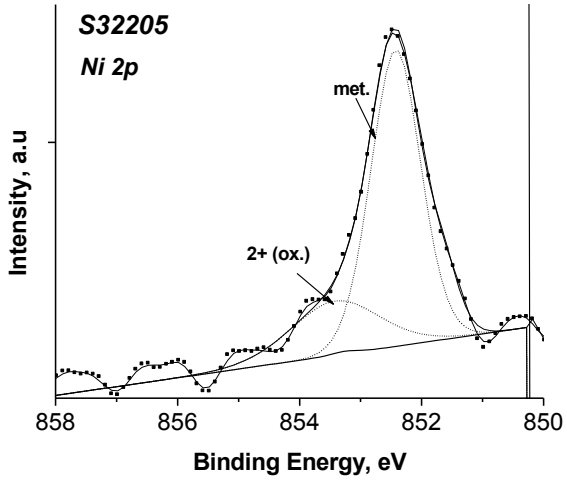


(c)

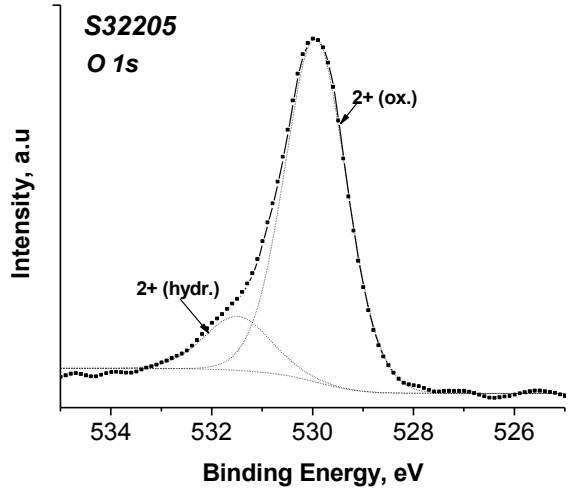


(d)

***Figure 4.44 (cont'd):*** ***Peak fitting results for high resolution X-ray photoelectron spectra from surface film formed on standard DSS S32205 formed at corrosion potential in 2.5 M NaOH at 170 $^{o}$C for (c) Ni 2p and (d) O 1s. Curve fitting was performed at the half maximum O 1s peak intensity (ca. 1920 nm).***

Results for the oxidation states and approximate ratios for S32101 were similar to S32205, with the exception of Mn and Mo species. The Mo signal in S32101 was weak and did not enable curve fitting. The spectra of high resolution scans of Mo 3d from the

top surface layers formed on S32205 are shown in Figure 4.45a. Peak fitting results (Fig 4.45b) of the Mo signal at 1280 nm show that the primary oxidation state was $Mo^{+4}$, which is not consistent with thermodynamic predications; however, the relative amount of oxidized Mo was limited with respect the amount of metallic Mo in the film. It is likely that molybdate ions ($Mo^{6+}$) were soluble in the NaOH solution [5-7]. Peak fitting of Mn spectra for S32205 was not possible due to the limited signal. High resolution scans of Mn 2d the top surface layers of S32101 signal are shown in Figure 4.46. Curve fitting of the Mn spectra at the half maximum O 1s was attempted, but the high signal to noise ratio resulted in a poor fit; there was a broad high BE shoulder near the peak for Mn metal indicating Mn was oxidized as $Mn^{2+}$ or $Mn^{3+}$ [34]. The relative ratio of the integrated peak area indicates that Mn is present primarily as MnO or $MnO_2^{2+}$, which is consistent with thermodynamic predictions.

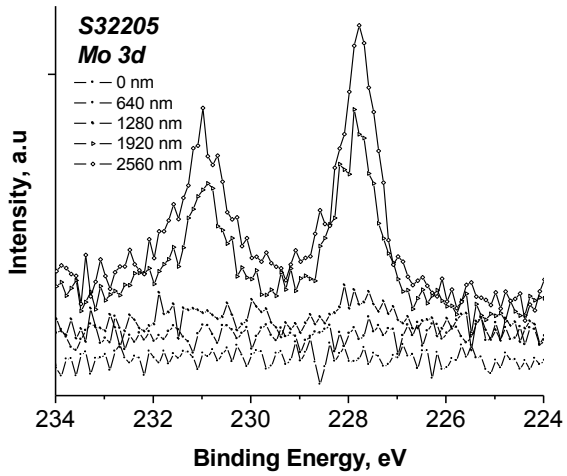


(a)

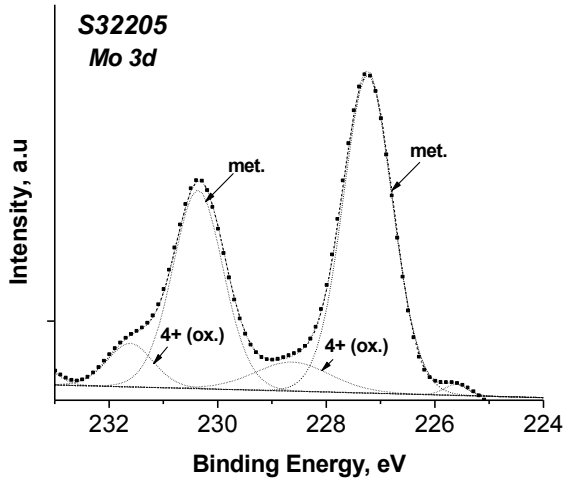


(b)

*Figure 4.45:* ***(a) High resolution X-ray photoelectron spectra from surface film formed on standard DSS S32205 formed at corrosion potential in 2.5 M NaOH at 170 $^{o}$C for Mo $3d_{5/2}$. (b) Peak fitting results for Mo $3d_{5/2}$. Curve fitting was performed at the half maximum O 1s peak intensity (ca. 1920 nm).***

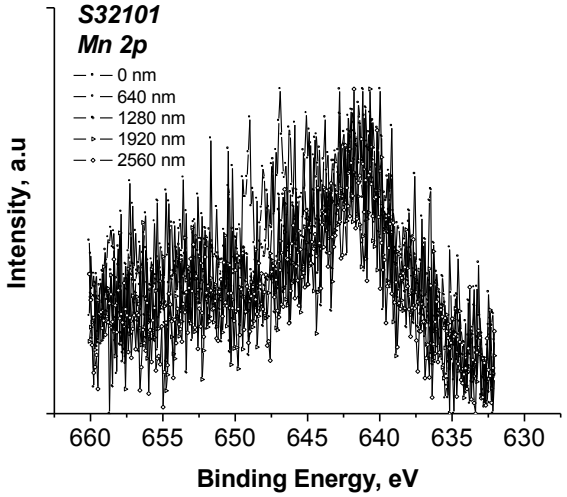


***Figure 4.46:*** ***High resolution X-ray photoelectron spectra from surface film formed on standard DSS S32205 formed at corrosion potential in 2.5 M NaOH at 170 $^{o}$C for Mn 2p.***

Characterization of the surface films formed on DSS in hot alkaline environments showed that selective dissolution of Fe, Mo, and Mn from the oxide/metal interface lead to a Cr- and Ni – enriched, inner layer and an outer, discontinuous layer than was enriched in iron as $Fe^{2+}$ and $Fe^{3+}$ and chromium as $Cr^{3+}$. The outermost layer of the film contained mainly hydroxide compounds of Fe and Cr. Ni remaining near the oxide/metal interface was unoxidized and was likely due to the signal from the base material. Mo and Mn were detected in limited amounts owing to their activity in alkaline environments. Mo was not detected in oxidized form, while Mn was found be oxidized primarily as $Mn^{2+}$or $Mn^{3+}$. The results from EDS were consistent with the XPS results.

## 4.5 Conclusions

Phenomological understanding of the corrosion susceptibilities and underlying corrosion mechanisms of DSS in hot alkaline environments was acquired in this work through the use of *in-situ* and *ex-situ* corrosion rate measurements (anodic polarization,

weight loss, and LPR) electrochemical measurements (EIS), and film characterization (EDS and XPS). Austenitic and superferritic grades of stainless steels were also studied in the alkaline environments to understand single phased materials for comparison. The influence of alloy composition was evaluated by studying pure elements in the alkaline environments. Behavior of the alloys and elements were studied at 90 $^{o}$C and 170 $^{o}$C to evaluate temperature effects. The role of alkalinity on the corrosion susceptibility were evaluated for lean and standard grade DSS at 170 $^{o}$C. Finally, film composition and morphology were studied to understand the oxidation states and relative amounts of oxidized species in the surface films. Based on the findings of this work, the following main conclusions were made:

- Corrosion rates for Mo-containing superferritic grade S44660 were similar to or slightly greater than those of DSS grades in alkaline environments. Mo-free superferritic grade S44627 had superior corrosion resistance. Superferritic grades were generally less susceptible to an increase in corrosion rate with increasing alkalinity than the other tested alloys.
- DSS grades S32205 and S32101 underwent preferential localized corrosion of austenite phase. Super DSS S2507 did not show this trend. Corrosion was uniform on the single-phase alloys.
- Mo [5-7] and Mn were detrimental to corrosion resistance of stainless steels in alkaline environments based on electrochemical measurements that showed lower polarization resistance and higher corrosion rates. Cr and Ni were beneficial as they increased the corrosion potential and reduced the critical current density required for passivation [5-6, 9-10].

- Temperature had a significant effect on increasing the corrosion susceptibility of the alloys [5-6]. Corrosion rates at 170 $^{o}$C increased by nearly an order of magnitude as compared to 90 $^{o}$C. The films were generally less resistive and more capacitive with increased temperature.
- Film formation in S32101 differed from the other grades of stainless steel. Two or three distinct RC time constants were detected in all of the grades tested in 2.5 M NaOH at 170 $^{o}$C. The analogous electrical circuit was similar to a modified Randles circuit that had a redox reaction that was rate limited by diffusion at the metal/film interface. The exposed surface area of the films increased with time based on the augmented capacitance values.
- Mo and Mn were mostly dissolved from the outer surface layers of S32205 and S32101. Mn was present in the surface film mainly as $Mn^{2+}$ or $Mn^{3+}$. Mo and Ni were present primarily in the unoxidized form. Cr was oxidized in the form of $Cr^{3+}$. Fe was found in both as $Fe^{3+}$ and $Fe^{2+}$. Surface films for both grades of DSS were Fe-enriched on the outer layers and had a Cr-rich inner layer. Ni and Mn were present near the oxide/metal interface.
- Increased alkalinity did not alter the film formation process of S32101; however, differences in the anodic polarization and EIS behavior were pronounced for S32205. Increased alkalinity favors the transpassive breakdown of the passive film through the oxidation of Fe species. The oxidation of $Fe_3O_4$ [11] was the predominant reaction near the corrosion potentials of S32205 and S32101.
- Based on the electrochemical measurements, thermodynamic predictions, and film composition, the surface film on DSS exposed to alkaline environments had

an outer hydroxide layer and inner oxide layer that was Fe and Cr enriched. Stability of the film was favored in the stainless steels with higher Cr content and compromised in those with higher Mo and Mn contents.

## 4.6 REFERENCES


[1] Wensley, A., Moskal, M., and Wilton, W., "Materials Selection for Kraft Batch Digesters," Corrosion/97, NACE Paper No. 378, 1997, Houston, TX.

[2] Wensley, A., and Champagne, P. NACE Corrosion, Paper No. 281, 1999, Houston, TX.

[3] Wensley, A., NACE Corrosion, Paper No. 589, 2000, Houston, TX.

[4] A. Wensley, Proc. of the 9th Int. Symposium on Corrosion in the Pulp and Paper Industry, Ottawa, Ontario, 1998, pp. 27-37.

[5] A. Bhattacharya, Georgia Institute of Technology Ph.D. Dissertation, 2008, Atlanta, GA.

[6] A. Bhatttacharya and P.M. Singh, Corr. Sci. 53 (2010) 71.

[7] L. Troselius, Proc. 11th International Pulp and Paper Industry, Corrosion in the Pulp and Paper Industry, Charleston, SC (2004).

[8] A. Laitinen, and H Hanninen, Corr. 52 (1996) 295.

[9] J.H. Zheng, W.F. Bogaerts, and M.J. Brabers, Corr. 48 (1992) 320.

[10] J.H. Zheng and W.F. Bogaerts, Proc. Eurocorr 1996, 2nd International Conference on Corrosion-Deformation Interactions, Nice, France ed. T. Magnin, The Institute of Materials (1997) 104.

[11] A.K. Agarwal, K.G. Sheth, K. Poteet, and R.W. Staehle, J. Electrochem. Soc. 119 (1972) 1637.

[12] J.D. Hem, Chem. Geo. 21 (1978) 199-218.

[13] F. Chouaib, P.H. Huebel, M.D. Sanson, G. Picard, B. Tremillion, J. Electroanal. Chem. 127 (1981) 179-193.

[14] HSC Chemistry 5.11, Outokumpu Technology Engineering Research.

[15] I. Betova, M. Bojinov, O. Hyokyvirta, and T. Saario, Corr. Sci 52 (2010) 1499-1507.

[16] P.A. Brooks, Corr. Sci. 12 (1972) 297.

[17] M. Pourbaix, Atlas of Electrochemical Equilibria in Aqeuous Solutions (Houston, TX: NACE) (1974).

[18] B. Beverskog, M. Bojinov, A. Englund, P. Kinnunen, T. Laitinen, K. Makela, T. Saario, P. Sirkia, Corr. Sci. 44 (2002) 1901.

[19] E.L. Shock, H.C. Helgeson, D.A. Sverjensky, Geochim. Cosmochim. Acta 53 (1989) 2.

[20] D.A. Sverjensky, E.L. Shock, H.C. Helgeson, Geochim. Cosmochim. Acta 61 (1997) 1359.

[21] M. Bojinov, G. Fabricius, P. Kinnunun, T. Laitinen, K. Makela, T. Saario, G. Sundholm, K. yliniemi, Electrochim. Acta 47 (2002) 1697.

[22] C. Andrade, P. Merino, X.R. Novoa, M.C. Perez, L. Soler, Mater. Sci. Forum 192-194 (1995) 891.

[23] S. Joiret, M. Keddam, X.R. Novoa, M.C. Perez, C. Rangel, H. Takenouti, Cement and Concrete Composities 24 (2002) 7-15.

[24] B. Beverskog, M. Bojinov, A. Englund, P. Kinnunen, T. Laitinen, K. Makela, T. Saario, P. Sirkia, Corr., Sci 44 (2002), 1901.

[25] M. Bojinov, P. Kinnunen, G. Sundholm, Corrosion 59 (2003) 91.

[26] M. Bojinov, P. Kinnunen, K. Lundgren, G. Wikmark, J. Electrochem. Soc. 152 (2005) B250.

[27] M. Bojinov, A. Galtayries, P. Kinnunen, A. Machet, P. Marcus, Electrochima Acta 52 (2007) 7475.

[28] M. Bojinov, K. Gaonkar, S. Ghosh, V. Kain, K. Kumar, T. Saario, Corr. Sci. 51 (2009) 1146.

[29] Dieter Landolt, “Corrosion and Surface Chemistry of Metals,” CRC Press, Boca Raton, FL (2007).

[30] F. Falkenberg, V.S. Raja, E. Ahlberg, J. Electrochem. Soc. 148 (2001) B132.

[31] D.D. Macdonald, Ru-Yu Liang, B.G. Pound, J. Electrochem. Soc. 134 (1987) 2981.

[32] D.D. Macdonald and S.I. Smedley, Electrochim. Acta 35 (1990) 1949.

[33] X.P. Guo, Y. Tomoe, H. Imaizumi, and K. Katoh, J. Electroanal. Chem. 445 (1998) 95.

[34] M. Keddam, H. Takenouti, N. Yu, Corr. Sci. 27 (1987) 107.

[35] R.C. Newman and A. Mehta, Corr. Sci. 28 (1988) 1183.

[36] I. Olefjord, B. Brox., and U. Jelvestam, J. Electrochem. Soc. 132 (1985) 2854.

[37] N. De Cristofano, M. Piantini, and N. Zacchetti, Corr. Sci. 39 (1997) 2181-2191.

[38] P. Marcus and J.M. Grimal, Corr. Sci. 33 (1992) 805.

[39] W. Fredriksson, K. Edstrom, C.-O.A. Olsson, Corr. Sci. 52 (2010) 2505-2510.

# CHAPTER 5

# INFLUENCE OF SULFIDE AND CHLORIDE ON CORROSION OF DUPLEX STAINLESS STEELS IN HOT ALKALINE ENVIRONMENTS

## 5.1. Introduction

The chemical composition of alkaline-sulfide kraft pulping liquors is complex and varies in the concentrations of sodium hydroxide (NaOH) and sodium sulfide ($Na_2S$) within a single digester. Moreover, North American kraft pulping uses white liquors that have a composition up to 150 g/l NaOH (3.75 M) and 50 g/l $Na_2S$ (0.64 M), while those in Scandinavian countries vary from 100 – 125 g/l NaOH (2.5 – 3.13 M) and 50 – 55 g/l $Na_2S$ (0.64 – 0.70 M) depending on the wood species being pulped. Other aggressive inorganic anions may also be present in these environments: sulphite ($SO_3^{2-}$), sulphate ($SO_4^{2-}$), thiosulphate ($S_2O_3^{2-}$), carbonate ($CO_3^{2-}$), and chloride ($Cl^-$). The latter anion may be present in the wood feed stock or as a non-process element. Moreover, a greater environmental awareness throughout the industry has resulted in considerable reuse of water, which can further lead to the accumulation of non-process elements and metallic salt compounds.

There are only a few studies on the effect of alkalinity, sulfidity, or chloride content on the corrosion behavior of stainless steels in hot alkaline environments described in the literature [1-3]. The corrosion resistance of stainless steel has primarily been studied in simulated liquors containing various concentrations of NaOH and $Na_2S$ to replicate the most aggressive conditions in a kraft digester [1-22]. Other research efforts in the field have used *in-situ* corrosion monitoring of digesters [23-27] or have carried out laboratory studies using extracted pulping liquors [28-31].

There has been no systematic work to understand the combined role of alkalinity, sulfidity, and chloride content on the corrosion behavior of stainless steels in hot alkaline-sulfide environments. Efforts to understand chloride effects in alkaline-sulfide environments have been limited to low temperatures. Corrosion of stainless steel in marine environments has facilitated studies on the combined role of chloride and sulfide formed through sulfate-reducing bacteria (SRB) [32-34]. There has also been extensive research on chloride effects in stainless steel reinforced concrete for infrastructure [35-37]. Studying environmental effects on the general corrosion and electrochemical behavior of different types of stainless steel (austenitic, ferritic, and duplex) will also clarify the role of alloy composition on corrosion behavior in hot alkaline environments.

The following chapter will describe the effect of sulfide and chloride ions on the corrosion susceptibilities of select grades of DSS (S32101 and S32205) in several caustic environments having different percent sulfidity and effective alkali content. Austenitic, superferritic, and other DSS samples have been tested for comparison.

## 5.2. Effect of Sulfide

### 5.2.1 Influence of Environment on Corrosion Rates and Morphology

Corrosion rates of austenitic (N08904, S31703, S31603, S30403), superferritic (S44660, S44627), and DSS (S32705, S32205, S32101, S32003) grades of stainless steel are shown in Figure 5.1 for several sulfide-containing caustic environments at 170 $^{O}$C: 100 g/l NaOH (2.5 M) + 55 g/l $Na_2S$ (0.70 M), 125 g/l NaOH (3.13 M) + 75 g/l $Na_2S$ (0.96 M), and 150 g/l NaOH (3.75 M) + 50 g/l $Na_2S$ (0.64 M). Alloy compositions and solution compositions are provided in Chapter 3.

Effective alkali (in g/l) correlated well to the corrosion rates observed in Figure 5.1. Percent sulfidity had an appreciable effect on the corrosion rates of the stainless

steels with lower Cr content and higher Ni content. The definitions for EA and percent sulfidity were provided in Chapter 3. The austenitic grades typically had the highest corrosion rates in sulfide-containing caustic environments. DSS were generally more resistant than austenitic grades but less resistant than the superferritic grades. Alloys in Figure 5.1 are arranged by decreasing Ni content within each type of stainless steel. Corrosion rates of all grades of stainless steel are still far lower than reported for carbon steel in alkaline-sulfide environments [26-28, 31].

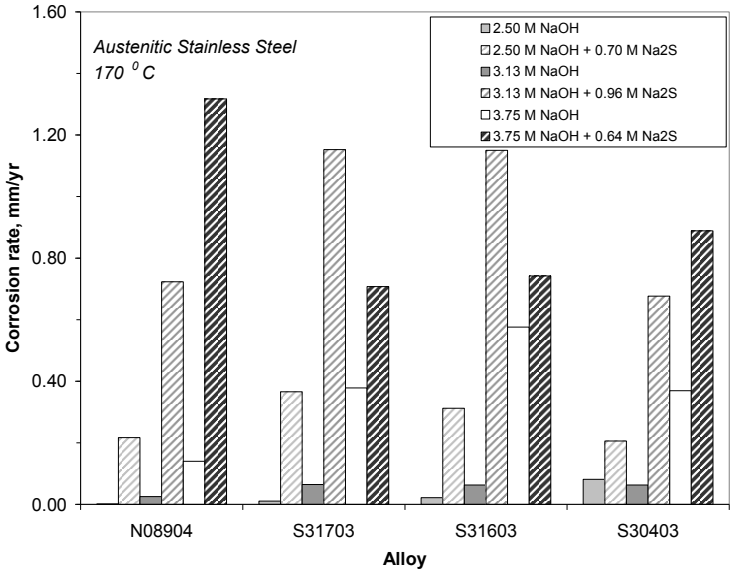


(a)

***Figure 5.1:*** ***Corrosion rates of austenitic (N08904, S31703, S31603, S30403) stainless steel tested in alkaline-sulfide and alkaline solutions at 170 $^{O}$C. Alloys have been arranged by left to right by decreasing Ni content within each type of stainless steel.***

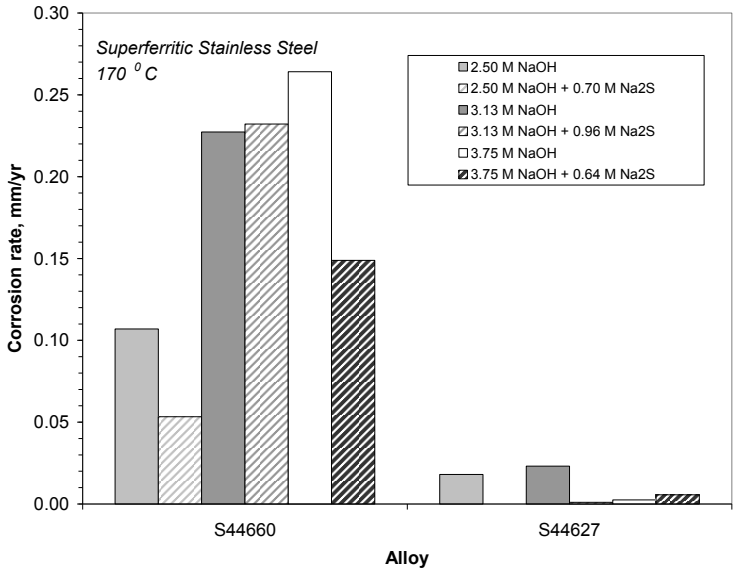


(b)

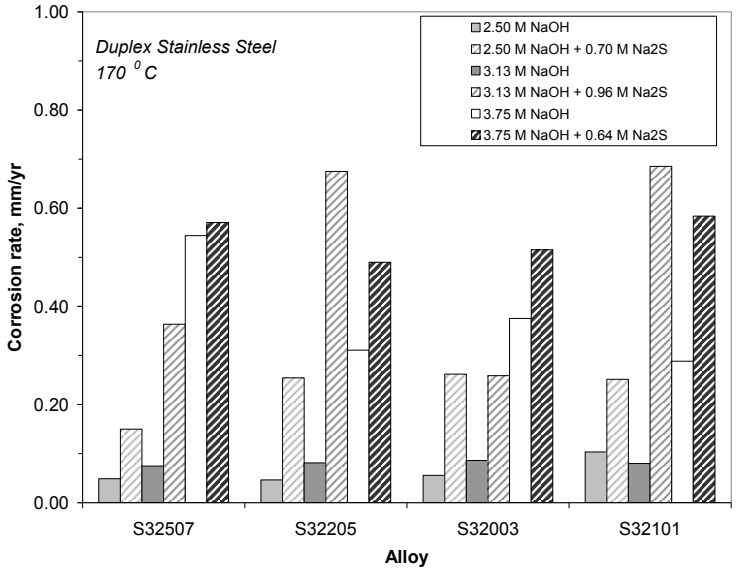


(c)

***Figure 5.1 (cont'd):*** ***Corrosion rates of (b) superferritic grades (S44660, S44627) and (c) duplex (S32705, S32205, S32101, S32003) of stainless steel tested in alkaline-sulfide and alkaline solutions at 170 $^{O}$C. Alloys have been arranged by left to right by decreasing Ni content within each type of stainless steel.***

Previous studies [2-3, 29-30] have also shown the improved corrosion resistance of austenitic and DSS in hot alkaline-sulfide solution is due to a higher amount of Cr.

Wensley et al [30] evaluated the corrosion rate and corrosion potential of several austenitic stainless steels and DSS used in mixed white and black (3:1) liquors used in pulping digester applications. The results showed that increasing the Cr content above 25 wt % was necessary for enhanced corrosion resistance. The austenitic phase was attacked preferentially in DSS at potentials more noble than the corrosion potential. A separate study [7] of select DSS tested in different simulated pulping liquors showed lower corrosion rates for lean DSS S32304 as compared to S32205 and S32101. DSS S32003 and S32705 had better overall corrosion resistance than S32205 and S32101 in the current study, which suggests environment and material composition have a complex role of corrosion in alkaline-sulfide solution. However, the differences within the DSS alloys tested were relatively small compared to the corrosion behavior of austenitic or ferritic alloys tested. The increase in corrosion rates was proportional to the Ni content of the stainless steel and inversely proportional to the Cr content, particularly in high sulfidity solutions.

High percent sulfidity and effective alkali were more detrimental to Ni-containing stainless steels with lower Cr contents, i.e. austenitic grades. Corrosion rates of austenitic and DSS tested in the lowest effective alkali solution (100 g/l NaOH + 55 g/l $Na_2S$) were similar in the current study. Superferritic grade S44627, which has low Ni (<0.5 wt %) and Mo (0.75 – 1.5 wt %), had superior performance to other all grades in alkaline-sulfide solutions. Mo was detrimental to the corrosion performance of stainless steels in the NaOH solution (Chapter 4), but the role of Mo on corrosion resistance of stainless steels in sulfide-containing caustic solution was less clear based on Figure 5.1. Indeed, corrosion rates of S30403 (0 wt % Mo) were lower than S31603 (2 -3 wt % Mo) in the

solutions with highest percent sulfidity, yet corrosion rates of S30403 were higher in the solution with the lowest sulfidity. Matrix composition will also have a role on the corrosion behavior.

The form of corrosion on each material was examined following exposure using optical and scanning electron microscopy (SEM). General corrosion for austenitic grades S31603 (12 wt % Ni, 17 wt % Cr) and S30403 (10 wt % Ni, 19 wt % Cr) in the 3.75 M NaOH + 0.64 M $Na_2S$ sulfide-containing caustic solution can be seen in the micrographs in Figure 5.2. Ferrite grain boundaries were attacked slightly more than other regions of the microstructure, but general corrosion was the predominant form of degradation for austenitic grades. A residual grain boundary oxide was found on S31603 after cleaning with inhibited hydrochloric acid. Energy dispersive X-ray spectra (EDS) showed that this oxide was enriched in S. Other grades of austenitic stainless steel had similar behavior in all of the environments regardless of the percent sulfidity and effective alkalinity.

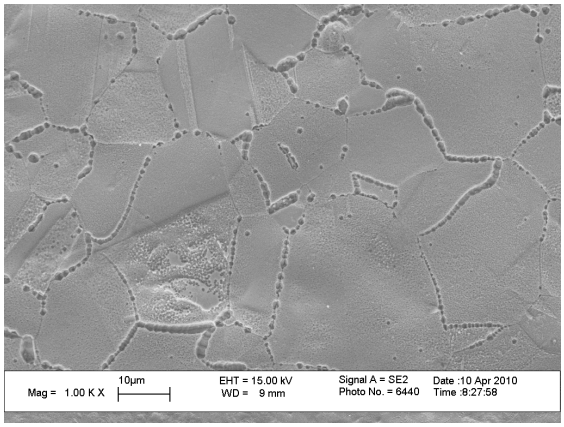


(a)

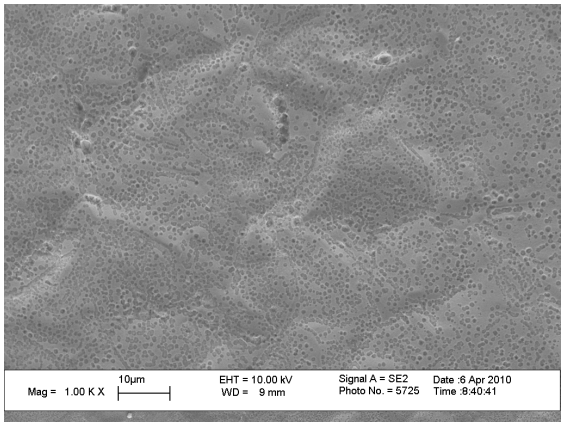


(b)

***Figure 5.2:*** ***SEM micrograph showing general corrosion on austenitic grades (a) S31603 and (b) S30403 tested in 3.75M NaOH + 0.64 M $Na_2S$ at 170 $^{O}$C.***

Superferritic grade S44627 underwent intergranular corrosion (IGC) in all of the sulfide-containing caustic environments. The severity of the attack increased with percent sulfidity. Figure 5.3 shows IGC after exposure to 3.75 M NaOH + 0.64 M $Na_2S$ alkaline-sulfide solution. EDS of the grain boundary region revealed the grain boundaries were enriched in S, C, Ti, and Nb. Ti and Nb are present in S44627 in lower concentrations (0.020 – 1.00) because they strongly bind to C and prevent sensitization through chromium carbide formation [38]. Superferritic S44627, which does not have Ti and Nb

additions, was relatively free of corrosion in these environments based on the morphology and corrosion rates.

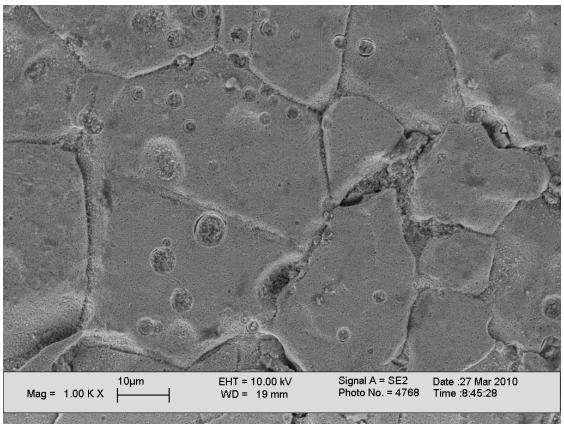


(a)

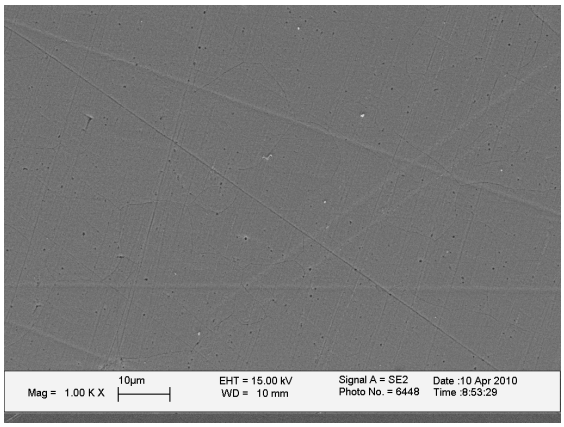


(b)

***Figure 5.3:*** ***SEM micrographs showing (a) intergranular corrosion on superferritic grade S44660 and (b) negligible attack on superferritic grade S44627 tested in 3.75 M NaOH + 0.64 M $Na_2S$ at 170 $^{O}C$.***

Percent sulfidity had an important role on the preferential corrosion of the DSS tested in sulfide-containing caustic environments. Lean grade DSS S32101 showed differences in the relative corrosion rates of localized regions on the surface depending

on the solution as shown in Figure 5.4. Standard grade S32205 showed similar behavior (Figure 5.5), whereby preferential attack was more apparent in the solution of higher percent sulfidity (Figure 5.5a) despite the lower overall corrosion rates in this solution.

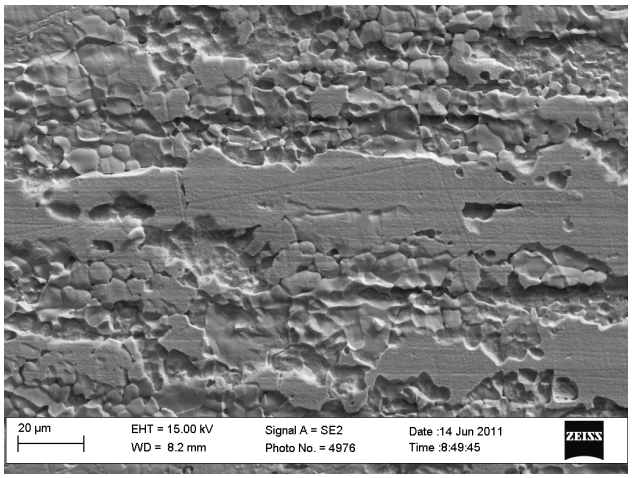


(a)

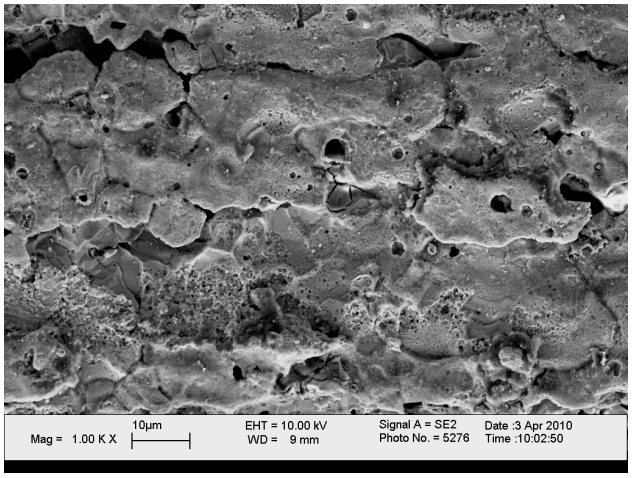


(b)

***Figure 5.4:*** ***SEM micrograph showing preferential corrosion on lean DSS (S32101) tested in solutions of (a) 35 % sulfidity (2.5M NaOH + 0.70 M $Na_2S$) and (b) 25 % sulfidity (150 g/l NaOH + 0.64 M $Na_2S$) at 170 $^{O}$C.***

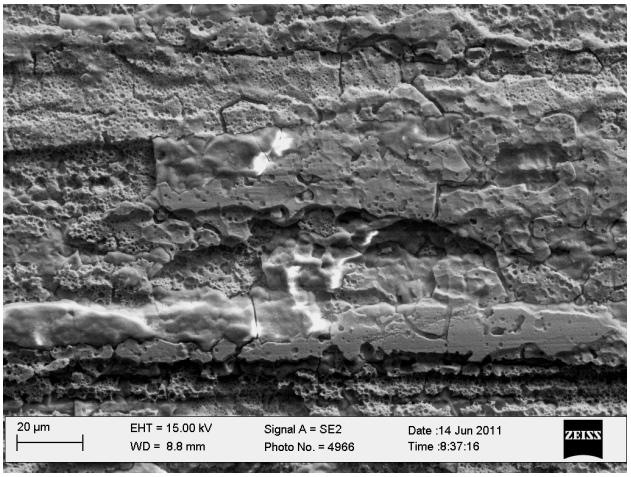


(a)

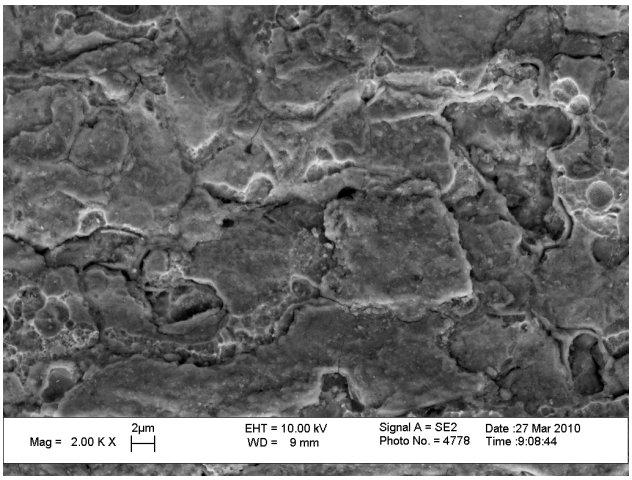


(b)

***Figure 5.5:*** ***SEM micrograph showing preferential corrosion on standard DSS (S32205) tested in solutions of (a) 35 % sulfidity (2.5M NaOH + 0.70 M $Na_2S$) and (b) 25 % sulfidity (150 g/l NaOH + 0.64 M $Na_2S$) at 170 $^{O}$C.***

Nearly uniform corrosion of lean S32101 grade DSS is shown in the cross-sectioned samples of Figure 5.6. Preferential corrosion of standard S32205 (Fig 5.7) due to selective attack of the austenite phase was more apparent in standard grade DSS S32205 as compared to lean grade DSS 32101 in the 2.5 M NaOH + 0.70 M $Na_2S$ solution (35 % sulfidity). Phase determination was accomplished using EDS based on the assumption that Cr and Mo are partitioned to the ferrite phase and Ni is partitioned to the

austenite phase (Chapter 3). Figure 5.6 shows a high magnification view of S32205 and the corresponding EDS spectra of regions indicted by arrows. Oxidation of the Cr-enriched ferrite phase was not as evident as the Ni-rich austenite phase. The oxide that formed in the austenite phase was S-rich.

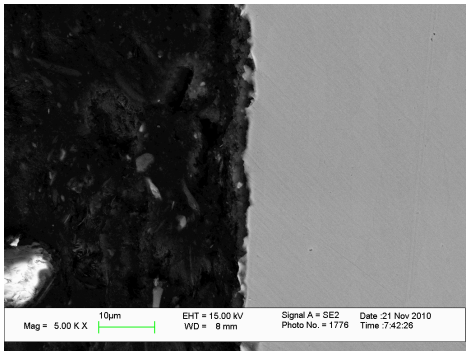


***Figure 5.6:*** ***Cross-sectional SEM micrographs showing relatively uniform corrosion on lean DSS (S32101) stainless steel tested in 35 % sulfidity solution (2.5M NaOH + 0.70 M $Na_2S$) at 170 $^{O}$C.***

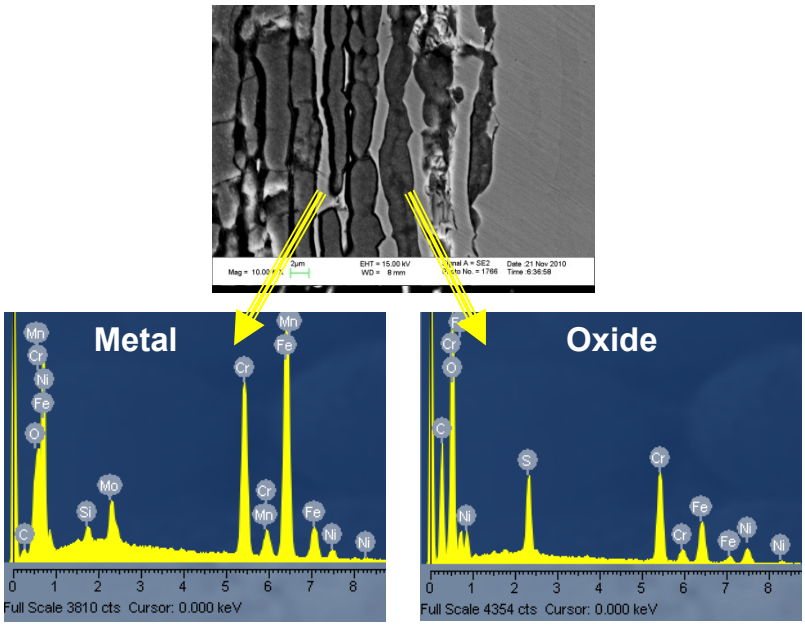


***Figure 5.7:*** ***Cross-sectional SEM micrograph of standard DSS S32205 exposed to 35 % sulfidity solution (2.5M NaOH + 0.70 M $Na_2S$) at 170 $^{O}$C. Arrows correspond to EDS spectra of Cr-rich region (ferrite) that was unoxidized and EDS spectra of S-rich, oxidized region.***

The synergistic role of sulfidity and effective alkali on corrosion behaviour for the DSS tested in alkaline-sulfide solutions is complex. Rämo et al [2-3] have explained the relationship between hydroxide and sulfide in austenitic and DSS in terms of S adhesion. The adhesion of S on the surfaces of austenitic type 304 and 316 was stronger than DSS S31803 and S32304 in their work, thus the authors tentatively ascribed the difference to Ni content. Higher sulfidity and effective alkalinity also had an appreciable effect on the corrosion rates of the austenitic and DSS in the current study. Preferential corrosion of the austenite phase was more apparent in S32205 as compared to S32101, which is attributed to the higher Ni content of S32205. Corrosion rates in alkaline-sulfide solution were nearly an order of magnitude higher as compared to the alkaline solution. Sulfide was clearly a corrosion activator of the stainless steels tested in alkaline environments, which has been shown extensively [26-28, 39] for carbon steel in pulping liquors.

Marcus et al [40-45] have studied the mechanism of S adsorption on Fe, Ni, Cr and their alloys on well-defined surfaces. Their studies clearly showed that adsorbed atomic S layers accelerate metal dissolution and inhibit the passivation of these materials. Electrochemical studies by Betova et al [15] of AISI 316L in simulated kraft pulping liquor also attributed the detrimental effects of S due to adsorption on the surface leading to unstable passivity and metal dissolution. Corrosion rates of the austenitic and DSS in the alkaline-sulfide solutions as compared to the simple alkaline environments (Chapter 4) supports earlier findings that showed enhanced metal dissolution of stainless steel in the presence of S species [2-3, 7, 15, 28-30].

### 5.2.2 Effect of Sulfide on Electrochemical Behavior

Anodic polarization was carried out to assess the influence of sulfide on the electrochemical behavior of select austenitic (S31603), superferritic (S44660), and DSS (S32205 and S32101) in alkaline-sulfide solution. Alloying elements (Fe, Cr, Ni, Mo, and Mn) were also tested to understand compositional effects in alkaline-sulfide solution. Alloy composition was shown to have a strong influence on the electrochemical behavior in alkaline environments (Chapter 4).

5.5.5.1 Anodic Polarization of Individual Alloying Elements

Figure 5.8 shows that with the exception of Mn, the anodic polarization curves for the alloying elements tested in 2.5 M NaOH + 0.70 M $Na_2S$ at 90 $^{O}$C showed similar trends. The effect of sulfide on the current density near the corrosion potential was more pronounced for Fe and Ni as compared to Cr and Mo. The increase in current density in the sulfide-containing caustic solution is distinct as compared to the 2.5 M NaOH solution (Chapter 4). Increased cathodic activity was apparent in the presence of sulfide, particularly for Fe. Mn was the only material that appeared to be passive at the corrosion potential.

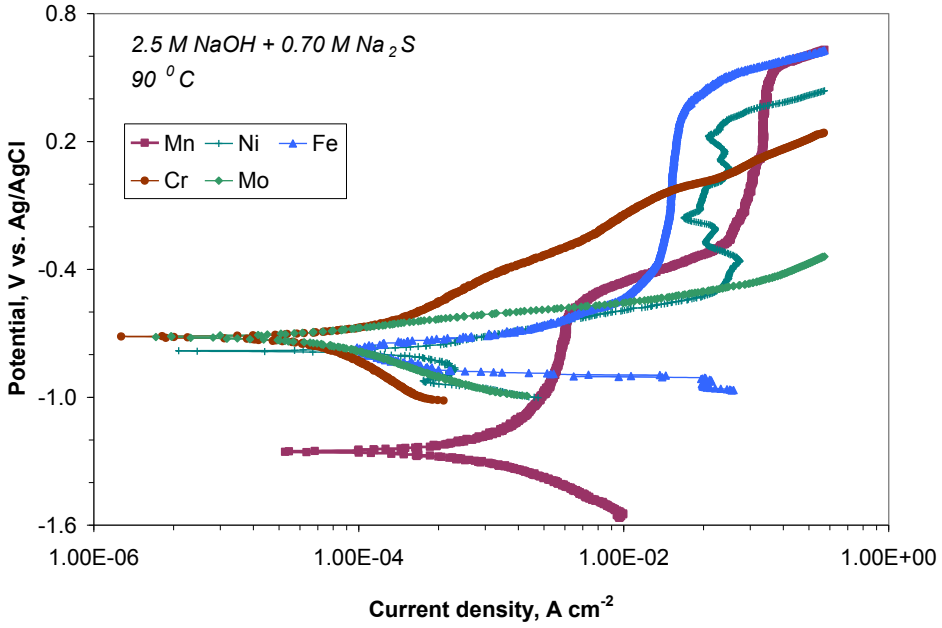


***Figure 5.8:*** ***Anodic polarization curves for Fe, Cr, Ni, Mo, and Mn tested in 2.5M NaOH + 0.70 M $Na_2S$ at 90 $^{O}$C.***

Comparisons in the electrochemical behavior of the alloying elements in the NaOH (2.5 M NaOH) and sulfide-containing caustic solution (2.5 M + 0.70 M $Na_2S$) solution based on Tafel extraction are provided in Table 5.1. It was tempting to assume the increase in anodic current density was due to enhanced dissolution of the metal based on the observed increase in corrosion rates. However, the oxidation of sulfur species also had a significant influence on the observed electrochemical behavior and will be discussed in more detail for the results at 170 $^{O}$C. All materials had higher corrosion rates in the alkaline-sulfide solution based on Tafel extraction. The increased rates for Mo and Mn and were relatively low compared to the other materials. Corrosion potentials were lower in the presence of sulfide, owing to the increased activity.

***Table 5.1:*** ***Anodic polarization parameters of Fe, Cr, Ni, Mo, and Mn tested in alkaline (A) and alkaline-sulfide (AS) solution at 90 $^{O}$C determined from Tafel extraction***

| *Alloy* | *Env.* | *jcorr, μA cm$^{-2}$* | *Ecorr, mV vs. Ag/AgCl* | *Ba, mV dec$^{-1}$* | *Bc, mV dec$^{-1}$* | *Corrosion rate, mm yr$^{-1}$* |
|---|---|---|---|---|---|---|
| Fe | A | 92 | -319 | 100000 | 1090 | 1.07 |
| Fe | AS | 226 | -860 | 91 | 54 | 3.06 |
| | | | | | | |
| Cr | A | 9 | -326 | 228 | 179 | 0.10 |
| Cr | AS | 160 | -731 | 331 | 1317 | 3.71 |
| | | | | | | |
| Ni | A | 2 | -189 | 371 | 310 | 0.02 |
| Ni | AS | 286 | -786 | 128 | 144 | 3.33 |
| | | | | | | |
| Mo | A | 41 | -648 | 47 | 356 | 0.48 |
| Mo | AS | 44 | -713 | 81 | 197 | 0.51 |
| | | | | | | |
| Mn | A | 2600 | -1370 | 100000 | 422 | 30.28 |
| Mn | AS | 227 | -1250 | 2239 | 419 | 52.86 |

The effect of temperature on the electrochemical behavior of the alloying elements is evident by comparing the results at 90 $^{O}$C (Figure 5.8) to those at 170 $^{O}$C (Figure 5.9). Mn was not tested at 170 $^{O}$C due to the limitation of the experimental setup. Increased temperature resulted in higher current densities and lower corrosion potentials of the alloying elements. Fe was particularly active in alkaline-sulfide solution at 170 $^{O}$C based on the low corrosion potential and high current density. The cathodic reaction was diffusion limited for Ni in Figure 5.9 based on Tafel slope. The other materials had an approximately linear trend at potentials more negative than the corrosion potential, indicating that a charge-transfer process was rate limiting in this region. Betova et al. [15] studied AISI 316L and its alloying elements in alkaline-sulfide solution of varying sulfide concentration and attributed this linear trend to hydrogen evolution. The authors tentatively interpreted the behavior as promoting the effect of adsorbed sulfide or hydrosulfide anions based on the following reactions shown on carbon steel [39, 46-48]:

$$Na_2S + H_2O = 2Na^+ + HS^- + OH^- \quad (5.1)$$

$$2HS^- + 2e^- = 2S_{ad}^{2-} + 2H_{ad} \quad (5.2)$$

$$2H_{ad} = H_2 \quad (5.3)$$

There were clear differences in the cathodic current density among the materials near the corrosion potential, although the variation in the anodic behavior was negligible. The anodic current density of Pt and Cr were lower than those of the other materials at potentials more noble than the corrosion potential. Pt is an inert electrode and should only show increased current for the hydrogen and oxygen evolution reactions in alkaline environments unless other reactions in the solution are occurring. Therefore, the increase in current near the corrosion potential was due the reaction of sulfur species.

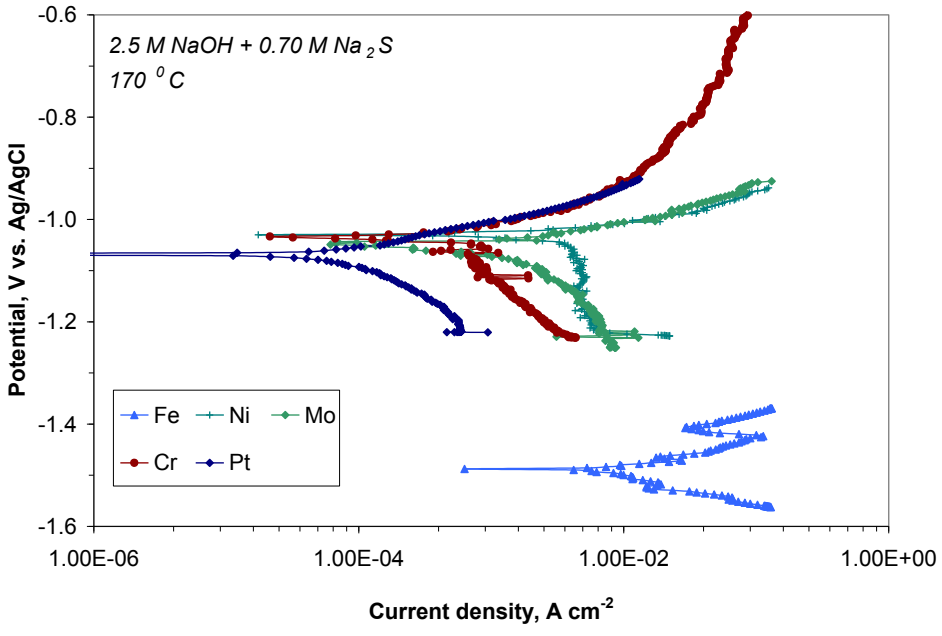


***Figure 5.9:*** ***Anodic polarization curves for Fe, Cr, Ni, Mo, and Mn tested in 2.5M NaOH + 0.70 M $Na_2S$ at 170 $^{O}$C.***

The anodic polarization curves of Pt tested in alkaline (2.5 M NaOH) and alkaline-sulfide (2.5 M NaOH + 0.70 M $Na_2S$) solution at 170 $^{O}$C is shown in Figure 5.10. The cathodic Tafel slopes are similar in the two environments, which further supports the conclusion that the cathodic reaction was due to hydrogen evolution. Due to the high current densities for the anodic reaction in the 35 % sulfidity solution, it was not possible to determine the polarization behavior beyond 0.100 V noble to the corrosion potential. The corrosion potential of Pt in the alkaline-sulfide solution was approximately -1.100 ± 0.050 V vs. Ag/AgCl.

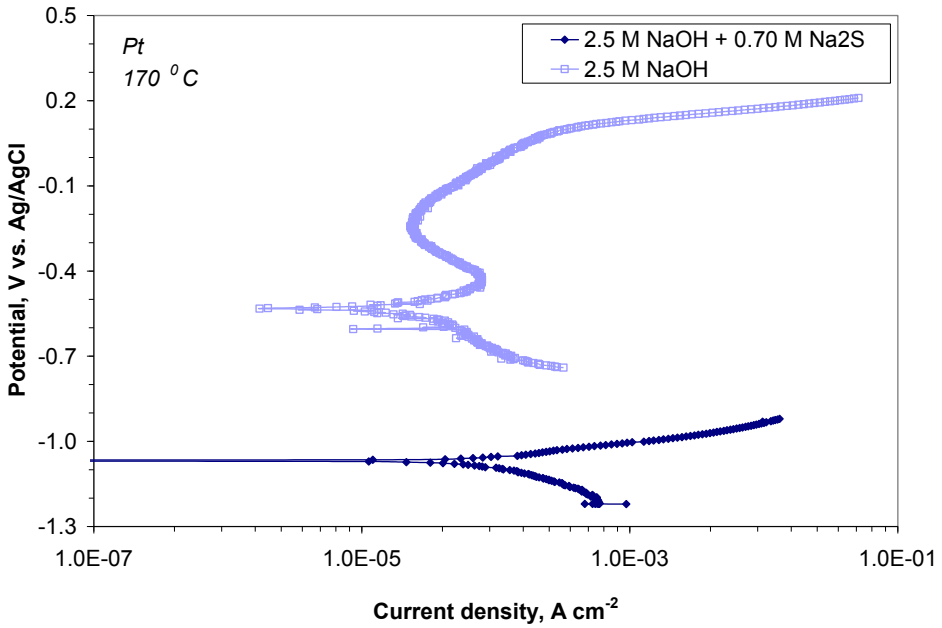


***Figure 5.10:*** ***Anodic polarization curves for Pt tested in alkaline (2.5M NaOH) and alkaline-sulfide (2.5 M NaOH + 0.70 M $Na_2S$) solution at 170 $^{O}$C.***

The E-pH diagram was used to determine the stability regions for the S – $H_2O$ system at 170 $^{O}$C (Figure 5.11) [49] to determine the adsorbed sulfide anions that accounted for the increased activity observed near the corrosion potential. Other studies

on the thermodynamics of the S – $H_2O$ system were performed at 25 $^{O}$C and 300 $^{O}$C [50-52] showed differences in the absolute potential values, but the trends were similar. The solution pH (T) in the current study was approximately 11.5 at 170 $^{O}$C based on extrapolation from the pH measured at room temperature (pH 13.4). The sulfide concentration [$S^{2-}$] was assumed to be 0.70 M even though it was expected the concentration was lower due to reaction of the $Na_2S$ added at the start of the experiment. Using the corrosion potential of Pt in Figure5.10 (E = -1.100 V vs. Ag/AgCl), sulfide ($S^{2-}$) and polysulfides ($S_n^{2-}$) were the stable species which has been described by others [50-52]. The oxidation of sulfide to polysulfide proceeds by the following reaction:

$$nHS^- = S_n^{2-} + nH^+ + 3(n-1)e^- \qquad (5.4)$$

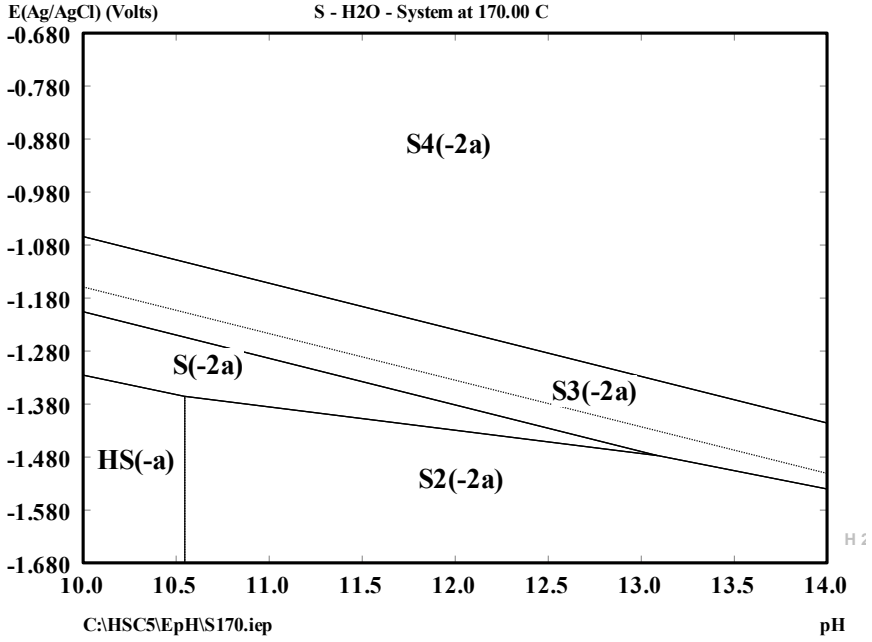


***Figure 5.11:*** ***E-pH diagram for the S- $H_20$ system at 170 $^{O}$C and 0.77 MPa. Molar concentration of sulfur is 0.70 M [49].***

Others [39, 46-48] have attributed the large increase in anodic current density to the reactive adsorption of sulfide on the surface of carbon steel and Fe, which hampers the growth of the passive film and increases its defective structure. The sulfide reacts with metallic cations in the outer layer and leads to the formation of sulfur-containing phases through the following reaction:

$$M_M^{2+} + HS_{ad}^- = MHS_{ad}^+ + V_M'' \tag{5.5}$$

$$MHS_{ad}^+ = MS_{1-x} + xHS^- + (1-x)H^+ \tag{5.6}$$

Results from more recent studies [2-3, 15] on the role of sulfide on the passivation of select stainless steels have lead to similar conclusions. These sulfur-containing phases result in a higher defect concentration of the film, thus increasing its ionic conductivity and ionic current density in the oxide. Furthermore, the formation of metal sulfides also leads to local acidification and increased dissolution of the surface film. The individual contributions of the alloying elements will be discussed with respect to the behavior of the alloys in alkaline-sulfide solution.

5.5.5.1 Anodic Polarization of Stainless Steel Alloys

The anodic polarization behavior of S31603, S44660, S32101, and S32205 were compared at 90 $^{O}$C and 170 $^{O}$C in 2.5 M NaOH + 0.70 M $Na_2S$. A previous electrochemical study [7-8] used thermodynamic predictions to determine the principle reactions for different grades of DSS in alkaline-sulfide environments. The various electrochemical reactions that can occur on stainless steels in sulfide environments were

described in detail in this earlier study and will not be discussed further. Based on the electrochemical behavior of the alloying elements in Figure 5.9 – 5.10, the precise reactions could not be determined using thermodynamic predictions as shown for the alkaline environment (Chapter 4). Therefore, the current study was focused on understanding the effect of sulfide with regards to the differences in the grades of stainless steel.

Results of alloys tested at 90 $^{O}$C are shown in Figure 5.12. Appreciable discrepancy was found with respect to the cathodic activity. The Tafel slopes were approximately linear at potentials just negative to the corrosion potential, indicating a charge-transfer process. The cathodic current density was nearly an order of magnitude greater for S31603, thus this process was enhanced on the surface of this material. The anodic activity was enhanced in S32205 and S316L as compared to S32101 and S44660. The secondary passivation behavior did not exhibit the same dependence on alloy composition as was found in the 2.5 M NaOH solution (Chapter 4). The corrosion potential of S44660 was lower than the other alloys. The composition of S31603 and S4460 were similar to the austenite and ferrite phases of S32205, respectively. S31603 was more active than S44660 near the corrosion potential of S32205. Assuming the compositions of the individual phases of DSS were similar to the single phase alloys, the austenite acted as the anodic site and the ferrite phase acted as the cathodic site. The SEM micrograph in Figure 5.7 supports this assumption.

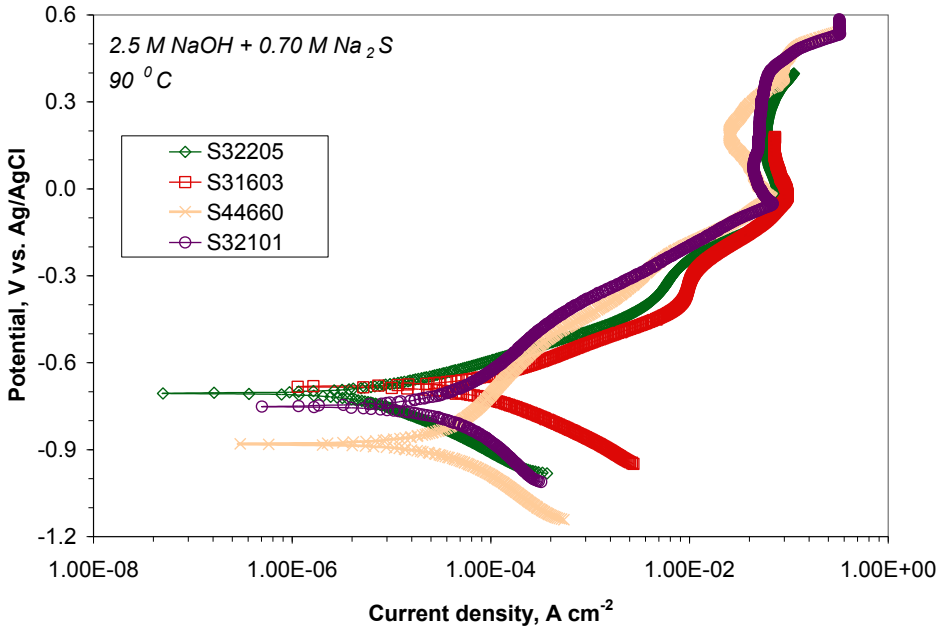


***Figure 5.12:*** ***Anodic polarization curves for austenitic (S31603), superferritic (S44660), and DSS (S2205 and S32101) tested in alkaline-sulfide (2.5 M NaOH + 0.70 M $Na_2S$) solution at 90 $^{O}$C.***

Dependence on temperature can be seen by comparing the behavior of the alloys in Figure 5.12 to those in Figure 5.13. An appreciable reduction in the corrosion potentials was observed at 170 $^{O}$C. Differences in the corrosion potentials were minimal at 170 $^{O}$C, which was caused by the increased reaction rate for the oxidation of sulfide. Metal sulfide compounds can also form near the corrosion potential of these alloys in alkaline-sulfide solution, which has been shown using X-ray diffraction [7-8]. The corrosion potential of the alloys was near the region where nickel sulfide ($Ni_3S_2$) and iron sulfide (FeS) may form based on the E-pH diagram for the S-Fe-Cr-Ni–$H_2O$ system at 170 $^{O}$C (Figure 5.14) [49]. Complex metal salts, such as sodium ferric sulfide ($NaFeS_2$), can also form in these environments [7-8].

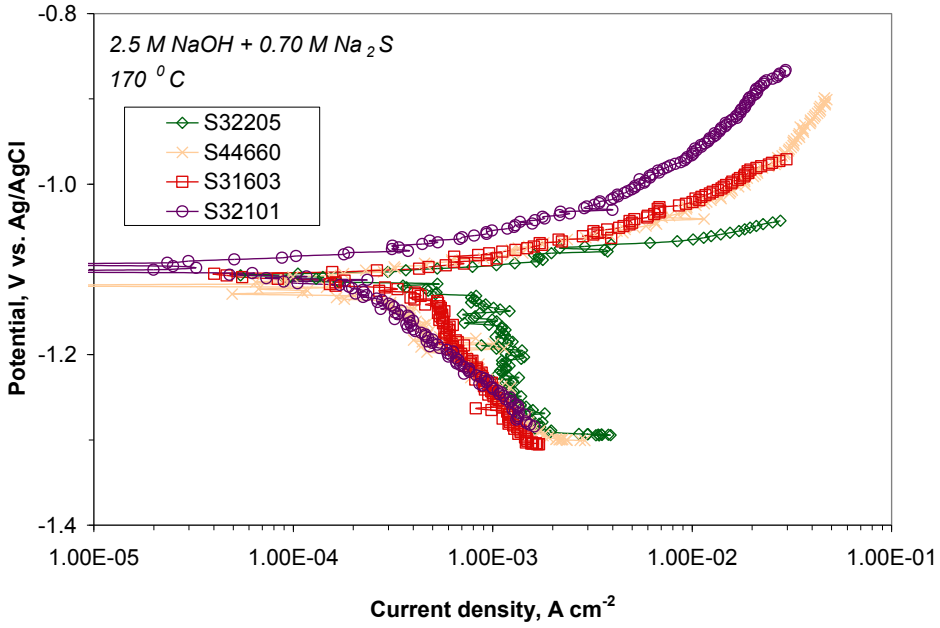


*Figure 5.13:* ***Anodic polarization curves for austenitic (S31603), superferritic (S44660), and DSS (S32205 and S32101) tested in alkaline-sulfide (2.5 M NaOH + 0.70 M $Na_2S$) solution at 170 $^{O}$C.***

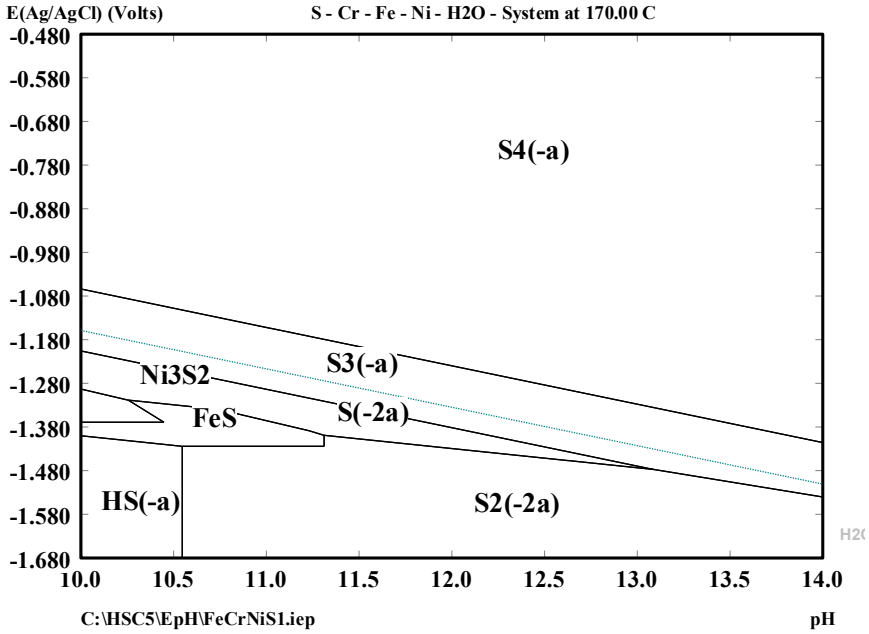


*Figure 5.14:* ***E-pH diagram for the Fe-Cr-Ni-S $H_20$ system (S dominant) at 170 $^{O}$C and 0.77 MPa [49]. Molar concentration of metal cations is 0.001 M and sulfur is 0.70 M.***

Further comparisons on the influence of temperature on the electrochemical behavior of the alloys can be drawn from Table 5.2, which shows the current densities and corresponding corrosion rates were nearly an order of magnitude greater at 170 $^{O}$C. The increase in current density was greatest for S31603 and S32205. The anodic Tafel slopes were considerably lower at 170 $^{O}$C, further indicating the reaction near the corrosion potential occurred more readily with increased temperature. Alloys S32101 and S44660 were already passivated at the corrosion potential based on the anodic Tafel slopes. Previous attempts [36] to measure in situ corrosion rates of carbon steel in alkaline-sulfide kraft pulping liquors showed poor agreement between linear polarization (LPR) and weight loss; however, the ratio of β to z was found to be a function of the solution at a given temperature, where z is the number of electrons released in the dissolution reaction, and β is given as:

$$\beta = \frac{\beta_a * \beta_c}{(\beta_a + \beta_c)} \qquad [5.1]$$

Equation [5.1] is based on the theory of Stern and Geary [53]. Values for the Tafel slopes at different temperatures are therefore indicative of the effectiveness of sulfide oxidation more than metal dissolution, which is further supported by the behavior of Pt in the alkaline-sulfide solution.

***Table 5.2:*** ***Anodic polarization parameters of S31603, S44660, S32101, and S32205 tested in alkaline-sulfide solution at 90 $^{O}$C and 170 $^{O}$C determined from Tafel extraction. Pt is shown for comparison.***

| *Alloy* | *T, $^{O}$C* | *jcorr, μA cm$^{-2}$* | *Ecorr, mV vs.Ag/AgCl* | *βa, mV dec$^{-1}$* | *βc, mV dec$^{-1}$* | *Corrosion rate, mm yr$^{-1}$* |
|---|---|---|---|---|---|---|
| S31603 | 90 | 75 | -682 | 134 | 158 | 0.86 |
| S31603 | 170 | 226 | -1030 | 81 | 1000000 | 217.90 |
| | | | | | | |
| S44603 | 90 | 62 | -878 | 571 | 315 | 0.71 |
| S44603 | 170 | 423 | -1043 | 66 | 283 | 31.52 |
| | | | | | | |
| S32101 | 90 | 69 | -750 | 409 | 419 | 1.59 |
| S32101 | 170 | 190 | -1015 | 54 | 208 | 48.69 |
| | | | | | | |
| S32205 | 90 | 56 | -706 | 90 | 154 | 0.65 |
| S32205 | 170 | 439 | -1004 | 53 | 216 | 114.80 |
| | | | | | | |
| Pt | 170 | 125 | -1070 | 83 | 190 | 9.04 |

### 5.2.3 Role of Sulfide on Surface Film Formation

A systematic study of the composition and physicoelectrical properties of passive films formed on select grades of stainless steel exposed to alkaline-sulfide solution (2.5 M NaOH + 0.70 M $Na_2S$) at 170 $^{o}$ C was carried out to understand the mechanism for sulfide adsorption. Previous attempts to show sulfide adsorption on stainless steels due to SRB [32-34] were performed using X-ray photoelectron spectroscopy (XPS) on materials exposed to near-neutral solutions at room temperature. Other efforts [15] to study the electrochemical behavior of AISI 316L and its alloying elements at 170 $^{o}$ C used electrochemical impedance spectroscopy (EIS). EIS and XPS were used in conjunction to study sulfide adsorption in the current study.

#### 5.2.3.1 Role of Physicoelectrical Properties of Surface Film

The *ac* impedance spectra for the studied alloying elements, i.e., Fe, Cr, Ni, and Mo, at the corrosion potential in a 2.5 M NaOH + 0.70 M $Na_2S$ solution at 170 $^{o}$ C are

shown in Figure 5.15 – 5.18, respectively. The effect of sulfide can be made by comparing the results for the 2.5 M NaOH solution (Chapter 4). It was established that film formation in the NaOH solution was limited by solid state transport in the oxide layer for the alloys based on the low frequency behavior in the spectra for the alloying elements and alloys.

The behavior of the passive films was significantly altered by the addition of sulfide as shown in Figure 5.15 – 5.18 with the possible exception of Mo (Figure 5.18). Mo had a single RC time constant in the NaOH solution, but the emergence of an additional time constant was clear in the alkaline-sulfide solution. Other authors [54] have attributed the difference in the NaOH solution to the nature of the self-passivation of Mo, which forms a monolayer of oxidized Mo, in comparison to the other materials that form 3D films. The additional time constant is likely the response of the passive film while the lower frequency response is due to interfacial processes. The impedance moduli at the lowest frequencies decreased by nearly an order of magnitude and the phase angle curves were displaced to lower frequencies for nearly all of the materials. The altered behavior in the alkaline-sulfide solution indicted that the response of the passive films was disappearing and the impedance was dominated by interfacial processes.

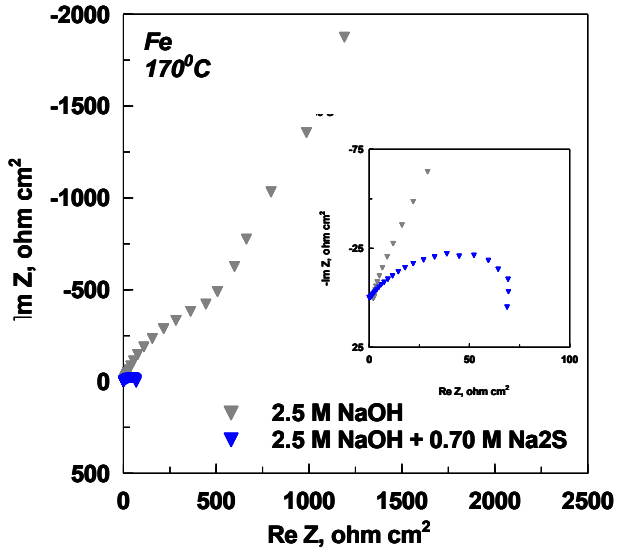


(a)

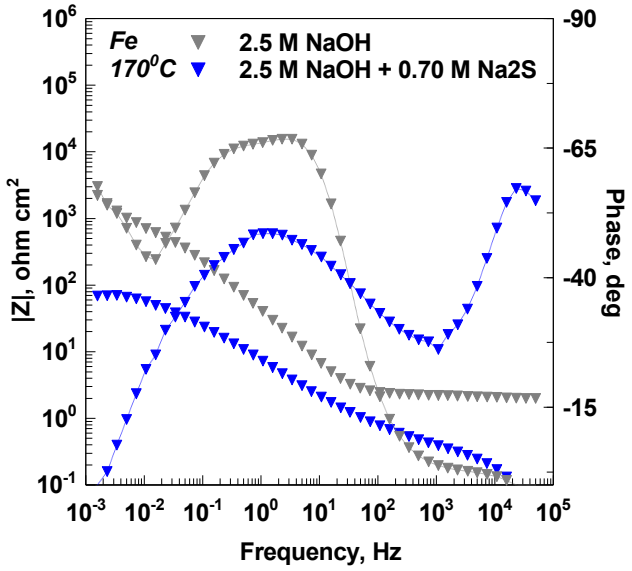


(b)

*Figure 5.15:* *Comparison of electrochemical impedance spectra at the corrosion potential for Fe tested in 2.5 M NaOH and 2.5 M NaOH + 0.70 $Na_2S$ at 170 $^{O}C$.*

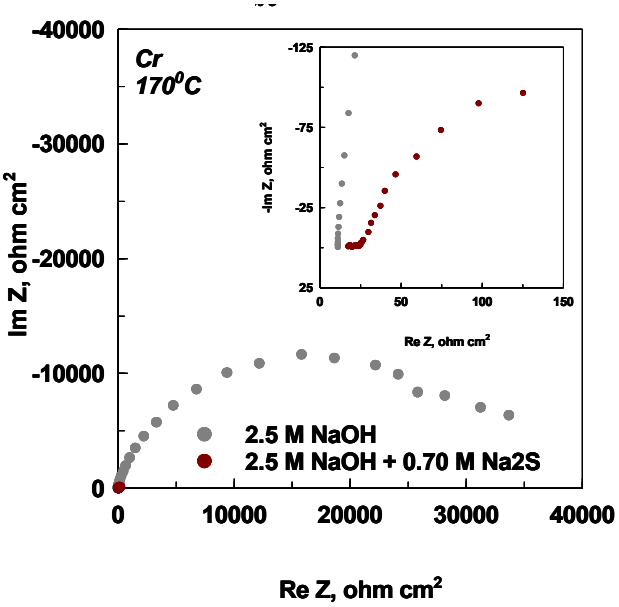


(a)

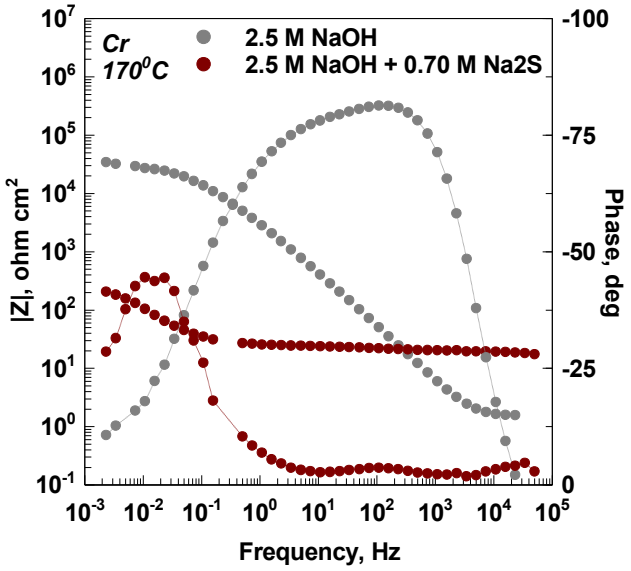


(b)

*Figure 5.16:* *Comparison of electrochemical impedance spectra at the corrosion potential for Cr tested in 2.5 M NaOH and 2.5 M NaOH + 0.70 $Na_2S$ at 170 $^{O}$C.*

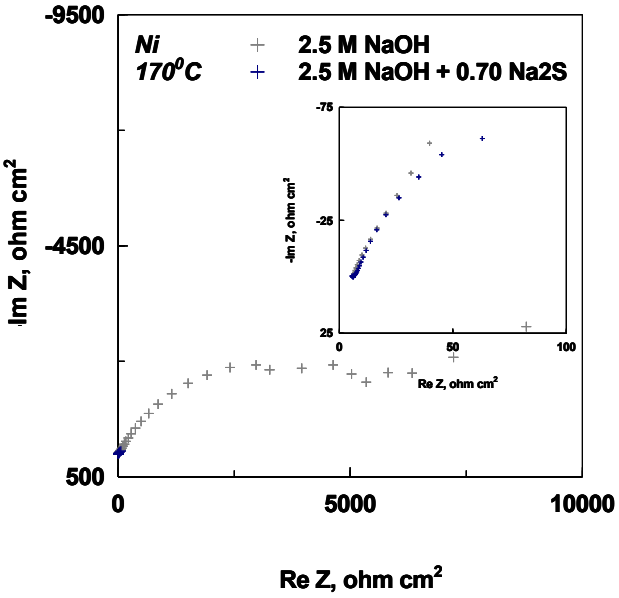


(a)

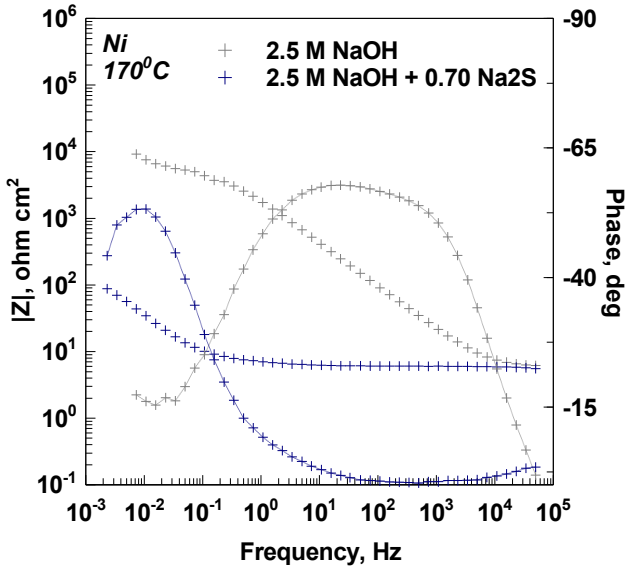


(b)

*Figure 5.17:* ***Comparison of electrochemical impedance spectra at the corrosion potential for Ni tested in 2.5 M NaOH and 2.5 M NaOH + 0.70 $Na_2S$ at 170 $^{O}$C.***

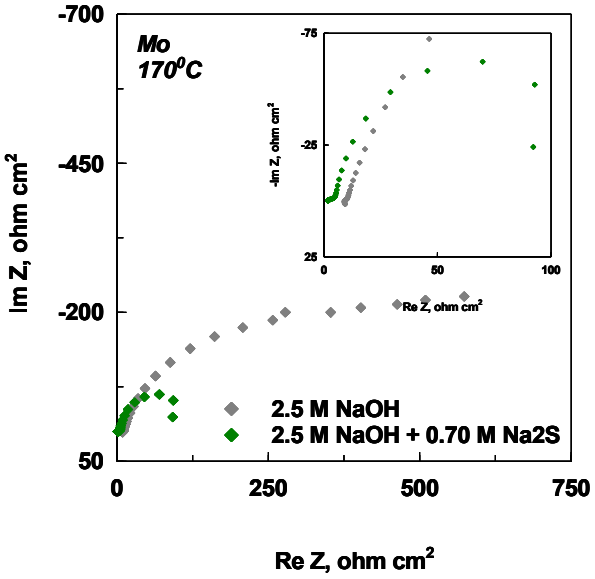


(a)

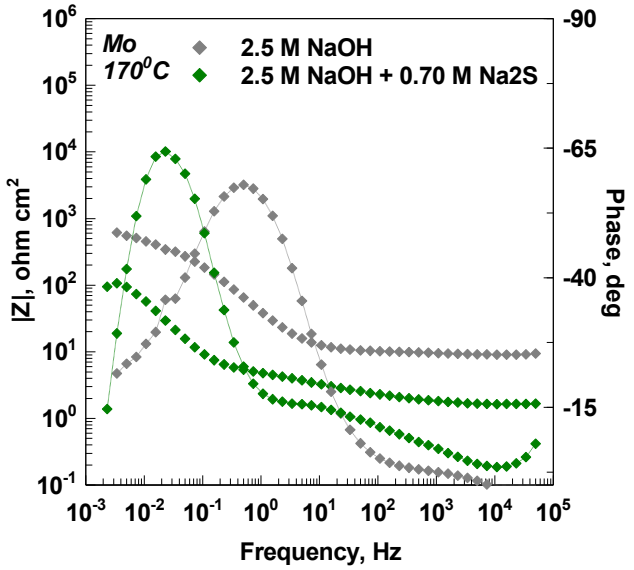


(b)

*Figure 5.18:* ***Comparison of electrochemical impedance spectra at the corrosion potential for Mo tested in 2.5 M NaOH and 2.5 M NaOH + 0.70 $Na_2S$ at 170 $^{O}$C.***

Betova et al [15] developed a kinetic model to describe the adsorption process of sulfide on AISI 316L and its alloying elements in hot alkaline solution. For this purpose, a transfer function based on the sequence of reactions, i.e., a two-step reaction with an adsorbed sulfur-containing intermediate was employed:

$$Z = R_s + \left[ j\omega C_{DL} + R_t^{-1} + \frac{R_{ad}^{-1}}{j\omega R_{ad} C_{ad} + 1} \right]^{-1} \quad [5.2]$$

$$R_t = \frac{k_1 + k_2}{F\left(b_1 + b_2\right)k_1 k_2}, \; R_{ad} = \frac{(k_1 + k_2)^2}{F\left(k_2 - k_1\right)\left(b_1 - b_2\right)k_1 k_2} \quad [5.3]$$

$$C_{ad} = \frac{\beta F(k_2 - k_1)\left(b_1 - b_2\right)k_1 k_2}{\left(k_1 + k_2\right)^3} \quad [5.4]$$

where $R_t$ is the charge-transfer resistance, $R_{ad}$ the resistance of the adsorption of the intermediate, and $C_{ad}$ is the adsorption psuedocapicitance. These parameters depend on the rate constants and potential coefficients of the two consecutive charge-transfer steps, the rate of which follows a Tafelian dependence on potential:

$$k_i = k_i^0 \exp(b_i E), \; i = 1, 2 \quad [5.5]$$

The authors assumed the corrosion process is limited by irreversible anodic reactions, and the cathodic reaction acts as a sink of electrons at the corrosion potential.

The spectra for S31603, S44660, S32101, and S32205 are shown in Figure 5.19. An attempt was made to fit a simplified analogous circuit model (Chapter 4) using a complex non-linear least squares (CNLS) linear regression algorithm that substituted

constant phase elements (CPE) for $C_{dl}$ and $C_{ad}$ to the results for S32101. Reasonable agreement between the modified model and experimental data was found, which shows that the behavior is dominated by two interfacial processes. The impedance spectra for S32205 differed from S32101, an unsurprising result considering the thick layer adsorbed on the surface of S32205 (Fig 5.6). S44660 also had an additional time constant in the mid-frequency range. The simplified model was also fit to S32205 (Figure 5.20) with poor agreement for a circuit having two CPE components, thus an additional RC circuit was added in series (Figure 5.21) to account for the high frequency response of the surface film. The surface film shown in cross section on S32205 (Figure 5.6) was thick (ca. 10 μm) and would account for the observed increase in impedance at high frequencies.

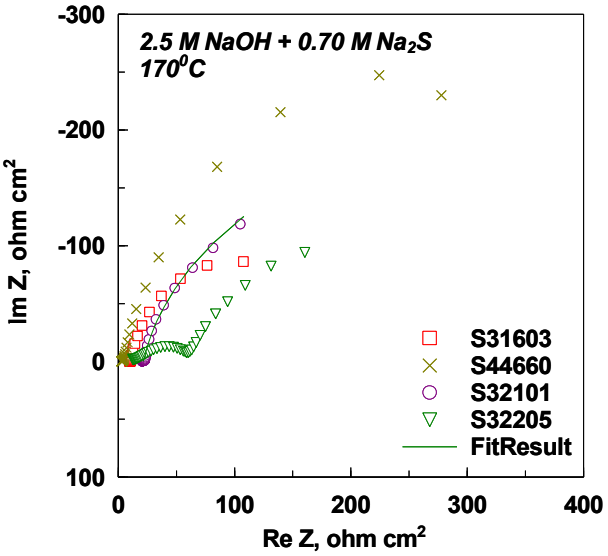


(a)

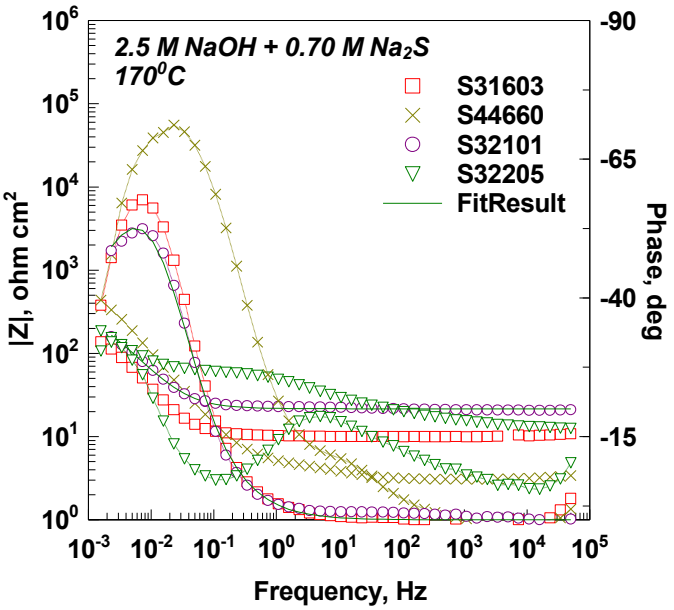


(b)

*Figure 5.19:* ***Comparison of electrochemical impedance spectra at the corrosion potential for S31603, S44660, S32101, and S32205 tested in 2.5 M NaOH + 0.70 $Na_2S$ at 170 $^{O}$C. Points – experimental points, lines – best fit results obtained from simulation on S32101. The best fitting parameters are: $R_s$ = 21.58 Ω cm$^2$, $R_1$ = 368 Ω cm$^2$, $CPE_1$ =189.9 mF cm$^{-2}$, $\alpha_1$ = 0.855, $R_2$ = 375 Ω cm$^2$, $CPE_2$ = 957 mF cm$^{-2}$, and $\alpha_2$= 0.98. ($\chi^2$ = 8.94e-3)***

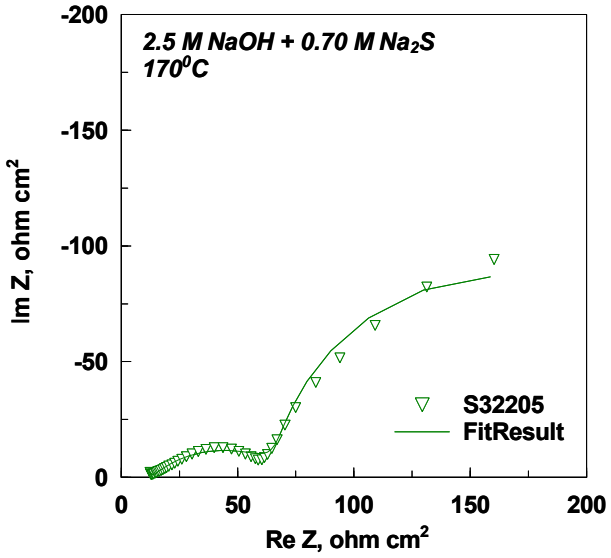


(a)

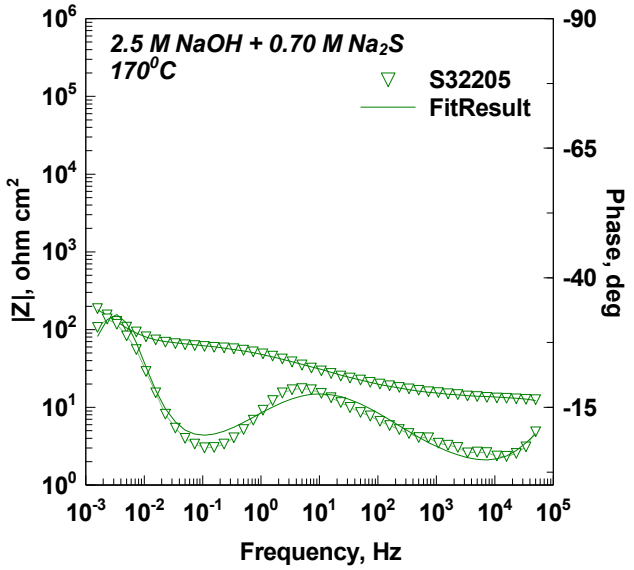


(b)

*Figure 5.20:* ***Electrochemical impedance spectra at the corrosion potential for S32205 tested in 2.5 M NaOH + 0.70 $Na_2S$ at 170 $^{O}$C. Points – experimental points, lines – best fit results obtained from simulation. The best fitting parameters are: $R_s$ = 8.73 Ω cm$^2$, $R_1$ = 61.8 Ω cm$^2$, $CPE_1$ =5.89 mF cm$^{-2}$, $\alpha_1$ = 0.455, $R_2$ = 206 Ω cm$^2$, $CPE_2$ = 369 mF cm$^{-2}$, $\alpha_2$= 0.947, R3=4.02 Ω cm$^2$, and C1 = 46.9 μF. ($\chi^2$ = 2.74e-3)***

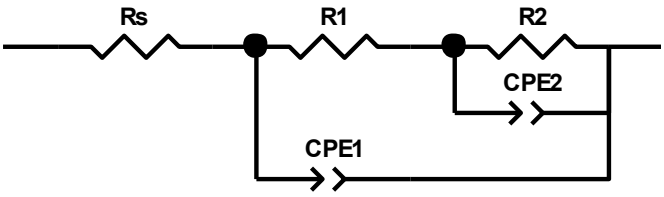


(a)

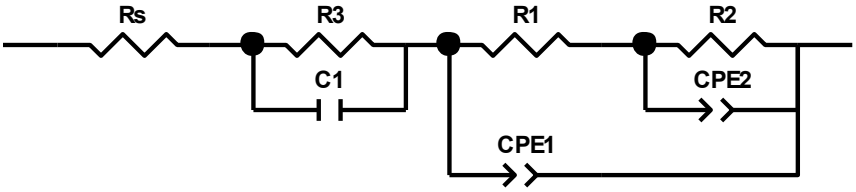


(b)

*Figure 5.21:* ***Equivalent circuits used to simulate the electrochemical behavior of (a) S31603, S44603, S32101, and (b) S32205 in 2.5 M NaOH + 0.70 M $Na_2S$ at the corrosion potential at 170 $^{O}$C.***

The impedance moduli at the lowest frequency corresponded reasonably well to the results from linear polarization resistance (LPR) of the alloys (ca. 200 - 500 Ω $cm^2$) shown in Figure 5.19. The clear trend towards lower resistance of the passive film in the presence of sulfide is supported by the impedance and LPR results. In other words, sulfide adsorption enhances the conductivity of the passive films. The film resistances of the alloys were close to the alloying elements in the alkaline-sulfide environment. Brandy and Jones [55] have evaluated errors arising from non-linearity of the polarization behavior in the range of -10 mV to 10 mV and showed errors as high a 50 % in the anodic region and 30 % in the cathodic region. The errors due to nonlinearity in the results shown in Figure 5.19 were determined by averaging the anodic and cathodic currents.

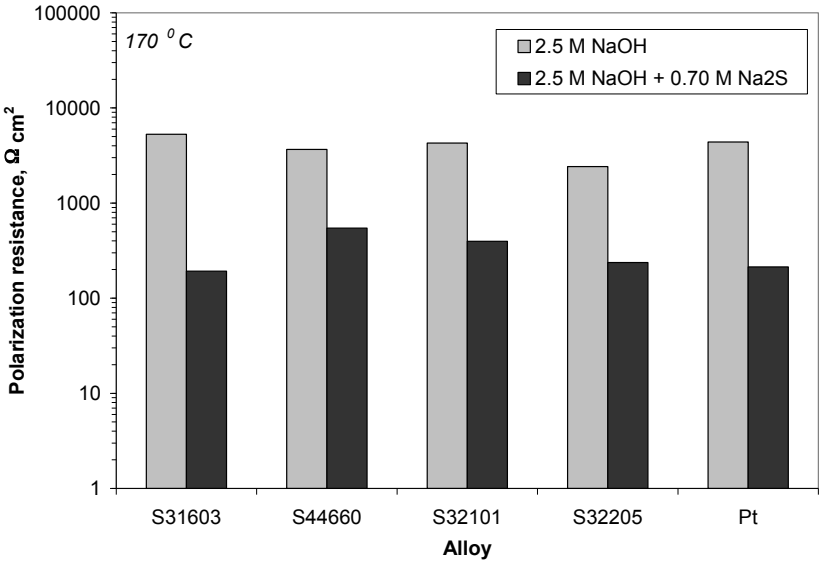


***Figure 5.22:*** ***Linear polarization resistance values for austenitic S31603, superferritic S44660, lean DSS S32101 and standard DSS S32205 tested in 2.5 M and 2.5 M NaOH + 0.70 M $Na_2S$ at 170 $^O$C. Pt is shown for comparison.***

The agreement between the experimental data and analogous circuits indicate that a heterogeneous reaction involving adsorptive interaction between the oxide surface and sulfur species had occurred in the presence of sulfide. Based on earlier findings for Fe [46-47], carbon steel [39, 48], AISI 316L [2-3, 15] in alkaline-sulfide environments, sulfide anions formed by hydrolysis of $Na_2S$ adsorb strongly on the surface of the respective materials and hinder the oxide film growth. Film growth is also unstable due to formation of soluble metal sulfide compounds, which more readily dissolve into the solution. The adsorptive process leads to a significant change in the reaction kinetics to a process limited by ionic diffusion in the film (Chapter 4) to an interfacial process similar to active dissolution. The adsorption process appeared to be favored on the alloys with lower Cr contents and higher Ni content based on the impedance and LPR data. Owing to the complexity associated with oxidation of S species in sulfide-containing caustic solution, electrochemical approaches to determine corrosion rates are difficult.

5.2.3.2 Effect of Film Composition

The corrosion rates, film morphologies, and impedance results indicated that sulfide enhanced dissolution of the DSS through a modification of the oxide film in an adsorption process. The films formed at the corrosion potential on austenitic S31603, superferritic S44660, lean DSS S32101, and standard DSS S32205 were characterized with XPS after exposure to 2.5 M NaOH + 0.70 M $Na_2S$ at 170 $^{O}$C. Film compositions and oxidation states of the various compounds were determined for the alloying elements after exposure for comparison. Thermodynamic predictions in conjunction with XPS spectra of DSS exposed to the NaOH solution (Chapter 4) demonstrated that films were composed of an outer hydroxide layer and inner, mixed Fe-Cr oxide. A similar approach was used to determine the film composition in the sulfide-containing caustic solution.

Cross-sectional SEM micrographs of the surface film that formed on superferritic S44660 is shown in Figure 5.23. The presence of sulfide resulted in a defective film morphology, which is evident by the film thickness and non-uniform nature. Representative spectra from EDS of the high magnification image showed that the surface film was enriched in S. The EDS spectra were normalized and compared based on the ratio of each cation to total cation percentage for qualitative comparisons. Outer layer was (61 wt % Fe, 28 wt % Cr, and 11 wt % Ni) and inner layer was approximately (69 wt % Fe, 28 wt % Cr, and 3 wt % Ni) based on the average of 15 measurements, thus Ni enrichment of the film was detected in presence of sulfide. The S - $K_{\alpha}$ peak was approximately 4 and 1 wt % for the outer and inner layers, respectively.

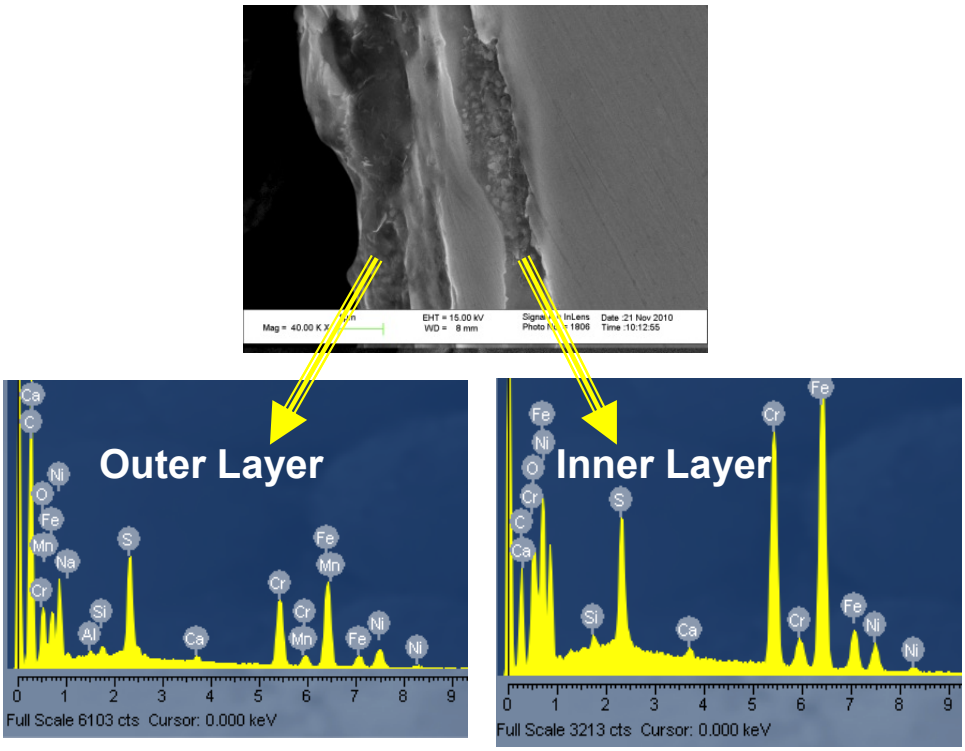


***Figure 5.23:*** ***Cross-sectional SEM micrograph of superferritic S44660 exposed to 35 % sulfidity solution (2.5M NaOH + 0.70 M $Na_2S$) at 170 $^{O}$C. Arrows correspond to EDS spectra of S-rich outer layer and EDS spectra of Fe and Cr enriched inner layer.***

Cross-sectional SEM micrographs of the surface film that formed on austenitic S31603 is shown in Figs. 5.24. The presence of sulfide also resulted in a defective film morphology, which is evident by the film thickness and non-uniform nature. The corrosion product on the surfaces was ca. 4-5 μm. Representative spectra from EDS of the high magnification image showed that the surface film was enriched in S. The EDS spectra were normalized and compared based on the ratio of each cation to total cation percentage for qualitative comparisons. Outer layer was (27 wt % Fe, 38 wt % Cr, and 32 wt % Ni) and inner layer was approximately (62 wt % Fe, 24 wt % Cr, and 14 wt % Ni) based on the average of 15 measurements, thus Ni and Cr enrichment of the film was detected in presence of sulfide. The S- $K_{\alpha}$ peak was approximately 8 and 3 wt % for the

outer and inner layers, respectively. Sulfidation of the film was more favorable in the austenitic grade as compared to the superferritic grade based on these results.

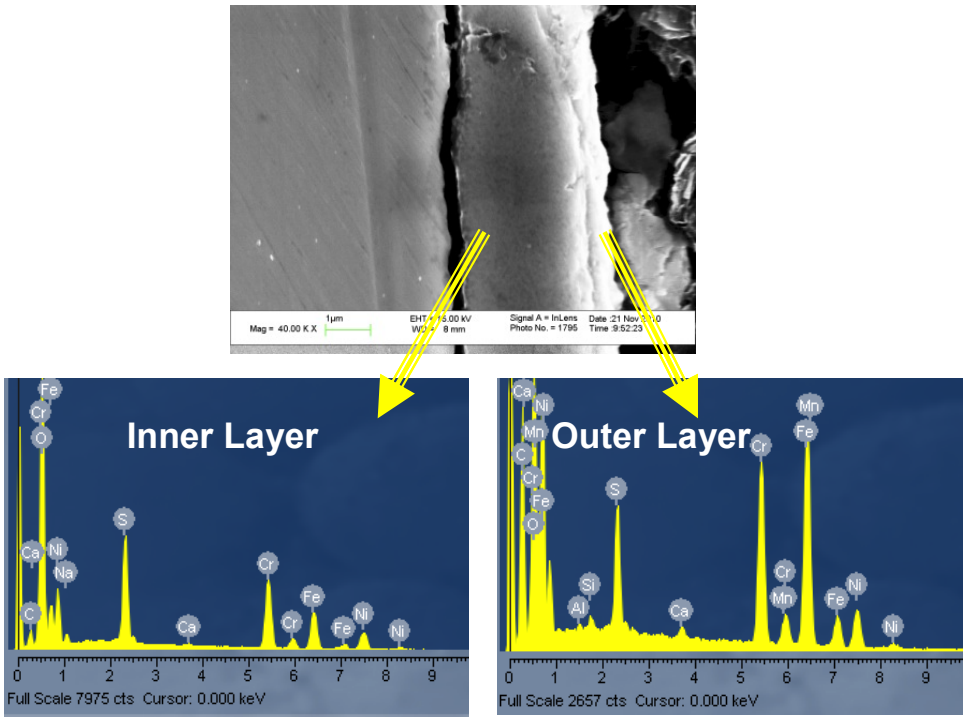


***Figure 5.24:*** ***Cross-sectional SEM micrograph of austenitic S31603 exposed to 35 % sulfidity solution (2.5M NaOH + 0.70 M $Na_2S$) at 170 $^{O}$C. Arrows correspond to EDS spectra of S-rich outer layer and EDS spectra of Cr and Ni enriched inner layer.***

The surface film that formed at the corrosion potential on S32205 after 168 h exposure to 2.5 M NaOH + 0.70 M $Na_2S$ at 170 $^{O}$C was analyzed using XPS with sputtering capability. Superferritic S44660 and austenitic S31603 were also studied to understand film composition in single phase materials. An argon (Ar) ion sputtering gun was used to evaluate the composition and oxidation state of the ionic species in the surface film as a function of depth.

Reference materials of Fe, Cr, and Ni were also studied to determine the binding energies (BE) of the Fe $2p_{3/2}$, Ni $2p_{3/2}$, and Cr $2p_{3/2}$ oxide and sulfur species in alkaline-sulfide solution. No sulfur was detected in the high resolution scans of Cr, thus only the oxide has been identified. All binding energy (BE) values were corrected using the carbon (C 1s) peak at 284.6 eV. Values for the BE of the various chemical states of alloys and reference materials are provided in Table 5.3. Results in Table 5.3 are consistent with the published data shown in Table 5.4 for model compounds measured under controlled conditions to prevent oxidation of the sulfur species.

***Table 5.3:*** ***Binding Energies (BE) of the Different Chemical States for Fe($2p_{3/2}$), Cr($2p_{3/2}$), Ni($2p_{3/2}$), and O(1s) Photoelectron Spectra of Control Samples (this study).***

| *Species* | *Chemical State* | *BE (eV)* |
|---|---|---|
| *Fe $2p_{3/2}$* | | |
| | Fe(II) - S | 707.5 |
| | Fe (II) - O | 709.7 |
| | Fe (III)- S | 708.5 |
| | Fe (III) - O | 712.4 |
| *Ni $2p_{3/2}$* | | |
| | Ni (II) - S | 853.2 |
| | Ni (II) - O | 854.4 |
| *Cr $2p_{3/2}$* | | |
| | Cr (III) - O | 576.2 |
| *S $2p_{3/2}$* | | |
| | $S^{2-}$ | 161.5 |
| | $S_n^{2-}$ | 163.2 |
| | $S^o$ | 164.6 |
| *O 1s* | | |
| | $O^{2-}$ | 530.4 |
| | $OH^-$ | 531.6 |

***Table 5.4:*** ***Binding Energies (BE) of the Different Chemical States for Fe($2p_{3/2}$), Cr($2p_{3/2}$), Ni($2p_{3/2}$), and O(1s) Photoelectron Spectra for References on Various Model Compounds.***

| *Species* | *Chemical State* | *BE (eV)* | *Reference* |
|---|---|---|---|
| *Fe $2p_{3/2}$* | | | |
| | Fe(II) - S | 707.0 | [56] |
| | Fe(II) - S | 707.1 | [56] |
| | Fe(II) - S | 707.3 | [56] |
| | Fe (II) - O | 709.5 | [56] |
| | Fe (II) - O | 709.0 | [56] |
| | Fe (II) - O | 708.0 | [56] |
| | Fe (III)- S | 709.2 | [56] |
| | Fe (III)- S | 709.1 | [56] |
| | Fe (III)- S | 708.7 | [56] |
| | Fe (III) - O | 711.6 | [56] |
| | Fe (III) - O | 711.0 | [56] |
| | Fe (III) - O | 712.0 | [56] |
| *Cr $2p_{3/2}$* | | | |
| | Cr (III)- S | 575 | [57] |
| | Cr (III)- S | 574.6 | [58] |
| | Cr (III)- S | 574.4 | [59] |
| | Cr (III) - O | 576.3 | [57] |
| | Cr (III) - O | 576.2 | [58] |
| | Cr (III) - O | 576.5 | [59] |
| *Ni $2p_{3/2}$* | | | |
| | Ni (II) - S | 853.4 | [60] |
| | Ni (II) - S | 853.0 | [60] |
| | Ni (II) - S | 854.2 | [60] |
| | Ni (II) - O | 854.0 | [60] |
| | Ni (II) - O | 854.8 | [60] |
| | Ni (II) - O | 853.8 | [60] |
| *S $2p_{3/2}$* | | | |
| | $S^{2-}$ | 161.3 | [56] |
| | $S^{2-}$ | 160.9 | [56] |
| | $S^{2-}$ | 162.3 | [61] |
| | $S_2^{2-}$ | 162.5 | [61] |
| | $S_2^{2-}$ | 162.3 | [61] |
| | $S_2^{2-}$ | 163.1 | [62] |
| | $S_n^{2-}$ | 163.3 | [56] |
| | $S_n^{2-}$ | 163.4 | [56] |
| | $S_n^{2-}$ | 163.8 | [61] |
| | $S^o$ | 164.0 | [56] |
| | $S^o$ | 164.4 | [56] |
| | $S^o$ | 164.2 | [61] |

Figure 5.25 shows a comparison of the major constituents of the surface film between XPS sputter depth profiles acquired from S32205, S31603, and S44660. The primary y-axis shows the normalized cation concentration (at %), and the secondary y-axis shows the measured anion concentration (at. %). Sulfidation of the oxide films is clear for each alloy. The surface films were enriched in Cr and Ni, particularly in the outer layers. Ni enrichment near the oxide/metal interface of S44660 is apparent in Figure 5.25b. Mo and Mn were mostly dissolved in the alkaline-sulfide environment. Spot size for these measurements was 400 μm, which is larger than the phase regions for this S32205 material (ca. 50 μm).

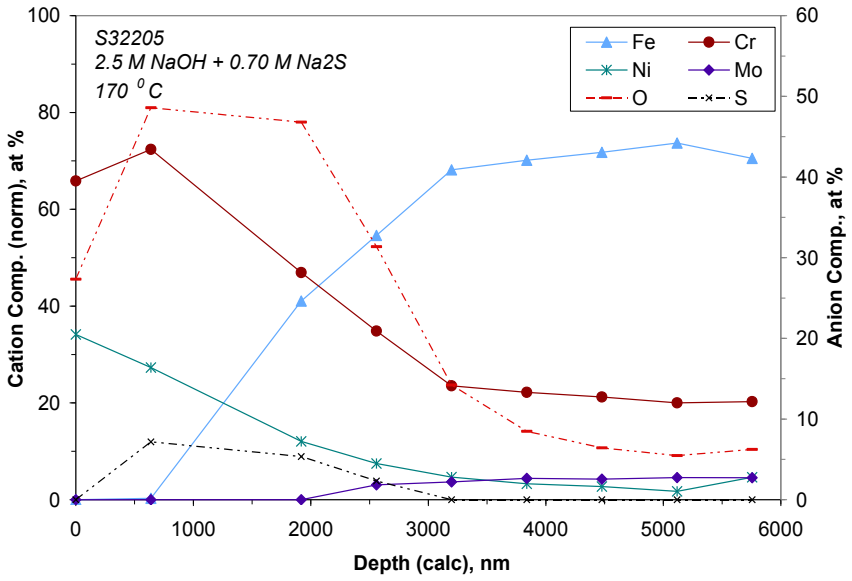


(a)

***Figure 5.25:*** ***X-ray photoelectron spectroscopy depth profile of surface film on (a) austenitic S3160 formed at corrosion potential in 2.5 M NaOH + 0.70 M $Na_2S$ at 170 $^{O}$C.***

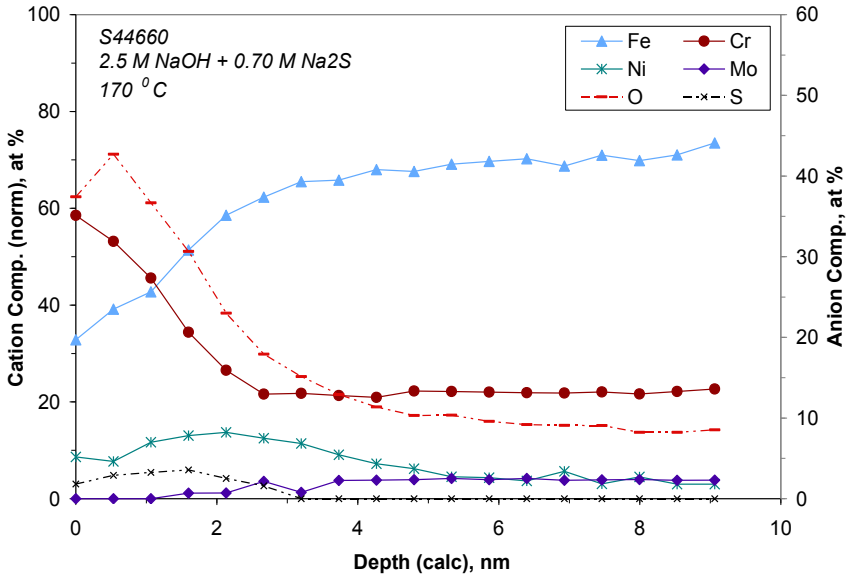


(b)

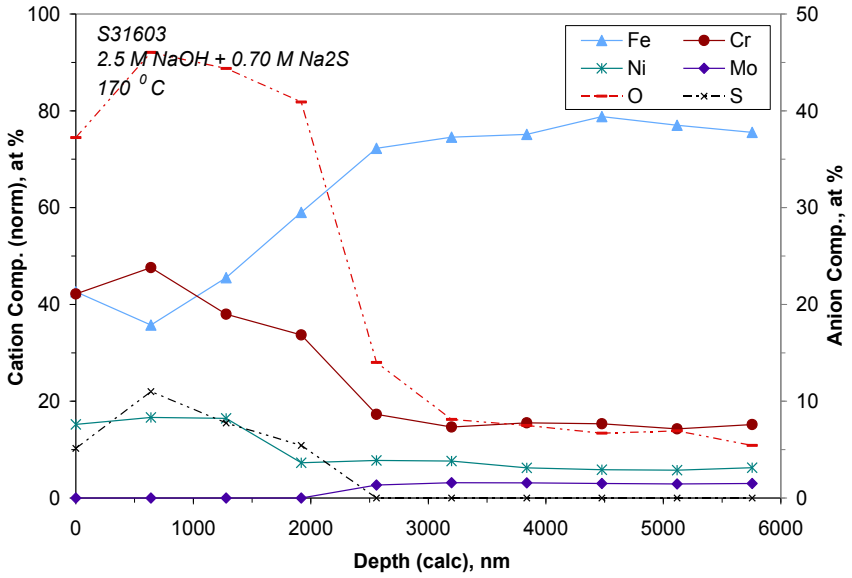


(c)

***Figure 5.25(cont'd):*** ***X-ray photoelectron spectroscopy depth profile of surface film (b) superferritic S44660, (c) lean DSS S32101, and (d) standard DSS S32205 formed at corrosion potential in 2.5 M NaOH + 0.70 M $Na_2S$ at 170 $^{O}$C.***

XPS spectra of high resolution scans of Fe 2p, Ni 2p, and Cr 2p and O 1s from the top surface layers formed on S32205 are shown in Figure 5.26. The spectra corresponding to half the maximum of the O 1s signal (ca. 1920 nm depth) are plotted using filled symbols. There is a broad high BE shoulder associated with each of the spectra, indicating that there is an appreciable amount of oxidation in the presence of sulfide. Moreover, considerable hydration of the surface Cr compounds took place based on the broad shoulder for the Cr spectra. A broad shoulder was also associated with Ni, which was not apparent in the NaOH solution (Chapter 4). The BE of the O 1s signal on the outer levels was consistent with a hydroxide layer. The surface films that form on Fe-Cr-Ni alloys in many environments [63-65] have been shown to have two primary layers: an outer hydroxide layer and inner oxide layer. The spectra from half the maximum O 1s signal depth (ca. 1920 nm) were analyzed to determine the oxidation states of each element.

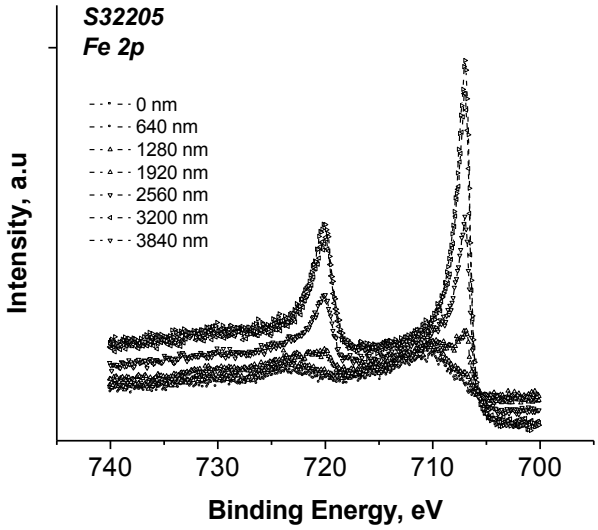


(a)

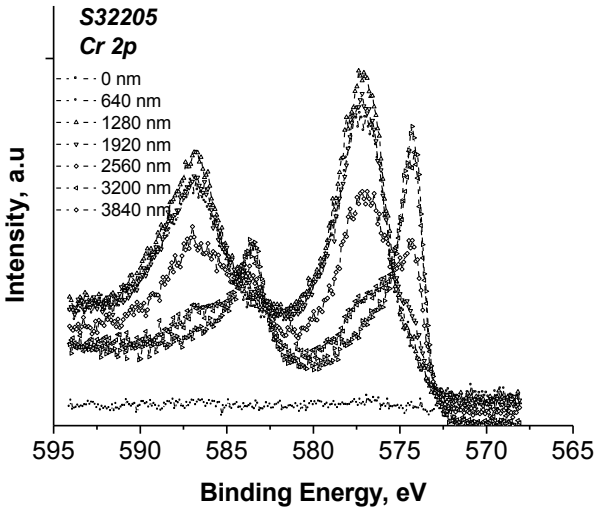


(b)

*Figure 5.26:* ***High resolution X-ray photoelectron spectra from surface film formed on standard DSS S32205 formed at corrosion potential in 2.5 M NaOH + 0.70 M Na2S at 170 $^{O}$C for (a) Fe 2p and (b) Cr 2p. Filled symbols represent the scan corresponding to the half maximum O 1s peak intensity (ca. 1920 nm).***

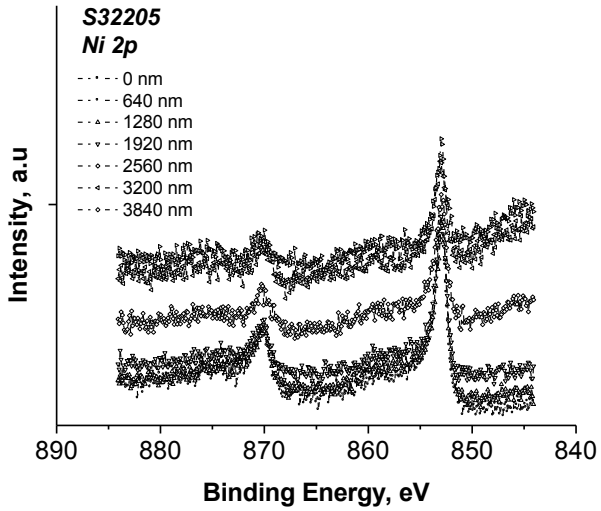


(c)

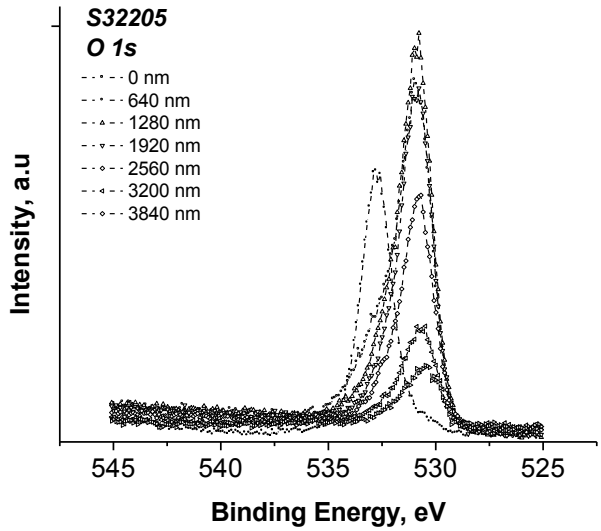


(d)

*Figure 5.26 (cont'd): High resolution X-ray photoelectron spectra from surface film formed on standard DSS S32205 formed at corrosion potential in 2.5 M NaOH + 0.70 M Na2S at 170 $^{o}$C for (c) Ni 2p and (d) O 1s. Filled symbols represent the scan corresponding to the half maximum O 1s peak intensity (ca. 1920 nm).*

Peak fitting of Fe 2p signal was attempted using Gaussian-Lorentzian line shapes after Savitzky - Golay smoothing and Shirley background subtraction indicated that sulfide compounds had formed in the oxide based on the broad high BE shoulder of Fe and Ni. Ionization due to sputtering is possible with depth profiling, thus semi-quantitative interpretation of the data showed that Fe was present as either $Fe^{2+}$ or $Fe^{3+}$. Fe was present as an oxide and a sulfide based on the differences between the caustic and sulfide-containing caustic environment. Cr was predominantly in the form of $Cr^{3+}$ as chromium oxide or chromium hydroxide. There were also $Cr^{+6}$ species detected, which likely formed through transpassive dissolution of the oxide film. Ni was in metallic form with limited amount of $Ni^{2+}$, which was likely nickel oxide and nickel sulfide based on thermodynamic predictions. The O 1s signal at the oxide/metal interface corresponded to a mixed oxide and hydroxide.

High resolution scans of the S 2p region for austenitic S31603 and superferritic S44660 (Figure 5.27) as well as DSS S32205 (Figure 5.28) show that sulfur species were identified in the 160 – 165 eV region. The BE values in this region correspond to either monosulfide ($S^{2-}$), disulfide ($S_2^{2-}$), or polysulfide ($S_n^{2-}$) compounds in Table 5.4. The relative amount of sulfide was greater in S31603.

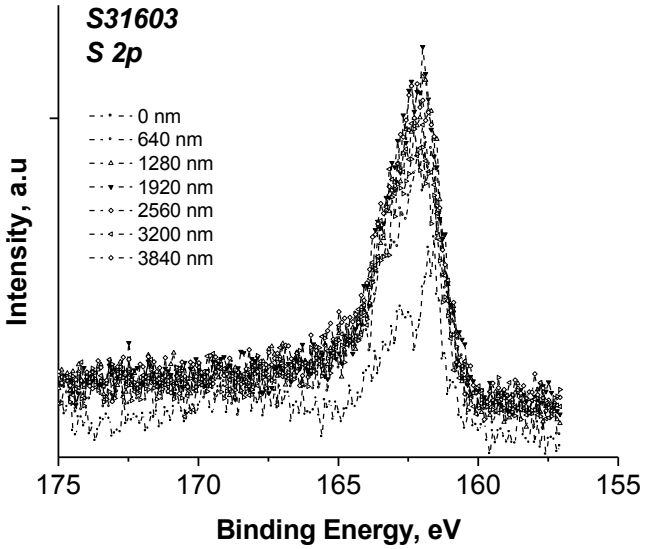


(a)

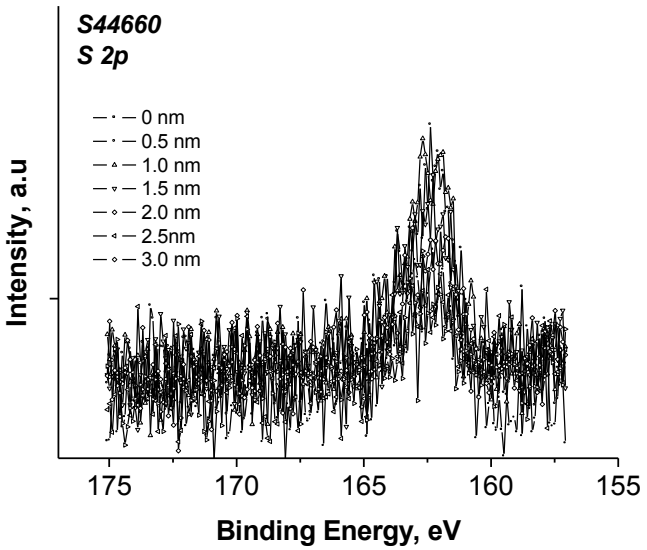


(b)

*Figure 5.27:* ***High resolution X-ray photoelectron spectra of S $2p_{3/2}$ from surface film formed at corrosion potential in 2.5 M NaOH + 0.70 M $Na_2S$ at 170 $^{O}$C for (a) austenitic S31603 and (b) superferritic S44660.***

An attempt was made to fit curves to the S 2p spectra for S32205 (Figure 5.29) to determine the sulfur compounds that formed near the corrosion potential in alkaline-sulfide solution. The fitting was performed at a depth corresponding to the oxide/metal interface (half the maximum O 1s signal, i.e., 1920 nm). The reduced sulfur was present in various forms of sulfide. Sulfur peaks corresponded to $S^{2-}$ at 161.9 eV (FWHM = 1.3 eV), and $S_n^{2-}$ at 163.4 eV (FWHM = 1.0 eV). The S 2p peaks for the $S_2^{2-}$ and $S_n^{2-}$peaks were detected at 162.5 eV and 164.7, respectively. The peaks had similar FWHM and BE values as those identified in the literature (Table 5.4). The relative amount of monosulfide to polysulfide increased with sputtering depth and was approximately 2:1 at the oxide/metal interface. The relative ratio of Fe, Cr, or Ni metal compounds could not be determined from the XPS data, but based on the relative concentration after sputtering to the oxide/metal interface (Figure 5.25), sulfides of Fe and Ni were most likely predominant in the outer layers of the film. The results imply that sulfur binds to the metal surface and is integrated into the oxide film, preventing stable passivation.

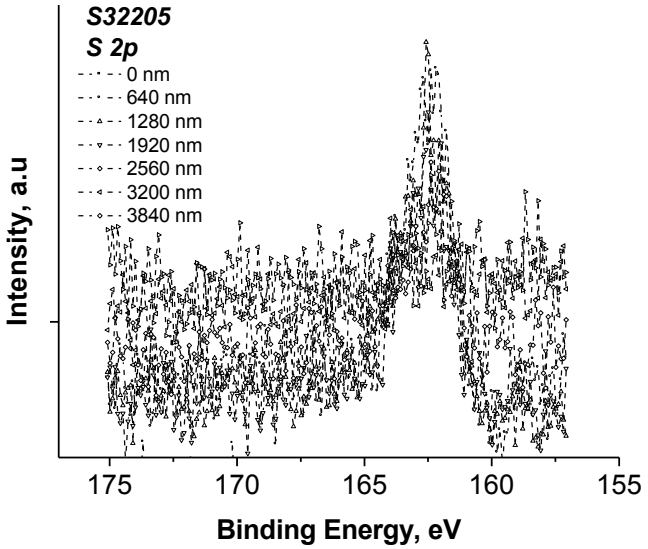


*Figure 5.28:* ***High resolution X-ray photoelectron spectra of S $2p_{3/2}$ from surface film formed at corrosion potential in 2.5 M NaOH + 0.70 M $Na_2S$ at 170 $^{O}C$ for DSS S32205.***

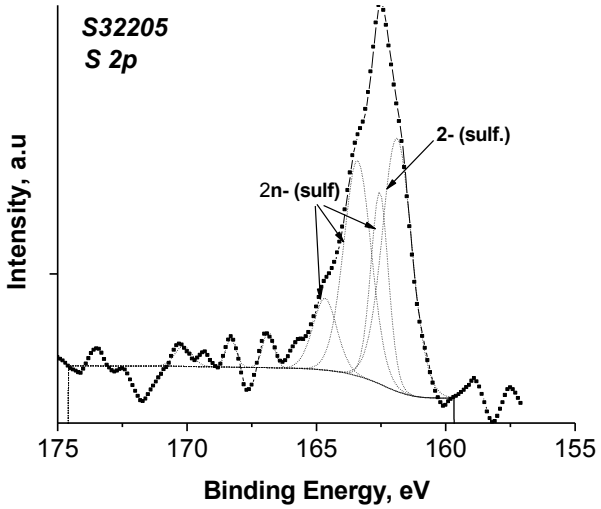


(b)

*Figure 5.29:* ***Peak fitting results for high resolution X-ray photoelectron spectra from surface film formed on standard DSS S32205 formed at corrosion potential in 2.5 M NaOH + 0.70 M $Na_2S$ at 170 $^{O}C$ for S $2p_{3/2}$ . Curve fitting was performed at the half maximum O 1s peak intensity (ca. 1920 nm).***

Thermodynamic predictions (E-pH diagrams) were used to determine the stable species that can form near the corrosion potential in the Fe-Cr-Ni-S-$H_2O$ system at 170 $^{O}$C. The E-pH diagrams for the dominant Fe, Cr, and Ni species are shown in Figure 5.30-5.32 [49]. All molar concentrations are assumed to be $10^{-3}$ M for the cations and 0.70 M for sulfur. Cr did not form metal sulfide compounds in the E-pH region (ca. -1.10 V vs. Ag/AgCl and pH 11.5) in this study based on the thermodynamic predictions. This finding was confirmed by the XPS measurements on the alloys and pure Cr sample. Others [7-8] have detected $Cr_2S_3$ using X-ray diffraction on select DSS (S32101 and S32304) exposed to alkaline-sulfide solution at the corrosion potential. Based on the E-pH diagrams, FeS (ferric/ferrous sulfide) (Figure 5.30) [49] and $Ni_3S_2$ (heazlewoodite) (Figure 5.32) [49] were more likely to form under the conditions in this study.

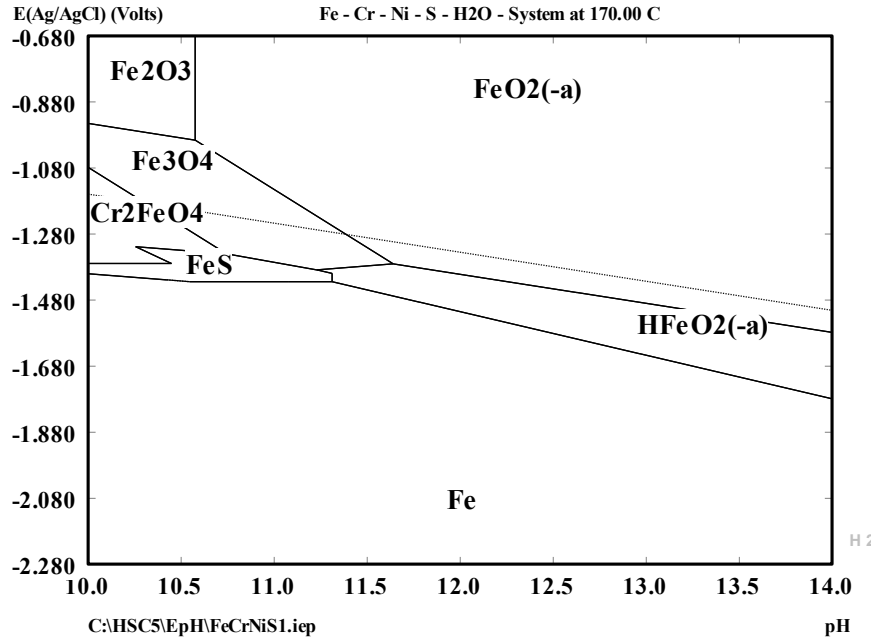


***Figure 5.30:*** ***E-pH diagram for the Fe-Cr-Ni-S $H_20$ system (Fe dominant) at 170 $^{O}$C and 0.77 MPa. Molar concentration of metal cation is 0.001 M and sulfur is 0.70 M [49].***

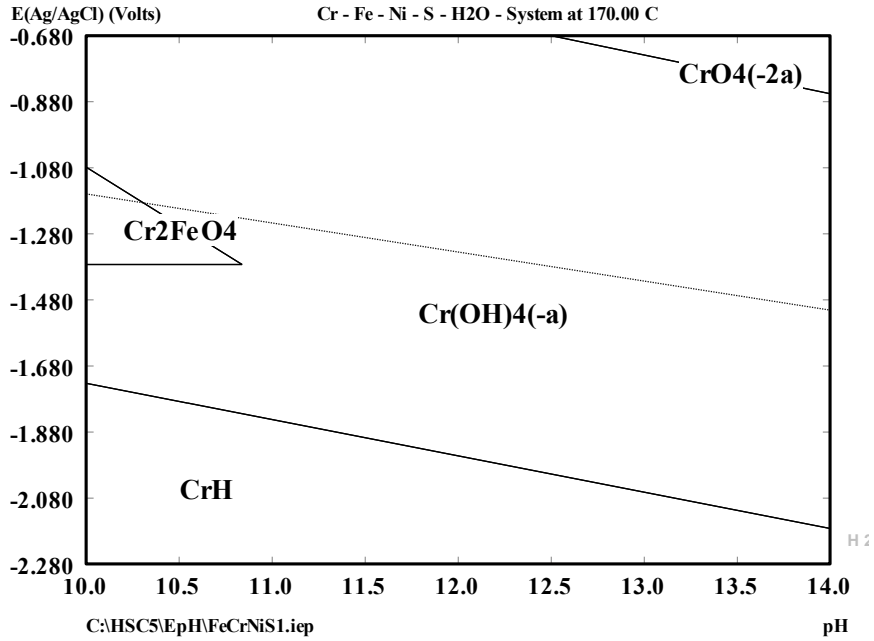


*Figure 5.31:* ***E-pH diagram for the Fe-Cr-Ni-S $H_20$ system (Cr dominant) at 170 $^{O}$C and 0.77 MPa. Molar concentration of metal cation is 0.001 M and sulfur is 0.70 M [49].***

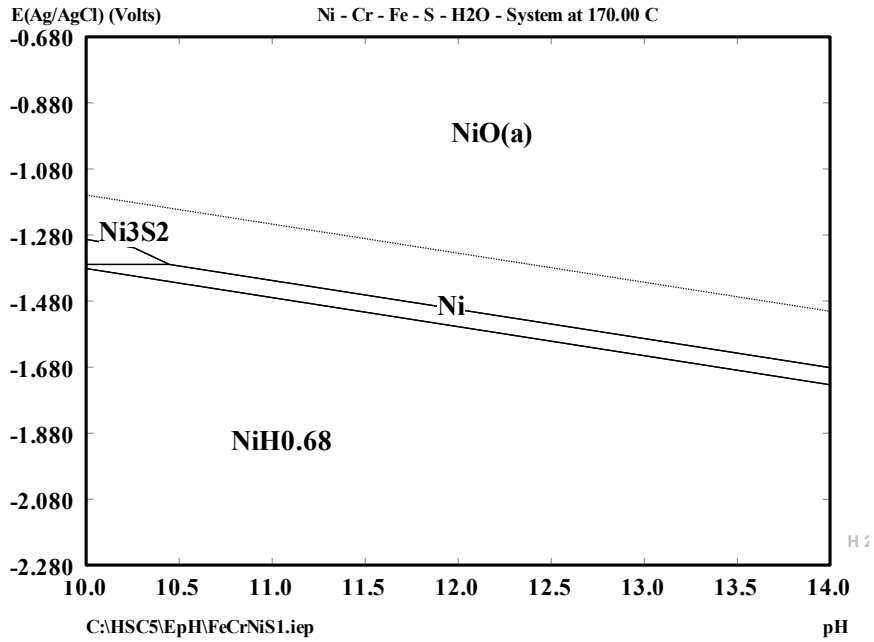


*Figure 5.32:* ***E-pH diagram for the Fe-Cr-Ni-S $H_20$ system (Ni dominant) at 170 $^{O}$C and 0.77 MPa. Molar concentration of metal cation is 0.001 M and sulfur is 0.70 M [49].***

The solubility products and standard free energies of formation for the sulfide compounds that could form under the conditions in this study are compared in Table 5.5. The Fe, Cr, and Ni sulfide compounds in this work were assumed to be stoichiometric. In reality, metal sulfide compounds are rarely stoichiometric due to the numerous oxidation numbers of sulfur [66]. In general, the more negative the free energy of formation ($\Delta G^o$) and lower the solubility product ($K_{sp}$), the greater the likelihood the specie was stable in the film. The sulfide compounds have higher solubility products than the oxides. Limited solubility of the sulfide compounds in the oxide film is one explanation for the observed enrichment of S on the outer surface layers in the EDS (Figure 5.23 – 5.24) and XPS (Figure 5.25) spectra. Redeposition of the sulfide compounds following dissolution could also account for the surface enrichment of S. The film on S44660 was less prone to sulfidation due to the higher Cr content of this alloy, which resulted in the formation of a more stable oxide film.

***Table 5.5: Solubility Products for the Dominant Species the Fe-Cr-Ni ternary System at 170 $^oC$.***

| *Element* | *Specie* | *- log Ksp* | *$\Delta G^o$, kcal $mol^{-1}$* |
|---|---|---|---|
| Fe | | | |
| | FeO | 14.81 | -56.3 |
| | $Fe_3O_4$ | 26.75 | -230.9 |
| | $Fe_2O_3$ | 20.04 | -167.7 |
| | $HFe0_2^-$ | 28.47 | -80.4 |
| | FeS (II) | -15.55 | -24.5 |
| | FeS (III) | -66.66 | -135.2 |
| Cr | | | |
| | $Cr_2FeO_4$ | 0.70 | -312.3 |
| | $CrO_4^{2-}$ | -41.55 | -153.7 |
| | $Cr(OH)_4^-$ | -35.46 | -227.3 |
| | $Cr_2S_3$ (III) | -42.42 | -86.0 |
| Ni | | | |
| | $Ni_3S_2$ (II) | -52.52 | -49.4 |
| | NiO | 6.68 | -47.3 |

FeS and $Ni_3S_2$ were most likely to form under the conditions in this study. There are numerous FeS compounds reported in the literature [56, 61-62]. Mackinawite ($Fe_{1+x}S$) has been reported for carbon steel [39, 48] and pure Fe [46-47] previously. This form of iron sulfide is relatively unstable and difficult to characterize with XPS. Other forms of iron sulfide, i.e., pyrrhotite ($Fe_{1-x}S$), troilite (FeS), pyrite ($FeS_2$), and greigite ($Fe_3S_4$), may also form. The BE value from S32205 was close to those reported for $Fe_{1+x}S$ in XPS studies of SRB, but it cannot be concluded if this form was present in the current study due to the complexity of the surface composition. Moreover, reported BE values for $Ni_2S_3$ (Table 5.4) are close to those for the FeS compounds, thus it cannot be determined whether one specie was prevalent over another. Spectroscopy techniques, i.e., XPS and EDS, have their inherent limitations such as quality of peak fitting and degradation during analysis. Nonetheless, the findings of this work support a corrosion mechanism of DSS based on the adsorption of sulfide compounds, which hinder the formation of a stable passive film.

### 5.3 Effect of Chloride

Preferential corrosion of DSS is a function of the individual behavior of the austenite and ferrite phases in a particular environment. Previous studies showed that the ferrite phase of DSS is more susceptible to localized corrosion in hot chloride-containing environments [67-71]. The understanding of corrosion behavior of austenitic and ferritic stainless steels in hot alkaline chloride environments is generally limited [72-74]. Most efforts to study chloride-induced corrosion of DSS in alkaline environments centered on rebar [35-36] and pre-stressing steels [37] in concrete pore solutions at ambient temperatures. No studies have focused on the role of chloride on the corrosion behavior

of DSS in hot caustic environments. Therefore, the following effort focused on understanding the preferential corrosion behavior of DSS due to chloride in hot caustic solutions with and without sulfide.

### 5.3.1 Role of Chloride in NaOH Environments

Environments prevailing in a typical kraft digester contain varying amounts of sulfide and chloride. These aggressive anions will have a synergistic effect on the corrosion susceptibility of plant equipment depending on their relative concentration in the pulping liquor. Anodic polarization and impedance spectroscopy of austenitic, superferritic, DSS, and their alloying elements was carried out in an alkaline chloride solution at 90 $^{O}$C to evaluate electrochemical behavior. The morphological features and surface composition of DSS S32101 and DSS S32205 were evaluated after exposure to an alkaline chloride solution at 170 $^{O}$C to study selective dissolution.

#### 5.3.1.1 Influence on Electrochemical Behavior

Figure 5.33 shows that the anodic polarization curves for the alloying elements tested in 2.5 M NaOH + 0.17 M NaCl at 90 $^{O}$C showed similar trends to the NaOH solution (Chapter 4). Analogous findings were found for the alloys (Figure 5.34). A negligible effect of chloride on the electrochemical parameters of the alloys and their alloying elements based on Tafel extraction is shown in Table 5.6. Impedance measurements of the alloys and alloying elements in the alkaline chloride solution also showed minor differences due to chloride up to a 24 h exposure. Therefore, there was no effect of chloride on the electrochemical behavior of the alloying elements under the conditions in this study. The 0.17 M concentration was expected to be the upper limit in kraft pulping based on the literature [1-31].

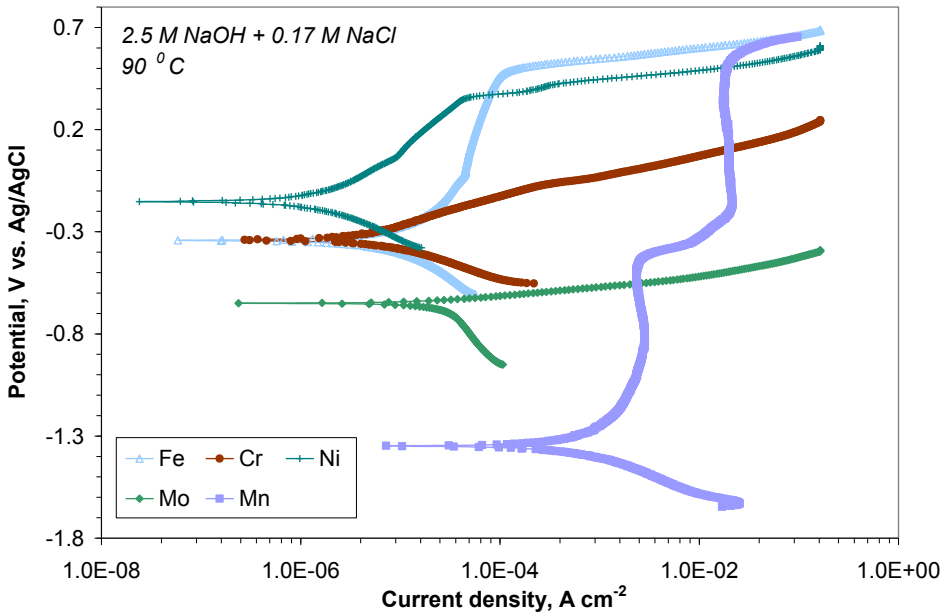


*Figure 5.33:* ***Anodic polarization curves for alloying elements (Fe, Cr, Ni, Mo, and Mn) tested in alkaline chloride (2.5 M NaOH + 0.17 M NaCl) solution at 90 $^{O}$C.***

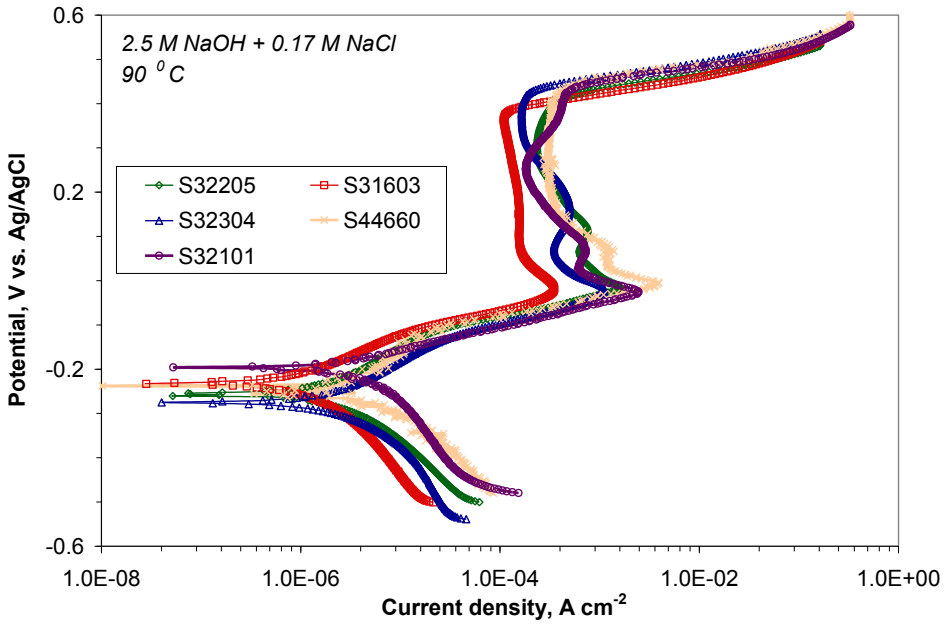


*Figure 5.34:* ***Anodic polarization curves for alloys (S31603, S44660, S32101, S32205, S32304) tested in alkaline chloride (2.5 M NaOH + 0.17 M NaCl) solution at 90 $^{O}$C.***

***Table 5.6:*** ***Anodic polarization parameters of alloys (S31603, S44660, S32101, S32205, S32304) and their alloying elements (Fe, Cr, Ni, Mo, Mn) tested in alkaline (A) and alkaline chloride (AC) solution at 90 $^{O}$C determined from Tafel extraction***

| *Mat.* | *Env.* | *jcorr, μA cm$^{-2}$* | *Ecorr, mV vs.Ag/AgCl* | *Ba, mV dec$^{-1}$* | *Bc, mV dec$^{-1}$* | *Corrosion rate, mm yr$^{-1}$* |
|---|---|---|---|---|---|---|
| S31603 | A | 7 | -250 | 278 | 181 | 0.08 |
| S31603 | AC | 2 | -228 | 150 | 247 | 0.02 |
| S44660 | A | 2 | -188 | 109 | 214 | 0.02 |
| S44660 | AC | 5 | -236 | 188 | 160 | 0.05 |
| S32101 | A | 4 | -195 | 104 | 338 | 0.04 |
| S32101 | AC | 6 | -195 | 87 | 289 | 0.13 |
| S32205 | A | 7 | -236 | 247 | 241 | 0.08 |
| S32205 | AC | 4 | -213 | 130 | 199 | 0.04 |
| S32304 | A | 6 | -241 | 213 | 185 | 0.07 |
| S32304 | AC | 4 | -271 | 184 | 213 | 0.04 |
| Fe | A | 92 | -319 | 100000 | 1090 | 1.07 |
| Fe | AC | 41 | -336 | 1507 | 968 | 0.57 |
| Cr | A | 9 | -326 | 228 | 179 | 0.1 |
| Cr | AC | 7 | -330 | 203 | 165 | 0.8 |
| Ni | A | 2 | -189 | 371 | 310 | 0.02 |
| Ni | AC | 2 | -187 | 331 | 299 | 0.03 |
| Mo | A | 41 | -648 | 47 | 356 | 0.48 |
| Mo | AC | 29 | -648 | 57 | 646 | 0.33 |
| Mn | A | 2600 | -1370 | 100000 | 422 | 30.28 |
| Mn | AC | 925 | -1350 | 1621 | 296 | 34.8 |

5.3.1.3 Film Morphology and Composition in Chloride-Containing NaOH Solution

DSS S32205 and S32101 were exposed to 2.5 M NaOH + 0.17 M NaCl at 170 $^{O}$C and examined with optical microscopy to show the localized selectivity of the corrosion behavior due to Figure 5.35 shows that preferential attack of the austenite phase (light etching phase) was more apparent in lean grade DSS S32101 as compared to standard grade DSS S32205. Pitting was not found on the surfaces of either sample. The difference in selectivity is due to the composition differences among these grades of DSS. Earlier work [71] showed that selective corrosion of the austenite or ferrite phase of DSS in $CaCl_2$ solution at 100 $^{O}$C with pH 6.5 depended on alloy composition.

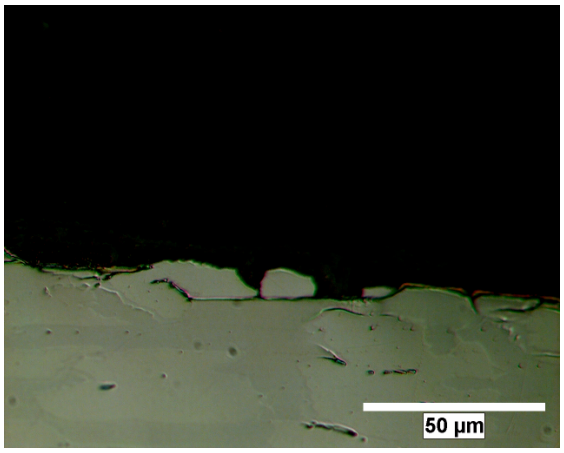


(a)

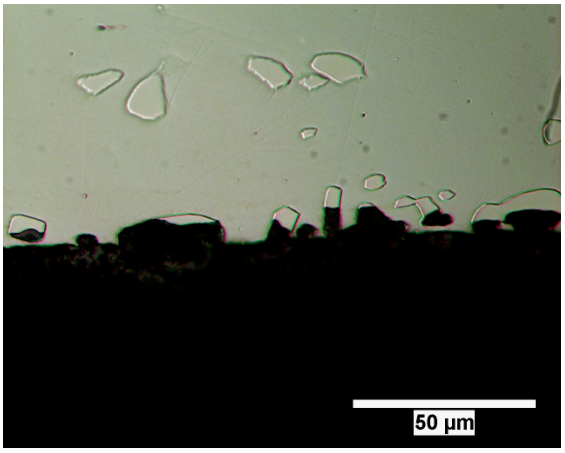


(b)

***Figure 5.35:*** ***Optical micrographs showing (a) relatively uniform corrosion of S32205 and (b) preferential corrosion of austenitic phase in S32101 tested in 2.5 M NaOH + 0.17 M NaCl at 170 $^{O}$C.***

Cross-sectional SEM micrographs of the surface film that formed on DSS S32205 are shown in Figs. 5.36. The presence of chloride did not appreciably alter the film morphology with respect to the NaOH solution (Chapter 4). The corrosion product on the surfaces was ca. 2-3 µm. Representative spectra from EDS of the high magnification image showed that the outer surface film was enriched in Fe. The EDS spectra were normalized and compared based on the ratio of each cation to total cation percentage for

qualitative comparisons. Outer layer was (89 wt % Fe, 8 wt % Cr, 3 wt % Ni, and < 1 wt % Mo) and inner layer was approximately (43 wt % Fe, 32 wt % Cr, 18 wt % Ni, and 7 wt % Mo) based on the average of 15 measurements. Depletion of Fe with chloride addition caused Ni and Mo enrichment of the inner layer with respect to the NaOH solution. The Mo-$L_{\alpha}$ peak with emission energy of 2.3 keV overlaps with the S- $K_{\alpha}$ peak, accounting for the erroneous S in the spectra.

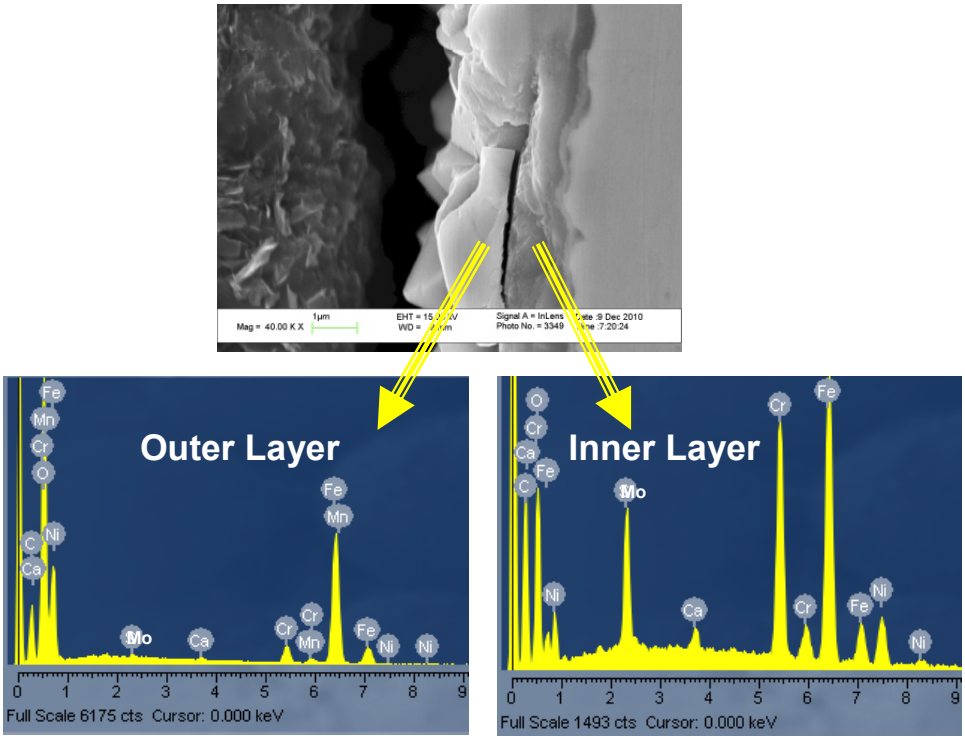


***Figure 5.36:*** ***Cross-sectional SEM micrograph of S32205 exposed to 2.5M NaOH + 0.17 M NaCl at 170 $^{O}$C. Arrows correspond to EDS spectra of Fe-rich outer layer and EDS spectra of Cr and Ni enriched inner layer.***

Cross-sectional SEM micrographs of the surface film that formed on DSS S32101 are shown in Figs. 5.37. The film morphology became more defective and less adherent with respect to the film that formed in the NaOH solution (Chapter 4). The corrosion product on the surfaces (when present) was ca. 1-2 μm. Representative spectra from EDS

of the high magnification image showed that the outer surface film was enriched in Fe. The EDS spectra were normalized and compared based on the ratio of each cation to total cation percentage for qualitative comparisons. Outer layer was (75 wt % Fe, 23 wt % Cr, 4 wt % Mn, and 2 wt % Ni,) and inner layer was approximately (67 wt % Fe, 27 wt % Cr, 4 wt % Mn, and 2 wt % Ni) based on the average of 15 measurements. Chloride addition caused Cr enrichment of the surface layer with respect to the NaOH solution.

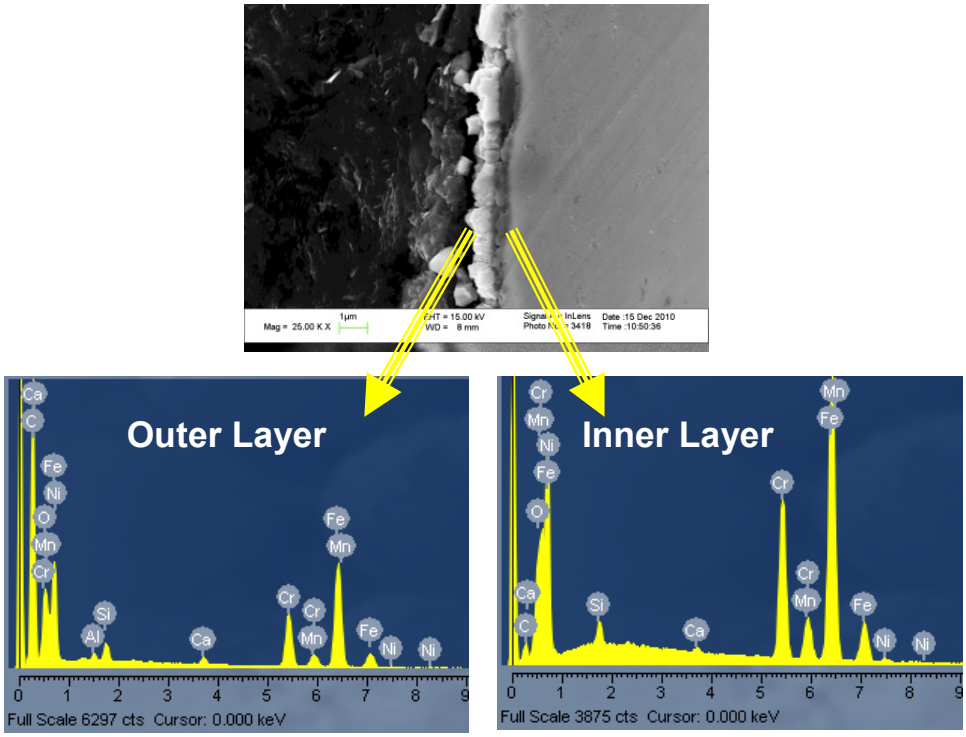


***Figure 5.37:*** ***(a) & (b) Cross-sectional SEM micrograph of S32101 exposed to 2.5M NaOH + 0.17 M NaCl at 170 $^{O}$C. Arrows correspond to (c) EDS spectra of Fe-rich outer layer and (d) EDS spectra of Cr enriched inner layer.***

Figure 5.38 shows a comparison of the major constituents of the surface film between XPS sputter depth profiles acquired from S32205 and S32101. The surface films were generally enriched in Fe, particularly in the outer layers. Cr enrichment near the oxide/metal interface was observed in both materials, but the enrichment relative to the

base composition was greater in S32101. Mo and Mn were dissolved from the outer layers, which was consistent with results from the NaOH solution. Ni enrichment of the surface layer on S32205 was not observed in the XPS spectra as it was with EDS. The disparity was likely caused by the limited lateral and depth resolution of EDS. Chloride was not detected using XPS or EDS, indicating that these ions do not penetrate the surface films that dissolve in a heterogeneous manner.

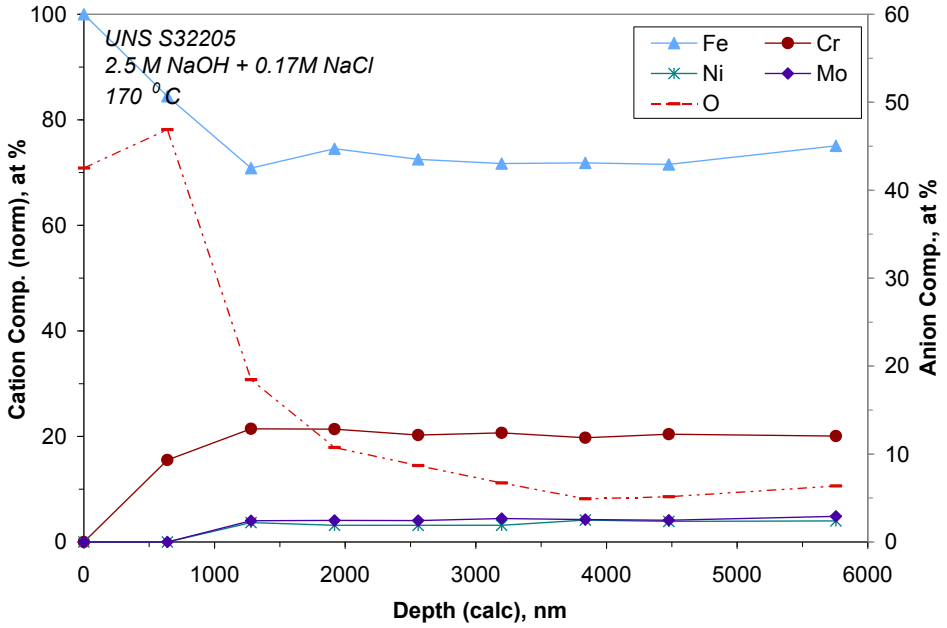


(a)

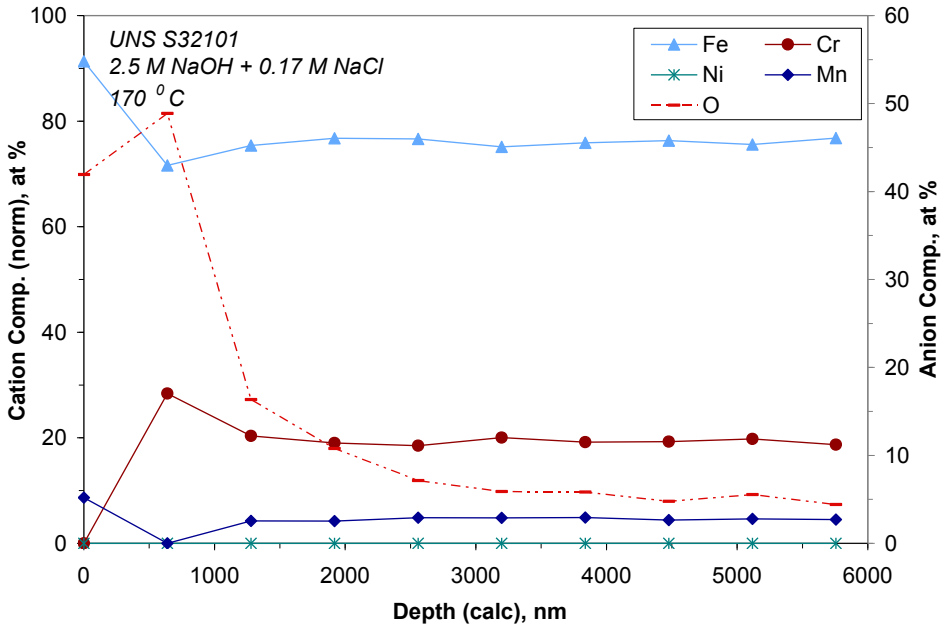


(b)

***Figure 5.38:*** ***X-ray photoelectron spectroscopy depth profile of surface film on (a) standard DSS S32205 and (b) lean DSS S32101 formed at corrosion potential in 2.5 M NaOH + 0.17 M NaCl at 170 °C.***

Addition of 0.17 M NaCl to the 2.5 M NaOH solution had a minor effect on the film compositions of DSS S32205 and S32101 at 170 $^{O}$C under the conditions in this study. However, surface films that formed in the chloride solution were more defective based on the cross-section micrographs (Figure 5.36 and Fig 5.37). Similar findings have been shown for austenitic stainless steel tested in alkaline-buffered solution (pH 11.5) at room temperature, whereby lower pH and higher chloride concentration caused the surface films to become unstable [75]. An early study of 18-8 austenitic stainless steel in hot alkaline solution showed that high concentrations of chloride (above 1 M) were required to have any effect on the localized corrosion behavior [72]. On the basis of the electrochemical and film composition results of the current study, 0.17 M NaCl had a minimal effect on the corrosion behavior of S32101 and S322205 in hot alkaline environments.

### 5.3.2 Role of Chloride in NaOH + $Na_2S$ Environment

Alkaline pulping liquors can vary in composition, thus it was of interest to understand if there was a synergistic effect between chloride and sulfide ions on the corrosion behavior of DSS in alkaline environments. Recent field experience showed that a DSS S32205 hot black liquor tank operating at 110 $^{o}$C with 1.0 wt % NaCl (0.17 M) failed due to selective corrosion of austenite and SCC [76], thus a NaCl molar concentration of 0.17 M was chosen in the current study. Corrosion rates of austenitic, superferritic, and DSS in simulated pulping liquors containing 2.5 – 3.75 M NaOH, 0.64 – 0.96 M $Na_2S$, and 0.17 M NaCl were determined from weight loss at 170 $^{O}$C. The morphology and composition of the surface films that formed on select samples in the solution with the highest ratio of chloride to sodium hydroxide (2.5 M NaOH + 0.70 M

$Na_2S$) were evaluated. The physicoelectrical properties of the films in this environment were also studied to understand chloride effects on film formation in alkaline-sulfide solution.

5.3.2.1 Influence on Corrosion Rates and Morphology

Corrosion rates of austenitic (N08904, S31703, S31603, S30403), superferritic (S44660, S44627), and DSS (S32705, S32205, S32101, S32003) grades of stainless steel are shown in Figure 5.33 for several alkaline solutions (2.5 – 3.75 M) at 170 $^{O}$C. The results indicate that there is an inhibiting effect of chloride with increased alkalinity. Indeed, corrosion rates in the 2.5 M NaOH + 0.70 M $Na_2S$ solution were generally greater in the presence of chloride, while those for the 3.75 M NaOH + 0.64 M $Na_2S$ were generally lower. The effect of chloride was most apparent for the grades of stainless steel with higher Cr contents in the least alkaline solution (2.5 M NaOH + 0.70 M $Na_2S$). These steels, which generally had lower corrosion rates in the absence of chloride, became more susceptible.

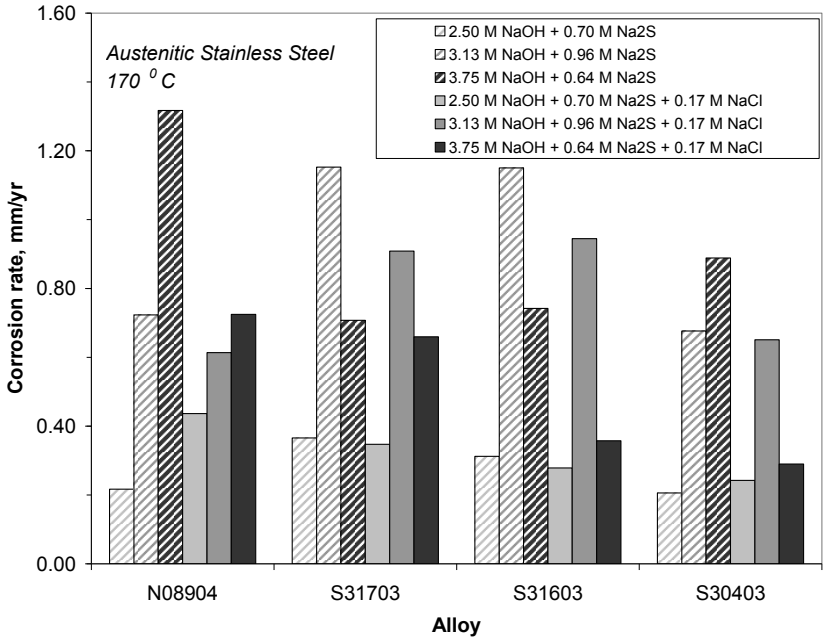


(a)

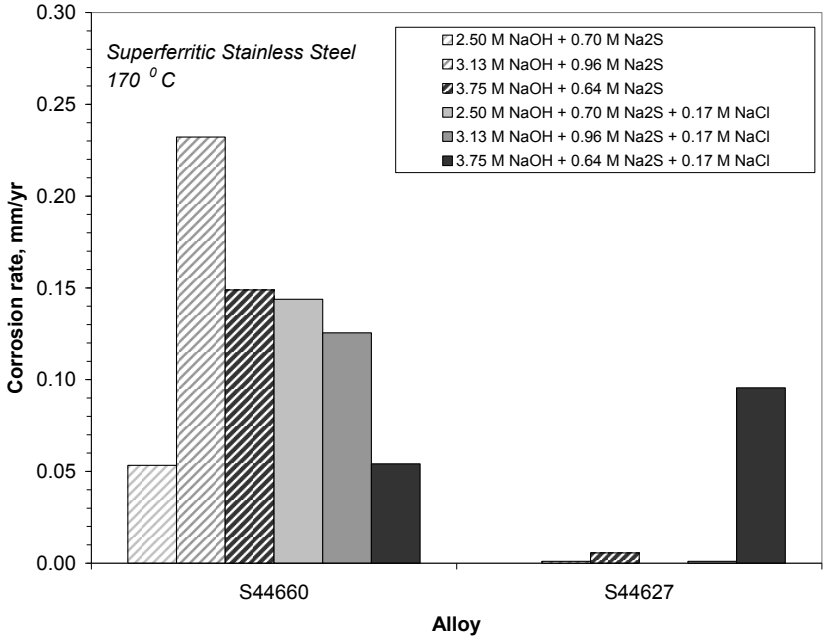


(b)

***Figure 5.39:*** ***Corrosion rates of (a) austenitic (N08904, S31703, S31603) and (b) superferritic grades (S44660, S44627) of stainless steel tested in alkaline-sulfide solutions at 170 $^O$C. Alloys have been arranged by left to right by decreasing Ni content within each type of stainless steel.***

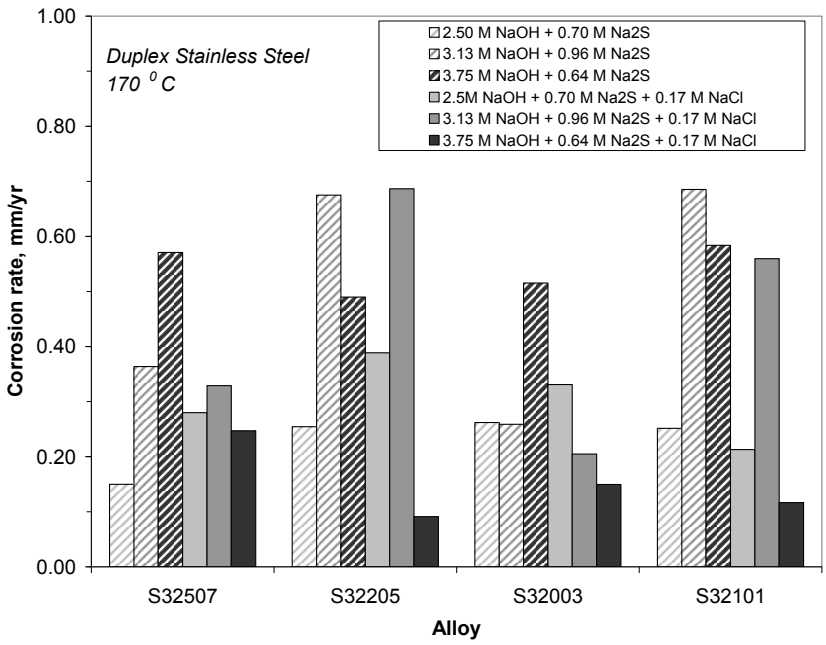


(c)

***Figure 5.39 (cont'd):*** ***Corrosion rates of (c) DSS (S32705, S32205, S32101, S32003) tested in alkaline-sulfide solutions at 170 $^{O}$C. Alloys have been arranged by left to right by decreasing Ni content within each type of stainless steel.***

Solutions used in this study were compared on the basis of their chloride ratio. The chloride ratio was a relevant parameter for determining the corrosivity of chloride in the alkaline-sulfide solutions.

$$Chloride\ Ratio = \frac{[NaCl]}{[NaOH]} \qquad [5.6]$$

where $[Na_2S]$, [NaCl], and [NaOH] are the salt concentrations in g $l^{-1}$. The corrosion rates with respect to the chloride-free solutions typically increased with this ratio. An analogous ratio has been developed for concrete pore solutions at lower temperatures [35-36]. Work in these environments has shown that the normally protective oxide that forms

in alkaline conditions may break down in the presence of chloride, leading to localized dissolution at active sites. Other studies on the corrosion of stainless steel in hot chloride solutions [67-74] have shown that the stability of the passive film is a strong function of pH, chloride content, and temperature. An electrochemical study of austenitic 18-8 stainless steel in hot alkaline chloride environments showed a reduction in the zero-current potentials and an increase in the current densities with lower NaOH and higher NaCl concentrations [72].

Based on the results of Figure 5.39, it can be stated that chloride does have an effect on the corrosion behaviour of DSS in alkaline-sulfide environments, particularly as the concentration of NaCl increases with respect to NaOH, i.e., the chloride ratio increases. The corrosion rates in alkaline-sulfide solution are therefore a function of percent sulfidity and chloride ratio. The following relationship, caustic chloride ratio (CCR), corresponds to the trends observed in the corrosion rates of the environments that were tested in this study with reasonable agreement.

$$Caustic\ Chloride\ Ratio = \frac{[Na_2S] + [NaCl]}{[NaOH] + [Na_2S] + [NaCl]} \qquad [5.7]$$

Preferential corrosion of the austenite phase of S32205 in the cross-sectional SEM micrograph of Figure 5.40 was less apparent after exposure to 2.5 M NaOH + 0.70 M $Na_2S$ + 0.17 M NaCl at 170 $^{o}$ C as compared to the chloride-free solution. Austenite/ferrite phase interfaces were more susceptible in the presence of chloride. The film morphology became more defective and less adherent with respect to the film that formed in the chloride-free solution. Chloride has been shown extensively [53] to be an

aggressive anion that hinders stable film formation. Representative spectra from EDS of the high magnification image showed that the outer surface film was enriched in Ni and S. Indeed the surface film had ~ 10 wt % S with more enrichment near the surface. The EDS spectra were normalized and compared based on the ratio of each cation to total cation percentage for qualitative comparisons. Outer layer was (23 wt % Fe, 43 wt % Cr, and 34 wt % Ni,) and inner layer was approximately (27 wt % Fe, 48 wt % Cr, and 25 wt % Ni) based on the average of 15 measurements. Mo and Mn were mostly dissolved. Chloride addition enhanced sulfidation of both phases in S32205, although the sulfidation of austenite occurred more readily than ferrite as evident by the islands that are selectively corroded in Figure 5.40.

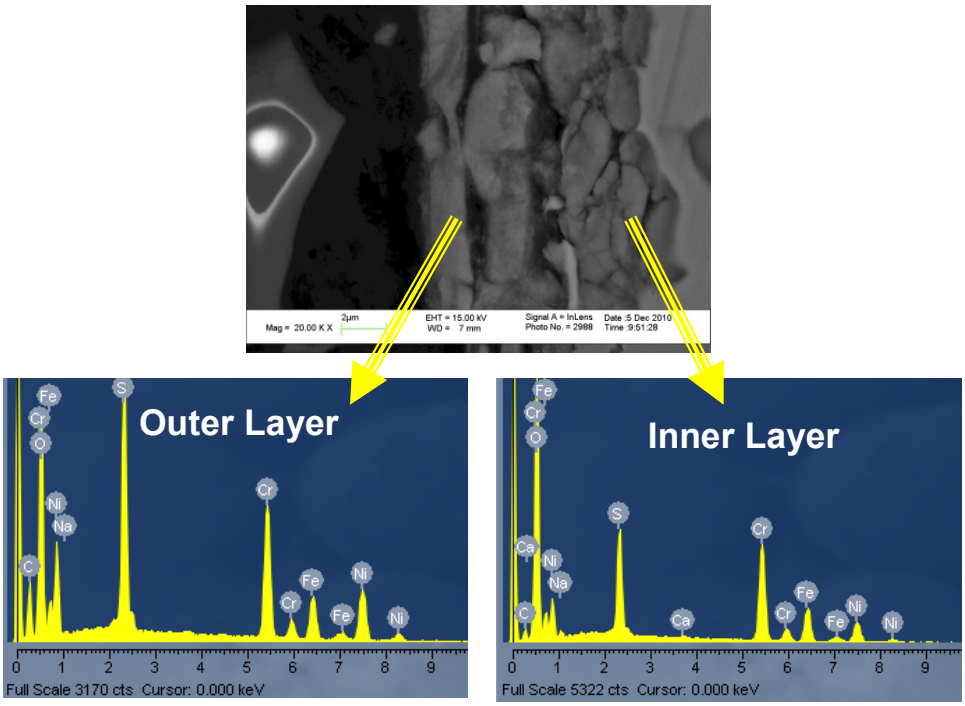


***Figure 5.40:*** ***Cross-sectional SEM micrograph of S32205 exposed to 2.5M NaOH + 0.70 M $Na_2S$ + 0.17 M NaCl at 170 $^{O}$C. Arrows correspond to EDS spectra of Ni and S-rich outer layer and EDS spectra of Cr and Ni enriched inner layer.***

Preferential corrosion of the austenite phase of S32101 was observed in the cross-sectional SEM micrograph of Figure 5.41 after exposure to 2.5 M NaOH + 0.70 M $Na_2S$ + 0.17 M NaCl at 170 $^{o}$ C. Representative spectra from EDS of the high magnification image showed that the outer surface film was enriched in Fe and S. Indeed the surface film had ~ 5 wt % S with more enrichment near the surface. The EDS spectra were normalized and compared based on the ratio of each cation to total cation percentage for qualitative comparisons. Outer layer was (72 wt % Fe, 14 wt % Cr, 11 wt % Ni, and 3 wt % Mn) and inner layer was approximately (43 wt % Fe, 43 wt % Cr, 12 wt % Ni, and 1 wt % Mn) based on the average of 15 measurements. Mn and Fe were mostly dissolved from the inner layer. Chloride addition enhanced the sulfidation of the austenite phase with respect to the ferrite phase.

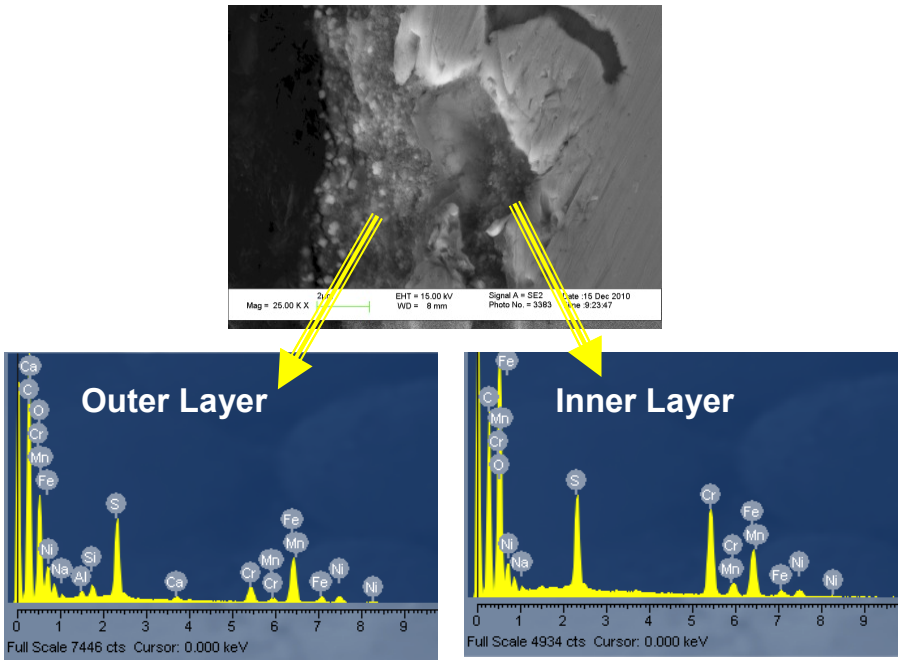


***Figure 5.41:*** ***(a) & (b) Cross-sectional SEM micrograph of S32101 exposed to 2.5M NaOH + 0.70 M $Na_2S$ + 0.17 M NaCl at 170 $^{O}$C. Arrows correspond to (c) EDS spectra of Fe and S -rich outer layer and (d) EDS spectra of Cr and Ni enriched inner layer.***

5.3.2.2 Surface Film Properties

*5.3.2.2.1 Role of Physicoelectrical Behavior of Surface Films*

The impedance spectra for S31603, S44660, S32101, and S32205 are shown in Figure 5.42. Results were generally similar to those in the alkaline-sulfide solution (Figure 5.18), although the mid-frequency response of the surface film of S32205 was not present. The behavior in chloride-containing, alkaline-sulfide solution is determined by a two-step process: a charge transfer process associated with the metal/film interface and an adsorption process. A simplified model using two CPE elements (Figure 5.20a) was fit to S32205 (Figure 5.43) and S32101 (Figure 5.44) with good agreement.

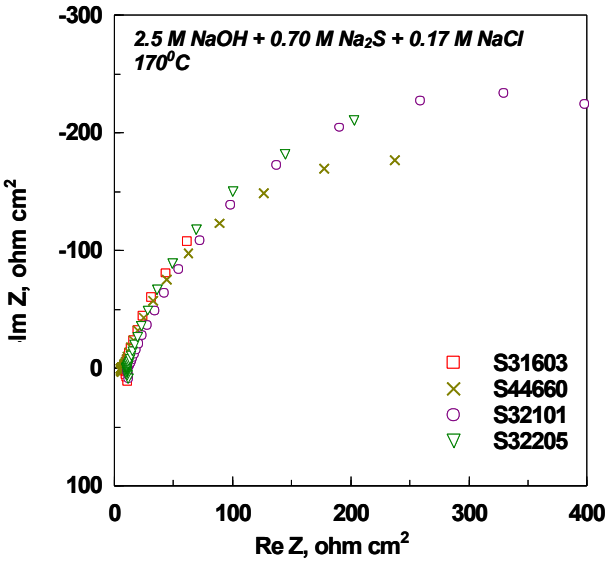


(a)

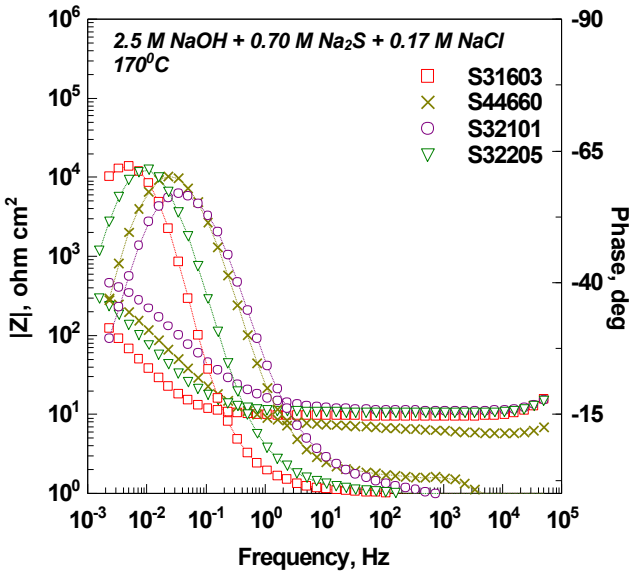


(b)

*Figure 5.42:* ***Comparison of electrochemical impedance spectra at the corrosion potential for S31603, S44660, S32101, and S32205 tested in 2.5 M NaOH + 0.70 $Na_2S$ + 0.17 M NaCl at 170 $^{O}$C.***

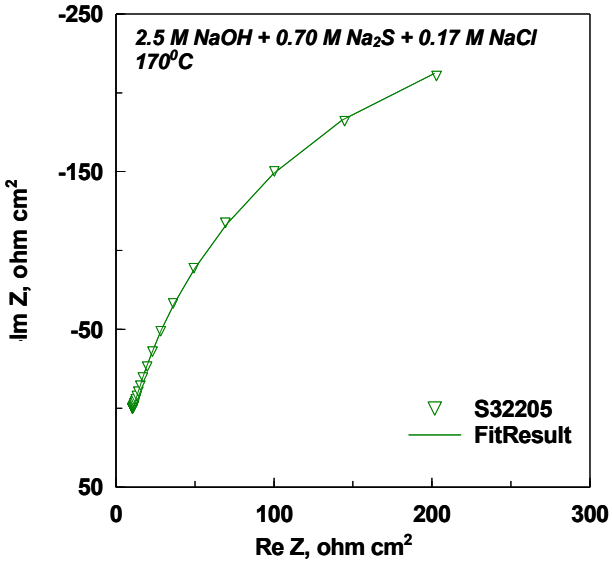


(a)

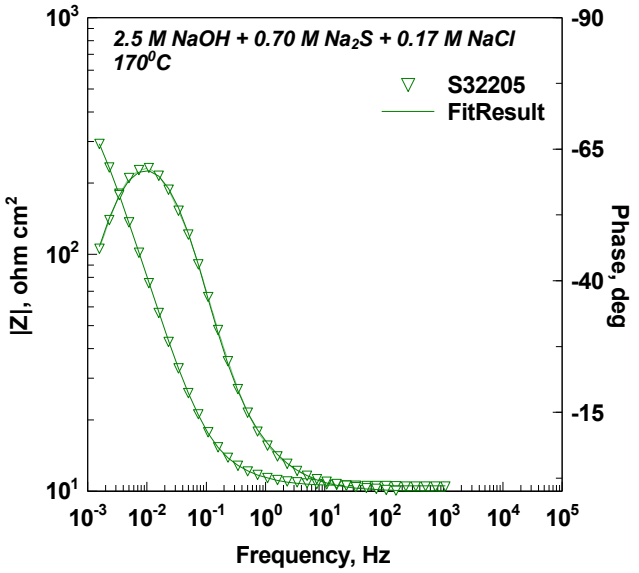


(b)

*Figure 5.43:* ***Electrochemical impedance spectra at the corrosion potential for S32205 tested in 2.5 M NaOH + 0.70 $Na_2S$ + 0.17 M NaCl at 170 $^{O}$C. Points – experimental points, lines – best fit results obtained from simulation. The best fitting parameters are $R_s$ = 10.5 Ω cm$^2$, $R_1$ = 8.24 Ω cm$^2$, $CPE_1$ =8.99 mF cm$^{-2}$, $\alpha_1$ = 0.850, $R_2$ = 594 Ω cm$^2$, $CPE_2$ =40.3 mF cm$^{-2}$, $\alpha_2$ = 0.816. ($\chi^2$ = 6.98e-4)***

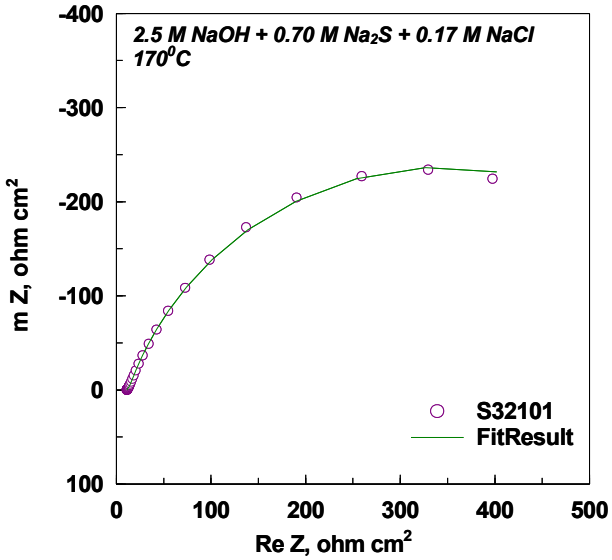


(a)

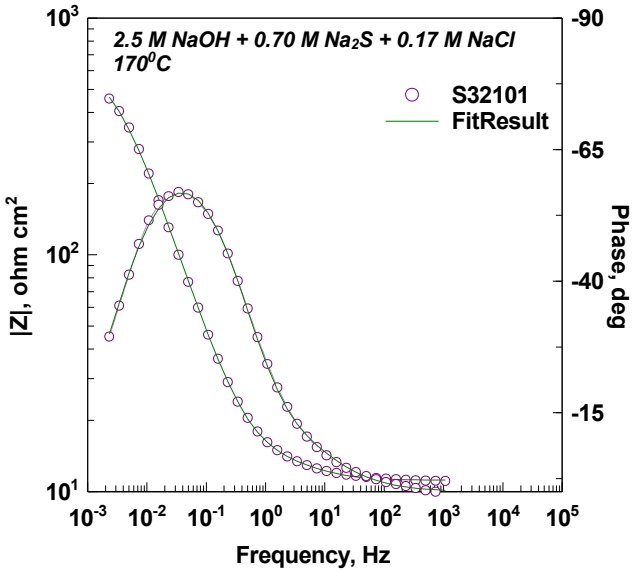


(b)

*Figure 5.44:* ***Electrochemical impedance spectra at the corrosion potential for S32101 tested in 2.5 M NaOH + 0.70 $Na_2S$ + 0.17 M NaCl at 170 $^{o}$C. Points – experimental points, lines – best fit results obtained from simulation. The best fitting parameters are: $R_s$ = 11.2 Ω cm$^2$, $R_1$ = 5.45 Ω cm$^2$, $CPE_1$ =15.4 mF cm$^{-2}$, $\alpha_1$ = 0.802, $R_2$ = 660 Ω cm$^2$, $CPE_2$ =18.3 mF cm$^{-2}$, $\alpha_2$ = 0.778. ($\chi^2$ = 3.57e-4)***

There are some differences in the fit parameters from the chloride-free alkaline-sulfide solution. The resistance associated with the charge transfer process ($R_1$) decreased in the presence of chloride, indicating that the surface film was more conductive. Conversely, the charge transfer resistance values ($R_2$) increased with chloride, which indicates there was an increased resistance associated with the adsorption process; however, the resistance values associated with adsorption had a range of values (200 – 600 Ω $cm^2$) due to the heterogeneous surface morphology. More significant results were found with respect to the pseudo-capacitance behavior of the films. The phase angle curves were displaced towards lower frequencies with chloride indicating that the response of the film was disappearing and the impedance was dominated by interfacial processes.

Linear polarization resistance (LPR) was used to validate the findings from the EIS measurements. The impedance moduli at the lowest frequency corresponded reasonably well to the results from LPR of the alloys (ca. 200 - 500 Ω $cm^2$). There was no clear trend to indicate that the films were less protective in the presence of sulfide and chloride. Indeed, the only alloy that had a lower LPR value in the chloride solution was superferritic S44660. The lower resistance of this alloy supports the EIS results, which showed S44660 had the highest impedance modulus at low frequencies (Figure 5.18) in the absence of chloride, but behaved like to other alloys in the presence of chloride. Based on the corrosion rates, morphologies, and film resistances it can be stated that chlorides have a greater effect on the ferrite phase of DSS as compared to the austenite phase.

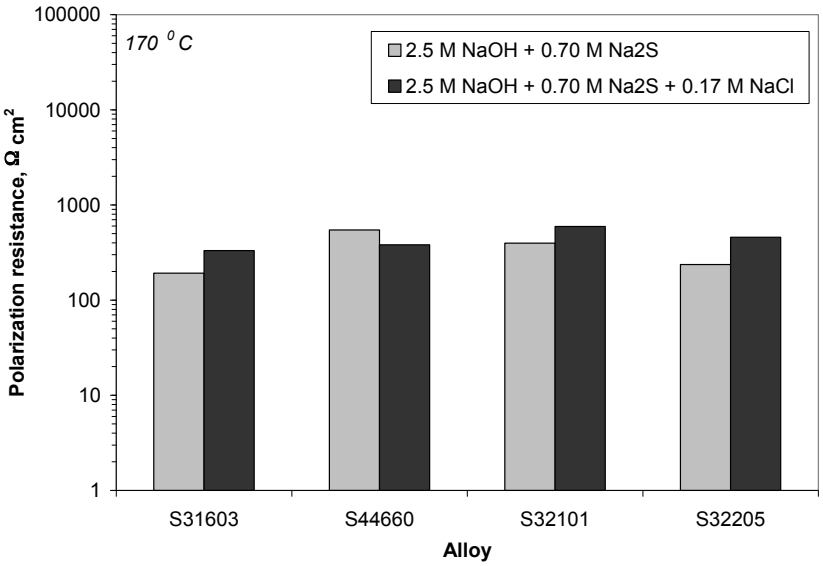


***Figure 5.45:*** ***Linear polarization resistance values for austenitic S31603, superferritic S44660, lean DSS S32101 and standard DSS S32205 tested in 2.5 M NaOH + 0.70 M $Na_2S$ with and without 0.17 M NaCl at 170 $^O$C.***

*5.3.2.2.2 Effect of Surface Film Composition*

Figure 5.46 shows a comparison of the major constituents of the surface film between XPS sputter depth profiles acquired from S32205 and S32101. The surface films were generally enriched in Cr, particularly in the outer layers. Some Ni enrichment of the surface film was found in S32101, but not in the S32205 sample. Cr enrichment near the oxide/metal interface was also observed in both materials, but the enrichment relative to the base composition was greater in S32205. Mo was mostly dissolved from the outer layers of S32205, which was consistent with results from alkaline-sulfide solution. Ni enrichment of the surface layer on S32205 was not observed in the XPS spectra as it was with EDS. Chloride was not detected using XPS or EDS indicating chloride compounds were soluble in the test solution.

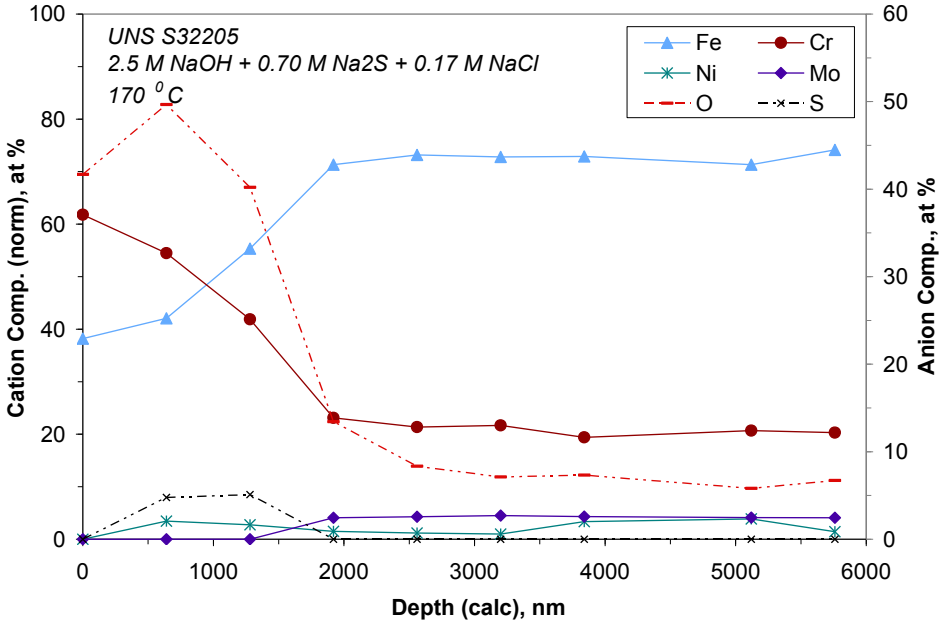


(a)

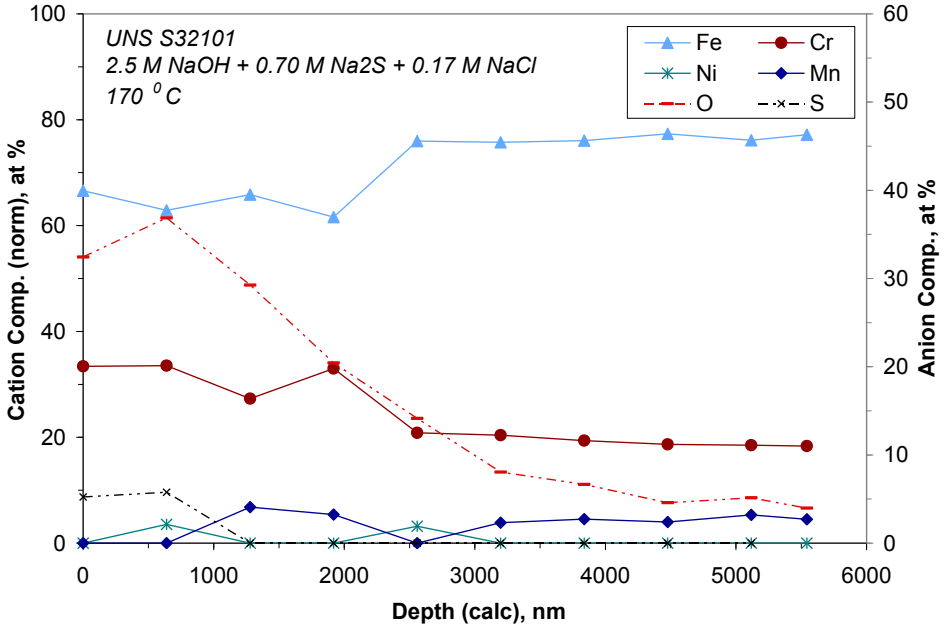


(b)

***Figure 5.46:*** ***X-ray photoelectron spectroscopy depth profile of surface film on (a) standard DSS S32205 and (b) lean DSS S32101 formed at corrosion potential in 2.5 M NaOH + 0.70 M $Na_2S$ + 0.17 M NaCl at 170 $^{O}$C.***

High resolution XPS spectra of Fe 2p, Ni 2p, and Cr 2p and O 1s from the top surface layers formed on S32205 are shown in Figure 5.47. The effect of chloride can be observed by comparing with the chloride-free, sulfide-containing caustic solution (Figure 5.26). There is a broad shoulder associated with each of the spectra, indicating that there was an appreciable amount of oxidation in the presence of sulfide and chloride. Moreover, considerable hydration of the surface Cr compounds took place based on the broad shoulder for the Cr spectra. The Ni signal was lower in S32205 in the presence of chloride as compared to the alkaline-sulfide solution without chloride, which may be due to the absence of an outer sulfide layer that was present in the chloride-free solution (Figure 5.6). The BE of the O 1s signal on the outer levels was consistent with a hydroxide layer. Curve fitting of the high resolution spectra was performed and the relative ratios of oxidized species were similar to the alkaline-sulfide solution indicating that the film composition was not appreciably altered by chloride.

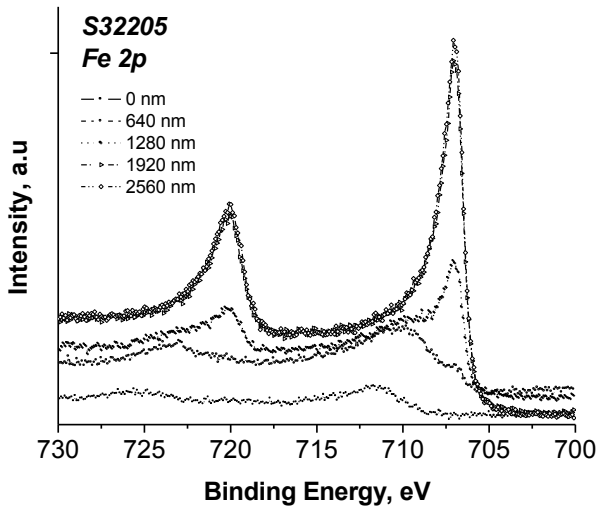


(a)

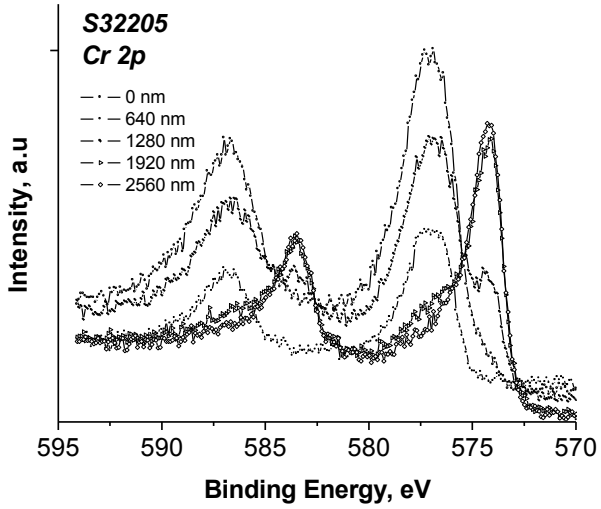


(b)

*Figure 5.47:* ***High resolution X-ray photoelectron spectra from surface film formed on standard DSS S32205 formed at corrosion potential in 2.5 M NaOH + 0.70 M Na2S at 170 $^{O}$C for (a) Fe 2p and (b) Cr 2p. Filled symbols represent the scan corresponding to the half maximum O 1s peak intensity (ca. 1920 nm).***

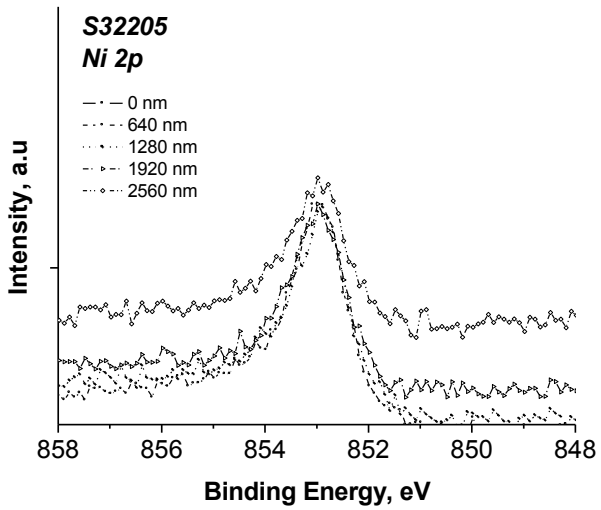


(c)

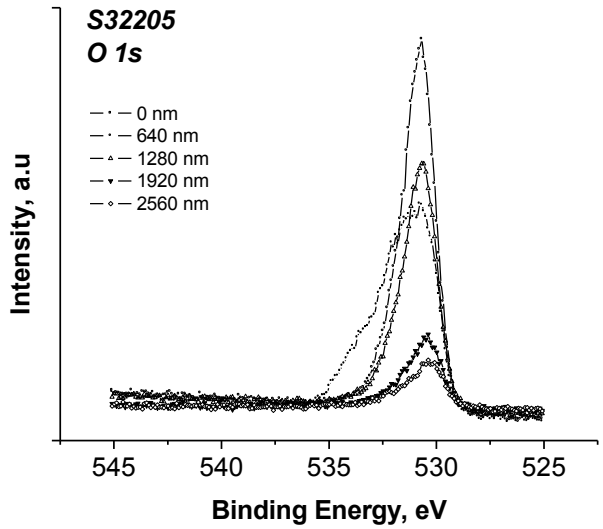


(d)

***Figure 5.47(cont'd):*** ***High resolution X-ray photoelectron spectra from surface film formed on standard DSS S32205 formed at corrosion potential in 2.5 M NaOH + 0.70 M Na2S at 170 $^{O}$C for (c) Ni 2p and (d) O 1s. Filled symbols represent the scan corresponding to the half maximum O 1s peak intensity (ca. 1920 nm).***

High resolution scans of the S 2p region for S32205 and S32101 (Figure 5.48) show that adsorption of sulfide species occurred in the chloride-containing solution. Curve fitting to the spectra showed that monosulfide ($S^{2-}$), disulfide ($S_2^{2-}$), and polysulfide compounds were present. The relative amount of monosulfide increased closer to the film/metal interface. The relative amount of sulfide based on the integrated peak areas was greater in S32205, which was also shown in the depth profiles of Figure 5.46.

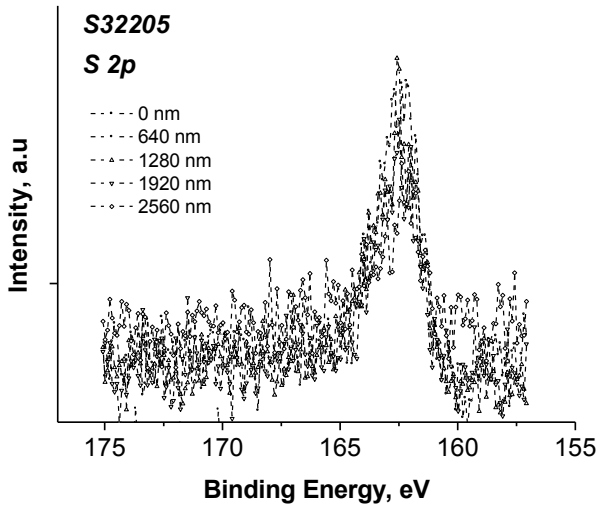


(a)

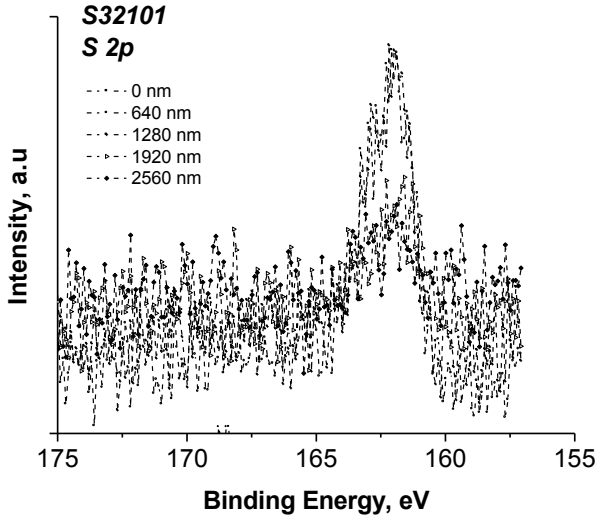


(b)

*Figure 5.48:* ***High resolution X-ray photoelectron spectra of S $2p_{3/2}$ from surface film formed at corrosion potential in 2.5 M NaOH + 0.70 M $Na_2S$ + 0.17 M NaCl at 170 $^{O}$C for (a) S32205 and (b) S32101.***

The S32205 and S32101 samples exposed to sulfide-containing caustic solutions at the corrosion potential in the presence of chloride showed convincing evidence for the adsorption of sulfide species in the oxide film. Analogous to the chloride-free solution, sulfide adsorption favored the formation of a defective film. Films were also defective because sulfide reacted with the steel to form non-protective metal sulfide compounds. The surface films that formed on DSS in sulfide-containing caustic solution in the presence of chloride were composed largely of a mixed oxide-hydroxide of Fe and Cr. On the basis of film composition, there were no appreciable differences with respect to the relative ratio of oxidized species in the presence of chloride indicating that film formation mechanism was similar with or without chloride. The lack of Ni enrichment of the outer surface layers in the chloride solution (Figure 5.46) was likely caused by the defective nature of the film (Figure 5.40) leading to more sulfide compound dissolution. Increased sulfidity was shown in earlier sections to enhance the preferential corrosion of the austenite phase. Chloride addition reduced the extent of preferential corrosion of austenite in S32205 by favoring the sulfidation of ferrite. Conversely, there was an increase in the extent of austenite sulfidation in S32101. The difference in behavior was due to the compositional differences of Ni and Mn in these alloys.

## 5.4 Conclusions

Further understanding of the role of sulfide and chloride on the corrosivity of hot caustic solutions was acquired through the use of corrosion rate (weight loss), electrochemical measurements (anodic polarization, LPR, and EIS), and film characterization (EDS and XPS) of select grades of stainless steel. Austenitic and superferritic grades were studied to understand the behavior of the individual phases of

DSS. The relative ratio of chloride and sulfide was also varied with respect to the hydroxide concentration to understand combined effects of reactive constituents. Based on the findings of this work, the following main conclusions were made:

- Corrosion rates of stainless steel in sulfide-containing caustic solution increased as function of effective alkali and percent sulfidity. Detrimental effect of sulfide was clear by the increased corrosion rates with respect to the sulfide-free, alkaline solution.
- Superferritic grades had lower corrosion rates than austenitic or DSS grades, particularly in the solutions with higher effective alkali contents. Austenitic grades generally had higher corrosion rates than the DSS grades.
- Increased sulfidity enhanced preferential corrosion of the austenite phase of DSS. Preferential corrosion was more apparent in S32205 than S32101 in 35 % sulfidity, but no clear differences were found in 25 % sulfidity.
- Electrochemical behavior of stainless steel in alkaline-sulfide solutions was a strong function of sulfide oxidation/reduction based on analogous behavior of Pt tested in the same environments.
    - Corrosion potential corresponded to oxidation/reduction of sulfide to polysulfide based on thermodynamic predictions.
    - Oxidation and reduction current densities increased significantly at 170 $^{o}$C as compared to 90 $^{o}$C.
    - Anodic polarization behavior of Ni and Fe were most influenced by sulfide addition. FeS and $Ni_3S_2$ were the most likely metal sulfide

compounds to form near the corrosion potential at 170 $^{o}$C based on thermodynamic predictions.

- Impedance spectroscopy in conjunction with film composition showed that sulfides enhanced corrosion at the metal/film interface through a two-step charge transfer process that involved adsorption and active dissolution.
    - Film resistances were nearly an order of magnitude higher in the NaOH solution as compared to the alkaline-sulfide solution. Similar trends were found for Pt indicating that the behavior was also a function of sulfide oxidation/reduction.
    - Mo was least affected by the addition of sulfide and had an extra time constant with respect to the NaOH solution.
    - An extra time constant associated with a strongly adhered surface film composed of sulfur species was found on S32205 and S44660. This surface film was not found on S31603 or S32101.
- Surface films in sulfide-containing caustic environments contained a defective, outer hydroxide layer and an inner barrier oxide layer that was enriched in Fe and Cr.
    - Lower concentrations of oxidized Fe ($Fe^{+2}$ and $Fe^{+3}$) in the surface films indicated Fe species were more soluble in the presence of sulfide owing to the formation of iron sulfide compounds. The precise compounds could not be determined in this study due to their reactivity and non-stoichiometric nature.

- Cr in the film primarily detected as oxidized $Cr^{+3}$, most likely it was present as $Cr_2O_3$ or $Cr(OH)_3$. The oxide to hydroxide ratio increased near the oxide/metal interface.
- Ni enrichment of the surface films was attributed to the lower solubility of nickel sulfide compounds in the oxide film. Ni was found in both oxidized ($Ni^{+2}$) and unoxidized ($Ni^{o}$) forms.
- Mo and Mn were mostly dissolved from the surface films based on the XPS depth profiling.

➢ Chloride further destabilizes the Cr-rich surface film formed on the surface of stainless steels in alkaline environments, particularly in the presence of sulfide.

- Corrosion rates increased with the ratio of chloride to hydroxide (chloride ratio). The corrosion rates in chloride-containing, alkaline-sulfide solution were a strong function of percent sulfidity and chloride ratio.
- Surface films generally became more defective in the presence of chloride.
- DSS S32101 underwent preferential localized corrosion of the austenite phase in alkaline-sulfide solution that contained chloride. Relatively uniform attack of the phases in S32205 under these conditions indicated that chloride addition enhanced corrosion of the ferrite phase.
- Chloride reduced the charge transfer resistance associated with the oxide/metal interface and shifted the response of the films to lower frequencies indicating the films were less protective.
- Chloride did not alter the relative ratio of oxidized species in the surface layer of DSS as compared to the chloride-free solution.

## 5.5 REFERENCES


[1] Wensley, A., NACE Corrosion, Paper No. 589, 2000, Houston, TX.

[2] Ramo, J., Sillanpaa, Kujalao, A., Hyokyvirta, O., and Peltonen, S., Mat. Corr. 52 (2001) 531.

[3] Ramo, J., Sillanpaa, Kujalao, A., Hyokyvirta, O., and Peltonen, S., Mat. Corr. 52 (2001) 741.

[4] Rondelli, G., Vicentini, B., and Sivieri, E., Corrosion Science, 39 (6): 1037 (1997).

[5] Reid, C., "Stress corrosion cracking of austenitic and duplex stainless steels in the kraft pulp mill," 1999 TAPPI Engineering/Process and Product Quality Conference, September 12-16, 1999, Anaheim, CA.

[6] L. Troselius, Proc. 11th International Pulp and Paper Industry, Corrosion in the Pulp and Paper Industry, Charleston, SC (2004).

[7] A. Bhattacharya, Georgia Institute of Technology Ph.D. Dissertation, 2008, Atlanta, GA.

[8] A. Bhatttacharya and P.M. Singh, Corr. Sci. 53 (2010) 71.\

[9] Svensson, C., Pulliainen, M., Huttunen, M., and Niemelainen, P., 2005 TAPPI Engineering, Pulping, Environmental Conference, August 28-31, 2005, Philadelphia, PA.

[10] Gorog, M., "Digester outlet device scraper arm cracking," 2006 Engineering, Pulping and Environmental Conference, November 5-8, 2006, Atlanta, GA.

[11] Singh, P.M., Mahmood, J., and Conde, P. "Stress Corrosion Cracking and CorrosionSusceptibility of Duplex Stainless Steels in Caustic Solutions," CORROSION/2005, Paper No. 05196. (Houston, TX: NACE, 2005).

[12] Leinonen, H.T. and Pohjanne, P., " Stress corrosion cracking susceptibility of duplex stainless steels and their welds in simulated cooking environments," NACE Corrosion 2006, Paper No. 06244, March 12-16, 2006, San Diego, CA.

[13] ERC Project Report, Institute of Paper Science and Technology at Georgia Tech, August 2006.

[14] Bhattacharya, A., Singh, P.M., Leinonen, H.T., and Mahmood, J., NACE Corrosion 2006, Paper No. 06497, March 12-16, 2006, San Diego, CA.

[15] I. Betova, M. Bojinov, O. Hyokyvirta, and T. Saario, Corr. Sci 52 (2010) 1499-1507.

[16] Truman, J.E. and Pirt, K.R., Duplex Stainless Steel, ed. Lula, R.A. ASM, p. 113-142, 1983, Materials Park, OH.

[17] Bhattacharya, A. and Singh, P.M. Stress Corrosion Cracking of Welded 2205 Duplex Stainless Steel in Sulfide-Containing Caustic Solution, Journal of Failure Analysis and Prevention, Vol. 7 (5) (2007), p. 371.

[18] Bhattacharya, A. and Singh, P.M. "Corrosion and Stress Corrosion Cracking of Duplex Stainless Steels in Pulping Liquors," CORROSION/2007, Paper No. 07206. (Houston, TX: NACE, 2007).

[19] Bhattacharya, A., and Singh, P.M. "Effect of Heat Treatment on Corrosion and Stress Corrosion Cracking of S32205 Duplex Stainless Steel in Caustic Solution." Metallurgical and Materials Transactions A: Physical Metallurgy and Materials Science, Vol. 40A (6) (2009), p.1388.

[20] Jordan, J.M. and Bryant, P.S. IPST Technical Paper Series Number 585, Submitted to TAPPI Pulping Conference, 1995, Chicago, IL.

[21] M. Honda et al., "Stress Corrosion Cracking of Stainless Alloys in Alkaline-Sulfide Solutions.," 1991.

[22] M. Honda, Y. Kobayashi, and A. Tamada, "Stress Corrosion Cracking of Stainless Alloys in Alkaline-sulfide Solutions," Corrosion (USA), vol. 48, 1992, pp. 822-829.

[23] D.C. Bennet, "Cracking in Continuous Digesters-History of the Problem and the Search for Predicitive Meassures," Tappi J. 65 (1982) 43-45.

[24] A. Laitinen and M. Pulliainen, "On-Line Monitoring of Recovery Boilers," Proc. 9th Int. Symp. On Corrosion in the Pulp and Paper Industry, Ottawa, Ontario, 1998, pp. 251-254.

[25] H. Leinonen, "Corrosive Environments in Different Process Stages of Modern Kraft Batch Cooking," Proc. NACE Corrosion 2000, paper no. 590, Houston, TX, 2000, 9p.

[26] D.C. Crowe and R.A. Yeske, "Corrosion Rate Monitoring in Kraft Pulping Process Liquors," IPC Technical Paper Series No. 191, July 1986, 17p.

[27] D.C. Crowe and R.A. Yeske, "Kraft White Liquor Composition and Long Term Corrosion Behavior," IPC Technical Paper Series No. 265, November 1987, 13p.

[28] Wensley, A., NACE Corrosion, Paper No. 589, 2000, Houston, TX.

[29] A. Wensley, Proc. of the 9th Int. Symposium on Corrosion in the Pulp and Paper Industry, Ottawa, Ontario, 1998, pp. 27-37.

[30] Wensley, A., Moskal, M., and Wilton, W., "Materials Selection for Kraft Batch Digesters," Corrosion/97, NACE Paper No. 378, 1997, Houston, TX.

[31] Singbeil, D.L., and Garner, A., NACE Corrosion 84, April 2-6, 1984, New Orleans, LA.

[32] G. Chen and C. R. Clayton, J. Electrochem. Soc 144 (1997) 3140-3146.

[33] J. Duan, B. Hou, and Z. Yu, Mat. Sci. and Eng. C 26 (2006) 624-629.

[34] P.J. Antony, S. Chongdar, P. Kumar, and R. Raman, Electrochima Acta 52 (2007) 3985-3994.

[35] J.T. Houston, E. Atimay, and P.M. Ferguson, "Corrosion of Reinforcing Steel Embedded in Structural Concrete." Report No. CFHR-3-5-68-112, Center for Highway Research, Univ. of Texas, Austin, TX, (1972).

[36] M.F. Hurley, J.R. Scully, G. Clemena, "Selected Issues in the Corrosion Resistance of Stainless Steel Clad Rebar," Proc. CORROSION 01, paper no. 01646, NACE International, (2001).

[37] R. Moser, P.M. Singh, L.F. Kahn, K.E. Kurtis, Corros. 67 (2011) 14p.

[38] R.E. Reed-Hill, R. Abbaschian, "Physical Metallurgy Principles," Third ed., PWS Publishing Co, Boston, MA (1994).

[39] D. Tromans, J.Electrochem. Soc. 127 (1980) 1253-1256.

[40] J. Oudar and P. Marcus, Appl. Surf. Sci. 3 (1979) 48.

[41] P. Marcus, N. Barbouth, and J. Oudar, C.R. Acad. Sci. Paris 280 (1975) 1183.

[42] P. Marcus and J. Oudar, "Fundamental Aspects of Corrosion Protection by Surface Modification" (E. McCafferty, C.R. Clayton, and J. Oudar, eds.) The Electrochemical Society, Pennington, NJ, 1984, p. 173.

[43] P. Marcus, A. Teissier, and J. Oudar, Corros. Sci. 24 (1984) 259.

[44] P. Marcus and J.M. Grimal, Corros. Sci. 31 (1990) 377.

[45] A. Elbiache and P. Marcus, Corros. Sci. 33 (1992) 261.

[46] D.W. Shoesmith, P. Taylor, M.G. Bailey, and B. Ikeda, Electrochimica Acta 23 (1978) 903-916.

[47] D.W. Shoesmith, M.G. Bailey, and B. Ikeda, Electrochimica Acta 23 (1978) 1329-1339.

[48] R.C. Salvarezza, H.A. Videla, and A.J. Arvia, Corr. Sci. 22 (1982) 815-829.

[49] HSC Chemistry 5.11, Outokumpu Technology Engineering Research.

[50] P. Marcus, E. Protopopoff, J. Electochem. Soc. 137 (1990) 2709.

[51] P. Marcus, E. Protopopoff, J. Electrochem. Soc. 140 (1993) 1571.

[52] P. Marcus, E. Protopopoff, J. Electrochem. Soc. 144 (1997) 1586.

[53] D.A. Jones, Principles and Prevention of Corrosion, Prentice Hall, 1996.

[54] F. Falkenberg, V.S. Raja, E. Ahlberg, J. Electrochem. Soc. 148 (2001) B132.

[55] R. Brandy, D.A. Jones, Corros. 32 (1976) 126-134.

[56] M. Mullet, S. Boursiquot, M. Abdelmoula, J.M. Genin, J.J. Ehrhardt, Geochimica et Cosmochimica Acta 66 (2002) 829.

[57] A.N. Buckley and R. Woods, Appl. Surf. Sci. 22/23 (1985) 280-287.

[58] A.R. Pratt, H.W. Nesbitt, I.J. Muir, Geochem. Cosmochim. Acta 85 (1994) 827-841.

[59] C.D. Wagner, J.E. Moulder, L.E. Davis, W.M. Riggs, "Handbook of X-Ray Photoelectron Spectroscopy," Perking-Emer Corp., Eden Prairie, MN (1979).

[60] D. Legrand, H.W. Nesbitt, and G.M. Bancroft, American Mineralogist 83 (1998) 1256-1265.

[61] A.L. Neal, S. Techkarnjanaruk, A. Dohnalkova, D. McCready, B.M. Peyton, and G.G. Geesey, Geochimica et Cosmochimica Acta 65 (2001) 223-235.

[62] J. Duan, B. Hou, Z. Yu, Mat. Sci. and Eng. C 26 (2006) 624-629.

[63] I. Olefjord, B. Brox., and U. Jelvestam, J. Electrochem. Soc. 132 (1985) 2854.

[64] N. De Cristofano, M. Piantini, and N. Zacchetti, Corros. Sci. 39 (1997) 2181-2191.

[65] P. Marcus and J.M. Grimal, Corros. Sci. 33 (1992) 805.

[66] M. Pourbaix, Atlas of Electrochemical Equilibria in Aqeuous Solutions (Houston, TX: NACE) (1974).

[67] C.M. Tseng, W.T. Tsai, Mat. Chem. And Phys. 84 (2004) 162-170.

[68] E. Symniotis, Corros. 46 (1990) 2.

[69] E. Symniotis, Corros, 51 (1995) 571.

[70] W.T. Tsai, M.S. Chen, Corros. Sci. 42 (200) 545-559.

[71] A. Laitinen, H. Hanninen, Corros. 52 (1996) 12p.

[72] S.S. Abd El Rehim, S.M. Abd El Haleem, S.M. Abd-El Wahaab, M.S. Shalaby, Surf. Tech. 19 (1983) 261-271.

[73] T. J. Nichol, I.A. Franson, G.E. Moller, Proc. CORROSION/81, Paper No. 117, NACE International, Houston, TX (1981) 357-401.

[74] L. Dahl, T. Dahlgren, and N. Lagmyr, High Temperature High Pressure Electrochemistry in Aqueous Solutions, NACE-4 (ed. R.W. Staehle, D. De G. Jones and J.E. Slater), NAVE, Houston, TX, (1976), p.533.

[75] T. Zakroczymski, C.J. Fan, Z. Szklarska-Smialowska, J. Electrochem. Soc. 132 (1995) 2868-2871.

[76] Bergquist, A., and Wegrelius, W. “Experiences in Pulp and Paper Industry of a 30 Years Old Steel Grade,” 2009 TAPPI Conference, Paper No. Memphis, TN.

# CHAPTER 6

# EFFECT OF SULFIDE AND CHLORIDE ON STRESS CORROSION CRACKING OF DUPLEX STAINLESS STEELS IN HOT ALKALINE ENVIRONMENTS

## 6.1. Introduction

Duplex stainless steels (DSS) have widely been selected for applications requiring high strength and corrosion resistance in aggressive pulping environments. Laboratory and field experience [1-19] has shown that DSS are susceptible to general corrosion and stress corrosion cracking (SCC) in hot alkaline-sulfide solution. Industrial pulping liquors contain multiple corroding agents in addition to sulfide and hydroxide, i.e., sulfites, sulfates, thiosulfate, carbonate, and chloride. The combined effect of these aggressive ions will influence the resistance of DSS to SCC. SCC of carbon steel and austenitic stainless steel in complex, industrial process streams has been well known for decades [20]. Much less is known about the SCC behavior of DSS in solutions containing several reactive constituents.

Chloride contamination can influence the stability of the oxide layers formed on the surface of DSS equipment in caustic alkaline pulping liquors (Chapter 5). The effect of chloride concentration on the corrosion susceptibility of DSS has widely been studied in acidic or near neutral environments [21-24]. However, there is limited understanding of the interaction between chlorides and sulfides in caustic environments. Indeed, recent field experience [25] showed that elevated chloride content (ca. 10 g $l^{-1}$ or 0.17 M NaCl)

resulted in accelerated corrosion and SCC of a heavy black liquor tank constructed of DSS S32205. It is therefore of technical and economic importance to evaluate the role of chloride and sulfide on the SCC behavior of DSS in hot alkaline-sulfide solution.

The role of chloride and sulfide on SCC of standard DSS S32205 and lean DSS S32101 grades in hot alkaline-sulfide solution was evaluated in this work. The primary objective was to obtain an understanding of SCC resistance as a function of environment. The fracture behavior was characterized to understand crack initiation and crack propagation after slow strain rate tests (SSRT) in environments containing different concentrations of NaOH, $Na_2S$, and NaCl. Film morphology and composition was studied with a scanning electron microscope (SEM) equipped with energy dispersive X-ray spectroscopy (EDS) to understand the relationship between solution composition and film characteristics near the crack tip.

## 6.2 Effect of Alkalinity

### 6.2.1 Stress Corrosion Cracking Susceptibility of DSS in Caustic Solutions

The engineering stress vs. percent elongation (% el.) curves from SSRT of DSS S32205 tested at an initial strain rate of $2 \times 10^{-6}$ $s^{-1}$ in several caustic solutions at 170 $^{o}$C are shown in Figure 6.1. The curves for lean DSS S32101 tested in the same solutions are shown in Figure 6.2. A sample tested in sand at 170 $^{o}$C is shown for comparison in each figure. The elastic part of the data has been truncated to remove the influence of system compliance. The differences observed among the % el. values at failure for the S32205 were not distinct based on Figure 6.1. Conversely, evident reduction in the % el. at failure was measured for S32101 with increasing concentrations of NaOH. The results also show the differences in mechanical behavior of the two alloys. The yield strength and tensile

strength of S32205 were greater than those of S32101, but the % el. values for S32101 indicating that lean DSS had greater ductility and lower strength than the standard DSS.

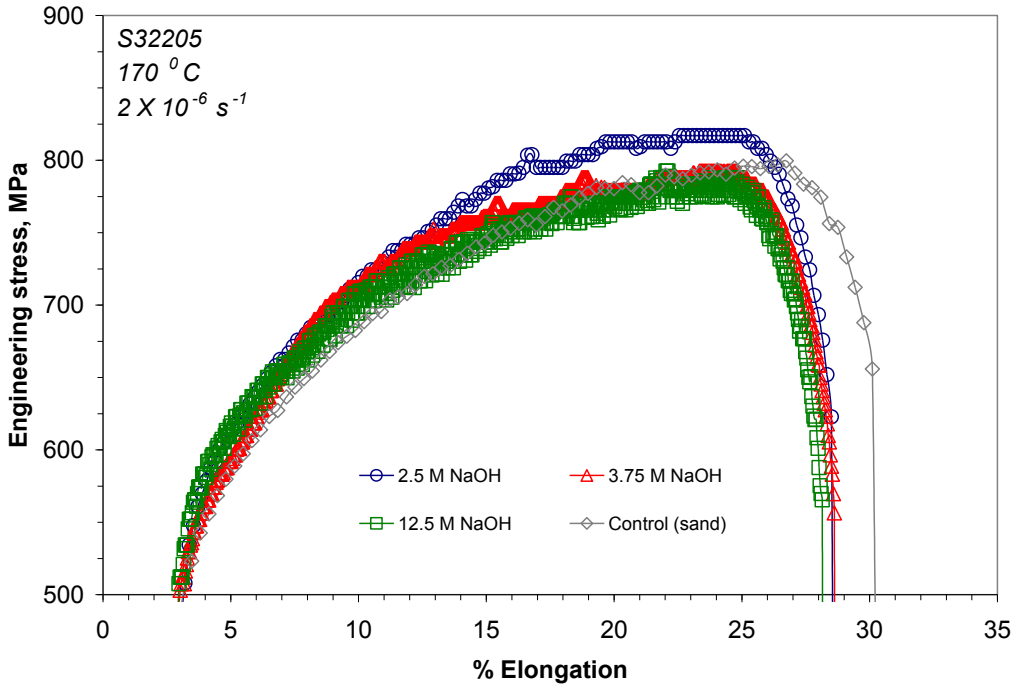


***Figure 6.1:*** ***Engineering stress - % elongation curves for S32205 tested at an initial strain rate of 2 x 10$^{-6}$ s$^{-1}$ in different alkaline environments at 170 $^{o}$C.***

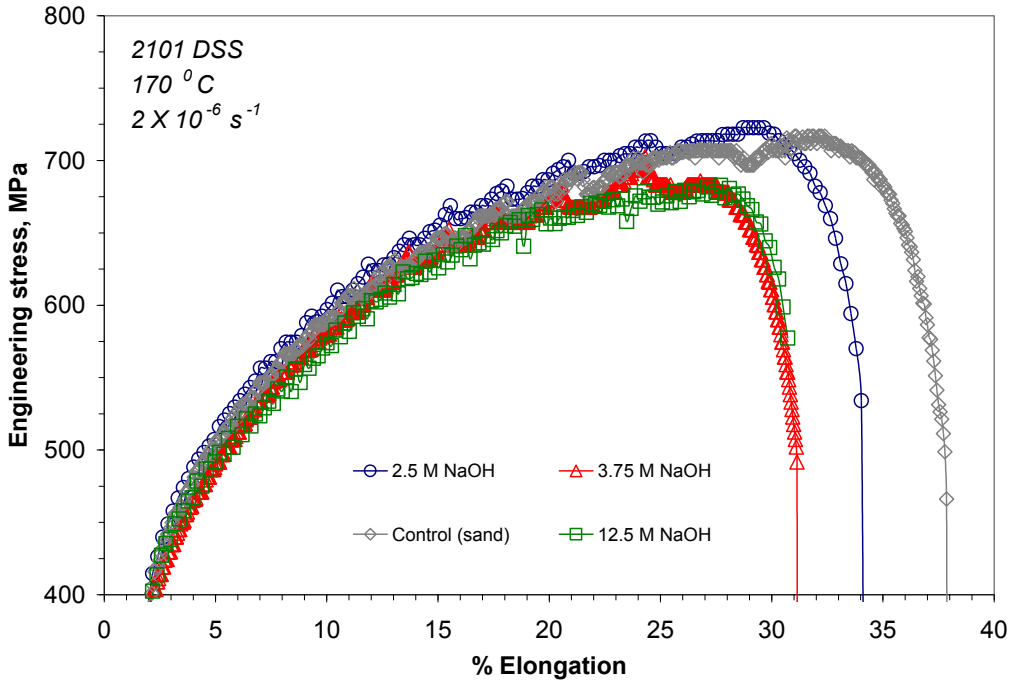


***Figure 6.2:*** ***Engineering stress - % elongation curves for S32101 tested at an initial strain rate of 2 x $10^{-6}$ $s^{-1}$ in different alkaline environments at 170 °C.***

Clearer differences in the SSRT results were found by comparing the maximum crack velocity, average crack density, and percent reduction in area (% RA) in Table 6.1. Maximum crack velocity was calculated from the deepest crack that was measured in mounted specimens. Average crack density was calculated from the number of cracks in 2 mm of the gage section. The % RA was determined by comparing the area of the fracture surface to the nominal cross-sectional area at the beginning of the test. Results from the NaOH solutions show that S32205 was not susceptible to SCC in solutions with 2.5 or 3.75 M NaOH. Severe transgranular SCC (TGSCC) was observed in 12.5 M NaOH. The % RA was reduced significantly in 12.5 M NaOH as compared to the other solutions. S32101 was susceptible to TGSCC in all of the alkaline solutions tested. The severity generally increased with increasing concentration of NaOH as shown by the

results in Table 6.1. The increased severity was particularly clear for the 12.5 M NaOH solution. The severity of SCC has been shown to increase with NaOH concentration for austenitic (300 series) [26-27] and DSS [6-10] tested in caustic solutions previously.

***Table 6.1: SCC data for S32205 and S32101 tested in alkaline environments at 170 $^{o}$C.***

| *Alloy* | *Solution Composition* | *Cracking Susceptibility* | *Max. Crack Velocity, mm $s^{-1}$* | *Avg. Crack Density, $mm^{-1}$* | *% Reduction in Area* |
|---|---|---|---|---|---|
| S32205 | 2.50 M NaOH | No SCC | - | - | 83 |
| S32205 | 3.75 M NaOH | No SCC | - | - | 83 |
| S32205 | 12.5 NaOH | TGSCC | 1.7E-06 | 15 | 23 |
| | | | | | |
| S32101 | 2.50 M NaOH | TGSCC | 3.0E-07 | 6 | 69 |
| S32101 | 3.75 M NaOH | TGSCC | 1.5E-07 | 8 | 70 |
| S32101 | 12.5 M NaOH | TGSCC | 6.6E-07 | 23 | 47 |

Corrosion potential or open-circuit potential (OCP) measurements were made on the S32205 and S32101 samples tested in the 12.5 M NaOH solution. The OCP measurements were made every 2 minutes versus a molybdenum pseudo-reference electrode (-1050 mV vs. Ag/AgCl) for the duration of the tests. The procedure used to determine the reference electrode potential is in Appendix B. Results from S32205 (Figure 6.3) and S32101 (Figure 6.4) show that the OCP dropped immediately after the onset of plastic deformation indicating that the surfaces were undergoing active corrosion. The reduction in potential was more gradual in S32205. The OCP values for S32205 and S32201 are similar to values acquired during electrochemical measurements

(Chapter 4). It is worth noting that the electrical connection on S32101 failed shortly after yield, but the downward trend in OCP was clear. The results show that the onset of SCC was associated with active dissolution on the metal surface.

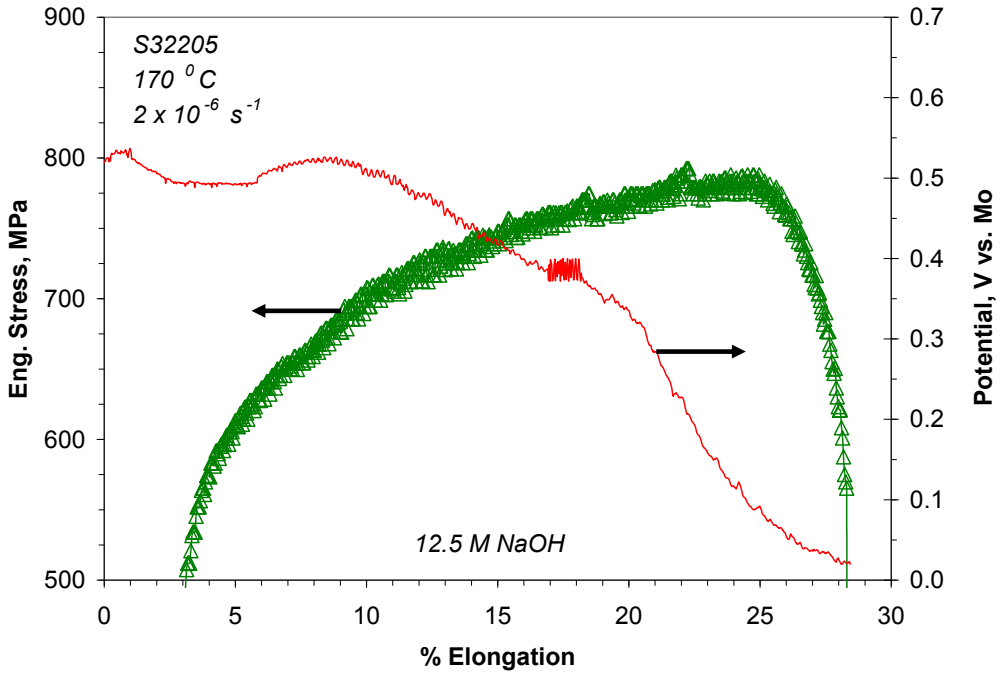


***Figure 6.3:*** ***Engineering stress - % elongation curves for S32205 tested at an initial strain rate of 2 x $10^{-6}$ $s^{-1}$ in 12.5 M NaOH at 170 $^{o}$C while monitoring the corrosion potential.***

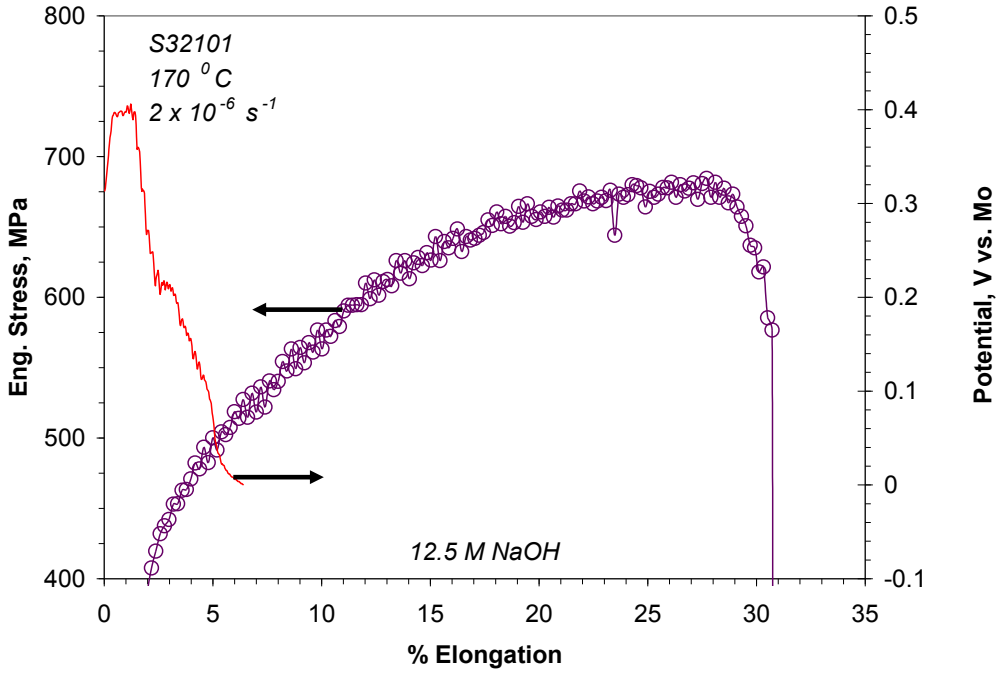


*Figure 6.4:* ***Engineering stress - % elongation curves for S32101 tested at an initial strain rate of 2 x $10^{-6}$ $s^{-1}$ in different alkaline environments at 170 °C.***

### 6.2.2 Crack and Fracture Surface Morphology

Optical micrographs showing differences in the SCC behavior S32101 tested in 2.5 M (Figure 6.5a) and 3.75 M NaOH (Figure 6.5b) indicated that the susceptibility of the phases changed with concentration of NaOH. Cracking was limited primarily to austenite in 2.5 M NaOH, but the ferrite (dark etching phase) was more susceptible in 3.75 M NaOH. Preferential corrosion of the austenite phase was identified throughout the gage section of the sample tested in 3.75 M, which suggests that crack initiation occurred in the austenite phase and crack propagation occurred in the ferrite phase.

α γ

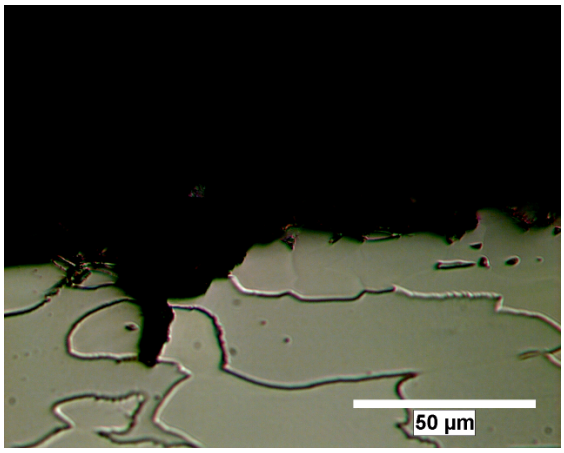


(a)

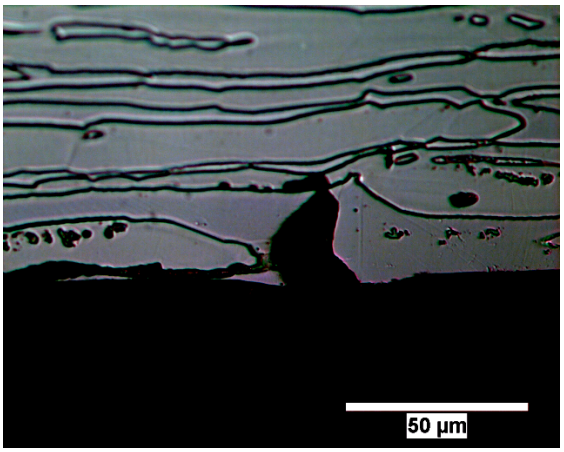


(b)

***Figure 6.5:*** ***Optical micrograph showing stress corrosion cracks for lean DSS S32101 in (a) 2.5 M NaOH in austenite (light etching phase) and (b) 3.75 M NaOH in ferrite phase (dark etching phase) tested at 170 $^{o}$C.***

Secondary cracks and quasi-cleavage fracture were observed on the surface of S32101 tested in 3.75 M NaOH at 170 $^{o}$C (Figure 6.6). EDS spectra taken near the secondary cracks showed the phase was enriched in Cr and Mo showing the phase was ferrite. The role of hydrogen cannot immediately be ruled out under hot alkaline conditions. Such a mechanism may account for the increased susceptibility of the ferrite phase. Conflicting points of view exist in the literature for the role of hydrogen on the

cracking process [11, 28-31]. Dahl et al [29] tested AISI 304 in de-aerated (200 g $l^{-1}$ NaOH) at 220 $^{o}$C and showed the OCP was situated in the active range; hence, hydrogen available at cathodic sites could play a role in the SCC process. Rondelli et al [11] made similar conclusions about austenitic and DSS tested in strong alkaline (300 g $l^{-1}$ NaOH) environments at 200 $^{o}$C. Susceptibility increased monotonically with decreasing strain rate indicating hydrogen played a role in the SCC mechanism. Others [28, 30-31] have reported that SCC of stainless steels is due to an anodic control through breakdown and repair of a passive film.

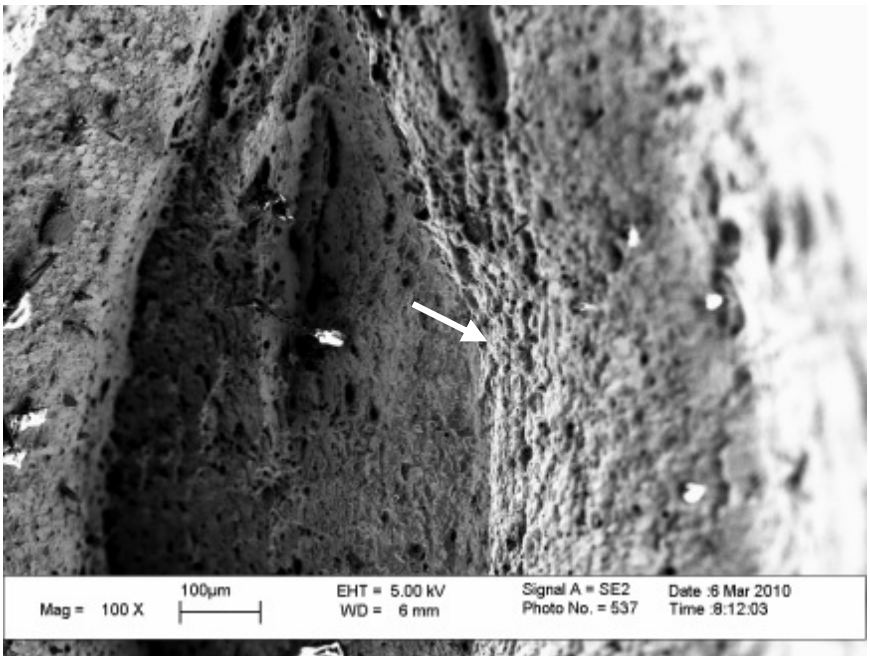


(a)

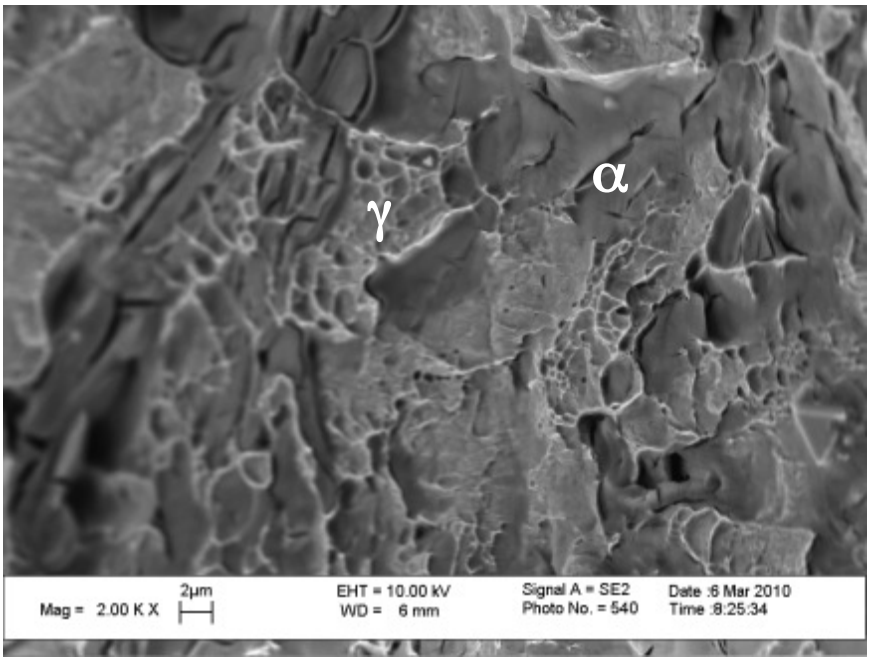


(b)

***Figure 6.6:*** ***(a) Low magnification and (b) high magnification SEM micrographs showing fracture surface of lean DSS S32101 tested in 3.75 M NaOH at 170 $^{o}$C. Arrow corresponds to region shown in (b).***

The severity of SCC was far greater in the 12.5 M NaOH solution at 170 $^{o}$C. The stress corrosion cracks on the surfaces of S32205 and S32101 are shown in Figure 6.7 and 6.8, respectively. Samples tested in sand at 170 $^{o}$C are shown for comparison. These samples show typical ductile failure. Limited ductility was associated with failure in the NaOH solution as evident by the lack of necking near the fracture surfaces, particularly for S32205. Furthermore, a large amount of surface cracks indicates crack initiation was favorable under the test conditions. Mounted samples that were polished, etched and observed under optical microscope (Figure 6.9) showed severe TGSCC associated with both phases of the DSS, although crack branching was favored in the austenite phase. Crack growth in the austenite phase was more apparent in S32101 (Figure 6.9b).

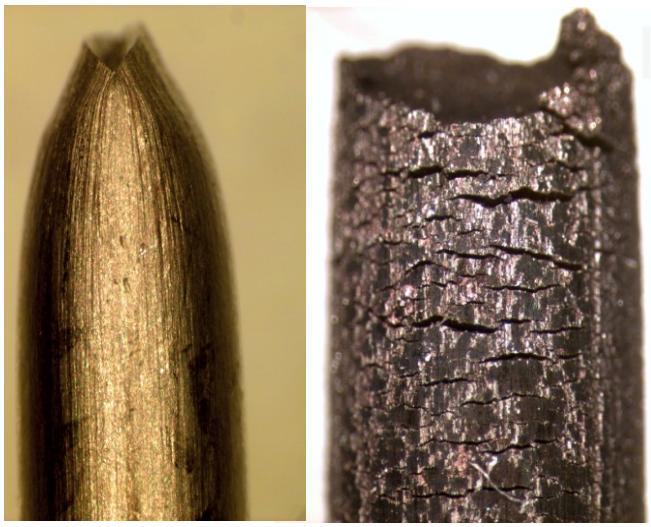

***Figure 6.7:*** ***Micrographs of DSS S32205 tensile specimens tested in (left) sand and (right) 12.5 M NaOH at 170 $^{o}$C show influence of environment.***

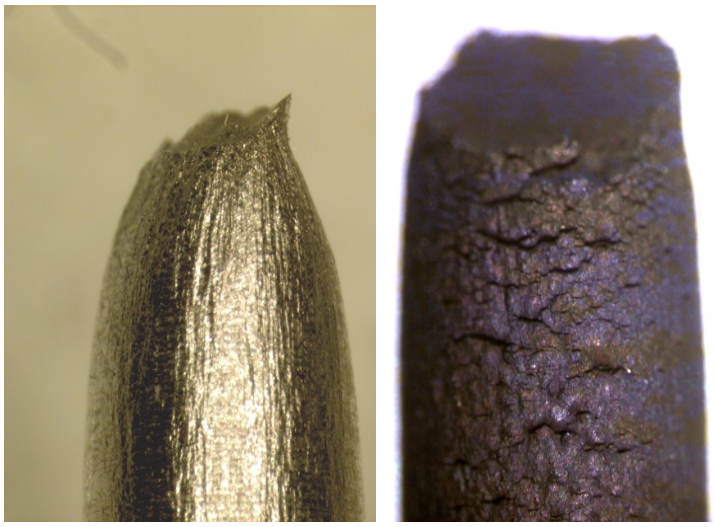

*Figure 6.8:* ***Micrographs of DSS S32101 tensile specimens tested in (left) sand and (right) 12.5 M NaOH at 170 $^{o}$C show influence of environment.***

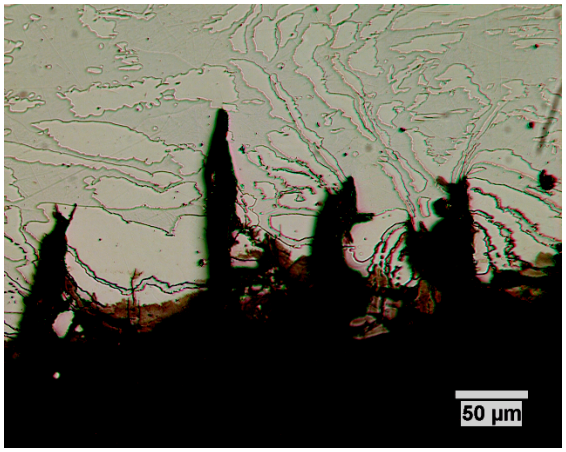


(a)

*Figure 6.9:* ***Optical micrograph showing stress corrosion cracks for (a) standard DSS S32205 tested in 12.5 M NaOH at 170 $^{o}$C.***

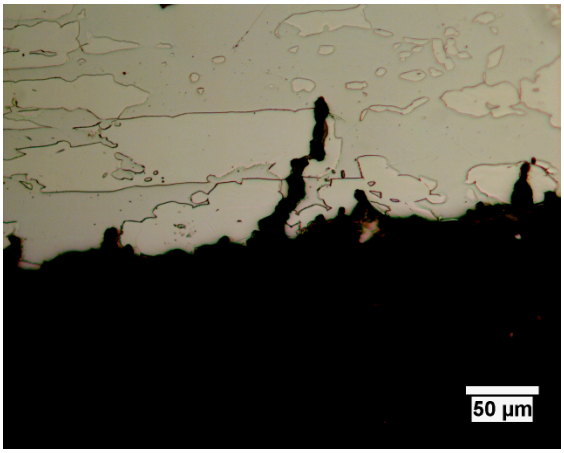


(b)

***Figure 6.9(cont'd):*** ***Optical micrograph showing stress corrosion cracks for (b) lean DSS 32101 tested in 12.5 M NaOH at 170 $^{o}$C.***

The growth of stress corrosion cracks in S32205 tested in 12.5 M NaOH at 170 $^{o}$C was associated with a Fe depleted, porous oxide layer as seen in the high resolution backscattered electron image and EDS spectra of Figure 6.10. Ni and Cr enrichment was observed in the oxide. Na was enriched in the regions with high O content. The clear partitioning of Mo and Ni indicated that sharp cracks with many branches grew preferentially in the austenite phase, although crack growth occurred in both the ferrite and austenite phases. Blunt cracks were associated with the Cr- and Mo-rich, ferrite phase. Crack growth beyond the oxide layer was not observed at the crack tips. Two distinct regions could be observed in the affected surface layer. Higher O content in the surface layer was favored in regions with high Cr contents based on the EDS analysis. Mo and Mn were depleted from the affected surface layers. No attempt was made to quantify the results of the EDS analysis.

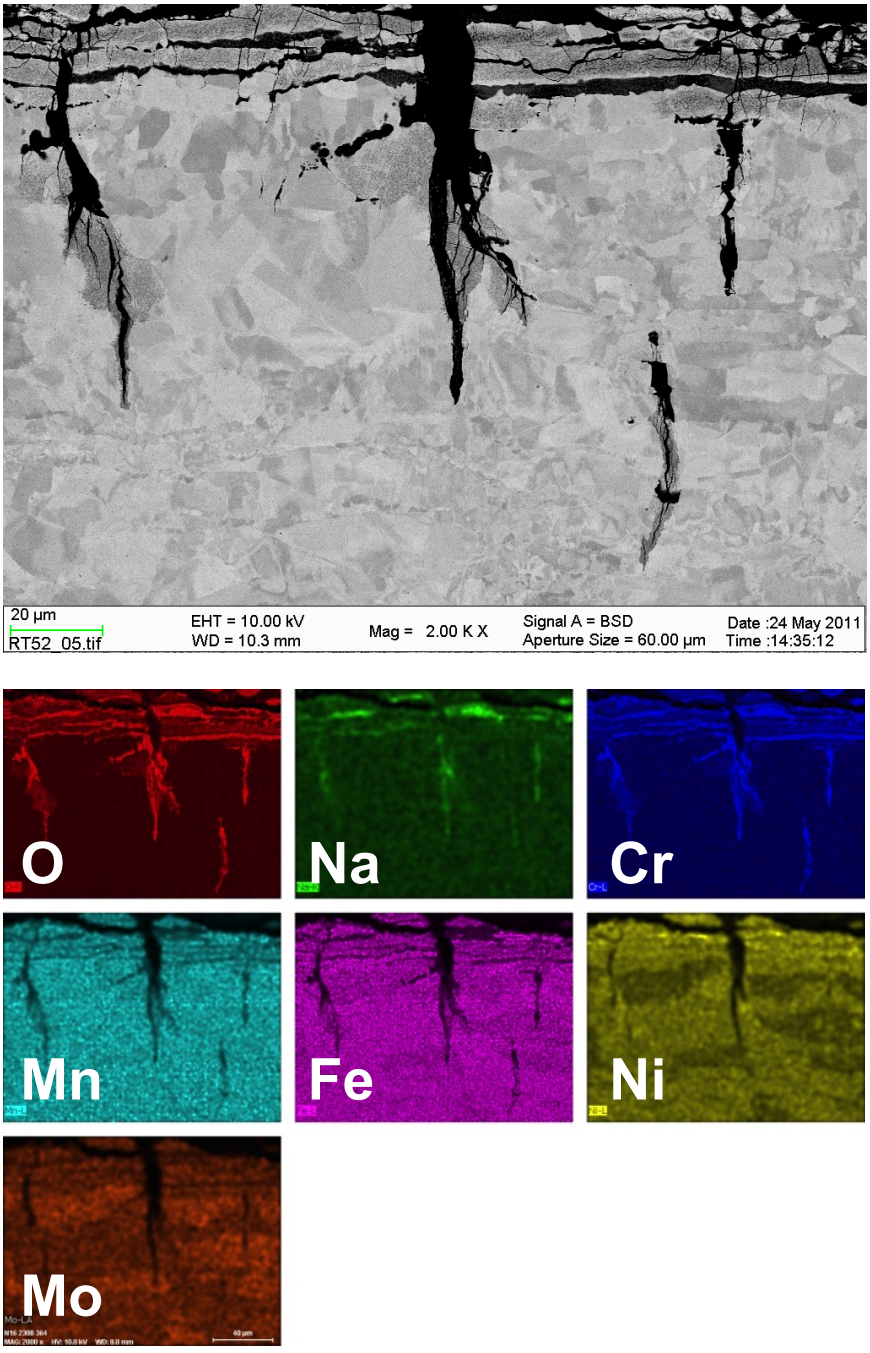


*Figure 6.10:* ***High resolution backscattered image and energy dispersive X-ray spectra maps of the surface of a standard DSS S32205 slow strain rate specimen tested in 12.5 M NaOH at 170 $^{o}$C.***

Electron backscattered diffraction (EBSD) maps showed the respective phases (austenite is dark and ferrite is light), regions of high misorientation, and crystal orientation near the crack tip of the S32205 specimen tested in 12.5 M NaOH at 170 $^{o}$C (Figure 6.11). Crack growth occurred in both phases, but appeared to be inhibited by the ferrite phase. The austenite phase showed more misorientation indicating this phase was more highly strained. The point-to-point misorientation (0.3 μm step size) in the highly strained regions was approximately 1 – 2 $^{o}$. High regions of strain were associated with crack growth. The pole Figure crystal orientation maps showed the material was highly textured. Texture was strongest in the ferrite phase along the {101} planes. The {hkl} indices give the orientation of the crystal planes parallel the observed surface of the grains. Branching in the austenite phase did not occur along preferential crystal planes. The aligned crystal structure may have been due to deformation, but it was unclear because the as-received condition was not evaluated.

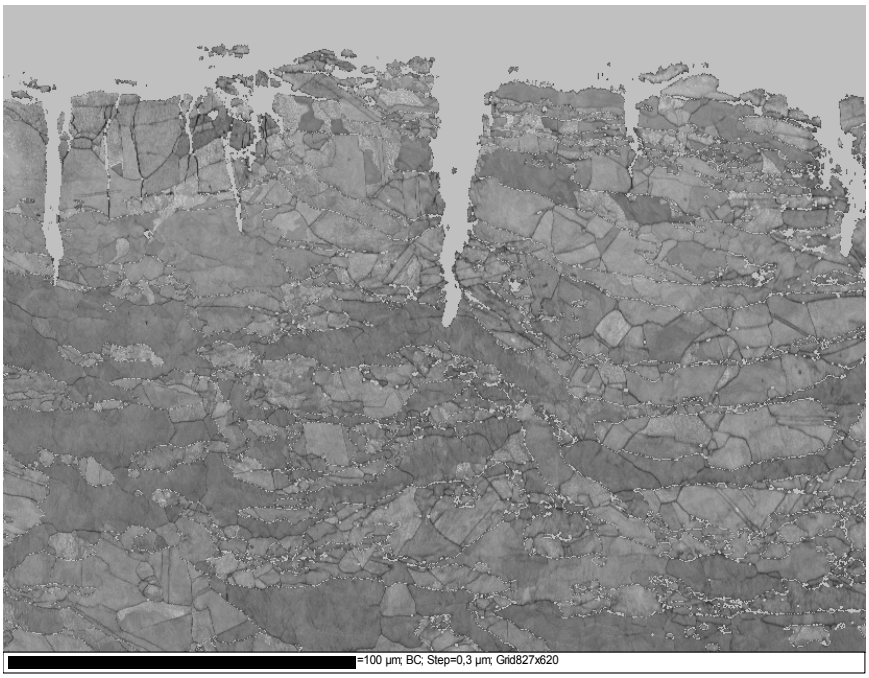


(a)

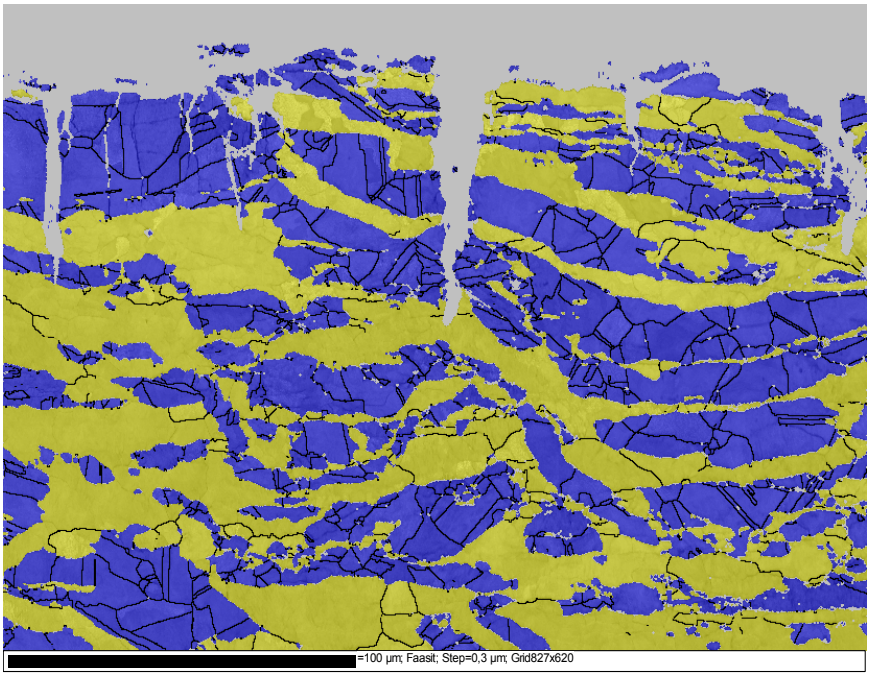


(b)

*Figure 6.11:* ***(a) Backscatter scanning electron micrograph of surface of a standard DSS S32205 slow strain rate specimen and corresponding electron back scattered diffraction maps of the tested in 12.5 M NaOH at 170 °C. (b)Phase map showing austenite (dark) and ferrite phases (light).***

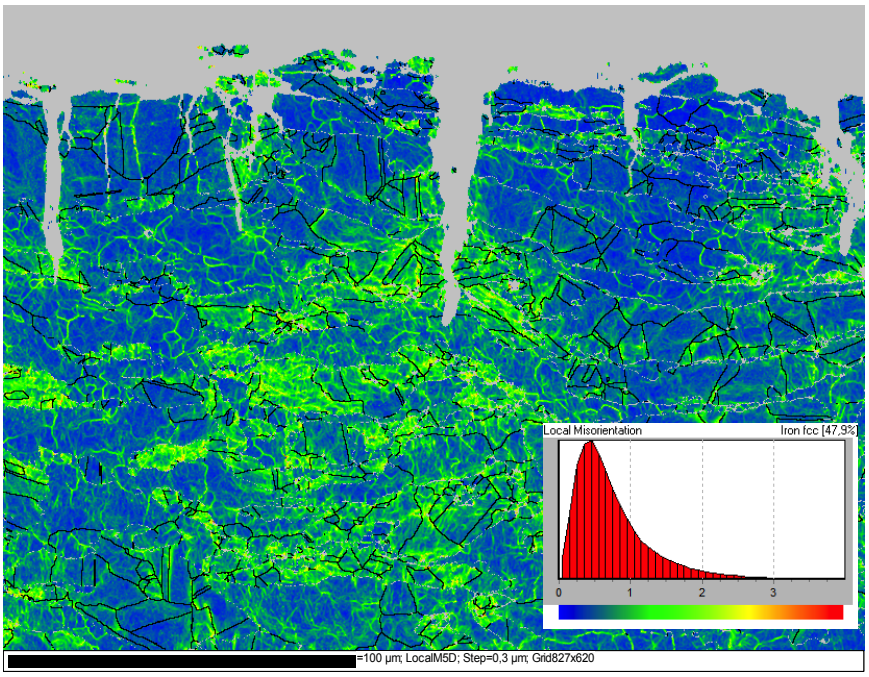


(c)

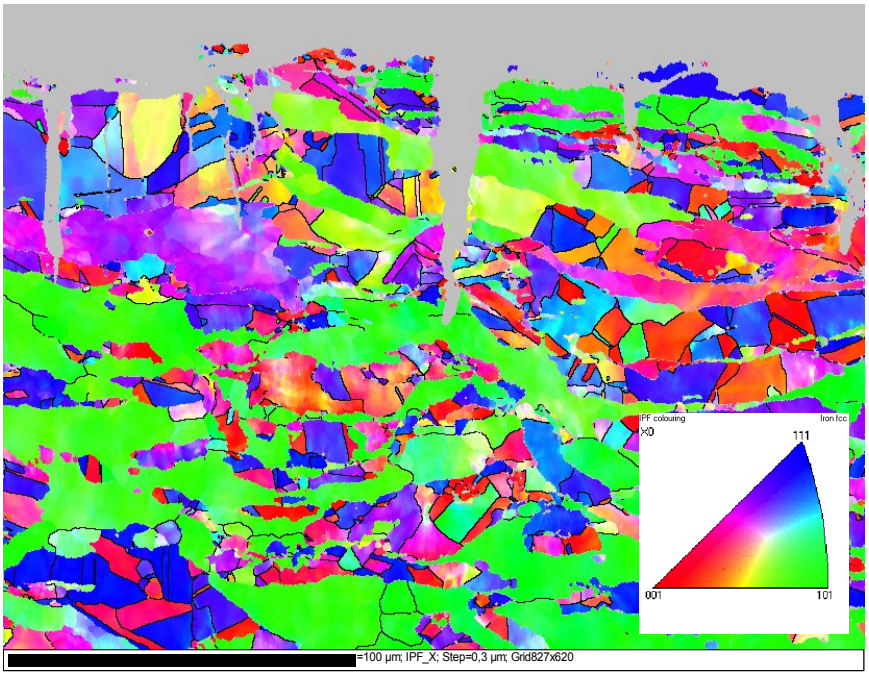


(d)

***Figure 6.11 (cont'd):*** ***Electron back scattered diffraction maps of the tested in 12.5 M NaOH at 170 $^{o}$C: (c) misorientation maps (step size 0.3µm), and (d) pole Figure crystal orientation map.***

The growth of stress corrosion cracks in S32101 tested in 12.5 M NaOH at 170 $^{o}$C was associated with a Cr-rich oxide layer as seen in the backscattered image and EDS maps of Figure 6.12. Na was enriched in the regions with high O content. Partitioning of Mo was not evident in the EDS maps for S32101 owing to the low concentrations of this element. Ni enrichment was observed near the crack tip, which was either due to preferential dissolution of other elements or redeposition. Similar findings have been reported elsewhere [32-34] Crack growth behavior could not be connected to any particular phase based on the EDS maps, although cracks were more bulbous and discontinuous (more crack interruptions) in S32101 as compared to S32205. These findings suggest the crack growth process was associated with dissolution. Higher Cr and O content were observed in the affected surface layer. Fe, Mo, and Mn were depleted from the affected surface layers.

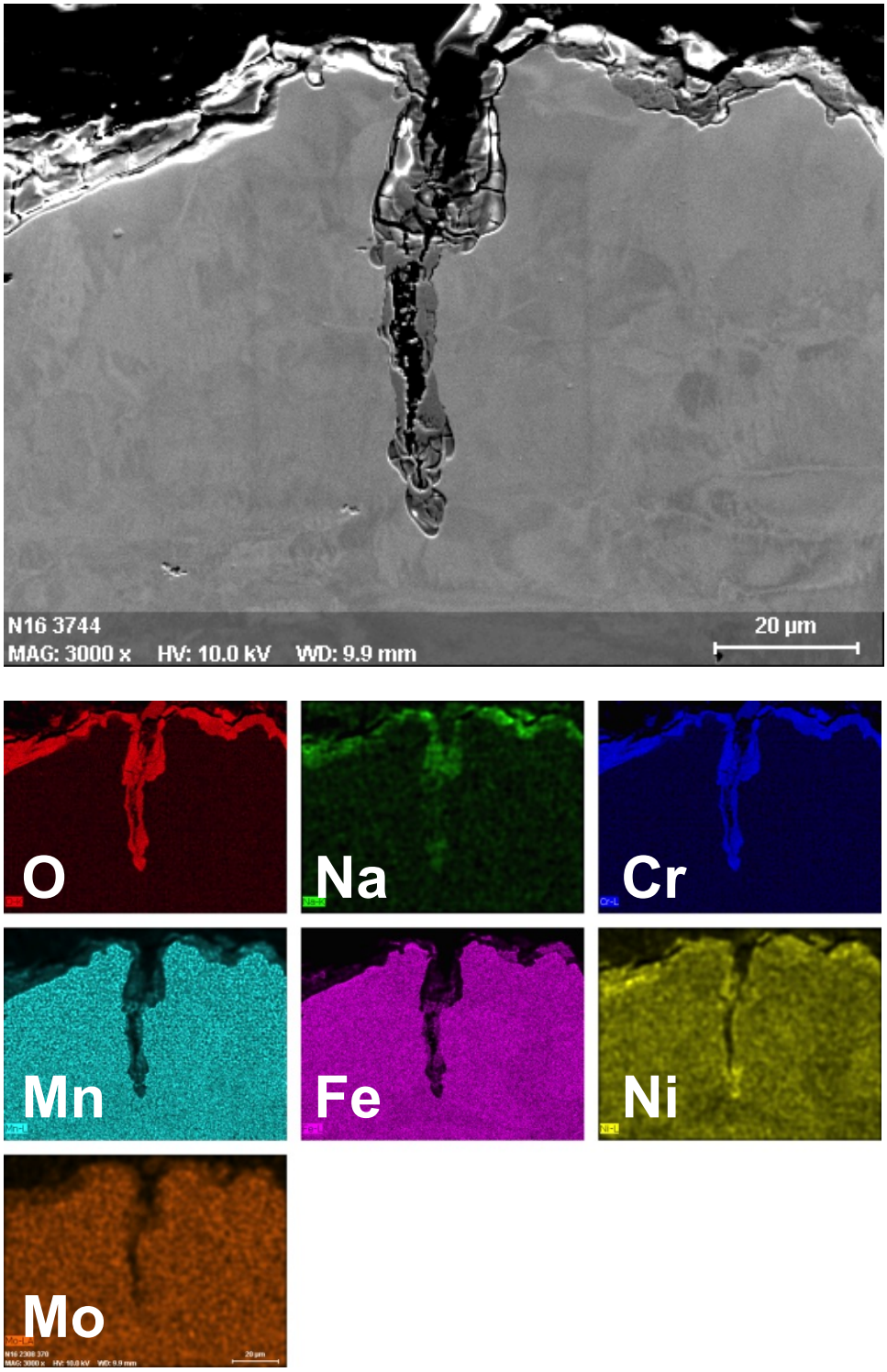


*Figure 6.12:* ***Energy dispersive X-ray spectra maps of the surface of a lean DSS S32101 slow strain rate specimen tested in 12.5 M NaOH at 170 $^{o}$C.***

EBSD maps of the S32101 specimen tested in 12.5 M NaOH at 170 $^{o}$C are shown in Figure 6.13. Crack growth occurred in both phases, and appeared to terminate in the austenite phase. The austenite phase showed appreciably more misorientation that the ferrite phase indicating the relative strain ratio between the two phases was greater in S32101 as compared to S32205. The point-to-point misorientation (ca. 1 – 2 $^{o}$) in the highly strained regions of austenite was independent of the crack tip. Moreover, a number of deformation twins were found in the highly textured austenite phase. The pole Figure crystal orientation maps showed texture was strongest in the austenite phase along the {00l} and {111} planes. Branched stress corrosion cracks were not observed in S32101.

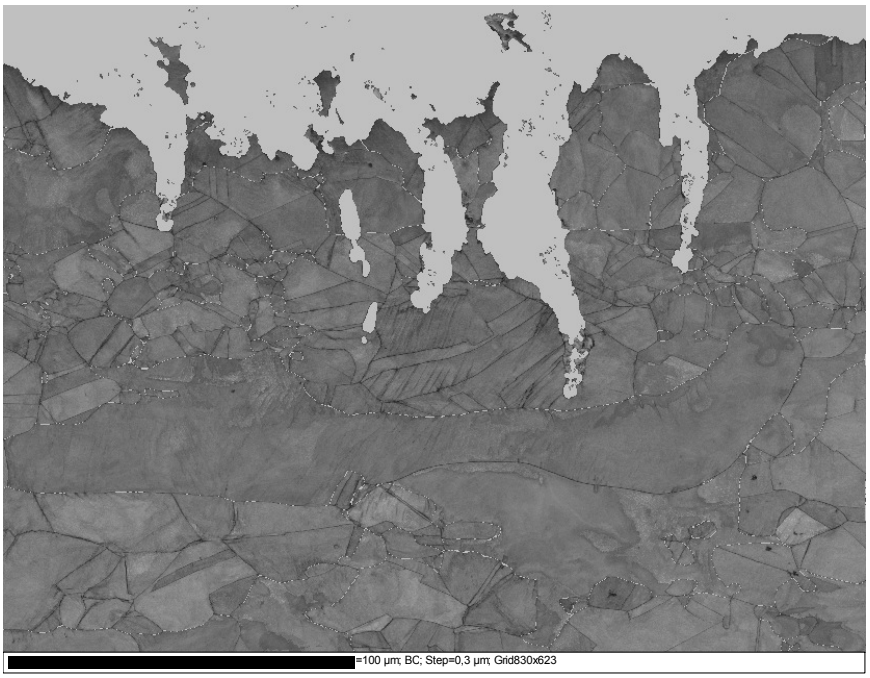


(a)

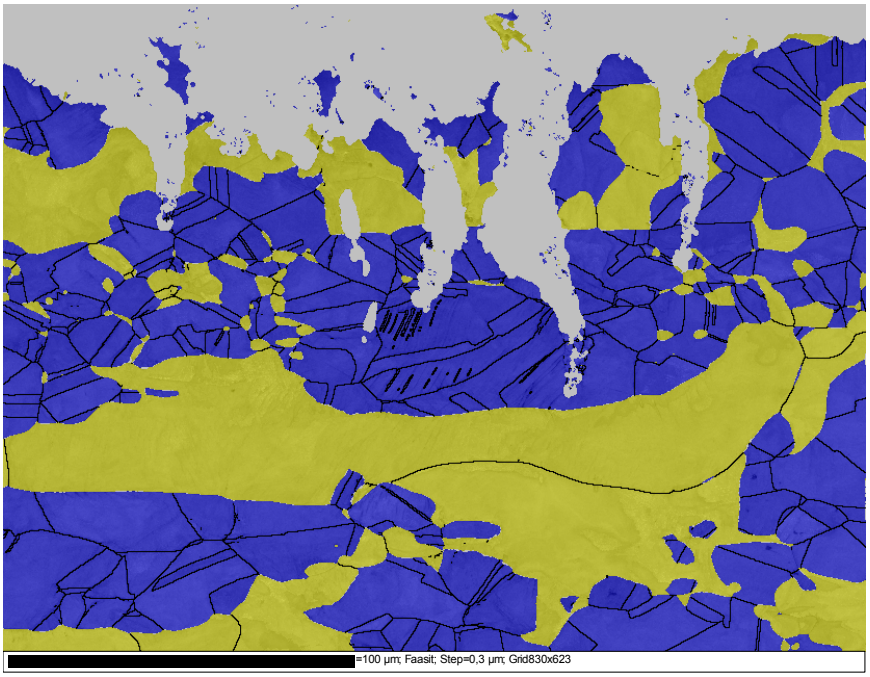


(b)

*Figure 6.13:* ***(a) Backscatter scanning electron micrograph of surface of a lean DSS S32101 slow strain rate specimen and corresponding electron back scattered diffraction maps of the tested in 12.5 M NaOH at 170 $^{o}$C: (b) phase map showing austenite (dark and ferrite (light.***

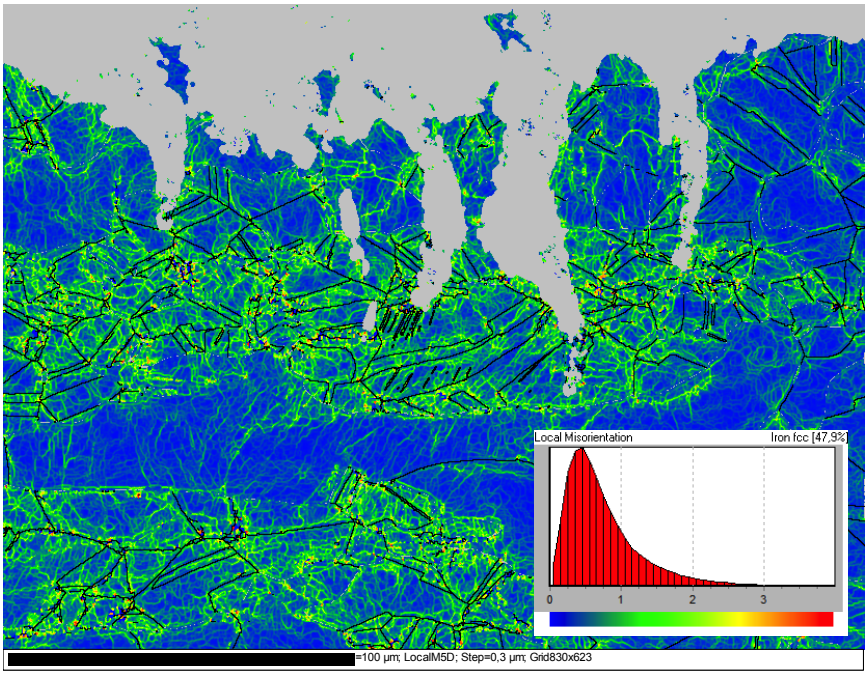


(c)

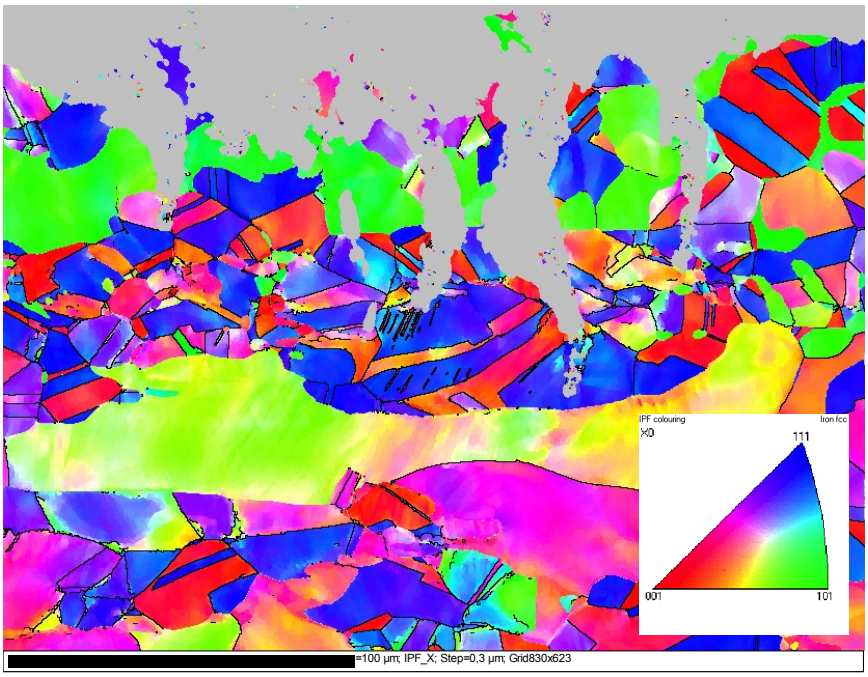


(d)

***Figure 6.13(cont'd):*** ***(c) Misorientation maps (step size 0.3µm), and (d) pole Figure crystal orientation map.***

Results from S32205 and S32101 tested in alkaline solutions at 170 $^{o}$C showed that the severity of SCC depended on material composition and alkalinity. Lean DSS S32101 was more susceptible to SCC in the tested environments than standard DSS S32205. The growth of SCC cracks in the two materials was dependent on the selective dissolution of Fe as evident by the enrichment of Cr and Ni near the crack tip. Secondary cracking and quasi-cleavage in the ferrite phase of S32101 suggests hydrogen may have had a role in the cracking process of this material. The corrosion potential for the two materials was in the active region and did not differ from materials tested under static condition (Chapter 4). Differences in the crack propagation behavior were identified in the 12.5 M NaOH solution. Crack branching in a porous oxide in the austenite phase was observed in S32205 but not in S32101. The austenite phase was more highly strained than the ferrite phase in both materials, although the relative strain between austenite and ferrite was greater in S32101.

Deakin et al [33] proposed selective dissolution of Fe and Cr, i.e. de-alloying, as a mechanism for SCC of 316L tested in 12.5 M at 140 $^{o}$C. This mechanism has also been proposed for a number of other materials, [35-37] whereby selective dissolution facilitates the formation of a nanoporous metallic layer enriched in the noble element that supports crack initiation. Coull and Newman [38] also studied the conditions required for SCC due to de-alloying in the Fe-Cr-Ni system in terms of critical Ni concentration and corrosion potential.

The corrosion potentials of S32205 and S32101 were in the region where de-alloying is expected to occur [38]. However, based on the relative ratios of Fe and Ni in S32205 (Fe/Ni ≅ 13) and S32101 (Fe/Ni ≅ 50), which are much higher than 316L (Fe/Ni

≅ 7.5), the de-alloyed layers likely lacked sufficient mechanical integrity to support cracking. Both DSS materials were both susceptible to SCC in 12.5 M NaOH despite the relatively low concentrations of Ni. S32205 (ca. 5.5 wt % Ni) showed different crack growth behavior than S32101 (ca. 1.5 wt % Ni), which can be attributed to the properties of the oxide layers that formed on tested DSS alloys. The absence of cracks beyond the oxide layers in S32205 and S32101 and enrichment of Cr suggests a mechanism involving the breakdown and repair of a protective film occurred in NaOH solutions, analogous to what has been shown for carbon steel in these environments [28, 39]. Crack growth rates increased with concentration of NaOH because the conditions favored selective dissolution. Hydrogen may have influenced the SCC behavior of S32101, but it was not possible to determine the extent of the involvement from this work

## 6.3 Effect of Sulfide

### 6.3.1 Stress Corrosion Cracking Susceptibility of DSS in Sulfide-Containing Caustic Solutions

The engineering stress vs. % elongation curves from SSRT of DSS S32205 at an initial strain rate of 2 x $10^{-6}$ $s^{-1}$ in several sulfide-containing caustic solutions at 170 $^{o}$C are shown in Figure 6.14. The curves for lean DSS S32101 tested in the same solutions are shown in Figure 6.15. A sample tested in sand at 170 $^{o}$C is shown for comparison in each figure. Sulfide addition reduced the % el. values at failure for the S32205; conversely, an increase in the % el. at failure was found for S32101 with sulfide addition. However, in both cases the % el was lower in sulfide-containing caustic solutions compared to the inert sane environment.

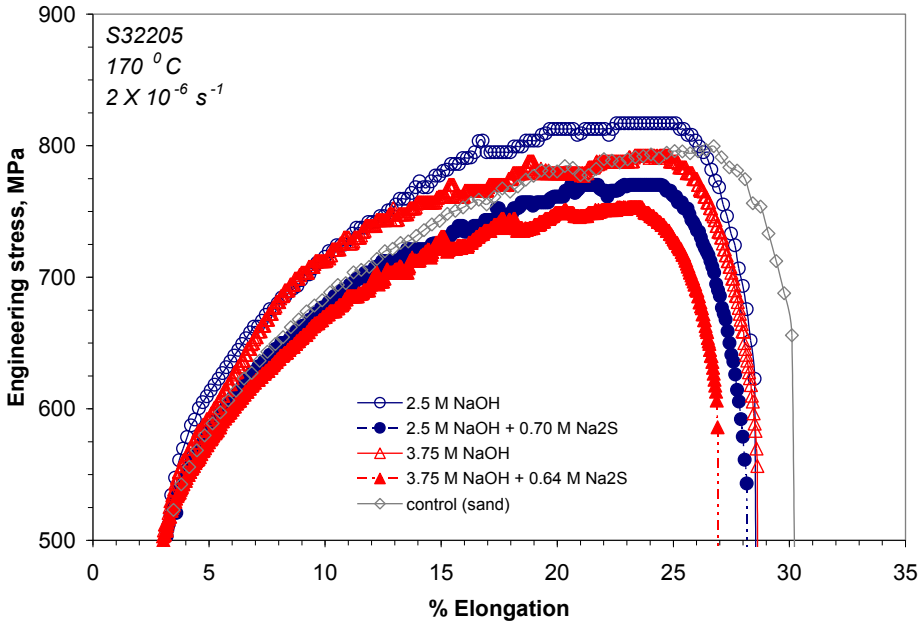


*Figure 6.14:* ***Engineering stress - % elongation curves for S32205 tested at an initial strain rate of 2 x $10^{-6}$ $s^{-1}$ in different alkaline environments with and without $Na_2S$ at 170 $^{O}$C.***

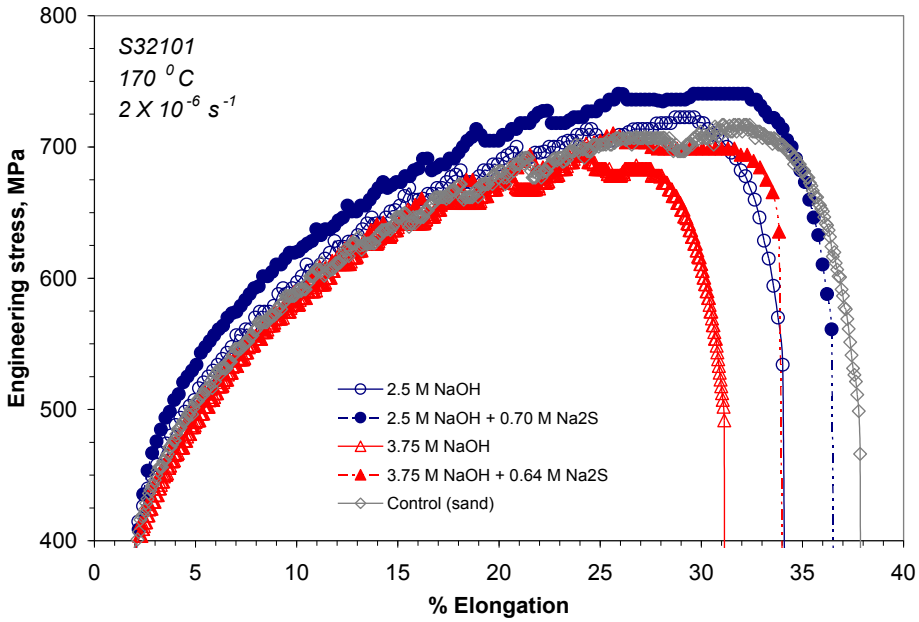


*Figure 6.15:* ***Engineering stress - % elongation curves for S32101 tested at an initial strain rate of 2 x $10^{-6}$ $s^{-1}$ in different alkaline environments with and without $Na_2S$ at 170 $^{O}$C.***

The SSRT results for S32205 and S32101 tested in alkaline-sulfide solutions are shown in Table 6.2. Results show that S32205 was not susceptible to SCC in the solution with 2.5 NaOH + 0.70 M $Na_2S$, but TGSCC was observed in 3.75 M NaOH + 0.64 M $Na_2S$. The % RA was reduced significantly in this solution. S32101 was susceptible to TGSCC in the two alkaline solutions that were tested. The severity increased appreciably in 3.75 M NaOH + 0.64 M $Na_2S$. Other work [8] on the SCC susceptibility of DSS in similar alkaline-sulfide solutions have shown that lean DSS S32101 is more susceptible to SCC than S32205. Superferritic S44660 and S44627 were also tested for comparison in 2.5 NaOH + 0.70 M $Na_2S$ at 190 $^oC$ using U-bend specimens. The specimens were pre-loaded such that the stress at the apex was above the yield strength of the materials. These materials did not experience SCC after a two-week exposure.

***Table 6.2:*** ***SCC data for S32205 and S32101 tested in alkaline-sulfide environments at 170 $^oC$. S44660 and S44627 were tested for comparison using U-bend specimens.***

| *Alloy* | *Solution Composition* | *Cracking Susceptibility* | *Max. Crack Velocity, mm $s^{-1}$* | *Avg. Crack Density, $mm^{-1}$* | *% Reduction in Area* |
|---|---|---|---|---|---|
| S32205 | 2.5 M NaOH + 0.70 M $Na_2S$ | No SCC | - | - | 86 |
| S32205 | 3.75 M NaOH+ 0.64 M Na2S | TGSCC | 5.3E-07 | 15 | 44 |
| | | | | | |
| S32101 | 2.5 M NaOH + 0.70 M Na2S | TGSCC | 1.6E-07 | 9 | 70 |
| S32101 | 3.75 M NaOH + 0.64 M Na2S | TGSCC | 1.3E-06 | 21 | 44 |
| | | | | | |
| S44660 | 2.5 M NaOH + 0.70 M Na2S | No SCC | - | - | N/A |
| S44627 | 2.5 M NaOH + 0.70 M Na2S | No SCC | - | - | N/A |

### 6.3.2 Crack and Fracture Surface Morphology

Micrographs in Figure 6.16 show the surface morphology of the S32205 SSRT specimens tested to failure in alkaline-sulfide solution at 170 $^{o}$C. A sample that was tested in sand is shown for comparison. Surface cracks were observed on the 3.75 M NaOH + 0.64 M $Na_2S$, but not in the 2.5 M NaOH + 0.70 M $Na_2S$ solution. SCC was observed on S32101 (Figure 6.17) in the two alkaline-sulfide solutions. SCC was not observed at the apex of the S44660 and S44627 U-bend specimens tested in 2.5 M NaOH + 0.70 M $Na_2S$ at 190 $^{o}$C (Figure 6.18). Superficial intergranular corrosion was observed on the surface layer of these two specimens.

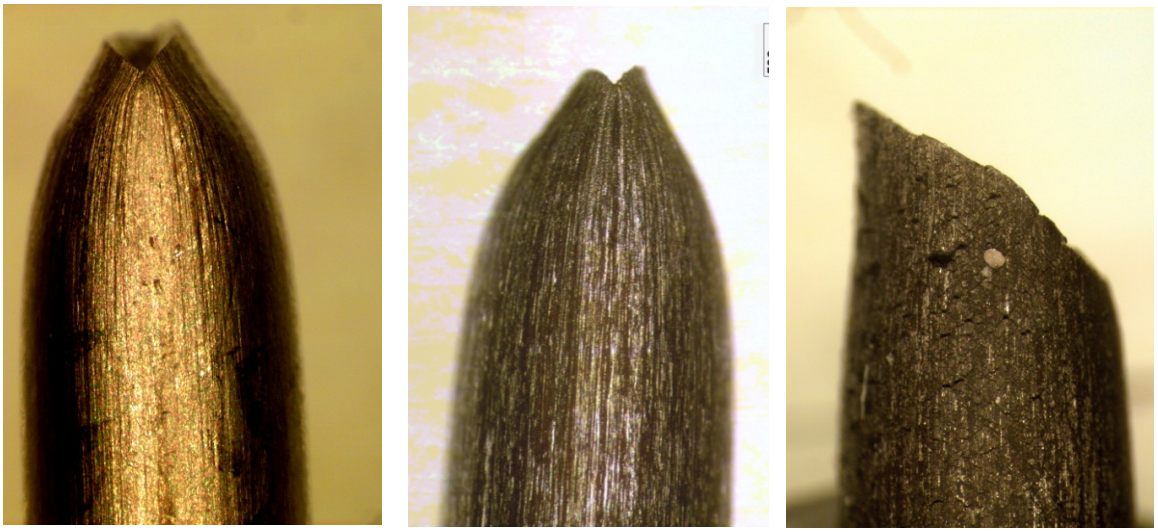

***Figure 6.16:*** ***Micrographs of DSS S32205 tensile specimens tested in (left) sand, (center) 2.5 M NaOH + 0.70 M $Na_2S$, and (right) 3.75 M NaOH + 0.64 M $Na_2S$ at 170 $^{o}$C show the influence of environment on SCC.***

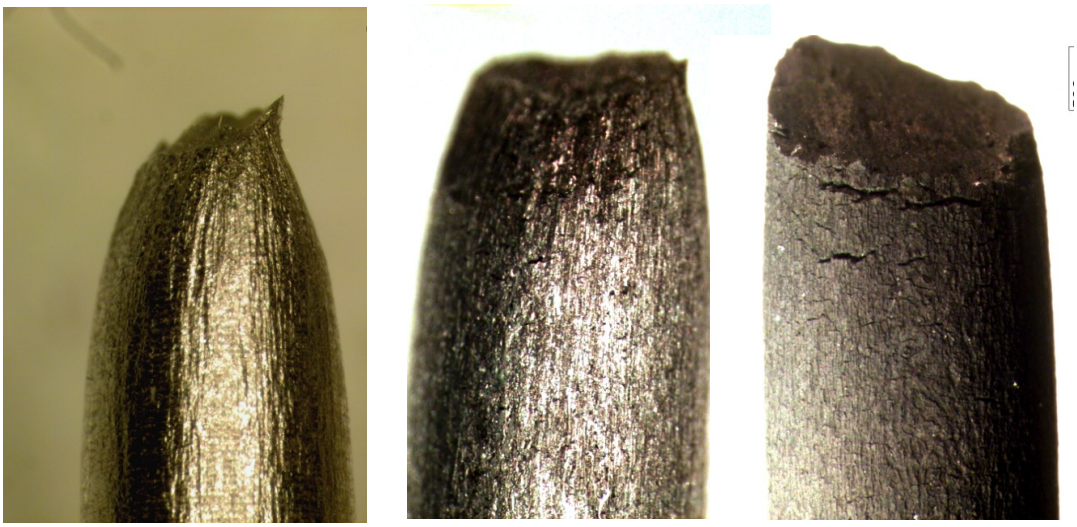

*Figure 6.17:* ***Micrographs of DSS S32101 tensile specimens tested in (left) sand, (center) 2.5 M NaOH + 0.70 M $Na_2S$, and (right) 3.75 M NaOH + 0.64 M $Na_2S$ at 170 $^oC$ show the influence of environment on SCC.***

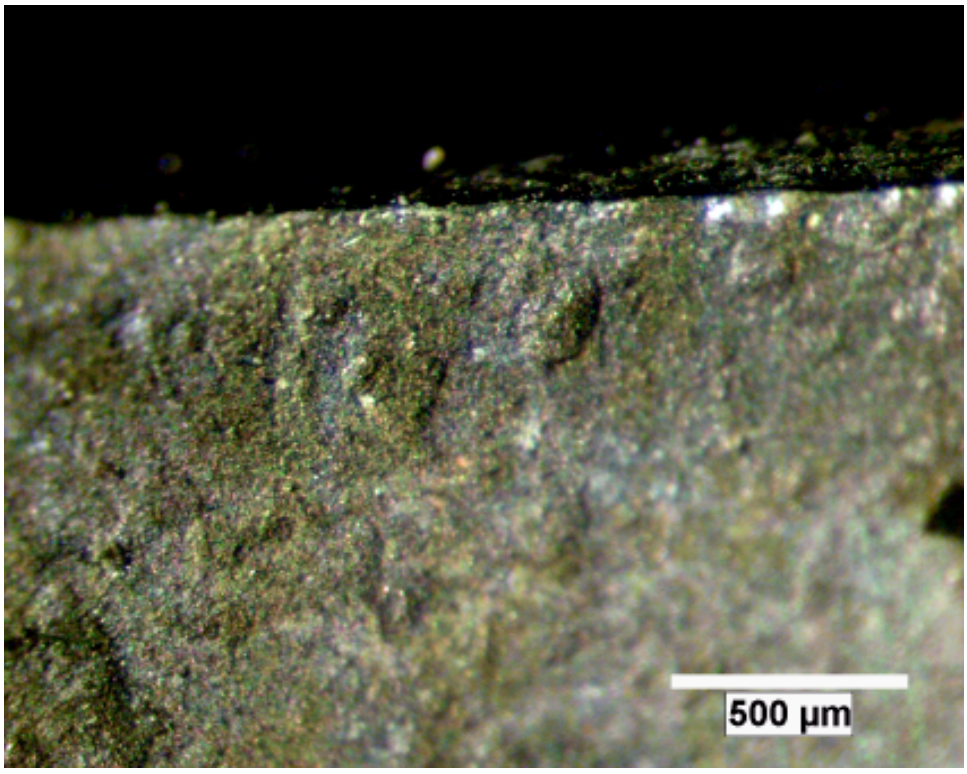


(a)

*Figure 6.18:* ***(a) Micrographs of S44660 and U-bend specimens tested in 2.5 M NaOH + 0.70 M $Na_2S$ at 190 $^oC$ show the influence of environment. No SCC was observed on these superferritic steel samples in tested environments.***

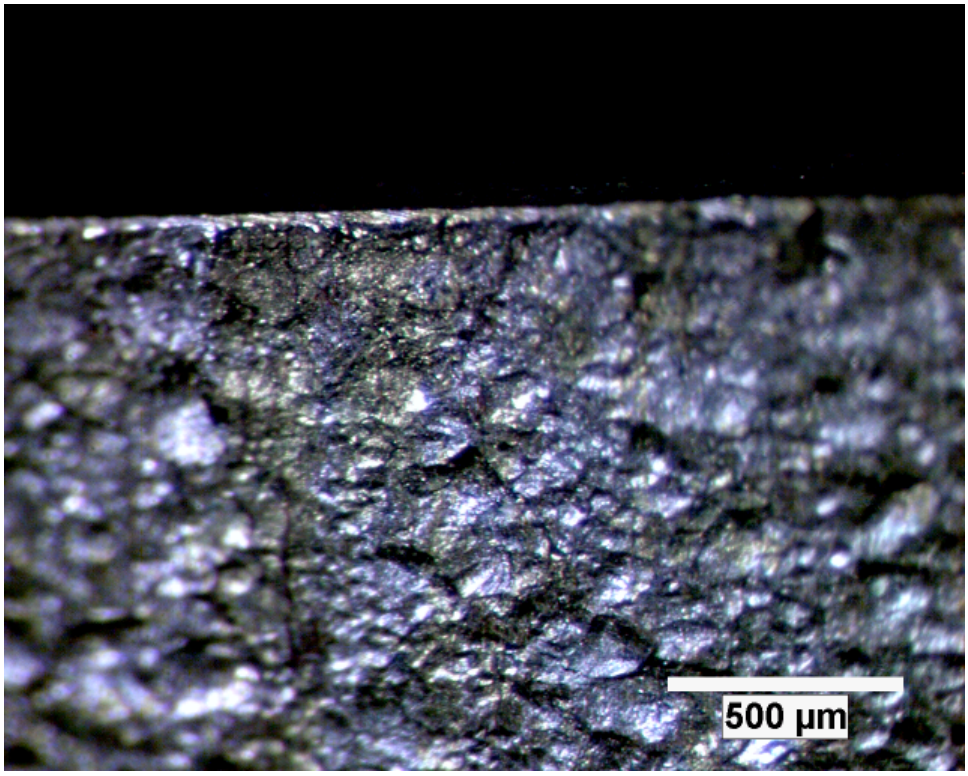


(b)

***Figure 6.18(cont'd):*** ***(b) Micrographs of S44627 U-bend specimens tested in 2.5 M NaOH + 0.70 M $Na_2S$ at 190 $^oC$ show the influence of environment. No SCC was observed on these superferritic steel samples in tested environments.***

Figure 6.19 shows SCC of S32205 tested in 3.75 M NaOH + 0.64 M $Na_2S$ at170 $^oC$. Crack growth was primarily along austenite/ferrite phase boundaries and through the austenite phase in the standard DSS grade. S32205 was not susceptible to SCC in the simple alkaline environments. Optical micrographs in Figure 6.20 show differences in the SCC behavior of S32101 tested in 2.5 M + 0.70 M $Na_2S$ and 3.75 M NaOH + 0.64 M $Na_2S$ at 170 $^oC$ indicated that the crack growth behavior varied with environment. Cracking was primarily in the austenite phase in both environments. Preferential corrosion of the austenite phase was more prevalent in the solution with higher sulfidity

(2.5 M NaOH + 0.70 M $Na_2S$). Crack initiation and crack propagation occurred in the austenite phase in alkaline-sulfide environments.

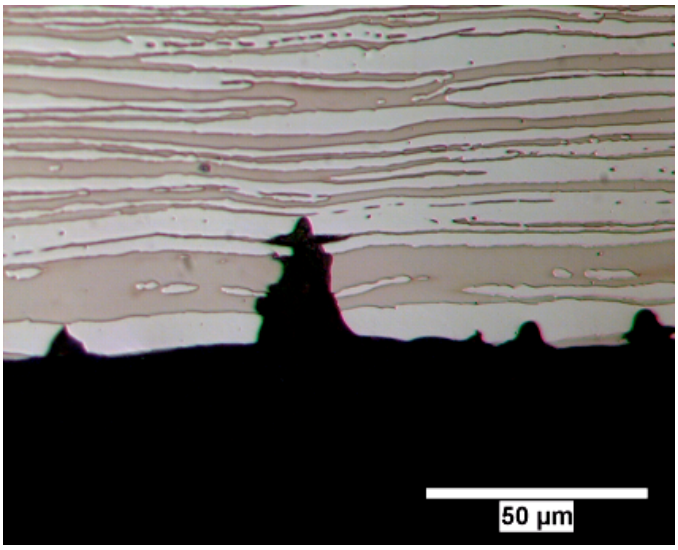


(a)

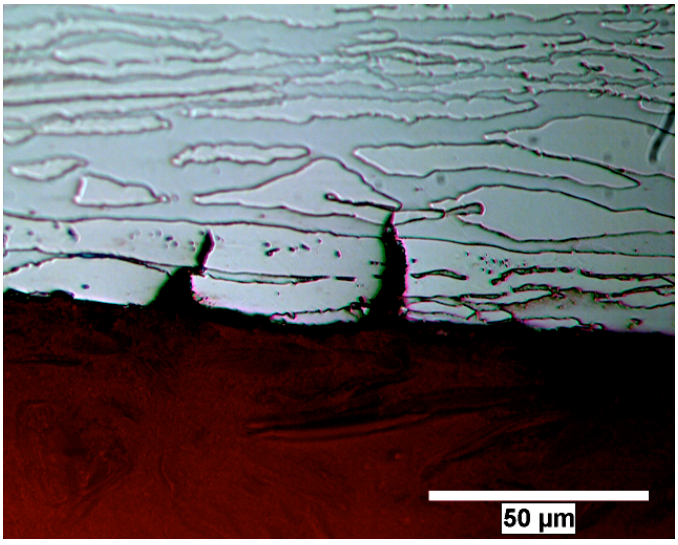


(b)

***Figure 6.19:*** ***Optical micrograph showing stress corrosion crack growth (a) along austenite/ferrite phase boundaries and (b) through austenite phase in standard DSS S32205 tested in 3.75 M + 0.64 M $Na_2S$ at 170 $^{o}$C.***

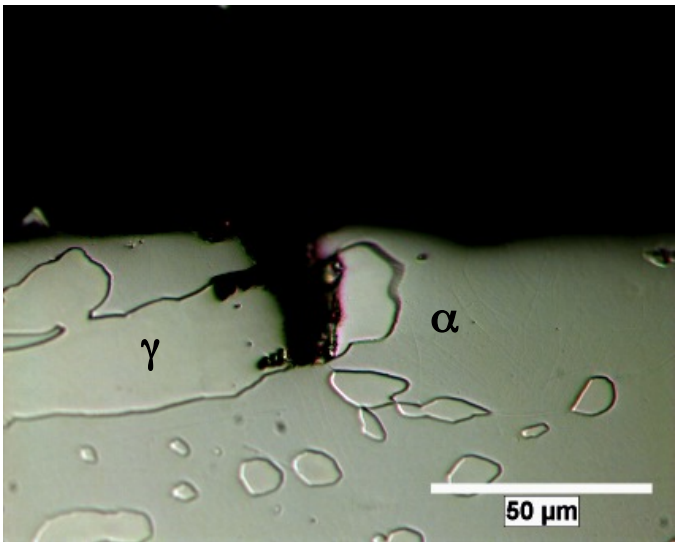


(a)

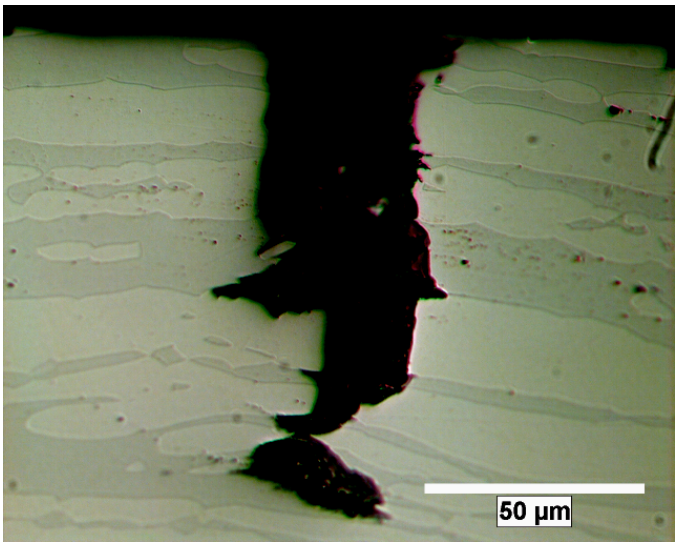


(b)

***Figure 6.20:*** ***Optical micrograph showing stress corrosion cracks for lean DSS S32101 in (a) 2.5 M + 0.70 M $Na_2S$ and (b) 3.75 M + 0.64 M $Na_2S$ tested at 170 $^oC$.***

The surface of S32205 tested in 3.75 M NaOH + 0.64 M $Na_2S$ at 170 $^oC$ (Figure 6.21a) showed brittle fracture associated with failure by TGSCC. Cleavage fracture in the high magnification micrograph (Figure 6.21b) shows that both phases failed in a brittle manner. Grain boundaries were crossed without apparent effect although austenite/ferrite

phase boundaries were favorable paths for crack growth. Secondary cracks were observed due to the propagation of cracks along austenite/ferrite phase boundaries. The anisotropic microstructure clearly had an appreciable influence on crack growth behavior (Chapter 7).

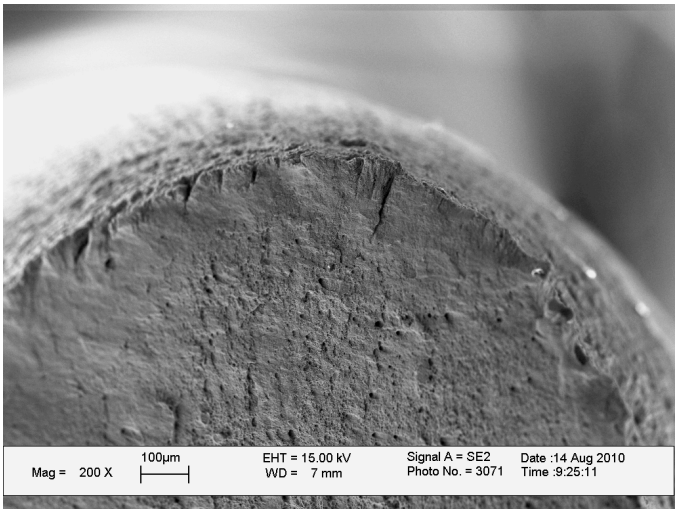


(a)

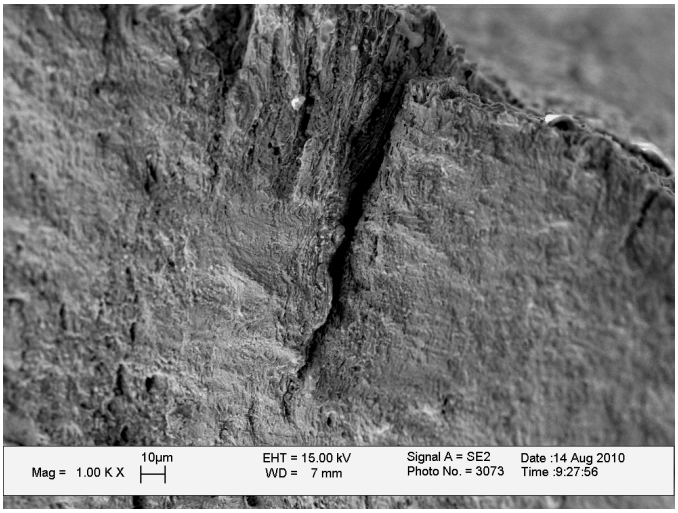


(b)

***Figure 6.21:*** ***(a) Low magnification and (b) high magnification SEM micrographs showing fracture surface of lean DSS S32205 tested in 3.75 M NaOH + 0.64 M $Na_2S$ at 170 $^{o}$C. Arrow corresponds to region shown in (b).***

A cross-sectioned specimen of S32205 tested in 3.75 M NaOH + 0.64 M $Na_2S$ at 170 $^oC$ was mounted in conductive resin, polished, and examined under SEM (Figure 6.22). Crack growth along austenite/ferrite phase boundaries was evident in two orientations (normal to loading direction and along loading direction). Microcracks were observed in the defective oxide near the crack tip, although no cracks were observed in the base material. Representative spectra from EDS were taken near the crack tip to determine the composition of the oxide film. The spectra were normalized and compared based on the ratio of each cation to total cation percentage for qualitative comparisons. Outer layer was approximately (9 wt % Fe, 16 wt % Cr, and 75 wt % Ni) and inner layer was approximately (26 wt % Fe, 62 wt % Cr, and 10 wt % Ni) based on the average of 15 measurements. S was enriched in the film (ca. 10 wt %), particularly in the Ni-rich, outer layer. This layer may have been the redeposition of nickel sulfide.

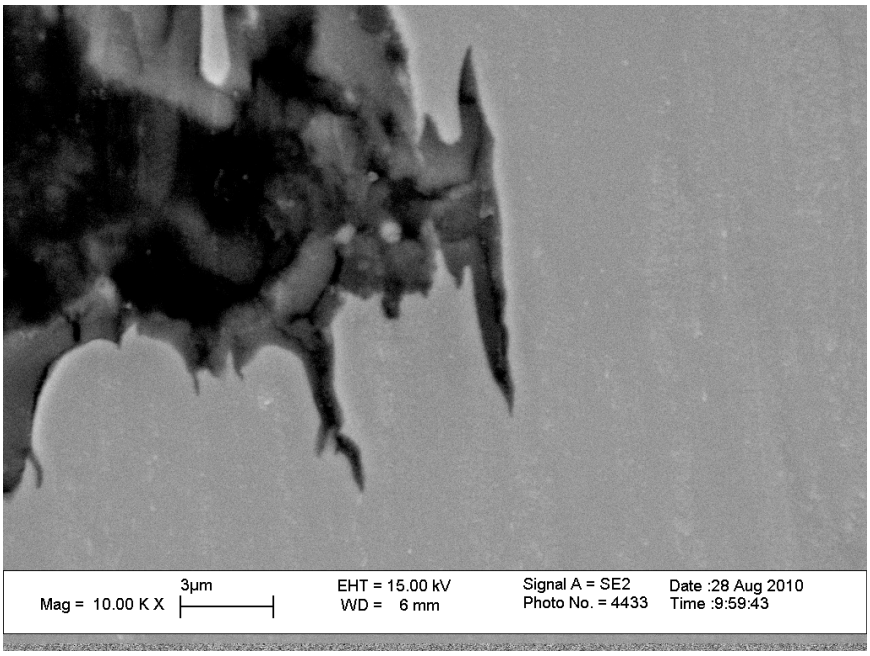


(a)

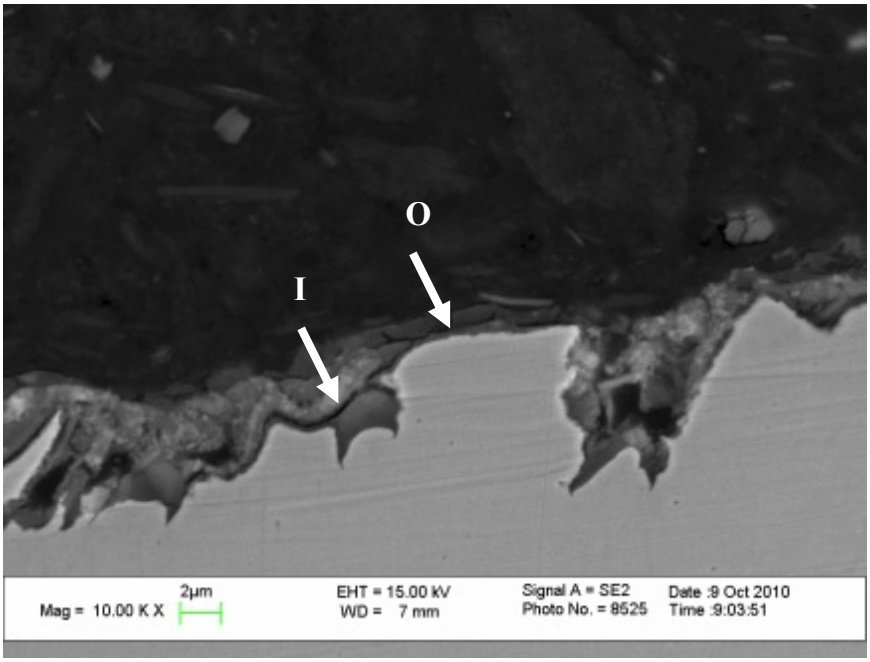


(b)

***Figure 6.22:*** ***SEM micrographs showing cross-sectional views of SCC cracks oriented (a) along the loading direction and (b) normal to load direction on standard DSS S32205 slow strain rate specimen tested in 3.75 M NaOH + 0.64 M $Na_2S$ at 170 $^oC$. The "O" and "I" indicate the outer and inner regions of the surface layers examined with EDS, respectively.***

The surface of S32101 tested in 3.75 M NaOH + 0.64 M $Na_2S$ at 170 $^oC$ (Figure 6.23a) showed brittle, quasi-cleavage fracture associated with failure by TGSCC. River patterns associated with the re-initiation of crack growth at either austenite grain boundaries or austenite/ferrite phase boundaries were seen in the high magnification image. Areas of ductile rupture (microvoids) are also evident in the figure, but it is not clear whether these regions correspond to different grains or phases. The orientation of the largest crack in Fig 6.22a corresponds to the micro-features in Figure 6.22b (indicated by arrow). Secondary cracks were observed (Figure 6.22a) due to the propagation of cracks along austenite/ferrite phase boundaries.

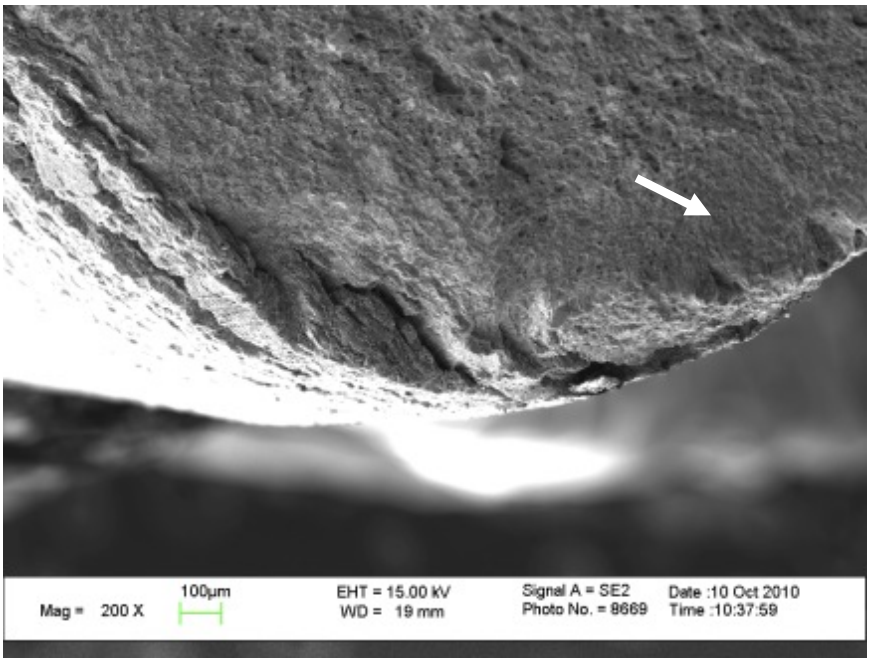


(a)

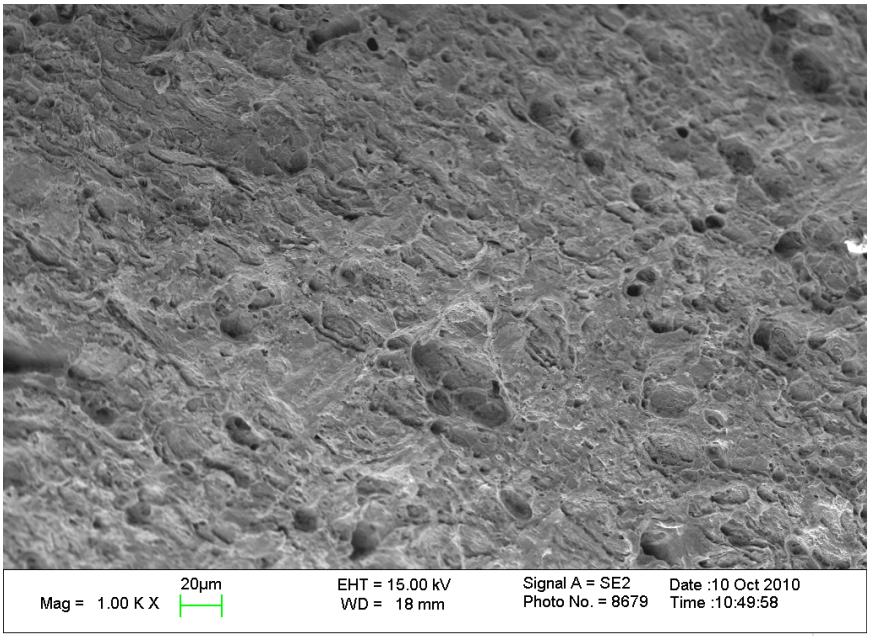


(b)

***Figure 6.23:*** ***(a) Low magnification and (b) high magnification SEM micrographs showing fracture surface of lean DSS S32101 tested in 3.75 M NaOH + 0.64 M $Na_2S$ at 170 $^{o}$C. Arrow corresponds to region shown in (b).***

SEM micrographs (Fig 6.24) of the S32101 specimen tested in 3.75 M NaOH + 0.64 M $Na_2S$ at 170 $^oC$ show crack growth along austenite/ferrite phase boundaries in two orientations (normal to loading direction and along loading direction). The contrast in the secondary electron micrograph was sufficient to show distinct phase regions. Representative spectra from EDS were taken near the crack tip to determine the composition of the defective oxide film. Outer layer was approximately (89 wt % Fe, 9 wt % Cr, 1 wt % Mn, and < 1 wt % Ni) and inner layer was approximately (76 wt % Fe, 20 wt % Cr, 4 wt % Mn, and 1 wt % Ni) based on the average of 15 measurements. S was detected in small amounts (< 1 wt %) independent of spectra location. Results show that the film composition was Fe and Cr rich, which differed from the S32205 sample tested under the same conditions.

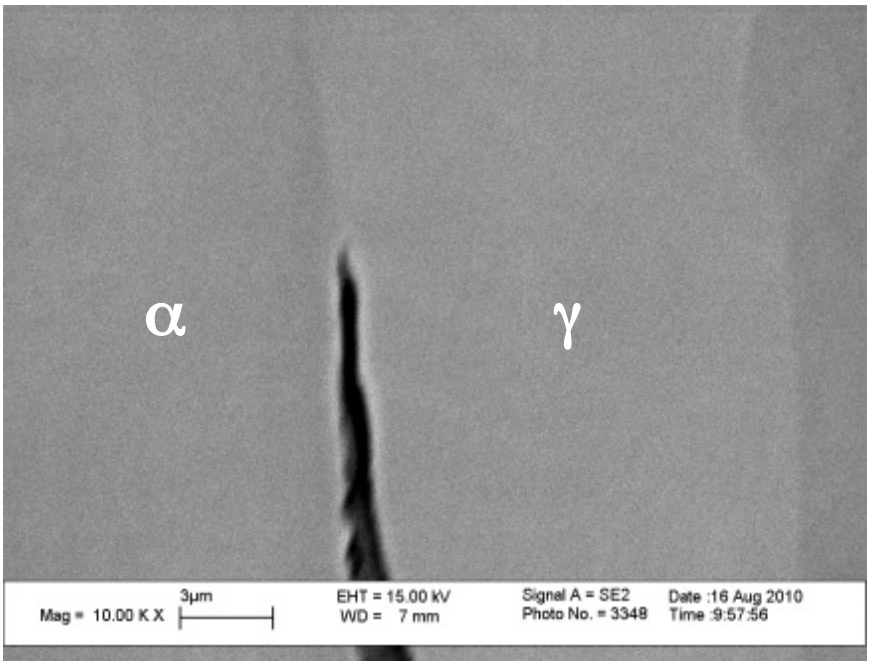


(a)

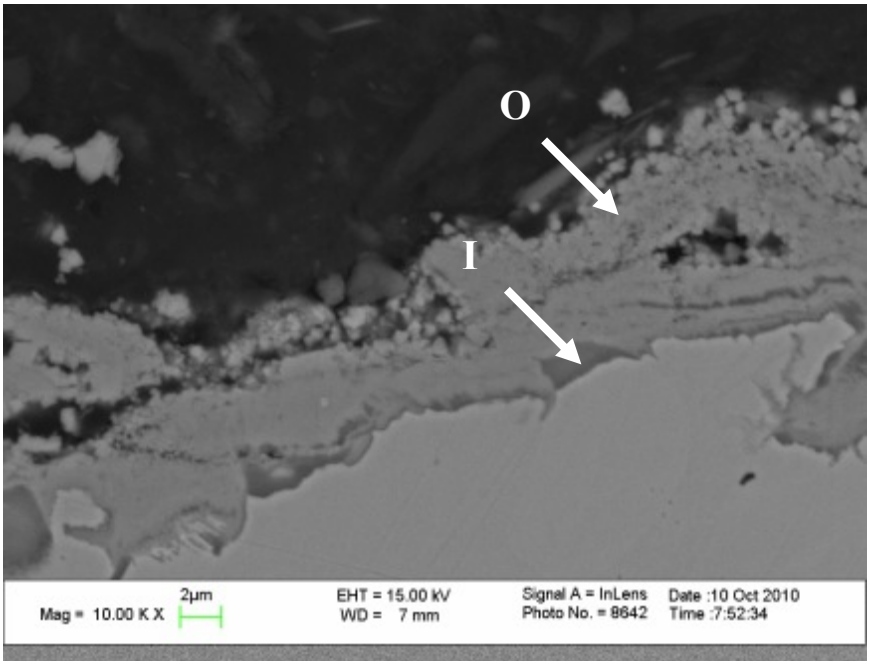


(b)

***Figure 6.24:*** ***SEM micrographs showing cross-sectional views of SCC cracks oriented (a) along the load direction and (b) normal to the loading direction on standard DSS S32101 slow strain rate specimen tested in 3.75 M NaOH + 0.64 M $Na_2S$ at 170 $^{o}$C. The "O" and "I" indicate the outer and inner regions of the surface layers examined with EDS, respectively.***

The results of the SSRT testing indicated that standard DSS S32205 and lean DSS S32101 were susceptible to SCC in sulfide-containing caustic environments at 170 $^{o}$C, and the susceptibility increased with the effective alkali content (defined in Chapter 3) of the alkaline-sulfide solution. Superferritic S44660 and S44627 U-bend specimens were not susceptible to SCC in the 155 g/l $Na_2O$ solution (2.5 M NaOH + 0.70 $Na_2S$) even at 190 $^{o}$C, but did undergo intergranular corrosion. Austenitic (300 series) grades were not tested in the current study, but have been shown to be highly susceptible to SCC in hot alkaline-sulfide solution [1-7].

Standard DSS 32205 was not susceptible to SCC in the solution with an effective alkali of 155 g $l^{-1}$ $Na_2O$ and 35 % sulfidity, but was susceptible in the 200 g $l^{-1}$ $Na_2O$ and 25 % sulfidity (3.75 M NaOH + 0.64 $Na_2S$) solution. Increased sulfidity enhanced preferential corrosion of the austenite phase, but did not necessarily correlate to increased crack growth rates. Crack growth rates for S32101 tested in the 155 g $l^{-1}$ $Na_2O$ solution were nearly an order of magnitude lower than those in the 200 g $l^{-1}$ $Na_2O$ solution.

Analysis of the failed DSS specimens showed that TGSCC growth corresponded to brittle features (quasi-cleavage) on the fracture surface. Crack growth occurred primarily in the austenite phase and along austenite/ferrite phase boundaries. Crack initiation was also in the austenite phase. Bhattacharya [8] also showed SCC crack initiation and growth was primarily in the austenite phase for different grades of DSS tested in alkaline-sulfide solution at 140 - 170 $^{o}$C. Field studies of failed DSS equipment [10,12,25] have shown a similar behavior.

The oxide film composition near the crack tip of S32205 tested in sulfide-containing caustic solution was enriched in Cr and Ni indicating that other elements (Fe,

Mo, and Mn) were selectively dissolved in the presence of sulfide. Results for the film composition and morphology suggest that the adsorption of sulfide favored defective film formation. Dissolution was favored along austenite/ferrite phase boundaries as evident by the crack growth behavior. Cracks were isolated to the oxide layer and were not identified in the base metal. The oxide film of S32101 was enriched in Fe. However, the general crack initiation and growth mechanism was similar to S32205. The difference in film composition showed the significant influence of Ni on film formation. Results of this work are consistent with a film breakdown and repair mechanism for SCC.

## 6.4 Effect of Chloride

### 6.4.1 NaOH + NaCl Environments

6.4.1.1 Stress Corrosion Cracking Susceptibility of DSS in Chloride-Containing Caustic Solutions

The engineering stress vs. % elongation curves from SSRT of DSS S32205 at an initial strain rate of 2 x $10^{-6}$ $s^{-1}$ in several chloride-containing caustic solutions at 170 $^{o}$C are shown in Figure 6.25. The curves for lean DSS S32101 tested in the same solutions are shown in Figure 6.26. A sample tested in sand at 170 $^{o}$C is shown for comparison in each figure. The DSS samples tested in the environments always had a lower % el at failure even in the absence of SCC (S32205). Chloride addition caused a minimal reduction in the % el. values at failure for S32205; however, the trend in the % el. at failure for S32101 was dependent on the solution alkalinity. An increase in the ratio of NaCl to NaOH enhanced the severity of SCC, which is consistent with the trend for corrosion behavior (Chapter 5).

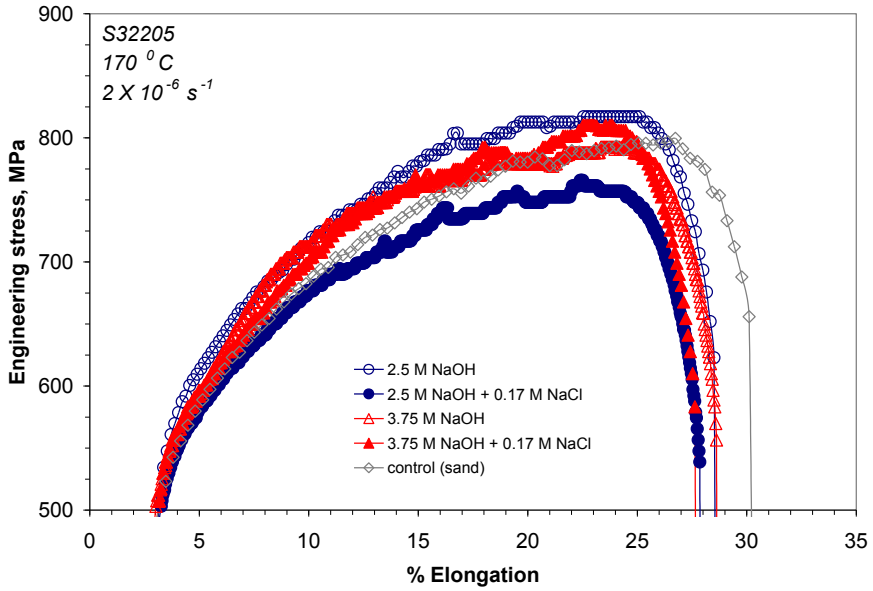


*Figure 6.25:* ***Engineering stress - % elongation curves for S32205 tested at an initial strain rate of 2 x $10^{-6}$ $s^{-1}$ in different alkaline environments with and without NaCl at 170 $^{O}$C.***

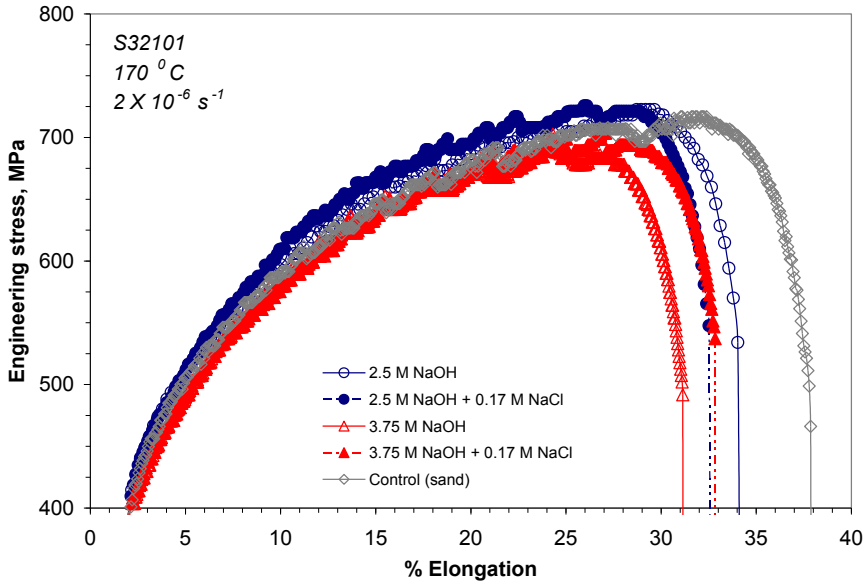


*Figure 6.26:* ***Engineering stress - % elongation curves for S32101 tested at an initial strain rate of 2 x $10^{-6}$ $s^{-1}$ in different alkaline environments with and without NaCl at 170 $^{O}$C.***

The SSRT results for S32205 and S32101 tested in alkaline-chloride solutions are shown in Table 6.3. Results show that S32205 was not susceptible to SCC at 170 $^{o}$C, thus chloride did not alter the SCC susceptibility of this material with respect to the NaOH solutions. S32101 was susceptible to TGSCC in the two solutions that were tested. The severity was greater in 2.5 M NaOH + 0.17 M NaCl due to the higher ratio of NaCl to NaOH, although there were more crack initiation sites in the solution with higher alkalinity based on the average crack density. Crack initiation in the more alkaline environment was facilitated by enhanced corrosion of the ferrite phase. Lean DSS S32101 was more susceptible to SCC in alkaline-chloride solution as compared to standard DSS S32205, which is consistent with the NaOH environment

***Table 6.3: SCC data for S32205 and S32101 tested in alkaline chloride environments at 170 $^{O}$C.***

| *Alloy* | *Solution Composition* | *Cracking Susceptibility* | *Max. Crack Velocity, mm s$^{-1}$* | *Avg. Crack Density, mm$^{-1}$* | *% Reduction in Area* |
|---|---|---|---|---|---|
| S32205 | 2.5 M NaOH + 0.17 M NaCl | No SCC | - | - | 83 |
| S32205 | 3.75 M NaOH+ 0.17M NaCl | No SCC | - | - | 85 |
| | | | | | |
| S32101 | 2.5 M NaOH + 0.17 M NaCl | IGSCC & TGSCC | 3.8E-07 | 8 | 63 |
| S32101 | 3.75 M NaOH + 0.17 M NaCl | IGSCC & TGSCC | 1.9E-07 | 28 | 64 |

6.4.1.2 Crack and Fracture Surface Morphology

Micrographs in Figure 6.27 and Figure 6.28 show the surface morphology of the S32205 and S32101 SSRT specimens, respectively, that were tested to failure in 2.5 M NaOH with and without 0.17 M NaCl at 170 $^{o}$C. Surface cracks on the surface of S32101 can not be resolved in the figure. The surface films that formed on the S32205 specimens

appeared to be relatively uniform and adherent, whereas the films on the S32101 specimens were defective and non-adherent. There was a visible reduction in the ductility of the S32101 tested in the chloride-containing solution based on the limited necking near the fracture

***Figure 6.27:*** ***Micrographs of DSS S32205 tensile specimens tested in (left) 2.5 M NaOH and (right) 2.5 M NaOH + 0.17 M NaCl at 170 $^{o}$C show influence of environment.***

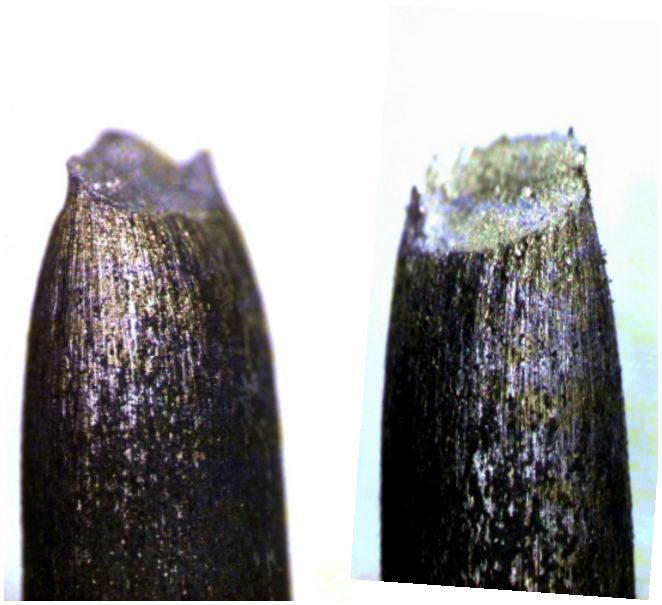

*Figure 6.28:* ***Micrographs of DSS S32101 tensile specimens tested in (a) 2.5 M NaOH and (b) 2.5 M NaOH + 0.17 M NaCl at 170 $^{o}$C show influence of environment.***

Optical micrographs in Figure 6.29 show the SCC behavior of S32101 in the 2.5 M NaOH + 0.17 M NaCl environment. Preferential corrosion of the austenite phase favored crack initiation in the austenite phase at austenite/ferrite phase boundaries (Figure 6.29a). Crack propagation (Figure 6.29b) was primarily in the austenite phase and along ferrite grain boundaries. Figure 6.30 shows SCC of S32101 tested in 3.75 M NaOH + 0.17 M NaCl at 170 $^{o}$C. Crack initiation occurred mainly at ferrite grain boundaries, but the growth of SCC cracks was primarily through ferrite grains. Chloride addition has been shown to enhance the susceptibility of the ferrite phase of DSS [21-24], but this finding was not shown elsewhere in hot caustic environments.

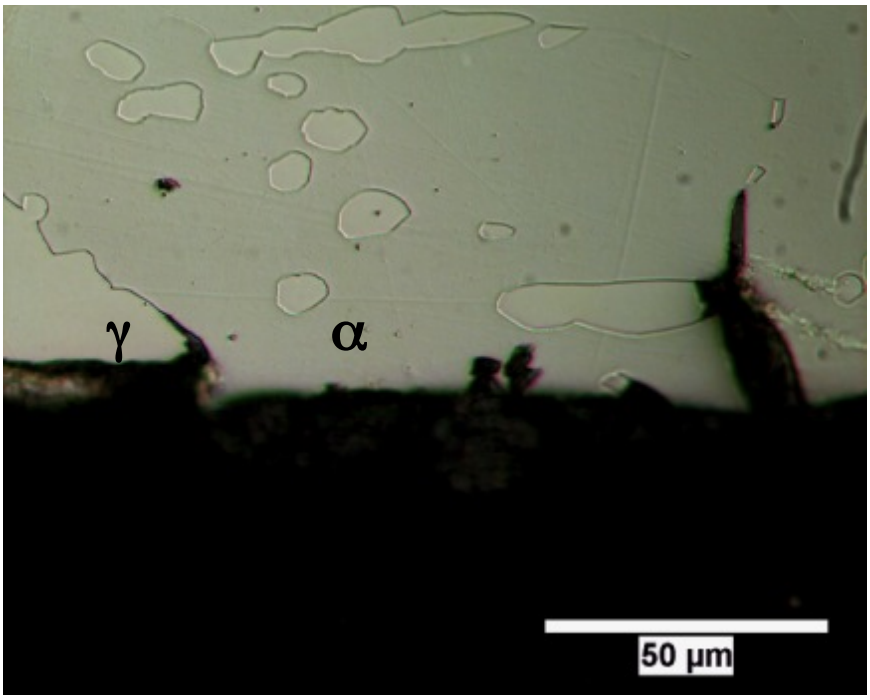


(a)

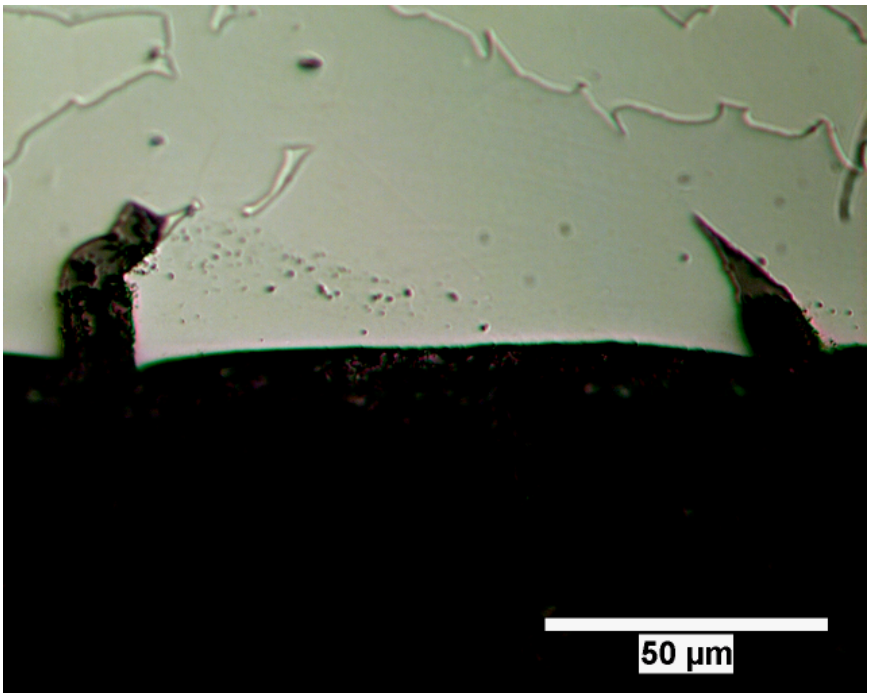


(b)

***Figure 6.29:*** ***Optical micrograph showing stress corrosion cracks for lean DSS S32101 in (a) 2.5 M NaOH + 0.17 M NaCl showing in austenite (light etching phase) and (b) 3.75 M NaOH in ferrite phase (dark etching phase) tested at 170 $^{o}$C.***

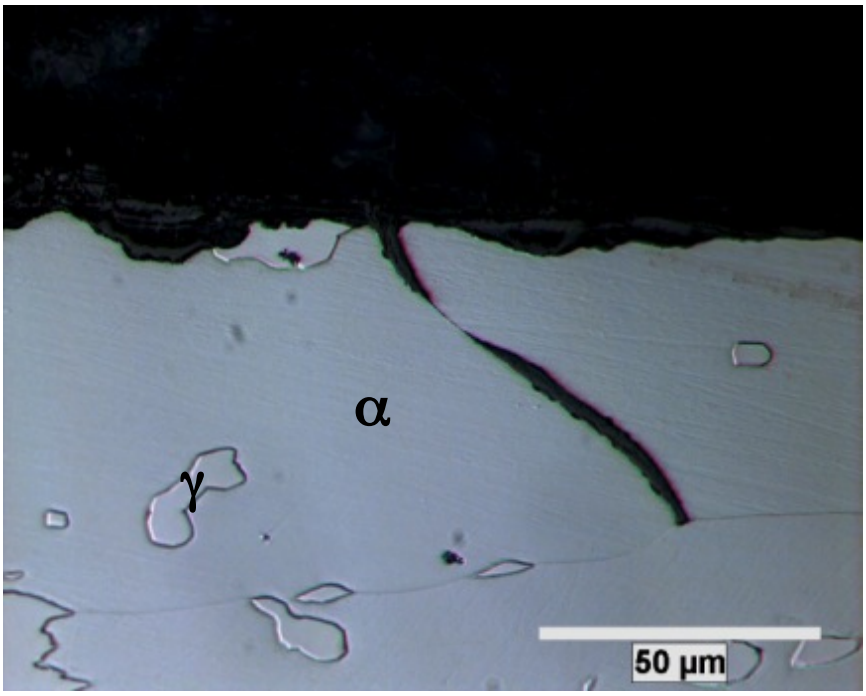


(a)

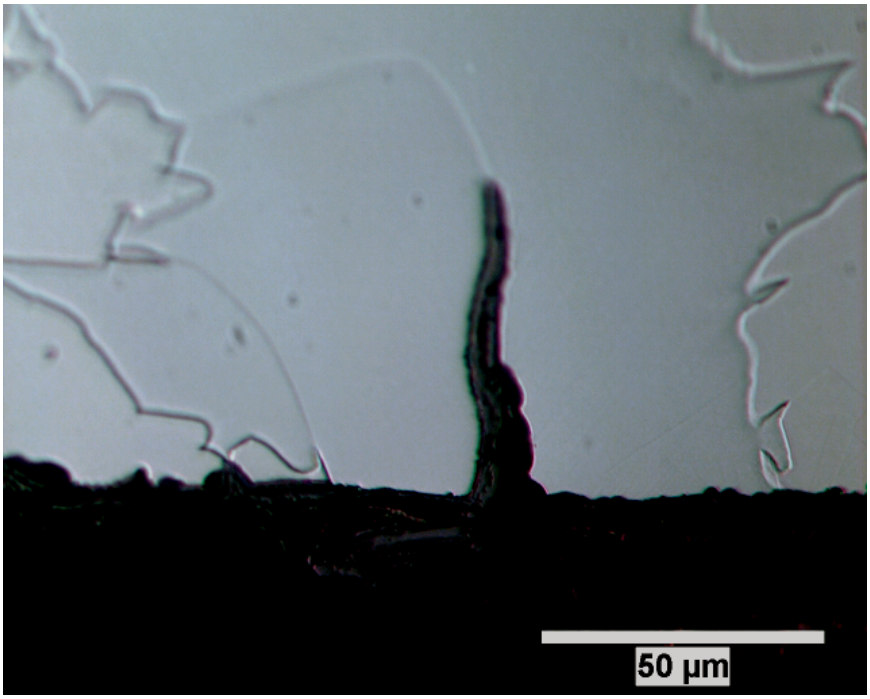


(b)

***Figure 6.30:*** ***Optical micrograph showing stress corrosion cracks for lean DSS S32101 in (a) 2.5 M NaOH + 0.17 M in ferrite (dark etching phase) and (b) 3.75 M NaOH + 0.17 M in ferrite phase (dark etching phase) tested at 170 $^{o}$C.***

The surface of S32101 tested in 3.75 M NaOH + 0.17 M NaCl at 170 $^{o}$C (Figure 6.31) showed a mixed fracture mode associated with failure. Cracks grew by intergranular stress corrosion cracking (IGSCC) or intergranular corrosion for a few grains and then transitioned to TGSCC (Figure 6.31b). IGSCC is evident in Figure 6.31c by the faceted surface appearance near the edge of the specimen. TGSCC growth was associated with rapid fracture; however, crack initiation and the initial stages of crack growth were associated with intergranular corrosion. Microvoid formation was observed near the crack initiation site, although microvoid coalescence was not the failure mechanism.

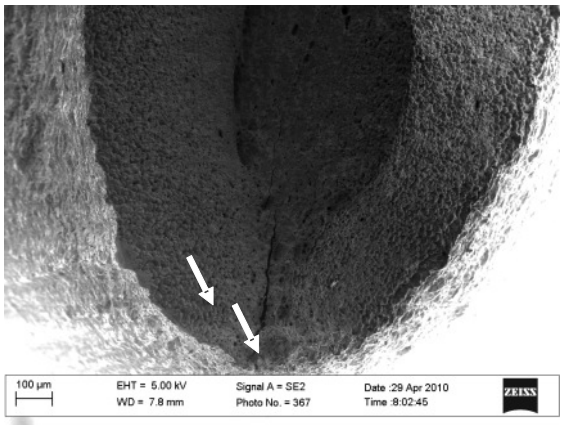


(a)

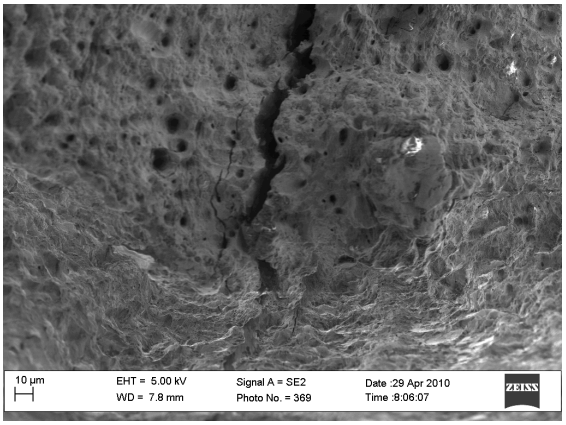


(b)

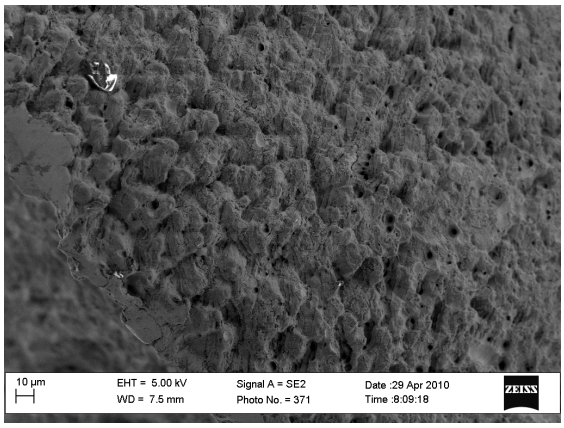


(c)

***Figure 6.31:*** ***(a) Low magnification and (b) high magnification SEM micrographs showing fracture surface of lean DSS S32101 tested in 3.75 M NaOH + 0.17 M NaCl at 170 $^{o}$C. Arrows corresponds to regions shown in (b) and (c).***

### 6.4.2. NaOH + $Na_2S$ + NaCl Environments

6.4.2.1 Stress Corrosion Cracking Susceptibility of DSS in Chloride- and Sulfide-Containing Caustic Solutions

Chloride had an effect on the engineering stress vs. % elongation curves for standard DSS S32205 tested alkaline-sulfide solutions at 170 $^{o}$C as shown in Figure 6.32. The results indicate that there was an appreciable reduction in the % elongation at failure for the specimen tested in 3.75 M NaOH + 0.64 M $Na_2S$ + 0.17 M NaCl. Figure 6.33 shows the engineering stress vs. % el for lean DSS S32101. There are no notable differences between the curves for S32101 in the presence or absence of 0.17 M chloride.

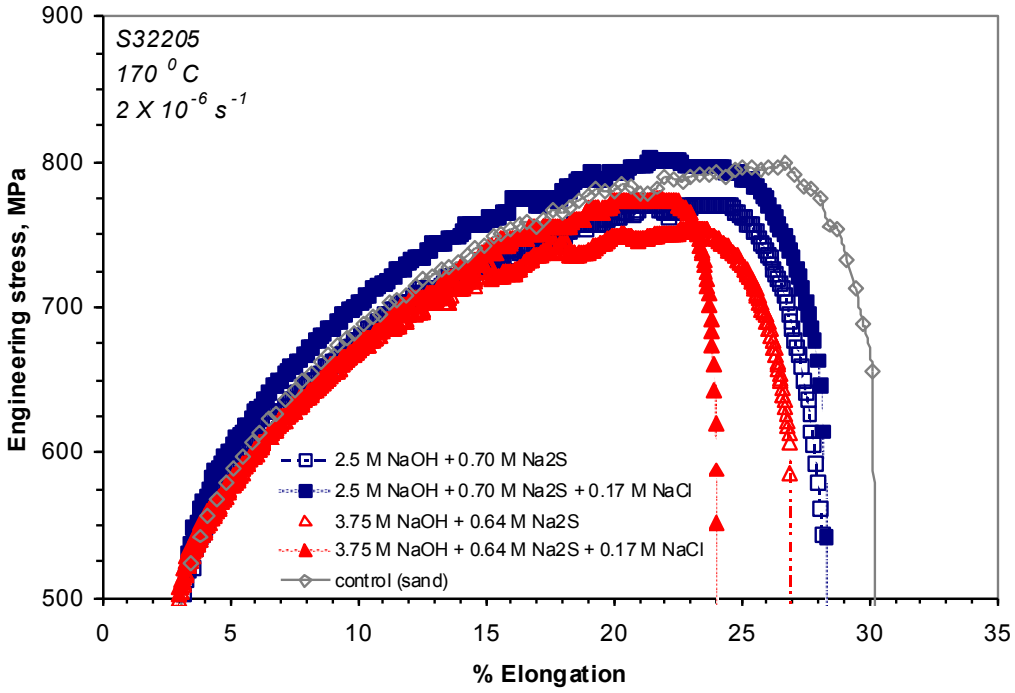


***Figure 6.32:*** ***Engineering stress - % elongation curves for S32205 tested at an initial strain rate of 2 x 10$^{-6}$ s$^{-1}$ in different alkaline-sulfide environments with and without NaCl at 170 $^{O}$C.***

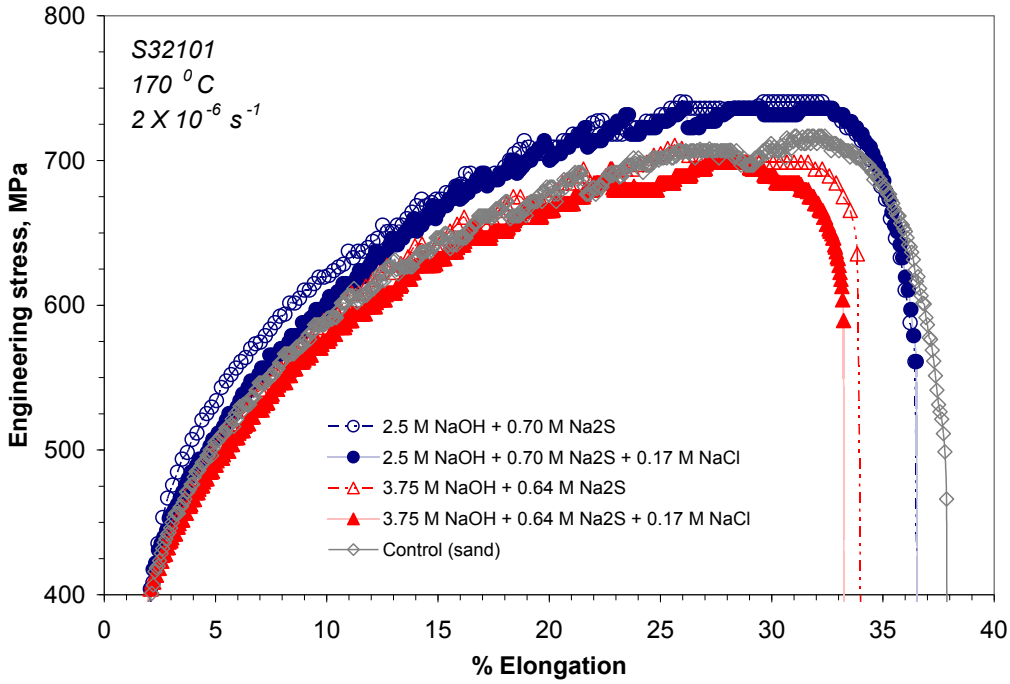


***Figure 6.33:*** ***Engineering stress - % elongation curves for S32101 tested at an initial strain rate of 2 x $10^{-6}$ $s^{-1}$ in different alkaline-sulfide environments with and without NaCl at 170 $^{O}$C.***

The SSRT results for S32205 and S32101 tested in sulfide-containing caustic solutions are shown in Table 6.4. Results show that S32205 was not susceptible to SCC in the 2.5 M NaOH + 0.70 $Na_2S$ at 170 $^{o}$C with or without chloride. TGSCC of S32205 did occur in the solution with a higher effective alkalinity. S32101 was susceptible to TGSCC in all of the solutions that were tested, but chloride did not appear to have an effect on the SSRT results as compared to the results for the sulfide-containing caustic solutions without chloride. The severity of SCC in both materials was greater in the higher effective alkali solution based on the maximum crack velocity, average crack densities and % RA. Maximum crack velocity was nearly an order of magnitude greater and crack density doubled for S32101 tested in the higher effective alkali solution (3.75

M NaOH + 0.64 M Na2S) as compared with the chloride- and sulfide-containing caustic solution.

***Table 6.4:*** ***SCC data for S32205 and S32101 tested in alkaline-sulfide environments with and without 0.17 M NaCl at 170 $^{O}$C.***

| *Alloy* | *Test Solution Composition* | *Cracking Susceptibility* | *Max. Crack Velocity, mm $s^{-1}$* | *Avg. Crack Density, $mm^{-1}$* | *% Reduction in Area* |
|---|---|---|---|---|---|
| S32101 | 2.5 M NaOH + 0.70 M $Na_2S$ | TGSCC | 1.6E-07 | 9 | 70 |
| S32101 | 2.5 M NaOH + 0.70 M $Na_2S$ + 0.17 M NaCl | TGSCC | 2.8E-07 | 6 | 67 |
| S32101 | 3.75 M NaOH + 0.64 M $Na_2S$ | TGSCC | 1.3E-06 | 21 | 44 |
| S32101 | 3.75 M NaOH + 0.64 M $Na_2S$ + 0.17 M NaCl | TGSCC | 9.1E-07 | 21 | 56 |
| | | | | | |
| S32205 | 2.5 M NaOH + 0.70 M $Na_2S$ | No SCC | - | - | 86 |
| S32205 | 2.5 M NaOH + 0.70 M $Na_2S$ + 0.17 M NaCl | No SCC | - | - | 80 |
| S32205 | 3.75 M NaOH + 0.64 M $Na_2S$ | TGSCC | 5.3E-07 | 13 | 44 |
| S32205 | 3.75 M NaOH + 0.64 M $Na_2S$ + 0.17 M NaCl | TGSCC | 4.7E-07 | 12 | 41 |

A systematic study of the effect of chloride at 170 $^{o}$C was conducted in the alkaline-sulfide solution (3.75 M NaOH + 0.64 M $Na_2S$) that was found to be more aggressive. Various concentrations of NaCl were evaluated to determine if there was threshold for chloride content associated with SCC. The engineering stress vs. % elongation curves for S32205 (Figure 6.34) showed an appreciable influence on the severity of SCC based on the reduction in the % el. at failure. The ductility of the sample tested in alkaline-sulfide solution with 0.034 M NaCl (2 g $l^{-1}$) was reduced by nearly 50

%. There was gradual recovery in ductility with increasing chloride content thereafter. Conversely, the macro behavior of lean DSS S32101 in the presence of chloride (Figure 6.35) did not change considerably with respect to the chloride-free solution based on the % el. at failure. There was a limited reduction in ductility associated with failure in the higher concentrations of NaCl (0.17 – 1.7 M).

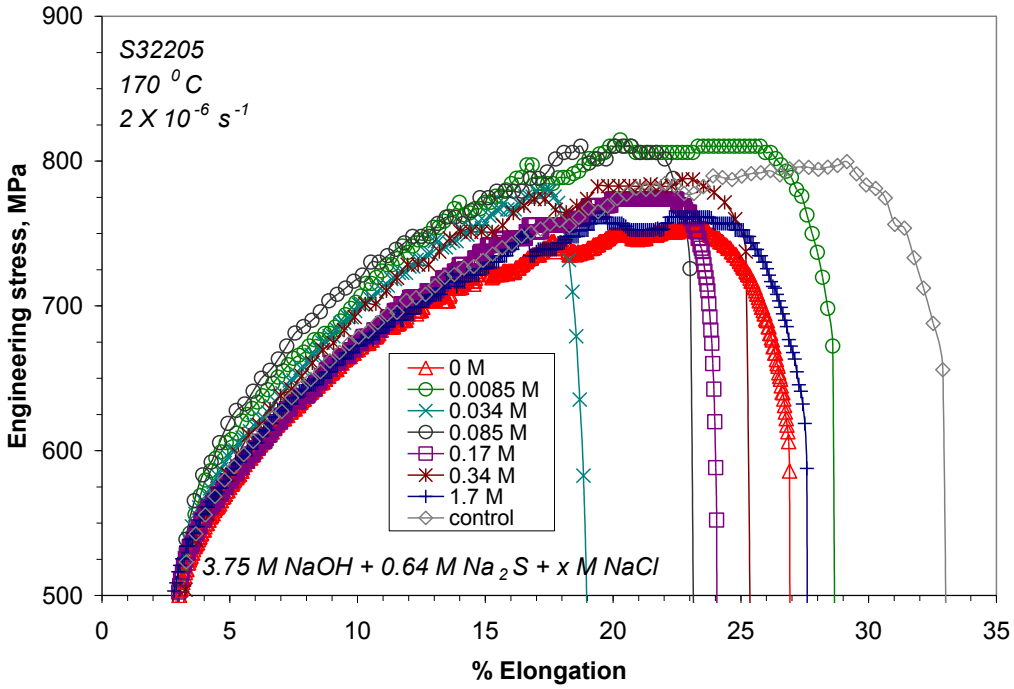


***Figure 6.34:*** ***Engineering stress - % elongation curves for S32205 tested at an initial strain rate of 2 x $10^{-6}$ $s^{-1}$ in different alkaline-sulfide environment (0.375 M NaOH + 0.64 M $Na_2S$) with various amounts of NaCl at 170 $^{O}$C.***

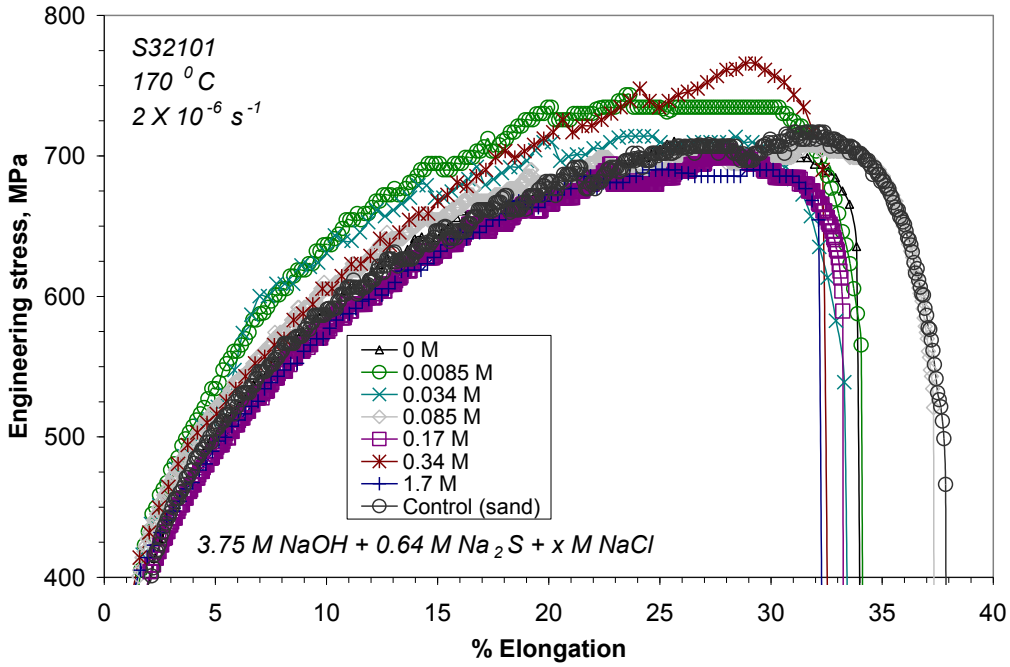


***Figure 6.35:*** ***Engineering stress - % elongation curves for S32101 tested at an initial strain rate of 2 x $10^{-6}$ $s^{-1}$ in alkaline-sulfide solution (0.375 M NaOH + 0.64 M $Na_2S$) with various amounts of NaCl at 170 $^{O}$C.***

The SSRT results for the specimens tested in different concentrations of chloride are shown in Table 6.5. The maximum number of crack initiation sites, i.e. crack density, in the tested materials correlated to an intermediate chloride content of 0.034 – 0.085 M (2 – 5 g $l^{-1}$ NaCl). As expected, the severity of SCC was also greatest for S32205 in this range of concentrations based on the maximum crack velocity and % RA. Crack density and maximum crack velocity generally increased together, indicating there was interaction among neighboring cracks. The most severe SCC in S32101 occurred with the highest concentrations of NaCl (0.17 M – 1.7 M).

***Table 6.5:*** ***SCC data for S32205 and S32101 tested in alkaline-sulfide solution (3.75 M NaOH + 0.64 M $Na_2S$) with various amounts of NaCl at 170 $^{O}$C.***

| *Alloy* | *Chloride Conc. (M)* | *Cracking Susceptibility* | *Max. Crack Velocity, mm $s^{-1}$* | *Avg. Crack Density, $mm^{-1}$* | *% Reduction in Area* |
|---|---|---|---|---|---|
| S32101 | 0 | TGSCC | 1.3E-06 | 21 | 44 |
| S32101 | 8.5E-04 | TGSCC | 2.5E-07 | 5 | 68 |
| S32101 | 3.4E-02 | TGSCC | 4.3E-07 | 28 | 67 |
| S32101 | 8.5E-02 | TGSCC | 3.0E-07 | 13 | 59 |
| S32101 | 1.7E-01 | TGSCC | 9.1E-07 | 21 | 56 |
| S32101 | 3.4E-01 | TGSCC | 1.8E-06 | 20 | 39 |
| S32101 | 1.7 | TGSCC | 8.4E-07 | 17 | 39 |
| | | | | | |
| S32205 | 0 | TGSCC | 5.3E-07 | 13 | 44 |
| S32205 | 8.5E-04 | TGSCC | 6.1E-07 | 24 | 48 |
| S32205 | 3.4E-02 | TGSCC | 2.0E-06 | 11 | 48 |
| S32205 | 8.5E-02 | TGSCC | 9.9E-07 | 35 | 22 |
| S32205 | 1.7E-01 | TGSCC | 4.7E-07 | 12 | 33 |
| S32205 | 3.4E-01 | TGSCC | 7.9E-07 | 16 | 41 |
| S32205 | 1.7 | TGSCC | 6.8E-07 | 15 | 57 |

The relationship between the severity of SCC and the molar concentration of NaCl is clearly shown in Figure 6.36, which compares the % RA for S32205 and S32101. The S32205 and S32101 specimens tested in chloride-free, alkaline-sulfide solution 3.75 M NaOH + 0.64 M $Na_2S$) both had a 44 % RA for comparison. The effect of chloride on SCC susceptibility was apparent with 0.085 M NaCl for both materials. A gradual reduction in the severity of SCC was observed with higher concentrations than 0.085 M for S32205. There was a steady increase in the severity of SCC with increasing chloride found for S32101.

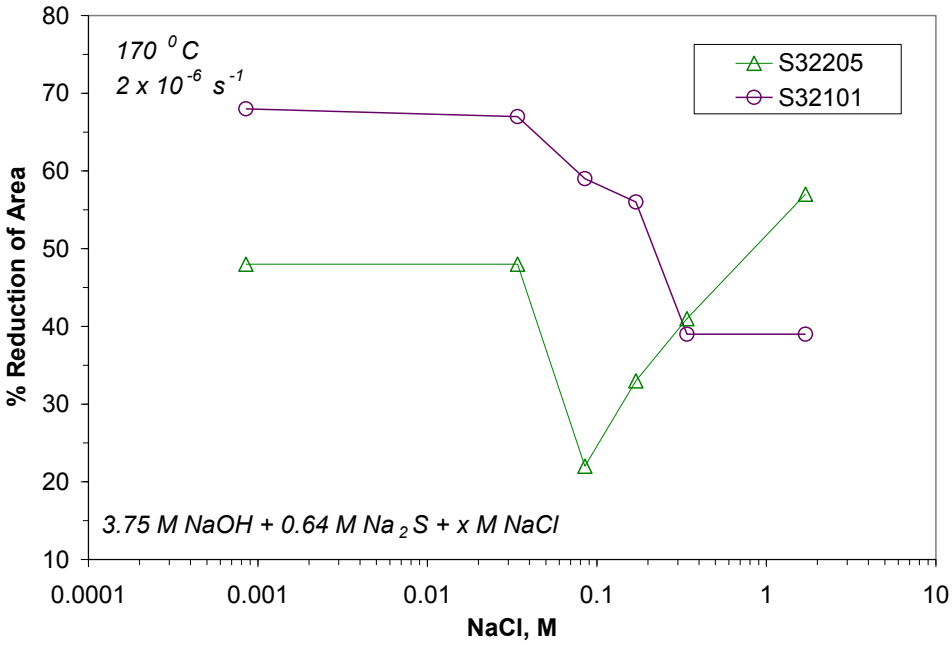


***Figure 6.36:*** ***Percent reduction in area for standard DSS S32205 and lean DSS S32101 tested at an initial strain rate of 2 x $10^{-6}$ $s^{-1}$ in alkaline-sulfide environment (0.375 M NaOH + 0.64 M $Na_2S$) with various amounts of NaCl at 170 $^{O}$C.***

The influence of chloride on stress corrosion crack initiation and coalescence can be seen in the necked regions of the failed DSS S32205 SSRT specimens (Figure 6.37). Crack coalescence is defined as the propensity for neighboring cracks to interact and combine to form larger cracks. The interaction of neighboring cracks is indicated by arrows in Figure 6.37. Singh and Parkins [41] studied crack coalescence of pipeline steel exposed to bicarbonate solution. The relative amount of short cracks increased with respect to the chloride-free solution when chlorides are present, thus chlorides favored crack initiation. With increasing chloride content (0.034 – 0.085 M), the number of total cracks begins to decrease, but the amount of longer cracks increased with respect to the number of short cracks. Crack coalescence was favored in the presence of chloride, which enhanced the severity of SCC.

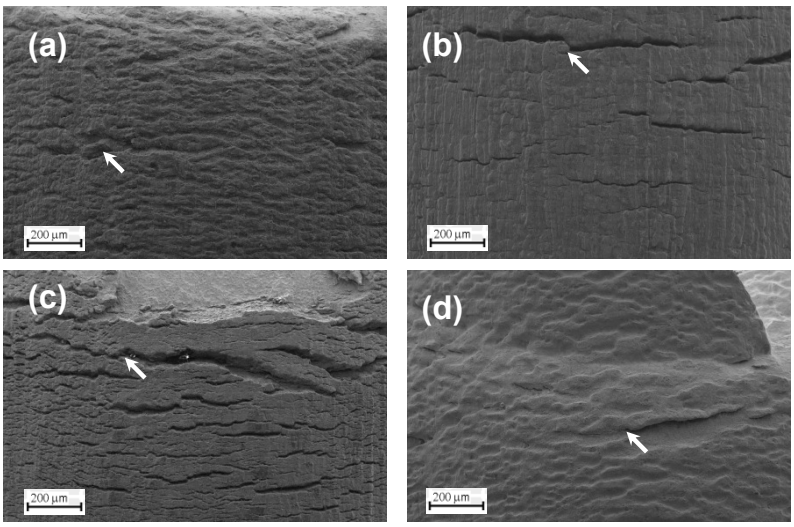


***Figure 6.37:*** ***Micrographs showing crack coalescences in the necked region of S32205 specimens tested at an initial strain rate of 2 x $10^{-6}$ $s^{-1}$ in alkaline-sulfide solution (0.375 M NaOH + 0.64 M $Na_2S$) with (a) 0 M, (b) 0.034 M, (c) 0.17 M, and (d) 1.7 M NaCl at 170 $^{O}$C.***

6.4.1.2 Crack and Fracture Surface Morphology

Chlorides enhanced the dissolution of the austenite and ferrite phases of DSS in sulfide-containing caustic solution, which had an influence on both crack initiation and crack propagation. Figure 6.38 shows the effect of increased dissolution on the crack morphologies that evolved in the S32205 specimens tested in alkaline-sulfide solution with chlorides. Preferential corrosion of the austenite phase was particularly noticeable in the concentration range of 0.034 – 0.085 M NaCl (Figure 6.39). The cracks that formed under these conditions often initiated in the austenite phase and grew through crack branching along slip planes. The corrosion of the two phases became more uniform with increasing chloride content. The increased corrosion facilitated crack blunting, which accounts for the reduction in the severity of SCC under the most concentrated chloride conditions.

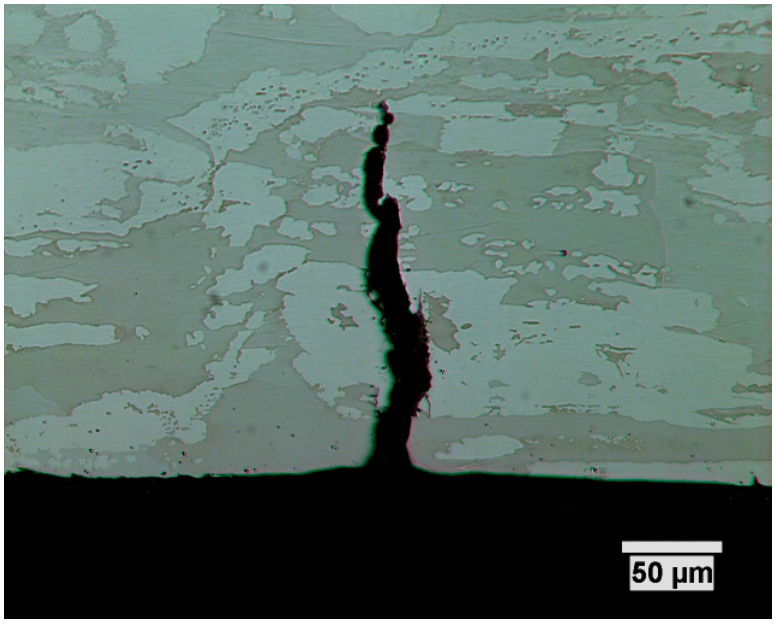


(a)

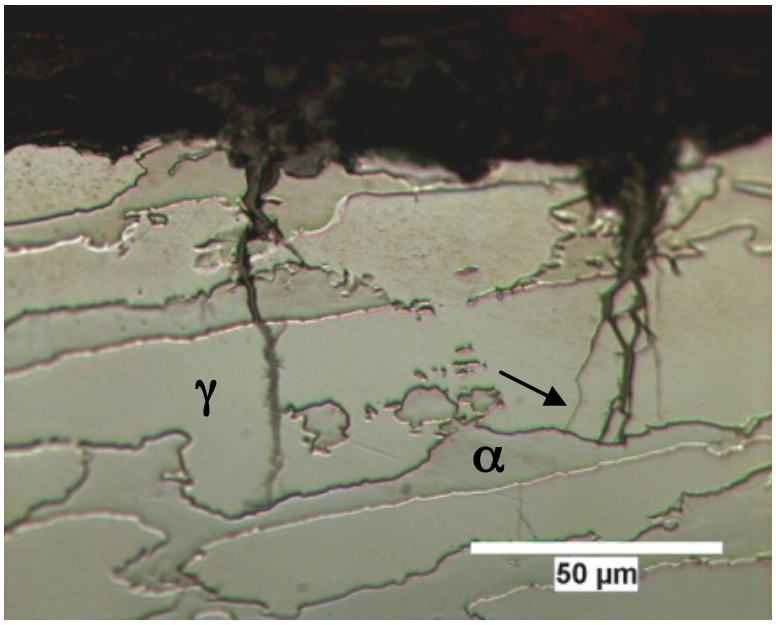


(b)

*Figure 6.38:* ***Micrographs showing the typical crack morphologies on SSRT S32205 specimens tested in alkaline-sulfide solution (150 g/l NaOH + 50 g/l $Na_2S$) containing (a) 0.034 M and (b) 0.085. Arrow indicates slip-step emergence.***

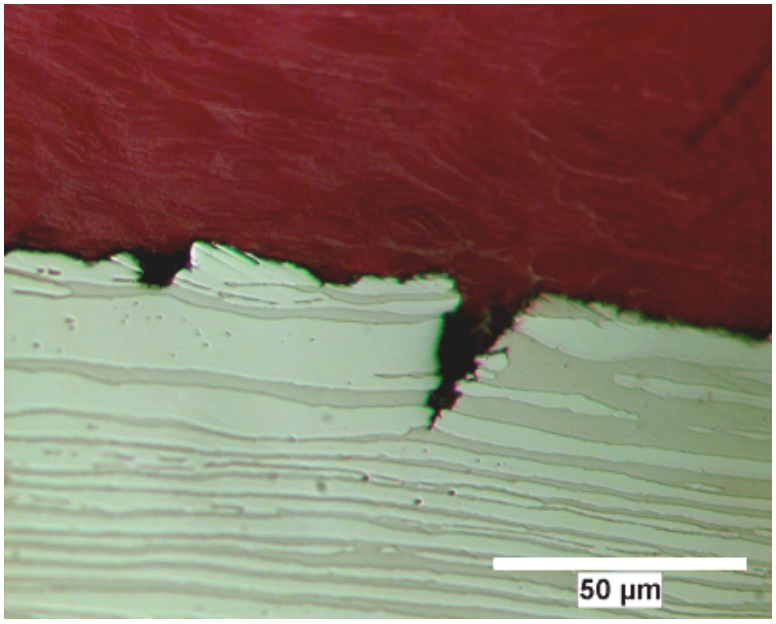


(c)

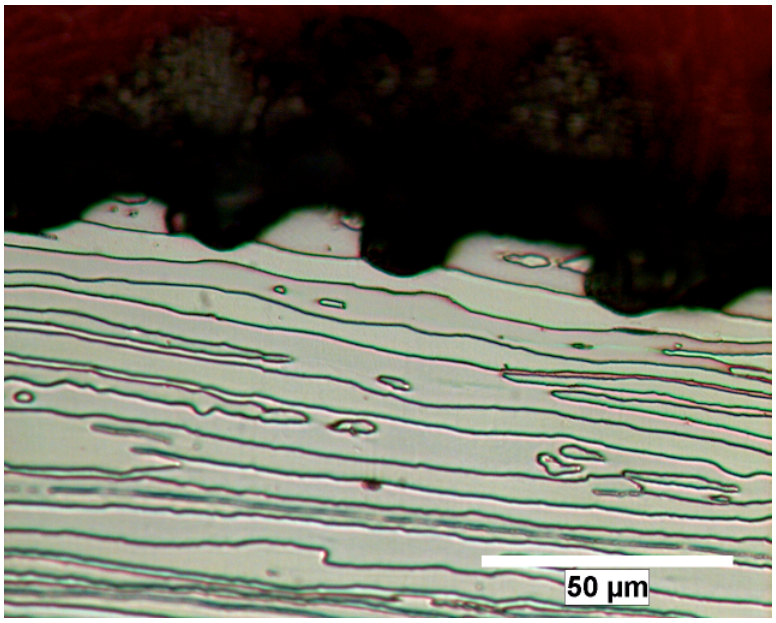


(d)

***Figure 6.38(cont'd):*** ***Micrographs showing the typical crack morphologies on SSRT S32205 specimens tested in alkaline-sulfide solution (150 g/l NaOH + 50 g/l $Na_2S$) containing (c) 0.17 M, and (d) 1.7 M NaCl at 170 $^{o}$C. Arrow indicates slip-step emergence.***

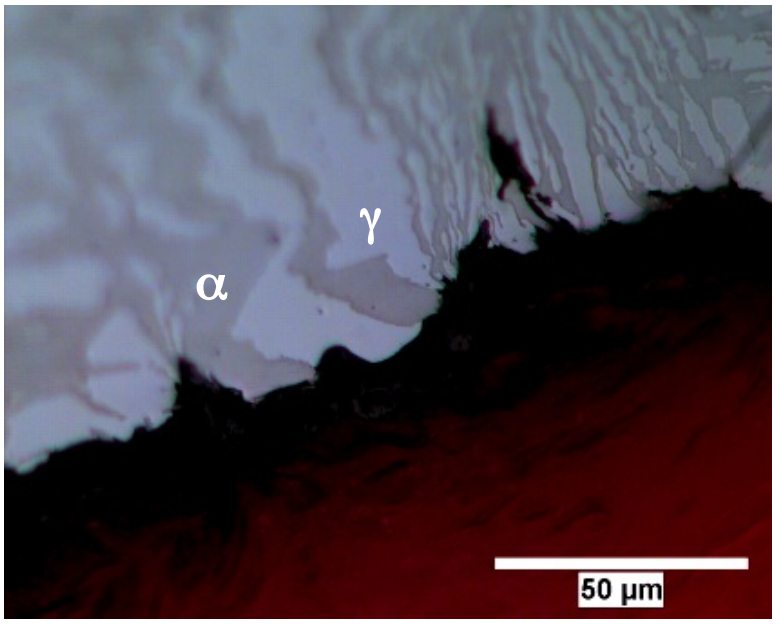


(a)

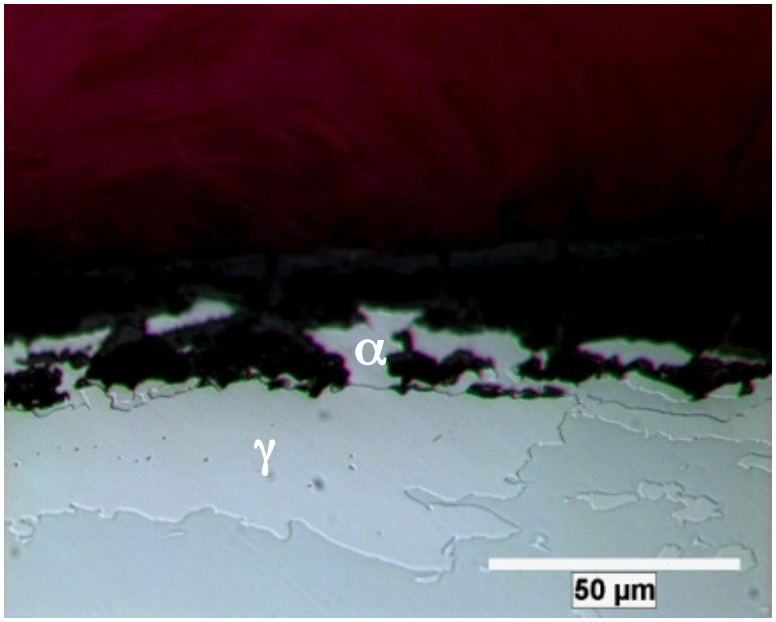


(b)

***Figure 6.39:*** ***Micrographs showing preferential corrosion of the austenite phase (γ) of S32205 specimens tested in alkaline-sulfide solution (150 g/l NaOH + 50 g/l $Na_2S$) containing (a) 0.034 M, and (b) 0.085 M NaCl at 170 $^{o}$C.***

Chlorides also enhanced corrosion activity near the crack tips of S32101 DSS in sulfide-containing caustic solution, which influenced the SCC mechanism. Figure 6.40 shows the effect of increased chloride had on the crack initiation and growth behavior in alkaline-sulfide solution. Analogous to S32205, preferential corrosion of the austenite phase was evident in the concentration range of 0.0085 – 0.085 M NaCl (Figure 6.41). The cracks that formed under these conditions often initiated in the austenite phase and grew through crack branching along favored orientations. The arrow in Figure 6.41a indicates slip-step formation. The corrosion of the two phases became more uniform with increasing chloride content, and the crack tips exhibited fewer branches. The increased corrosion of ferrite phase enhanced the severity of SCC under the most concentrated chloride conditions.

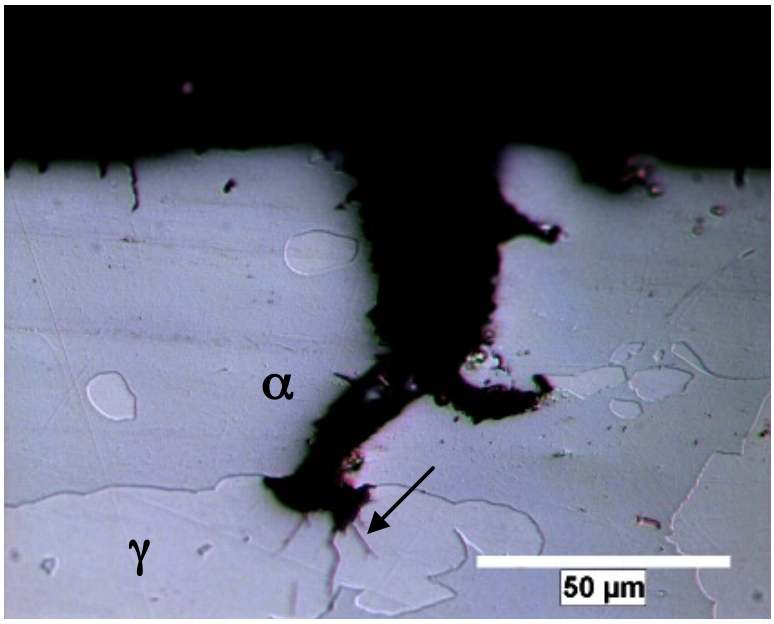


(a)

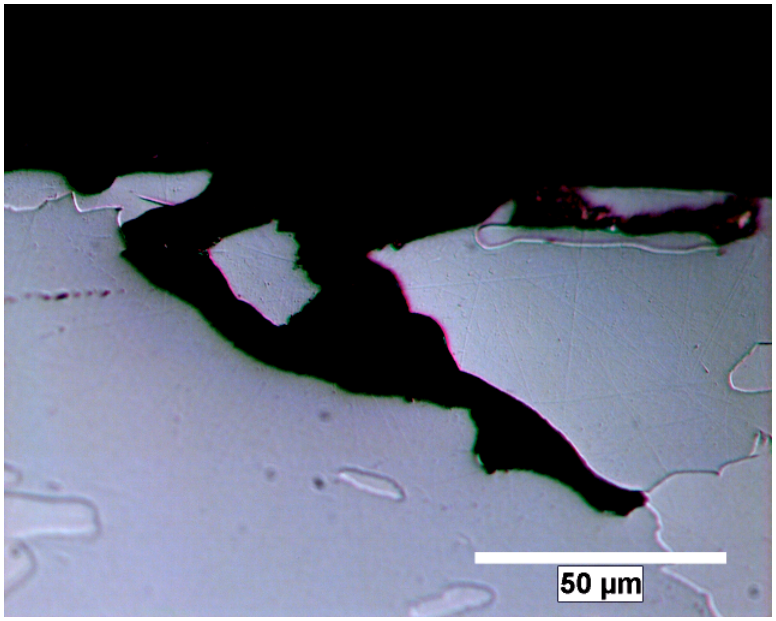


(b)

*Figure 6.40:* ***Micrographs showing the typical crack morphologies on SSRT S32101 specimens tested in alkaline-sulfide solution (150 g/l NaOH + 50 g/l $Na_2S$) containing (a) 0.034 M and (b) 0.085 M, (c) 0.17 M at 170 $^oC$.***

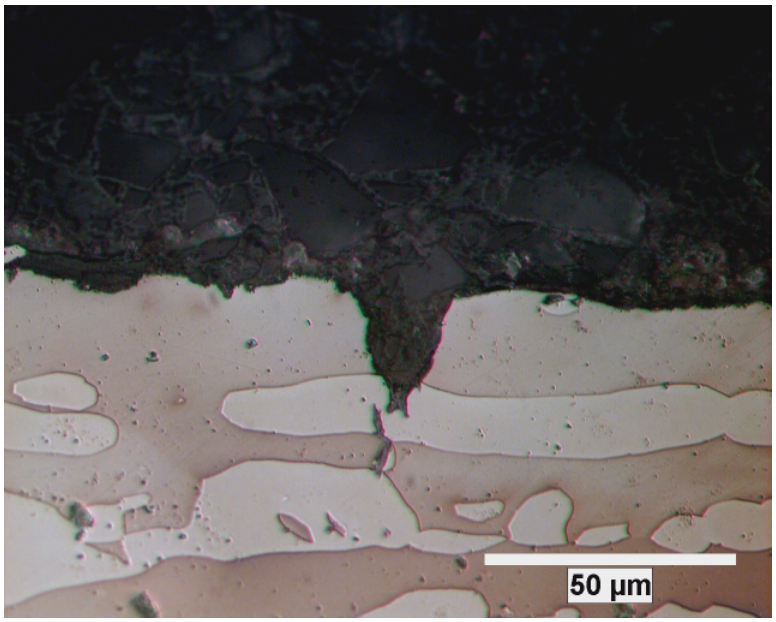


(c)

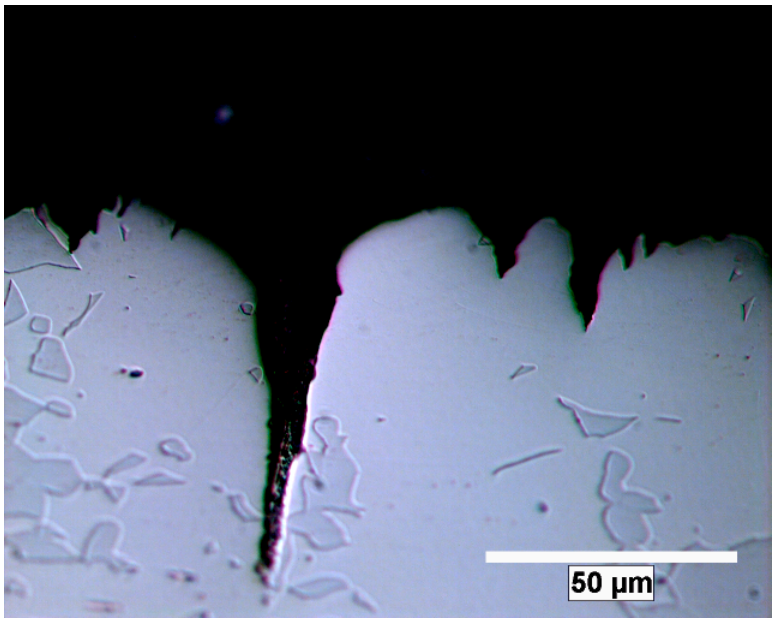


(d)

***Figure 6.40 (cont'd):*** ***Micrographs showing the typical crack morphologies on SSRT S32101 specimens tested in alkaline-sulfide solution (150 g/l NaOH + 50 g/l $Na_2$ with (c) 0.17 M, and (d) 1.7 M NaCl at 170 $^{o}$C.***

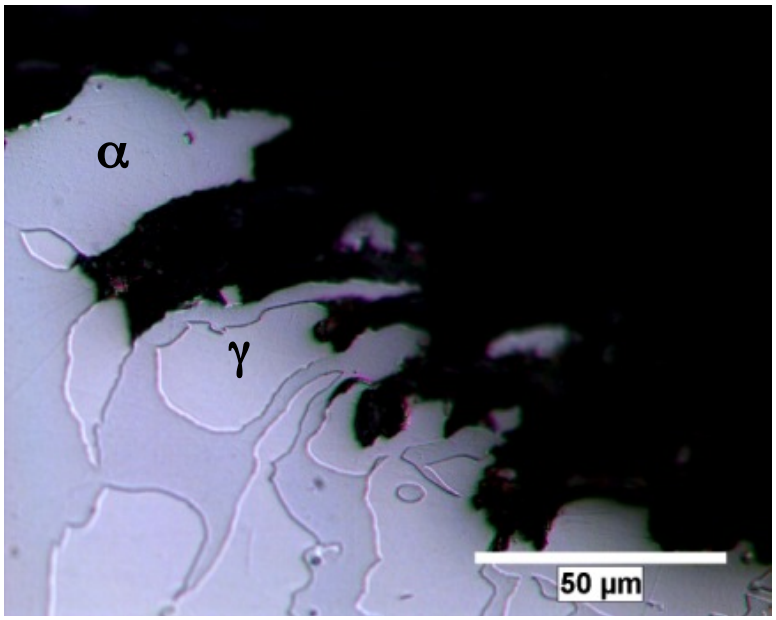


(a)

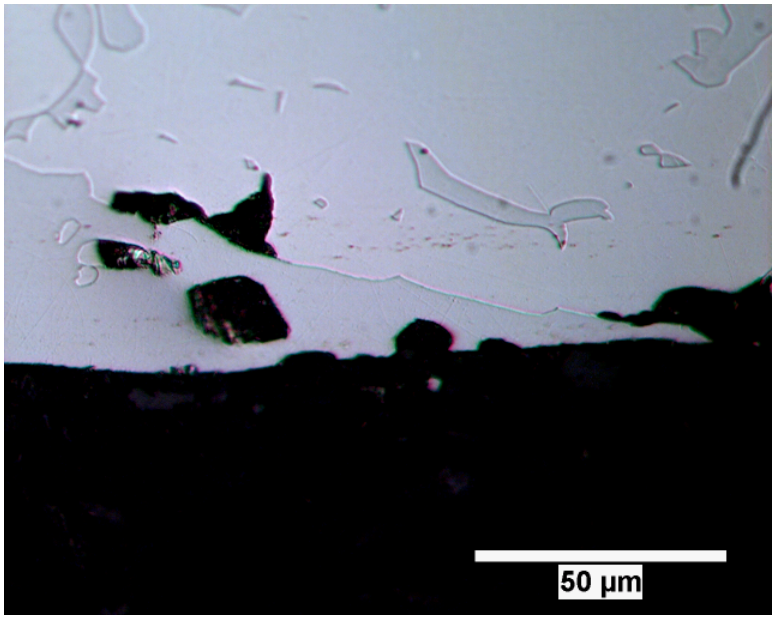


(b)

***Figure 6.41:*** ***Micrographs showing preferential corrosion of the austenite phase (γ) of S32101 specimens tested in alkaline-sulfide solution (150 g/l NaOH + 50 g/l $Na_2S$) containing (a) 0.034 M, and (b) 0.085 M NaCl at 170 $^{o}$C.***

The surface of DSS S32205 specimens tested in sulfide-containing caustic solution with different amounts of chloride at 170 $^{o}$C showed the macroscopic fracture behavior (Figure 6.42). Large secondary cracks associated with crack growth along austenite/ferrite phase boundaries along the loading direction, particularly for chloride concentrations greater than 0.034 M NaCl. The surface of the S32205 sample tested with 0.17 M NaCl (Figure 6.43) showed brittle, quasi-cleavage fracture associated with failure by TGSCC. The austenite phase was smooth and failed due to cleavage, whereas the ferrite phase exhibited limited ductility based on the occurrence of dimple rupture. Analogous features were found for S32101 tested under the same conditions (Figure 6.44). The propagation of cracks along austenite/ferrite phase boundaries was favored in the presence of chloride and resulted in higher crack growth rates supported by the results in Table 6.5. The crack growth behavior was strongly influenced by the banded microstructure. Microstructural effects are the subject of Chapter 7.

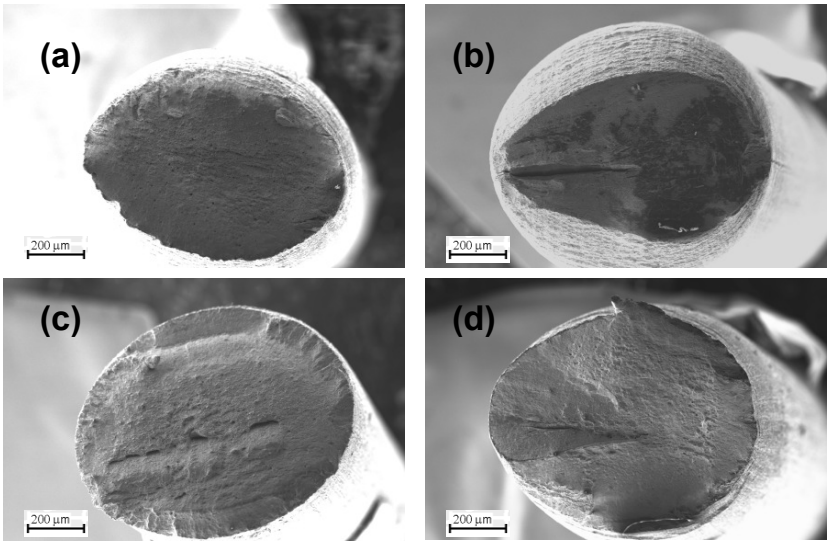


***Figure 6.42:*** ***Micrographs showing the fractured surface of SSRT S32205 specimens tested in alkaline-sulfide solution (3.75 M NaOH + 0.64 M $Na_2S$) containing (a) 0 M, (b) 0.034 M, (c) 0.085 M, and (d) 0.17 M NaCl at 170 $^{o}$C.***

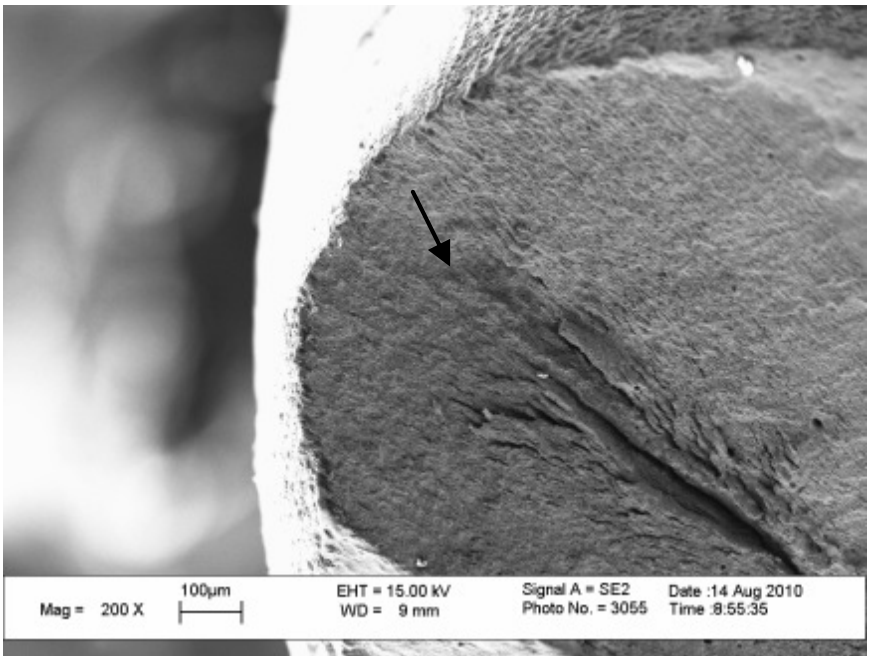


(a)

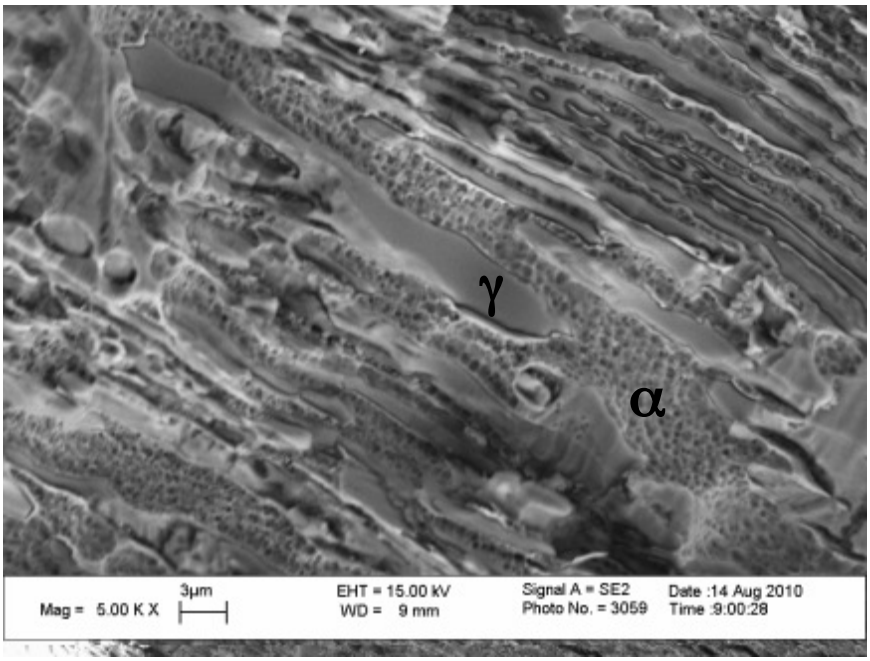


(b)

***Figure 6.43:*** ***(a) Low magnification and (b) high magnification SEM micrographs showing fracture surface of lean DSS S32205 tested in 3.75 M NaOH + 0.64 M $Na_2S$ + 0.17 M NaCl at 170 $^oC$. Arrow corresponds to region shown in (b).***

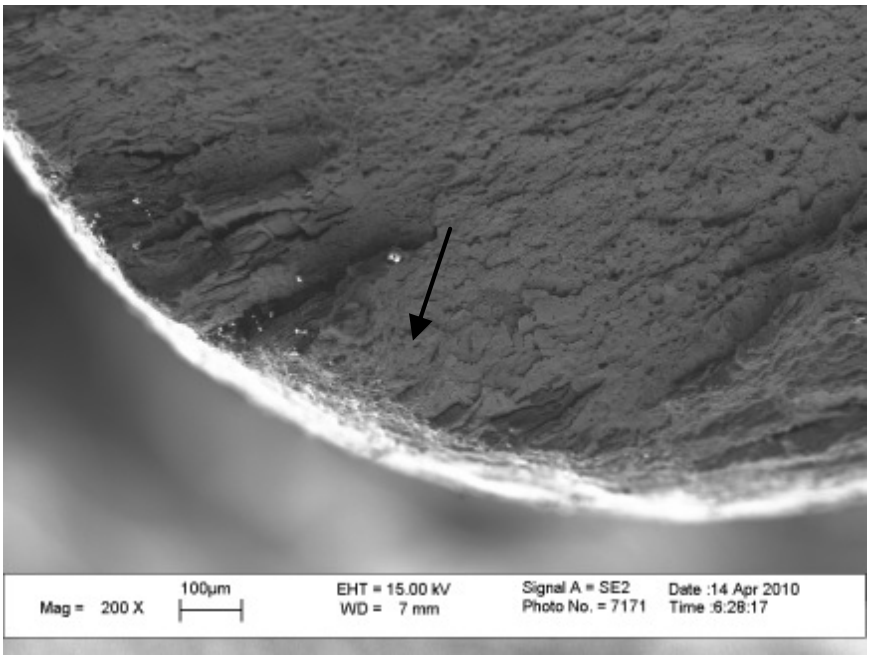


(a)

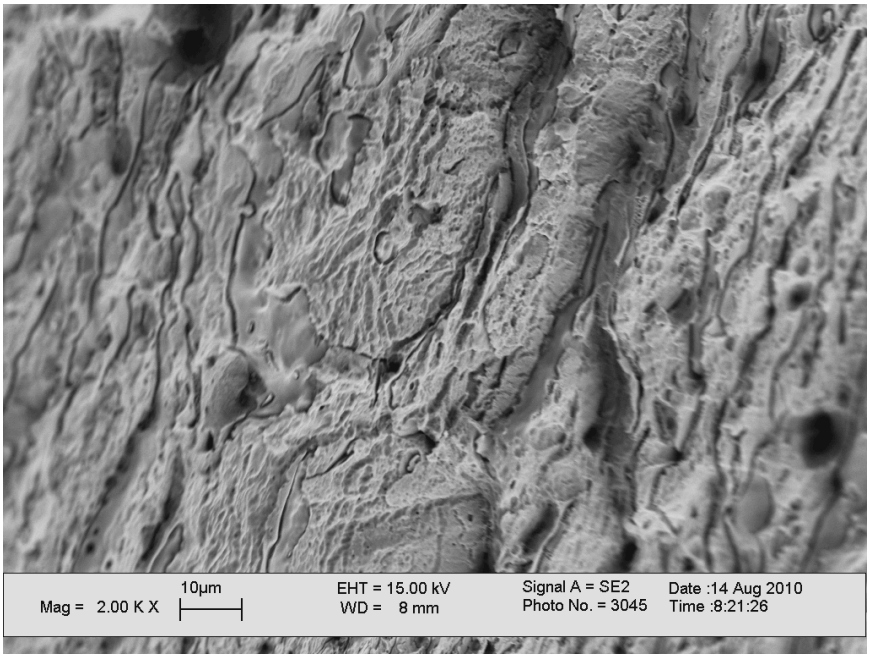


(b)

***Figure 6.44:*** ***(a) Low magnification and (b) high magnification SEM micrographs showing fracture surface of lean DSS S32101 tested in 3.75 M NaOH + 0.64 M $Na_2S$ + 0.17 M NaCl at 170 $^{o}$C. Arrow corresponds to region shown in (b).***

SSRT S32205 and S32101 samples tested in sulfide-containing caustic solution with varying molar concentrations of NaCl were mounted, polished, and observed under SEM equipped with EDS to study the composition and morphology of the surface films. Figure 6.45 shows the S32205 and S32101 samples tested with 0.17 M NaCl. Chloride addition enhanced the defective nature of the film. A non-adherent inner, barrier film layer can be seen in Figure 6.45a and 6.45b. This inner, barrier film layer was seen on both DSS specimens. The inner layer was approximately (54 wt % Fe, 35 wt % Cr, and 11 wt % Ni) in S32205 based on the average of 15 measurements. Sulfur was detected in the inner layer (ca. 5 wt %). The inner layer of S32101 was approximately (47 wt % Fe, 41 wt % Cr, 5 wt % Ni, and 6 wt % Mn). Sulfur was also detected in the inner layer (ca. 3 wt %). The EDS spectra showed similar trends for the two materials: the inner, barrier film was enriched in Cr and Ni and contained S.

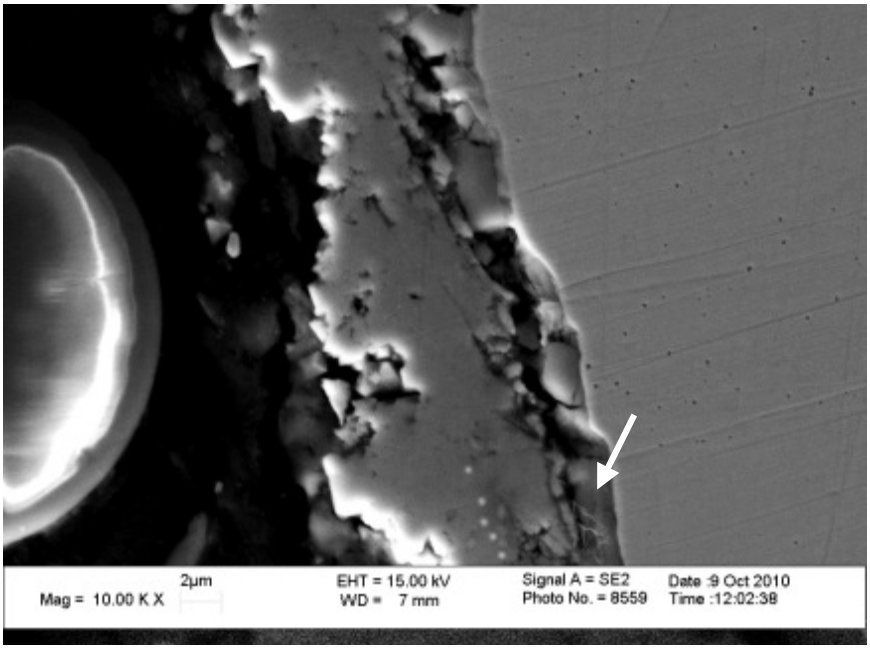


(a)

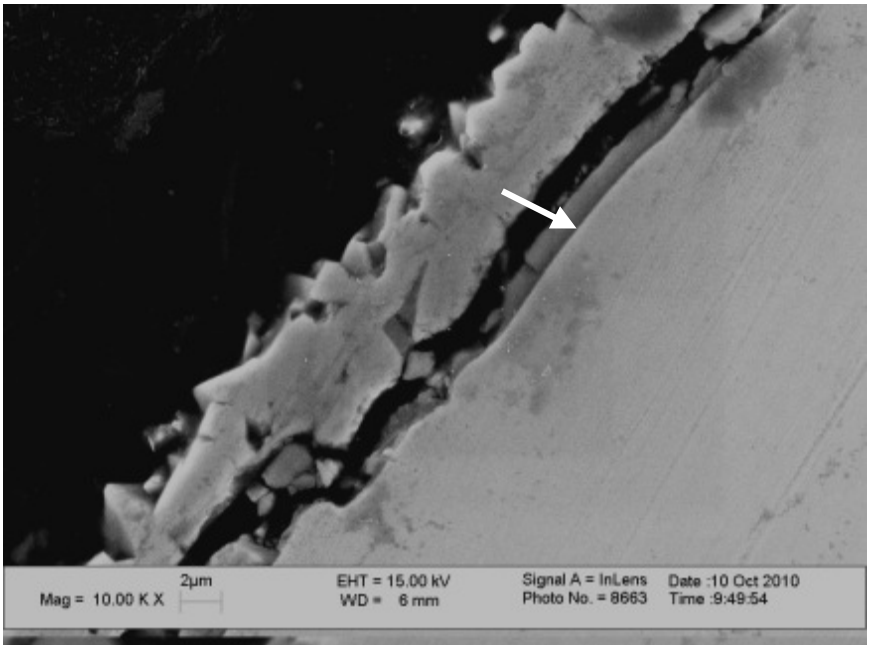


(b)

***Figure 6.45:*** ***Cross-sectional view of oxide film of (a) S32205 and (b) S32101 DSS samples tested in alkaline-sulfide solution (3.75 M NaOH + 0.64 M $Na_2S$) with 0.17 M NaCl at 170 $^{o}$C. Arrows indicate the sites where inner, barrier film composition was measured with EDS.***

Further evidence of a defective film can be seen in the top-down images of the S32205 DSS samples (Figure 6.46) tested with increasing chloride content. The defective nature of the film is clear, particularly for 0.085 M NaCl (Figure 6.46c) and 1.7 M NaCl (Figure 6.46d). Chloride addition to alkaline-sulfide solution clearly influenced the stability of the passive film. A more defective film formed in the presence of chloride, thereby enabling sulfide and chloride ions to react with the metal. The cross-sectioned images revealed that there was a multi-layered film present on the DSS in alkaline-sulfide solution. The ability of aggressive ions in the solution to react with the base material was enhanced in the chloride-containing solutions because the surface film was more defective and less protective.

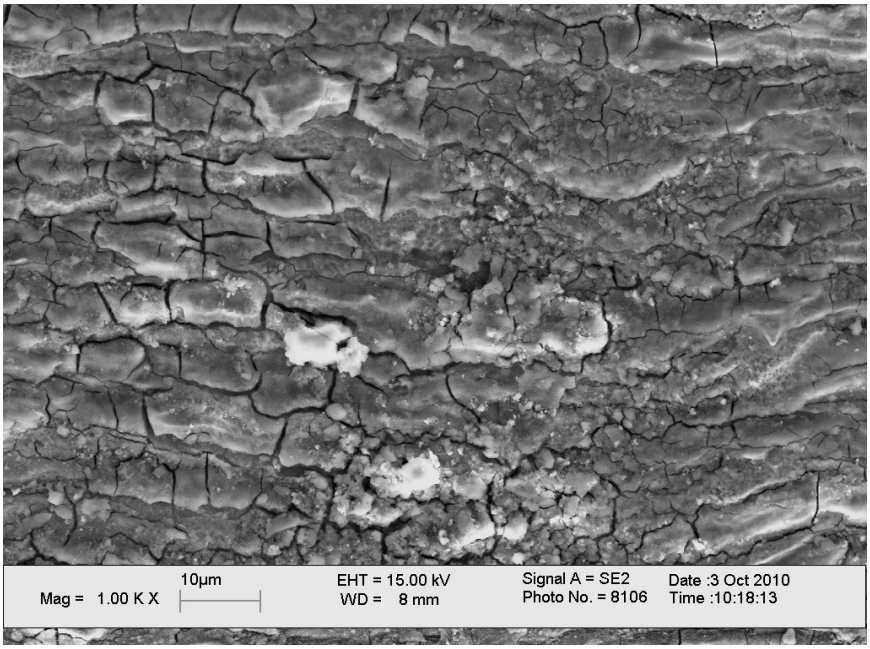


(a)

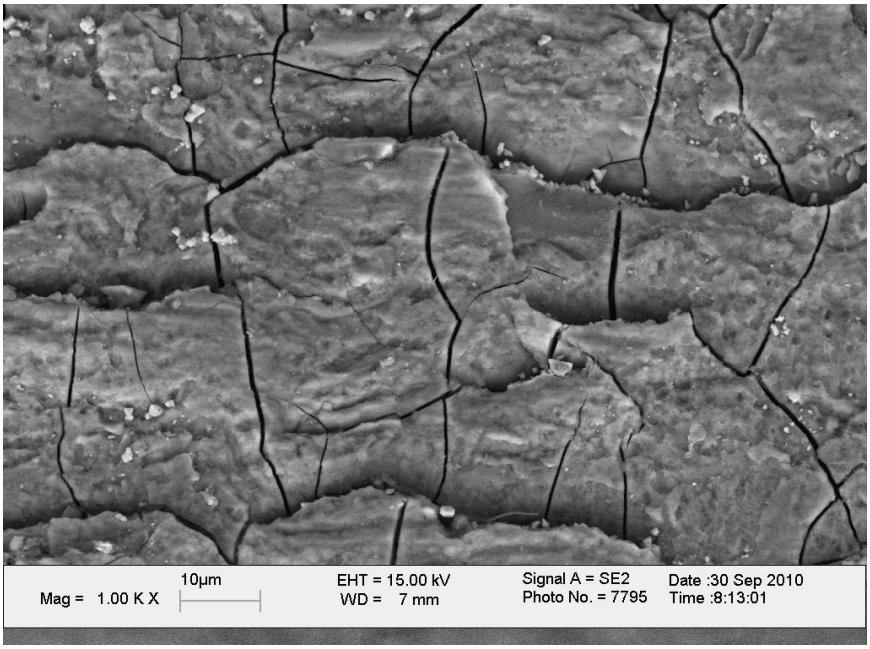


(b)

***Figure 6.46:*** ***Top-down SEM micrographs showing film morphology of S32205 samples tested in alkaline-sulfide solution (3.75 M NaOH + 0.64 M $Na_2S$) with (a) 0 M, and (b) 0.034 M at 170 $^{o}$C.***

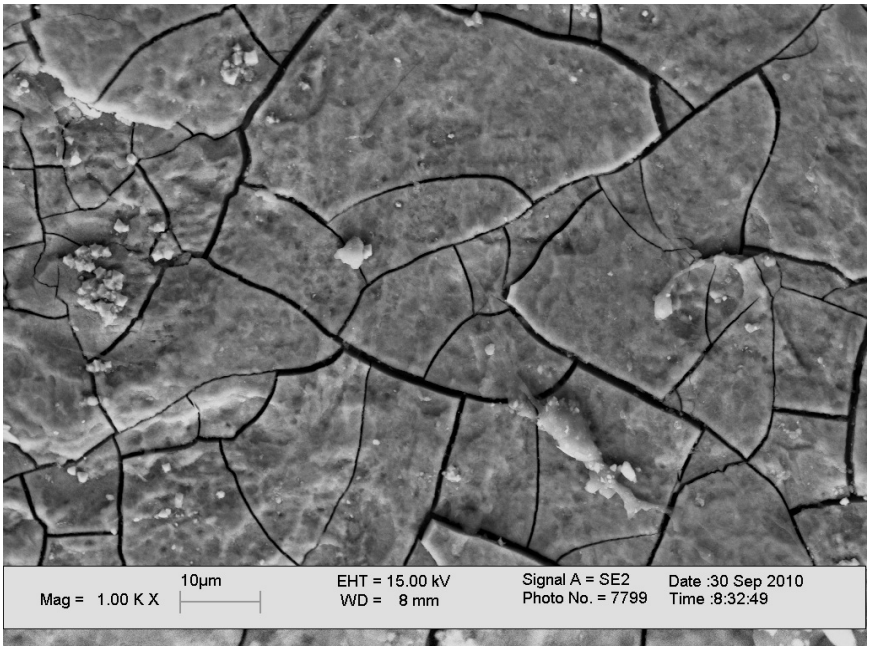


(c)

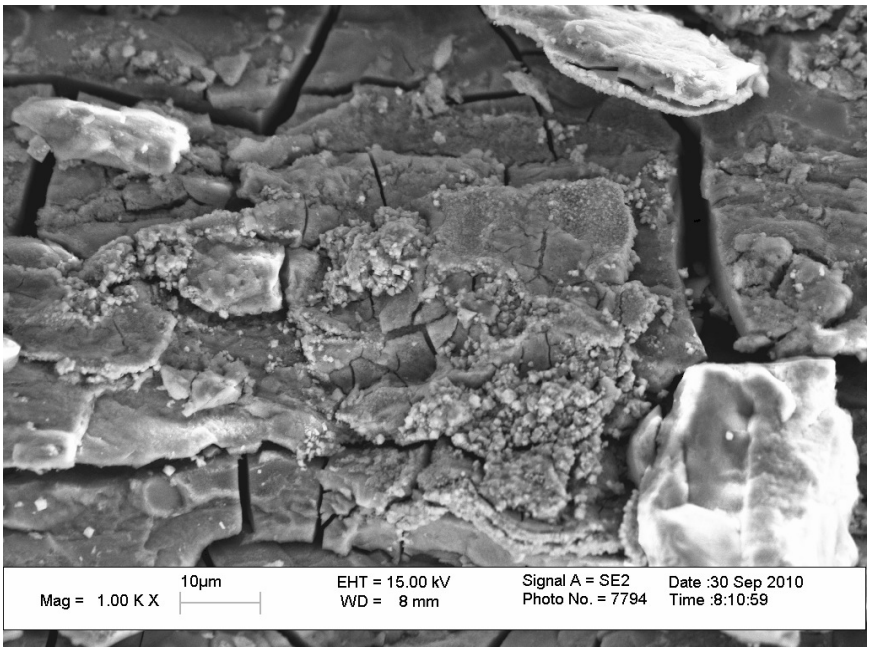


(d)

***Figure 6.46 (cont'd):*** ***Top-down SEM micrographs showing film morphology of S32205 samples tested in alkaline-sulfide solution (3.75 M NaOH + 0.64 M $Na_2S$) with (c) 0.085 g/l, and (d) 1.7 M NaCl at 170 $^oC$.***

The work in sulfide-containing caustic solution with and without chloride showed that chlorides affect the initiation and growth behavior of stress corrosion cracks. The susceptibility of S32205 and S32101 was a strong function of the chloride content in the solution, whereby preferential corrosion of the austenite phase and enhanced corrosion of the ferrite phase enhanced SCC susceptibility of S32205 and S32101, respectively. The phase distribution and material composition accounted for the differences in susceptibility [8]. Despite the difference in the composition of these alloys, the properties of the inner surface film, including its composition and morphology were similar. Chlorides and sulfides resulted in the formation of a defective surface film that was enriched in metal sulfur compounds (Chapter 5). Crack initiation was therefore favored in the presence of chloride due to destabilization of the Cr-rich passive film. The emergence of slip-steps indicated that the growth of SCC cracks occurred by an active path mechanism such as the slip-step dissolution (film rupture) model [42]. Based on the fractography and crack morphology, the growth of SCC cracks was favored along austenite/ferrite phase boundaries showing there was a strong role of the banded microstructure formed during hot rolling.

## 6.5 Conclusions

The addition of sulfide and chloride to NaOH environments strongly influenced the SCC susceptibilities of S32205 and S32101 based on the SSRT testing and subsequent characterization in this work. Crack behavior was quantified in terms of maximum crack velocity, average crack density, and % RA to compare the relative susceptibilities of the DSS in different environments. The phase distribution and material composition altered the crack initiation and growth behavior in each environment based

on fractographs and micrographs of the failed specimens. The following general conclusions can be made based on the results of the current work:

- The SCC initiation and growth mechanisms of DSS S32205 and S32101 tested in NaOH environments depended largely on the alkalinity of the solution:
  - S32101 was susceptible to SCC in 2.5 M and 3.75 M NaOH at 170 $^{o}$C, and S32205 was not susceptible in these environments.
  - DSS S32205 and S32101 were highly susceptible to SCC in 12.5 M NaOH at 170 $^{o}$C. The growth of TGSCC cracks proceeded by a discontinuous process through the austenite and ferrite phases, which was not hindered by austenite/ferrite phase boundaries.
  - Crack growth was favored along highly stressed regions in the material based on the misorientation maps from EBSD.
- Chlorides alone did not have an effect on the SCC susceptibility of DSS S32205 tested in NaOH environments at 170 $^{o}$C in the absence of sulfide.
- DSS S32101 underwent a mixed mode failure of IGSCC and TGSCC in 3.75 M NaOH + 0.17 M NaCl at 170 $^{o}$C. Cracks initiated at ferrite grain boundaries.
- Chloride addition to alkaline-sulfide solution favors preferential dissolution of the austenite phase, particularly in the concentration of 0.034 – 0.085 M for DSS S32205 and 0.0085 – 0.085 M for DSS S32101.
- Preferential dissolution of the austenite phase lead to severe SCC in S32205 as these sites served as precursors to crack initiation. Less severe SCC was observed for S32101 when preferential dissolution occurred.

- Lean grade DSS S32101 showed an increased severity of SCC as the concentrations were increased higher than 0.085 M NaCl.
- The coalescence of SCC cracks was more prominent in the presence of chloride in DSS S32205 and S32101 most likely due to the increase in crack density. The growth of these cracks was predominantly along the austenite/ferrite phase boundaries in the banded microstructure.
- Sulfur was present in the oxide film of DSS S32205 and S32101 tested in sulfide-containing caustic solution indicating that the adsorption of sulfides results in the formation of a defective film in the presence or absence of chloride.
- Chlorides generally destabilized the Cr-rich passive film that formed on DSS S32205 and S32101 in alkaline-sulfide environments.
- Ni and Cr enrichment of the oxide surface film was observed for DSS S32205 and S32101 tested in alkaline-sulfide solution with and without chloride.
- The initiation and growth of stress corrosion cracks for DSS S32205 and S32101 tested in alkaline environments generally depended on a film breakdown and repair mechanism such as slip-step dissolution.

## 6.6 REFERENCES


[1] M. Honda et al., "Stress Corrosion Cracking of Stainless Alloys in Alkaline-Sulfide Solutions.," 1991.

[2] M. Honda, Y. Kobayashi, and A. Tamada, "Stress Corrosion Cracking of Stainless Alloys in Alkaline-sulfide Solutions," Corrosion (USA), vol. 48, 1992, pp. 822-829.

[3] A.J. Sedriks, "Corrosion of Stainless Steel," John-Wiley & Sons, New York, 1979.

[4] G. Rondelli and B. Vicentini, “Susceptibility of Highly Alloyed Stainless Steels to Caustic Stress Corrosion Cracking,” Materials and Corrosion, Vol. 53, 2002, pp. 813-819.

[5] Wensley, A., Moskal, M., and Wilton, W., "Materials Selection for Kraft Batch Digesters," Corrosion/97, NACE Paper No. 378, 1997, Houston, TX.

[6] Wensley, A., and Champagne, P. NACE Corrosion, Paper No. 281, 1999, Houston, TX.

[7] Wensley, A., NACE Corrosion, Paper No. 589, 2000, Houston, TX.

[8] Bhattacharya, A., Georgia Institute of Technology Ph.D. Dissertation, 2008, Atlanta, GA.

[9] Bhattacharya, A. and Singh, P.M.”Corrosion and Stress Corrosion Cracking of Duplex Stainless Steels in Pulping Liquors,” CORROSION/2007, Paper No. 07206. (Houston, TX: NACE, 2007).

[10] Bhattacharya, A., and Singh, P.M. “Effect of Heat Treatment on Corrosion and Stress Corrosion Cracking of S32205 Duplex Stainless Steel in Caustic Solution.” Metallurgical and Materials Transactions A: Physical Metallurgy and Materials Science, Vol. 40A (6) (2009), p.1388.

[11] G. Rondelli, B. Vicentini, and E. Sivieri, “Stress Corrosion Cracking of Stainless Steels in High Temperature Caustic Solutions,” Corrosion Science, vol. 39, 1997, pp. 1037-1049.

[12] C. Reid, “Stress Corrosion Cracking of Austenitic and Duplex Stainless Steels in the Pulp and Paper Industry,” TAPPI Engineering Conference Proceedings, 1999, pp. 1315-1357.

[13] H.T. Leinonen, P. Pohjanne, “Stress Corrosion Cracking Susceptibility of Duplex Stainless Steels and their Welds in Simulated Cooking Environments. NACE Corrosion 2006, paper no. 06244, San Diego, CA, USA, 12-16 March 2006.

[14] M. Gorog, “Digester Outlet Device Scraper Arm Cracking,”2006 Engineering, Pulping and Environmental Conference, Atlanta, GA, USA, 5-8 November 2006.

[15] P.M. Singh, J. Mahmood, P. Conde, “Stress Corrosion Cracking and Corrosion Susceptibility of Duplex Stainless Steels in Caustic Solutions,” NACE Corrosion 2005, paper no. 05196, Houston, TX, USA, 3-7 April 2005.

[16] P.M. Singh and A. Anaya, “Effect of Wood Species on Corrosion Behavior of Carbon Steel and Stainless Steels in Black Liquors,” Corrosion Science, vol. 49, 2007, pp. 497-509.

[17] Truman, J.E. and Pirt, K.R., Duplex Stainless Steel, ed. Lula, R.A. ASM, p. 113-142, 1983, Materials Park, OH.

[18] Svensson, C., Pulliainen, M., Huttunen, M., and Niemelainen, P., 2005 TAPPI Engineering, Pulping, Environmental Conference, August 28-31, 2005, Philadelphia, PA.

[19] Ramo, J., Sillanpaa, Kujalao, A., Hyokyvirta, O., and Peltonen, S., Mat. and Corr. Vol. 52 (2001), p741.

[20] ERC Project Report, Institute of Paper Science and Technology at Georgia Tech, August 2006.

[21] Singh, P.M., Perdomo, J.J., Oteng, J.E., and Mahmood, J., Corrosion, "Stress corrosion cracking and corrosion fatigue cracking of a duplex stainless steel in white water environments," 60 (9): 852 (2004).

[22] Svensson, C., Pulliainen, M., Huttunen, M., and Niemelainen, P., 2005 TAPPI Engineering, Pulping, Environmental Conference, August 28-31, 2005, Philadelphia, PA.

[23] Bhattacharya, A., Singh, P.M., Leinonen, H.T., and Mahmood, J., NACE Corrosion 2006, Paper No. 06497, March 12-16, 2006, San Diego, CA.

[24] Bhattacharya, A. and Singh, P.M. Stress Corrosion Cracking of Welded 2205 Duplex Stainless Steel in Sulfide-Containing Caustic Solution, Journal of Failure Analysis and Prevention, Vol. 7 (5) (2007), p. 371.

[25] Bergquist, A., and Wegrelius, W. "Experiences in Pulp and Paper Industry of a 30 Years Old Steel Grade," 2009 TAPPI Conference, Paper No. Memphis, TN.

[26] J.R. Kearns, M.J. Johnson, "The Corrosion of Stainless Steels and Nickel Alloys in Caustic Solutions," CORROSION/84, paper no. 146 (Houston, TX: NACE International, 1984).

[27] Guidelines for PReventing Stress Corrosion Cracking in the Chemical Process Industries, MTI Publication no. 15 (Houston, TX: NACE, 1985), p. 40-42.

[28] R.W. Staehle et el, Stress Corrosion Cracking and Hydrogen Embrittlement of Iron Base Alloys, R.W. Staehle et al, eds. NACE-5, NACE, Houston, (1977) p. 193.

[29] L. Dahl, T. Dahlgren, and N. Lagmyr, High Temperature High Pressure Electrochemistry in Aqueous Solutions, NACE-4 (ed. R.W. Staehle, D. De G. Jones and J.E. Slater), NAVE, Houston, TX, (1976), p.533.

[30] T. Cassagne and P. Combrade, Innovation in Stainless Steels Vol. 3, AIM, Milano (1993), p.215.

[31] D.V. Subrahmanyam, A.K. Agarwal, and R.W. Staehle, Proc. 7th International Congress on Metallic Corrosion, ABRACCO, Rio de Jeneiro (1978), p. 783.

[32] G. Santarini and J.Y. Boos, "Corrosion of Austenitic Stainless Steels in Hot Concentrated Aqueous NaOH Solutions," Corr. Sci 19 (1979), pp. 261-281.

[33] J. Deakin et al., "De-alloying of Type 316 Stainless Steel in Hot, Concentrated Sodium Hydroxide Solution," Corrosion Science, vol. 46, 2004, pp. 2117-2133.

[34] H.T. Leinonen, P. Pohjanne, T. Saukkonen, T. Schildt, J. Romu, and H. Hanninen, "Effect of Selective Dissolution on Stress Corrosion Cracking Susceptibility of Austenitic and Duplex Stainless Steels in Alkaline Solutions," NACE Corrosion 2011, Houston, TX, 13-17 March 2011, paper no. 11160, 17p.

[35] K. Sieradzki et al., "The Relationship Between Dealloying and Transgranular Stress-Corrosion Cracking of Cu-Zn and Cu-Al Alloys," Journal of the Electrochemical Society, vol. 134, 1987, p. 1635.

[36] K. Sieradzki and R.C. Newman, "Brittle Behavior of Ductile Metals During Stress-Corrosion Cracking," Philosophical Magazine A, vol. 51, 1985, pp. 95-132.

[37] K. Sieradzki and R.C. Newman, "Stress-Corrosion Cracking," J. Phys. Chem. Solids, vol. 48, 1987, pp. 1101-1113.

[38] Z.L. Coull and R.C. Newman, "Selective Dissolution and Oxidation Zones in Ni-Cr-Fe Space and their relationship to stress corrosion cracking," Proc. NACE Corrosion 2007, T. Cassagne and S. Shipilov eds., Nashville, TN, 5p.

[39] R.N. Parkins, Proc. 5th Symposium on Line Pipe Research, Am. Gas Assoc. Arlington, VA (1974), P. U-1.

[40] D.L. Singbeil, "A Study of the Stress Corrosion Cracking of Mild Steel in Alkaline and Alkaline Sulphide Solutions," University of British Colombia, M.S. Thesis, Vancouver, BC, 1981.

[41] R.N. Parkins and P.M. Singh, "Stress Corrosion Crack Coalescence" Corrosion 46 (1990), pp. 485-499.

[42] F.P. Ford, "Slip Dissolution Model," Corrosion Sous Contrainte-Phénoménologie et Mécanismes Les Editions de Physique, Les Ulis, France, vol. 307, 1992.

# CHAPTER 7

# ROLE OF ANISOTROPIC MICROSTRUCTURE ON STRESS CORROSION CRACKING BEHAVIOR OF DUPLEX STAINLESS STEELS IN HOT ALKALINE ENVIRONMENTS

## 7.1 Introduction

Hot or cold deformation to produce wrought duplex stainless steels (DSS) leads to alignment of grains along the deformation direction. Furthermore, deformation induces microstructural fibering, producing elongated grains or bands in the microstructure. Owing to pronounced microstructural anisotropy, mechanical anisotropy is seen in these materials. A large number of mechanical and physical properties describing the macroscopic behavior of DSS, such as uniaxial yield and ultimate strength, fatigue resistance, fracture toughness, and stress corrosion cracking (SCC) behavior are influenced by anisotropy [1-7]. Directionality effects due to the anisotropic microstructure were shown for S32205 (DSS 2205) by both Hutchinson et al [1] and ul-Haq et al [2-3]. These effects were shown to be more significant in the cold rolled case as compared to hot rolled steel case, with greater anisotropy for decreasing plate thickness (i.e. increasing rolling reduction).

DSS obtain a balanced microstructure of primarily face-centered cubic (fcc) austenite ($\gamma$) and body-centered cubic (bcc) ferrite ($\alpha$) phase through hot and/or cold rolling followed by suitable annealing and quenching. Careful selection of the processing parameters has generally ensured favorable mechanical properties and corrosion

resistance of DSS equipment in the pulp and paper industry, although experience [8-26] has shown that DSS may become susceptible to general corrosion and SCC under certain conditions. The implication of microstructural anisotropy on SCC of DSS remains unclear from the published literature. Former laboratory efforts to study the corrosion and SCC behavior of DSS in hot alkaline-sulfide solution have shown that the austenitic phase was less resistant than the ferrite phase [8-13]. Other studies in hot chloride solutions [27-30] have shown that the ferrite phase is more susceptible. The susceptibility of individual phases will be a function of alloy composition, microstructural anisotropy, and mechanical anisotropy.

The microstructures of as-received standard DSS S32205 and lean DSS S32101 were studied in terms of relative phase distribution and mechanical behavior of each phase (Chapter 3). Round tensile samples were machined from the as-received material, which was provided as 9.5 mm thick, hot rolled and coil-processed DSS plate with a No. 1 finish in accordance with ASTM A480. These samples were tested for their SCC susceptibility by the slow strain rate testing (SSRT) method. The SCC susceptibility was quantified in terms of maximum crack velocity and average crack density for different microstructure orientations in a hot sulfide-containing caustic solution, where SCC had been observed previously [12] (Chapter 6). Annealed and cold worked (20 % rolling reduction) specimens were also studied to understand residual stress distribution in the phases after cold work. The mechanical properties of these samples were compared for the different microstructural orientations as well with respect to the hardness of the austenite and ferrite phases.

## 7.2 Anisotropy in Mechanical Properties

The current work was performed to understand the macro- and microscopic anisotropic properties of standard DSS 32205 due to large plastic deformation and annealing. Plate specimens that were cold rolled to a target thickness were used to understand the role of large plastic deformation on mechanical behavior (section 7.2.1). Round tensile specimens machined from the as-received material and characterized in Chapter 3 were not used to understand cold work effects due to experimental setup limitations associated with the X-ray measurements. The as-received DSS S32205 material in Chapter 3 was used in a separate study to understand the effect of annealing on the mechanical behavior of the individual phases (section 7.2.2).

### 7.2.1 Effect of Large Plastic Deformation

DSS S32205 sheet was cold rolled to a thickness of 2 mm. The material was then water quenched from a temperature of 1050 $^{o}$C to avoid precipitation of secondary phases. The annealed material was also rolled to a final thickness of 1.6 mm to attain 20 % cold work. The microstructures of the annealed and cold worked conditions are shown in Figure 7.1 and Figure 7.2, respectively. A heavily banded microstructure for both conditions was found in all three orientations with austenitic islands in a ferritic matrix. The method of point counting [31] revealed the approximate area fraction of ferrite in the DSS S32205 specimens was approximately 60 % in each orientation.

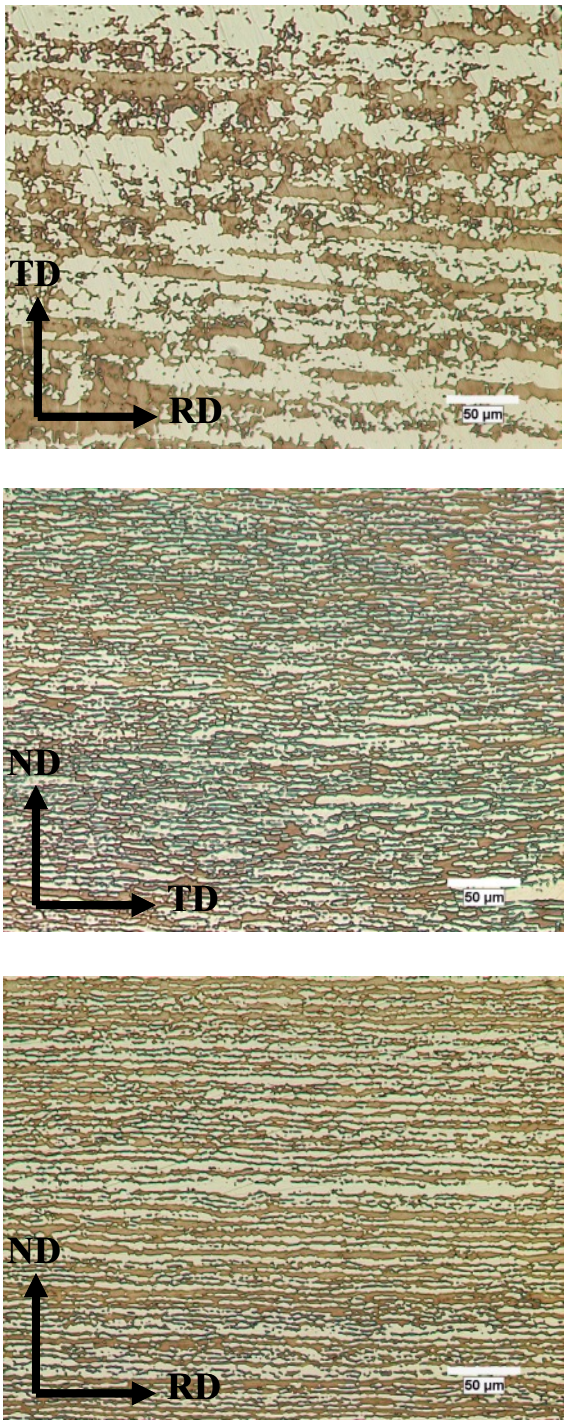


*Figure 7.1:* ***Micrographs showing the (a) RL orientation, (b) TS orientation, and (c) TL orientation microstructure of annealed standard DSS S32205 evaluated in this study.***

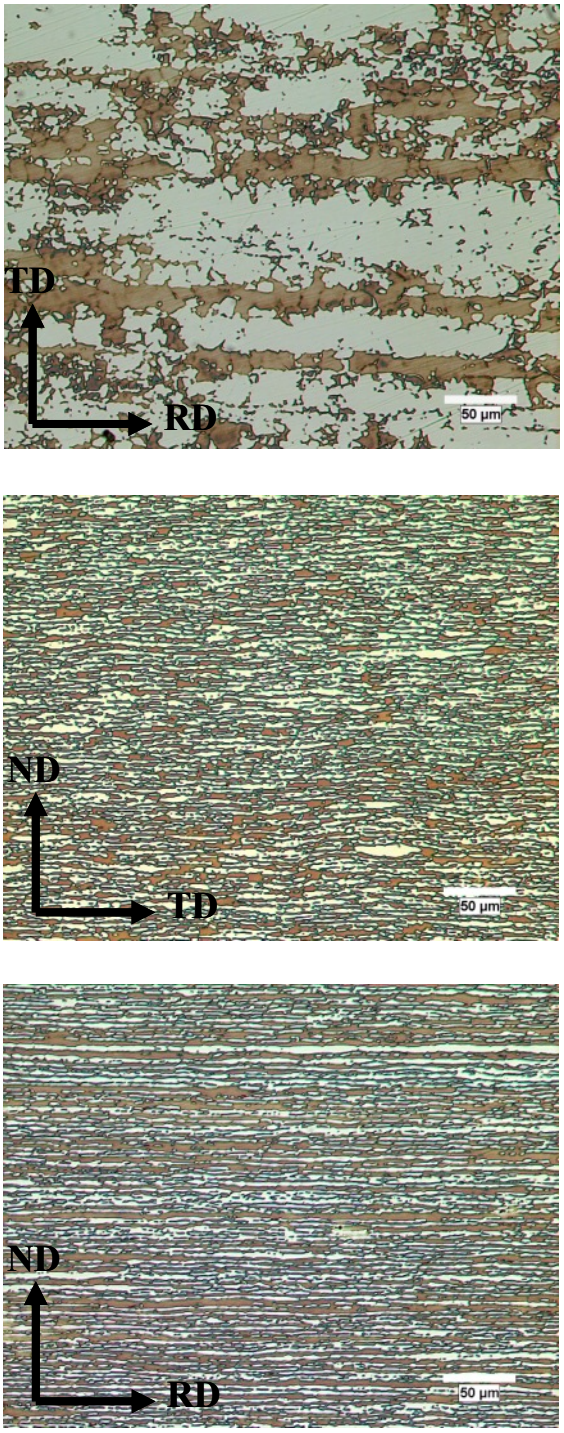


*Figure 7.2:* ***Micrographs showing the (a) RL orientation, (b) TS orientation, and (c) TL orientation microstructure of 20 % cold worked standard DSS S32205 evaluated in this study.***

The macroscopic mechanical behavior and microhardness of the individual phases indicated there was appreciable effect of cold work. The room temperature macroscopic material properties of the S32205 plate specimens (Table 7.1) were investigated by tensile testing of plate specimens that were machined in accordance with ASTM E8 [32]. The test results were provided by the VTT Technical Research entre of Finland and are shown in Appendix C. The gauge length of the specimens was 80 mm. The material exhibited anisotropic material properties as a result of rolling texture. Higher yield and tensile strengths in the transverse direction than in the longitudinal direction relative to the banded microstructure is common for DSS [1-3]. The 20 % cold work reduction in plate thickness nearly doubled the strength of the material and reduced the ductility by nearly 75 %. The relative strength of the TD as compared to the RD did not change due to the cold working. The Vickers microhardness of the austenite and ferrite phases (Table 7.2) increased in proportion the macroscopic properties. Figure 7.3 shows that the indents in the austenite and ferrite phases were similar. The indent size was too large to evaluate the microhardness in orientations other than RL.

***Table 7.1:*** ***Macroscopic mechanical properties for rolling direction (RD) and transverse direction (TD) of standard DSS S32205 tested by VTT Technical Research Centre of Finland.***

| | *Annealed* | | *20 % Cold Work* | |
|---|---|---|---|---|
| | *RD* | *TD* | *RD* | *TD* |
| Proof strength $R_{p0.2}$ (MPa) | 585 | 617 | 999 | 1034 |
| Tensile Strength $R_m$ (MPa) | 820 | 830 | 1079 | 1138 |
| Strain to failure A80 (%) | 29 | 28 | 9 | 7 |

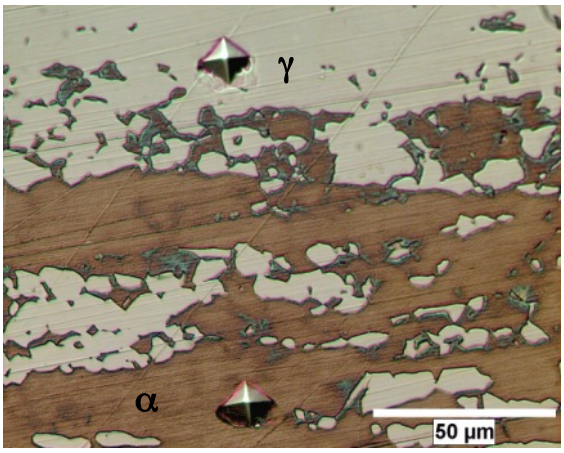


(a)

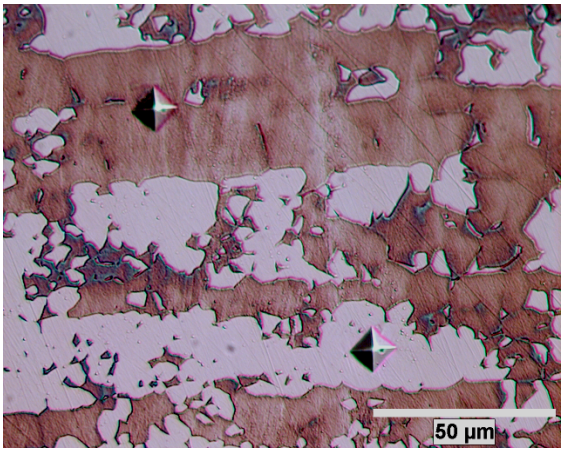


(b)

***Figure 7.3:*** ***Micrographs showing the microstructure (RL orientation) of (a) annealed and (b) 20 % cold worked standard as-received DSS S32205 evaluated in this study. Microhardness indents show similarity in hardness of the two phases and increased hardness of the cold worked specimen.***

***Table 7.2:*** ***Microhardness values ($HV_{25}$) of austenite and ferrite phase in rolling direction (RD) of as-received annealed and 20 % cold worked standard DSS S32205***

| | *Annealed Condition* | *20 % Cold Work Condition* |
|---|---|---|
| Austenite | 254±4 | 372±26 |
| Ferrite | 247±8 | 389±13 |

The residual microstresses in the austenite and ferrite phase of standard DSS S32205 were compared in the annealed condition and after 20 % cold work in this study.

The stresses were determined with X-ray diffraction in accordance with the techniques in the experimental section (Chapter 3).

Experimental and fitted $\sin^2\psi$ curves determined using X-ray diffraction on the electropolished surface of the annealed and 20 % cold worked DSS S32205 specimens are shown in Figure 7.4 and Figure 7.5 for austenite and ferrite, respectively. The anisotropy of single-crystal elastic constants and pronounced textures caused small non-linearities on the $\sin^2\psi$ plots fitted to the experimental points. The latter effects have been reviewed elsewhere [33]. A positive slope corresponding to tensile stress was observed for the austenite phase (Figure 7.4). A negative slope corresponding to compressive stress was seen in the ferrite phase (Figure 7.5). The slopes were greatest for $\phi = 90$ degrees indicating the highest residual stresses were in the transverse direction.

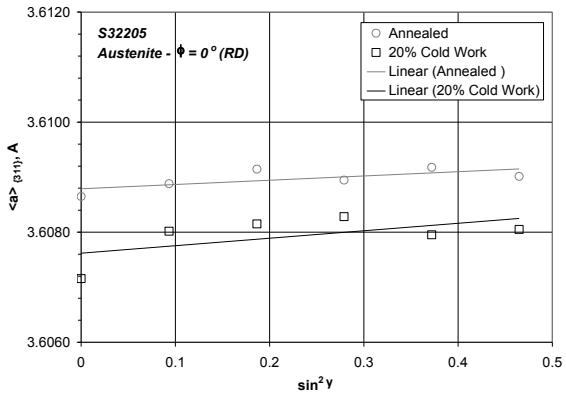


(a)

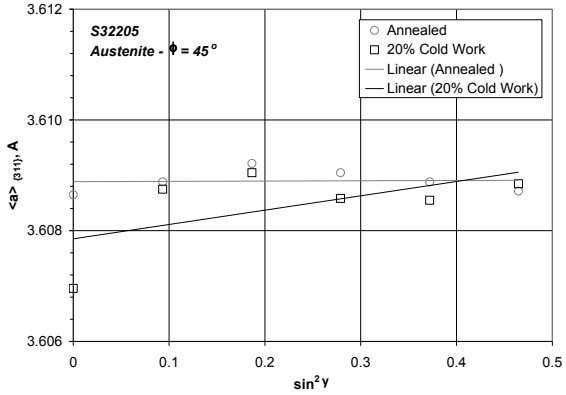


(b)

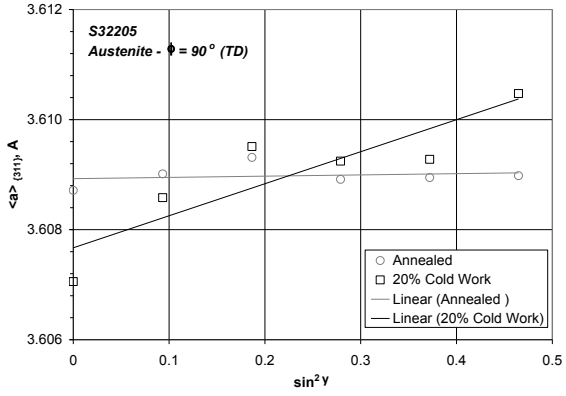


(c)

*Figure 7.4:* ***Experimental and fitted $\sin^2\psi$ curves for (a) $\psi = 0^o$, (b) $\psi = 45^0$, and (c) $\psi = 90^0$ determined using X-ray diffraction for the annealed and 20 % cold worked standard DSS S32205 (scattering vector is parallel to RD for $\psi = 0^o$). Lattice spacing of austenite {311} is shown.***

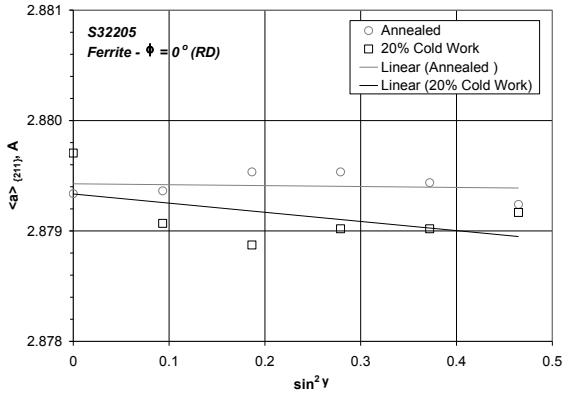


(a)

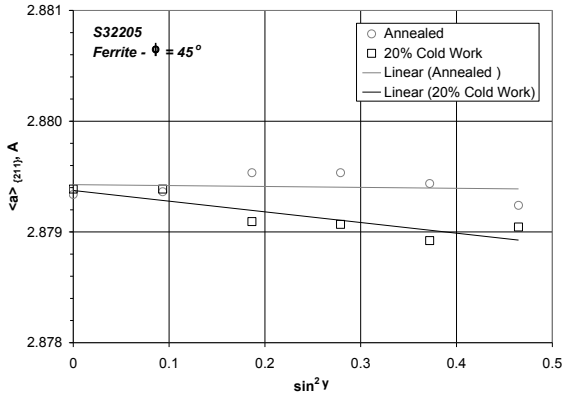


(b)

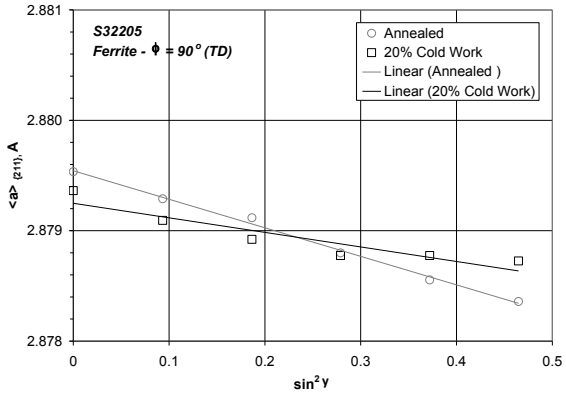


(c)

***Figure 7.5:*** ***Experimental and fitted $\sin^2\psi$ curves for (a) $\psi = 0^o$, (b) $\psi = 45^0$, and (c) $\psi = 90^0$ determined using X-ray diffraction for the annealed and 20 % cold worked standard DSS S32205 (scattering vector is parallel to RD for $\psi = 0^o$). Lattice spacing of ferrite {211} is shown.***

The average total stress measured from the ferrite and austenite phases are shown in Table 7.3 for several orientations. Refer to Chapter 3 for equations and assumptions used calculate the macrostresses $^{M}\sigma$ and microstresses. Measurements at zero applied load indicated there was a small macroscopic residual stress in the annealed sample and a relatively large tensile macrostress in the 20 % cold worked specimen. The microstresses were tensile in the austenite phase and compressive in the ferrite phase. The microstresses were higher in the transverse direction ($\phi = 90^{o}$) as compared to the rolling direction ($\phi = 0^{o}$). Errors associated with the experimentally measured average total stresses are also provided.

***Table 7.3:*** ***Residual microstresses of austenite and ferrite for different orientations (scattering vector is parallel to RD for $\psi = 0$ degrees) of annealed and 20 % cold rolled standard DSS S32205.***

| *Condition* | *Orientation ($\phi$, degree)* | $^{t}\sigma^{\gamma}$ *(MPa)* | *Error (±)* | $^{t}\sigma^{\alpha}$ *(MPa)* | *Error (±)* | $^{M}\sigma$ *(MPa)* | $^{\mu}\sigma^{\gamma}$ *(MPa)* | $^{\mu}\sigma^{\alpha}$ *(MPa)* |
|---|---|---|---|---|---|---|---|---|
| Annealed | 0 | -142 | 21 | 16 | 9 | -47 | -95 | 63 |
| | 45 | -72 | 10 | 26 | 9 | -13 | -59 | 39 |
| | 90 | 20 | 5 | 22 | 6 | 21 | -1 | 1 |
| | | | | | | | | |
| 20% Cold Work | 0 | -57 | 1 | 73 | 26 | 21 | -78 | 52 |
| | 45 | -39 | 5 | 120 | 14 | 56 | -95 | 64 |
| | 90 | -15 | 3 | 260 | 14 | 150 | -165 | 110 |

The influence of morphology and microstresses on the macroscopic behavior of a material was first studied by Winholtz and Cohen [34] in 1080 steel with pearlitic and spheroidal microstructure during low-cycle fatigue. Their results showed microstresses were higher in the pearlitic condition than in the spheroiditic condition. The authors

concluded that the differences were due to morphology; the pearlitic lamellae more effectively transfer load to the cementite phase. The higher microstresses gave the pearlitic condition a higher work-hardening rate than the spheroiditic condition. The microstresses in the current investigation were larger in the austenite phase of S32205 DSS, which indicates this phase would yield prior to the ferrite phase during large plastic deformation and further undergo work hardening with deformation

Microstresses have been studied on samples that were loaded to large plastic strains [35-38] or during thermal cycling [4-5] in earlier studies. These efforts showed that the microstresses increased with increasing plastic strain and the microstresses were always tensile in the austenite and compressive in the ferrite. Behavior was attributed to the faster hardening rate of austenite. The triaxial residual stress state in UNS S32304 (lean DSS 2304) was studied [6] *in-situ* during axial loading with X-ray diffraction and compared to results from finite element modeling. The authors concluded that the initial stress state influenced the stress evolution beyond the yield strength of the material, and the microstresses were primarily due to the initial thermal stresses. The results of the current study on S32205 are consistent with earlier studies on other grades of DSS.

### 7.3.2 Effect of Annealing and Quenching

DSS S32205 SSRT specimens were heated in a furnace at 1150 $^{o}$C and quenched in water to avoid precipitation of secondary phases. The microstructure of the annealed condition is shown in Figure 7.6. The as-received condition was shown in Chapter 3. A heavily banded microstructure was apparent for the annealed condition in all three orientations with austenitic islands in a ferritic matrix. The method of point counting [31] was used to determine the average area fraction of austenite ($A_\gamma$), number of point

interceptions per test length ($N_L$), and lineal fraction ($L_L$) for the RL and TL orientations in the annealed condition. The as-received material is compared to the annealed condition in Table 7.4. The results show that austenite phase was distributed more uniformly in the ferrite matrix (i.e., less continuous phase distribution) with larger regions of ferrite separating islands due to the annealing process.

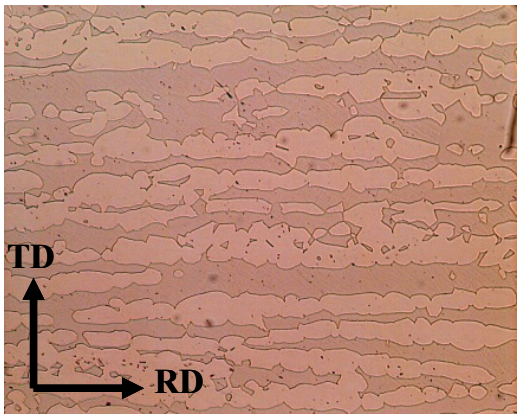


(a)

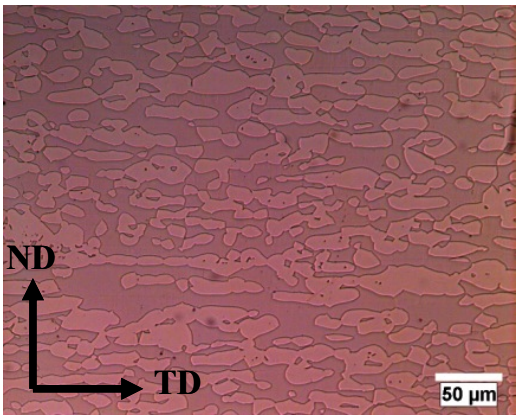


(b)

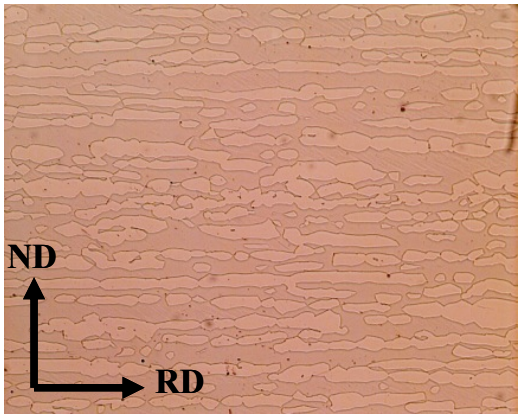


(c)

*Figure 7.6:* ***Micrographs showing the (a) RL orientation, (b) TS orientation, and (c) TL orientation microstructure of annealed standard DSS S32205 evaluated in this study.***

***Table 7.4:*** ***Quantitative stereology parameters for the austenite phase (light etching phase) of as-received and annealed standard DSS S32205 materials evaluated in this study***

| | *RL Orientation* | | | | *TL Orientation* | | | |
|---|---|---|---|---|---|---|---|---|
| *Condition* | $A_\gamma$ *(%)* | $N_L$ *($\mu m^{-1}$)* | $L_L$ | $L_L/N_L$ *($\mu m$)* | $A_\gamma$ *(%)* | $N_L$ *($\mu m^{-1}$)* | $L_L$ | $L_L/N_L$ *($\mu m$)* |
| As-received | 43±2 | 0.046±0.006 | 0.68±0.09 | 15 | 48±3 | 0.121±0.008 | 0.69±0.04 | 6 |
| Annealed | 48±4 | 0.033±0.008 | 0.52±0.13 | 33 | 51±4 | 0.061±0.004 | 0.57±0.04 | 16 |

Vickers microhardness ($HV_{25}$) was measured for the austenite and ferrite phases of as-received and annealed DSS S32205 as shown in Table 7.5. Ten measurements were made in the two phases for each orientation of the materials. The results show that the austenite and ferrite phases had generally similar hardness in DSS S32205, although the ferrite phase was slightly harder in the annealed condition. There was also a relatively small difference in hardness for the different orientations. There was an increase in the hardness of the as-received material as compared to the annealed material, particularly in the austenite phase. Hot rolling altered the mechanical properties of the two phases of the as-received material based on the hardness values.

***Table 7.5:*** ***Vickers microhardness ($HV_{25}$) of as-received and annealed DSS S32205***

| | *Austenite Phase* | | | *Ferrite Phase* | | |
|---|---|---|---|---|---|---|
| *Condition* | *RL* | *TS* | *TL* | *RL* | *TS* | *TL* |
| As-received | 306±14 | 306±9 | 306±9 | 317±20 | 297±14 | 287±13 |
| Annealed | 283±18 | 266±12 | 274±8 | 279±18 | 283±4 | 292±13 |

## 7.3 Stress Corrosion Cracking Behavior

### 7.3.1 Slow Strain Rate Testing in Chloride- and Sulfide-Containing Caustic Solution to Determine Anisotropic Effects in Microstructure on Fracture Features

SSRT was conducted in an autoclave at 170 $^{o}$C to evaluate the effect of microstructural anisotropy on the SCC behavior of S32205 and S32101 DSS. Samples were tested at an initial strain rate of $2x10^{-6}$ $s^{-1}$, and the load was applied along the RD. Tests on control specimens were conducted in sand at 170 $^{o}$C for comparison. Fractured tensile specimens were mounted and polished using standard laboratory practices. The maximum crack velocity ($\mu m\ s^{-1}$) and average crack density ($mm^{-1}$) in the plastically deformed (necking) region of the samples were measured in order to quantify the severity of SCC for the RL and TL orientations.

Test solutions were composed of 150 g/l (3.75 M) sodium hydroxide (NaOH) and 50 g/l (0.64 M) sodium sulfide ($Na_2S$) with 0 – 100 g/l (0.0085 – 1.7 M) of sodium chloride (NaCl). Previous laboratory studies [12] have used solutions containing only 3.75 M NaOH and 0.64 M $Na_2S$ to simulate environments used in the pulp and paper industry to show that DSS S32205 was susceptible to SCC. Recent field experience [26] also suggests that DSS S32205 is susceptible to SCC in pulping liquors containing high concentrations of chlorides. Chlorides were thus added to the solutions. Results from the SSRT in these environments are provided in Chapter 6.

Due to anisotropy in the material microstructures, elliptical fracture surfaces were observed in the fracture surfaces as shown for DSS S32205 in Figure 7.7. Elliptical fracture surfaces were associated with more ductility as evident by the % elongation at failure (Chapter 6). Similar behavior was found for DSS S32101 (not shown). Severe

SCC cracks were apparent along the TD, particularly with 0.034 – 0.087 M of NaCl for UNS S32205 and 0.17 – 1.7 M NaCl for DSS S32101. It is worth mentioning that cracks along the TD were observed in the RL orientation and cracks in the ND were observed in the TL orientation.

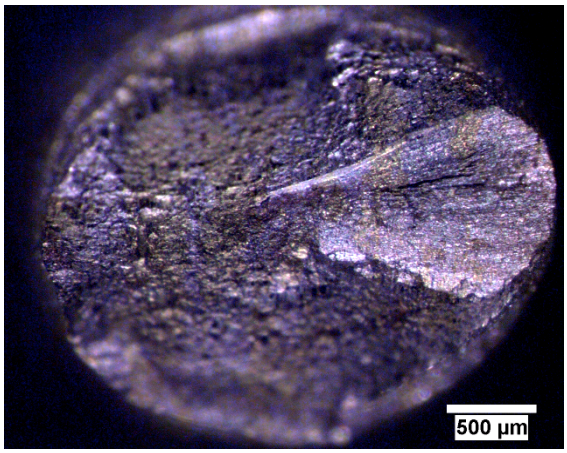


(a)


(b)

***Figure 7.7:*** ***(a) Micrograph showing the relatively round fracture surface of DSS S32205 tested in 3.75 M NaOH + 0.64 M Na2S + 0 M NaCl at 170 $^{o}$C. (b) A more elliptical fracture surface was observed for the fracture surface of a DSS S32205 sample tested in 3.75 M NaOH + 0.64 M Na2S + 1.7 M NaCl due to increased ductility associated with the failure.***

### 7.3.2 Crack Statistics

The crack length distribution resulting from chloride addition is expressed as a histogram plot for DSS S32205 (Fig 7.8) and S32101 (Figure 7.9). Chlorides clearly had a role on SCC initiation behavior based on the frequency of cracks as a function of concentration. The chloride concentrations that corresponded to preferential corrosion of the austenite phase in S32205 in the alkaline-solution (Chapter 6) was related to a greater number of cracks. Conversely, the number of cracks in lean DSS S32101 increased with chloride concentrations, which indicates that dissolution enhanced crack initiation in this material. The increased number of cracks was directly related to the severity of SCC in both DSS materials.

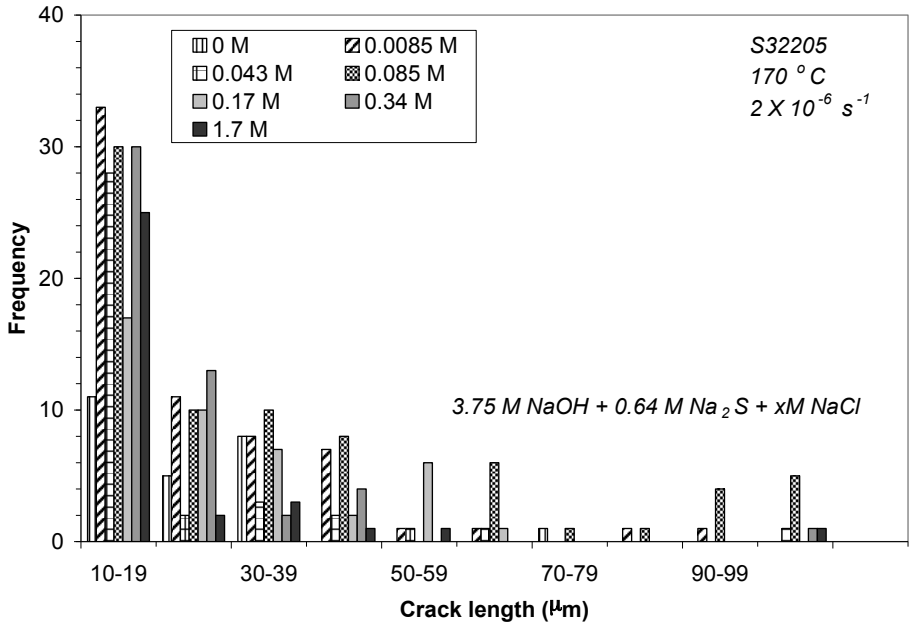


***Figure 7.8:*** ***Histogram showing the frequency of cracks of a given length in DSS S32205 tested by SSRT in 3.75 M NaOH + 0.64 M $Na_2S$ with various amounts of chloride at 170 °C.***

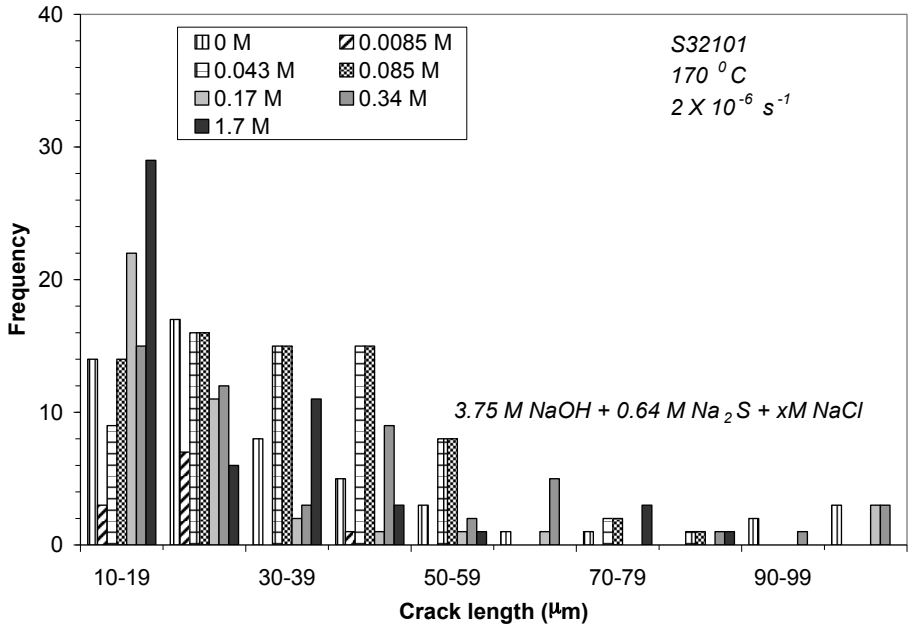


***Figure 7.9:*** ***Histogram showing the frequency of cracks of a given length in DSS S32101 tested by SSRT in 3.75 M NaOH + 0.64 M $Na_2S$ with various amounts of chloride at 170 °C.***

Significant differences in the maximum crack velocity and average crack density were found for the RL orientation and TL orientation in DSS S32205 and S32101 as shown in Figure 7.10 and Figure 7.11, respectively. Maximum crack velocity was determined from the length of the longest crack divided by the total time of the test. The only measured crack growth was normal to the RD or the applied load. Crack density was defined as the number of cracks per mm of the gage section. Higher crack density indicated there were a greater number of nucleation sites for crack initiation.

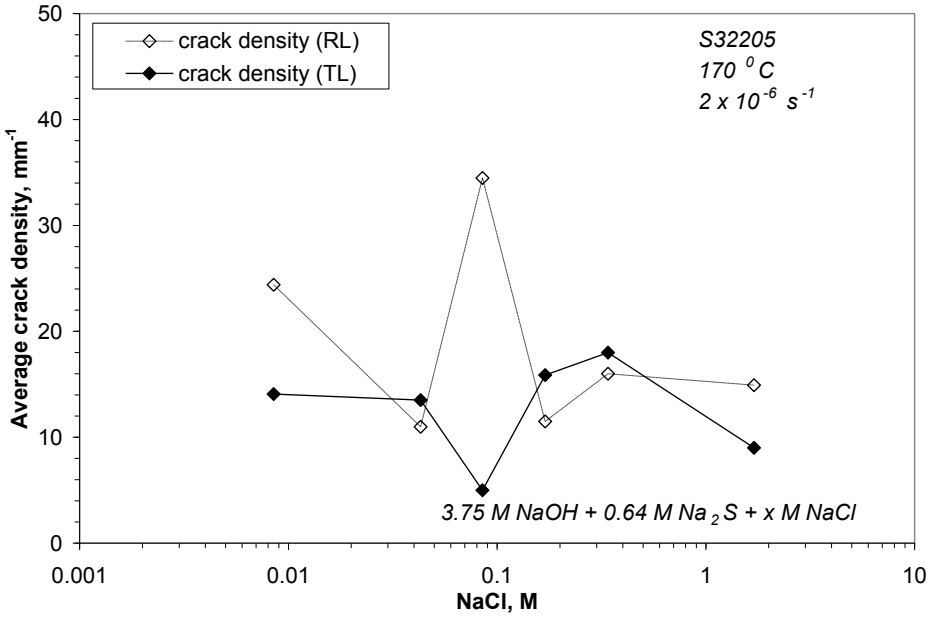


(a)

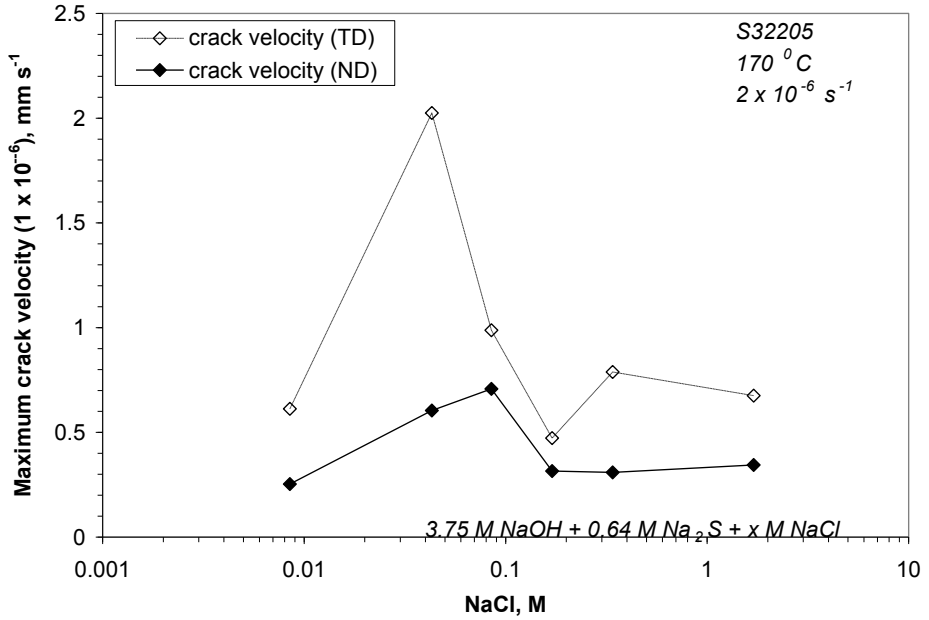


(b)

*Figure 7.10:* ***(a) Average crack density and (b) maximum crack velocity measured on the surface of DSS S32205 SSRT specimens tested in 3.75 M NaOH + 0.64 M $Na_2S$ with various amounts of chloride at 170 °C.***

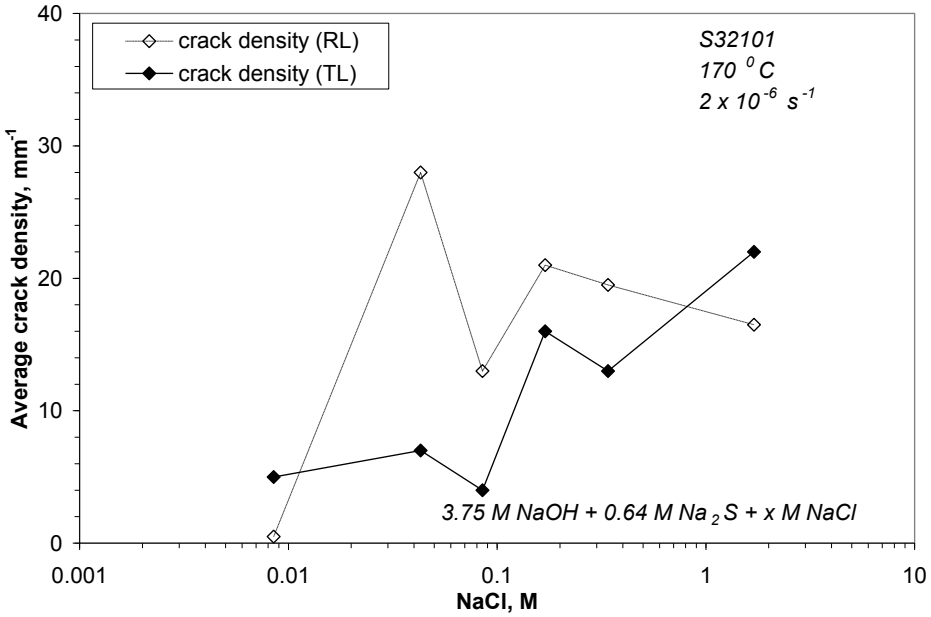


(a)

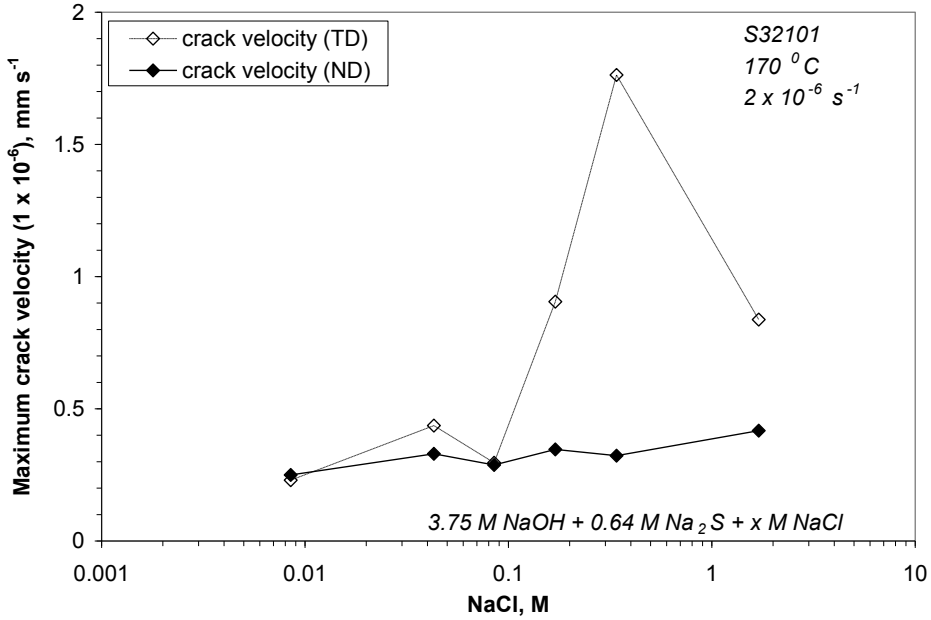


(b)

*Figure 7.11:* ***(a) Average crack density and (b) maximum crack velocity measured on the surface of DSS S32101 SSRT specimens tested in 3.75 M NaOH + 0.64 M $Na_2S$ with various amounts of chloride at 170 °C.***

The difference in crack density and maximum crack velocity between the two orientations indicated that crack initiation was easiest in the RL orientation and crack propagation was fastest in the TD. This behavior occurred more readily in DSS S32101 than DSS S32205 in the highest concentrations of chloride (0.17 – 1.7 M). However, DSS S32205 became more susceptible to TGSCC in lower concentrations of chloride (0.034 – 0.085 M) where selective corrosion of the austenite phase had occurred (Chapter 6). While the relative propensity for crack initiations with respect to the microstructures of the two materials was similar, the crack growth rates varied depending on the chloride concentration. Most cracks were found in the necked region in this material-environment system, indicating that the stresses required for crack initiation were close to the ultimate tensile strength of these materials.

It has been shown previously [1-3] that hot rolled DSS plates can have unusually large anisotropy of strength due to texture hardening. Furthermore, the microstresses in the austenite and ferrite phases were measured during loading [6]. The austenite phase was shown to be under residual tension while the ferrite phase was under residual compression due to a coefficient of thermal expansion mismatch. The study on 20 % cold worked S32205 also showed there were large residual stresses in the two phases even after plastic deformation (section 7.2.1). The microhardness values measured in Chapter 3 indicated that the austenite was as hard as the ferrite phase in DSS S32205 and harder in DSS S32101. Therefore, the tensile strength of the austenite phase must have been equal to or higher than the ferritic phase in the two materials.

The susceptibility of a material to SCC in a given environment strongly depends on the propensity for crack nucleation and crack propagation. Crack initiation in both

tested DSS was found to be in the austenite phase or at the austenite/ferrite phase boundaries, which is similar to previously reported observations in sulfide-containing caustic solution [12]. Solution composition was found to strongly influence the crack initiation process, whereby cracks initiate where dissolution rates are the highest (i.e., the austenite phase due to lower chromium content as shown in Chapter 3).

Anisotropic microstructure of DSS in different directions influences the initiation and growth of stress corrosion cracks. Data in Chapter 3 indicated that the RL orientation had the highest mean intercept length in both DSS S32205 and S32101. The austenite phase was more susceptible in alkaline-sulfide solution, so the distribution of austenite phase at the surface affects the crack initiation while the crack growth depends on the continuation of susceptible phase in a particular direction. This observation was also reflected by the maximum crack velocities and average crack densities in the TD and ND for DSS S32205 and S32101 in Figure 7.8 – 7.11.

When multiple cracks initiate at the surface, crack coalescence can influence the overall crack growth rate and failure [39]. An increase in crack density and crack length will favor crack coalescence or the tendency of neighboring cracks to coalesce to form longer cracks. Due to anisotropy and differences in the crack densities in different orientation, the probability of crack coalescence is also influenced. SEM micrographs showed a greater number of crack coalescences along the TD as compared to the ND (Chapter 6). SEM micrographs also showed an increase in crack density and therefore the number of crack coalescences with increasing chloride content from 0.0085 to 0.17 M NaCl, followed by a decrease in coalescence with increasing chloride due to more dissolution of Fe, Mn, and Mo based on the composition of the surface films (Chapter 6).

Microhardness data in Chapter 3 showed that the austenite phase in the TL orientation was harder than the RL orientation for DSS S32101, while no difference was found for DSS S32205. The difference in crack nucleation may also be attributed to texture arising from hot rolling [1-3], but no attempt was made to characterize texture in these materials. Texture in rolled DSS S32205 is well documented, and the results have shown texture of primarily components (100)[011]$\alpha$ in the ferrite phase and (110)[-112]$\gamma$ and (110)[1-1-2]$\gamma$ in the austenite phase. Anisotropy influences the tendency for cracks to nucleate and grow at regions of high stress. The anisotropic behavior observed for the as-received material indicates that texture effects will also strongly influence the crack growth behavior in SCC.

## 7.4 Conclusions

The micro- and macroscopic mechanical properties of standard DSS S32205 and lean DSS S32101 were related to SCC behavior. Microstructural features were associated with SCC initiation and growth behavior. The results indicate that microstructural anisotropy affects the SCC susceptibility of hot rolled DSS. The following main results were determined from this work:

- DSS S32205 underwent work hardening due to 20 % cold work. The strength due to cold work was increased by nearly 100 %, and the ductility was reduced by approximately 25 % with respect to the annealed condition in the longitudinal direction.
- The hardness of the ferrite and austenite phases of DSS S32205 was similar after annealing and 20 % cold work.

- Residual tensile stresses were observed in the austenite phase and were balanced by compressive stresses in the ferrite phase of DSS S32205 plates.
    - The magnitude of the residual stresses increased with 20 % cold work in austenite and ferrite.
    - The residual stresses originated from thermal stresses caused by the CTE mismatch of the two phases as reported elsewhere.
- Large differences in the maximum crack velocities and average crack densities were found between the RL and TL orientations in both UNS S32205 and UNS S32101.
- Maximum crack velocity was a maximum along the TD, thus crack initiation and growth were favored along the TD.
- Crack growth and coalescence of neighboring cracks were influenced by microstructure. Large cracks formed through the coalescence of smaller cracks, particularly in the presence of chlorides.
- Chlorides enhanced anisotropy in crack growth behavior by facilitating crack initiation and growth along austenite/ferrite phase boundaries, which lead to more severe SCC in the sulfide-containing caustic environments that were studied.
- Microstructure orientation was important for accurately characterizing SCC, particularly for round specimens machined from hot rolled plate.

## 7.5 REFERENCES

[1] Hutchinson, W.B., Ushioda, K., and Runnsjő, G., "Anisotropy of tensile behavior in a duplex stainless steel sheet," Mat. Sci. and Tech, Vol. 1 (1985), p.728.

[2] A. ul-Haq, H. Weiland, and H.J. Bunge, Mat. Sci. and Tech. 10 (1994) 289-298.

[3] A. ul-Haq, H. Weiland, and H.J. Bunge, J. of Mat. Sci. 29 (1994) 2168-2176.

[4] E. Werner, T. Siegmund, and F. Fischer, "A Computer Study of the Thermomechanical Deformation Behavior of a Duplex Steel," Computational Materials Science, vol. 3, 1994, pp. 279-285.

[5] T. Siegmund, E. Werner, and F.D. Fischer, "On the Thermomechanical Deformation Behavior of Duplex-type Materials," Journal of the Mechanics and Physics of Solids, vol. 43, 1995, pp. 495-532.

[6] J. Johansson, M. Odén, and X.H. Zeng, "Evolution of the Residual Stress State in a Duplex Stainless Steel during Loading," Acta Materialia, vol. 47, 1999, pp. 2669-2684.

[7] V.V. Silberschmidt and E. Werner, "Analysis of Thermal Residual Stresses in Duplex-type Materials," Computational Materials Science, vol. 16, 1999, pp. 39-52.

[8] Rondelli, G., Vicentini, B., and Sivieri, E., Corrosion Science, 39 (6): 1037 (1997).

[9] Wensley, A., Moskal, M., and Wilton, W., "Materials Selection for Kraft Batch Digesters," Corrosion/97, NACE Paper No. 378, 1997, Houston, TX.

[10] Wensley, A., and Champagne, P. NACE Corrosion, Paper No. 281, 1999, Houston, TX.

[11] Reid, C., "Stress corrosion cracking of austenitic and duplex stainless steels in the kraft pulp mill," 1999 TAPPI Engineering/Process and Product Quality Conference, September 12-16, 1999, Anaheim, CA.

[12] A. Bhattacharya, "Stress Corrosion Cracking of Duplex Stainless Steels in Caustic Solutions, Ph.D. Thesis, Georgia Institute of Technology, Atlanta, GA (2008).

[13] Wensley, A., NACE Corrosion, Paper No. 589, 2000, Houston, TX.

[14] Singh, P.M., Perdomo, J.J., Oteng, J.E., and Mahmood, J., Corrosion, "Stress corrosion cracking and corrosion fatigue cracking of a duplex stainless steel in white water environments," 60 (9): 852 (2004).

[15] Svensson, C., Pulliainen, M., Huttunen, M., and Niemelainen, P., 2005 TAPPI Engineering, Pulping, Environmental Conference, August 28-31, 2005, Philadelphia, PA.

[16] Gorog, M., "Digester outlet device scraper arm cracking," 2006 Engineering, Pulping and Environmental Conference, November 5-8, 2006, Atlanta, GA.

[17] Singh, P.M., Mahmood, J., and Conde, P. "Stress Corrosion Cracking and CorrosionSusceptibility of Duplex Stainless Steels in Caustic Solutions," CORROSION/2005, Paper No. 05196. (Houston, TX: NACE, 2005).

[18] Leinonen, H.T. and Pohjanne, P., " Stress corrosion cracking susceptibility of duplex stainless steels and their welds in simulated cooking environments," NACE Corrosion 2006, Paper No. 06244, March 12-16, 2006, San Diego, CA.

[19] ERC Project Report, Institute of Paper Science and Technology at Georgia Tech, August 2006.

[20] Bhattacharya, A., Singh, P.M., Leinonen, H.T., and Mahmood, J., NACE Corrosion 2006, Paper No. 06497, March 12-16, 2006, San Diego, CA.

[21] Bhattacharya, A. and Singh, P.M. Stress Corrosion Cracking of Welded 2205 Duplex Stainless Steel in Sulfide-Containing Caustic Solution, Journal of Failure Analysis and Prevention, Vol. 7 (5) (2007), p. 371.

[22] Bhattacharya, A. and Singh, P.M. "Corrosion and Stress Corrosion Cracking of Duplex Stainless Steels in Pulping Liquors," CORROSION/2007, Paper No. 07206. (Houston, TX: NACE, 2007).

[23] Bhattacharya, A., and Singh, P.M. "Effect of Heat Treatment on Corrosion and Stress Corrosion Cracking of S32205 Duplex Stainless Steel in Caustic Solution." Metallurgical and Materials Transactions A: Physical Metallurgy and Materials Science, Vol. 40A (6) (2009), p.1388.

[24] Ramo, J., Sillanpaa, Kujalao, A., Hyokyvirta, O., and Peltonen, S., Mat. And Corr. Vol. 52 (2001), p741.

[25] M. Honda et al., "Stress Corrosion Cracking of Stainless Alloys in Alkaline-Sulfide Solutions.," 1991.

[26] Bergquist, A., and Wegrelius, W. "Experiences in Pulp and Paper Industry of a 30 Years Old Steel Grade," 2009 TAPPI Conference, Paper No. Memphis, TN.

[27] P.M Singh et al., "Stress Corrosion Cracking and Corrosion Fatigue Cracking of a Duplex Stainless Steel in White Water Environments," Corrosion (Houston, Tex.), vol. 60, 2004, pp. 852-861.

[28] R. Oltra, A. Desestret, E. Mirabal, J.P. Bizouard, "A Critical Study of Stress Corrosion Cracking of Duplex Stainless Steels in Environments Containing

Chlorides and $H_2S$. Study of the Ferrite Phase Behavior," Corrosion Science, Vol. 27, I. 10-11, 1987, pp. 1251-1269.

[29] H.S. Kwon and H.S. Kim, "Investigation of stress corrosion susceptibility of duplex (alpha+ gamma) stainless steel in hot chloride solution," Materials Science and Engineering A(Switzerland), 1993, pp. 159-166.

[30] M. Puiggali, D. Desjardins, L. Ajana, "A Critical Study of Stress Corrosion Cracking Testing Method for Stainless Steels in Hot Chloride Media," Corrosion Science, Vol. 27, I. 6, 1987, pp. 585-594.

[31] L.M. Karlsson and A.M. Gokhale, Journal of Microscopy, 186 (1997) 143-152.

[32] ASTM E8, "Standard Test Methods for Tension Testing of Metal Materials," Vol. 03.01, ASTM International, West Conshohocken, PA (2003), p. 1-27.

[33] K. Inal, P. Gergaud, M. Francois, and J.L. Lebrun, Stress Analysis in a duplex steel," Scan. J. of Mettal. 28 (1999), pp. 139-150.

[34] R. Winholtz, and J. Cohen, J. Metall. Trans. 23A (1992), p. 341.

[35] J.L. Lebrun and K. Inal, in Proc. 45$^{th}$ Annual Denver X-Ray Conference, Denver, CO. Plenum Press, NY (1995).

[36] V. Hauk, H. Nikolin, and L.Z. Pintschovius, Metallk. 81 (1990), p. 556.

[37] K. Inal, and J.L. Lebrun, in Proc. ICRS-5, Linkoping, Sweden. Linkoping University (1997), p. 472.

[38] K. Kamachi et al., in Proc. Prog. in Science and Engineering of Composites, ICCM-IV, Tokyo. JSCM, Tokyo (1982), p. 1383.

[39] R.N. Parkins and P.M. Singh, "Stress Corrosion Crack Coalescence" Corrosion 46 (1990), pp. 485-499.

# CHAPTER 8

# HYDROGEN EMBRITTLEMENT OF UNS S32205 DUPLEX STAINLESS STEEL IN ALKALINE-SULFIDE SOLUTION

## 8.1 Introduction

Austenitic-ferritic duplex stainless steels (DSS) are widely used in chemical processing industries, including process streams that utilize sulfide-containing caustic (alkaline-sulfide) solutions. The most common industrial processes utilizing alkaline-sulfide solutions include the modified Bayer processes used in alumina ore processing, the Girdler-sulfide process used in heavy water production, hydrocarbon processing for the treatment of acidic impurities such as hydrogen sulfide and mercaptans, and various process streams in pulp mills utilizing the kraft pulping process. Field and laboratory experience [1-15] has shown that DSS equipment may fail by environmentally assisted cracking (EAC), which includes stress corrosion cracking (SCC) and hydrogen embrittlement (HE).

The electrochemical conditions necessary to cause HE of DSS in alkaline-sulfide environments is not well understood. Anodic protection is commonly used for corrosion control in kraft pulping digesters. The corrosion potential that is chosen for anodic protection is determined by the construction material and pulping environment. The onset of EAC could occur if the applied potential does not correspond to the passive region due to faulty equipment or improper installation. Furthermore, less noble materials such as carbon or low alloy steel may come in contact with DSS in pulping environments [16].

The galvanic effect caused by the coupling of these materials could shift the corrosion potential into a region where HE becomes a concern.

The intent of this work was to ascertain the electrochemical conditions required for HE of DSS S32205 in an alkaline-sulfide solution at room temperature. Previous work [1-8] showed that the austenite phase is susceptible to EAC at elevated temperatures in alkaline-sulfide solution (Chapter 6). Therefore, it was also an objective to evaluate the affect of hydrogen on the austenite and ferrite phases of DSS and the implications that hydrogen absorption had on crack initiation and growth.

## 8.2 Electrochemical Conditions Required for Hydrogen Embrittlement

### 8.2.1 Effect of Sulfide on Cathodic Polarization

The cathodic polarization behavior of the DSS S32205 specimen tested in deaerated, sulfide-free (3.75 M NaOH) solution and sulfide-containing (3.75 M NaOH + 0.64 M $Na_2S$) solutions is shown in Figure 8.1. The results indicate that the initial corrosion potential, i.e. open-circuit potential (OCP), was approximately -1170 and -1210 mV vs. standard calomel electrode (SCE) for the sulfide-free and sulfide-containing solutions, respectively. The addition of sulfide shifted the OCP in the active direction. The general features of these curves are similar, although the sulfide-containing solution had a slightly higher cathodic current density.

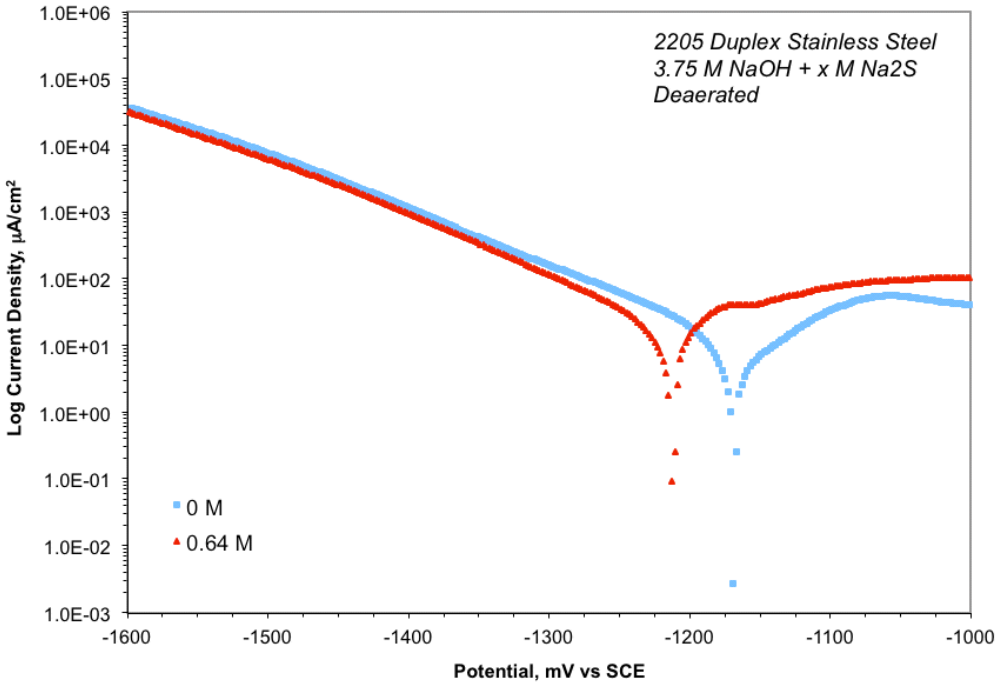


***Figure 8.1:*** ***Cathodic polarization behavior of DSS S32205 tested in deaerated 3.75 M NaOH with and without 0.64 M $Na_2S$ at room temperature. The potential was increased at a rate of 2 mV $s^{-1}$.***

### 8.2.2 Effect of Cathodic Polarization on Hydrogen Diffusion

Hydrogen permeation curves of DSS S32205 are shown in Figure 8.2. In this study, the steady-state permeation current density was used as indication of whether hydrogen produced on the sample surface could diffuse through a coupon of 200 µm within 1.6 x $10^6$ s (18 days) at select cathodic potentials. The results indicated that a small amount of hydrogen contributed to the permeation current density at -1500 mV vs. SCE. The OCP stabilized to approximately -700 mV vs. SCE after 1 h in the solution.

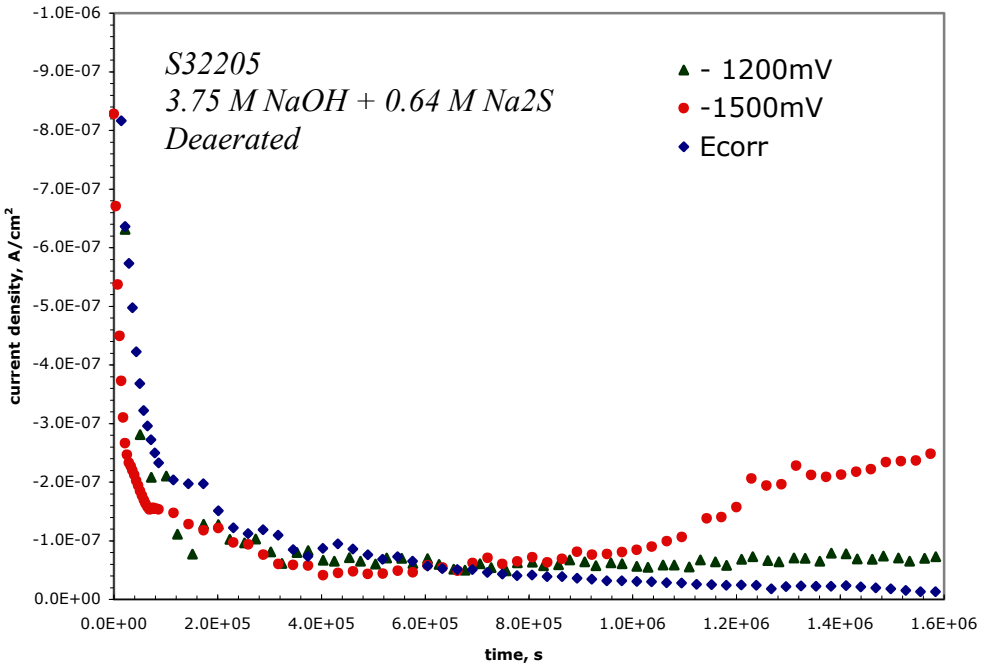


***Figure 8.2:*** ***Hydrogen permeation curves for DSS S32205 coupons tested in alkaline-sulfide solution (3.75 M NaOH + 0.64 M $Na_2S$) under applied cathodic potential of -1500 and -1200 mV vs. SCE as well as at the stabilized corrosion potential (~ -700 mV vs. SCE after 1 h) at room temperature.***

The hydrogen flux through the specimen was calculated in terms of the steady-state current density $i_p^{\infty}$ ($mA \cdot cm^{-2}$) and was converted into the steady-state hydrogen permeation flux, $J_{\infty}$ ($mol \cdot cm^{-2} \cdot s^{-1}$), according to

$$J_{\infty} = \frac{i_p^{\infty}}{nF} \qquad [8.1]$$

where n is the number of electrons transferred and F is Faraday's constant [17]. The hydrogen permeation rate ($mol \cdot cm^{-1} \cdot s^{-1}$) is given by

$$J_{\infty} L = \frac{i_p^{\infty}}{nF} L \qquad [8.2]$$

where L is the specimen thickness in mm. For diffusion as the rate-limiting step, the effective diffusivity, $D_{eff}$ ($cm^2 \cdot s^{-1}$) is related to the time lag, $t_L$ (s). The hydrogen permeation rate at -1500 mV vs. SCE can be estimated according to

$$D_{eff} = \frac{L^2}{6t_L} \qquad [8.3]$$

Taking the steady state current density as 3 X $10^{-7}$ $A \cdot cm^{-2}$, the value of $J_\infty$ is approximately 3.1 X $10^{-12}$ $mol \cdot cm^{-2} \cdot s^{-1}$. Sample thickness, L, for these tests was 200 μm. The hydrogen permeation rate for these DSS samples was found to be 6.2 X $10^{-12}$ $mol \cdot cm^{-1} \cdot s^{-1}$. If $t_L$ is taken as 9.5 x $10^5$ s, $D_{eff}$ for this study is 7.0 X $10^{-11}$ $cm^2 \cdot s^{-1}$. No hydrogen could be detected from the permeation current at -1200 mV vs. SCE or at the stabilized corrosion potential in the time period that was evaluated. This finding indicates that hydrogen at potentials more noble to -1500mV vs. SCE cannot be detected on the exit side by the electrochemical procedure used in this study.

Figure 8.3 shows a scanning electron microscope (SEM) image of the hydrogen microprinting [18] after a 24 h exposure at -1200 mV vs. SCE in the sulfide-free (3.75 M NaOH) solution for the S32205 material used in this investigation. Silver grains are predominantly on the surface of the Cr- and Mo- enriched phase (ferrite), which was confirmed by energy dispersive X-ray spectroscopy (EDS). The silver grains were primarily on the interior of the grains, without a preference for grain boundaries. Furthermore, there was no gradient in silver grains at the ferrite/austenite boundary.

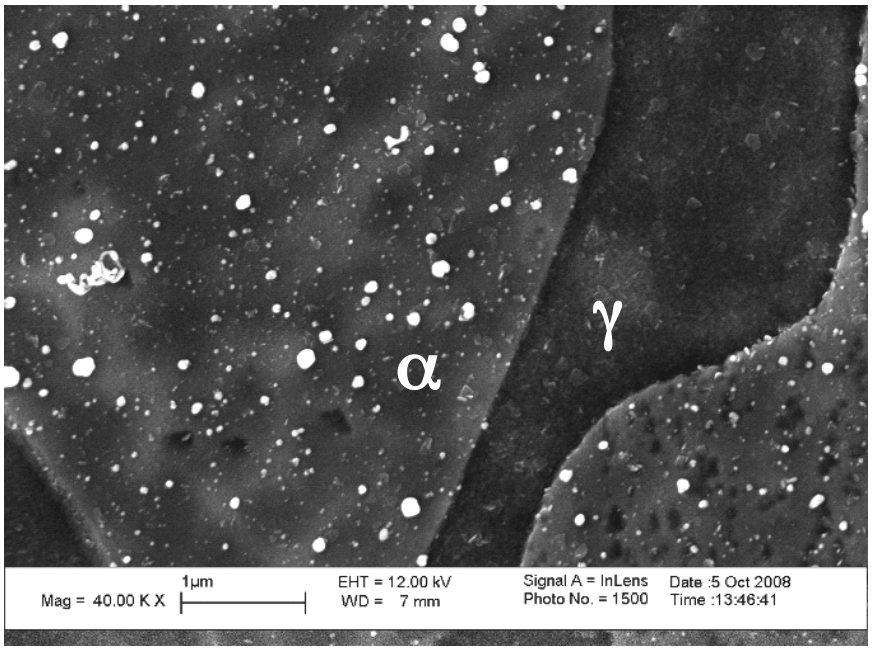


***Figure 8.3:*** ***Scanning electron micrograph of 2205 DSS polarized to -1200 mV vs. SCE in a sulfide-free (3.75 M NaOH) solution at for 24 h. Silver grains are present on ferrite phase.***

The equilibrium potential for the hydrogen evolution reaction in alkaline solutions given by the following reaction is -1026 mV vs. SCE,

$$2H_2O + 2e^- \rightarrow H_2 + 2OH^- \qquad (8.1)$$

At 25 $^oC$, the equilibrium potential for the oxidation of $Cr^{+2}$ (activity $10^{-6}$) given by (8.2) is -1330 mV vs. SCE, which is more active than OCP for DSS S32205 in an alkaline-sulfide solution of pH 13.3.

$$Cr \rightarrow Cr^{+2} + 2e^- \qquad (8.2)$$

The OCP will be between the dominant anodic and cathodic half-cell reactions for the equilibrium potentials for the reduction of water (8.1) and the oxidation of chromium (8.2) based on the mixed potential hypothesis of Wagner-Traud [19]. The addition of 0.64 M $Na_2S$ to the alkaline solution resulted in polarization of the reduction of water, thus sulfide affects the cathodic reaction as can been seen in Figure 8.1. Earlier work [20-22]

showed that sulfur-containing compounds blocked hydrogen adsorption and modified the Tafel relationship for the hydrogen evolution reaction. Based on a detailed study by Newman and Shreir [22], cathodic poisons can enhance the solubility of hydrogen absorption with an increase in poison concentration to a maximum when further increase in concentration produces little effect, which is known as the critical concentration. This result was supported by the findings of Tsai et al [14] who found that sulfur acted as a cathodic inhibitor in concentrations exceeding the critical concentration of 0.060 M in 3.5 % NaCl (0.06 M NaCl) solution. Based on the findings of Tsai et al, a concentration of 0.64 M $Na_2S$ is expected to decrease HE in 3.75 M NaOH.

The effective diffusivity (7.0 X $10^{-11}$ $cm^2 \cdot s^{-1}$) calculated from the coupon polarized to -1500 mV vs. SCE in Figure 8.2 indicates that hydrogen diffusion is slow in DSS S32205 exposed to the alkaline-sulfide solution at room temperature. Previous work [23-25] showed that the effective diffusivity of hydrogen in DSS S32205 at room temperature was 1.5 to 6.4 X $10^{-10}$ $cm^2 \cdot s^{-1}$, which is nearly an order of magnitude faster than in the alkaline-sulfide solution in the current study. Many factors can influence the diffusivity of hydrogen such as the metallurgical condition of the sample, sample thickness, stability of the charging media, hence the value obtained in this work is subject to a large variation from what has been found previously. Owing to the high permeability and slow diffusivity of hydrogen in the austenite phase, hydrogen diffusion occurred primarily through the ferrite lattice as would be expected. The diffusivity of hydrogen in the ferrite phase has been shown to be nearly 4 to 5 orders of magnitude greater than in the austenite phase [15]. Moreover, the microprinting results showed that silver grains

were predominantly on the ferrite phase, indicating that hydrogen did not have sufficient time to diffuse through the austenite phase to the surface in the time of the experiment.

## 8.3 Effect on Mechanical Behavior

### 8.3.1 Influence of Hydrogen Absorption on Microhardness

Microhardness of S32205 DSS samples polarized to cathodic potentials are shown in Figure 8.4. Microhardness was also conducted on a sample exposed to air (not shown) in order to confirm that the increase in hardness was not due to sample preparation. Data shown in Figure 8.4 was the average value from at least 20 hardness measurements for each condition. Standard deviation for hardness values was ~ 25 HV, which is large with respect to the differences in hardness between the samples exposed at OCP and -1200mV vs. SCE for different times. Hardness data in Fig 8.4 indicated that the influence of hydrogen absorption was minimal at -1200 mV vs. SCE, while there was no significant change in the hardness of DSS sample exposed at the OCP (approximately -700 mV. Vs. SCE after stabilization) for up to 24 hours. Owing to the experimental limitations of the microhardness tests, it was not possible to determine if hydrogen absorption had occurred at potentials more positive than -1200 mV vs. SCE. An increase in hardness was apparent for the DSS sample tested with applied potential of -1500 mV vs. SCE.

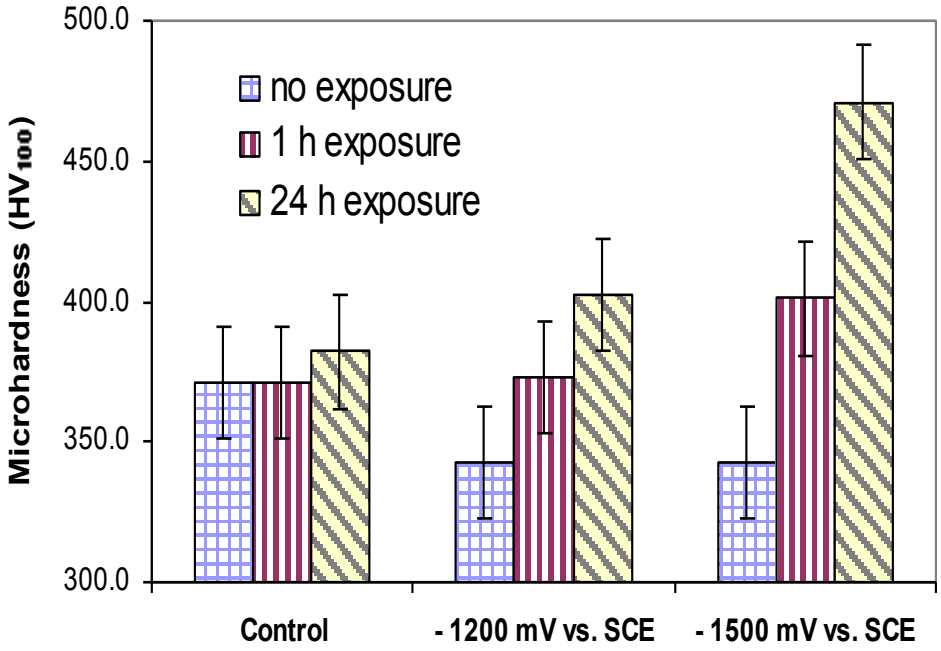


*Figure 8.4:* ***Vickers microhardness data for S32205 DSS polarized to -1200 mV vs. SCE and 1500 mV vs. SCE in alkaline-sulfide solution (3.75 M NaOH + 0.64 M $Na_2S$). The sample tested at the OCP (approximately -700 mV cs. SCE after stabilization) is shown for comparison (control).***

### 8.3.2 Effect of Cathodic Polarization on Slow Strain Rate Testing

The engineering stress vs. strain curves for DSS S32205 specimens tested at an initial strain rate of $2 \times 10^{-6}$ $s^{-1}$ in alkaline-sulfide solution at the free corrosion potential, i.e., stabilized OCP, and polarized to various potentials are shown in Figure 8.5. The curve of a control sample tested in air is also shown for comparison. The percent elongation at fracture ($\%\varepsilon_f$) for the sample tested in air and at the corrosion potential is similar owing to the absence of HE. There was a small reduction in ductility observed in the sample tested at the OCP due to the environment. At more negative potentials, however, there was a marked decrease in $\%\varepsilon_f$.

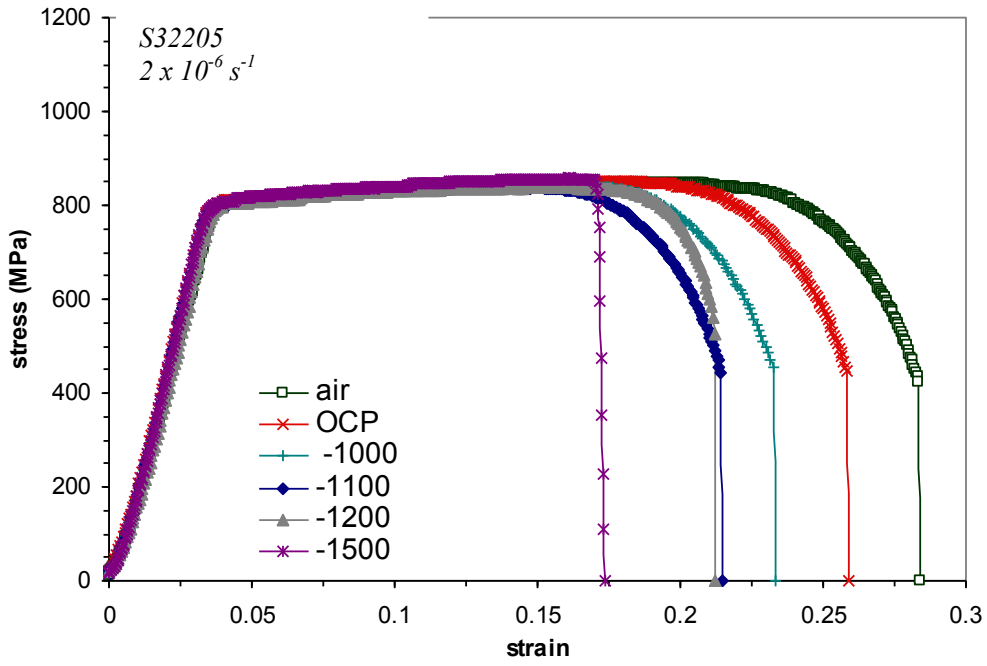


***Figure 8.5:*** ***Stress-strain curves measured on S32205 DSS tested in alkaline-sulfide solution (3.75 M NaOH + 0.64 M $Na_2S$) at the OCP and with applied potentials of -1500, -1200, -1100, and -1000 mV vs. SCE. A sample was tested in air for comparison.***

The slow strain rate testing (SSRT) results are provided in Table 8.1. As expected, the severity of HE was found to increase as a function of the magnitude of the applied cathodic potential. However, HE was not detected in the sample tested the OCP, which was found to be -700 mV vs. SCE by the end of the test. The percent reduction in area (% RA) correlated well with the fracture morphologies observed by optical microscopy. The time to failure decrease resulted from an increase in the applied cathodic potential. The longest crack from each specimen was measured and divided by the total test time to calculate the maximum crack velocity in mm $s^{-1}$. The crack velocity for the sample tested at -1200 mV vs. SCE was one order of magnitude greater than the sample tested at -1100 mV vs. SCE, which indicates that there is a significant increase in the hydrogen absorption at the more negative potential.

***Table 8.1*** ***SSRT results from DSS S32205 tested in alkaline-sulfide solution (3.75 M NaOH + 0.64 M $Na_2S$) at room temperature***

| *Potential, V vs. SCE* | *EAC Susceptibility* | *% RA* | *Time to Failure, h* | *Maximum Crack Velocity, mm/s* |
|---|---|---|---|---|
| -1500 | HE | 22 | 24.2 | 3.5 E-06 |
| -1200 | HE | 41 | 29.4 | 1.5 E-06 |
| -1100 | HE / SCC | 74 | 29.9 | 1.8 E-07 |
| -1000 | no HE | 78 | 32.4 | - |
| -700 (OCP) | no HE | 78 | 36.0 | - |
| air | no HE | 80 | 39.4 | - |

The % RA as a function of the potentials evaluated in this study is provided in Figure 8.6. There was a significant decrease in % RA at potentials that were more negative than -1100 mV vs. SCE, which indicates embrittlement. The samples tested in air and at the OCP had a % RA of 80 and 78, respectively, whereas this value was reduced to 41 at -1200 mV vs. SCE and to 22 at -1500 mV vs. SCE. The % RA is a favorable metric for qualitatively evaluating the onset of EAC.

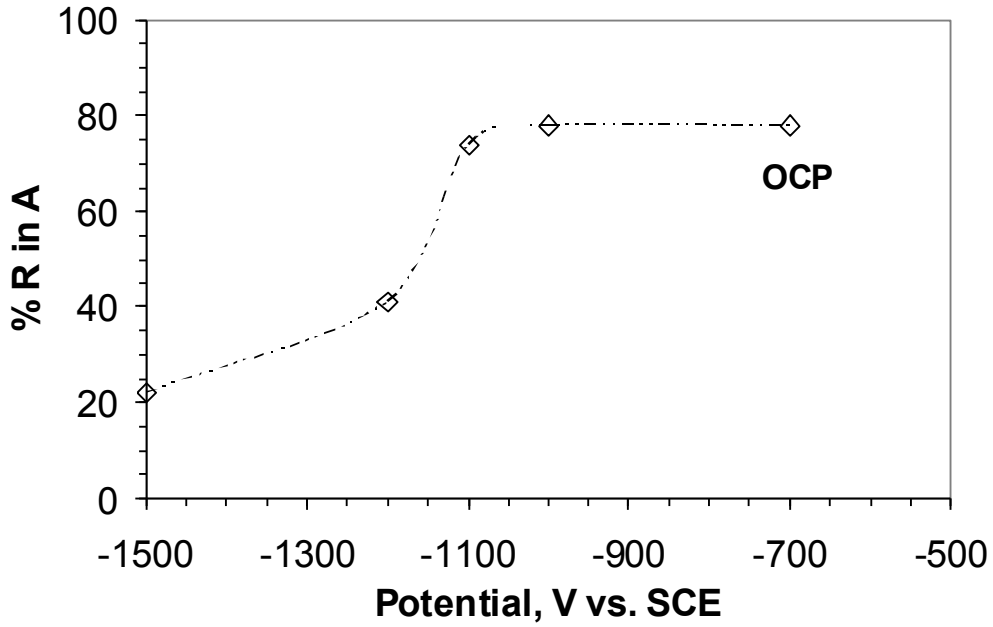


***Figure 8.6:*** ***The % RA values measured on the fracture surfaces of S32205 DSS tested in alkaline-sulfide solution (3.75 M NaOH + 0.64 M $Na_2S$) at the OCP and applied cathodic potentials.***

The metallographic observations of the samples tested at potentials more negative than -1100 mV vs. SCE showed the presence of many transgranular secondary cracks with limited branching. Micrographs for the sample tested at -1500 mV vs. SCE are provided in Figure 8.7. Crack initiation was in the ferrite phase (darker etching phase).

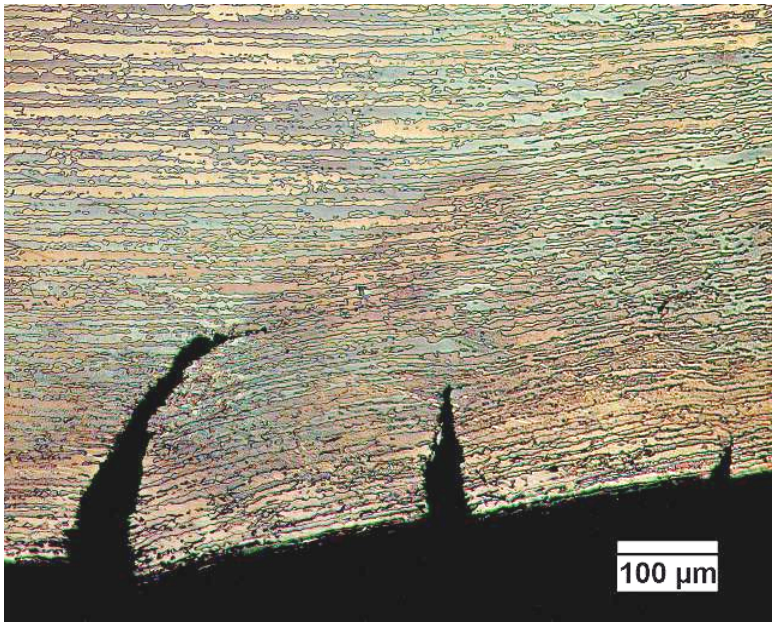


(a)

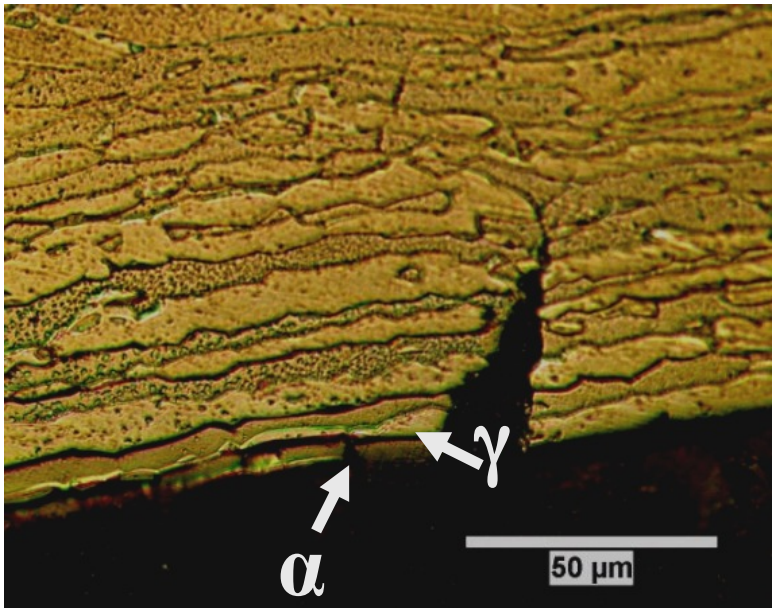


(b)

*Figure 8.7:* ***Optical micrographs (a) low magnification and (b) high magnification of S32205 DSS polarized to -1500 mV vs. SCE in alkaline-sulfide solution (3.75 M NaOH + 0.64 M $Na_2S$) at room temperature. Cracks initiated in the ferrite phase (darker etching phase) in (b).***

Figure 8.8 shows the gauge sections of the specimens polarized at -1500, -1200, and -1100 mV vs. SCE as well as the sample tested at the stabilized OCP (ca. 700 mV vs. SCE). There were fewer secondary cracks in the sample tested at -1500 mV vs. SCE than at -1200 mV vs. SCE. There was very limited necking in the latter samples. There was a limited amount of secondary cracks present in the sample tested at -1100 mV vs. SCE as compared to the samples tested at more negative potentials. Cracks in this sample were limited to the necked region. No cracks could be detected in the samples tested at -1000 mV vs. SCE or at the OCP.

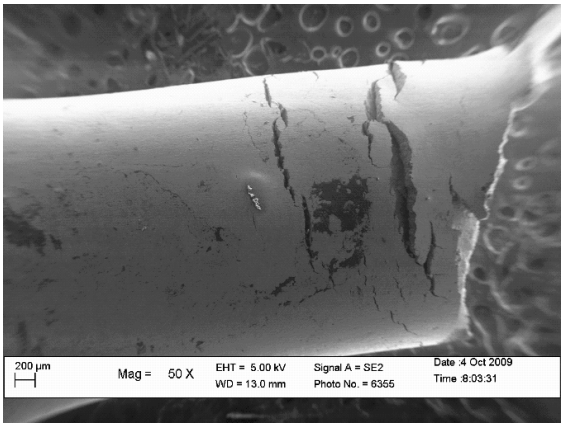


(a)

***Figure 8.8:*** ***(a) SEM fractographs of S32205 DSS that was strained to failure at 2 X $10^{-6}$ $s^{-1}$ in sulfide-containing (3.75 M NaOH + 0.64 M $Na_2S$) solution polarized to -1500 mV vs. SCE at room temperature.***

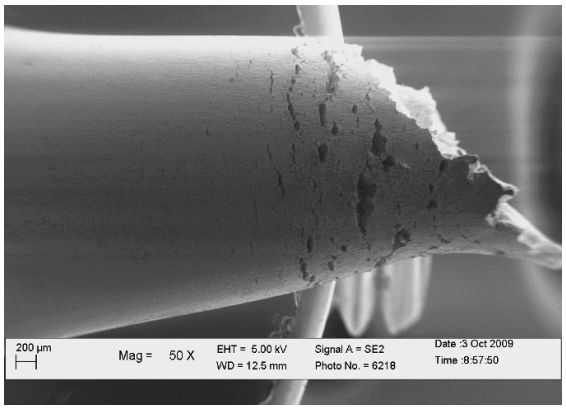


(b)

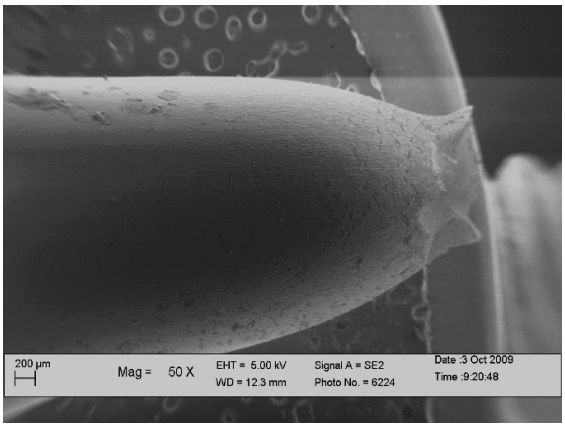


(c)

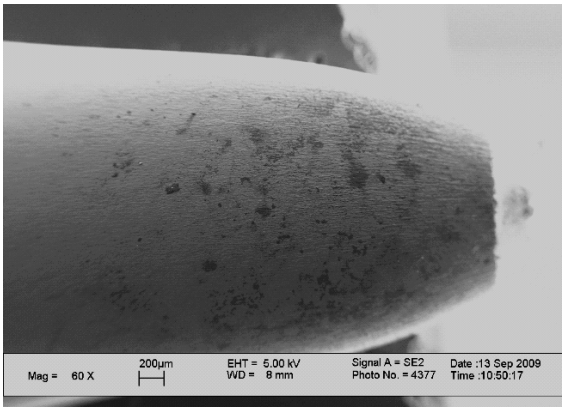


(d)

***Figure 8.8(cont'd):*** ***SEM fractographs of S32205 DSS that was strained to failure at 2 X $10^{-6}$ $s^{-1}$ in sulfide-containing (3.75 M NaOH + 0.64 M $Na_2S$) solution polarized to (a) -1500 mV vs. SCE (b) -1200 mV vs. SCE, (c) -1100 mV vs. SCE, and (d) OCP at room temperature.***

The fracture morphology was examined under SEM after each test, and the observations were consistent with the SSRT failure metrics. The fracture morphology was predominantly transgranular in the specimen tested in sulfide-containing solution at an applied potential of -1500 mV vs. SCE as shown in Figure 8.9. Cracks were initiated primarily in the ferrite phase and propagated transgranularly into the specimen. A transgranular cleavage failure associated with rough stepwise tearing developed at -1500 mV vs. SCE as shown in Figure 8.9b.

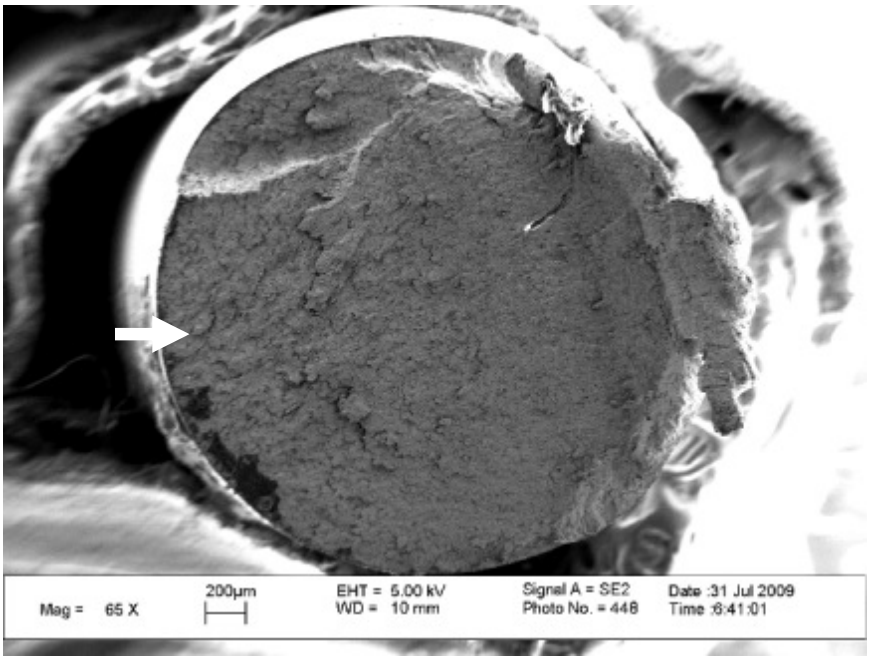


(a)

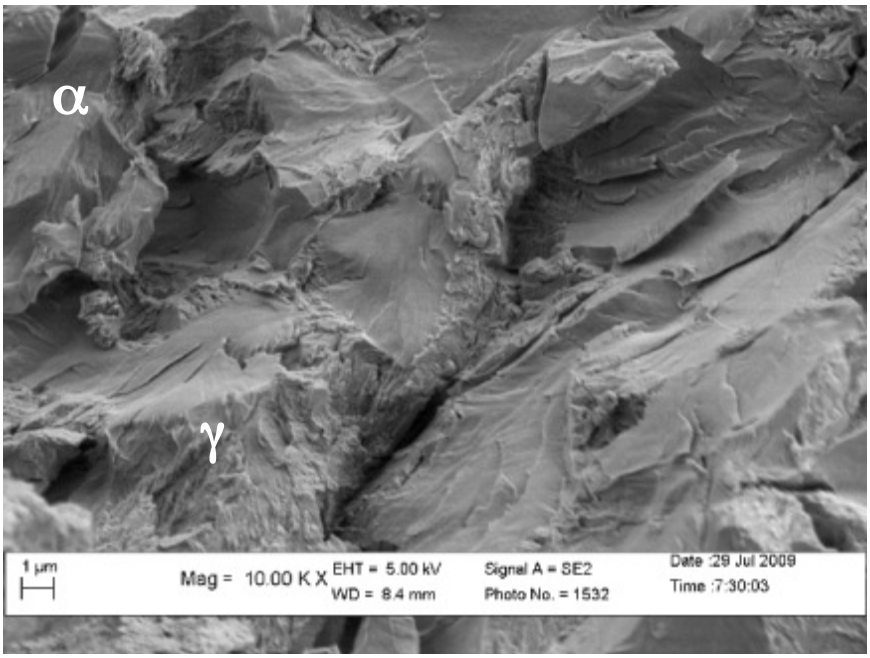


(b)

***Figure 8.9:*** ***Fracture surface of the S32205 DSS that was strained to failure at 2 X $10^{-6}$ $s^{-1}$ in alkaline-sulfide solution (3.75 M NaOH + 0.64 M $Na_2S$) polarized to -1500 mV vs. SCE at room temperature: (a) low magnification of surface and (b) high magnification of edge near failure initiation indicated by arrow.***

The samples tested at -1200 and -1100 mV vs. SCE also failed by a transgranular cleavage mode as shown in Figure 8.10. The ferrite grains showed a brittle cleavage failure mode at these potentials. The ferrite fracture facets frequently showed deep perpendicular cracks. Unlike the samples tested at -1500 and -1200 mV vs. SCE where a rough stepwise morphology developed in the austenite phase, there was a transition in failure mode to ductile tearing in this phase at -1100 mV vs. SCE as shown in Figure 8.10b.

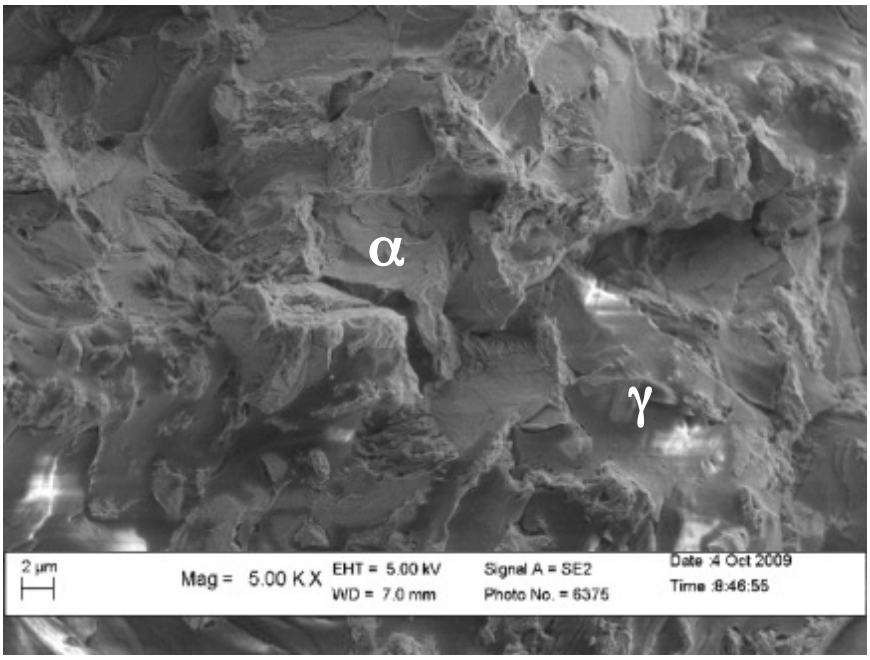


(a)

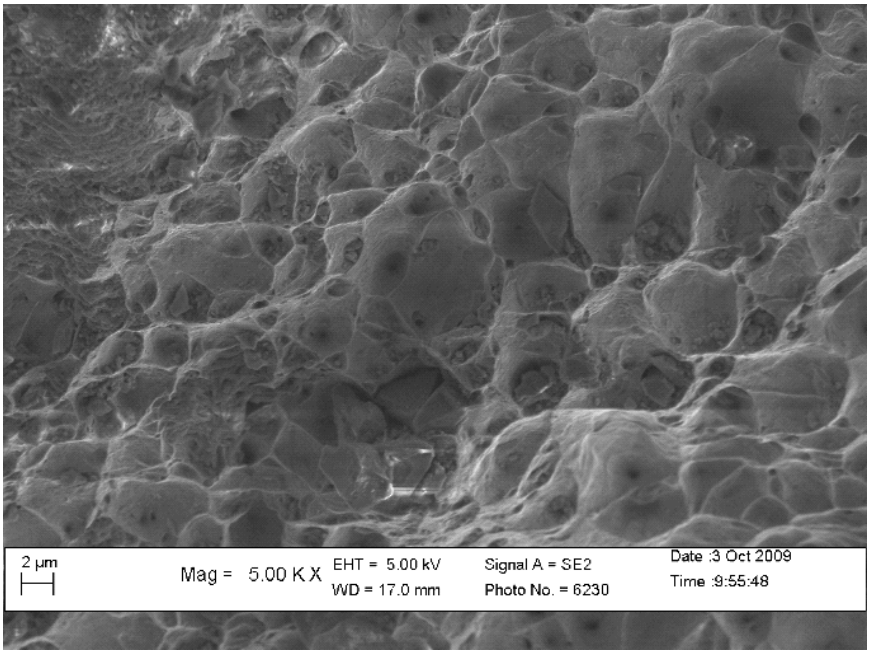


(b)

***Figure 8.10:*** ***Micrographs showing high magnification fracture features of the S32205 DSS strained to failure at 2 X $10^{-6}$ $s^{-1}$ in alkaline-sulfide solution (3.75 M + 0.64 M $Na_2S$) polarized to (a) -1200 mV vs. SCE and (b) -1100 mV vs. SCE.***

The fracture morphology of the samples tested in alkaline-sulfide solution at room temperature at -1000 mV vs. SCE and OCP were similar to that of a sample tested in air. The fracture morphologies of OCP and air are shown in Figure 8.11a and Figure 8.11b, respectively. There was no evidence of HE in the samples tested at potentials more noble than -1100 mV vs. SCE. Moreover, secondary cracks could not be detected on the sample surfaces. These samples failed by ductile fracture. Ductile dimples could frequently be observed on the fracture surfaces.

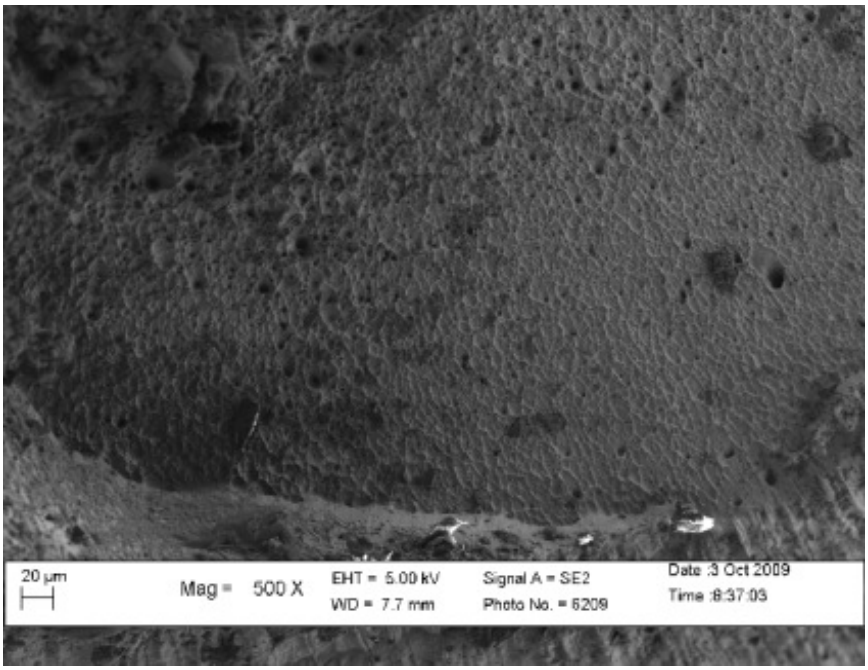


(a)

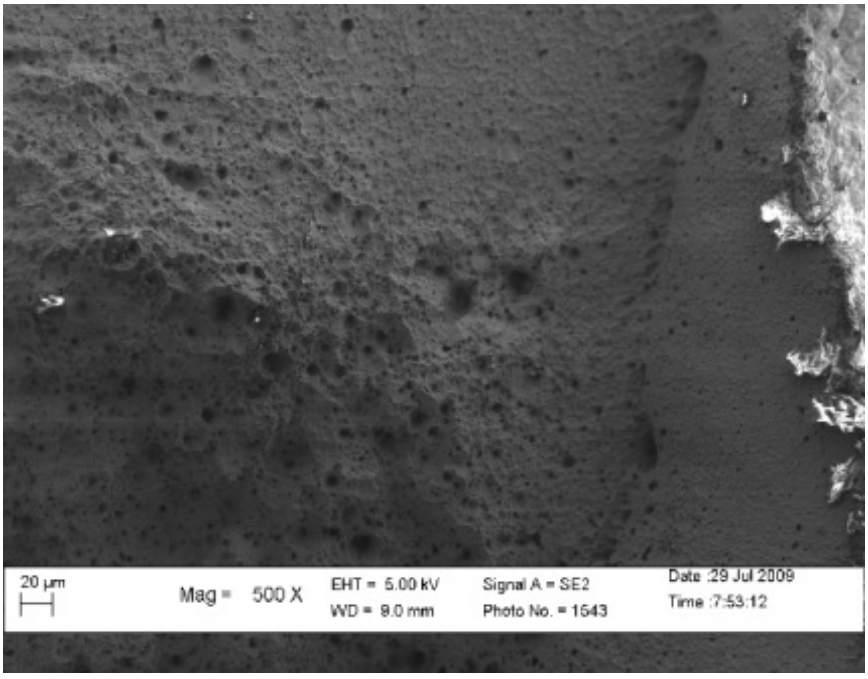


(b)

***Figure 8.11:*** ***SEM micrographs showing the fracture features of S32205 DSS that was strained to failure at 2 X 10-6 $s^{-1}$ at room temperature: (a) OCP (ca. -700 mV vs. SCE) in alkaline-sulfide solution (3.75 M NaOH + 0.64 M $Na_2S$) and (b) air.***

The results of the SSRT indicated that HE of DSS S32205 can occur in alkaline-sulfide solutions at sufficiently cathodic potentials applied at room temperature. The fracture surfaces clearly showed that the preferred phase for crack initiation is the ferrite phase. Indeed, the ferrite phase was more susceptible to the effects of HE under the conditions that were evaluated based on the fracture morphology examined under SEM. Brittle cleavage was observed in the ferrite phase for all cases where HE had occurred. The austenite phase became susceptible to HE at cathodic potentials that were less noble than -1100 mV vs. SCE. Cracking in the austenite phase was observed in Figure 8.9 for the sample tested at -1500 mV vs. SCE. At -1500 and -1200 mV vs. SCE, the austenite phase was susceptible to HE, which has previously been explained by the hydrogen-enhanced localized plasticity model [26]. The severity of HE was markedly increased when the austenite phase was rendered susceptible under an applied cathodic potential. Microhardness data did not show an increase in hardness at potentials nobler than -1200 mV vs. SCE because hydrogen had not embrittled the austenite phase at these potentials. For sample tested at -1100 mV vs. SCE cracks could only be detected in the necked region of the specimen, which indicated that stresses near the ultimate tensile strength were required for HE under these potentials. The fracture features at -1100 mV vs. SCE showed a brittle-to-ductile transition in the failure mode as compared to samples tested at less noble potentials.

Cathodic polarization of DSS S32205 specimens strained in alkaline-sulfide solution of 3.75 M NaOH and 0.64 M $Na_2S$ resulted in HE at potentials less noble than -1100 mV vs. SCE. Based on the potential gradient between the initial corrosion potential (-1210 mV vs. SCE) from Figure 8.1 and the applied cathodic potential, it was expected

that HE was not observed at potentials nobler than -1100 mV vs. SCE. Susceptibility to HE increased as a function of the applied potential, whereby severe HE was observed at potentials of -1200 and -1500 mV vs. SCE. At these potentials, the rapid ingress of hydrogen into the metal was favored due to the instability of the passive film, particularly if the film is damaged due to strain as well as a higher fugacity of hydrogen. The solution pH was measured before each test and found to be 13.3. For this system at 25 $^{o}$C and assuming a pH of 13.3, film formation was not thermodynamically favorable at -1200 or -1500 mV vs. SCE as predicted by the E-pH (Pourbaix) diagram of the Fe-Cr-Ni system at 25 $^{o}$C (Figure 8.12) [27].

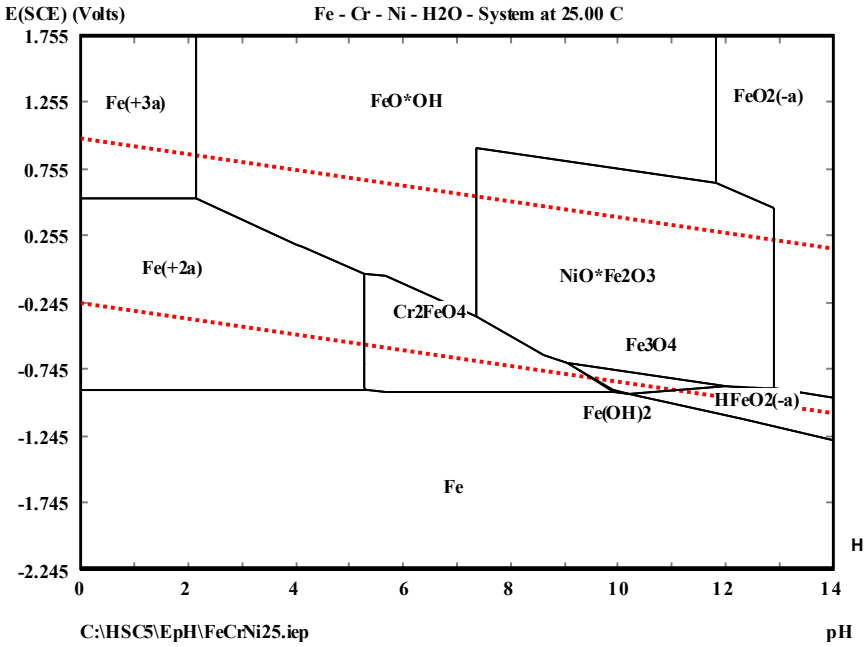


***Figure 8.12:*** ***E-pH diagram for the Fe-Cr-Ni system at 25 $^{o}$C [27] showing the thermodynamic stability of water as indicated by the solid red lines.***

The SSRT curves in conjunction with the fractography results showed that the threshold potential for HE of DSS tested in alkaline-sulfide solution was approximately -1100 mV vs. SCE in this investigation. At this potential, there was a change in the fracture morphology of the austenite phase. Owing to the higher diffusivity and lower solubility for hydrogen in the ferrite phase, hydrogen was transferred primarily through this phase during cathodic charging. At less cathodic potentials (i.e., more noble potentials), there was not a sufficient amount of hydrogen to render DSS S32205 susceptible to EAC due to the high solubility for hydrogen in the austenite phase. The austenite phase has a beneficial effect on preventing HE of DSS in alkaline-sulfide solutions, which is similar to the results of work conducted on acidic and neutral pH environments [9-15]. These findings highlight the likelihood that the EAC observed at higher temperatures [1-8] was likely attributed to an anodic dissolution process in lieu of an absorption mechanism (Chapter 6). Nonetheless, care should be exercised in industrial processes where there is a potential for galvanic coupling or improper anodic protection ($E \leq -1100$ mV vs. SCE) of DSS, even under strong alkaline conditions.

## 8.4 Conclusions

SSRT under applied potential and electrochemical techniques were used to study the influence of hydrogen on the EAC of DSS S32205 in alkaline-sulfide solution at room temperature in this work. The results indicated that an increase in the cathodic potential enhanced the severity of HE below a threshold potential of -1100 mV vs. SCE. DSS may therefore become susceptible to HE in alkaline-sulfide environments when hydrogen evolution is possible due to galvanic effects or applied potentials. The main results from this work were the following:

- The electrochemical measurements indicated that the addition of sulfide to an alkaline solution shifted the corrosion potential to a less noble potential.
- Hydrogen permeation in DSS S32205 was minimal after 1.6 x $10^{16}$ s (18 days) in alkaline-sulfide solution (3.75 M NaOH + 0.64 M $Na_2S$) even when polarized to -1500 mV vs. SCE at room temperature.
- An increase in the Vickers microhardness of DSS S32205 was apparent when the applied cathodic potential was less noble than -1200 mV vs. SCE in an alkaline-sulfide solution at room temperature.
- SSRT tests showed there was HE of DSS S32205 when the applied cathodic potential was less noble than -1100 mV vs. SCE, which was the threshold potential in the alkaline-sulfide solution evaluated in this study.
- The ferrite phase was more susceptible to HE in alkaline-sulfide solution as compared to the austenite phase, which has also been shown in acidic and near neutral pH environments.
- Care should be taken in industrial processes when there is a potential for galvanic coupling with a more active metal, such as carbon or low alloy steel, or where anodic protection is used in plant equipment.

## 8.5 REFERENCES


[1] G. Rondelli, B. Vicentini, E. Sivieri, Corr. Sci, Vol. 39 (1997), p. 1037.

[2] H.T. Leinonen, P. Pohjanne, "Stress Corrosion Cracking Susceptibility of Duplex Stainless Steels and Their Welds in Simulated Cooking Environments", CORROSION/2006, Paper No. 06244. (San Diego, CA: NACE, 2006).

[3] A. Bhattacharya and P. M. Singh, Stress Corrosion Cracking of Welded 2205 Duplex Stainless Steel in Sulfide-Containing Caustic Solution, Journal of Failure Analysis and Prevention, Vol. 7 (5) (2007), p. 371.

[4] P.M. Singh, J. Mahmood, P. Conde, "Stress Corrosion Cracking and Corrosion Susceptibility of Duplex Stainless Steels in Caustic Solutions," CORROSION/2005, Paper No. 05196. (Houston, TX: NACE, 2005).

[5] A. Bhattacharya, P.M. Singh, H.T. Leinonen, and J. Mahmood, NACE Corrosion/2006, Paper No. 06497. (San Diego, CA: NACE, 2006).

[6] A. Bhattacharya and P.M. Singh,"Corrosion and Stress Corrosion Cracking of Duplex Stainless Steels in Pulping Liquors," CORROSION/2007, Paper No. 07206. (Houston, TX: NACE, 2007).

[7] A. Bhattacharya, P. M. Singh, Effect of Heat Treatment on Corrosion and Stress Corrosion Cracking of S32205 Duplex Stainless Steel in Caustic Solution. Metallurgical and Materials Transactions A: Physical Metallurgy and Materials Science, Vol. 40A (6) (2009), p.1388.

[8] A. Bhattacharya and P. M. Singh, Effect of heat treatment on corrosion and Stress Corrosion Cracking of 2205 and 2101 duplex stainless steels in caustic solutions, Corrosion. Vol. 64, (6) (2008), p. 532.

[9] M. Barteri, F. Mancia, A. Tamba, and G. Montagna**, "**Engineering Diagrams and Sulphide Stress Corrosion Cracking of Duplex Stainless Steels in Deep Sour Well Environment," Corr. Sci, Vol. 27 (10/11) (1987), p. 1239.

[10] K. Van Gelder, J.G. Erlings, J.W. M. Damen, and A. Visser, "The Stress Corrosion Cracking of Duplex Stainless Steel in $H_2S/CO_2/Cl^-$ Environments," Corr. Sci., Vol. 27 (10/11) (1987), p. 1271.

[11] A.A. El-Yazgi and D. Hardie, "Stress Corrosion Cracking of Duplex and Super Duplex Stainless Steels in Sour Gas Environments," Corr. Sci. Vol. 40 (6) (1998), p.909.

[12] A. Turnbull, A. Griffiths, and T. Reid, "Hydrogen Embrittlement of Duplex Stainless Steels – Simulating Service Experience," CORROSION/1999, Paper No. 00148. (Houston, TX: NACE, 1999).

[13] F. Zucchi et al. "Hydrogen Embrittlement of Duplex Stainless Steel under Cathodic Protection in Acidic Artificial Sea Water in the Presence of Sulphide Ions," Corr. Sci., Vol. 48 (2006), p. 522.

[14] S.T. Tsai, K.P. Yen, and H.C. Shih, "The Embrittlement of Duplex Stainless in Sulfide-Containing 3.5% NaCl Solution," Corr. Sci, Vol. 40 (2/3) (1998), p. 281.

[15] T. Zakroczymski, A. Glowacka, and W. Swiatnicki, "Effect of Hydrogen Concentration on the Embrittlement of Duplex Stainless Steel," Corros. Sci., Vol. 47 (2005), p. 1403.

[16] A. Wensley, "Corrosion of Carbon and Stainless Steels in Kraft Digesters," CORROSION/2000, Paper No. 00589. (Houston, TX: NACE, 2006).

[17] ASTM G148, "Standard Practice for Evaluation of Hydrogen Uptake, Permeation, and Transport in Metals by an Electrochemical Technique," ASTM International, West Conshohocken, PA (2003), p. 1-10.

[18] T.E. Pérez, J. Ovejero García, Scripta Metallurgica, Vol. 16 (1982), p. 161.

[19] C. Wagner, and W. Traud, Z. Electrochem. Vol. 44 (1938), p391.

[20] J.H. Barber and B.E. Conway*, J. Chem. Soc. Faraday Trans*. Vol. 92 (20) (1996) p. 3709.

[21] P. Kedzierzawski, Z. Szklarska-Smialowska, and M. Smialowski, *J. Electrochem. Soc*. Vol. 127 (1980), p. 2550.

[22] J.F. Newman, and L.L. Shreir, *Corrosion Science*, Vol. 9: (1969) p. 631.

[23] S.S. Chen, T.I. Wu, J.K Wu, Journal of Material Science, Vol. 39 (2004), p. 67.

[24] W.C. Luu, P.W. Liu, J.K. Wu, Corrosion Science, Vol. 44 (2002), p. 1783.

[25] E. Owczarek and T. Zakroczymski, "Hydrogen Transport in a Duplex Stainless Steel," Acta Mater., Vol. 48 (2000), p. 3059.

[26] R. Oltra, C. Bouillot, and T. Magnin, *Scr. Mat*., Vol. 35 (9) (1996), p1101.

[27] HSC Chemistry 5.11, Outokumpu Technology Engineering Research.

# CHAPTER 9

# PROPOSED MECHANISM FOR STRESS CORRROSION CRACKING OF DUPLEX STAINLESS STEELS IN HOT ALKALINE-SULFIDE ENVIRONMENTS

## 9.1 Introduction

The main objective of this study was to understand the influence of microstructure and environment on the stress corrosion cracking (SCC) mechanism of standard UNS S32205 (2205) and lean UNS S32101 (2101) duplex stainless steels (DSS) in hot alkaline-sulfide environments. The role of different anions (i.e., $OH^-$, $S^{2-}$, and $Cl^-$) was studied using exposure coupons and slow strain rate specimens ($2 \times 10^{-6}$ $s^{-1}$ initial strain rate) in hot alkaline pulping liquors (170 $^oC$). Microstructural features of DSS were related to the corrosion and SCC behavior. The results from select environments have been reviewed and related to existing corrosion and SCC models to burgeon scientific understanding in this alloy-environment combination in this chapter.

## 9.2 Summary of Results

Phenomenological understanding of the effect of liquor composition on the corrosion and SCC susceptibilities of standard and lean DSS in hot alkaline environments was acquired in simulated pulping liquors at 170 $^oC$ (Chapters 4 and 5). Earlier studies showed that sulfide influenced the corrosion and SCC susceptibilities of austenitic and DSS [1-16], but no studies had previously compared different types of stainless steel (austenitic, superferritic, lean DSS, and super DSS) as well as their alloying elements in

different simulated pulping liquors to understand compositional effects. Increased effective alkali had an appreciable effect on increasing the corrosion rates of all of the materials that were studied (Chapter 5). Presence of sulfide, measured as percent sulfidity, was most detrimental to the austenitic grades (N08904, S31703, S30403, and S31603). Increased sulfidity enhanced preferential corrosion of the austenite phase of DSS (S32205 and S32101), thereby increasing the overall corrosion rates during coupon exposure and also increased the tendency for crack nucleation under constant initial strain rate (Chapter 6). Preferential corrosion did not correlate to more severe SCC of DSS S32101 but did correlate in the case of DSS S32205 tested in 3.75 M NaOH + 0.64 M $Na_2S$ with chlorides (Chapters 6 and 7).

Chlorides had previously been shown [17-18] to influence SCC behavior of DSS in acidic and near neutral environments, but no studies had ever systematically evaluated chloride effects in hot alkaline-sulfide solution. The chloride threshold corresponding to increased severity of SCC in both DSS alloys was approximately 0.034 M NaCl. The influence of chlorides on the corrosion rates of the DSS alloys was reduced with increasing alkalinity. However, SCC behavior was influenced by the presence of chlorides regardless of the solution alkalinity. On the basis of the corrosion rate measurements, a relationship between the corrosivity of the pulping liquor due to chlorides, caustic chloride ratio, was proposed as

$$Caustic\ Chloride\ Ratio = \frac{[Na_2S]+[NaCl]}{[NaOH]+[Na_2S]+[NaCl]} \qquad [9.1]$$

where $[Na_2S]$, [NaCl], and [NaOH] are the salt concentrations in g $l^{-1}$.

The onset of SCC of DSS in hot alkaline environments is dependent on a surface film that formed near the corrosion potential (Chapters 4-7). Surface film formation is known to be an important factor in SCC resistance [1-2]; however, the morphology and composition of the surface film that forms on the surface of DSS in caustic solutions was not known prior to this research. The outer surface film that formed on S32205 and S32101 was enriched in Fe in pure NaOH at 170 $^{o}$C. Ni and Cr were enriched near the film/metal interface in this surface film. However, Fe was depleted near the film/metal interface. Mo and Mn were selectively dissolved in this solution. The outer, discontinuous layer of the surface film contained hydroxide compounds and the inner, continuous (barrier or passive) layer contained a mixture of oxides based on thermodynamic predictions [19]. The film that formed on the strained samples was more defective supporting earlier reports [16] that corrosion rates of strained samples were greater than during static exposure. Impedance measurements showed that the behavior of the surface film was consistent with a Mixed –Conduction Model for oxide films [20-23]. Reasonable agreement was found between the experimental EIS data and a simplified electrical circuit model. Corrosion rates increased with temperature because the films formed on the DSS alloy surfaces were more conductive.

Selective dissolution influenced the corrosion behavior of the different grades of steel as shown in a recent study for austenitic type S30403 and DSS S32205 [24] (Chapters 4 and 5). An earlier study [25] also showed that austenitic type S31603 underwent selective dissolution in strong caustic conditions. Corrosion rates for Mo-containing superferritic grade S44660 (3 - 4 wt. %) were similar to or slightly greater than those of DSS grades in alkaline environments. Whereas, superferritic grade S44627

(0 wt. % Mo) had superior corrosion resistance to all of the grades that were tested. Corrosion rates of austenitic and DSS grades were generally similar in NaOH environments. Electrochemical measurements show that the selective dissolution of Fe was favored by increased alkalinity of the solution based on the electrochemical measurements. Alloying DSS with Cr reduced selective dissolution by favoring the formation of a stable passive film. SCC of DSS in hot alkaline environments was associated with selective dissolution of Fe, Mo, and Mn based on the active corrosion potential and film composition of the strained samples. The austenite phase of S32205 underwent preferential corrosion due to selective dissolution of Fe and Mo. However, for the S32101 alloy, selective dissolution was favored in austenite and at ferrite grain boundaries in alkaline environments due to the lower Cr content and higher Mn content of this steel.

Sulfide addition to the NaOH solution significantly altered the inner, barrier film composition and morphology, resulting in higher corrosion rates and increased susceptibility to SCC of the DSS that were studied (Chapters 5 and 6). Corrosion resistance of each type of stainless steel was a strong function of the Cr content, whereby Cr favored the formation of a stable film. Impedance spectroscopy in conjunction with film composition studies showed that sulfides enhanced corrosion at the metal/film interface through a two-step charge transfer process that involved adsorption and active dissolution. Sulfide adsorption on the surface hindered the formation of a stable passive film, which lead to appreciable metal oxidation and a more conductive film as has been shown for iron [26] and mild steel [27-28]. The formation of metal sulfides further compromised the protective nature of the film.

Earlier work [16, 29-30] used potentiodynamic scans to study the electrochemical behavior of alloying elements of Fe-Cr-Ni alloys in caustic environments, but these studies did not also evaluate film composition. Attempts to use electrochemical techniques to study selective dissolution and SCC behavior of DSS in alkaline-sulfide solution were compromised by the reactive nature of sulfur compounds (Chapter 5). The oxidation of sulfide was shown to be the predominant reaction determining the corrosion potential of a platinum electrode. Therefore, current measured on the metal electrodes (i.e., corrosion rates based on Faraday's Law) was due to metal oxidation as well as sulfide oxidation. The *dc* techniques such as anodic polarization and linear polarization resistance in highly concentrated alkaline pulping liquors provided information about the rates of sulfide oxidation/reduction on a particular electrode surface as well a basis for qualitative comparisons among alloys. The *ac* impedance measurements were useful for mechanistic understanding of corrosion processes occurring on the electrode surfaces.

Chloride effects were studied in the absence and presence of sulfide in NaOH environments (Chapter 5) and related to their SCC behavior (Chapter 6), which had never been evaluated in DSS. The properties of the surface film that formed on DSS alloys in chloride-containing NaOH solution were not appreciably different from the NaOH solution, although corrosion rates increased with an increase in the ratio of chloride to hydroxide in the test solution. Chloride further destabilized the Cr-rich surface film that formed on stainless steels in the presence of sulfide by reducing the charge transfer resistance associated with the oxide/metal interface and shifted the response of the films to lower frequencies, which was consistent with austenitic type 316L in a recent study

[23]. The shift to lower frequencies indicated that the oxide/metal interface had a more capacitance response, either due to internal porosity or defects.

The mechanism of crack initiation and growth varied depending on the relative amount of sulfide and chloride in the pulping liquor (Chapters 6 and 7). Surface films on DSS in alkaline-sulfide solution generally became more defective with increasing chloride (Chapters 5-7). The corrosion morphology in chloride-containing, alkaline-sulfide solution was a strong function of percent sulfidity and chloride ratio. DSS S32205 underwent preferential localized corrosion of the austenite phase in alkaline-sulfide solution (35 % sulfidity) in the absence of chloride. However, in the presence of 0.17 M NaCl, relatively uniform attack of the phases in S32205 indicated that chloride addition enhanced corrosion of the ferrite phase. Relatively uniform attack of the phases was observed in a solution with 25 % sulfidity and no chloride; the addition of 0.0034 M NaCl caused preferential corrosion of the austenite phase. Phase interfaces were also more susceptible to corrosion in the presence of chloride. These findings demonstrated that chlorides altered the SCC mechanism by favoring crack initiation and growth at localized regions where austenite or austenite/ferrite phase boundaries were attacked by sulfide and chloride.

Microstructural features were related to the SCC susceptibilities of DSS tested in alkaline-sulfide solutions at 170 $^{o}$C (Chapter 7). Microstructure aspects of DSS had previously been studied with respect to mechanical behavior [31-37] or phase composition [38-41], but the mechanical behavior of the anisotropic microstructures had never previously been related to SCC in caustic solutions. The phase distribution and material composition altered the crack initiation and growth behavior in each alloy-

environment combination. Crack initiation was favored in the rolling longitudinal (RL) orientation as compared to the transverse longitudinal (TL) orientation due to the differences in austenite distribution. Crack growth was favored in austenite and along phase interfaces in the transverse direction (TD). Secondary cracks also grew normal to the applied stress along austenite/ferrite phase boundaries because the austenite phase was more continuous along the rolling direction of the banded microstructure. Crack coalescence [42] had an influence on the growth of cracks in DSS tested in hot alkaline solutions depending on the number of crack initiation sites, which depended on the concentration of sulfide and chloride.

Hot rolled and coil-processed DSS S32205 in the as-received condition was harder and less ductile than a specimen that was annealed in the laboratory (Chapter 7). The austenite phase had similar strength to the ferrite phase in either material condition. SCC was observed in the as-received material and not in the annealed specimen. A 20 % rolling reduction was shown to increase the magnitude of residual stresses in DSS S32205 and induced appreciable work hardening of both phases. Residual stresses were tensile in the austenite phase even after large plastic deformation. The residual tensile stress combined with the applied stress lead to plastic deformation of austenite prior to the macroscopic yield strength. Crack growth was favored along highly stressed regions in the austenite phase based on electron backscattered diffraction maps indicating this phase underwent a greater extent of plastic deformation than the ferrite phase.

Earlier studies have shown that DSS may become susceptible to hydrogen embrittlement under certain conditions [43-45], but there were no studies of the affect of hydrogen on DSS in alkaline-sulfide environments. Slow strain rate testing (SSRT) under

applied potential showed that hydrogen production near the corrosion potential was not thermodynamically favorable in alkaline environments at room temperature (Chapter 8). An applied cathodic potential enhanced the severity of HE of S32205 tested in 3.75 M NaOH + 0.64 M $Na_2S$ below a threshold of -1100 mV vs. standard calomel electrode (SCE). Fracture surface features for the samples that failed due to hydrogen embrittlement differed from those tested near the corrosion potential at 170 $^{o}$C. The ferrite phase was found to be the favored site of crack initiation and growth due to the lower solubility and higher diffusivity of the body-centered cubic (bcc) phase under applied cathodic potential; however, hydrogen effects were not systematically studied at 170 $^{o}$C so the results at room temperature were not directly comparable to those at 170 $^{o}$C. Hydrogen absorption was likely negligible in S32205 near the corrosion potential based on the electrochemistry and SSRT results at 170 $^{o}$C.

## 9.3 Proposed Mechanism for SCC of DSS

### 9.3.1 Crack Initiation

Crack initiation in hot alkaline solutions was related to the selective dissolution of Fe, Mo, and Mn in S32101 and S32205 in hot alkaline environments based on the composition of the surface film. The morphology of the surface films consisted of an outer, discontinuous layer and an inner, continuous (barrier or passivation) layer. The composition and physicoelectrical properties of the film were altered appreciably by the addition of sulfide and chloride. Examination of the failed specimens tested by the SSRT method at 2 x 10 $^{-6}$ s $^{-1}$ with various ratios of hydroxide, sulfide, and chloride at 170 $^{o}$C indicated that the fracture features associated with SCC were affected by the addition of

these anions. Therefore, the initiation mechanism is not necessarily the same in all hot alkaline environments and is a function of the relative ratio of tested anions.

The microscale initiation mechanism for S32205 and S32101 in hot alkaline solution in the absence of other corrosive constituents is shown in Fig 9.1. The main features of this mechanism [46-53] are determined by the dissolution rate along active paths in the material controlled by diffusion at the crack tip and charge transfer activation. The rate of film breakdown and repair will be a function of the environment in the crack tip opening including local pH, concentration of cations at the metal surface, ohmic losses, and corrosion potential. Mechanical factors such as local heterogeneity due to slip-step immergence will promote damage to the film on the surface. Intergranular active paths may also become susceptible in the ferrite phase due to the local depletion of Cr. A model based on film rupture and repair explains the discontinuous crack process observed in both phases of DSS tested in 12.5 M NaOH at 170 $^{o}$C. Crack growth was not observed beyond the surface affected layers near the crack tip further supporting a dissolution-based mechanism.

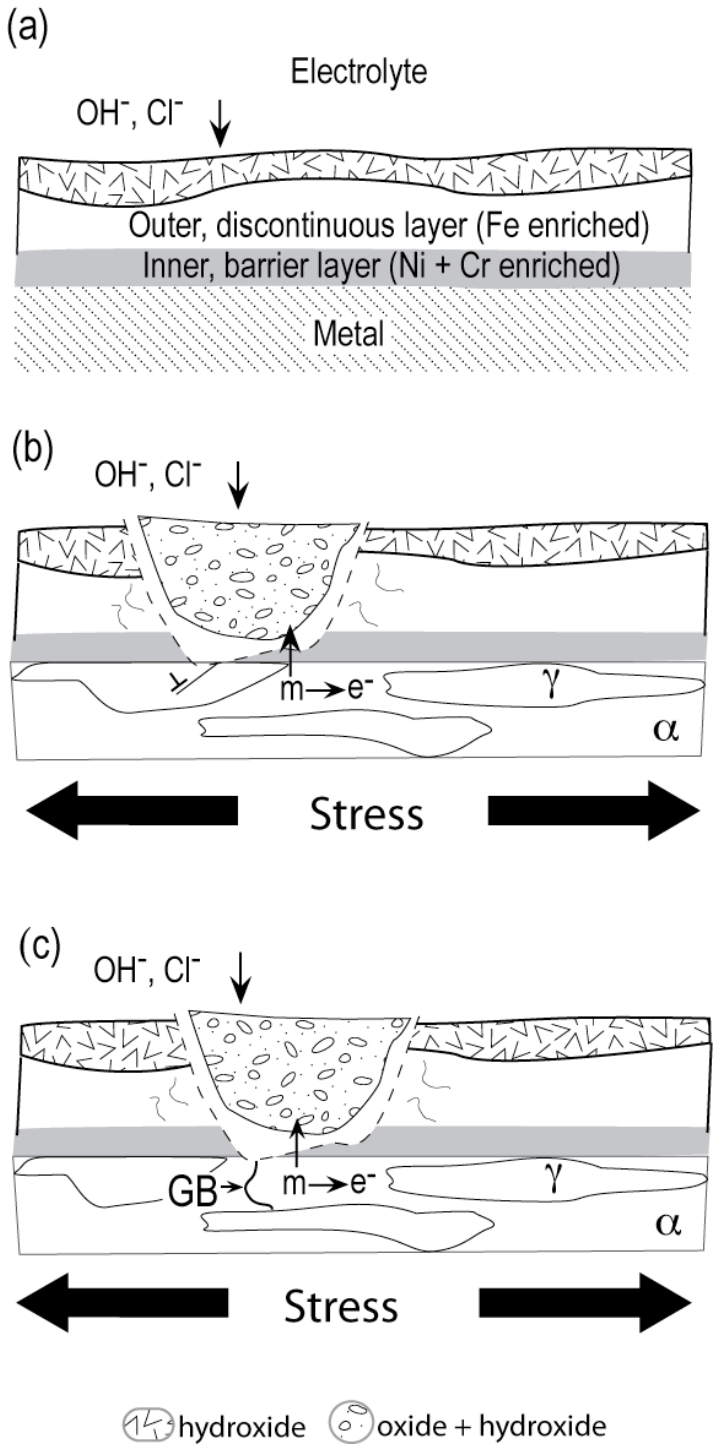


*Figure 9.1:* ***Schematic showing steps involved in crack initiation caused by selective dissolution of DSS tested in hot alkaline environments in the absence of other anions: (a) material forms film in absence of stress (b) initiation in austenite phase (γ) due to film rupture model, and (c) intergranular corrosion at ferrite (α) grain boundaries.***

Sulfidation of the inner barrier film resulted in unstable passivation and metal dissolution through the formation of sulfides. Anodic polarization showed that the current densities were significantly higher in the presence of sulfide (0.64 – 0.70 M $Na_2S$) owing to the increased surface activity. Weight loss measurements verified that the current was also due to dissolution as well as sulfide oxidation. The increased Tafel slopes on the Pt electrode with respect to the NaOH solution indicated that the cathodic activity was enhanced by sulfide addition. The increase in anodic activity indicated that sulfides were able to increase the rate of anodic interaction by formation of unstable species and increased electrical conductivity of the film. X-ray measurements verified the existence of sulfide species in a complex form. Deterioration of the film was further verified by the formation of active compounds. Dissolution of Fe, Mo, and Mn caused a concentration gradient in the film. Based on the corrosion potential of the S32205 and S32101 and X-ray spectra, Cr is expected to be present in the form of chromium oxide ($Cr_2O_3$) and chromium hydroxide ($Cr(OH)_3$) in the inner layer. Presence of chloride in sulfide-containing caustic solutions enhanced sulfidation and favored crack initiation, which was related further destabilization of the Cr-rich oxide and hydroxide film in Cr-depleted regions such as austenite/ferrite phase boundaries.

Many factors were shown to influence the extent of sulfidation and subsequent instability of the inner, barrier film. Austenite and austenite/ferrite phase boundaries were favorable initiation sites because of their lower Cr composition. The integrity and stability of the film that formed at these sites were also compromised in the presence of sulfide. Because sulfides are more effective electron conductors and structurally more permeable than dense chromium compounds, sulfur enriched region of the film become

sites for further metal oxidation by $OH^-$, $S^{2-}$, or $Cl^-$ in a manner analogous to pitting by sulfate-reducing bacteria [53]. The structural features of the base material are another factor. The face-centered cubic (fcc) austenite phase can undergo slip more readily than the bcc ferrite, which would further compromise the integrity of the surface film under an applied strain. On the basis of the experimental observations in this work, the proposed microscale initiation mechanism(s) based on slip-step emergence in the austenite phase in alkaline-sulfide are shown in Fig 9.2.

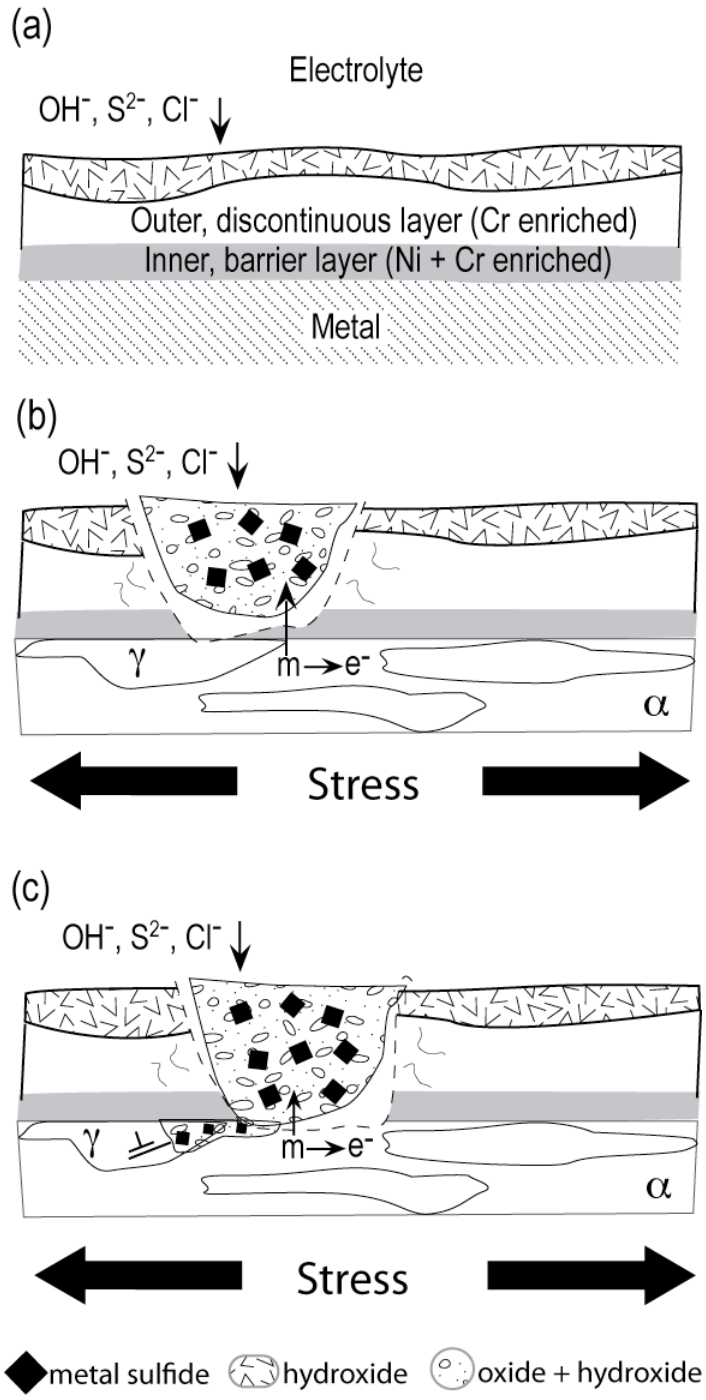


***Figure 9.2:*** ***Schematic showing steps involved in crack initiation caused by sulfidation of the inner, barrier film formed on DSS tested in hot alkaline environments in the presence of sulfide and chloride: (a) film on alloy in absence of stress, (b) initiation in austenite phase due to film rupture (slip-step dissolution) model , and (c) sulfides are adsorbed on the surface and enhance metal oxidation by $OH^-$, $S^{2-}$, or $Cl^-$ , and (c) sulfidation of the austenite phase (γ) is enhanced by the presence of $Cl^-$.***

### 9.3.2 Crack Propagation

Crack propagation mechanisms were not explicitly explored in this research. SSRT was particularly useful for indentifying crack initiation mechanisms and SCC susceptibilities of DSS in various alkaline environments due to the aggressive test conditions that accelerate testing; however, SSRT cannot easily be used to determine if crack propagation will occur in the presence of an existing flaw. Thorough understanding of the crack propagation behavior requires knowledge of the threshold stresses needed for crack growth. Furthermore, the growth mechanism is dependent on the plastic zone at the crack tip. The loading condition at the crack tip, such as the stress intensity and size of the plastic zone cannot be determined from smooth SSRT specimens. The growth mechanism must be valid for different loading conditions (constant load and strain) and deformation rates. A fracture mechanics approach in conjunction with electrochemical modeling is required to quantify the stresses at the crack tip to fully understand crack propagation behavior in each alloy-environment system.

Qualitative understanding of the crack propagation mechanism can be gleaned from the fractography and maximum crack velocities of failed S32205 and S32101 specimens tested in different environments. The fracture features varied depending on the alloy and environment in this work, thus several mechanisms may account for SCC of DSS in alkaline environments. Hydrogen embrittlement did not appear to be the propagation mechanism based on the fractography results and electrochemical studies. Austenite and austenite/ferrite phase boundaries were typically the favored paths for transgranular crack advance. The exception was S32101 tested in 3.75 M NaOH + 0.17 M NaCl, which showed intergranular fracture in the ferrite phase. The failure of this

specimen may have been related to the processing history of the as-received material, but ferrite was also susceptible in the 3.75 M solution indicating the effect was due to the environment. Ferrite grain boundaries were sites for crack propagation in the strong caustic solutions, particularly in the presence of chlorides. The growth of cracks along ferrite grain boundaries in caustic environments had not been shown prior to this research.

The emergence of slip-steps was evident in optical micrographs for DSS tested in alkaline-sulfide solution with additions of chloride. Other alkaline-sulfide environments often resulted in wide and blunt cracks with limited features near the crack tip due to dissolution. An oxide was present in these cases. Cracks were not observed to grow beyond the oxide/metal interface. Selective dissolution near the oxide/metal interface based on EDS measurements indicted the growth behavior was based on a film rupture and repair mechanism due to selective dissolution of Fe, Mo, and Mn. Results from impedance measurements also supported a film-controlled mechanism due to adsorption of sulfide and/or chloride and dissolution processes under exposure conditions. Crack initiation and growth occurred along slip-steps supporting a model based on slip-step dissolution.

One model for SCC crack propagation that is consistent with the observations in this study attributes corrosion-deformation interactions at the crack tip with the growth of cracks [54-55]. Selective dissolution at the crack tip interacts with dislocations leading to cleavage-like failure of austenite. This model has been applied to austenitic stainless steel in alkaline [54] and chloride environments [55]. Dislocations consume vacancies generated by corrosion processes at the crack tip, thereby enhancing creep. The

electrochemical results and analysis of the surface films in hot alkaline environments support this model based on the selective dissolution of Fe, Mo, and Mn. Sulfides and chlorides enhanced dissolution at the crack tip enabling crack advance along electrochemically active paths in the microstructure. A schematic view for the SCC initiation and growth mechanisms in DSS in hot alkaline solution is shown in Figure 9.3. The mechanism is modified for alkaline-sulfide solutions in Figure 9.4.

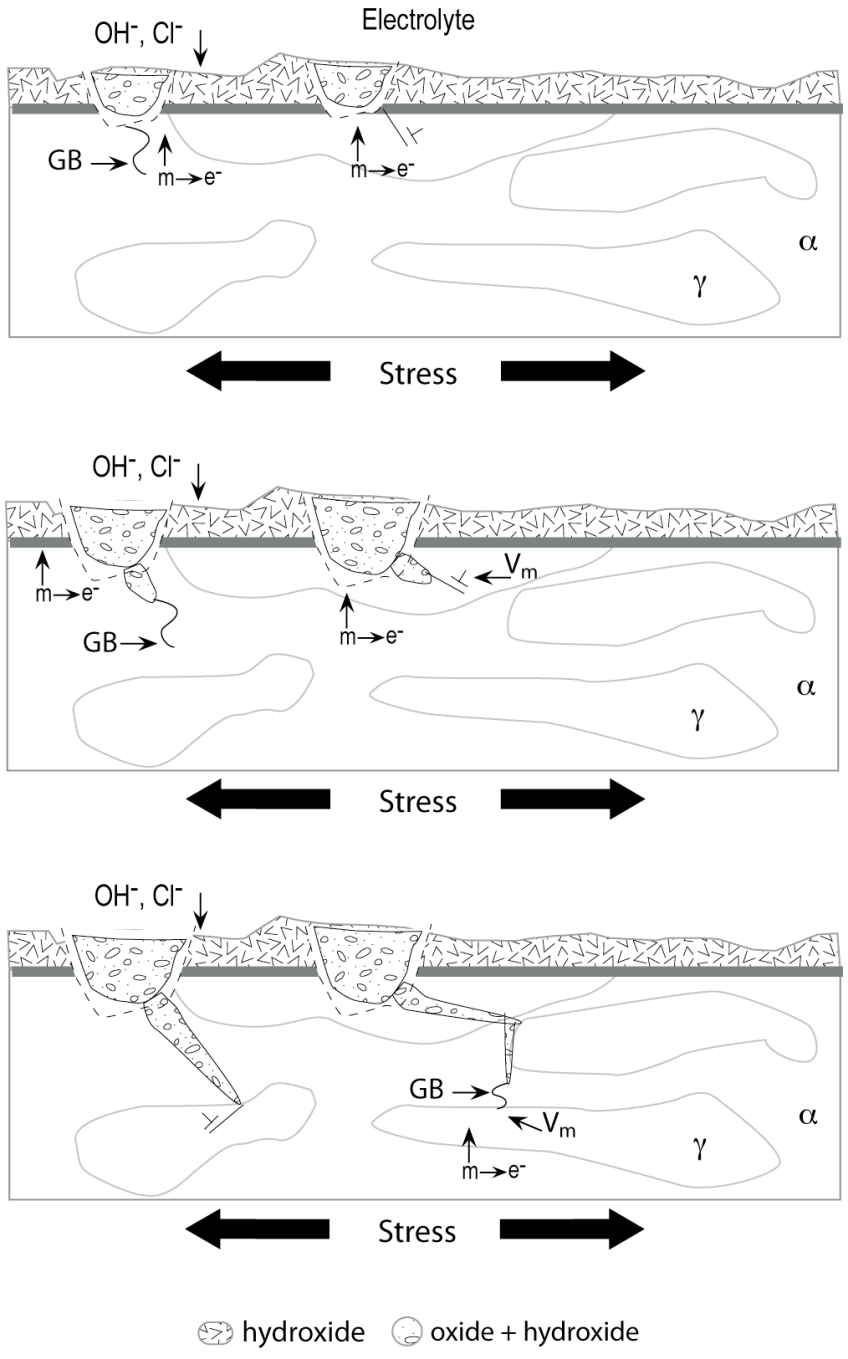


***Figure 9.3:*** ***Schematic showing steps involved in stress corrosion crack initiation and growth on DSS tested in hot alkaline environments in the absence of sulfide and chloride: (a) initiation in austenite phase due to film rupture (slip-step dissolution model) or in ferrite phase at grain boundaries, (b) selective dissolution of Fe, Mo, and Mn creates vacancies near crack tip, and (c) vacancies are consumed by dislocations and enable crack advance through creep.***

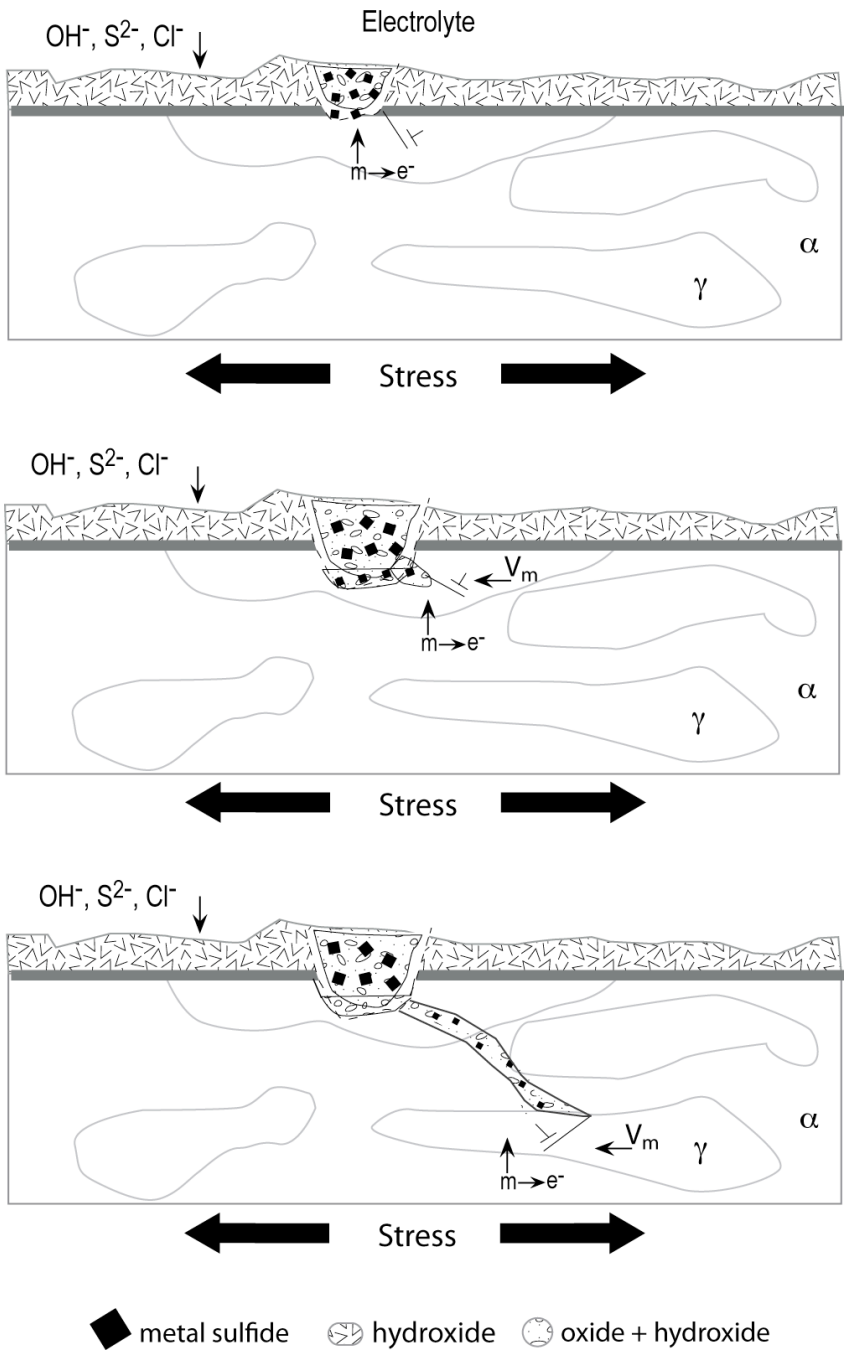


*Figure 9.4:* ***Schematic showing steps involved in stress corrosion crack initiation and growth on DSS tested in hot alkaline environments in the presence of sulfide and chloride: (a) initiation in austenite phase due to sulfidation of the inner, barrier layer causes unstable passivity at the crack tip, (b) dislocations are dissolved at slip-steps (slip-step dissolution model), and (c) crack advance proceeds in discontinuous steps due to unstable passivity.***

## 9.4 Conclusions

This work showed that the mechanism of SCC of DSS in hot alkaline environments depended on the rate of rupture and repair of a passive film that formed along active paths in the material, which was a function of the sulfide and chloride concentration in the solution. The primary results for understanding the mechanism of SCC of DSS in caustic environments are the following:

- The film on austenite and ferrite phase became more defective in the presence of sulfide and chloride due to anion adsorption on the surface, hindering stable passivation as supported by electrochemical and film composition studies.
- Superferritic grades more readily formed a stable passive film than austenitic grades due to the differences in Cr content.
- Selective dissolution resulted in SCC growth in DSS tested in caustic solution.
    - Ferrite grain boundaries were favored sites in the lean DSS in the absence of sulfide due to the lower Cr content of this steel.
    - Crack initiation and growth in DSS occurred at slip steps in the austenite phase or at austenite/ferrite phase boundaries in the presence of sulfide and chloride due to selective dissolution of Fe, Mo, and Mn at the active crack tip, resulting in a Cr enriched layer.

## 9.5 REFERENCES

[1] R.W. Staehle et el, Stress Corrosion Cracking and Hydrogen Embrittlement of Iron Base Alloys, R.W. Staehle et al, eds. NACE-5, NACE, Houston, (1977) p. 193.

[2] A.J. Sedriks, “Corrosion of Stainless Steel,” John-Wiley & Sons, New York, 1979.

[3] M. Honda et al., “Stress Corrosion Cracking of Stainless Alloys in Alkaline-Sulfide Solutions.,” 1991.

[4] M. Honda, Y. Kobayashi, and A. Tamada, “Stress Corrosion Cracking of Stainless Alloys in Alkaline-sulfide Solutions,” Corrosion (USA), vol. 48, 1992, pp. 822-829.

[5] C. Reid, “Stress Corrosion Cracking of Austenitic and Duplex Stainless Steels in the Pulp and Paper Industry,” TAPPI Engineering Conference Proceedings, 1999, pp. 1315-1357.

[6] Wensley, A., Moskal, M., and Wilton, W., "Materials Selection for Kraft Batch Digesters," Corrosion/97, NACE Paper No. 378, 1997, Houston, TX.

[7] Wensley, A., and Champagne, P. NACE Corrosion, Paper No. 281, 1999, Houston, TX.

[8] Wensley, A., NACE Corrosion, Paper No. 589, 2000, Houston, TX.

[9] Ramo, J., Sillanpaa, Kujalao, A., Hyokyvirta, O., and Peltonen, S., Mat. and Corr. Vol. 52 (2001) 531.

[10] Ramo, J., Sillanpaa, Kujalao, A., Hyokyvirta, O., and Peltonen, S., Mat. and Corr. Vol. 52 (2001) 741.

[11] P. Combrade and J.P. Audouard, “Duplex Stainless Steels' 91, 28.±30.10. 1991, Beaune, Bourgonge, France, J,” S, pp. 257-270.

[12] P.M. Singh, J. Mahmood, P. Conde, “Stress Corrosion Cracking and Corrosion Susceptibility of Duplex Stainless Steels in Caustic Solutions,” NACE Corrosion 2005, paper no. 05196, Houston, TX, USA, 3-7 April 2005.

[13] Svensson, C., Pulliainen, M., Huttunen, M., and Niemelainen, P., 2005 TAPPI Engineering, Pulping, Environmental Conference, August 28-31, 2005, Philadelphia, PA.

[14] H.T. Leinonen, P. Pohjanne, “Stress Corrosion Cracking Susceptibility of Duplex Stainless Steels and their Welds in Simulated Cooking Environments. NACE Corrosion 2006, paper no. 06244, San Diego, CA, USA, 12-16 March 2006.

[15] ERC Project Report, Institute of Paper Science and Technology at Georgia Tech, August 2006.

[16] A. Bhattacharya, ”Stress Corrosion Cracking of Duplex Stainless Steels in Caustic Solutions, Ph.D. Thesis, Georgia Institute of Technology, Atlanta, GA (2008).

[17] S.T. Tsai and S.L. Chou, “Environmentally Assisted Cracking Behavior of Duplex Stainless Steel in Concentrated Sodium Chloride Solution,” Corrosion Science, vol. 42, 2000, pp. 1741-1762.

[18] P.M Singh et al., “Stress Corrosion Cracking and Corrosion Fatigue Cracking of a Duplex Stainless Steel in White Water Environments,” Corrosion (Houston, Tex.), vol. 60, 2004, pp. 852-861.

[19] HSC Chemistry 5.11, Outokumpu Technology Engineering Research.

[20] B. Beverskog, M. Bojinov, A. Englund, P. Kinnunen, T. Laitinen, K. Makela, T. Saario, P. Sirkia, Corr. Sci. 44 (2002) 1901.

[21] M. Bojinov, P. Kinnunen, K. Lundgren, G. Wikmark, J. Electrochem. Soc. 152 (2005) B250.

[22] M. Bojinov, A. Galtayries, P. Kinnunen, A. Machet, P. Marcus, Electrochima Acta 52 (2007) 7475.

[23] I. Betova, M. Bojinov, O. Hyokyvirta, and T. Saario, Corr. Sci 52 (2010) 1499-1507.

[24] H.T. Leinonen, P. Pohjanne, T. Saukkonen, T. Schildt, J. Romu, and H. Hanninen, “Effect of Selective Dissolution on Stress Corrosion Cracking Susceptibility of Austenitic and Duplex Stainless Steels in Alkaline Solutions,” NACE Corrosion 2011, Houston, TX, 13-17 March 2011, paper no. 11160 17 p.

[25] J. Deakin et al., “De-alloying of Type 316 Stainless Steel in Hot, Concentrated Sodium Hydroxide Solution,” Corrosion Science, vol. 46, 2004, pp. 2117-2133.

[26] D. W. Shoesmith, M.G. Bailey, and B. Ikeda, Electrochim. Acta 23, (1978) 1329-1338.

[27] D. Tromans, J. Electrochem. Soc. 127 (1980) 1253.

[28] R. C. Salvarezza, H. A. Videla, and A.J. Arvia, Corr. Sci 22 (1982) 815-829.

[29] A.K. Agrawal et al., “The Polarization Behavior of Fe-Ni-Cr Alloys in Concentrated Sodium Hydroxide Solutions in the Temperature Range 25° to 150° C,” Journal of The Electrochemical Society, vol. 119, 1972, p. 1637.

[30] J.H. Zheng, W.F. Bogaerts, and M.J. Brabers, “Stress Corrosion Cracking and Anodic Dissolution of 316L Stainless Steel in Hot Lithium Hydroxide,” Corros. (1992).

[31] E. Werner, T. Siegmund, and F. Fischer, "A Computer Study of the Thermomechanical Deformation Behavior of a Duplex Steel," Computational Materials Science, vol. 3, 1994, pp. 279-285.

[32] T. Siegmund, E. Werner, and F.D. Fischer, "On the Thermomechanical Deformation Behavior of Duplex-type Materials," Journal of the Mechanics and Physics of Solids, vol. 43, 1995, pp. 495-532.

[33] V.V. Silberschmidt and E. Werner, "Analysis of Thermal Residual Stresses in Duplex-type Materials," Computational Materials Science, vol. 16, 1999, pp. 39-52.

[34] J. Johansson, M. Odén, and X.H. Zeng, "Evolution of the Residual Stress State in a Duplex Stainless Steel during Loading," Acta Materialia, vol. 47, 1999, pp. 2669-2684.

[35] Hutchinson, W.B., Ushioda, K., and Runnsjő, G., "Anisotropy of tensile behavior in a duplex stainless steel sheet," Mat. Sci. and Tech, Vol. 1 (1985), p.728.

[36] A. ul-Haq, H. Weiland, and H.J. Bunge, Mat. Sci. and Tech. 10 (1994) 289-298.

[37] A. ul-Haq, H. Weiland, and H.J. Bunge, J. of Mat. Sci. 29 (1994) 2168-2176.

[38] H. Okamoto, The Effect of Tungsten and Molybdenum on the Performance of Super Duplex Stainless Steels, Proceedings of Application of Stainless Steel '92, Stockholm, Sweden, Jernkontoret, 1992, p. 360.

[39] C.M. Tseng, H.Y. Liou, and W.T. Tsai, "The Influence of Nitrogen Content on Corrosion Fatigue Crack Growth Behavior of Duplex Stainless Steel," Materials Science & Engineering A, vol. 344, 2003, pp. 190-200.

[40] M. Femenia, J. Pan, and C. Leygraf, "Characterization of Ferrite-Austenite Boundary Region of Duplex Stainless Steels by SAES," Journal of The Electrochemical Society, vol. 151, 2004, p. B581.

[41] F. El-Taib Heakal, A.A. Ghoneim, and A.M. Fekry, "Stability of Spontaneous Passive Films on High Strength Mo-containing Stainless Steels in Aqueous Solutions," Journal of Applied Electrochemistry, vol. 37, 2007, pp. 405-413.

[42] .N. Parkins and P.M. Singh, Corros 46 (1990) 485.

[43] S.L. Chou and W.T. Tsai, "Effect of Grain Size on the Hydrogen-Assisted Cracking in Duplex Stainless Steels," Materials Science and Engineering: A, vol. 270, 1999, pp. 219-224.

[44] E. Owczarek and T. Zakroczymski, "Hydrogen Transport in a Duplex Stainless Steel," Acta Materialia, vol. 48, 2000, pp. 3059-3070.

[45] S.S. Chen, T.I. Wu, and J.K. Wu, "Effects of Deformation on Hydrogen Degradation in a Duplex Stainless Steel," Journal of Materials Science, vol. 39, 2004, pp. 67-71.

[46] F.A. Champion, in Symp. Internal Stresses in Metals and Alloys, Inst. of Metals, (1948) 468.

[47] H.L. Logan, J. Res. Natl. Bur. Stand. 48 (1952) 99.

[48] T.J. Smith, R.W. Staehle, Corrosion 23 (1967) 117-129.

[49] R.N. Parkins, Proc. 5th Symposium on Line Pipe Research, Am. Gas Assoc. Arlington, VA (1974), P. U-1.

[50] R.N. Parkins, Corr. Sci. 20 (1980) 147-166.

[51] R.N. Parkins, Corrosion 43, (1987) 130-139.

[52] T. Magnin, Advances in Corrosion-Deformation Interactions, Materials Science Forum, vol. 202, Trans Tech Publications, 1996, 15.

[53] G. Chen and C. R. Clayton, J. Electrochem. Soc. 144, (1997) 3140-3146.

[54] J.H. Zheng and F. Bogaerts, "Transpassive Chromium Dissolution – Interactions with Stress Corrosion Cracking of Austenitic Stainless Steel in Caustic Solutions." In: Magnin, T. (ed.) Second Int. Conf. on Corrosion-Deformation Interactions. Nice, France, 24-26 September 1996. European Federation of Corrosion Publications No. 21. The institute of Metals, (1997), 131-139.

[55] H.T. Leinonen and H. Hanninen, "Prediction of Stress Corrosion racking Susceptibility of Austenitic Stainless Steels in 50 % CaCl2 Solution." In: Magnin, T. (ed.) Second Int. Conf. on Corrosion-Deformation Interactions. Nice, France, 24-26 September 1996. European Federation of Corrosion Publications No. 21. The institute of Metals, (1997), 131-13915] N. Sridhar and J. Kolts, "Corrosion 43 (1987)," p. 646.

# CHAPTER 10

# CONCLUSIONS

## 10.1 Practical Implications

Industrial process environments may contain different amounts of sulfide and chloride; however, the combined role of these ions on the stress corrosion cracking (SCC) of duplex stainless steels (DSS) had never been studied previously. This work showed that chlorides in caustic environments actually have a significant role on the performance of these alloys. A mechanism for SCC of DSS in hot alkaline environments in the presence of sulfide and/or chloride was proposed on the basis of the results and was consistent with a film breakdown and repair mechanism similar to slip-step dissolution. The onset of SCC was related to the stability of the surface film that formed under different environmental conditions, and the extent of selective dissolution in the austenite phase. Selective dissolution depended on percent sulfidity, alkalinity, and chloride content. Chlorides enhanced crack initiation and coalescence along the austenite/ferrite phase boundaries. Considerations for practical implications of this research and suggestions for future studies are provided in this chapter.

### 10.1.1 Process Optimization Considerations

- Process changes that result in increased temperature, increased effective alkali content, increased chloride to hydroxide ratio, or % sulfidity will reduce the life of plant equipment. Corrosion rates were significantly higher when the effective alkali content increased from 128 g/l $Na_2O$ to 175 g/l $Na_2O$ at 170

$^{o}$C. As-received DSS S32205 was immune to SCC in the alkaline pulping liquor with the former effective alkali and susceptible to TGSCC in the latter.

- Chloride concentrations in hot alkaline pulping liquors should be kept to a minimum, especially below 0.034 M NaCl, to reduce SCC susceptibility of standard and lean grade DSS.
- Preferential corrosion of the individual phases of the DSS alloys, particularly austenite in the presence of sulfide and chloride, can enhance the corrosion and SCC susceptibilities of plant equipment.
- DSS alloys may become susceptible to hydrogen embrittlement in alkaline-sulfide environments when hydrogen evolution is thermodynamically possible due to galvanic effects from coupling with an active material or improper control of the applied potential to values lower than -1100 mV vs. standard calomel electrode.

### 10.1.2 Material Considerations

- Developing DSS grades of stainless steel with microstructures that are designed to have larger grain boundaries and fewer austenite/ferrite phase boundaries could hinder SCC growth processes in alkaline-sulfide environments.
- DSS grades with higher Cr and lower Ni would have improved resistance as compared S32205 and S32101. N or Cu could be used to stabilize the austenite phase in lieu of Mn. Mo and Mn did not benefit DSS in alkaline environments and were selectively dissolved from the surface layer.

- Post heat treatment of regions expected to have high residual stress (welds or cold worked sections) is recommended following fabrication.

## 10.2 Suggestions for Future Work

### 10.2.1 Crack Tip Chemistry and Morphology

Film characterization was conducted with *ex-situ* techniques that had limited lateral or depth resolution. X-ray photoelectron spectroscopy provided useful information for understanding corrosion film compositions in different environments, but due to the spot size of the X-ray beam (400 μm) it was not possible to determine the composition of the individual phases or at crack tips. Similarly, energy dispersive x-ray spectroscopy provided information about composition at the crack tip, but it was limited by its depth resolution. Characterization of the crack tip oxide in a microscope equipped with Auger electron spectroscopy would enable further understanding of the crack tip oxide film formed in each phase in hot alkaline environments.

Transmission electron microscopy (TEM) should be considered in future work to understand the dislocation substructures that form near crack tips. Recent developments in focused ion beam lift-out techniques have enabled these regions to be examined in TEM specimens. Analysis of the crack tip chemistry could be undertaken in these studies. Of particular interest would be understanding the dislocation structures that form in the individual phases near the crack tip as compared to the based material. Understanding the submicron mechanisms could also illustrate the effects of precipitation on substructural features that cannot be resolved by other microscopy tools.

### 9.4.2 Electrochemical Behavior

The limits for de-alloying and selective dissolution in DSS as a function of composition, temperature, solution chemistry, and applied oxidation/reduction potential still remain unclear from this research. The mechanism was generally similar in pure NaOH, but the film morphology had significantly different features with 12.5 M NaOH as compared to 3.5 M NaOH. The maximum crack velocities were an order of magnitude greater for S32101 conditions. S32205 became susceptible with 12.5 M NaOH and not in the 3.5 M NaOH solution. Further work electrochemical work with *ac* and *dc* techniques during mechanical tests could provide greater insight into the features of de-alloying and its relationship to SCC. The kinetic aspects of sulfidation of the oxide film were unclear from this work and further film studies should be conducted to understand the reaction rates at the film/oxide interface.

### 9.4.3 Fracture Mechanics Approach

The slow strain rate test for SCC does not provide quantitative information about the mechanical conditions at the crack tip. Modeling that accounts for dissolution effects at the crack tip in two phase materials would clarify the mechanochemical behavior that occurs in DSS. A fracture mechanics approach that uses pre-notched specimens would provide information about the size of the plastic zone and quantifiable information about the stress intensity ahead of the crack tip. The crack growth rates could be monitored with potential drop technique to determine *in-situ* environmental effects. The threshold stresses in different alloy-environment combinations could also be measured to make well-informed decisions about material selection. Such an approach could also

demonstrate the similarities or differences in stress corrosion crack propagation behavior between constant strain and constant load conditions.

# APPENDIX A

# MATERIAL CERTIFICATION SHEETS

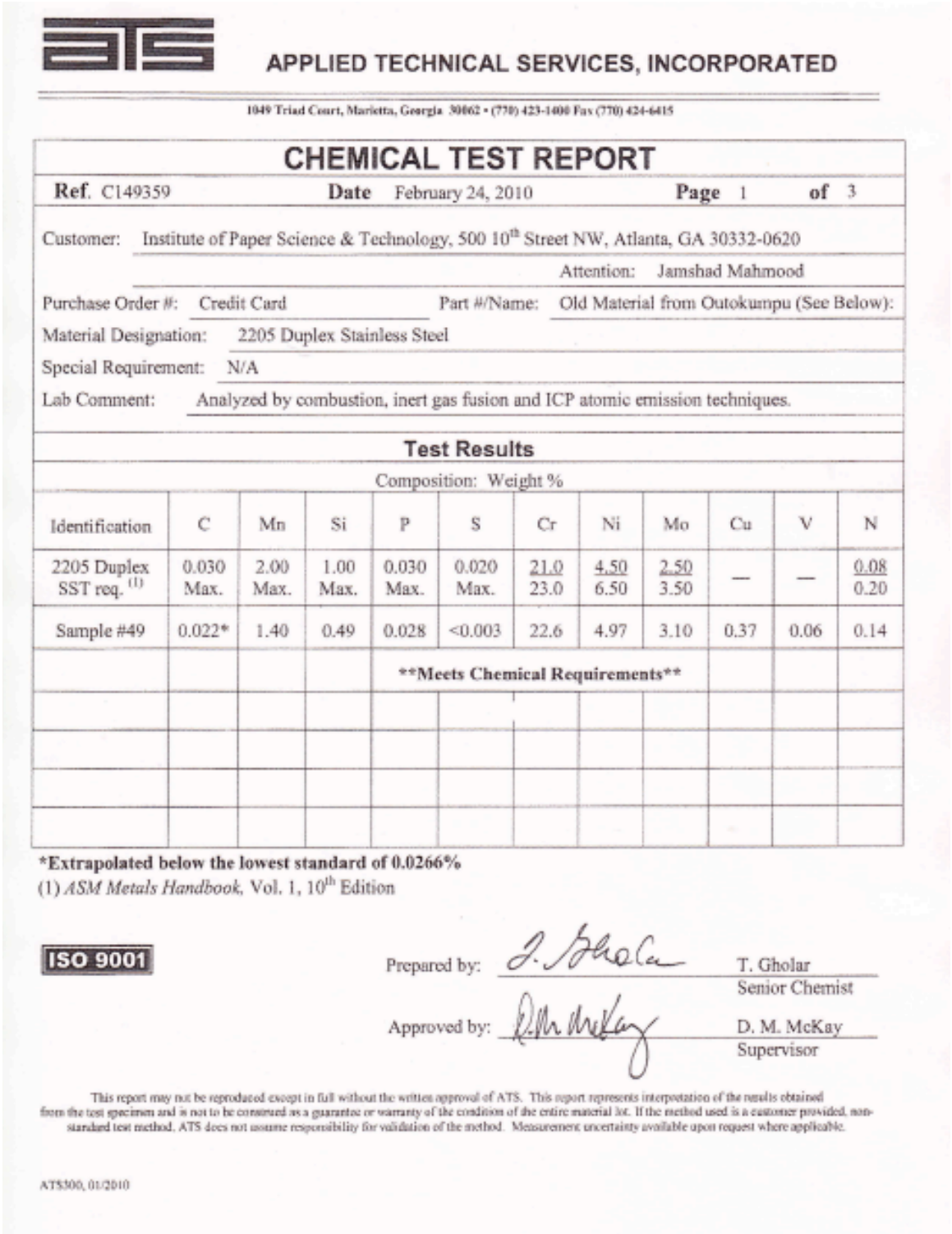

APPLIED TECHNICAL SERVICES, INCORPORATED

1049 Triad Court, Marietta, Georgia 30062 • (770) 423-1400 Fax (770) 424-6415

# CHEMICAL TEST REPORT

**Ref.** C149359 **Date** February 24, 2010 **Page** 1 **of** 3

Customer: Institute of Paper Science & Technology, 500 10th Street NW, Atlanta, GA 30332-0620

Attention: Jamshad Mahmood

Purchase Order #: Credit Card Part #/Name: Old Material from Outokumpu (See Below):

Material Designation: 2205 Duplex Stainless Steel

Special Requirement: N/A

Lab Comment: Analyzed by combustion, inert gas fusion and ICP atomic emission techniques.

## Test Results

Composition: Weight %

| Identification | C | Mn | Si | P | S | Cr | Ni | Mo | Cu | V | N |
|---|---|---|---|---|---|---|---|---|---|---|---|
| 2205 Duplex SST req. (1) | 0.030 Max. | 2.00 Max. | 1.00 Max. | 0.030 Max. | 0.020 Max. | 21.0 23.0 | 4.50 6.50 | 2.50 3.50 | — | — | 0.08 0.20 |
| Sample #49 | 0.022* | 1.40 | 0.49 | 0.028 | <0.003 | 22.6 | 4.97 | 3.10 | 0.37 | 0.06 | 0.14 |
| | | | | **Meets Chemical Requirements** | | | | | | | |

***Extrapolated below the lowest standard of 0.0266%**

(1) *ASM Metals Handbook*, Vol. 1, 10th Edition

ISO 9001

Prepared by: T. Gholar, Senior Chemist

Approved by: D. M. McKay, Supervisor





**Figure A.1: Material certification sheet for standard grade DSS UNS S32205 used in slow strain rate tests for stress corrosion cracking susceptibility.**

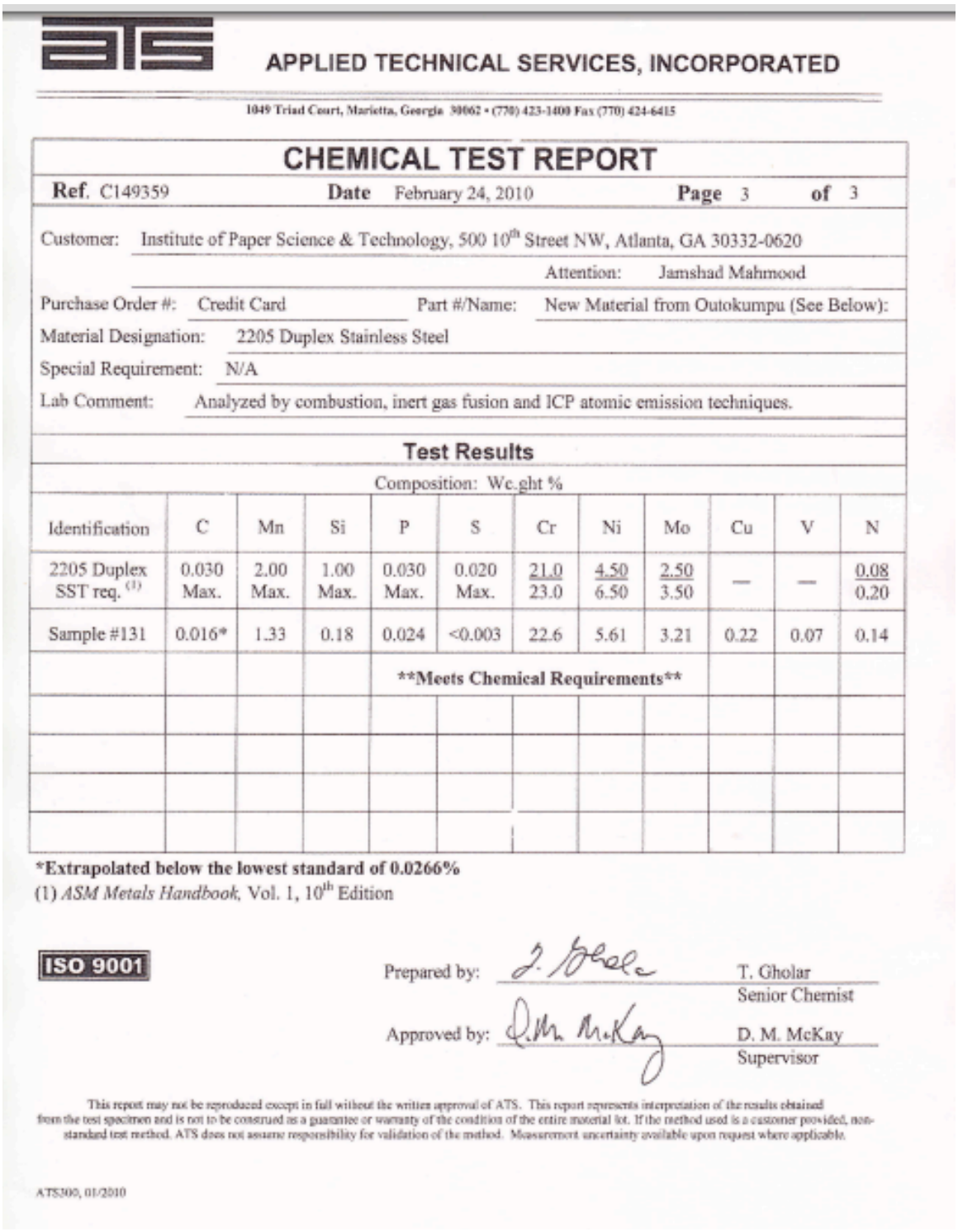

APPLIED TECHNICAL SERVICES, INCORPORATED

1049 Triad Court, Marietta, Georgia 30062 • (770) 423-1400 Fax (770) 424-6415

## CHEMICAL TEST REPORT

**Ref.** C149359 **Date** February 24, 2010 **Page** 3 **of** 3

Customer: Institute of Paper Science & Technology, 500 10th Street NW, Atlanta, GA 30332-0620

Attention: Jamshad Mahmood

Purchase Order #: Credit Card Part #/Name: New Material from Outokumpu (See Below):

Material Designation: 2205 Duplex Stainless Steel

Special Requirement: N/A

Lab Comment: Analyzed by combustion, inert gas fusion and ICP atomic emission techniques.

### Test Results

Composition: Weight %

| Identification | C | Mn | Si | P | S | Cr | Ni | Mo | Cu | V | N |
|---|---|---|---|---|---|---|---|---|---|---|---|
| 2205 Duplex SST req. (1) | 0.030 Max. | 2.00 Max. | 1.00 Max. | 0.030 Max. | 0.020 Max. | 21.0 23.0 | 4.50 6.50 | 2.50 3.50 | — | — | 0.08 0.20 |
| Sample #131 | 0.016* | 1.33 | 0.18 | 0.024 | <0.003 | 22.6 | 5.61 | 3.21 | 0.22 | 0.07 | 0.14 |
| | | | | **Meets Chemical Requirements** | | | | | | | |

***Extrapolated below the lowest standard of 0.0266%**

(1) *ASM Metals Handbook*, Vol. 1, 10th Edition

ISO 9001

Prepared by: T. Gholar, Senior Chemist

Approved by: D. M. McKay, Supervisor

This report may not be reproduced except in full without the written approval of ATS. This report represents interpretation of the results obtained from the test specimen and is not to be construed as a guarantee or warranty of the condition of the entire material lot. If the method used is a customer provided, non-standard test method, ATS does not assume responsibility for validation of the method. Measurement uncertainty available upon request where applicable.

ATS300, 01/2010

**Figure A.2: Material certification sheet for standard grade DSS UNS S32205 used in hydrogen embrittlement studies.**

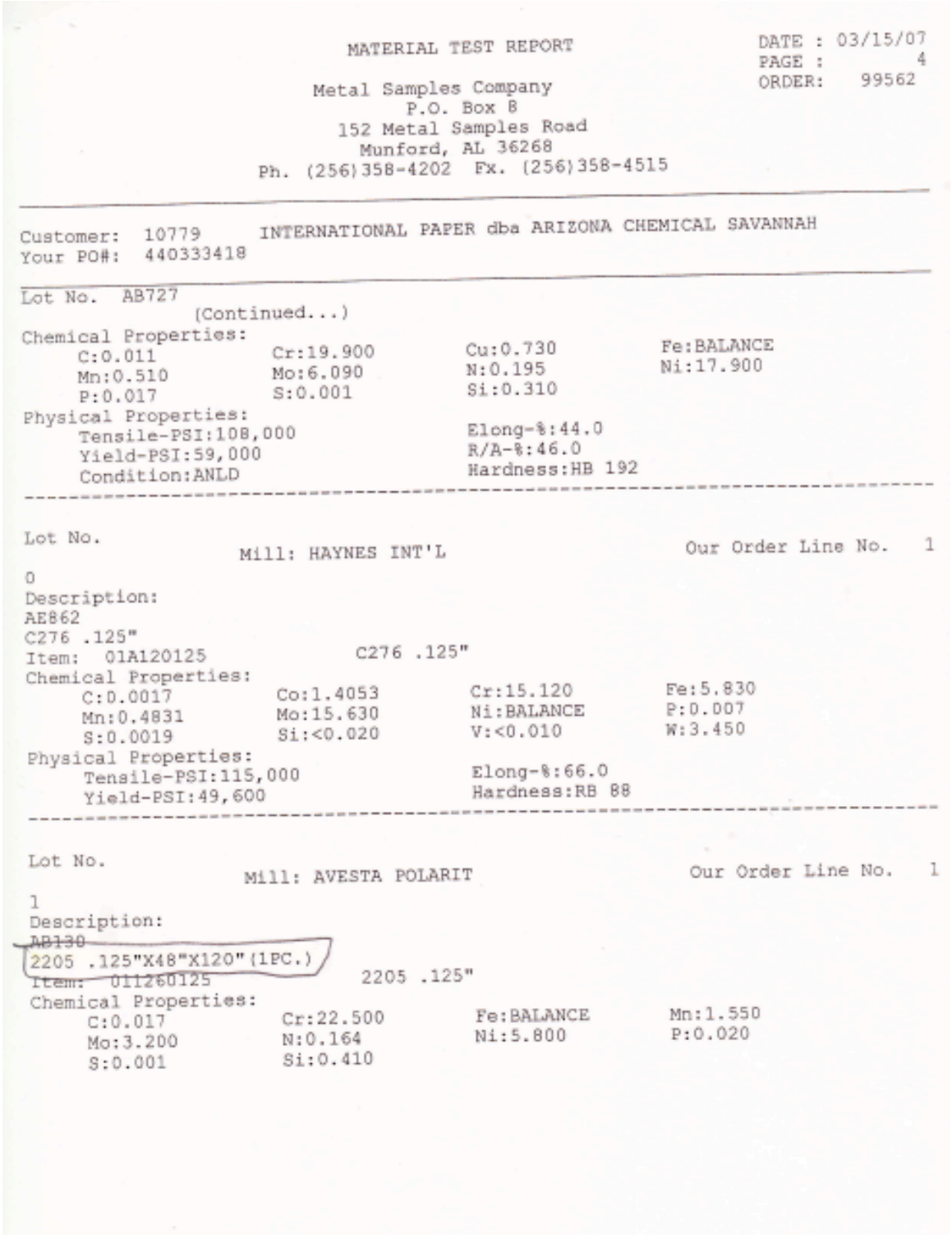

MATERIAL TEST REPORT

DATE : 03/15/07
PAGE : 4
ORDER: 99562

Metal Samples Company
P.O. Box B
152 Metal Samples Road
Munford, AL 36268
Ph. (256)358-4202 Fx. (256)358-4515

Customer: 10779 INTERNATIONAL PAPER dba ARIZONA CHEMICAL SAVANNAH
Your PO#: 440333418

Lot No. AB727
(Continued...)
Chemical Properties:
C:0.011 Cr:19.900 Cu:0.730 Fe:BALANCE
Mn:0.510 Mo:6.090 N:0.195 Ni:17.900
P:0.017 S:0.001 Si:0.310
Physical Properties:
Tensile-PSI:108,000 Elong-%:44.0
Yield-PSI:59,000 R/A-%:46.0
Condition:ANLD Hardness:HB 192

Lot No.
Mill: HAYNES INT'L Our Order Line No. 1
0
Description:
AE862
C276 .125"
Item: 01A120125 C276 .125"
Chemical Properties:
C:0.0017 Co:1.4053 Cr:15.120 Fe:5.830
Mn:0.4831 Mo:15.630 Ni:BALANCE P:0.007
S:0.0019 Si:<0.020 V:<0.010 W:3.450
Physical Properties:
Tensile-PSI:115,000 Elong-%:66.0
Yield-PSI:49,600 Hardness:RB 88

Lot No.
Mill: AVESTA POLARIT Our Order Line No. 1
1
Description:
~~AB130~~
2205 .125"X48"X120"(1PC.)
Item: 011260125 2205 .125"
Chemical Properties:
C:0.017 Cr:22.500 Fe:BALANCE Mn:1.550
Mo:3.200 N:0.164 Ni:5.800 P:0.020
S:0.001 Si:0.410

**Figure A.3: Material certification sheet for standard grade DSS UNS S32205 (2205) used for exposure coupons to understand film formation and role of composition.**

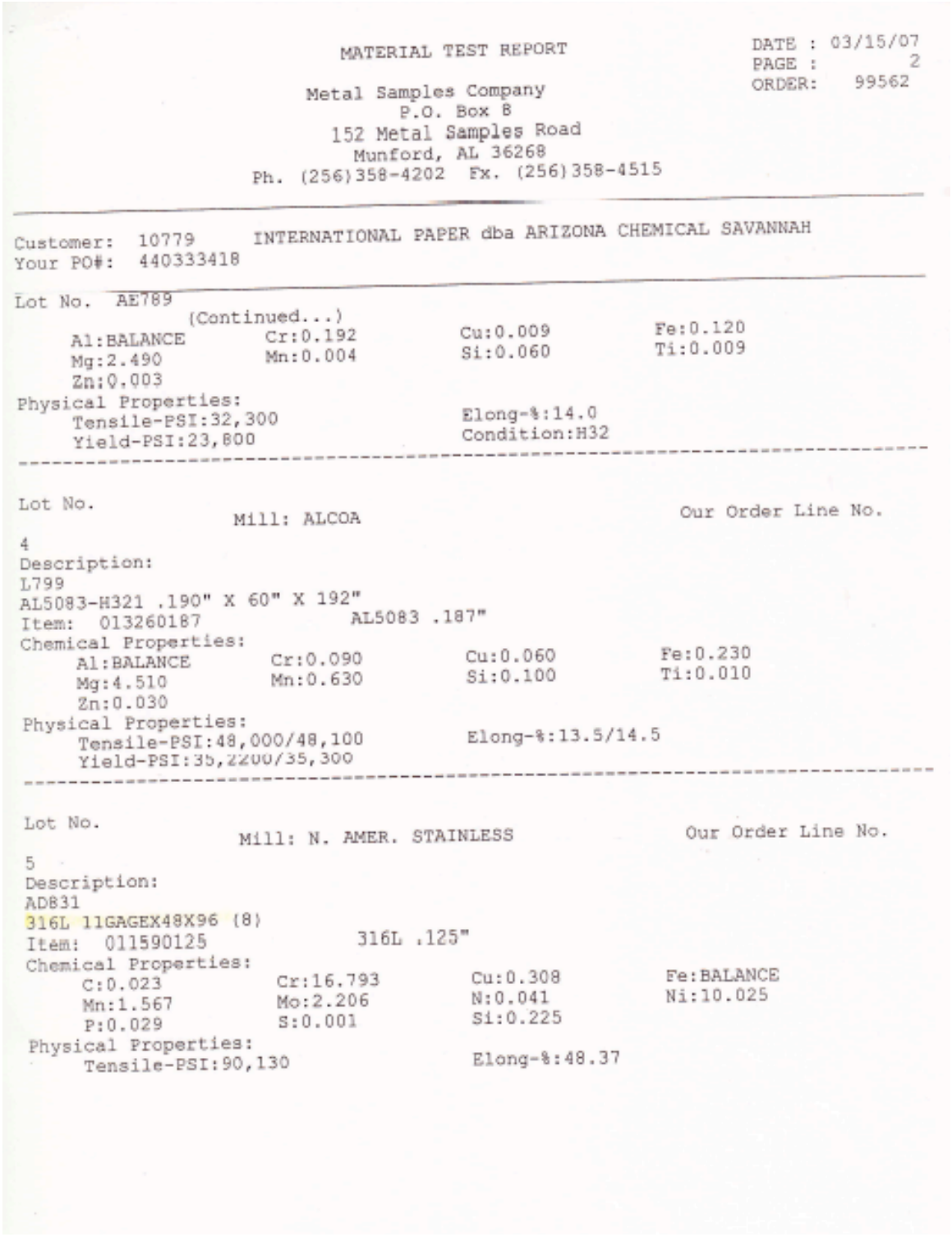

MATERIAL TEST REPORT

DATE : 03/15/07
PAGE : 2
ORDER: 99562

Metal Samples Company
P.O. Box 8
152 Metal Samples Road
Munford, AL 36268
Ph. (256)358-4202 Fx. (256)358-4515

Customer: 10779 INTERNATIONAL PAPER dba ARIZONA CHEMICAL SAVANNAH
Your PO#: 440333418

Lot No. AE789
(Continued...)
Al:BALANCE Cr:0.192 Cu:0.009 Fe:0.120
Mg:2.490 Mn:0.004 Si:0.060 Ti:0.009
Zn:0.003
Physical Properties:
Tensile-PSI:32,300 Elong-%:14.0
Yield-PSI:23,800 Condition:H32

Lot No. Mill: ALCOA Our Order Line No.
4
Description:
L799
AL5083-H321 .190" X 60" X 192"
Item: 013260187 AL5083 .187"
Chemical Properties:
Al:BALANCE Cr:0.090 Cu:0.060 Fe:0.230
Mg:4.510 Mn:0.630 Si:0.100 Ti:0.010
Zn:0.030
Physical Properties:
Tensile-PSI:48,000/48,100 Elong-%:13.5/14.5
Yield-PSI:35,2200/35,300

Lot No. Mill: N. AMER. STAINLESS Our Order Line No.
5
Description:
AD831
316L 11GAGEX48X96 (8)
Item: 011590125 316L .125"
Chemical Properties:
C:0.023 Cr:16.793 Cu:0.308 Fe:BALANCE
Mn:1.567 Mo:2.206 N:0.041 Ni:10.025
P:0.029 S:0.001 Si:0.225
Physical Properties:
Tensile-PSI:90,130 Elong-%:48.37

**Figure A.4: Material certification sheet for austenitic grade UNS S31603 (type 316L) used for exposure coupons to understand film formation and role of composition.**

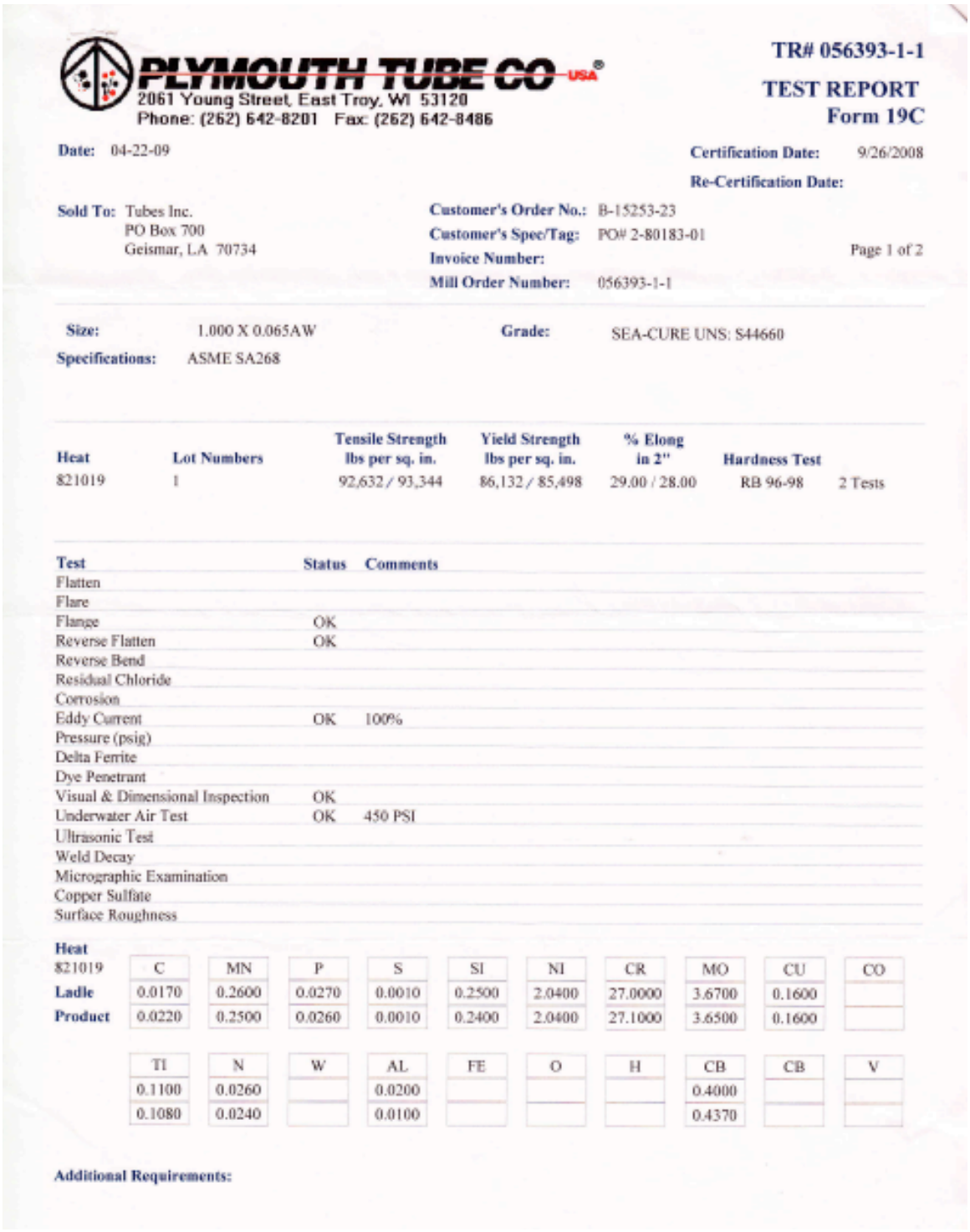

PLYMOUTH TUBE CO USA®
2061 Young Street, East Troy, WI 53120
Phone: (262) 642-8201 Fax: (262) 642-8486

TR# 056393-1-1

TEST REPORT
Form 19C

Date: 04-22-09

Certification Date: 9/26/2008

Re-Certification Date:

Sold To: Tubes Inc.
PO Box 700
Geismar, LA 70734

Customer's Order No.: B-15253-23
Customer's Spec/Tag: PO# 2-80183-01
Invoice Number:
Mill Order Number: 056393-1-1

Page 1 of 2

Size: 1.000 X 0.065AW

Grade: SEA-CURE UNS: S44660

Specifications: ASME SA268

| Heat | Lot Numbers | Tensile Strength lbs per sq. in. | Yield Strength lbs per sq. in. | % Elong in 2" | Hardness Test | |
|---|---|---|---|---|---|---|
| 821019 | 1 | 92,632 / 93,344 | 86,132 / 85,498 | 29.00 / 28.00 | RB 96-98 | 2 Tests |

| Test | Status | Comments |
|---|---|---|
| Flatten | | |
| Flare | | |
| Flange | OK | |
| Reverse Flatten | OK | |
| Reverse Bend | | |
| Residual Chloride | | |
| Corrosion | | |
| Eddy Current | OK | 100% |
| Pressure (psig) | | |
| Delta Ferrite | | |
| Dye Penetrant | | |
| Visual & Dimensional Inspection | OK | |
| Underwater Air Test | OK | 450 PSI |
| Ultrasonic Test | | |
| Weld Decay | | |
| Micrographic Examination | | |
| Copper Sulfate | | |
| Surface Roughness | | |

| Heat | C | MN | P | S | SI | NI | CR | MO | CU | CO |
|---|---|---|---|---|---|---|---|---|---|---|
| Ladle | 0.0170 | 0.2600 | 0.0270 | 0.0010 | 0.2500 | 2.0400 | 27.0000 | 3.6700 | 0.1600 | |
| Product | 0.0220 | 0.2500 | 0.0260 | 0.0010 | 0.2400 | 2.0400 | 27.1000 | 3.6500 | 0.1600 | |

| TI | N | W | AL | FE | O | H | CB | CB | V |
|---|---|---|---|---|---|---|---|---|---|
| 0.1100 | 0.0260 | | 0.0200 | | | | 0.4000 | | |
| 0.1080 | 0.0240 | | 0.0100 | | | | 0.4370 | | |

Additional Requirements:

**Figure A.5: Material certification sheet for superferritic grade UNS S44660 used for exposure coupons to understand film formation and role of composition.**

# APPENDIX B

# REFERENCE ELECTRODE POTENTIAL DETERMINATION

The work conducted in hot alkaline environments was performed using a molybdenum/molybdenum sulfide ($Mo/MoS_2$) pseudo reference electrode threaded onto a PTFE-insulated lead in the autoclave lid. Calibration of the reference electrode was performed in an autoclave using commercially available (InterCorr International PB-REF$^{TM}$ Pressure Balanced Reference Electrode System Model SS/5000) external pressure-balanced reference electrode (Figure B.1) prior to the electrochemical measurements. Further information on the EPBRE is provided by the manufacturer [1]. The external cell was maintained at room temperature. A salt bridge containing the reference cell solution was connected to the autoclave with high-pressure PTFE tubing. The cell solution was concentrated potassium chloride (KCl) in the pure caustic environments and 2.5 M NaOH + 0.70 M $Na_2S$ in the sulfide-containing caustic environments. A valve was used to contain the solution in the autoclave until the system was pressurized.

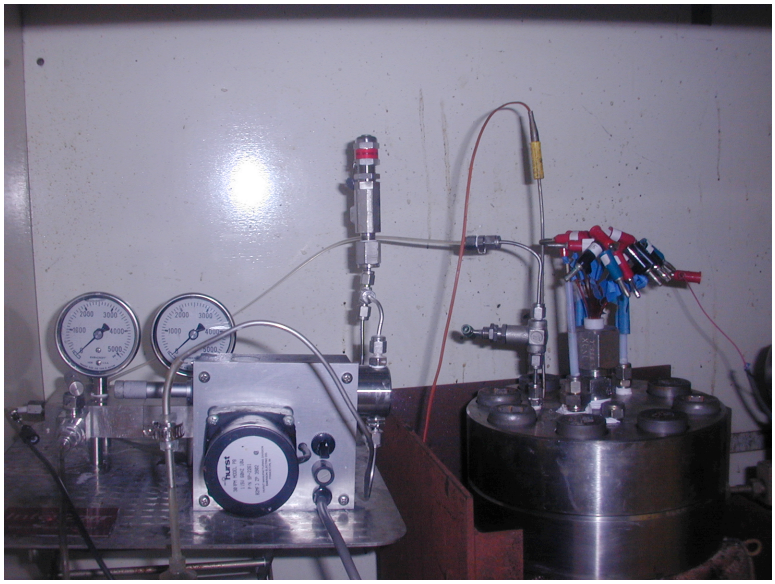

**Figure B.1: Image showing silver/silver sulfide external pressure-balanced reference electrode connected to lid of high temperature autoclave assembly using high pressure PTFE tubing.**

The potential of the $Mo/MoS_2$ electrode in the autoclave was determined versus a silver/silver sulfide (SSS) electrode that was threaded into the external reference electrode body for the caustic test environments containing sulfide. Further information on the SSS electrode preparation and features can be found in the work by Yeske and Sprague [2]. The SSS electrode was prepared by anodizing a silver rod, 3 mm diameter x 13 mm long, in alkaline-sulfide environment to form a surface film of silver sulfide. The silver rod was connected to the positive (+) terminal of a 1.5 V D cell battery and a stainless steel wire was connected to the negative (-) terminal. The silver rod and stainless steel wire were immersed in a solution containing 2.5 M NaOH and 0.70 M $Na_2S$ for several minutes to form a brittle, grey-black film.

The potential of the $Mo/MoS_2$ electrode in the autoclave was determined versus Ag/AgCl electrode for the pure caustic test environment to avoid sulfide contamination. The Ag/AgCl electrode that was threaded into the external reference electrode body was

prepared by anodizing a silver rod, 3 mm diameter x 13 mm long, in concentrated HCl to form a surface film of silver chloride. The silver rod was connected to the positive (+) terminal of a power supply and a stainless steel wire was connected to the negative (-) terminal. The silver rod and stainless steel wire were immersed in 20% HCl and the potential was maintained at 20 V for approximately 30 minutes to form a brittle, pink-purple-grey film.

The potentials for the SSS and Ag/AgCl reference electrodes were monitored over a 24 h period at room temperature prior to the electrochemical experiments. The potential of the SSS electrode was found to be approximately -900 mV vs. a standard calomel electrode (SCE) (+/- 5 mV) at room temperature. The electrode remained in this potential range for all of the alkaline-sulfide liquor compositions that were used throughout this study. The Ag/AgCl electrode was found to have a potential of -45 mV vs. SCE (+/- 2 mV) at room temperature in concentrated KCl.

The autoclave was heated to 170 $^{o}$C allowing the pressure to build at the valve/salt bridge interface. The valve was then opened to allow the liquid junction between the salt bridge and autoclave solution to reach equilibrium in the PTFE tube. No attempt was made to correct for the liquid junction potential at high temperatures, although the value was expected to be small due to the high conductivity of the solutions. The LJP at room temperature was measured and found to be negligible. Temperature compensation was calculated based on a Nernst relationship and found to be approximately 40 mV assuming the activity of the ionic species remained nearly constant with an increase in temperature. The potential of the Mo/$MoS_2$ electrode is plotted versus the SSS pressure balanced reference electrode in Figures B.2. The results show that the potential for Mo/$MoS_2$

pseudo reference electrode was approximately -150 mV vs. SSS or -1050 mV vs. Ag/AgCl (+/- 25 mV) at 170 $^{o}$C. Large error is due to the uncertainty in ionic concentration at the elevated temperature.

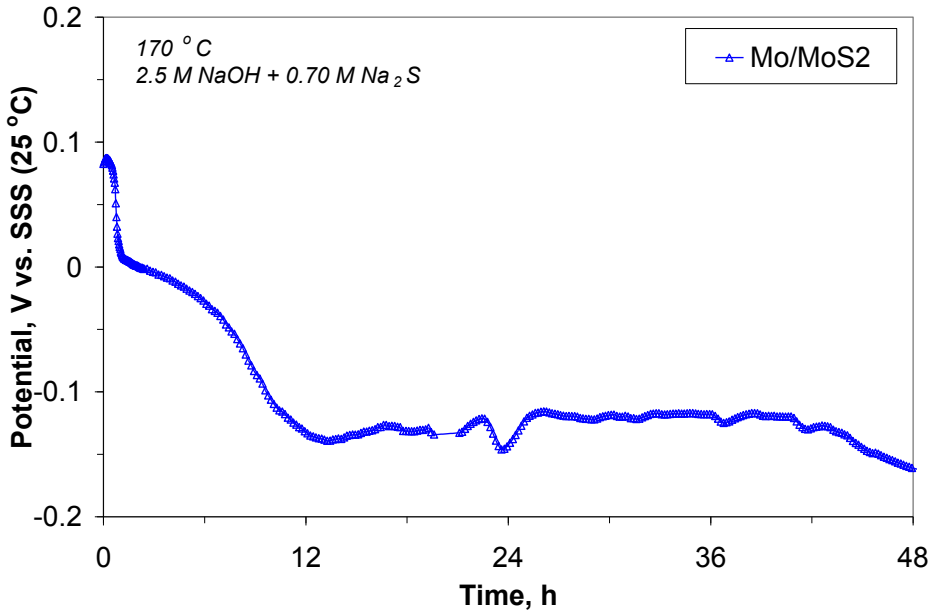


**Figure B.2: Potential measurement during a 48 h exposure for the Mo/$MoS_2$ pseudo reference electrode vs. a silver/silver sulfide (SSS) external pressure-balanced reference.**

## REFERENCES


[1] InterCorr International, "PB-Ref Pressure Balanced Reference Electrode System (Model SS/5000) User Manual," InterCorr International, Inc. Houston, TX, 1-10.

[2] R.A. Yeske and C.H. Sprague, "The Silver/Silver Sulfide Reference Electrode for Use in Corrosion Studies in Kraft White Liquor," Project 3556 Insutite of Paper Chemistry, Appleton, WI (1984), 1-26.

# APPENDIX C

# MECHANICAL TEST RESULTS AND SAMPLE DIMENSIONS FOR MATERIAL PROVIDED BY VTT TECHNICAL RESEARCH CENTRE OF FINLAND

**EN1.4462** [2205] [21Cr-4.5Ni-2.5Mo]

Chemical composition (wt%) Coil number 809955
Heat 80995

| C | Mn | S | Ni | Cr | Mo | N | Cu |
|---|---|---|---|---|---|---|---|
| 0.023 | 1.49 | <0.001 | 5.68 | 22.3 | 3.13 | 0.198 | 0.08 |

Delivered as 2B (EN 10088-2:1995 or ASTM A 480-01) 2/8/2010

| | annealed | cold rolled | cold rolled |
|---|---|---|---|
| **thickness (mm)** | 1.99 | 1.64 | 1.22 |

Mechanical properties

| | RT L/T | 200 °C L/T | RT L/T | 200 °C L/T | RT L/T | 200 °C L/T |
|---|---|---|---|---|---|---|
| **Rp0.2 (MPa)** | 585/617 | 419/453 | 999/1034 | 835/868 | 1191/1212 | 1083/1101 |
| **Rm (MPa)** | 820/830 | 700/719 | 1079/1138 | 943/1010 | 1286/1384 | 1136/1276 |
| **A80mm (%)** | 29/28 | | 9/7 | | 6/5 | |
| **A50mm (%)** | | 31/30 | | 6/6 | | 2/1 |

Ferrite content

| | | | | |
|---|---|---|---|---|
| **(%)** | | | | |

Finishing

| | | | |
|---|---|---|---|
| | 2B | 2B | 2B |

In store as steel coupons A4 (about 210 mm * 295 mm (rolling direction))

| | coupons | store/date | coupons | store/date | coupons | store/date |
|---|---|---|---|---|---|---|
| TRC | 12 | 6/17/2010 | | | | |
| VTT | 7 | 6/17/2010 | | | | |

**Figure C.1: Mechanical test results and nominal chemical composition of standard grade DSS UNS S32205 (2205) received from VTT Technical Research Centre of Finland.**

**EN1.4162** [2101] [21Cr-1.3Ni-4Mn-0.1Mo-0.2N]

Chemical composition (wt%) Coil number 813493
Heat 81349

| C | Mn | S | Ni | Cr | Mo | N | Cu |
|---|---|---|---|---|---|---|---|
| 0.014 | 4.96 | <0.001 | 1.64 | 21.4 | 0.31 | 0.216 | 0.30 |

Delivered as 2B (EN 10088-2:1995 or ASTM A 480-01) 10.12.2009

| | annealed | cold rolled | cold rolled |
|---|---|---|---|
| **thickness (mm)** | 1.52 | 1.20 | 0.91 |

Mechanical properties

| | RT L/T | 200 °C L/T | RT L/T | 200 °C L/T | RT L/T | 200 °C L/T |
|---|---|---|---|---|---|---|
| **Rp0.2 (MPa)** | 566/591 | 426/434 | 947/963 | 809/894 | 1152/1098 | 1036/1059 |
| **Rm (MPa)** | 762/765 | 640/641 | 1068/1127 | 888/985 | 1263/1331 | 1146/1207 |
| **A80mm (%)** | 31/29 | | 5/5 | | 4/2 | |
| **A50mm (%)** | | 30/31 | | 4/3 | | 3/2 |

Ferrite content

| | | | |
|---|---|---|---|
| **(%)** | | | |

Finishing

| | 2B | 2B | 2B |
|---|---|---|---|

In store as steel coupons A4 (about 210 mm * 295 mm (rolling direction))

| | coupons | store/date | coupons | store/date | coupons | store/date |
|---|---|---|---|---|---|---|
| TRC | 28 | 6/17/2010 | | | | |
| VTT | 7 | 6/17/2010 | | | | |

**Figure C.2: Mechanical test results and nominal chemical composition of lean grade DSS UNS S32101 (2101) received from VTT Technical Research Centre of Finland.**

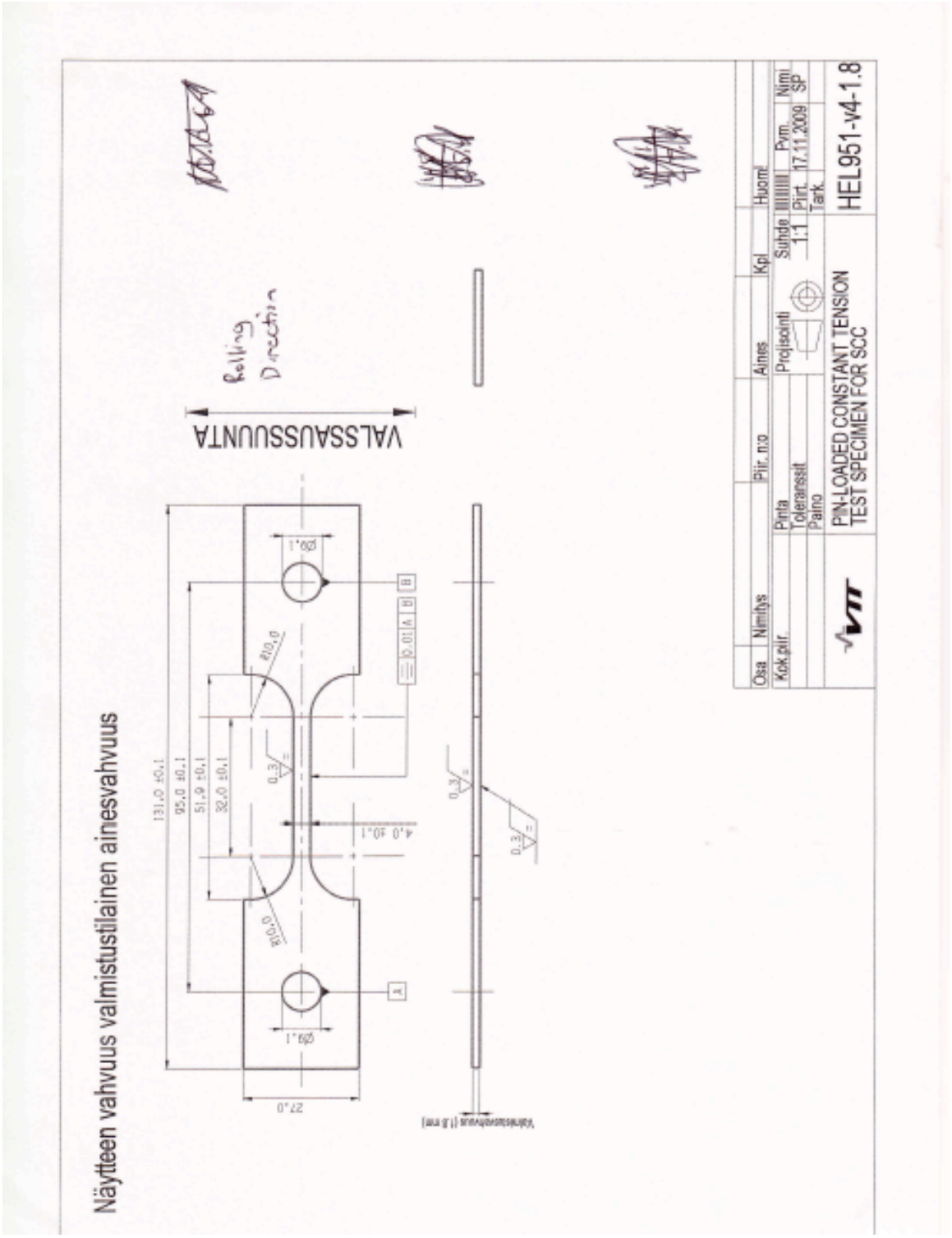


**Figure C.3: Sample dimensions for tensile specimens used to determine mechanical properties of standard grade DSS UNS S32205 (2205) and lean grade DSS UNS S32201 (2101) received from VTT Technical Research Centre of Finland.**

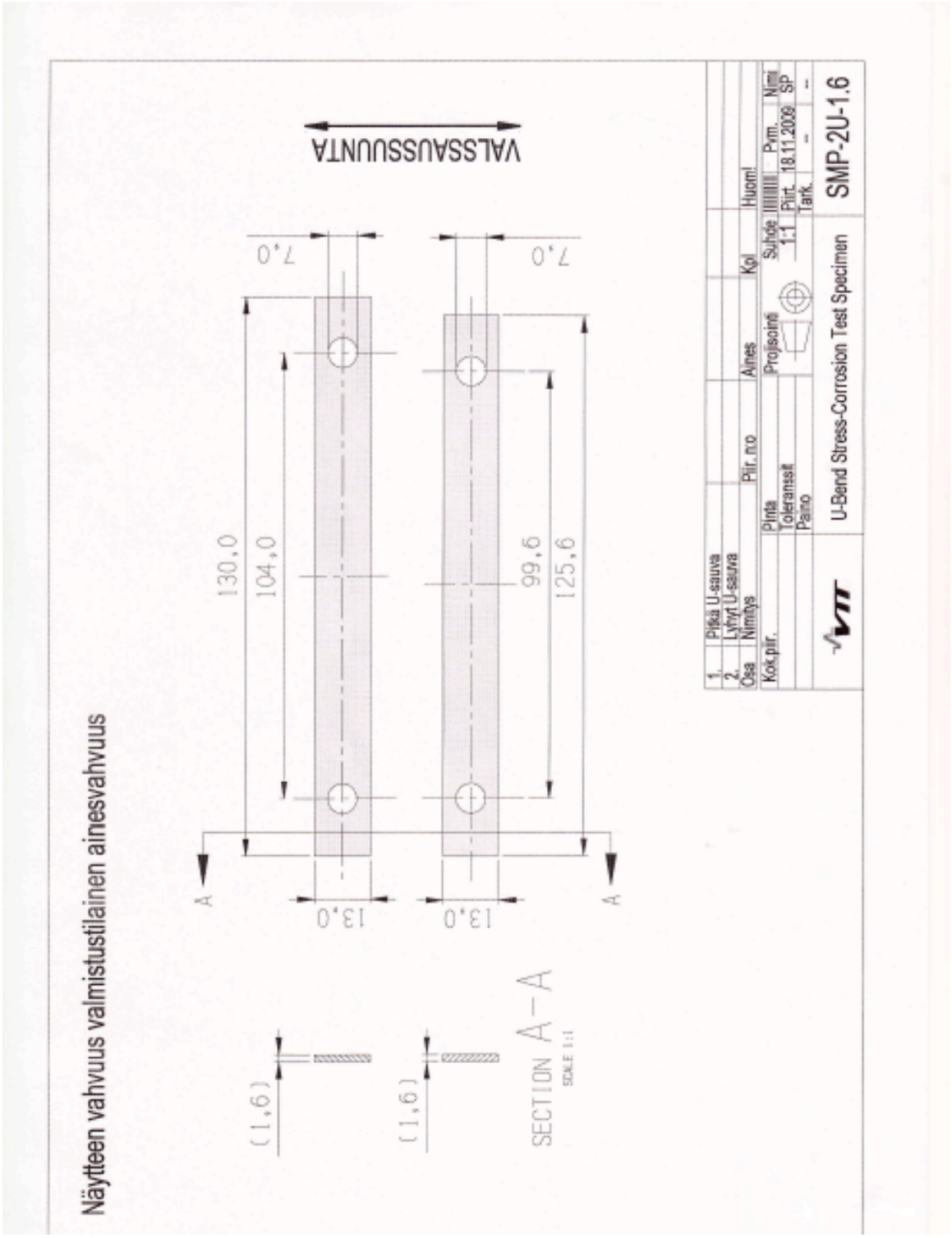


**Figure C.4: Sample dimensions for U-bend specimens used to determine stress corrosion cracking susceptibility of superferritic grades UNS S44660 and UNS S44427.**

# VITA

**Kevin R. Chasse**

Kevin grew up and attended high school in Blackstone, Massachusetts. He received a B.S. in mechanical engineering from Worcester Polytechnic Institute, Worcester, MA in 2002 and a M.S. in engineering from Brown University, Providence, RI in 2004 under the guidance of Dr. Clyde L. Briant. He worked for several years as a mechanical engineer before coming to Georgia Tech in 2007 to pursue a doctorate in materials science. He is currently a graduate student in the Corrosion and Materials Chemistry Laboratory under the guidance of Dr. Preet M. Singh.